In November 2025, the solar wind swept across the outer skin of our magnificent Spaceship Earth. This stunning image was captured in Norway by Frank Olsen.

Thermal Power and Climate Change: A Data-Driven Analysis of Cause and Effect, 1800-2100

Please note: These is a preprint and has not been peer reviewed. Data may be preliminary.

Tadeusz W. Patzek

Professor Emeritus
KAUST

December 6, 2025

First Edition

Camera-ready manuscript typeset with LaTeX(2e).

To Joanna, My Patient Wife
My Lovely Children:
Lucas, Sophie and Julie
And My Sweet Grandchildren:
Henry and June,
Atticus and Pearl-May

Contents

List of Tables

List of Figures

Chapter 1

Prologue

A springtime view of our home in Austin, Texas. The pump house and big rainwater tank are behind the gravel circle, and two solar PV arrays are on the far left. Peace is in the air.
Photo by T.W. Patzek, March 2020.

We cannot immunize the continents and the oceans against our contempt for small places and small streams. Small destructions add up, and finally they are understood as large destructions

Wendell Berry
Contempt for Small Places (2004)

In April 2025, we made the difficult decision to leave Austin, in Central Texas, and relocate to California's Bay Area. We sold our beloved 15-acre sanctuary – an oasis of peace with an inviting, energy-efficient home, a guest house, my workshop, a 16-kilowatt solar array, and a rainwater harvesting system fed by four tanks, the largest holding 30,000 gallons. It was more than just a property; it was a way of life. Yet with heavy hearts, we became early climate migrants from Texas. Why? Because two decades of my research point to a sobering conclusion: much of the Texas interior is on track to becoming a dry savannah or even desert within the next decade. The ever-longer drought periods will be punctuated by catastrophic rain bursts, with most rainwater running off to the Gulf of Mexico[1] and not recharging the local aquifers. This book is both a farewell to Texas – our cherished home and source of inspiration – and a hopeful embrace of coastal California, where we begin a new chapter, closer to our children and grandchildren.

In this book, I explore how human activities have overwhelmed Earth's natural systems, triggering a lightning-fast shift of global climate – unseen in the last 60 million years. As you read, I ask for your patience and persistence, because coming to terms with the hard truths ahead won't be easy. But your engagement is essential – especially for the sake of your children and grandchildren, who will bear the full impact of what is now unfolding.

I walk a tightrope between scaring you too much – so much that you might stop reading this book – and not scaring you enough, so that you dismiss the subject altogether and waste no more of your precious time on it. Climate change is not a single problem; it is like a giant Russian doll. Inside it are myriad smaller dolls – nested, hidden, interlinked crises – each containing its own unfolding disaster.

Some of these problems will be plainly visible; most will not. They will conspire silently to disrupt your life long before you understand where the chaos began. For example, burning fossil fuels increases the concentration of carbon dioxide in the atmosphere and oceans. Atmospheric CO_2 absorbs a portion of the infrared radiation that Earth emits into space. As less heat escapes into the cold Universe, the planet's surface and oceans warm – imperceptibly at first, but steadily and without pause.

Approximately 130 million people – over one-third of the U.S. population – live in the hottest states, including Florida, Hawaii, Arizona, Texas, Louisiana, Mississippi, Nevada, Alabama, Georgia, South Carolina, and California, where residents are regularly exposed to dangerous levels of heat (*HowStuffWorks Staff*, 2023, *FEMA National Risk Index*, n.d., *U.S. EPA*, 2022b). Extreme and increasingly frequent heatwaves not only elevate mortality rates but also pose serious public health threats, as evidenced by rising emergency department visits and hospital admissions among affected populations (*Gould et al.*, 2025).

When the Earth warms, snow and ice melt, reducing planetary albedo and accelerating further warming. When land surfaces heat, more soil moisture evaporates, drying out ecosystems, triggering mega-droughts (*Chandanpurkar et al.*, 2025), killing crops, and fueling megafires. Failed crops leave more poor people hungry or starving, pushing them toward migration. As rich countries face mass influxes of desperate migrants, their democratic institutions fray, and they become more authoritarian – ironically, resembling the impoverished nations and people they try to shut out.

More atmospheric CO_2 also means more dissolved CO_2 in seawater. Despite the ocean's vast buffering capacity via carbonate and bicarbonate ions, its pH drops steadily. Ocean acidification harms countless marine organisms that rely on calcium carbonate to build shells or skeletons. As listed in Table 1.1, creatures like corals, pteropods, and bivalves suffer or die. With the collapse of coral reefs – biodiverse marine oases – hundreds of millions of people lose access to their primary source of protein. When zooplankton –such as foraminifera and krill – and phytoplankton decline, so too will the whales and the highly productive cold-water fisheries that depend on them as a foundational food source.

[1] Recently renamed to the "Gulf of America" by current US regime. While the US initiated the war of 1846-1848, (*Henderson*, 2007) and benefited enormously from its victory by annexing California, Arizona, New Mexico, Nevada, and Utah (*Treaty of Guadalupe Hidalgo*, 1848), this was not an isolated act of "theft," but part of a broader pattern of imperial competition, nation-building, and colonial legacies (*Stephanson*, 1995). Although Texas declared independence from Mexico in 1836, Mexico never formally recognized the Republic of Texas. Thus, the 1845 US annexation of Texas violated Mexican sovereignty in the eyes of Mexico. Indigenous peoples were the greatest losers in these transfers: their lands changed hands from Spain to Mexico to the US, usually with no regard for their sovereignty and well-being.

Table 1.1: Representative impacts of ocean acidification on marine organisms

Group	Examples	Observed or Projected Impacts
Mollusks	Oysters, clams, mussels, scallops	Weakened shells, reduced larval survival, slower growth
Echinoderms	Sea urchins, starfish	Impaired larval development and skeleton formation
Crustaceans	Crabs, lobsters, shrimp	Mixed effects; reduced calcification, molting disruption
Cnidarians	Reef-building corals	Reduced calcification, increased bleaching susceptibility
Coccolithophores	*Emiliania huxleyi* (plankton)	Thinner calcium carbonate plates; altered marine carbon cycling
Pteropods	*Limacina helicina* ("sea butterflies")	Shell dissolution, vulnerability in polar food webs
Fish	Clownfish, cod, cobia	Altered behavior, reduced larval survival and growth
Zooplankton	Copepods, amphipods	Indirect effects via food web disruption
Seagrasses	*Zostera*, *Posidonia*	Potential enhancement due to CO_2 fertilization; ecosystem-dependent

Layer onto this the predation of global fish stocks by super-trawlers from China, Europe, and America. As fish vanish, destitute fishermen may turn to piracy or terrorism. Meanwhile, melting glaciers and thermal expansion of ocean water cause sea levels to rise rapidly, endangering hundreds of millions in low-lying coastal regions.

When global temperatures climb further, thriving tropical forests – vital reservoirs of biodiversity that stabilize the climate and sustain life – dry out, burn, or collapse from heat stress.

When glaciers melt everywhere on the ever-hotter planet, billions of people lose their main source of drinking water. Two billion of people in China, India, Pakistan, etc. get water from the Himalayan glaciers, see Figure 1.1. Where will they go?

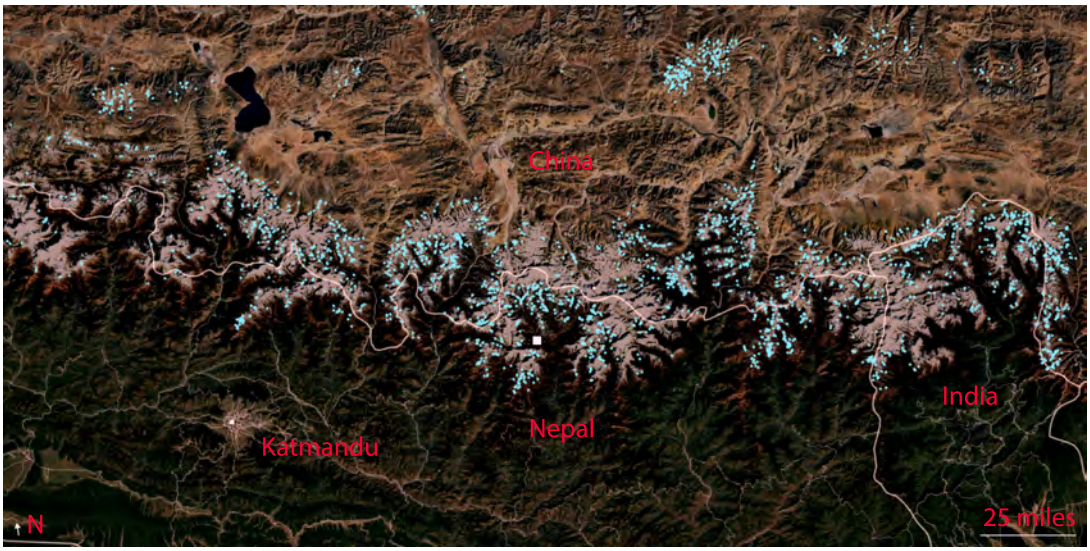

Figure 1.1: Thousands of glacier melt lakes now dot the Himalayas. Source: *Zhang et al.* (2025b), includes Landsat (USGS/NASA) and Copernicus Sentinel data (ESA).

With the global human population increasing and freshwater resources diminishing, groundwater aquifers are being depleted – many to the point of collapse. Excessive extraction causes land subsidence, and numerous cities and regions around the world are now physically sinking. It is important to note that intense rainfall events often lead to flash floods and rapid surface runoff, which limit infiltration and significantly reduce aquifer recharge.

Now a few examples. Jakarta – the capital of Indonesia – is a sprawling megacity of over 11 million people. In 2022, a combination of severe land subsidence caused by excessive groundwater extraction and chronic flooding driven by rising sea levels compelled the Indonesian government to begin relocating the capital from the island of Java to Borneo.

Other coastal megacities, such as Cairo, New Orleans, Houston and New York are already witnessing the dire effects of this dual threat.

Inland, in Mexíco City, home to more than 20 million residents, decades of overpumping have led to the collapse of underlying aquifers. As a result, this large urban basin is subsiding at an astonishing rate of up to $30 - 50$ cm/yr – the highest measured in any major city worldwide.

Tehran — the inland capital of Iran with 16 million inhabitants — must be relocated to the Gulf coast said[2] the Iranian president, Masoud Pezeshkian. Parts of the city subside at 30 cm/yr and water supplies disappear. "When we say the land subsides 30 centimeters each day, this means disaster," he said. He warned that mismanagement, construction in upstream areas and cuts to downstream water flows risk irreversible damage. "Protecting the environment is not a joke," Pezeshkian said. "Ignoring it means signing our own destruction."

But wait, there is more.

Worldwide, topsoil is increasingly inundated by intensifying winter storms, only to dry, crack, and degrade during ever more prolonged, widespread, and hotter summer droughts. These amplifying seasonal swings – from saturated to desiccated conditions – cause soil to swell and shrink, damaging the foundations of homes, roads, and critical infrastructure. As of 2025, 75% of the world's population lived in regions experiencing freshwater loss due to soil desiccation, shrinking rivers and lakes, and retreating groundwater tables (*Chandanpurkar et al.*, 2025). These losses undermine food production, sanitation systems, and climate resilience. A persistent, continent-scale drying trend is accelerating desertification in areas already plagued by insufficient rainfall. Emerging "mega-dry" regions now span the western coasts of North and Central America, the Middle East, and large parts of Southeast Asia. These insidious impacts of climate change remain almost entirely uninsured globally – and they threaten regions that collectively generate nearly $8 trillion in annual economic activity.

According to the European Central Bank, land subsidence could result in potential losses exceeding $2.9 billion across EU-27 financial institutions. Europe is currently the fastest-warming continent, but the greatest exposure to subsidence lies in China and India.

In Europe, the Netherlands faces the most severe impacts: subsidence is the primary reason that roughly 25% of the country lies below mean sea level, substantially increasing its vulnerability to coastal flooding.

Are you beginning to feel my pain? Even if you're living comfortably in the states of Florida, Louisiana, or Texas? It is odd to proclaim these states to be climate-change-free, really, because when the good people there head to the beach, their children now play in water that feels more like a hot tub than the ocean.

Such abnormally warm coastal waters fuel violent rainfall of almost biblical proportions and ever-larger hurricanes[3] – monsters that threaten to obliterate entire coastal cities and towns. This isn't some distant hypothetical threat for places like Miami, Tampa, New Orleans, or Houston. Persistently elevated ocean temperatures will do exactly that,[4] even in the absence of broader global climate change.

[2] https://www.iranintl.com/en/202511209098.

[3] A recent study by *Keenan et al.* (2025) supports other research showing that hurricanes have prolonged health consequences, such as: (i) Chronic diseases, e.g., cardiovascular disease, diabetes, and mental health disorders that continue well beyond the immediate aftermath of a hurricane; (ii) Persistent social and environmental disruptions, such as mold and housing instability lasting ∼3 years post-Katrina, business closures, and eroded social infrastructure; and (iii) Psychological effects, such as persistent PTSD, depression, and anxiety that often follow extreme weather events.

[4] During an August 2025 conference in San Antonio, TX, Josh Salter, a Risk & Insurance Management Society's staffer, expressed a common frustration. The same week last month that Texas Hill Country experienced deadly flooding, he noted,

But of course, climate change is here – compounding all of these natural hazards.

In addition to emotions, writing and reading a book like this presents several other profound challenges. First, there exists a vast universe of data about the Earth – her ancient past, ecosystems, human history, patterns of resource extraction, and much more. Then there is an ocean of information chronicling past and present climate changes.

Following the terminology in *Rubin* (2023), I will use the word Source to describe this nearly infinite reservoir of knowledge about the Earth system. To build a coherent mental model of the Source, we must first reduce its size and complexity. Our ability to remember the myriad facts that constitute the Source is limited. Our senses, moreover, may distort how we perceive essential images, sounds, words, and numbers. And our cognitive capacity may fall short of grasping the fantastically complex models that would do justice to the Source's reality.

To cope with this overwhelming flood of information, we inevitably choose only those fragments that seem meaningful to us, while filtering out the rest.

Yet I, as your guide, aspire to a different path. I would like to preserve everything I know and perceive with all my senses – and to communicate this experience to you as clearly and honestly as possible. I want you to feel the awe and wonder I feel, without being constrained by your own limited time, interests, or the immediate utility you might perceive in this work.

Paraphrasing Rubin somewhat:

> As readers, our filters inevitably reduce the intelligence of the Source by interpreting the data that arrive, rather than letting them pass through us freely. As our perception fills with these recast fragments, relationships form with the material already stored within us.
>
> These relationships give rise to beliefs and stories: about who we are, about the people around us, and about the nature of the world itself. Over time, these stories coalesce into a worldview.
>
> As an author, I strive to hold these stories lightly to leave space for the vast amounts of information that do not easily fit within the bounds of my own belief system. The more raw data I can take in, and the less I shape them prematurely, the closer I come to touching nature itself.

In other words, I want you to feel not only my sense of wonder, but also the sheer pain of navigating through the dark alleys of our fraught relationship with this miraculous, living Earth – the only Mothership we will ever have, and one we must allow at all costs to protect us from ourselves.

Of course, there is nothing new under the Sun. Sir Francis Bacon, that great architect of empirical thought, taught us to lay aside dogma and lift instead the subtle, multiple veils that obscure our understanding of natural world.

In 1620, Bacon classified in *Novum Organum* the intellectual fallacies of the human mind as idols of the Tribe, the Cave, the Marketplace and the Theater. An idol is a mental image which receives veneration but is devoid of substance.

Bacon did not regard idols as symbols, but rather as human fixations. His model of human perceptions is as true today as it was in the 17th century. Some things never change – but in the age of social media, when falsehoods spread like wildfire, the consequences of humanity's common fallacies have become far more destructive.

Idols of the Tribe are deceptive beliefs inherent in the minds of all humans. They are abstractions of error arising from common human tendencies of exaggeration, distortion, and disproportion:

- **We rely on immediate sensory experience:** We are genetically programmed to trust what we can see, hear, smell and touch. We can't see or smell carbon dioxide in the air, or see the inevitable depletion of subsurface oil and gas fields. Having witnessed two centuries of exponential growth

"a one-in-1,000-year storm hit North Carolina, and a one-in-1,000-year storm also hit Illinois. So how accurate can all this data be if we're getting things that are only supposed to happen once in 1,000 years, three times the same week?" We will answer Josh's questions in Appendix D.

in crude oil production, we are prone to extrapolate this trend indefinitely. Most policymakers, economists, and technologists view oil as ubiquitous and assume it will always remain so. This belief, however, is at odds with the geological reality that fossil fuels are, by definition on human timescales, "dead" and nonrenewable deposits requiring millions of years to form from organic matter.

- **We resort to wishful thinking:** People often believe what they were true. It is far more comfortable to imagine that our current way of life is sustainable, or that climate change is neither real nor caused by humans. Religious sects, social media, and even a recent DOE report *Christy et al.* (2025) exploit this deeply human vulnerability.

- **We tend to see patterns and oversimplify things:** The human mind is predisposed to find order, even where none exists. It is easier to believe in simple, linear narratives—such as the notion that the Earth has always cycled naturally through climate variations—than to confront the complex, unprecedented reality of human-driven climate change. Once again, climate deniers and preachers prey on this weakness.

Idols of the Cave are those that arise within the mind of an individual. The human mind is symbolically a cavern: thoughts wander in this dark cave and are shaped by temperament, education, habit, environment, and chance. Thus, an individual who devotes himself to a particular branch of learning often becomes captive to its peculiar interests, interpreting all other knowledge through that narrow lens.

- **Self-interest:** Someone who works in the oil industry (as I did for many years) or lives in a town heavily dependent on fossil-fuel extraction may be reluctant to admit that their livelihood contributes to a global problem. Their personal experience and financial well-being create a powerful bias against inconvenient facts.

- **Place of residence:** A person living in a coastal area threatened by rising sea levels will likely hold a different perspective on climate change than someone in a landlocked region that has not yet experienced significant, observable impacts. Their personal "caves" of experience shape their beliefs.

- **Education and media exposure:** The information people digest – whether from specific news outlets, social-media echo chambers, or academic cliques—can strongly bias their views. For example, if one reads only sources that question climate science, it becomes very difficult to accept established evidence. A slick collection of essays, *The Deniers* by *Solomon* (2008), preys upon precisely this vulnerability of the human mind.

Idols of the Marketplace are errors that arise from the false significance bestowed upon words. Language, intended to communicate thought, often distorts it instead. Carelessly used words, stripped of precise meaning, breed confusion and fallacy. In this way, words betray their purpose, obscuring the very realities they were meant to reveal.

- **Vague or misleading terminology:** Terms such as "clean coal," "natural gas," "net-zero," or "green hydrogen" can create the false impression that these technologies are environmentally benign. Even the phrase "climate change," which sounds less threatening than "climate breakdown" or "climate bifurcation" (as used in this book), can be a source of confusion.

- **Politicization of language:** When phrases like "renewables," "carbon tax," "Green New Deal," or "climate activist" become politicized, they lose their objective meaning and are deployed as tools of attack or defense rather than for genuine understanding. This politicization undermines reasoned discussion of policy solutions.

- **Semantic confusion:** People often use terms such as "weather" and "climate" interchangeably. For example, after a cold winter day, how many times I have heard: "So much for global warming!" Such misunderstandings of basic scientific concepts make it difficult to engage seriously with the actual evidence, data, and long-term trends (see Appendix A – Appendix E in this book).

Idols of the Theater are dogmas and belief systems imposed upon the mind by philosophy, ideology, or tradition. They are received rather than discovered, and are often defended without question. In the context of climate breakdown, several such "theatrical idols" are especially damaging:

- **Unquestioning belief in economic systems:** The neoliberal dogma of unlimited economic growth is a powerful idol of the theater. The assumption that the economy must always expand, and that such growth is an unmitigated good, stands in direct conflict with the reality of a finite planet—one with limited resources and limited capacity to absorb pollution. This doctrine makes it difficult to imagine sustainable alternatives.
- **Blind faith in technological salvation:** The conviction that human ingenuity and technology will inevitably solve the climate crisis is another form of this idol. This belief, often framed as technological optimism, can justify inaction, as it undermines both the urgency and the perceived necessity of profound behavioral and systemic changes needed to avert catastrophe.
- **Political ideologies:** Rigid political ideologies can also become idols of the theater. If a major US party dismisses climate change as a hoax or exaggeration – and tries to destroy science and its tools – its followers may adopt this view uncritically, regardless of the scientific evidence. Here ideology functions as a pre-packaged belief system, replacing inquiry with conformity.

If you can muffle the voices of these idols reverberating in your mind, you will be able to read this book with an open spirit. And, having considered all the facts, be joyful—as my friend Wendell Berry once wrote...

1.1 Book layout

Figure 1.2 charts the trajectory of human societal and technological development against the rising likelihood of anthropogenic systemic failure. The flowchart shows that growth in energy use, population, and material consumption is ultimately constrained by impacts on the ecosphere, climate, and human well-being. After a transitional period, outcomes may range from stabilization at lower population and consumption levels to partial or total collapse of complex civilization. No previous complex civilization has approached the scale of today's – with 8 billion people and global interconnectivity. Life on Earth will persist, as it always has...

This book is organized as follows:

Chapter 2 has a glossary of key terms used in the book and a brief description of energy units.

Chapter 3 illustrates that Earth is a vast far-from-equilibrium system that continually dissipates the high-energy photons intercepted from the Sun. Life itself is an intrinsic and essential component of this planetary dissipation. Over the past 3 billion years, the coupled dynamics of plate tectonics, volcanism, and life have governed Earth's climate and maintained its long-term habitability. The human perturbation of the global carbon cycle is modest in magnitude compared with several natural fluxes, yet it strikes directly at the biosphere – where it inflicts a disproportionate harm on the stability of the climate system. This pivotal chapter establishes the interwoven narrative of our book.

Chapter 4 examines 6,000 years of combustion by humans of biomass and fossil fuels, with a particular focus on the past two centuries. We demonstrate the persistent global reliance on thermal sources of primary power and highlight the socio-political risks of compelling societies to abandon these sources prematurely, especially without the necessary technological and institutional preparation.

Chapter 5 investigates the physical constraints on emissions of CO_2 and other greenhouse gases. We contrast the anthropogenic emissions of the last 200 years with those triggered by the Chicxulub impact event and by extreme volcanism during the Paleocene-Eocene Thermal Maximum (PETM). Using mass-balance methods, we estimate the fraction of emitted CO_2 that remains in the atmosphere, and we calibrate our simplified emissions model against IPCC's RCP4.5 and RCP6.0 scenarios as well as the simulations of *Zickfeld et al.* (2009). Finally, we explicitly link the current trajectory of climate change to its principal driver – combustion-based thermal emissions – and identify the onset of a global climate bifurcation around 1976.

Chapter 6 compares two emissions scenarios developed by Patzek: a physics- and geology-constrained trajectory of CO_2 emissions from fossil fuels and agriculture and land-use change (FF+AL), which culminates at 568 ppm_v by 2100, and a simplified alternative scenario reaching 720 ppm_v. These are evaluated alongside five IPCC RCP and SSP scenarios. We demonstrate that the three major fossil

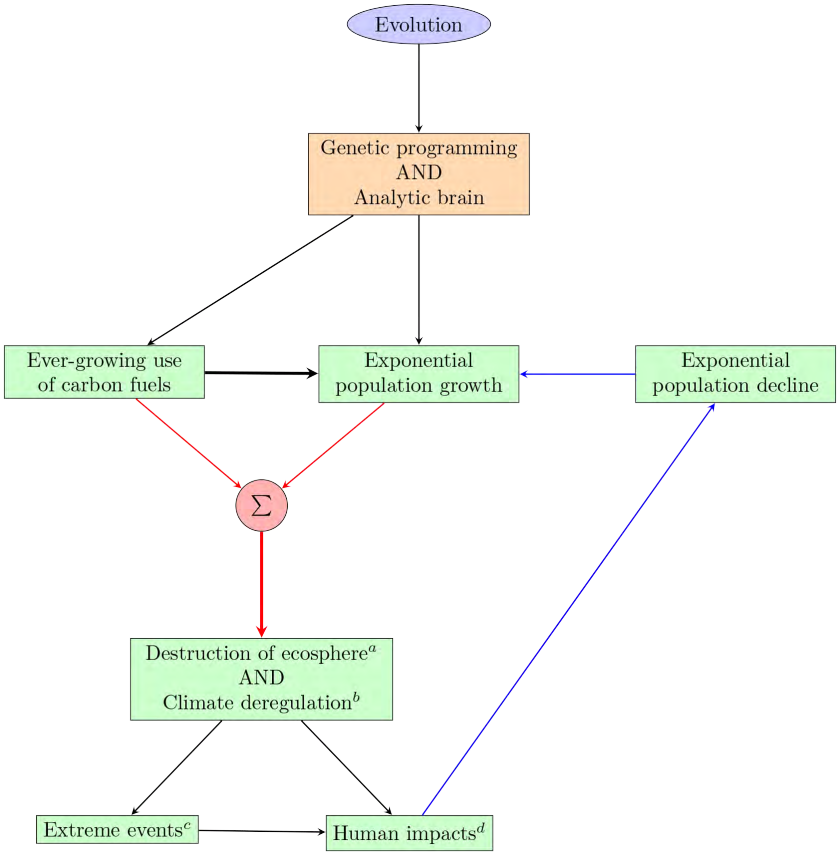

Figure 1.2: The story of human evolution and impacts on Earth is sketched by this flowchart and unfolds throughout this book. [a]Destruction of the ecosphere refers to ecological overshoot by humans, including ocean acidification, loss of biodiversity, wetland degradation, soil depletion, resource exhaustion, and the pervasive pollution of air, water, and land. [b]Climate breakdown denotes the intensifying thermal imbalance caused by greenhouse gas emissions – including the bifurcation of land and ocean warming, destabilization of the atmosphere, disruption of the water cycle, and weakening of major oceanic currents. [c]Extreme events encompass heatwaves, super-droughts, megafires, rain bombs and atmospheric rivers, hurricanes, tornadoes, and the collapse of ice sheets and glaciers. [d]Human impacts are – among others – air, soil, and water pollution; plastic saturation; freshwater scarcity; crop failures; forest collapse; rising epidemics and pandemics; increasing mortality and morbidity; hunger & starvation; mass migration (possibly 1-3 billion people); conflicts and wars; declining sperm counts; and the spread of invasive species.

fuel sources have each undergone approximately ten doublings in power output. Patzek's fossil fuel production trajectories are then decomposed into the minimal number of Gaussian functions necessary to approximate future extraction of coal, oil, and natural gas.

Chapter 7 introduces key aspects of the Sun-Earth system relevant to climate science. In particular, Section 7.4 describes Earth's parent star – the Sun – including how much solar radiation is intercepted by the planet, and how the Sun's radiative stability and orbital geometry determine the average solar energy flux per square meter of Earth's surface, which drives virtually all climate-related processes. Section 7.5 presents eleven essential definitions related to radiative energy fluxes and Earth's albedo, along with methods for measuring these quantities. Section 7.6 discusses the spectral distribution of solar radiation. Section 7.7 derives Earth's effective blackbody radiation temperature as a function of the Sun's temperature, Earth-Sun geometry, and planetary albedo. Section 7.8 introduces Earth's infrared emission spectrum, including the absorption features of water vapor and CO_2, and the fundamental physics of infrared photon interactions with atmospheric gases. Section 7.9 provides a concise explanation of the greenhouse effect. Section 7.10 decomposes the total greenhouse effect into contributions from individual greenhouse gases other than water vapor. Section 7.11 explains the different time scales associated with

Earth's climate response to a doubling of atmospheric CO_2 concentration. Finally, Section 7.12 explores how Earth's radiation energy imbalance has evolved over the past two decades.

Chapter 8 examines the global distribution of greenhouse gas and aerosol emissions, with particular emphasis on the largest historical contributors – Europe, the United States, the EU-27, China, and other parts of Asia – which together account for over 80% of cumulative CO_2 emissions. Section 8.5 presents historical case studies of prolonged air pollution episodes in Europe (including England, Germany, Eastern Europe, and Russia), the United States, and Asia, highlighting their temporary suppressive effects on global warming. We then review key environmental legislation enacted in these regions and assess its long-term implications for the climate. Section 8.6 documents the ongoing human-caused reduction of Earth's albedo and quantifies the resulting increase in radiative forcing projected between 2010 and 2035, a decade from today.

Chapter 9 compares the modern climate regime with paleoclimate regimes across three geologic periods: the past 800,000 years, the Mid-Pleistocene Transition (MPT; $\sim$1.25$-$0.7 Ma), and the broader Paleocene-Oligocene epochs spanning the last 57 million years. In particular, we demonstrate that the equilibrium climate sensitivity (ECS) to greenhouse gas concentrations during past interglacial periods was higher than in the present-day climate system.

Chapter 10 describes the satellite- and surface-based observational systems that collect vast amounts of climate data, as well as the algorithms and models used to compute global land and ocean temperature anomalies. This chapter also introduces the use of generalized extreme value (GEV) distributions for monthly maxima and minima of global and land surface temperatures, highlighting their utility in capturing the 1976 climate bifurcation and in properly parameterizing climate change as a function of cumulative CO_2 emissions.

Chapter 11 directly links observed global warming to its principal cause – combustion-based CO_2 emissions (CTE) – and presents a statistical projection of global temperature through 2100, including associated 2σ confidence intervals. We compare Patzek's FF+AL (568ppm$_v$) and 720ppm$_v$ scenarios with their closest IPCC analogs to highlight key divergences in assumptions.

Chapter 12 demonstrates how the already-committed melting of polar ice caps and the resulting rise in sea level – along with their respective rates of acceleration – are linked to cumulative CO_2 emissions.

Chapter 13 traces how the limitations of nineteenth- and early twentieth-century spectroscopic equipment, combined with a fundamental misunderstanding of Earth's radiative energy balance, gave rise to a persistent argument among climate change deniers – that CO_2 has little or no effect on global climate. We critically examine why Knut Ångström's conclusions were flawed and demonstrate how modern infrared spectroscopy and satellite observations have transformed our understanding of the Earth as a radiating blackbody. The chapter also highlights the pioneering contributions of Exxon scientists, who, for over a decade, were at the forefront of climate research and correctly predicted the climatic consequences of fossil carbon emissions.

Chapter 14 summarizes the principal technologies currently promoted by the industrialized world as candidates for planetary-scale geoengineering. We show how their substantial environmental costs are reframed as quick, simple fixes to the most pressing climate problems, with the aim of soothing – and deceiving – the restless publics in affluent countries.

Chapter 15 presents the key scientific conclusions of this book and explores the roles of human psychology, journalism, religion, and art in shaping our perception of climate change and in coping with its consequences.

The book ends with five appendices and a long bibliography.

In Appendix A we define global carrying capacity and relate it to the Earth system state vector $\mathbf{E}$. Through examples, we reveal the nonlinear dynamics of $\mathbf{E}$: equilibria (fixed points), critical thresholds, and the three canonical bifurcations – saddle–node, pitchfork, and Hopf – with far-reaching implications for climate change and human well-being. Countries that ignore the human impacts of climate change imperil themselves and the rest of the world.

In Appendix B, we use quantum mechanical statistics to derive the Planck Law of blackbody radiation

and the Stefan-Boltzmann Law. We also derive the key macroscopic quantities, irradiance, spectral irradiance and radiance that are used throughout the book.

In Appendix C we derive the dependence of climate temperature response on a doubling of CO_2 concentration.

In Appendix D we delineate the fundamentals of Generalized Extreme Value (GEV) statistics and use GEV to quantify 132 years of temperature changes and rainfall in Dallas, Texas.

In Appendix E we analyze 46 years of daily polar ice-extent observations – collected by U.S. and Japanese satellites – to show that claims of little or no change in Arctic and Antarctic sea-ice area, as propagated in the recent DOE report (*Christy et al.*, 2025), are demonstrably false. The continuing loss of polar sea ice is a key driver of the destabilization of both the global climate system and the security of the world's food supply.

Chapter 2

Energy and its units

A village museum in Normandy, France.
Photo by T.W. Patzek, July 2007.

The historical development of thermodynamics has been ... particularly susceptible to logical insecurity, ... and there has been no adequate reexamination of the fundamentals

Percy Williams Bridgman

The Nature of Thermodynamics (1961 edition, p. 226)

2.1 Glossary

To be readable, many of the descriptions below are *not* most rigorous:

Ecosystem: A system that consists of living organisms (plants, bacteria, fungi, animals) and inanimate substrates (soil, minerals, water, atmosphere, etc.), on which these organisms live.

Energy, Etymology: The word *energy* originated from the Greek term (*energeia*): (*en*) – "in" and (*ergon*) – "work" or "activity" It was used by Aristotle to describe the state of being "at work" or "in activity." Thus, *energeia* means "being at work" or "in activity." The term entered Latin as *energia*, and then passed into Middle English via Old French.

Energy, Definition: A direct consequence of the First Law of Thermodynamics is that the amount of work performed during an adiabatic process (i.e., with no heat exchange) defines the change in an important system property. We designate this property as the system's total energy, E, and define its change between two states, 1 and 2 ($1 \to 2$) of a system by the relation:

$$\Delta E := E_2 - E_1 = -W^a_{1\to 2} \tag{2.1}$$

where $W^a_{1\to 2}$ is the work done by the system in *any* adiabatic process from state 1 to state 2. Total energy is the sum of internal, potential and kinetic energies. Energy is the ability of a system to lift a weight in a process that involves no heat exchange (is adiabatic). In general

$$\Delta E = \Delta U + \Delta E_P + \Delta E_K = -\underbrace{W_{1\to 2}}_{\textbf{by}\ \text{system}} + \underbrace{Q_{1\to 2}}_{\textbf{on}\ \text{system}} \tag{2.2}$$

where U is the internal or thermal energy E_P and E_K are the potential and kinetic energies of the system, and $W_{1\to 2}$ and $Q_{1\to 2}$ are the quantities of work and heat transferred into the system during a *non-adiabatic* process $1 \to 2$ that also involves a heat interaction with the surroundings. Equation (2.2) is stated as a fact in some books on thermodynamics, e.g., *Abbott and Van Ness* (1972).

Energy, Free: The portion of a system's total energy that is available to perform useful work. Free energy quantifies the maximum amount of work that can be extracted from a system as it transitions from an initial to a final state, under specified constraints (e.g., constant temperature and pressure in the case of Gibbs free energy, or constant temperature and volume for Helmholtz free energy). A helpful analogy is to think of free energy as the amount of electricity that could be generated from a physical or chemical transformation, such as burning a lump of coal and converting the resulting heat into mechanical or electrical work.

Energy, Primary: is energy embodied in natural resources – such as coal, crude oil, natural gas, uranium, solar radiation, wind, and flowing water – before any conversion or transformation. For example, primary energy could be the heat of combustion (HHV) of a fuel (coal, crude oil, natural gas, biomass, etc.), the potential energy of water behind a dam, or the amount of heat from uranium fission necessary to generate electricity in a nuclear power plant.

Enthalpy: Enthalpy is the ability of a system to rotate a turbine shaft in a process that involves no heat exchange (is adiabatic).

Exergy: (Gibbs free energy relative to the environment.) Exergy is equal to the shaft work or electricity necessary to produce very slowly a material in its specified state from materials common in the environment, heat being exchanged with the environment at 1 atmosphere and 15°C.

Entropy: Entropy is proportional to the part of internal energy that is *transformed* into heat, *not* work, in any process conducted very, very *slowly*. The coefficient of proportionality is 1 over the temperature of the transformation.

Higher Heating Value (HHV): HHV is determined in a sealed insulated vessel by charging it with a stoichiometric mixture of fuel and air (e.g., two moles of hydrogen and air with one mole of oxygen) at 25^0 C. When hydrogen and oxygen are combined, they create hot water vapor. Subsequently, the vessel and its content are cooled down to the original temperature and the HHV of hydrogen is determined by measuring the heat released between identical initial and final temperature of 25^0 C.

Petroleum, conventional: Petroleum, excluding lease gases and condensate, as well as tar sands, oil shales, ultra-deep offshore reservoirs, etc.

System: A region of the world *we pick* and separate from the rest of the world (the *environment*) by an imaginary closed *boundary*. We may not describe a system by what happens inside or outside of it, but only by what *crosses* its boundary. An *open* system allows for matter to cross its boundary, otherwise the system is *closed*.

Other forms of energy can be expressed by the three forms defined above:

- **Chemical energy** is the potential energy stored in the bonds of chemical compounds (such as molecules and atoms). This energy is released or absorbed during a chemical reaction when bonds are broken or formed.
- **Electricity** is the most useful form of free energy of electrons flowing down the gradient of electrical potential. Energetic electrons are like water behind a dam. Electricity can be converted into mechanical work with an almost 100% efficiency, it can be degraded to generate heat and light, and can drive chemical reactions.
- **Nuclear energy** is released from the nucleus of an atom when it undergoes a change, either by splitting (fission) or combining (fusion). It is governed by the laws of nuclear physics and results from the conversion of mass into energy. In nuclear fission, a heavy atomic nucleus (e.g., uranium-235 or plutonium-239) splits into two smaller fragments, releasing energy, neutrons, and radiation.
- **Radiant energy** is transported by *electromagnetic waves*, which consist of photons whose energies are proportional to the wave frequency. The relationship between frequency ν and wavelength λ is given by:

  $$\nu = \frac{c}{\lambda}$$

  where c is the speed of light.

  Electromagnetic radiation spans a broad spectrum, from the *longest wavelengths and lowest frequencies* (radio waves) to the *shortest wavelengths and highest frequencies* (gamma rays). The main categories, in order of increasing frequency, are:

  - Radio waves
  - Microwaves
  - Infrared radiation
  - Visible light
  - Ultraviolet radiation
  - X-rays
  - Gamma rays

  The radiant energy from **sunlight**, particularly in the visible and near infrared regions, is **the** energy source that powers all ecosystems on Earth.

In nature, energy is the universal currency of all processes. In both natural and human economies, it is explicitly free energy that serves as the only real currency – one that is continuously devalued through dissipation in every transformation that drives every process, from the metabolism of nutrients to the functioning of complex systems.

2.2 Units of Energy

For the unit of energy we will use 1 joule (J). It is a fairly small amount of energy. A little more than 4 joules are necessary to heat one teaspoon of water by one degree on the Celsius scale. For the unit

of power we will use one joule per second (J/s) or 1 watt (W). On average, an adult man at rest on an empty stomach needs about 100 W continuously to live and function. This requirement makes a human equivalent to one 100 W bulb operating continuously.

Larger energy units are the powers of 1 joule. We use kilo joules (kJ), mega joules (MJ), giga joules (GJ), tera joules (TJ), peta joules (PJ), exa joules (EJ), and zeta joules (ZJ).

Here is the list of these derived energy units:

1kJ is 1 000 or 10^3 joules

1MJ is 1 000 000 or 10^6 joules

1GJ is 1 000 000 000 or 10^9 joules

1TJ is 1 000 000 000 000 or 10^{12} joules

1PJ is 1 000 000 000 000 000 or 10^{15} joules

1EJ is 1 000 000 000 000 000 000 or 10^{18} joules

1ZJ is 1 000 000 000 000 000 000 000 or 10^{21} joules

During one year, the US population requires approximately

$$100\frac{\text{J}}{\text{s}\times\text{person}}\times 330\ 000\ 000\ \text{persons}\times 3600\times 24\times 365\ \text{s/year}\approx 1\ \text{EJ/year} \tag{2.3}$$

as food.

> The amount of *power* (energy/time) required to feed the entire US population for one year, 1×10^{18} J/year or 1 EJ/year, is the fundamental unit in which all other energy flows in the US economy will be described.

A common unit of energy is 1 kWh (kilo watt-hour); it is equal to 3.6 MJ (mega joule), see Figure 2.1. This amount of energy is needed to lift slowly a compact car to the top of the Eiffel tower 324 m above ground level.

$$\begin{aligned}&\text{work} = mgh\\&\text{Hyundai Elantra: } 1200\text{kg}\times 9.81\text{ms}^{-2}\times 324\text{m} = 3.6\text{MJ} = 1\ \text{kWh}\end{aligned} \tag{2.4}$$

In Texas, an average household electricity bill is about 1000 kWh/month, or 3.6 GJ/month. To produce this electricity with an overall efficiency of 0.32, we need to burn 11.25 GJ/month of a fossil fuel, or 135 GJ/year. Thus, this average household demands lifting an Elantra up the Eiffel Tower every 43 minutes year-around.

135 GJ is equivalent to the total heat released by burning 2.9 metric tonnes of gasoline. So each household in Texas is responsible for burning almost 3 metric tonnes of gasoline equivalents per year just to obtain the needed electricity. When I was at KAUST in Saudi Arabia, the two powerful air conditioners in our house there would burn 30 tonnes of gasoline equivalents per year and could lift an Elantra up the Eiffel Tower every 4 minutes year-around.

A much larger unit of energy per unit time – power – is exemplified by the resting metabolic rate of a 40-ton male sperm whale: approximately 10,000 W. Remarkably, this is also the average exosomatic (external to our body metabolism) power consumed continuously by each man, woman, and child in the United States, primarily through our use of thermal primary energy sources, see Figure 2.2.

(a) (b)

Figure 2.1: A small unit of energy. 1 kWh = 3.6 MJ is work performed by combusting 250 grams of natural gas in a turbine. **(a)** It requires 1kWh to lift slowly a Hundai Selantra up the Eiffel Tower. **(b)** The Eiffel Tower in Paris is 324 m tall.

Figure 2.2: A large male sperm whale generates an average metabolic power of 10,000 W – equivalent to the continuous exosomatic power available to the average American over the course of a year.

Chapter 3

Global carbon cycle

Our living planet is a tapestry of far-from-equilibrium systems that ceaselessly dissipate the energy of the solar photons that power her. Left to themselves, these systems would relax toward a global equilibrium that is death. Everything that happens anywhere on Earth, happens only because of this continuous flux of high-energy photons and their dissipation.
Tad Patzek's lecture at AGH in Cracow (2025-10-29)

3.1 What are you going to learn?

There can be no description of the carbon cycle on the Earth without viewing the planet as a giant, far-from-equilibrium dissipative structure, in which global *biota* plays *the* major role as a dissipator of the incoming solar energy. The term *biota* (from the Greek *biōtē*, meaning "life") refers collectively to all living organisms inhabiting a given region, ecosystem, or the planet as a whole. It encompasses every form of life—plants, animals, fungi, protists, and microorganisms—as well as their functional and evolutionary relationships within the biosphere (*Whittaker and Likens*, 1973, *Ricklefs and Relyea*, 2011). In Earth-system science, the biota represents the active biological component that dissipates solar energy, and exchanges matter and energy with the atmosphere, hydrosphere, lithosphere, and cryosphere.

We will illustrate this vast spectrum of natural and anthropogenic dissipation with a few examples. Terrestrial and marine plants together continuously dissipate through photosynthesis roughly ten times more solar power than the entire primary energy flux generated by the human economy—which itself derives mostly from exploiting fossilized solar energy stored in the lithosphere. Hurricanes self-organize to dispose of excess heat when conduction and ordinary convection are insufficient in warm (≥ 25 °C) (*Webb*, 2021) or very warm (~ 35 °C) (*NASA Earth Observatory*, 2023) seawater. Each mature hurricane operates as a remarkably efficient Carnot engine, dissipating terawatts to tens of terawatts of latent and sensible heat in water vapor and condensed droplets while radiating thermal energy into space. A large school of fish may collectively dissipate by viscous drag the mechanical power equivalent to several large power plants. Over an average lifetime, a single human ingests about 140 tonnes of food, water, and air, expelling roughly the same quantity of physiological waste. With eight billion individuals, humanity constitutes a major physiological dissipator of solar energy and generator of chemical entropy—and, through our exosomatic metabolism, we produce roughly ten times more "mess" than our biological metabolism alone. For other details, see Chapters 4, 5 and 12 and Appendices A and E.

After this introduction, we will examine the major global fluxes and reservoirs of carbon, both today and in the geological past. In particular, we will analyze the mechanisms of ocean acidification and the ocean's buffering capacity during the industrial era—a period of unprecedented CO_2 emissions—and over the last 10,000 years, when the atmosphere, land, and ocean had sufficient time to reach quasi-equilibrium, limiting fluctuations in atmospheric CO_2 concentration to barely 100 ppm_v.

In passing, we will glance back into the ancient geologic eons, focusing on the supercontinent Rodinia about one billion years ago, and show that even the oldest known animals are the recent descendants of ancient bacteria and algae, which almost perished when Rodinia broke up. We humans occupy only a vanishingly small point in geologic time—and yet, within that instant, look at what we have managed to do to the planet and to all her species. As my Australian friend D. J. White quips: "The arc of the living Universe is long, but it bends toward Just Us."

3.2 Why is this important?

In this book, we explain how humanity's prolonged ecological overshoot, see Appendix A, drives the abrupt and brutal climate changes now unfolding, even though the direct perturbations we introduce into the Earth system are small compared with the immense natural fluxes of the global carbon cycle. The damage arises because our disruptions strike at the biosphere—the thin, fragile membrane on which nearly all life depends—and it is precisely here that the planet is most vulnerable. The familiar arguments of climate-change deniers overlook a simple but devastating fact: even a small, persistent imbalance in atmospheric CO_2 fluxes can produce disproportionately large and long-lasting warming effects that imperil all living systems. It is essential to grasp this principle before we enter the dense forest of nested, interconnected processes that make understanding the present crisis so breathtakingly challenging.

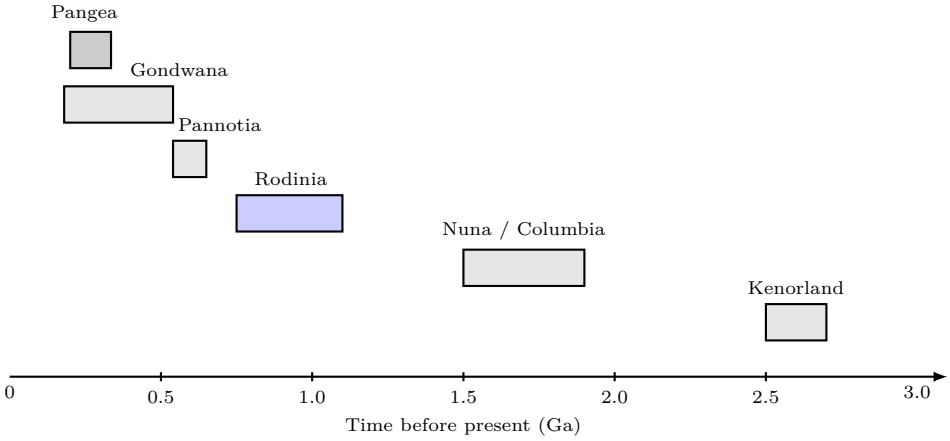

Figure 3.1: Approximate durations of major supercontinents over the last 3 billion years, plotted against time before present in billions of years (Ga). Ages are schematic and compiled from standard reconstructions of Kenorland, Nuna/Columbia, Rodinia, Pannotia, Gondwana, and Pangea. During and after the prolonged breakup of Rodinia, Earth plunged twice into a globally frozen, ice-covered state—the two "Snowball Earth" episodes—that together lasted for roughly 70 million years, about five million years longer than the time elapsed since the extinction of the dinosaurs to the present day.

3.3 What have we skipped?

The interplay of plate tectonics, global volcanism, and life has regulated Earth's climate for over 3 billion years. The extensive weathering of reactive volcanic rocks deposited during breakups of the ancient supercontinents shown in Figure 3.1, together with the burial of organic carbon, act to draw down atmospheric CO_2 and have plunged the planet into several deep freezes, two of which lasted for nearly 70 million years and almost extinguished the Precambrian life. Conversely, volcanism coupled with plate tectonics gradually restores atmospheric CO_2, warming the planet and allowing life to re-oxidize carbon and reassert its control over much of the carbon cycle described in this chapter. The full story is complex enough to deserve a book of its own.

For example, the late Mesoproterozoic (1.6-1.0 Ga) to early Neoproterozoic (1.0-0.54 Ga) supercontinent Rodinia, see Figure 3.1, assembled between about 1.3 and 0.9 Ga and persisted as a long-lived equatorial landmass until at least 0.8 Ga (*Li et al.*, 2008, *Evans*, 2009). Its breakup was protracted: plume-related rifting began by ∼ 830–800 Ma and progressed through 800–750 Ma[1], ultimately fragmenting most of Rodinia between ∼ 750 and 650 Ma (*Li et al.*, 2008, *Bogdanova et al.*, 2009). High-precision U–Pb geochronology and palaeomagnetism show that during the onset of the **Cryogenian Sturtian** glaciation (∼ 717–660 Ma), grounded ice sheets reached sea level on the low-latitude margins of Laurentia[2], which was then situated near the equator (*Macdonald et al.*, 2010a,b, *Hoffman et al.*, 2017). This global glaciation was perhaps the most severe challenge to the survival of early life on Earth. Life ultimately prevailed, aided by intense volcanic outgassing that released vast amounts of CO_2 into the ancient atmosphere. The resulting greenhouse effect warmed the planet sufficiently to melt the global ice cover and terminate the Snowball Earth state. A younger but still extreme **Marinoan** glaciation followed at ∼ 650–635 Ma (*Hoffman and Schrag*, 2002, *Hoffman et al.*, 1998). In most palaeogeographic reconstructions, these "Snowball Earth" episodes occur as Rodinia is rifting apart in low latitudes, so that intense silicate weathering of freshly exposed volcanic and rift-flank lithologies on an equatorial supercontinent provides a natural trigger for catastrophic CO_2 drawdown and runaway ice–albedo feedback (*Hoffman and Schrag*, 2002, *Schrag et al.*, 2002, *Li et al.*, 2008). Not too be nit-picking, the Marinoan glaciation occurred *after*

[1] Rodinia's formation and breakup may have lasted as long as the entire time span from the beginning of the Cambrian to the present—that is, even longer than it took for all modern species, except bacteria, algae and other protists, and multicellular eucaryotes, to evolve. Try to imagine this!

[2] Laurentia is the ancient geological core (craton) of North America, formed from some of Earth's oldest continental rocks. It includes the Canadian Shield and underlies much of present-day Canada and the central and northern United States. Laurentia has persisted as a stable continental block for more than 2.5 billion years and played a central role in the assembly and breakup of multiple supercontinents, including Rodinia and Pangea.

most of Rodinia had already fragmented, but *before* the complete assembly of Pannotia.

Silicate weathering is caused by a set of chemical reactions in which atmospheric CO_2 dissolves in rainwater to form carbonic acid (H_2CO_3), which reacts with silicate minerals in rocks. A simplified reaction for calcium silicate weathering is:

$$CaSiO_3 + 2\,CO_2 + H_2O \rightarrow Ca^{2+} + 2\,HCO_3{}^- + SiO_2,$$

followed by marine precipitation of calcium carbonate:

$$Ca^{2+} + 2\,HCO_3{}^- \rightarrow CaCO_3 \downarrow + CO_2, aq + H_2O.$$

Overall, one molecule of CO_2 is consumed per molecule of $CaSiO_3$ weathered, providing a long-term sink for atmospheric CO_2 and a key negative feedback in Earth's climate system.

Geochronological and geochemical data suggest that the initial breakup of Rodinia at ∼ 830–800 Ma was plume-related, marked by voluminous mafic[3] dike swarms[4] and bimodal volcanism[5] across Laurentia, Australia, South China, and India, consistent with the impingement of one or more mantle plumes beneath the supercontinent (*Li et al.*, 2008, *Bogdanova et al.*, 2009, *Donnadieu et al.*, 2004). Of course the processes of supercontinent breakup and subduction are even more complicated. *Gernon et al.* (2025) proposed that organized chains of Rayleigh-Taylor instabilities, which sweep along continental roots following breakup, can systematically flush ancient deep lithospheric reservoirs over tens of millions of years and leave chemical signatures of the distant past among the scattered breakup fragments today.

Table 3.1: Representative fossil and biomarker evidence for life surviving through the Cryogenian Sturtian Snowball Earth.

Evidence	**Approx. age (Ma)**	**Significance**	**Source**
Bangiomorpha pubescens (multicellular red alga)	∼1,047 (pre–Sturtian)	First known sexually reproducing eukaryote; persisted into Cryogenian	Butterfield (2000)
Proterocladus antiquus (green alga)	∼1,000	Early chlorophyte lineage ancestral to modern green algae	Tang *et al.* (2020)
Cryogenian steranes (C_{30} 24–isopropylcholestane)	717–635	Biomarkers of demosponges or ancestral animals	Love *et al.* (2009)
Acritarchs and filamentous cyanobacteria	720–660	Photosynthetic microbial life under ice or in meltwater	Cohen *et al.* (2017)
Stromatolitic and microbial laminites in glacial sediments	717–660	Evidence for benthic microbial mats during glaciation	Bosak *et al.* (2011)

Despite the near-global ice cover during the Sturtian Snowball Earth (∼ 717–660 Ma), life persisted in a variety of refugia. As Table 3.1 attests, microbial ecosystems survived in open or thin-ice regions near volcanic centers, subglacial and hydrothermal environments, and beneath the ice in brine channels or cryoconite holes[6]. Marine photosynthetic cyanobacteria, green and red algae (*Chlorophyta*, *Rhodophyta*),

[3]The term *mafic* refers to silicate rocks and magmas rich in magnesium (Mg) and iron (Fe)—hence the name—and relatively poor in silica (SiO_2). Typical mafic rocks include basalt and gabbro, which crystallize from low–viscosity magmas derived from partial melting of the mantle. Mafic lavas are dark in color and dense, with mineral assemblages dominated by pyroxene, olivine, and plagioclase feldspar. In contrast, *felsic* rocks (e.g., granite, rhyolite) are silica–rich, lighter in color, and less dense.

[4]A *dike swarm* is a large, geologically coherent array of near-vertical, sheet-like intrusions of mafic magma that cut across older rock formations. Such swarms may extend for hundreds to over a thousand kilometers and often radiate from a central source region or mantle plume head, marking zones of lithospheric stretching and continental rifting.

[5]*Bimodal volcanism* refers to the coexistence of both mafic (basaltic) and felsic (rhyolitic or granitic) magmas within the same volcanic or tectonic province, with few intermediate compositions. It typically develops in extensional settings, such as continental rifts, where mantle-derived mafic magmas trigger partial melting of the crust, producing silica-rich felsic magmas.

[6]*Cryoconite* (from Greek *kryos*, "cold," and *konis*, "dust") refers to dark, dust-like granules composed of mineral particles, soot, and microbial communities that accumulate on the surfaces of glaciers and ice sheets. By absorbing sunlight, cryoconite lowers the local albedo and melts small depressions, known as *cryoconite holes*, which provide liquid-water micro-habitats that can harbor photosynthetic cyanobacteria and other microorganisms even under globally glaciated conditions.

and heterotrophic protists continued to evolve, as evidenced by Cryogenian biomarkers such as steranes and preserved microfossils (e.g., *Bangiomorpha*, *Palaeopascichnus*). Bacterial mats and eukaryotic algae likely inhabited small polynyas or continental-margin meltwater oases, forming the biological foundation that allowed rapid diversification once the ice melted at the onset of the Ediacaran.

While reading this book, remember that CO_2, plate tectonics, volcanism, and life have always played disproportionately large roles in controlling the global climate system at different temporal and spacial scales.

3.4 Solar power dissipated by land plants

Terrestrial photosynthesis constitutes one of the largest continuous fluxes of energy on Earth. Each year, land vegetation fixes roughly $N_{\mathrm{PP,land}} \approx 60$ PgC yr^{-1} (1 PgC $= 10^{15}$ gC), according to multiple global carbon budget estimates (*Canadell et al.*, 2021, *Field et al.*, 1998, *Beer et al.*, 2010, *Running*, 2012). The chemical energy stored in this newly formed biomass represents the difference between absorbed solar radiation and the energy re-emitted as heat or longwave radiation.

The mean photosynthetic efficiency of land plants—the fraction of incoming solar radiation converted to chemical energy—is small,

$$\eta_{\mathrm{photo}} \approx (0.3\text{–}0.5)\%.$$

Given that the global average shortwave solar flux absorbed by vegetated land surfaces is roughly $F_{\mathrm{abs}} \approx 170$ W m^{-2} and that land covers $A_{\mathrm{land}} \approx 1.48 \times 10^{14}$ m^2 (29% of Earth's surface), the gross solar power incident on land is

$$P_{\odot,\mathrm{land}} = F_{\mathrm{abs}} A_{\mathrm{land}} \approx 2.5 \times 10^{16} \text{ W } (= 25{,}000 \text{ TW}).$$

Multiplying by the photosynthetic efficiency gives the global rate of *solar energy dissipation through photosynthesis*:

$$P_{\mathrm{photo,land}} = \eta_{\mathrm{photo}} P_{\odot,\mathrm{land}} \approx (0.003\text{–}0.005) \times 2.5 \times 10^{16} \approx (7.5\text{–}12.5) \times 10^{13} \text{ W},$$

or roughly **75–125 TW**. This estimate agrees with global-carbon-budget conversions from gross primary productivity, e.g, *Patzek* (2007):

$$60 \text{ PgC yr}^{-1} \times (39 \text{ kJ gC}^{-1}) \times \frac{1}{3.15 \times 10^7 \text{ s yr}^{-1}} \approx \mathbf{75\ TW}.$$

Thus, the Earth's land plants continuously dissipate of order $\mathcal{O}(100)$ TW of solar power as chemical free energy, later released as heat through respiration, decay and combustion, and radiated back to the Universe. For comparison, total human primary energy consumption in 2024 is $\sim$20 TW. Thus, the biosphere's natural "solar engine" on land alone exceeds anthropogenic energy use by 3-6 times.

3.5 Solar power dissipated by marine photosynthesis

Marine phytoplankton perform photosynthesis throughout the euphotic[7] zone, typically the upper 50–100 m of the ocean, converting a small fraction of absorbed solar radiation into chemical free energy. The global ocean produces approximately $N_{\mathrm{PP,ocn}} \approx 45\text{–}55$ PgC yr^{-1} according to satellite and carbon-cycle assessments (*Field et al.*, 1998, *Behrenfeld and Falkowski*, 1997, *Sarmiento and Gruber*, 2006, *Canadell et al.*, 2021). The average energy content of fixed organic carbon is ≈ 39 kJ gC^{-1} (*Whittaker and Likens*, 1973), yielding a global chemical-energy rate of

$$P_{\mathrm{photo,ocn}} = N_{\mathrm{PP,ocn}} \times (39 \times 10^3 \text{ J gC}^{-1}) / (3.15 \times 10^7 \text{ s yr}^{-1}).$$

[7] Euphotic zone = "the sunlight zone" in water.

For $N_{\mathrm{PP,ocn}} = 50$ PgC yr^{-1},

$$P_{\mathrm{photo,ocn}} \approx 6.2 \times 10^{13}\ \mathrm{W} = \mathbf{62\ TW}.$$

The photosynthetic conversion efficiency for the ocean as a whole is

$$\eta_{\mathrm{photo,ocn}} = \frac{P_{\mathrm{photo,ocn}}}{F_{\mathrm{abs,ocn}} A_{\mathrm{ocn}}} \approx 0.04\text{–}0.1\%,$$

where $F_{\mathrm{abs,ocn}} \approx 170$ W m^{-2} is the mean shortwave flux absorbed by the ocean surface (*Trenberth et al.*, 2009, *Wild et al.*, 2013) and $A_{\mathrm{ocn}} = 3.61 \times 10^{14}$ m^2 is the oceanic area fraction (71% of Earth's surface). Thus, the oceanic biosphere converts of order 10^{-3} of incident solar power into biochemical energy, subsequently dissipated as heat through respiration, microbial oxidation, and food-web metabolism.

Combining with the terrestrial photosynthetic flux ($\sim$ 75–125 TW; Section 3.4), the total planetary photosynthetic power is

$$P_{\mathrm{photo,global}} \approx P_{\mathrm{photo,land}} + P_{\mathrm{photo,ocn}} \approx (140\text{–}200)\ \mathrm{TW},$$

roughly an order of magnitude greater than the entire anthropogenic primary-energy consumption ($\sim$ 20 TW).

As shown by *Patzek* (2007) (see his Table 2[1]), the global gross primary productivity (GPP) of terrestrial and aquatic plants remains remarkably stable on decadal time scales, averaging about 110 GtC yr^{-1}. This flux corresponds to a continuous dissipation and conversion of roughly **114 TW** of solar power into chemical energy stored in biomass.

[1]Based on infrared emissions from plants measured continuously by the MODIS instrument on the now dying Aqua and Terra satellites.

3.6 Global thermal power imbalance induced by greenhouse gas forcing

By 2024, the increasing concentrations of long-lived greenhouse gases (e.g., CO_2, CH_4, N_2O) had introduced a persistent radiative forcing of approximately 2.5 W m^{-2} relative to the pre-industrial baseline (*Ciais et al.*, 2013, *Dlugokencky et al.*, 2025). When integrated over the Earth's surface area ($\sim 5.1 \times 10^{14}$ m^2), this forcing corresponds to a global power imbalance on the order of **1000 – 2000 TW**. This globally-distributed power dissipation occurs continuously as the Earth system stores most of additional absorbed heat in the oceans, and redistributes it via atmospheric, oceanic and cryospheric warming.

Long-lived greenhouse gases warm up Earth, while she dissipates the persistent radiative imbalance by emitting more longwave radiation to space, ultimately returning energy to the cold Universe at the cosmic microwave background temperature of 2.73 K.

3.7 Global atmospheric wind power dissipation

On a global, time-average basis the atmospheric circulation converts available potential energy into kinetic energy that is ultimately dissipated by friction at rates of order $\sim$1–3 W m^{-2}, i.e.,

$$P_{\mathrm{diss}} \approx (1\text{–}3) \times 5.1 \times 10^{14}\,\mathrm{m}^2 \approx 5 \times 10^{14}\,\mathrm{W}\text{–}1.5 \times 10^{15}\,\mathrm{W} = \mathbf{500\text{–}1500\ TW}.$$

(cf. Table 3.2), consistent with Lorenz-cycle energetics (*Lorenz*, 1955) and multiple independent estimates (*Roy and Traiteur*, 2010, *Kleidon*, 2012, *Makarieva et al.*, 2016, *Marvel et al.*, 2013).

Table 3.2: Published estimates relevant to global atmospheric kinetic-energy dissipation by winds.

Study	Method / Scope	Dissipation [$\mathrm{W\,m^{-2}}$]	Global Power [TW]
Roy and Traiteur (2010)	Empirical KE dissipation estimate (surface layer), consistency check with independent method	∼2.1	∼1070
Kleidon (2012)	Thermodynamic work budget / Lorenz-cycle perspective for the climate system (free-energy generation that is ultimately dissipated)	∼2–3 (order)	∼1000–1500
Makarieva et al. (2016)	Reformulation of global atmospheric power budget (moist atmosphere; condensation motions); total atmospheric power	∼0.8–1.0[†]	∼410–510
Marvel et al. (2013)	GCM perturbations of atmospheric drag; geophysical limits to extractable wind power; implies kinetic-energy dissipation capacity	(implied upper-bound regime)[‡]	$\lesssim$1600 (capacity limit)

[†]Definitions differ: "total atmospheric power" in *Makarieva et al.* (2016) is not identical to near-surface KE dissipation; thus values are somewhat lower but bracket the same order.
[‡]Not a direct climatological mean; rather a modeled upper bound where added drag increases whole-atmosphere kinetic-energy dissipation quasi-linearly up to ∼1600 TW.

The spread (∼0.8–3 $\mathrm{W\,m^{-2}}$) reflects differing definitions (*e.g.*, near-surface kinetic-energy dissipation versus "total atmospheric power" in a moist atmosphere) and methodological approaches. It is therefore reasonable to adopt ∼1,000 TW as a representative, order-of-magnitude value, with a plausible range of ∼500–1,500 TW.

3.7.1 Approximate power dissipated by tropical cyclones

Following *Emanuel* (1998, 1987), the surface-layer kinetic-energy dissipation per unit area is $D = C_D\,\rho\,u^3$, so that a storm's total instantaneous power is approximated by

$$P \;\approx\; \pi\,\rho\,C_D\,u^3\,r_0^2, \tag{3.1}$$

where u is a representative 10-m wind speed, r_0 a characteristic outer radius, ρ near-surface air density, and C_D the surface drag coefficient. Values below are illustrative, using $\rho = 1.15\ \mathrm{kg\,m^{-3}}$ and $C_D = 2.0 \times 10^{-3}$ (noting that C_D may level off at extreme winds (*Powell et al.*, 2003)). The hurricanes are categorized in Equation (3.1) by the Saffir-Simpson scale, see Table 3.3. The measured power and time-integrated power of real category 5 hurricanes are illustrated in Table 3.4. One of the strongest hurricanes ever measured, Irma, is shown in Figure 3.2.

3.7.2 The duration of peak sustained winds

In strong tropical cyclones, the peak wind-duration is limited by the stability of the eyewall[8] and environmental conditions. Major hurricanes (Category 3–5) typically maintain their maximum 1-minute sustained wind speeds for several hours, on the order of ∼3–12 h (*Landsea and Franklin*, 2013). Only the most intense and well-organized Category 5 storms sustain peak winds for much longer (∼18–36 h), generally in exceptionally favorable conditions of low vertical wind shear and high ocean heat content; examples include Hurricanes Irma (2017) and Dorian (2019) in the Atlantic. Eyewall replacement cycles, occurring every ∼6–24 h, often interrupt this peak phase and lead to temporary intensity fluctuations

[8]The *eyewall* is the ring of intense deep convection surrounding the hurricane's eye, where the strongest updrafts, heaviest rainfall, and maximum sustained winds occur. It is the primary engine of the storm's energy conversion, transporting heat and moisture upward and driving the extreme pressure gradient that sustains the cyclone.

Table 3.3: Illustrative instantaneous dissipation power by Saffir-Simpson category using (3.1).

Category	u (m s^{-1})	u (mph)	r_0 (km)	P (TW)
Cat 1	38	85	30	0.36
Cat 2	46	103	35	0.86
Cat 3	54	121	40	1.82
Cat 4	64	143	50	4.74
Cat 5	75	168	60	10.97

Notes: u values are representative 1-min sustained winds at 10 m (midpoints of Saffir-Simpson ranges). Radii r_0 are illustrative storm scales increasing with category. Because $P \propto u^3 r_0^2$, results are highly sensitive to these choices; real storms exhibit large spread in size and structure. Cf. *Emanuel* (1987, 1998) for canonical $P \sim 10^{12}$-10^{13} W estimates and *Emanuel* (2005) for the lifetime-integrated power dissipation index (PDI).

Table 3.4: Approximate peak power dissipation and total PDI for selected Category 5 hurricanes. Values from NOAA/NHC best-track data; PDIs from 6-hourly maxima (*Emanuel* 2005).

Hurricane	**Year**	**Peak Power (TW)**	**PDI ($\times 10^{10}$ m^{3}s^{-2})**	**Sources**
Wilma (Atl)	2005	3–36	∼20	NHC[a] TCR[b]; NWS[c]
Irma (Atl)	2017	5–72	∼60	NHC TCR; Klotzbach et al.
Dorian (Atl)	2019	4–36	∼30	NHC TCR
Patricia (EPac)	2015	3–14	∼12	NHC TCR; BAMS[d]
Otis (EPac)	2023	1–4	∼5	NHC advisories

PDI $= \sum u_{\max}^3 \Delta t$, 6-hourly 1-min winds (m s^{-1}); see *Emanuel* (2005), *Villarini and Vecchi* (2012).
[a]NHC = National Hurricane Center, the NOAA office responsible for forecasting and monitoring tropical cyclones in the Atlantic and eastern Pacific.
[b]TCR = Tropical Cyclone Report
[c]NWS = National Weather Service, the NOAA agency responsible for US weather forecasts, warnings, and climate monitoring.
[d]BAMS = The *Bulletin of the American Meteorological Society*, the flagship journal of the American Meteorological Society (AMS), well known for its annual "State of the Climate" reports and comprehensive hurricane-season summaries.

(*Kossin and Sitkowski*, 2009). Thus, a representative duration for the near-steady peak dissipation of a strong hurricane is τ_{hurr} ∼6–12 h.

Depending on the cube of the peak wind speed u, the square of the outer radius r_0, and the storm duration τ_{hurr}, a Category 5 hurricane—which operates as an almost perfect Carnot engine between the hot ocean surface and the cold tropopause at roughly 18 km altitude—can produce up to 70 TW of mechanical power, about three times more than the current primary power dissipated by humanity. Global warming tends to increase u, r_0, and τ_{hurr}, thereby amplifying the total energy throughput of such storms.

3.7.3 Power dissipated by storms and thunderstorms

Recent theoretical work suggests that the frictional dissipation associated with precipitation and convective turbulence in the tropics lies in the range of approximately 1-2 W m^{-2} globally averaged in convective regions (*Makarieva et al.*, 2013). If one assumes an effective tropical convective area of $\sim 5 \times 10^{13}$ m^2,

Figure 3.2: One of the strongest hurricanes ever recorded, *Irma* (6 September 2017), spanned an area comparable to that of France (effective radius of tropical-storm force winds = ∼240 km)—the strongest on record remains *Patricia* (2015). Irma formed on August 30 and dissipated on September 13, 2017, making it a very long-lasting hurricane. At peak intensity and because of her large size, Irma's instantaneous power output was estimated to be nearly four times greater than the total primary power consumption of the global human economy at that time. Irma swept east-west damaging Cape Verde, the Leeward Islands (Barbuda, Saint Barthélemy, Anguilla, Saint Martin and the Virgin Islands), Greater Antilles (Cuba and Puerto Rico (intercepting the hurricane in the picture), Turks and Caicos Islands, Jamaica, The Bahamas, and Eastern United States (mostly Florida). *Image source: NASA.*

then this corresponds to a total dissipation power of order

$$P \approx (1\,\text{to}\,2)\,\mathrm{W\,m^{-2}} \times 5 \times 10^{13}\,\mathrm{m^2} \sim (5 \times 10^{13}\,\mathrm{W\,to}\,1 \times 10^{14}\,\mathrm{W}),$$

i.e. on the order of 10^{14} W (**100 TW**) for convective-storm dissipation alone.

Globally, lightning occurs about 40–50 times per second, corresponding to roughly 1.3×10^9–1.6×10^9 flashes per year (*Christian et al.*, 2003). A typical lightning discharge releases on the order of 10^9–10^{10} J of energy (*Rakov and Uman*, 2003, *Christian et al.*, 2003). Multiplying by the global flash rate gives a total annual energy release of $\sim 10^{19}$ J, or an average dissipation power of

$$P_{\text{lightning}} \approx \frac{10^{19}\ \mathrm{J\ yr^{-1}}}{3.16 \times 10^7\ \mathrm{s\ yr^{-1}}} \approx 3 \times 10^{11}\ \mathrm{W},$$

i.e. about 0.3 TW globally. Thus, lightning contributes negligibly to Earth's total energy budget, being nearly three orders of magnitude smaller than the mechanical power dissipated by all thunderstorms ($\sim 10^{14}$ W).

3.8 Power dissipated by oceanic waves and currents

The global power dissipated by wind-generated ocean surface waves results from the continuous transfer of momentum from the atmosphere to the ocean. Satellite altimetry and wave reanalysis products indicate a total dissipation rate of approximately **2–3 TW** globally (*Ardhuin et al.*, 2009). Most of this energy is lost

through wave breaking and turbulent mixing in the upper ocean, where it contributes to surface-ocean mixing and the generation of oceanic turbulence.

The global power dissipation associated with oceanic currents includes contributions from mesoscale eddies, large gyres, boundary-layer drag and the broader overturning circulation. Observational estimates suggest that mesoscale eddy kinetic-energy dissipation alone is on the order of ~ 0.7 TW (*Torres et al.*, 2023). Additional dissipation occurs through deep-ocean bottom boundary drag and the large-scale overturning circulation (*Scott and Marshall*, 2018), although a full global integrated power estimate remains elusive.

On a global, annually averaged basis, ocean surface waves dissipate a surprisingly small amount of mechanical power–only about 2–3 TW.

3.9 Power dissipated by largest earthquakes

The radiated seismic energy E of an earthquake with moment magnitude M_w can be estimated from *Kanamori* (1977):

$$\log_{10} E = 1.5\, M_w + 4.8, \;\; E \text{ in J} \tag{3.2}$$

Using representative fault rupture durations $\Delta t \sim 200$–300 s for the largest events (*Lay et al.*, 2011), the instantaneous radiated power $P \approx E/\Delta t$ during a large earthquake far exceeds the continuous primary power consumption of modern civilization ($\sim$20 TW). For example, the 1960 Chile ($M_w = 9.5$) and 2004 Sumatra–Andaman ($M_w = 9.1$) earthquakes released $\sim 1.1 \times 10^{19}$ J and $\sim 2.8 \times 10^{18}$ J of seismic energy, corresponding to peak radiated powers of $\sim$ (4–6) $\times 10^{16}$ W and $\sim$ (1–2) $\times 10^{16}$ W, respectively. Thus, for 2–5 minutes, the largest earthquakes dissipate mechanical energy at rates 1,000–10,000 times larger than the average power generated and consumed by 8 billion humans.

3.9.1 Note on total dissipation

The fraction of mechanical work W on the slipping fault that is converted into radiated seismic energy E is known as the *seismic efficiency* η. Observational and theoretical studies indicate that η is typically low, on the order of a few percent (rarely exceeding 10%), with the remainder dissipated as frictional heating, off-fault damage, and other inelastic processes (*Kanamori and Brodsky*, 2004). Since $W = E/\eta$, the corresponding instantaneous dissipation rate may be at least an *order of magnitude larger* than the radiated-power values listed above and in Table 3.5.

Table 3.5: Ten largest instrumental-era earthquakes with approximate radiated energy E, rupture duration Δt, and peak radiated power $P \approx E/\Delta t$. Energy estimates follow $\log_{10} E = 1.5 M_w + 4.8$ (*Kanamori*, 1977).

Event (Location)	**Year**	**M_w**	E **(J$\times 10^{17}$)**	P **(PW)**
Chile, Valdivia	1960	9.5	110	~ 400
Alaska, Prince William Sound	1964	9.2	40	~ 15
Sumatra-Andaman	2004	9.1	28	~ 10
Japan, Tohoku	2011	9.1	28	~ 10
Kamchatka	1952	9.0	20	~ 8
Maule, Chile	2010	8.8	8.9	~ 4
Ecuador-Colombia	1906	8.8	8.9	~ 3
Rat Islands, Alaska	1965	8.7	5.6	~ 3
North Sumatra (Nias)	2005	8.6	3.5	~ 2
Andreanof Islands, Alaska	1957	8.6	3.5	~ 2

Notes: Duration assumptions used for power estimates: Valdivia $\sim$250 s, Alaska 1964 $\sim$250 s, Sumatra 2004 $\sim$300 s, Tohoku 2011 $\sim$180 s, other great quakes $\sim$150-250 s based on rupture inversions and aftershock zone lengths.

3.10 Geothermal power dissipation

The continuous geothermal heat flow from the Earth's interior to the surface is estimated at approximately 4.3×10^{13} W to 4.9×10^{13} W (43-49 TW), corresponding to an average surface heat flux of roughly 0.08-0.10 W m^{-2} (*Lucazeau*, 2019, *Pollack et al.*, 1993). Although modest compared to the incident solar radiation, this internal-heat dissipation represents a persistent, planet-scale power loss that contributes to mantle convection, plate tectonics, and long-term molten-core cooling.

The geothermal power radiated upward through the Earth's surface is tiny compared with absorbed solar radiation ($\sim 1.2 \times 10^5$ TW) yet comparable with other planetary mechanical and heat fluxes. We adopt 47 ± 2 TW as a central value, consistent with multiple modern syntheses of continental and oceanic heat-flow databases. (*Davies and Davies*, 2010, *Davies*, 2013, *Furlong and Brown*, 2013, *Karlsen et al.*, 2021).

3.11 Energy dissipated by a school of fish

Suppose a school of $N = 10^4$ fish each with an effective drag are,a $a = 0.01$ m^2, swims at speed u.

Figure 3.3: A large ribbon school of fish. *Image source: Getty.*

This is an intriguing problem, and we shall devote to it more attention than it probably merits from a purely energy-dissipation standpoint. First we must ask how many fish are there in a large school, like the one in Figure 3.3? There is no single number (see Table 3.6) – school size depends on species, body size, behavior, and geometry of the aggregation. A practical way to estimate the count is to assume a number density n (fish per m^3) and a school volume V:

$$N = n\,V.$$

For many travelling schools, a representative number density is $n \sim 1$–10 m^{-3} (individuals typically spaced by $\sim$ 1 body length). For tight "bait balls" or dense defensive clusters, $n \sim 10$–100 m^{-3} is plausible.

Back-of-the-envelope link to spacing. If typical center-to-center spacing is s (m), a crude geometric

estimate is

$$n \approx \frac{1}{s^3},$$

so for $s = 0.3$ m (small sardine/anchovy), $n \sim 37$ m^{-3}; for $s = 0.6$ m, $n \sim 4.6$ m^{-3}.

Illustrative examples. Using simple shapes for the school geometry:

$$\begin{aligned} \text{Sphere (bait ball):} \quad & V = \tfrac{4}{3}\pi r^3, \\ \text{Cylindrical ribbon:} \quad & V = \pi R^2 L, \\ \text{Sheet/pancake:} \quad & V = L\,W\,H. \end{aligned}$$

Table 3.6: Order-of-magnitude fish counts for representative school geometries at number density n. Actual schools are highly variable; these examples are illustrative.

Geometry	**Dimensions**	$\boldsymbol{V}$ [m^3]	$\boldsymbol{n}$ [m^{-3}]	$\boldsymbol{N}$ (fish)
Tight bait ball (sphere)	$r = 15$ m	1.4×10^4	30	$\sim 4.2 \times 10^5$
Large travelling school (sheet)	500×200×20 m	2.0×10^6	5	$\sim 1.0 \times 10^7$
"Mega" ribbon (cylinder)	$L = 5$ km, $R = 150$ m	3.5×10^7	5	$\sim 1.8 \times 10^8$

Rule of thumb.

- *Small/medium schools:* 10^3-10^5 fish.
- *Large schools (hundreds of meters):* 10^6-10^7 fish.
- *Very large aggregations (km-scale runs/ribbons):* 10^7-10^8 fish (and, exceptionally, more).

Notes. "School" (coordinated) vs. "shoal" (loose) are often conflated; densities can be far lower in loose shoals. Hydrodynamic interactions usually reduce per-fish drag relative to swimming alone, so using $N = nV$ with large n provides an upper bound for dissipative power estimates.

3.11.1 Order-of-magnitude power dissipated by large fish schools

We approximate the instantaneous mechanical power dissipated against hydrodynamic drag by

$$P \approx F_D\, u \approx \tfrac{1}{2}\,\rho\, u^3 \sum_{i=1}^{N} C_{D,i}\, A_i \equiv \tfrac{1}{2}\,\rho\, u^3\, N\, \mathcal{A},$$

where ρ is seawater density, u a representative school swimming speed, N the number of fish, and $\mathcal{A} \equiv \langle C_D A \rangle$ an *effective drag area per fish* (drag coefficient times the chosen reference area). Schooling can reduce individual drag force by 75% via hydrodynamic interactions (*Weihs*, 1973, *Hemelrijk et al.*, 2015, *Verma et al.*, 2018, *Zhang et al.*, 2024), so this gives an upper bound if one adopts a solitary-fish $\mathcal{A}$. We take $\rho = 1025\,\mathrm{kg\,m^{-3}}$ and a baseline $\mathcal{A} = 1 \times 10^{-2}\,\mathrm{m^2}$ per fish (tunable; results scale linearly with $\mathcal{A}$).[9]

[9] For solitary fish, classical measurements (e.g., bluefish) decompose total drag into pressure + friction components and support quadratic drag scaling with speed (*Ogilvy and DuBois*, 1981).

School sizes used (from simple geometry).

$$N = nV, \qquad n = \text{fish number density } (\mathrm{m}^{-3}), \quad V = \text{school volume}.$$

We adopt the illustrative cases introduced earlier:

$$\begin{aligned}
&\text{Tight bait ball (sphere): } r = 15\,\mathrm{m},\ n = 30\,\mathrm{m}^{-3} \ \Rightarrow\ N \approx 4.24 \times 10^5,\\
&\text{Large travelling sheet: } L \times W \times H = 500\,\mathrm{m} \times 200\,\mathrm{m} \times 20\,\mathrm{m},\\
&n = 5\,\mathrm{m}^{-3} \ \Rightarrow\ N \approx 1.0 \times 10^7,\\
&\text{“Mega” ribbon (cylinder): } L = 5\,\mathrm{km},\ R = 150\,\mathrm{m},\\
&n = 5\,\mathrm{m}^{-3} \ \Rightarrow\ N \approx 1.77 \times 10^8.
\end{aligned}$$

A rough estimate of the power dissipated by these schools of fish is shown in Table 3.7. It appears that an exceptionally large school of fish could dissipate through viscous drag a total power approaching 70 GW. Even if schooling behavior reduced this estimate by $\sim 75\%$ through hydrodynamic synchronization, the effective dissipation would still be on the order of 20 GW—comparable to the combined electrical output of about twenty large power stations.

Table 3.7: Approximate instantaneous power dissipated by representative fish-school geometries. Computed from $P = \frac{1}{2}\rho u^3 N \mathcal{A}$ with $\rho = 1025\,\mathrm{kg\,m}^{-3}$ and $\mathcal{A} = 0.01\,\mathrm{m}^2$ per fish.

School geometry	N	P **at** u**=1 m/s (MW)**	P **at** u**=2 m/s (MW)**
Tight bait ball (r=15 m, n=30 m^{-3})	4.2×10^5	2	17
Large travelling sheet (500×200×20 m, n=5 m^{-3})	1.0×10^7	51	410
“Mega” ribbon (L=5 km, R=150 m, n=5 m^{-3})	1.8×10^8	9100	7.2×10^4

Note: Power scales as $P \propto u^3 N \mathcal{A}$; doubling speed increases P by roughly eightfold. Values assume no drag reduction from schooling, and hence represent upper bounds.

Large pelagic fish schools exhibit prolonged periods of coordinated motion that can persist from hours to days while the group travels together, feeds, or migrates (*Pitcher and Parrish*, 1993). Within these sustained episodes, coherent high-order structures (e.g., milling or polarized formations) may be maintained for tens of minutes to several hours, depending on external stimuli such as predators, foraging opportunities, and environmental gradients (*Ballerini et al.*, 2008). Rapid transitions between collective states can occur on timescales of seconds, yet the overall collective coherence of a large school is often preserved over very long distances and extended durations.

Scaling guidance. If your preferred $\mathcal{A}$ differs, rescale the tabulated (“tab”) values via

$$P^\star \;=\; P \times \left(\frac{\mathcal{A}}{0.01\,\mathrm{m}^2}\right) \times \left(\frac{N}{N_{\mathrm{tab}}}\right) \times \left(\frac{u}{u_{\mathrm{tab}}}\right)^3.$$

Because schooling can reduce individual drag or effective area, the values in Table 3.7 should be treated as *upper bounds* for a given N and u.

A mega-ribbon of fish, 5 km long and with a density of about 5 fish m^{-3}, dissipates roughly 72 GW of frictional heat, or, more conservatively, $0.25 \times 72 \approx 20$ GW when accounting for hydrodynamic coherence within the school. If the 72 GW of heat were converted to electricity at efficiency $\eta = 0.35$ – typical of a 1 GW$_e$ thermal power plant – the resulting output would be $P_e = \eta P_{\mathrm{th}} \approx 0.35 \times 72 \approx 25$ GW$_e$, i.e., the equivalent of about 25 such plants. Using the reduced estimate of 20 GW gives $P_e \approx 0.35 \times 20 \approx 7$ GW$_e$, or roughly seven 1 GW$_e$ plants.

3.12 Physiological food, water, and oxygen uptake over a human lifetime

A refined analysis in Chapter 4 produces a comparable estimate – within a factor of two – underscoring the difficulty of quantifying both the energy humans metabolize through food and the average intensity of their activities.

A moderately active adult sustains an average metabolic power of

$$P_{\text{met}} \approx 150 \text{ W} \quad \Rightarrow \quad E_{\text{day}} = P_{\text{met}} \times 86400$$
$$\approx 1.3 \times 10^7 \text{ J day}^{-1} \approx 3.1 \times 10^3 \text{ kcal day}^{-1},$$

consistent with physiological and nutritional assessments (*FAO/WHO/UNU Expert Consultation*, 2004, *Mifflin et al.*, 1990, *Smil*, 2013, *Guyton and Hall*, 2020). Over an 80-year lifespan ($t_{\text{life}} = 2.52 \times 10^9$ s),

$$E_{\text{life}} = P_{\text{met}}\, t_{\text{life}} \approx 3.8 \times 10^{14} \text{ J}.$$

With this assumption, 8 billion humans develop the sustained power of approximately **1.2 TW**, or $1.2/20 \times 100 = 6\%$ of global primary power generation in 2024.

Given the international life-expectancy data for 2019–2024, the assumption of an average 80-year human lifespan is somewhat optimistic (see Table 3.8), though many populations are approaching it. The most recent demographic specifics for China and India are summarized in Table 3.9. Together, these two nations comprise approximately 3×10^9 people, or about 38% of the world's total population.

Table 3.8: Life expectancy at birth (years) by region and sex. WHO regional values are for 2019 (latest with region–sex detail); the UN WPP 2024 gives the updated global figure (both sexes combined).

Region	Both	Male	Female	ΔF–M
World (WHO, 2019)	73.3	70.8	75.9	5.1
Africa (WHO, 2019)	64.5	62.4	66.6	4.2
Americas (WHO, 2019)	77.2	74.5	79.8	5.3
Eastern Mediterranean (WHO, 2019)	69.7	68.3	71.3	3.0
Europe (WHO, 2019)	78.2	75.1	81.3	6.2
South-East Asia (WHO, 2019)	71.4	69.9	73.1	3.2
Western Pacific (WHO, 2019)	77.7	74.8	80.8	6.0
World (UN WPP 2024)[a]	73.3	–	–	–

[a] UN *World Population Prospects* (WPP) 2024 reports global life expectancy at birth of **73.3 years** in 2024 (both sexes combined). Regional and sex-specific values are from the WHO 2019 compilation, still used for consistent WHO regional comparisons.

Intake expressed as dry food + total water + inhaled oxygen. Using a representative energy density of dry food matter (17 kJ g^{-1}) and counting *all* water intake (beverages + moisture in food),

$$\text{Dry food (DFM):} \quad \text{DFM}_{\text{day}} = \frac{E_{\text{day}}}{17 \text{ kJ g}^{-1}} \approx 0.76 \text{ kg day}^{-1} \Rightarrow \text{DFM}_{80y} \approx \mathbf{22\ t},$$
$$\text{Total water:} \quad W_{80y} \approx (2.7\text{–}3.0) \text{ L day}^{-1} \times 365 \times 80 \approx \mathbf{79\text{–}88\ t},$$
$$\text{Inhaled oxygen:} \quad O_{2,80y} \approx 0.84 \text{ kg day}^{-1} \times 365 \times 80 \approx \mathbf{25\ t},$$

with the oxygen requirement grounded in standard respiratory physiology (*Guyton and Hall*, 2020, *Weibel*, 2005).

Table 3.9: Latest estimates of life expectancy at birth (years) for China and India, 2023–2024.

Country	Year	Both	Male	Female	Primary source
China	2024	79.0	77.0[a]	81.0[a]	National Health Commission (via Xinhua)
China	2023	78.6	76.5[b]	80.7[b]	National Health Commission
China	2023	77.95	74.8	81.0	Macrotrends (UN / World Bank aggregation)
India	2023	72.0	70.2	73.8	Wikipedia summary (UN & national data)
India	2022–23	70.42	68.6	72.2	Macrotrends (World Bank)

[a] Sex-specific 2024 figures inferred from NHC trend reporting (male ˜77, female ˜81 years).
[b] Sex-specific 2023 breakdown consistent with prior NHC demographic reporting.

Table 3.10: Lifetime physiological intake and principal outputs for an 80-year life at $P_{\text{met}} \approx 150\,\text{W}$.

Quantity	Daily mean	Lifetime total (80 yr)
Dry food (DFM)	$\sim$0.76 kg d^{-1}	$\sim$22 t
Total water (all sources)	2.7-3.0 L d^{-1}	79-88 t
Inhaled O_2	0.84 kg d^{-1}	$\sim$25 t
CO_2 exhaled [†]	—	$\sim$41 t
H_2O excreted [‡]	—	$\sim$95 t
Dry fecal solids	—	$\sim$1 t
Other (skin, hair, nails, menses)	—	$\lesssim$0.1 t

Notes. [†]Assumes carbon mass fraction of DFM $f_C \approx 0.5$, giving $M_C \approx 11\,\text{t}$ and $M_{CO_2} = M_C(44/12) \approx 41\,\text{t}$. [‡]Includes urine, fecal water, sweat/skin, respiratory water, and $\sim$10 t of metabolic water from food oxidation. Diet composition, hydration, climate, and activity introduce $\mathcal{O}(10\%)$ variability.

Mass conservation and reconciliation. Earlier tallies that listed "food (wet)" and then *also* listed "water intake" inadvertently double-counted the moisture already contained in food. Expressing intake as *dry food* + *total water* + O_2 avoids this error and closing the budget requires including gaseous outputs (CO_2, H_2O). With the representative values above,

$$\underbrace{22 + (79\text{–}88) + 25}_{\text{inputs } \approx 126\text{–}135\ \text{t}} \approx \underbrace{41}_{CO_2} + \underbrace{95}_{H_2O} + \underbrace{1}_{\text{dry solids}} + \underbrace{0.1}_{\text{other}} \approx 137\ \text{t},$$

closing the mass balance to within expected uncertainty ranges in diet, hydration, and activity. Only a small, transient body-mass storage term (tens of kg over the life course) remains, and it is largely offset between growth and late-life catabolism.

3.12.1 Daily ATP turnover in humans

A typical human continuously regenerates adenosine triphosphate (ATP), the universal energy carrier of metabolism, at an astonishing rate (*Alberts et al.*, 2015, *Milo and Phillips*, 2015, *Lane and Martin*, 2010).

ATP: The electric coin of life. Adenosine triphosphate (ATP) is often called the "energy currency" of the cell, but it would be more accurate to describe it as an *electric battery* at the molecular scale (*Skulachev*, 1999, *Nicholls and Ferguson*, 2013, *Lane*, 2009). Each ATP molecule stores chemical potential in the three negatively charged phosphate groups packed close together like compressed springs of electrostatic repulsion. When one phosphate bond is cleaved, these charges relax, releasing about 30 kJ mol^{-1} of free

energy. This energy does not appear as heat alone; it drives electric currents and field gradients that power life.

ATP fuels ion pumps—notably the Na^+/K^+ ATPase—that continually separate charge across cellular membranes, maintaining transmembrane potentials of -70 to -200 mV. The resulting electric fields, exceeding 10^7 V m^{-1}, are among the strongest steady fields known in nature, exceeding those in a lightning.[10] By coupling chemical energy to electrical polarization, cells turn ATP hydrolysis into directed motion, signal propagation, and biosynthesis. Every heartbeat, nerve impulse, and muscle contraction ultimately traces back to these electric actions of ATP, whose turnover—tens of kilograms per day in an adult human—sustains the continuous conversion of chemical to electrical work in the living state.

Assuming an average of 10^7 ATP molecules hydrolyzed per cell per second and a body containing $\sim 3 \times 10^{13}$ cells, the total daily turnover is

$$N_{\mathrm{ATP,day}} \approx 2.6 \times 10^{25} \text{ molecules day}^{-1} = 43 \text{ mol day}^{-1}.$$

With a molar mass of $M_{\mathrm{ATP}} = 507$ g mol^{-1}, this corresponds to a regenerated mass of roughly

$$m_{\mathrm{ATP,day}} \approx 22 \text{ kg}.$$

Thus, an adult human recycles on the order of 20 kg of ATP each day, despite possessing at any instant only ∼50 g of ATP molecules. The entire cellular ATP pool therefore turns over about 400 times per day, or once every few minutes. This daily ATP production rate is 4.5 times larger than the daily food, water and oxygen uptake by the same average human.

Over a lifetime, an average human consumes about **137 metric tons** of essential dry food, water, and oxygen, and produces ∼600[1] metric tons of ATP. For eight billion people, this amounts to roughly **one teraton** of vital mass inputs required to live and work. The corresponding metabolic power sustaining humanity is on the order of ~ 1.2 **TW**.

[1] Human cells hydrolyze ATP to ADP and phosphate to release energy, but nearly all ADP and phosphate are rapidly **recycled** to new ATP; the only excreted products are CO_2, H_2O, urea, creatinine, and small amounts of phosphate generated upstream in metabolism rather than from ATP breakdown itself.

[10] Lightning discharges are preceded by intense electric fields that approach or exceed the dielectric strength of air. Under standard atmospheric pressure the breakdown threshold is on the order of

$$E_{\mathrm{breakdown}} \approx 3 \times 10^6 \text{ V m}^{-1},$$

though in practice leader initiation and propagation often occur at somewhat lower field strengths, due to ionization, branching, and field enhancement effects. In situ measurements in thunderclouds have recorded vertical electric fields of $\sim 6.3 \times 10^5$ V m^{-1}, with estimated peaks up to $\sim 9.3 \times 10^5$ V m^{-1} in the final leader stages (*Marshall et al.*, 2006). Near the surface beneath an electrified storm, fields of several kV m^{-1} are common; e.g., values above 2000 V m^{-1} are often cited as warning thresholds for elevated lightning risk (*Mission Instruments*, 2024).

Table 3.11: Approximate mechanical or thermal power dissipation by selected Earth system processes. Peak values are instantaneous during the most energetic phase; global values are quasi-steady.

Process	Power (W)	Notes / Scaling
Largest earthquakes (M_w 9.5)	$\sim 10^{16}$-10^{17}	Peak, few minutes (*Kanamori*, 1977)
GHG forcing (2.5 W m^{-2})	$\sim 1.3 \times 10^{15}$	Continuous (*Dlugokencky et al.*, 2025)
Wind power dissipation	$\sim$ (5-15) $\times 10^{14}$	Continuous (*Marvel et al.*, 2013)
Global photosynthesis	$\sim 2 \times 10^{14}$	Continuous(*Canadell et al.*, 2021)
Major hurricanes (Cat 4-5)	$\sim 10^{13}$-10^{14}	Peak, 6-12 h (*Emanuel*, 1986)
Geothermal heat flow	$\sim 5 \times 10^{13}$	Continuous (*Pollack et al.*, 1993)
Human primary power use	$\sim 2 \times 10^{13}$	Continuous (*International Energy Agency*, 2024)
Global ocean wave dissipation	$\sim$ 2-3 $\times 10^{12}$	Continuous (*Ardhuin et al.*, 2009)
Global tropical cyclones	$\sim 10^{12}$	Global annual mean (*Emanuel*, 2020)
Schools of fish	$\sim 0.4 - 70 \times 10^{9}$	Average, hours-days (*Pitcher and Parrish*, 1993)

3.13 Summary of power dissipation by the discussed Earth systems

Approximate ranges of mechanical and thermal power dissipation from key Earth-system processes—including global photosynthesis, the strongest hurricanes, the largest instrumental-era earthquakes, large pelagic fish schools, the collective metabolism of humanity, and the primary power produced and dissipated by industrial society—are synthesized in Figure 3.4 and Table 3.11.

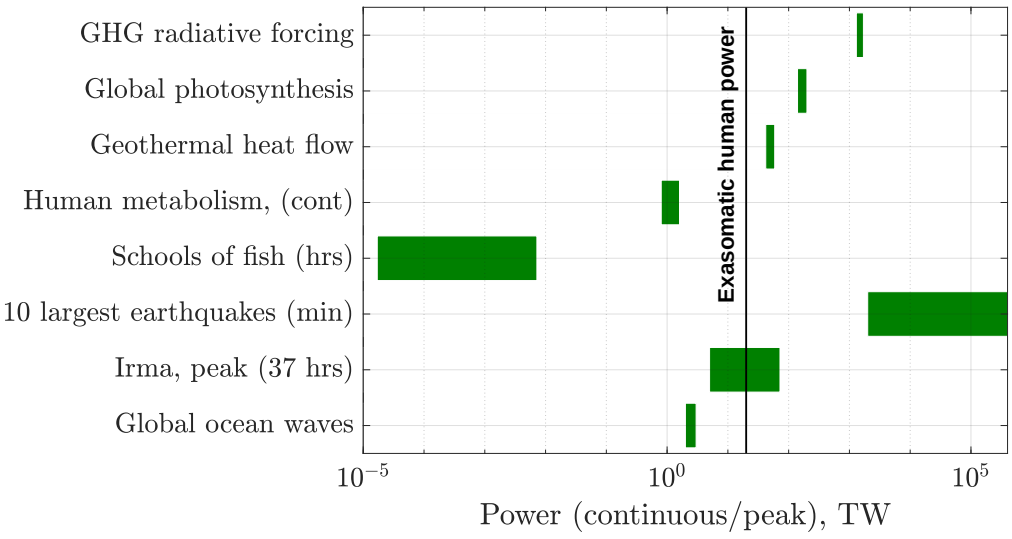

Figure 3.4: Power dissipation by major natural and anthropogenic Earth systems. Calculations by Patzek.

Large dissipative events release extraordinary power that can translate into severe economic losses and human tragedy. The inflation-adjusted damages from some of the costliest hurricanes and the 2025 Los Angeles wildfire are shown in Figure 3.5. Importantly, events that obliterated Caribbean island nations appear far less costly in economic terms, not because they were less destructive, but because the affected

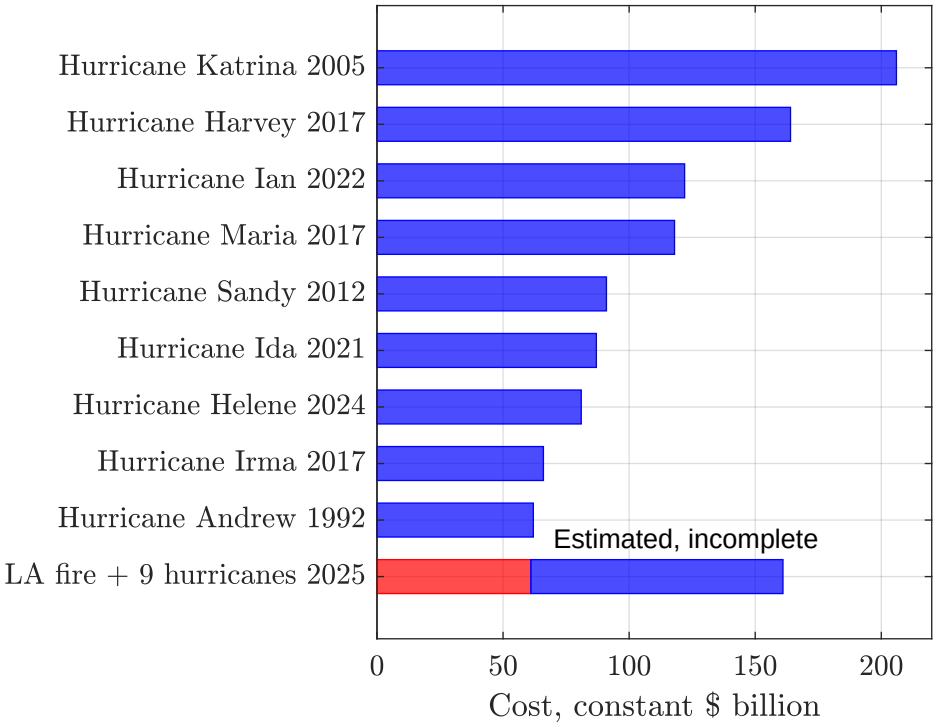

Figure 3.5: Some of the most expensive hurricanes (blue). Data from (*Milman and Witherspoon*, 2025).

populations are far poorer and possess fewer insurable assets, despite catastrophic loss of life, homes, and livelihoods.[11]

3.14 Global carbon cycle: Now and through deep time

3.14.1 Essentials and notation

Let C_i [PgC] denote the carbon inventory of reservoir i and $F_{i\to j}$ [PgC yr^{-1}] the flux from i to j. The contemporary major reservoirs are the atmosphere ($C_{\mathrm{atm}} \approx 875$ PgC in 2024), surface ocean (~ 900 PgC), intermediate/deep ocean ($\sim 37{,}000$ PgC), terrestrial biosphere ($\sim 2{,}500$ PgC, living + soils), and lithosphere (carbonates + kerogen $\gtrsim 10^7$ PgC) (*Sarmiento and Gruber*, 2006, *Canadell et al.*, 2021, *Ciais et al.*, 2013). Mass balance reads

$$\frac{dC_{\mathrm{atm}}}{dt} = E_{\mathrm{FF+LUC}} - F_{\mathrm{atm}\to\mathrm{ocean}} - F_{\mathrm{atm}\to\mathrm{land}}, \tag{3.3}$$

with $E_{\mathrm{FF+LUC}}$ fossil + land-use emissions and the sinks partitioned between oceanic invasion + carbonate chemistry adjustment and land uptake (CO_2 fertilization, nitrogen–phosphorus constraints, climate stresses).

[11] Loss estimates vary according to the normalization methodology used to account for inflation, exposure changes, and wealth accumulation (e.g., *Pielke and Landsea*, 1998). Monetary losses for U.S. events are based primarily on NOAA's National Centers for Environmental Information (*NCEI (NOAA)*, 2024), while international losses are supplemented by the EM-DAT International Disaster Database maintained by the Centre for Research on the Epidemiology of Disasters (*CRED*, 2024).

3.14.2 Characteristic times of the atmospheric CO_2 decay function

Following *Joos et al.* (2013) and *Archer and Brovkin* (2008), the decay of an atmospheric CO_2 perturbation can be represented as a weighted sum of exponential terms:

$$\frac{\Delta C_{\mathrm{atm}}(t)}{E_0} = a_0 + \sum_{k=1}^{3} a_k \, e^{-t/\tau_k}, \tag{3.4}$$

where E_0 is the pulse emission (PgC), a_k are fractional weights, and τ_k are the characteristic time constants [yr] corresponding to distinct physical processes in the global carbon cycle.

The first three terms describe rapid to intermediate exchanges with the ocean and biosphere, while the constant residual a_0 represents the quasi-permanent tail governed by ocean-sediment-weathering equilibration on 10^4-10^5-year timescales.

Table 3.12: Characteristic times and fractional weights of the Bern carbon-cycle impulse-response function (from *Joos et al.* 2013; see also *Archer and Brovkin* 2008).

Component	Fraction a_k	Time scale τ_k [yr]	Dominant process
a_0	0.217	∞	Millennial tail governed by sediments and silicate weathering
a_1	0.186	1.19	Rapid air–sea and biospheric exchange
a_2	0.338	18.5	Upper-ocean equilibration
a_3	0.259	173	Deep-ocean invasion and carbonate buffering

In this formulation,

- approximately half of a CO_2 pulse is removed within $\sim$ 30 years (biosphere ($t \geq 2\tau_1 = 2.4$ yr + surface ocean, ($t \geq 2\tau_2 \approx 30$ yr),
- another $\sim$ 30% within a few centuries (deep-ocean uptake, ($t \geq 2\tau_3 = 3.5$ centuries), and
- the remaining $\sim$ 20% persists for millennia,

underscoring the long atmospheric residence time of anthropogenic CO_2.

3.14.3 The Industrial Revolution perturbation (1850–present)

Total anthropogenic emissions since 1850 exceed 2,700 $PgCO_2$ ($\sim$740 PgC), of which $\sim$46% remains in the atmosphere (airborne fraction), $\sim$24% is taken up by the ocean, and $\sim$30% by land (decadal means; interannual variability driven by ENSO, fires, drought) (*Friedlingstein et al.*, 2025, *Canadell et al.*, 2021). The ocean sink is controlled by the Revelle (buffer) factor, vertical transport, and high-latitude deep-water formation; acidification proceeds at ~ -0.002 pH yr^{-1} in surface waters (*Sarmiento and Gruber*, 2006, *Canadell et al.*, 2021). Land sinks arise from CO_2 fertilization, climate change, nitrogen deposition, and management; their sensitivity to heat and water stress yields large semi-arid variability (*Ciais et al.*, 2013, *Friedlingstein et al.*, 2006).

The 2024 global carbon-cycle balance shown here is adapted from *Friedlingstein et al.* (2025) and visualized in Figure 3.6. Figure 3.7 summarizes the rapidly changing anthropogenic fluxes that dominate the present-day perturbation, while the remaining internal fluxes – and the resulting annual net accumulation of atmospheric CO_2 – represent the Earth system's response. The gross primary productivity of the terrestrial biosphere, about 130 Gt C yr^{-1}, and the corresponding marine photosynthetic flux of roughly 80 Gt C yr^{-1}, each exceed by an order of magnitude the anthropogenic fluxes plotted in Figure 3.7. On annual timescales, however, these large photosynthetic uptakes are nearly balanced by plant respiration and heterotrophic decomposition on land, and by respiration and remineralization processes in the ocean. Most long-term carbon reservoirs therefore remain effectively steady, with the notable exceptions of

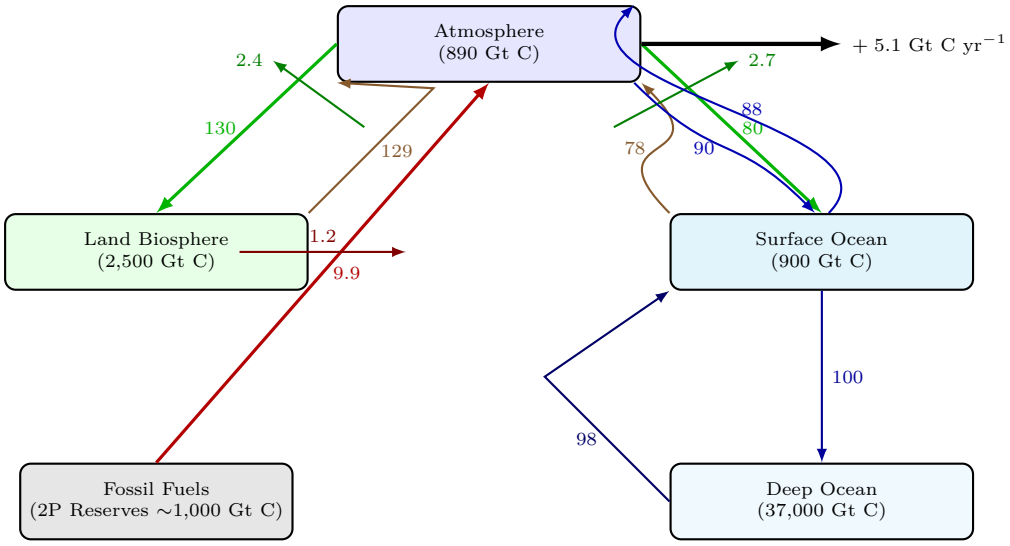

Figure 3.6: Major reservoirs and annual carbon fluxes in the contemporary (2024) global carbon cycle. Large gross biological fluxes (photosynthesis and respiration) are nearly balanced on annual timescales, while anthropogenic emissions and air–sea/air–land imbalances produce the observed atmospheric accumulation. Data source (*Friedlingstein et al.*, 2025).

fossil-fuel reserves and the relatively small but persistent accumulations in coastal sediments and marine biota. By far the largest carbon reservoir outside Earth's mantle is the dissolved inorganic carbon (DIC) stored in the global ocean, as detailed in Figure 3.8.

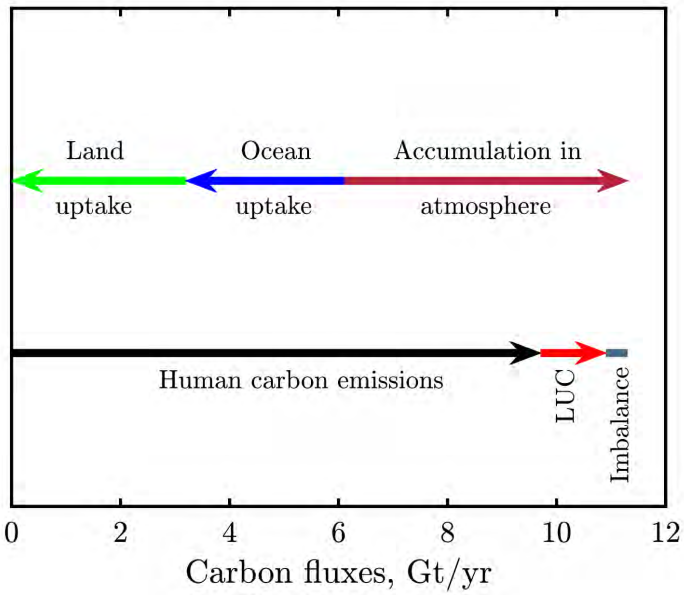

Figure 3.7: These fast-changing fluxes in the global carbon cycle matter most for climate change on an annual basis. LUC = Land Use Change. Other parts of the cycle are likely to adjust over decades, centuries and millennia. The annual accumulation in the atmosphere is roughly 5 Gt of C or 18 Gt CO_2. To absorb this accumulation, we would need 550,000 giant direct air capture machines like the one depicted in Figure 14.5. Data source (*Friedlingstein et al.*, 2025).

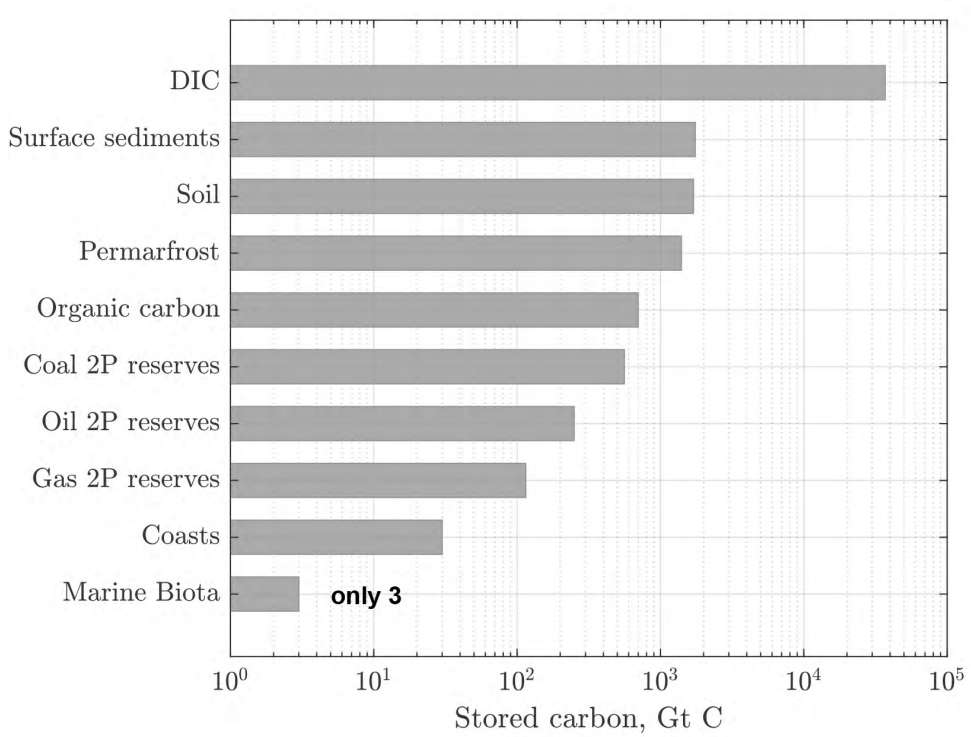

Figure 3.8: Most carbon reservoirs on Earth are enormous, and the largest near-surface store by far is the dissolved inorganic carbon (DIC) in the global ocean. By contrast, the *proved plus probable* (2P) fossil-fuel reserves – consistent with the IPCC AR6 definitions – constitute one of the smallest human-accessible carbon accumulations. If the *possible* category is added, the total fossil-fuel endowment expands to the industry's 3P estimate, giving an ultimately technically recoverable fossil carbon resource of 3P $\approx$ 5,000 Gt C. Data source (*Friedlingstein et al.*, 2025).

3.15 Lysocline and carbonate compensation depth (CCD)

The *lysocline* is the depth in the ocean below which the rate of dissolution of calcium carbonate ($CaCO_3$) begins to increase rapidly due to higher pressure, lower temperature, and elevated CO_2 concentrations. Deeper still lies the *carbonate compensation depth* (CCD), defined as the depth at which the rate of $CaCO_3$ supply from above (biogenic rain) equals its rate of dissolution in seawater. Below the CCD, essentially all $CaCO_3$ particles dissolve before reaching the seafloor, and the sediments become carbonate-poor and clay-rich.

In other words, the lysocline marks the onset of enhanced carbonate dissolution, while the CCD marks the depth where dissolution is complete.

3.15.1 Shoaling of the lysocline and CCD during climate cooling and warming

The vertical positions of the lysocline and the carbonate compensation depth (CCD) are governed by the balance between the delivery of biogenic calcium carbonate ($CaCO_3$) from the surface ocean and its dissolution at depth. Their behavior reflects the interplay of ocean circulation, respiration, and carbonate chemistry across very different timescales.

Oceanic controls on the carbonate system

The saturation state of calcium carbonate is given by

$$\Omega_{CaCO_3} = \frac{[Ca^{2+}][CO_3^{2-}]}{K^*_{sp}(T, S, P)}, \tag{3.5}$$

where K^*_{sp} is the apparent solubility product that depends on temperature, salinity, and pressure. When $\Omega_{CaCO_3} < 1$, seawater is undersaturated and $CaCO_3$ tends to dissolve; when $\Omega_{CaCO_3} > 1$, the mineral is stable and can accumulate in sediments. The depth of the lysocline marks the onset of rapid dissolution, and the CCD lies where dissolution equals supply.

Why shoaling occurs in both glacial and warming regimes?

Although both glacial deep oceans and the modern ocean warmed by anthropogenic climate change exhibit shoaling[12] of the lysocline and CCD, the underlying mechanisms and CO_2 flux directions are opposite.

- **Glacial (cooling) regime:** Enhanced biological pump efficiency (see Section 14.3.1) and sluggish ventilation lead to greater storage of respired CO_2 in the deep ocean and its flux from the *deep upward*. This raises deep-ocean Dissolved Inorganic Carbon (DIC) and carbonic acid, lowering pH and $[CO_3^{2-}]$. In this case, Ω_{CaCO_3} drops below unity, causing $CaCO_3$ to dissolve more readily and the CCD to shoal upward on a millennial time scale (*Broecker and Peng*, 1987, *Zeebe and Ridgwell*, 2011).
- **Anthropogenic (warming) regime:** The modern shoaling is driven not by respiration but by invasion of atmospheric CO_2 into surface and intermediate waters. Ocean acidification decreases pH and $[CO_3^{2-}]$, again lowering Ω_{CaCO_3}, but from the *top downward* (*Ridgwell and Zeebe*, 2005, *Boudreau et al.*, 2021). The deep ocean has not yet equilibrated, so the lysocline and CCD move upward rapidly on centennial timescales.

Timescales and feedbacks

During glacial cycles, carbonate compensation operates over 10^3–10^4 years: dissolution of $CaCO_3$ at shallower depths releases alkalinity, which eventually neutralizes the excess CO_2 and restores the CCD to greater depths. In contrast, anthropogenic ocean acidification acts over decades to centuries, far faster than the natural buffering response (*Archer and Brovkin*, 2008).

Recovery to preindustrial CCD depths will take many millennia once CO_2 emissions cease.

Conceptual summary

The apparent paradox of CCD shoaling during both cooling and warming vanishes when one distinguishes the *direction of CO_2 storage and flux*:

In glacial periods, CO_2 is trapped in the deep ocean, producing shoaling through respiratory acidification; during anthropogenic warming, CO_2 is driven into the ocean down from the atmosphere, producing shoaling through air–sea exchange. The processes are inverse, but both transiently reduce the carbonate saturation state and raise the dissolution horizons.

3.15.2 The Revelle (Buffer) Factor

The *Revelle factor*, also known as the *buffer factor* or *buffer capacity of the ocean*, quantifies the resistance of seawater to changes in atmospheric CO_2 due to the non-linear carbonate chemistry of the ocean surface layer (*Revelle and Suess*, 1957, *Sarmiento and Gruber*, 2006, *Zeebe and Ridgwell*, 2011). At constant

[12] Shoaling means the upward (toward shallower depth) movement of the lysocline.

Table 3.13: Conceptual summary of lysocline and CCD shifts in cooling and warming climate regimes.

Scenario	Dominant CO_2 flux	Deep-ocean [CO_2]	Atm [CO_2]	CCD response
Glacial (cooling)	Surface → deep (storage)	High	Low	Shoals (deep ocean acidifies; carbonate dissolves)
Deglacial (warming)	Deep → surface (release)	Low	Rising	Deepens (carbonate burial resumes)
Anthropogenic warming	Atmosphere → ocean (invasion)	Increasing (esp. intermediate)	Very high	Shoals (ocean acidification; delayed compensation)

total alkalinity (TA) and temperature, the Revelle factor is formally defined as

$$RF \doteq \frac{\frac{\Delta pCO_2}{pCO_2}}{\frac{\Delta DIC}{DIC}} \approx \frac{\partial \ln(pCO_2)}{\partial \ln(DIC)}, \tag{3.6}$$

where pCO_2 is the partial pressure of CO_2 in surface seawater and DIC is the dissolved inorganic carbon concentration (sum of aqueous CO_2, bicarbonate, and carbonate ions).

Thus, RF measures the fractional increase in pCO_2 per fractional increase in total dissolved inorganic carbon. Because most added carbon is converted to bicarbonate (HCO_3^-) and carbonate (CO_3^{2-}) rather than remaining as dissolved CO_2, the seawater buffer capacity varies strongly with temperature and alkalinity. In the present-day ocean,

$$RF \approx 8\text{–}15,$$

From Equation (3.6), it follows that lower values of the Revelle factor correspond to a *higher* seawater buffering capacity against dissolved CO_2, whereas higher values indicate a *lower* buffering capacity and greater chemical stiffness of the carbonate system. This relationship is *not* purely thermal; it's mediated through carbonate speciation and alkalinity.

As the NOAA/GLODAP data shown in Figure 3.9, demonstrate, RF tends to be **lower in warm, low-latitude waters** and **higher in cold, high-latitude waters**. This pattern arises because colder waters hold more CO_2 and have higher DIC/TA ratios, making pCO_2 more sensitive to changes in DIC and thus producing higher RF values. Conversely, warm, alkaline tropical waters have lower DIC/TA ratios and therefore exhibit smaller relative pCO_2 responses, corresponding to lower RF.

The total-scale pH, defined as $pH_T = -\log_{10}([H^+]_{free} + [HSO_4^-])$, is projected to decline from about 8.1 in the year 2000 to roughly 7.6 by 2100 under *high-emission* scenarios, which may be inaccurate for the reasons described elsewhere in this book. This decrease corresponds to an approximate *tripling* of hydrogen-ion activity in surface seawater on a global scale. Such acidification would severely *reduce* carbonate-ion availability, threatening coral reefs worldwide, and strongly impacting organisms that build calcium-carbonate shells and skeletons.

In view of Equation (3.6), a large Revelle factor, RF, indicates that a given perturbation in atmospheric CO_2 produces a relatively large change in seawater pCO_2, and therefore a smaller net uptake of additional carbon—that is, a lower buffer capacity. However, RF does not necessarily increase uniformly as the ocean acidifies. Its magnitude depends on temperature, alkalinity, and the DIC/TA ratio, and regional trends may either strengthen or weaken the oceanic CO_2 buffer depending on local biogeochemical conditions (*Egleston et al.*, 2010, *Hauck et al.*, 2020).

Therefore, RF is **not** a direct predictor of net air-sea CO_2 flux, which also depends on gas-exchange kinetics and circulation, and may change as TA, T, and mixing vary. Thus RF should be interpreted

Table 3.14: Typical surface-ocean Revelle buffer factor (RF) ranges and their interpretation (*Egleston et al.*, 2010, *Takahashi et al.*, 2014).

Region	RF	**Comment**
Warm subtropical gyres	8–9	Lower sensitivity; higher buffer capacity.
Mid-latitude waters	10–11	Intermediate response.
Cold polar regions	12–15	Higher sensitivity; lower buffer capacity.

strictly as a local thermodynamic sensitivity, not as the ocean's instantaneous ability to absorb atmospheric CO_2.

Currently on a multi-decadal time horizon, a large share of emitted CO_2 is taken up by the ocean, but full neutralization by $CaCO_3$ dissolution and silicate weathering requires 10^3–10^5 years (*Archer*, 2005, *Zeebe and Ridgwell*, 2011). Hence, a significant fraction of anthropogenic CO_2 effectively persists on millennial timescales.

In summary, as atmospheric CO_2 fugacity rises and surface seawater warms, the Revelle factor generally increases in much of the global ocean, indicating a gradual decline in the chemical buffer capacity for additional CO_2 uptake. However, the relationship is not spatially uniform: local variations in alkalinity, salinity, and circulation can partly offset or even reverse this trend in some regions.

Table 3.15: NOAA basin naming conventions in the Global Surface Ocean Acidification dataset (NCEI 0259391). "N" = Northern Hemisphere, "C" = Central/Equatorial band, "Southern" = Southern Ocean.

Basin Label	**Meaning**	**Geographic Extent (approx.)**
Arctic	Arctic Ocean	All waters north of ∼65–70°N, including the Canadian Archipelago, Barents, and Kara seas.
Pacific–N	North Pacific	North of the Equator (∼0–66°N); includes western/eastern sub-basins, Bering, and Okhotsk seas.
Atlantic–N	North Atlantic	North of the Equator (∼0–66°N); includes Gulf Stream, Caribbean, and Nordic seas.
Pacific–C	Central / Equatorial Pacific	Equatorial band (∼10°S–10°N); centered on the tropical Pacific upwelling region.
Atlantic–C	Central / Equatorial Atlantic	Equatorial belt (∼10°S–10°N); includes tropical Atlantic and Gulf of Guinea.
Indian	Indian Ocean	Extends from ∼30°N to 60°S; includes Arabian Sea, Bay of Bengal, and southern Indian sector.
Southern	Southern Ocean	Circumpolar waters south of ∼60°S, encircling Antarctica and bounded by the Antarctic Circumpolar Current (ACC).

The surface seawater temperature, DIC, Revelle factor, and pH are shown in Figure 3.9 for the oceanic regions defined in Table 3.15. Across the global ocean – despite large differences in surface temperature – the Revelle factor has generally increased since about 2010, reflecting the rise in the fugacity of atmospheric CO_2. Since preindustrial times (circa 1750), the Arctic and Southern Oceans have consistently exhibited the highest values of RF, indicative of lower buffer capacity. Projections beyond 2050, however, remain highly uncertain in the NOAA data and model ensembles.

3.15.3 Glacial–interglacial carbon cycling (past ∼800 kyr)

Ice-core records show atmospheric CO_2 oscillating between ∼180 and 280 ppm_v during Pleistocene cycles, tightly coupled to temperature via ocean circulation, the soft-tissue and carbonate pumps, sea ice, and iron

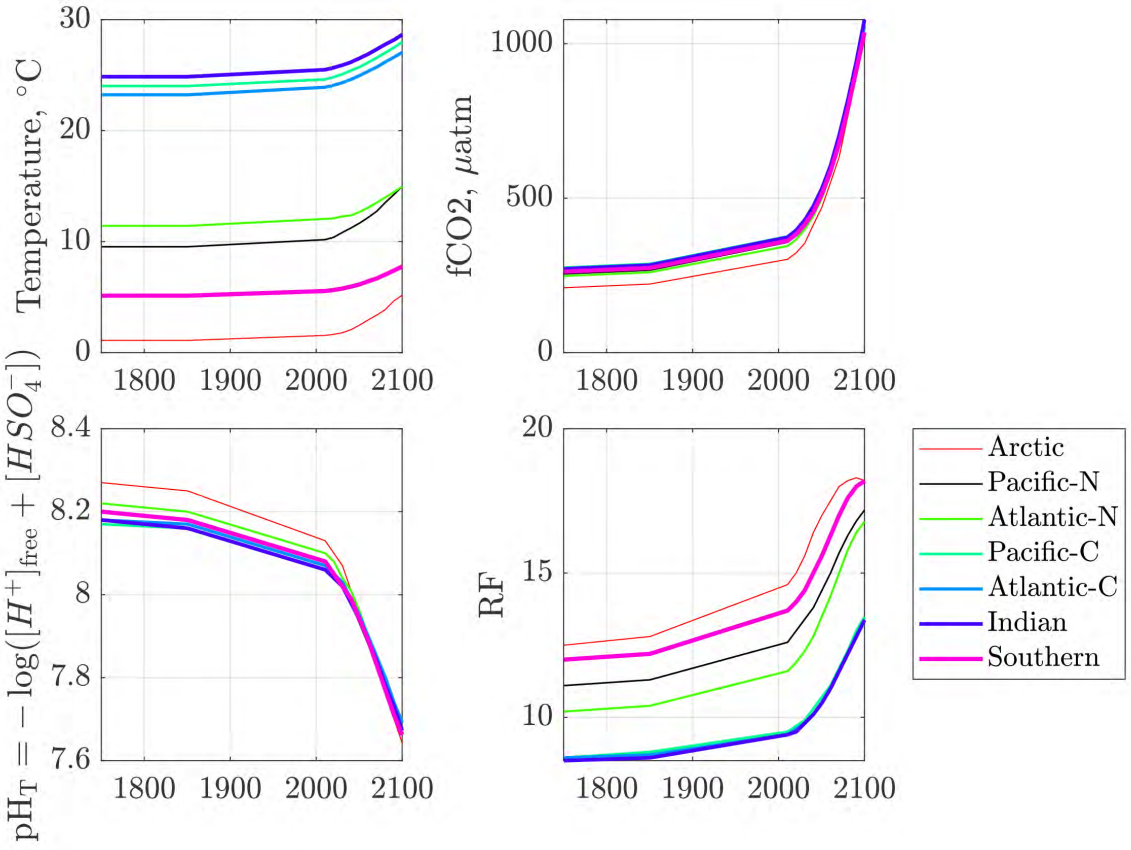

Figure 3.9: The key parameters characterizing the chemistry of surface seawater are shown. Note the abrupt changes in all of them after 2010. These trends reflect the accelerating global ocean warming and acidification driven by the rising atmospheric CO_2 concentration. Data source: NOAA, https://www.ncei.noaa.gov/data/oceans/ncei/ocads/data/0259391/.

fertilization (*Lüthi et al.*, 2008, *Petit et al.*, 1999a, *Hain et al.*, 2014). Deglacial rises in CO_2 and Antarctic temperature are phased by Southern Ocean processes and interhemispheric heat transport (*Shakun et al.*, 2012, *Hain et al.*, 2014). Carbonate compensation adjusts the lysocline/CCD over millennia, buffering alkalinity and contributing to the late deglacial CO_2 evolution (*Zeebe and Ridgwell*, 2011).

3.15.4 The geological carbon cycle (million-year scales)

On 10^6–10^7 yr horizons, the carbonate–silicate cycle sets atmospheric CO_2 via the balance of volcanic/metamorphic degassing, silicate weathering, burial of carbonates and organic carbon, and oxidative weathering of old organic matter (*Berner and Kothavala*, 2001, *Kump et al.*, 2004). Proxy syntheses (boron isotopes, alkenones, stomatal indices, paleosols) reconstruct large Cenozoic declines in CO_2 from Eocene warmth to Neogene ice ages (*Beerling and Royer*, 2011, *Foster et al.*, 2017). Extreme events—e.g., the Paleocene–Eocene Thermal Maximum (PETM; ∼56 Ma), Mesozoic Oceanic Anoxic Events, and Large Igneous Province (LIP) degassing—illustrate that rapid carbon release drives acidification, deoxygenation, and biotic stress.

Current anthropogenic release rates of CO_2 exceed known deep-time rates by an order of magnitude (*Zeebe et al.*, 2016, *Zeebe and Ridgwell*, 2011).

3.15.5 What it all means for CO_2 partitioning

- **Airborne fraction:** ∼0.46 (multi-decadal), but variable interannually (*Friedlingstein et al.*, 2025).
- **Ocean buffer:** Revelle factor ∼10 reduces fractional uptake efficiency as C_{atm} rises (*Sarmiento and Gruber*, 2006).
- **Millennial tail:** $\mathcal{O}$(10–20%) of a pulse persists >1,000 yr absent negative emissions (*Archer and Brovkin*, 2008, *Joos et al.*, 2013).
- **Glacial amplitude:** During the late Pleistocene, atmospheric CO_2 varied by about ∼100 ppm_v between glacial minima (∼180 ppm_v) and interglacial maxima (∼280 ppm_v) (*Lüthi et al.*, 2008, *Hain et al.*, 2014). This ∼100 ppm_v swing reflects the coupled response of the ocean and biosphere to orbital forcing and ice-sheet feedbacks. The dominant mechanisms include: (i) changes in ocean circulation and deep-water ventilation, which regulate the sequestration of carbon in the abyssal ocean; (ii) variations in biological nutrient utilization and export production—especially in the Southern Ocean, where enhanced iron supply during glacials increased biological pump efficiency; and (iii) carbonate compensation, the long-term adjustment of ocean alkalinity and the lysocline depth that modulates atmospheric CO_2 over millennial timescales. Together these processes determine the ∼100 ppm_v glacial amplitude observed in ice cores.

In the early 1800s, the mean atmospheric CO_2 concentration was about 280 ppm_v–essentially the interglacial maximum sustained throughout the Holocene. We are on course to *double* this value within two centuries, with most of the increase occurring in less than one. Geologically speaking, humanity is injecting a pulse of CO_2 into the atmosphere at an *unprecedented* rate–tens to hundreds of times faster than any natural carbon release recorded in the Cenozoic sediment record (*Lüthi et al.*, 2008).

3.15.6 Implications and uncertainties

Future carbon–climate feedbacks (permafrost, fire regimes, soil carbon, nutrient limitation, ocean stratification) can weaken sinks and raise the effective TCRE (transient climate response to cumulative emissions) (*Canadell et al.*, 2021, *Friedlingstein et al.*, 2006). Deep-time analogs warn that rapid carbon injections impose multi-millennial recovery and durable ocean chemical change (*Zeebe et al.*, 2016, *Archer*, 2005). In short, the Earth-climate system has been pushed by humans to an uncharted territory.

Minimal reading map

1. Contemporary budgets: (*Friedlingstein et al.*, 2025, *Canadell et al.*, 2021).
2. Ocean processes and buffering: (*Sarmiento and Gruber*, 2006, *Zeebe and Ridgwell*, 2011).
3. Land processes and feedbacks: (*Ciais et al.*, 2013, *Friedlingstein et al.*, 2006).
4. Pleistocene dynamics: (*Lüthi et al.*, 2008, *Hain et al.*, 2014, *Shakun et al.*, 2012).
5. Geological perspectives and proxies: (*Berner and Kothavala*, 2001, *Beerling and Royer*, 2011, *Foster et al.*, 2017, *Zeebe et al.*, 2016).

Chapter 4

Human population, economy and power use

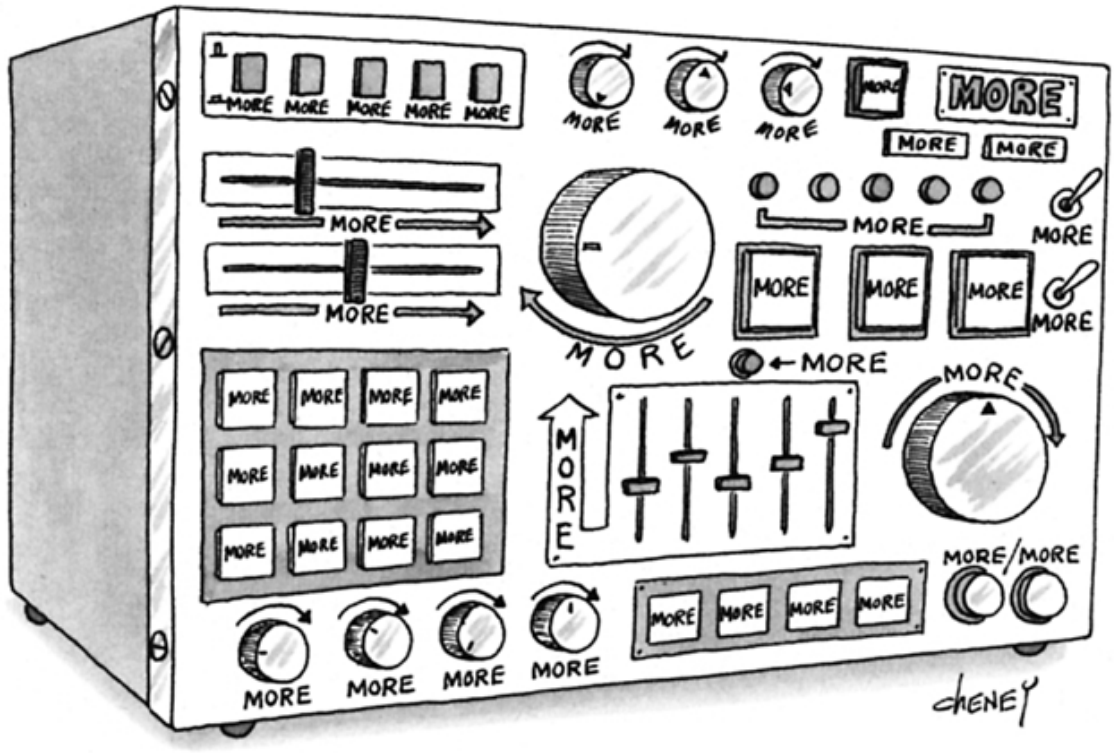

The More graphic appeared in *Mankoff and Bank* (2000), p. 63. Published with permission.

> The decadent international but individualistic capitalism in the hands of which we found ourselves after the war is not a success. It is not intelligent. It is not beautiful. It is not just. It is not virtuous. And it doesn't deliver the goods
>
> John Maynard Keynes
> *Collected Writings* (1971–80)

Close to everything that happens to humans has been determined by the amount of *free energy* (cf. Section 2.1) available to all of us. In times past, daily sunlight and its derivatives, wind, rain, floods and inundations delivered the free energy that built human civilizations. The key drivers of collapses of these civilizations (*Tainter*, 1990, *Tainter and Patzek*, 2011) have been the prolonged crop failures caused by climate change (*Fagan*, 2004), pandemics and die-off's (*Hays*, 2005), droughts, pests, soil destruction, deforestation, opportunistic invaders, and in some places earthquakes, e.g., (*Herodotus and de Sélincourt (translator)*, 1996, *Glassner*, 2004, *Guidoboni and Comastri*, 1994, *Keller and DeVecchio*, 2012). Our attempts to idealize the glorious past, the happy egalitarian hunter-gatherer bands (*Cavalli-Sforza and Cavalli-Sforza*, 1995), Tikopians (*White*, 1983), Mayas (*Hodell et al.*, 1995), Native Americans (*Cook et al.*, 2004), etc. have often been wishful idealizations. Humans have always been the ephemeral vessels struggling to propagate their immutable genes through geologic time and make sure their offspring survives. So we keep on multiplying (Figure 4.3(a)) at a frightening rate (Figure 4.3(b)).

What enabled this exponential procreation? The short answer: modern capitalism driven by vast flows of energy and energy-dependent technology. Today, we stand precariously close to a global disaster cliff. The survival of many of the eight billion people alive today depends on complex technological systems that sustain us every second. Remove this technology (or electricity) for a single day, and the cracks would immediately appear; after a week, chaos and hunger would dominate, trapping panicked and helpless populations. What happens to the modern world when electricity suddenly disappears was imagined in 1943 by René Barjavel in "Ravage." This all-time science-fiction masterpiece was translated into English (*Barjavel*, 1967) as "Ashes, Ashes," see Figure 4.1. Collectively, we accepted this Faustian bargain when we allowed the techno-human system to enframe[1] us – without most people fully comprehending the consequences. In 1954, *Heidegger* (1977) warned us about this inescapable trajectory.

Figure 4.1: Total grid failure and blackout in Spain. Fans walk through the dark gangways during a general power blackout during Day Seven of the Mutua Madrid Open at La Caja Magica on April 28, 2025 in Madrid, Spain. Spain's blackout showed a hidden flaw in high-renewable grids – when too many inverters mimic the grid's frequency, a small disturbance can trigger a rapid, system-wide collapse. Without stable, "grid-forming" (base-load coal- and gas-fired, and nuclear power plants) sources or better inverter coordination, high solar and wind penetration risks turning resilience into fragility. Sources: (*Fouda*, 2025, *The Honest Sorcerer*, 2025).

[1] Enframing is the mindset or ordering principle that forces nature, people, and resources to be viewed merely as "standing-reserve of energy" – that is, as things to be used, extracted, stored, and optimized for utilitarian purposes. It is not just about machines or devices, but also about people as objects with utility, and a way of thinking that reduces all existence to something available for control and consumption. Does this sound familiar? It should, because this definition is also a definition of modern capitalism. Heidegger was a member of NSDAP in Germany between 1933 and 1945.

4.1 Gold standard and inflation

In contrast to their parents, our adult children have experienced only prosperity and sustained economic growth, having come of age near the peak expansion of the Global Fossil Amoeba[2]. Consequently, no meaningful discussion of climate change and the necessity of economic degrowth can begin without addressing economics.

The reason is straightforward: the prevailing paradigm of *neoliberal economics*[3] is predicated on the expectation of perpetual Gross Domestic Product (GDP) growth – ideally every quarter, indefinitely.

This growth imperative mirrors the decision-making logic of approximately one billion affluent inhabitants of the Fossil Amoeba, including the author. We all reside within capitalist societies fundamentally organized around expansion. Let us begin, then, with four essential definitions.

Definition 1. Gross Domestic Product (GDP) is the total monetary value of all final goods and services produced within a country's borders during a year. GDP's annual increases lead to an unbounded exponential growth of human enterprise on the finite planet Earth.

Definition 2. A Purchasing Power Parity (PPP) dollar is a hypothetical unit of currency that equalizes the purchasing power of different countries by accounting for differences in price levels. One PPP dollar buys the same amount of goods and services in any country. PPP adjustments are commonly used by the International Monetary Fund and World Bank to compare economic indicators like GDP, income and living standards across countries more accurately than using market exchange rates, which can be distorted by speculation, inflation, or government intervention. The PPP dollar is an approximation subject to a significant uncertainty.

Definition 3. A consumer price index (CPI) measures changes in the price level of a market basket of consumer goods and services purchased by households. The CPI in the United States is defined by the Bureau of Labor Statistics as "a measure of the average change over time in the prices paid by urban consumers for a market basket of consumer goods and services. The inflation rate is calculated as the percent change in CPI from one accounting period to the next (typically month-over-month or year-over-year).

$$\text{Inflation Rate} = \frac{\text{CPI}_{\text{current}} - \text{CPI}_{\text{previous}}}{\text{CPI}_{\text{previous}}} \times 100\%$$

Definition 4. The FED, short for the Federal Reserve System, is the central bank of the United States, created in 1913 to provide the country with a safe, flexible, and stable monetary and financial system. The Fed operates through a network of 12 regional Federal Reserve Banks and is governed by the Federal Reserve Board of Governors in Washington, D.C. Fed chairmen are appointed by presidents, but their fiscal policy decisions are independent of the Executive Branch directives, at least until 2025.

The Bretton Woods Conference was held in July 1944 in Bretton Woods, New Hampshire (*Steil*, 2013). At this meeting, 44 Allied nations ratified a new global financial system after World War II (WWII). They established the International Monetary Fund (IMF) and the World Bank, and created a system of fixed exchange rates tied to the U.S. dollar, which in turn was convertible to gold. The Bretton Woods system sought to promote international economic stability, rebuild war-torn economies, and prevent competitive currency devaluations. The system lasted until 1971, when the U.S. ended dollar convertibility to gold, leading to the modern era of floating exchange rates, high inflation and stagflation.

[2]The term *Fossil Amoeba* was coined by Dr. Nate Hagens to describe the global energy and economic system powered by fossil fuels (*Hagens*, 2020).

[3]Neoliberal economics rose to prominence in the 1980s under Ronald Reagan in the United States and Margaret Thatcher in the United Kingdom. It has since shaped global policy frameworks through institutions such as the International Monetary Fund (IMF) and the World Bank.

Between 1959 and 1970, France reduced its dollar reserves, exchanging them for gold at the official exchange rate, to reduce economic influence of the US. This, along with the fiscal strain of federal expenditures on the Vietnam War and persistent balance of payments deficits, led the then US President, Richard Nixon, to end international convertibility of the dollar to gold on August 15, 1971 (the "Nixon Shock"), and subsequently all references to gold were removed ("Paper USD"), see Figure 4.2.

On August 13, 1971, President Nixon met secretly at Camp David with Federal Reserve chairman Arthur Burns, incoming Treasury Secretary John Connally, then Undersecretary for international monetary affairs, and with a future legendary Fed Chairman Paul Volcker, and other high-ranking White House and Treasury advisers. Quoting Wikipedia:

> There was great debate about what Nixon should do, but ultimately Nixon, relying heavily on the advice of the self-confident Connally, decided to break up Bretton Woods by suspending the convertibility of the dollar into gold, freezing wages and prices for 90 days to combat potential inflationary effects, and impose an import surcharge (tariffs) of 10 percent. "Connally brilliantly packaged the program not as America abandoning its commitment to the gold standard but as America taking charge. He turned the dollar's collapse, which could have appeared shameful, into a moment of hubris".

The Nixon import surcharge followed. It was authorized under the Trading with the Enemy Act of 1917, was applied broadly across all imports rather than targeting specific products. It remained in effect for approximately *four* months and was lifted in December 1971 following the Smithsonian Agreement, under which several major currencies were revalued against the US dollar. This temporary tariff formed a central component of Nixon's broader economic strategy to realign international monetary relations and protect U.S. economic interests amid growing financial instability (*Irwin*, 2011).

However, the concurrent abandonment of the gold standard contributed to the prolonged stagflation of the 1970s,resulting in a 45% cumulative inflation by 1976 (see Table 4.1). In contrast, the Trump 2 administration appears poised to inflict more severe economic damage through sustained tariffs ranging from 10–100%, with potentially far-reaching consequences for both the US and global economies.

Figure 4.2 shows the history of US CPI since January 1913 (a), and the annual inflation rate derived from it (b). In contrast, Table 4.1 lists the periods of highest inflation and highest deflation (negative inflation in a contracting economy) all the way back to the US Revolutionary War of 1777.

This interesting figure and table illustrate that

- From 1913 to 1971, the Federal Reserve gradually developed the tools and fiscal policies to dampen the wild spikes of inflation, achieving an exponential reduction in price volatility.
- In August 1971, the collapse of the Bretton Woods gold standard marked a fundamental shift in the global financial system. The Federal Reserve adapted its monetary approach, continuing to moderate inflationary swings with notable success.
- The COVID-19 pandemic emerged following a decade of massive monetary interventions triggered by the 2008 financial crisis: Quantitative Easing 1 (QE1, December 2008–March 2010) injected $2.35 trillion, followed by QE2 (November 2010–June 2011) which added an additional $600 billion.
- Between 2016 and 2020, the Trump administration stimulated the U.S. economy with approximately $1.9 trillion in corporate tax cuts (via the 2017 Tax Cuts and Jobs Act) and by lifting discretionary spending caps. In response to the COVID-19 crisis, the administration also enacted the $2.2 trillion CARES Act in March 2020, providing direct relief to individuals and businesses.
- The Biden administration followed with the $1.9 trillion American Rescue Plan Act (ARPA), signed into law on March 11, 2021. The plan provided direct payments, extended unemployment benefits, and support for businesses and state and local governments during the ongoing pandemic.
- In fiscal year 2021, the federal government spent approximately $6.8 trillion, aiming to mitigate the economic and social impacts of the pandemic and to accelerate recovery.

- Altogether, nearly $15 trillion[4] was injected into the U.S. economy over roughly 13 years. This extraordinary fiscal and monetary expansion marked the beginning of a new economic regime, associated with a sustained 9% inflation rate unfolding under the "Trump 2" administration (see the rightmost spike in the inflation rate, not seen for fifty years).
- What happens next is anybody's guess, but the news may not be happy.

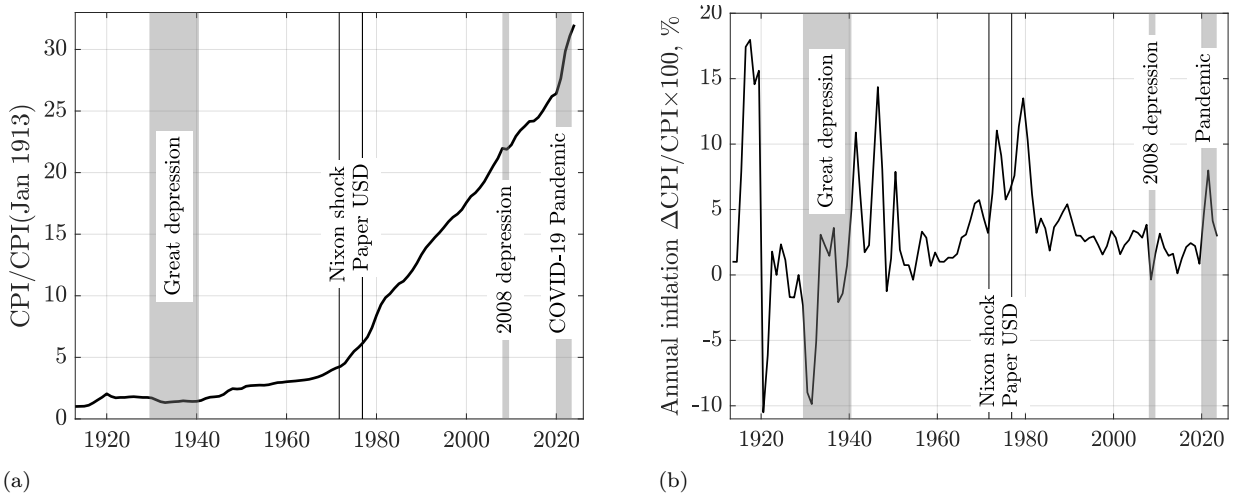

Figure 4.2: (**a**) The US CPI (Consumer Price Index) normalized by its initial published value for January 1913, so that it starts from one. Simply put, what cost you $1 in January 1913, would cost you $32 in December 2024. Note that the Great Depression of October 1929 – 1940 would have had a lesser impact on the CPI than the Depression of August 2008. But in 2008, the US Fed injected trillions of USD into the economy and the US inflated its way out of the crisis. The two vertical solid lines are the "Nixon shock" (left) and October 1976, when all references to gold were removed from the definition of the dollar. Between 1981 and 2109, the average slope of the CPI curve was 0.45/yr. (**b**) Annual inflation. Source: US Bureau of Labor Statistics, last accessed 04/27/2025.

4.2 Population and its exosomatic metabolism

Earth's carrying capacity, K, is a simple idea with far-reaching, complex consequences for the planetary system, as detailed in Appendix A. This appendix may be skipped on a first reading, or if the mathematical background feels insufficient. Those who continue, however, will find that carrying capacity is intricately interwoven with all aspects of the Earth system, like a spider's web of subtle connections—many of them not well recognized even thirty years ago by leading researchers, who were too often constrained by quasi-religious anthropomorphism.

Subtle changes in the Earth-system function may result in large an non-unique changes in carrying capacity of the planet.

For example, the jury is still out on how severely the 1976 bifurcation in global land and sea surface temperature anomalies will affect life on Earth and its carrying capacity, see Chapter 10 for details. This bifurcation occurred when the key climate control parameter—cumulative CO_2 emissions—crossed a critical threshold, after which global land areas began to warm more rapidly than the ocean surface, radiating additional heat to the cold Universe. Because of net downward convective heat transport from the ocean surface, seawater warms more slowly than land, which can only conduct heat away from its surface. Consequently, however, the global ocean absorbs the vast majority (about 90%) of the excess solar energy that remains out of equilibrium.

[4]For comparison, the 2011 U.S. nominal GDP was approximately $15.5 trillion. Therefore, an extra one year's GDP was plowed into the US economy over roughly a decade, igniting high inflation.

Table 4.1: Major inflationary and deflationary periods in US history

Period	Type	Peak Rate	Primary Cause(s)
1777–1779	Inflation	>300% annually	Revolutionary War; overprinting of Continental currency
1861–1864	Inflation	∼50% annually	Civil War; fiat "greenback" issuance to finance war spending
1917–1920	Inflation	∼20% annually	World War I mobilization; demand surge and postwar boom
1920–1921	Deflation	–10.5% (1921)	Post-WWI bust; Fed tightening; falling commodity prices
1929–1933	Deflation	–10.3% (1932)	Great Depression; the 1930 Smoot-Hawley 40% tariff on 20,000 goods; bank failures; collapse of economy
1946–1947	Inflation	14.4% (1947)	Post-WWII supply shortages and demand surge
1974–1975	Inflation	12.3% (1974)	Wage-price spiral & stagflation after abandonment of the gold standard; OPEC oil embargo
1979–1981	Inflation	13.5% (1980)	Second oil shock; loose 1970s monetary policy
2008–2009	Disinflation	∼0% (2009)	Global financial crisis; collapse in demand and credit
2021–2022	Inflation	9.1% (2022)	COVID-19 recovery; supply chain shocks; stimulus policies

Humans behave as "K-optimizers" – who increase population, resource consumption, and energy use up to – and temporarily above – the limits of Earth's carrying capacity. A striking early example of how the intensified agriculture and Industrial Revolution triggered population growth is Britain. In preindustrial times, approximately 80% of the British population lived in rural areas *Allen* (2017). By 1850, when reliable temperature records began, this ratio had reversed, and the population had surged, as illustrated in Figure 4.4(a).

Post-1650, the English Agricultural Revolution increased food production by both expanding arable land by 30% and industrializing farming practices. This agricultural transformation laid the groundwork for the coal-powered Industrial Revolution that accelerated after 1750. For instance, wheat production alone rose by 75% between 1700 and 1800.

Today, a mean global human averaged over 8 billion people is far from being a hard-physically working slave, as clarified in *Fajzel et al.* (2023), in their Fig. 1. These leisurely average lifestyles are possible only because of the gusher of mostly fossil energy powering the global human enterprise. This must end, and Plan B, i.e., the various Green Transitions (*Bolson et al.*, 2022a, 2023), are mired in systemic difficulties (Figure 4.1) and unrealistic expectations, while the world is careening irreversibly away from sustainability *Patzek* (2004), *Bolson et al.* (2022b).

It is not easy to calculate a human equivalent of a continuous, mostly fossil fuel- and biomass-based "laborer," whose work would replace the daily stay of primary power[5] an average earthling consumes continuously, currently ∼2,100 W/person, see Figure 4.5(a).

According to the US Occupational Safety and Health Administration (OSHA), a normal work shift is no more than 8 consecutive hours in a day, with each shift separated by at least 8 hours of rest. A normal workweek is 5 such work days. Let's assume that per week a human can work at most 90 hours, while

[5]Primary power is primary energy per unit time.

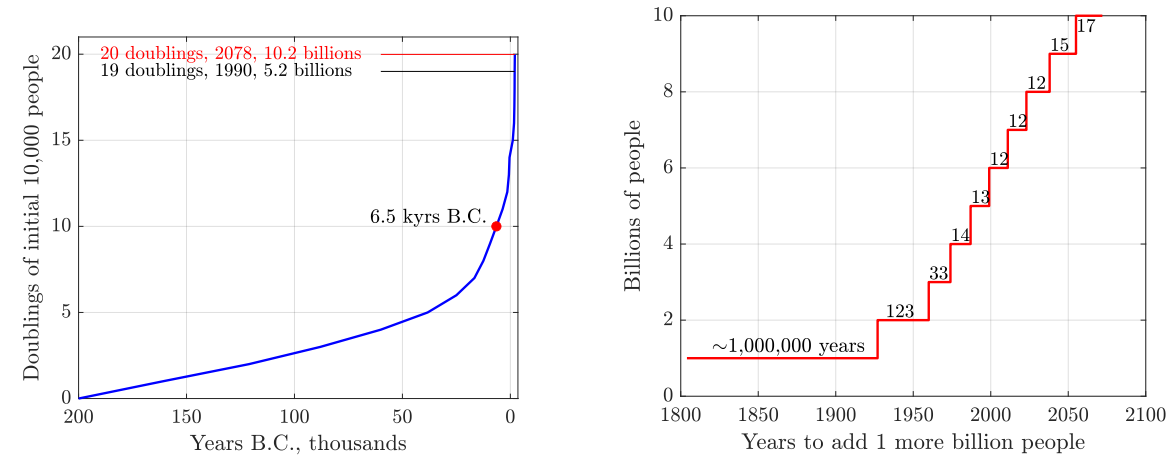

(a) (b)

Figure 4.3: The power of exponential growth is illustrated through the successive doublings (2^0, 2^1, 2^2, ...) of a human cohort initially numbering 10,000 individuals around 200,000 years BCE. The timing of these doublings is aligned with widely accepted reconstructions of historical human population sizes. Notably, between 900,000 and 800,000 years BCE, humans nearly went extinct, with only about 1,000 individuals surviving in Africa (*Hu et al.*, 2023). For the next 600,000 years, the global human population remained small, averaging only ∼27,000 individuals at any given time. Thus, a cohort of 10,000 people living 200,000 years ago could plausibly have represented nearly all of anatomically modern humanity. If such a cohort were to double 20 times, it would reach approximately 10.2 billion people by the year 2078. *There will not be a 21st doubling.* **(b)** Years required to add each successive billion people. Sources: Early population data from Rex Weyler, 2017, private communication; and UN Dept. of Economic and Social Affairs, Population Division, accessed 08/30/2023. Calculations by Patzek.

eating, resting and sleeping during the remaining $168 - 90 = 78$ hours. Thus, on a continuous 24/7 basis, the human labor efficiency is $90/168 = 0.54$.

Table 4.2 lists average power developed by humans when they engage in sustained physical activities. To obtain a continuous "primary power (PP) laborer" equivalent, we average normal manual work of a man and woman is used: $0.5 \times (145 + 113) \times 0.54 = 129$ W$\times 0.54 \approx 70$ W, continuously. Thus, the 2.1kW/capita continuously in Figure 4.5(a) is equivalent to some 30 human laborers, and fossil fuels effectively usher into existence around $8 \times 30 = 240$ billion person-equivalents, making it certain that the humans alive today overconsume the planet's resources.

As a consistency check, the UK minimum for a working man is 2500 kcal/day = 10465 kJ/day (121 W) in food uptake. A miner might need twice this rate, cf. *Anonymous* (2021). An average man needs energy at the basic metabolic rate of 7000 kJ per 24 hours (∼85 W) for a 30-year-old, 70 kg man, when he is lying down with an empty stomach. The average leisure power for a man doing nothing productive is an additional ∼2400kJ per day. Thus, a man engaged only in light leisure activities would use about 9400 kJ/day (109 W). Our equivalent fossil laborer must eat 24/7 and requires power at rest. This power in food must be produced by farmers with a certain efficiency and prepared by service workers, who are also helped by the primary power laborers.

Another consistency check is provided by the number of slaves per household in ancient Rome. This number varied significantly with wealth and social status. While modest households might have had two or three $(2 - 3)$ slaves, affluent Roman families, particularly those of the senatorial class, often possessed hundreds. Some elite households reportedly owned up to 500 slaves, and emperors could command as many as 20,000 (*History Learning*, n.d.). Thus, a male slave working hard physically could develop an average 24/7 power of 100 W (between a brick layer and miner in Table 4.2). Somewhat arbitrarily, we assume that there is a constant number of slaves (6) providing ample food and services for an affluent idle family and for each slave performing all other work at 100 W continuously. Thus we have two alternative

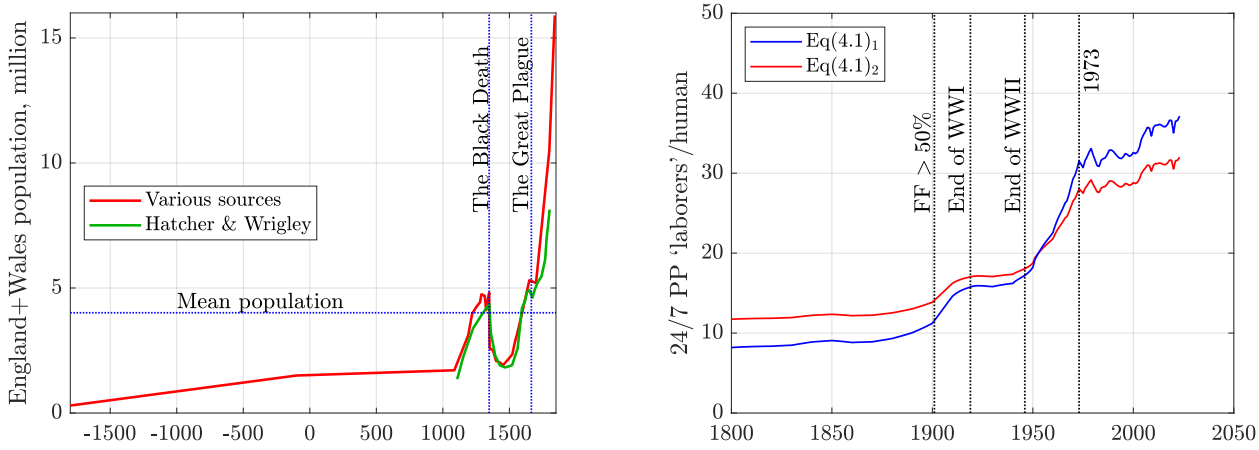

(a) (b)

Figure 4.4: (**a**) Estimated population of England and Wales over the Common Era. According to the *Domesday Book* – a manuscript record of the *Great Survey* of much of England and parts of Wales, completed in 1086 at the order of King William – the population at that time was fewer than 2 million people. By 1850, the population had increased to at least 16 million. This dramatic growth was driven by the expanding use of fossil energy and the technological advancements that accompanied it. (**b**) The number of primary power-equivalent 'laborers' (PP_E) available per human, as defined by Equation (4.1). Sources: Various, *Tucker* (1963), *Hatcher* (1983), *Wrigley and Schofield* (1989). Calculations by Patzek.

definitions of the number of primary power equivalents PP_E of a slave, whom we will call a 'laborer' from now on:

$$PP_E = \begin{cases} \dfrac{\text{Primary power/person available to society at time t}}{\text{Average continuous power of one person (70 W)}} & \text{or} \\ \\ \dfrac{\text{Primary power/person available to society at time t}}{\text{100 W}} + 6 \end{cases} \tag{4.1}$$

Both alternatives are similar, as illustrated in Figure 4.4(b). In subsequent calculations we will use the second alternative.

Table 4.2: The daily energy generated by a human performing different types of work.

Type of Work	Example	Men		Women	
		kJ /day	W	kJ /day	W
Rest	Lying down		81		
Light Work-Sitting	Accountant	9600	111	8400	97
Normal Manual Work	Production Engineer	12500	145	9800	113
Moderate bodily work	Bricklayer	15000	174	12000	139
Heavy manual work	Miner	19500	226		
Extreme effort	Lumberjack	20500	237		

4.2.1 Consumer Price Index (CPI)

The normalized consumer price index is shown in Figure 4.2. It increased 33-fold between Januray 1913 and December 2024. The post-WWII global economic expansion resulted in an acceleration of the world GDP after 1950. But, after abandoning the gold standard in August 1971, the US CPI started increasing

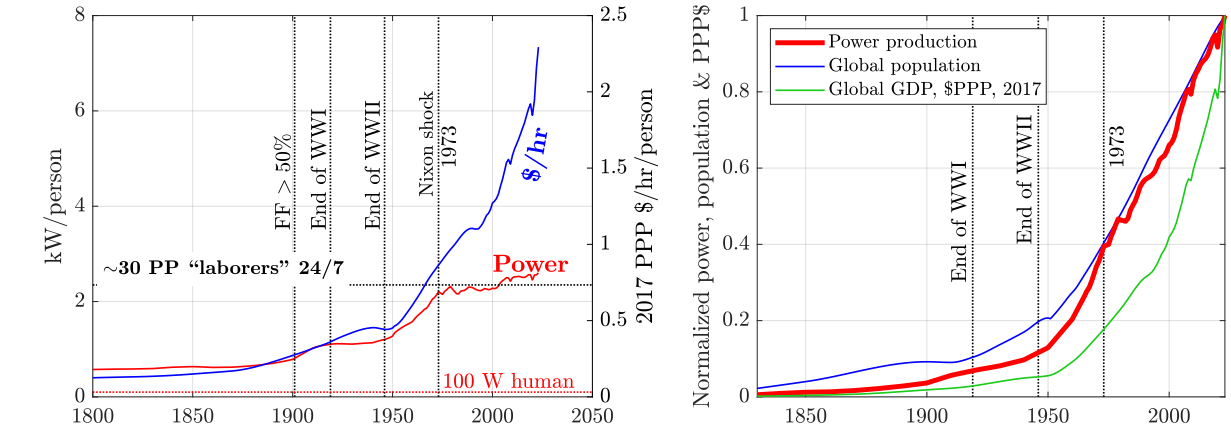

(a) (b)

Figure 4.5: **(a)** Global per capita power consumption in kW, and gross domestic product (GDP) generation power in Purchasing Power Parity (PPP) constant 2017 US dollars per hour per person. Both quantities grew more less in unison until 1973, and diverged afterwards. Oil and gas production peaked in the US in 1971 and 1972, followed by production decline and reservoir repressuring with peripheral waterfloods in the Middle East, and the Arab embargo after the Yom Kippur war in 1973. The growth rates of production of oil and lease condensate and natural gas have been markedly lower post-1973. **(b)** The total primary energy/time (PP), population and GDP histories are normalized so that they are zero in 1830 and 1 in 2023. Human population and global GDP have been following consumption of primary power, with the population leading until 1973 and the GDP always lagging. Sources: EIA, BP, UN Dept. of Economic and Social Affairs, Population Division and World Bank, accessed 08/30/2023; analysis by Patzek.

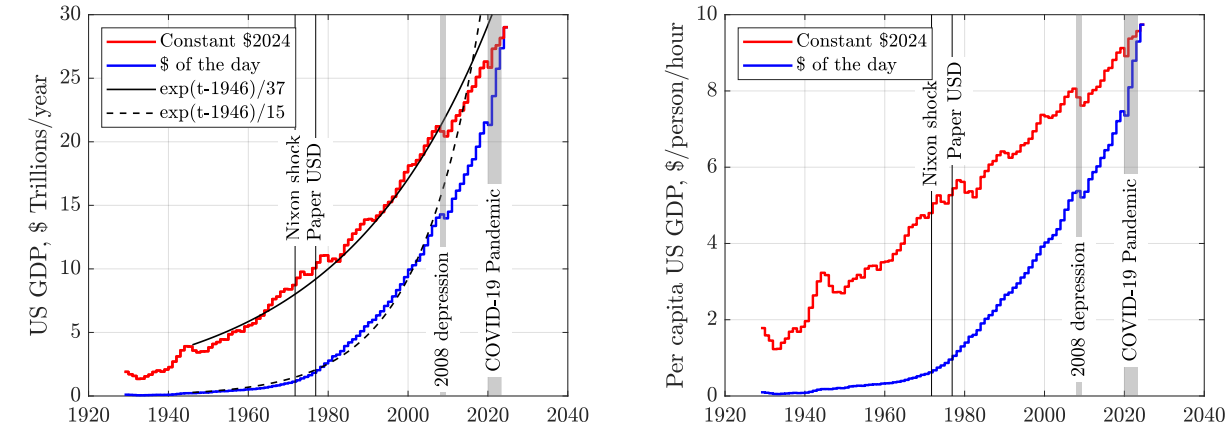

(a) (b)

Figure 4.6: History of US Gross Domestic Product (GDP) in constant ("chained") US dollars in 2024, and in dollars of the day. **(a)**. GDP in constant 2024 dollars increases exponentially at 2.7%/yr, and in dollars of the day at 6.5%/yr. **(b)**. GDP per capita in US dollars per person per hour. Sources US Bureau of Labor Statistics, and UN Dept. of Economic and Social Affairs, Population Division and World Bank, accessed 04/27/2025; analysis by Patzek.

at a significantly higher rate. Between 1971 and 1977, the United States CPI increased by 47%. The effect of floating currency exchange rates and high inflation spilled over to the global GDP post-1971, as

is clearly seen in Figure 4.5(a).

In this book, we use the CPI (Consumer Price Index) to adjust the prices of commodities – such as metals, petroleum, and natural gas – for inflation. Although the GDP deflator could also serve this purpose, the two inflation indices are practically equivalent for long-term analysis. As shown in Figure 4.2, since 1985 the CPI has been influenced by the Federal Reserve System ("Fed") through its control of credit and interest rates, maintaining an average inflation rate of approximately 3.3% per year since 1945. A notable deviation occurred during the 2008 financial crisis, when the downturn caused both GDP trends in Figure 4.6(a) to fall below their respective exponential growth trajectories. The surge in inflation during the COVID-19 pandemic was driven by several trillion dollars of quantitative easing (QE). While this wave of inflation may have politically benefited President Trump, it was not sufficient to restore GDP growth to its pre-crisis exponential path.

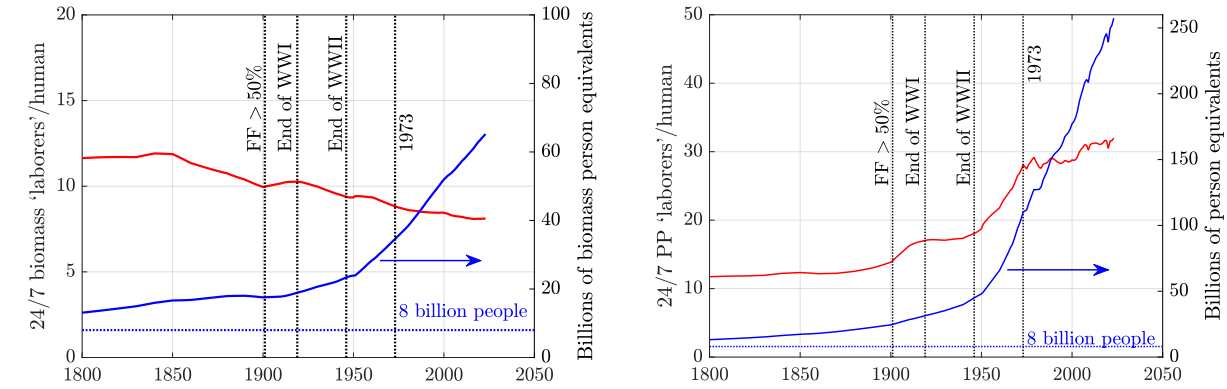

(a) (b)

Figure 4.7: The power from biomass and total primary power (PP) per capita are divided by the average power of a human (100 W), plus roughly six human-equivalents that provide food and other services for every primary power-laborer and themselves. This number of laborers is then multiplied by the corresponding human population, giving the number of person-equivalents on the Earth. **(a)** Biomass burning has always been an important source of primary power for humans. In 1800, there were 12 biomass laborers per human and by 2023 this number decreased to 8. But human population and quantity of biomass burned grew explosively over these 123 years, rendering 13 and 65 billion of biomass person-equivalents, respectively. **(b)** Since 1900, the 24/7 primary power 'laborers' (Equation $(4.1)_2$) working for an average human have been mostly fossil fuel-based. By 2024, this number was ∼260 billion person-equivalents. How can this be sustainable? Sources: EIA, OWID, UN Dept. of Economic and Social Affairs, Population Division, accessed 01/15/2025. Calculations by Patzek.

4.3 Primary energy that drives our civilization

Over the last 250 years, we have *augmented* the mostly current sunlight products (firewood, charcoal, draught animal and human food, and some coal) (*Patzek*, 2004) with the geological ones, mostly fossil fuel (FF) accumulations, and everything changed (*Marder et al.*, 2016, *Patzek*, 2007). Primary energy (PE) from burning these fossil fuels has accelerated societal metabolism by two or three orders of magnitude in the following sequence: more free energy from fossil fuels → more humans → more economic activity (GDP) → more technology → more free energy in an ever-tightening spiral, see Figure 4.5(a). What used to take 1,000 or 10,000 years, takes now a decade or 100 years, while we have overshot badly (*Catton*, 1980b), are destroying the ecosphere (*Patzek*, 2004, 2007), and are rapidly approaching practical exhaustion of resources (*Hubbert*, 1962, 1969) at current production rates. Close to all countries are already woefully unsustainable (*Bolson et al.*, 2022b).

A simple calculation shows that by 2023, each of the 8 billion living humans (cf. Figure 4.3) had ∼8 and ∼32, respectively, biomass- and total primary power-"laborers," who served us 24/7, see Figure 4.7.

Therefore, humanity exploded to 260 billion person-equivalents, and the US alone was 46 billion person-equivalents, see Figure 4.7(b). Our impact on the environment has increased many-fold (*Bradshaw et al.*, 2021) and the ever-growing global techno-civilization *must* implode within decades (*Patzek*, 2007, *Tainter and Patzek*, 2011, *Trust et al.*, 2025).

The main thesis of this work is that current climate change is a direct, immediate effect of the ecological overshoot cause (*Catton*, 1980b) that in turn is proportional to the consumption of primary energy per unit time or primary power (PP) ∼cubed, see Figure 4.8(a).

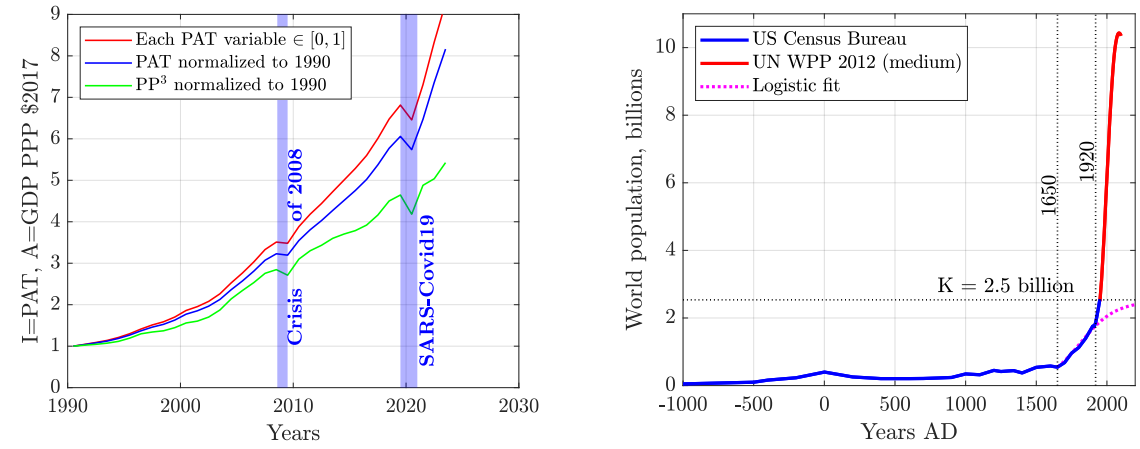

(a) (b)

Figure 4.8: **(a)** Human impact I = Population × Affluence × Technology (*Ehrlich and Holdren*, 1971). All impact models are normalized by their mid-1990 outcomes. Sources: EIA, OWID, UN Dept. of Economic and Social Affairs, Population Division, accessed 01/15/2025. **(b)** The historical and projected world population. Note the explosive population growth since 1650, the onset of Agricultural Revolution (the left vertical line), and its fastest stage since 1920, the start of large-scale production of ammonia fertilizer by the Haber-Bosch process (the right vertical line). Imagine yourself standing on the population high in 2050 and looking down. At the onset of Industrial Revolution (ca. 1760), the world population was about 1 billion people. In 2023, it was 8 times higher. The rate of population growth slowed down early in the Industrial Revolution because of the abhorrent living conditions of working poor, lack of nutrition, and meager wages. Source: US Census Bureau. Calculations by Patzek.

If one multiplies the three normalized curves in Figure 4.5(a) to represent the population (P), affluence (GDP in Purchasing Power Parity (PPP) constant USD), and technology (T, a function of total PE), and normalizes the result by its mid-1990 value to factor-out the coefficients of proportionality, one obtains the top red curve in Figure 4.8(a). The multiplication of the raw curves in Figure 4.5(a) gives the middle (blue) curve. The realization that since the year 1900, the global civilization has been driven exclusively by the ever-increasing fossil fuel primary power yields the bottom green curve. The conclusion is that by this measure, humans have increased their impacts on the planet by a factor of $5-8$ since 1990, and by a factor $10-20$ since 1977, when the original paper was published by *Ehrlich and Holdren* (1971).

Before we describe our global primary energy and fossil fuel energy production and forecast, and link the ensuing global heating to them, let's ask the following question: What might be a maximum ecologically permissible size of human population on the Earth?

Figure 4.8(b) shows an estimate of the human population between the years 1000 BCE and 2100 CE (the red curve). For the next 80 years, we use the middle-fertility population projection from the United Nations' Dept. of Economic and Social Affairs. This projection peaks at a little over 10.8 billion people.

We recognize that by 1650, the modern industrial revolution in Britain had started. Also the South and Central Americas were eventually repeopled by Spaniards, Portuguese and $10-11$ million slaves in the

150 years after the conquest and erasing the local population. Portuguese Brazil received by far the largest share – about 4.5 to 5 million slaves (roughly $40-45\%$ of the total Atlantic slave trade). Spanish colonies in the Caribbean, Central America, and northern South America (e.g., Cuba, Santo Domingo Colombia and Venezuela) imported around $2-2.5$ million slaves. French, Dutch, and British Caribbean colonies (e.g., Haiti, Jamaica, Barbados and Suriname) imported about 3 to 3.5 million slaves, with most flowing into what would be considered Central or northern South America (*Eltis and Richardson*, 2010, *Klein*, 2010).

North America imported many fewer slaves directly, about $388{,}000-450{,}000$ in total over the same period. But, between 1650 and 1920, about 35 to 40 million people migrated voluntarily to North America in three big waves, with some 34 million migrants arriving between 1820 and 1920 (*Daniels*, 2002). In comparison, between 1650 and 1920, South and Central America received only about 12 to 15 million voluntary migrants, mainly Europeans and Asians.

With the massive population redistribution and modernization, the global agricultural production could sustain a much faster growth of human population. Table 4.3 shows that the period 1650-1920 marks the transition from traditional subsistence farming to commercial, science-driven, mechanized agriculture, enabling the global population boom and industrial society we live-in today. We extrapolate this period of the highest pre-WWII population growth by fitting a logistic growth curve of the following form:

$$\text{Population} = \frac{K}{1+\exp\left((t-t^*)/\tau\right)} \tag{4.2}$$

where the carrying capacity of the planet is $K = 2.5$ billion people, the characteristic time of exponential growth is $\tau = 125$ years, and the year of peak population growth rate is $t^* = 1810$. All these coefficient values fit the population data between 1650 and 1920.

Table 4.3: Transformation of Global Agricultural Output (1650–1920)

Period	**Key Developments and Significance**
1650–1750	Second[1] agricultural revolution in England: expansion of crop rotation systems, selective breeding, improved plowing, and land privatization and fencing-off. Agricultural productivity per acre and worker increases.
1750–1850	Spread of agricultural innovations across Europe and North America. Rising food security supports population growth, lowers mortality, and frees labor for the industrial revolution.
1850–1920	Third agricultural revolution: mechanization (reapers, threshers, tractors), expansion of railroads, global trade of crops, chemical fertilizers (e.g., guano, early synthetics), and scientific breeding programs. Agricultural output per capita increases sharply.

[1]First agricultural revolution evolved in England through millennia. Crop rotation and types, and farm layout were pretty much the same in 1050 and in 1750. But common land, previously open to communal use by peasants for grazing, farming and gathering, was privatized, fenced-off ("enclosed"), and assigned to individual owners.

If humans were the rational, intelligent beings in charge of their fateful decisions (but we *never* were), human population might have resembled the projection in Figure 4.8(b), which shows that a reasonable logistic (*Verhulst*, 1838) extrapolation of world's population beyond the year 1920 might have resulted in 2.5 billion people today and beyond. However, there are several different constraints on an optimal[6] size of human population:

- 2.5 billion people on the Earth would require the 1850-1900 life expectancy, lifestyle, slavery, and conflicts.
- Average life expectancy in the year 1900 was 32 years (35-40 years in the 1920s), and in 2022 it was 71-73 years (*Roser and Ortiz-Ospina*, 2023).

[6]An optimum population size is not the same as the maximum number of people that could be packed onto Earth at one time. The maximum would have to be housed and nurtured by methods analogous to those used to rise cage chickens or pigs in metal crates, and the process would inevitably reduce the planet's long-term carrying capacity (*Daily et al.*, 1994).

- $2.5 \times 32/73 \sim 1$ billion people at today's life expectancy.
- World GDP per capita was 2450 PPP 2017 USD in 1900, vs. 18,880 in 2022 (*World Bank and OWID*, 2023) (a factor of ∼8 increase). Assume optimistically that progress of technology reduced the overall human impact on the Earth to a factor of 2, and we are down to 0.5 billion people.
- Assume that organic agriculture similar to that in the 1900s, might feed sustainably 4 times more or 2 billion people (1.65 billion people lived in 1900, consuming fossil fuel power of 24 billion person-equivalents, see Figure 4.7(b)).
- But we do *not* want to have wars, strife and pandemics like WWI and Spanish Flu, so the result is likely **∼1-1.5 billion people**, similar to the estimate in *Daily et al.* (1994). The latter estimate was obtained from ecological and primary power use arguments developed here in much more detail.
- Thus, optimistically, we have overshot the carrying capacity of the Earth by a factor of **5-8** by burning biomass and fossil fuels. The true human impact on the living Earth might be substantially higher, as indicated by Figure 4.7(b).

With the number of humans growing exponentially and demanding ever more resources from the finite Earth, a sustainable global economy is becoming elusive fast (*Bolson et al.*, 2022b). In summary, according to the sustainability definition in *Patzek* (2004), humanity could be only weakly unsustainable if we kept our numbers at or below 1.5 billion people, and each human used primary energy from biomass and fossil fuel as in the year 1900. *After* the deep cuts in fossil fuel power consumption, renewables[7] will become relevant *again* (*Bolson et al.*, 2022a, 2023).

4.4 Historic fossil fuel production

Figure 4.9 shows how many days per year Britain (a) and the world (b) *could* run on each source of primary energy. For example, by 1817, Britain depended on coal 300 days per year, as much as the world depended on all fossil fuels during my lifetime (1951.9-now). Conversely, in 1850, Britain (and to a much lesser degree the Continental Europe and US) depended on coal for 336 days/yr, and the world only for 27 days/yr. By the year 1900, the world exceeded 50% dependence on fossil fuels, see Figure 4.9(b).

One of the common misunderstandings is that humans began to rely on fossil energy only after 1750, the start of "Industrial Revolution." It turns out, however, that the easy-to-dig, outcropping coal was widely used for the last 6,000 years as a fuel for cooking, heating, smelting, pottery, etc. Coal was burned everywhere, starting in China (*Liang*, 2006), in Britain during Bronze Age and Roman times (*Durand*, 1993), and in many other countries (*Freese*, 2004), including North America (*Adams*, 1970).

Similarly, bitumen and oil & gas seeps were used pretty much everywhere for thousands of years (*Speight*, 2007); in China for 3000 years (*Needham*, 1964), in ancient Greece and Rome (*Heaton*, 2005), and in ancient Americas (*Langenkamp*, 2002).

We are sentenced to live on the Earth that is not increasing in size and gross primary productivity (*Patzek*, 2007). Compared with the radius of our planet of about 6,400 kilometers, we live on a very thin skin or "membrane," between 11 kilometers below sea level (the Mariana Trench in the Pacific or the deepest oil and gas wells) and 11 kilometers above (jet flights). Top soil, which gives us grain, fruit, wood, fiber and meat, is usually several meters thick, but often much less. This delicate membrane on which we live supports everything we do and if we damage it sufficiently, it won't.

But never mind the constraints imposed by the living Earth. Once humans found plentiful coal, crude oil and natural gas accumulations and vastly improved technologies of producing these fossil fuels (Figure 4.11-Figure 4.12(a)), their ever-higher consumption propelled exponentially the number of living people, and the global gross domestic product (GDP) these people generated each year (recall Figure 4.5).

Please notice that the exponentially growing production of coal, crude oil and natural gas went each through 10 doublings. The 11th doubling will *never* happen for any of them, because we are already

[7] A more precise description of "renewables" was proposed by my Spanish friend and coauthor of a paper relevant in this context (*Bolson et al.*, 2022a), Mr. Pedro Prieto: "Non-renewable systems for capturing renewable power flows."

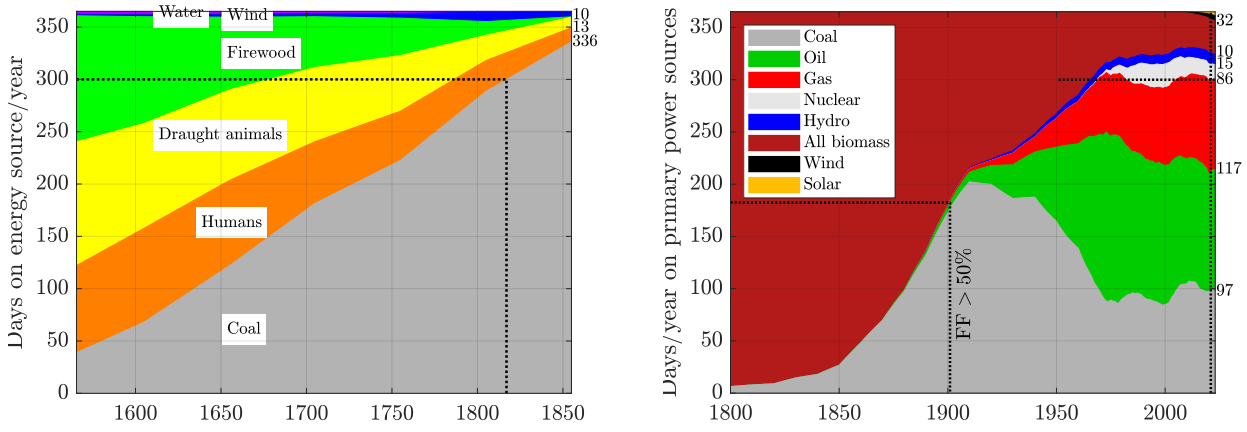

(a) (b)

Figure 4.9: Days per year on each primary power source for Britain **(a)** and the world **(b)**. The data from *Wrigley* (2016) were converted to days per year on a given primary energy source in Britain since 1565. The two horizontal lines at 300 days/year, denote Britain's dependence on coal by 1817 and world's dependence on fossil fuel since 1951. The vertical line on the right in the onset of the SARS-CoV-2 virus pandemic. Other sources: EIA, OWID, accessed 01/21/2025. Calculations by Patzek.

probing the resource limits. Please also notice that all human civilizations have been built on burning biomass and fossil fuels, see Figure 4.9 and Figure 4.7.

In modern times, the amount of primary energy from burning fossil fuels exceeded that from burning biomass only in 1900, see Figure 4.9(b). Contributions from nuclear reactors, water dams, solar PV and wind turbines have been barely noticeable (the upper right corner of Figure 4.9(b)). In 2023, thermal power sources (fossil fuels, biomass and uranium) delivered $347/365 = 95\%$ of primary power, while hydro, PV and wind delivered 18 days of primary power of 5%.

Figure 4.12(b) shows that in 2023 the world was a 19 TW primary power machine, which delivered ∼5 TW ($\sim 25 - 30\%$) as mechanical and electrical power, and ∼14 TW ($\sim 70 - 75\%$) as heat power (process heat, inefficiencies, thermal losses) (*IEA*, 2023a, *Smil*, 2017). Nota bene, the IEA and BP have been using the 'substitution method' for the primary power from PV arrays and wind turbines, while from the definition of primary energy and thermodynamics, EIA and I have been using the 'direct method' (more explanation soon).

This complex story about physical impossibility of transitioning **up** from thermal sources of power to some magic mixture of 'green technologies' is not just my say-so, compare Figure 4.10 with this quotation from *Tooze* (2025):

> What if [*'Industrial Revolution,' TWP*] and 'three energy transitions' [*biomass → coal → oil & gas → nuclear+hydro+PV+wind, TWP*] are a fairy tale dressed up in a business suit, a PR story or, worse, a mirage, an ideological snare, a dangerously seductive illusion? That wouldn't mean that the transition to green energy is impossible, just that it is unsupported by historical experience. Indeed, it runs counter to it. When we look more closely at the historical record, it shows not a neat sequence of energy transitions, but the accumulation of *ever more and different types of energy* [*italics by TWP*]. Economic growth has been based not on progressive shifts from one source of energy to the next, but on their interdependent agglomeration. Using more coal involved using more wood, using more oil consumed more coal, and [*using more PV and wind consumes more fossil fuels+uranium+hydro, TWP*]. An honest account of energy history would conclude not that [*multidecadal, TWP*] energy transitions were a regular feature of the past, but that what we are attempting - the deliberate exit from and suppression of the energetic mainstays of our modern way of life - is without precedent.

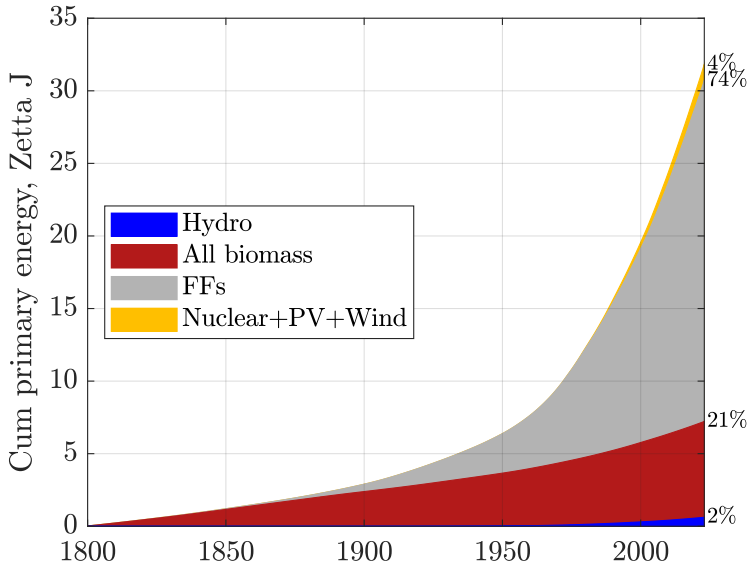

Figure 4.10: Global cumulative primary energy production by source. Please notice that in 2023, biomass and fossil fuels delivered 95% of the primary energy that drove our civilization for the last two centuries. The contribution of each energy source was rounded to an integer, and the results do not add to 100%. Sources: EIA, OWID, *Clark and Jacks* (2007), Patzek, accessed 01/12/2025.

Because we have not had an honest discussion of the cosmic shift of economic priorities necessary to *downsize* global primary power mix away from thermal sources, we now have a 'social energy transition': old political order → Trump's administration in the US and fascists gaining power in a growing number of other countries. Because we live in a post-truth era, let me add a disclaimer: I am a chemical engineer and physicist, who spent some of his life working for the oil & gas industry, was introduced to the internal Shell reports by M. King Hubbert in 1983, and has been worrying about global supply of energy for humanity since 1985.

To restate the obvious,[8] the so-called "green renewables" are not truly renewable. Rather, they are – or might become – the following:

- Periodically rebuildable machines that convert ambient energy flows (sunlight, wind, gravity) into usable forms such as electricity, mechanical work, or heat. According to a corollary to the First Law of Thermodynamics, energy is conserved and it cannot be "renewed."
- Potential components of a more sustainable future society – though not of our current one, which remains structurally dependent on fossil fuels.
- Industrial machines that we construct, deploy, and maintain using fossil fuels; crucially, they do not replace fossil fuels but supplement their use.

Finally, it is important to emphasize that we cannot construct and deploy these "renewables" relying solely on the energy output of their prior generation. I say this as a long-time owner and operator of three large ground-mounted photovoltaic arrays.

As explained in the Supporting Online Materials to *Bolson et al.* (2022a), my wife and I are a net electricity generator, use only rainwater, recycle almost all waste streams from our 15-acre property, and drive a hybrid car. Even though our 01/2025 electricity bill was -$1,663, we are completely embedded in the fossil power grid in Austin, TX, gorge on fossil fuels as food delivered by refrigerated diesel trucks to giant air-conditioned stores, and buy occasionally fossil fuel-imbued consumer products. As statistical Americans, each one of us "eats" primary power like a 40 ton male sperm whale (Figure 2.2), who

[8] Paraphrasing our article (*Bolson et al.*, 2022a) and a recent comment made by my wise friend, Dr. D.J. White.

consumes daily 3% of his body weight as squid, fish, etc. (*Clarke*, 1980), and metabolizes them at a rate of 100× that of a human. Cutting back on current primary power binge will be very painful and require long-term preparation of civil societies.

In summary, humans have been a flame burning through nature since times immemorial:

> Burning of undergrowth extended grazing lands for game. It is now recognized that many supposedly wild landscapes inhabited down to historic times by hunter gatherers – the North American prairies and the Australian outback, for instance – were shaped by deliberate fire-setting. "Man," wrote the great anthropologist and writer Loren Eiseley, "is himself a flame. He has burned through the animal world and appropriated its vast stores of protein for his own." *Wright* (2005), *Man is a flame* (Page 30).

Before, we were many separate fires burning different places at different times. By today, all these smaller fires have merged into a giant global conflagration, our *technosphere* (*Heidegger*, 1977), 260 billion burning man-equivalents strong.

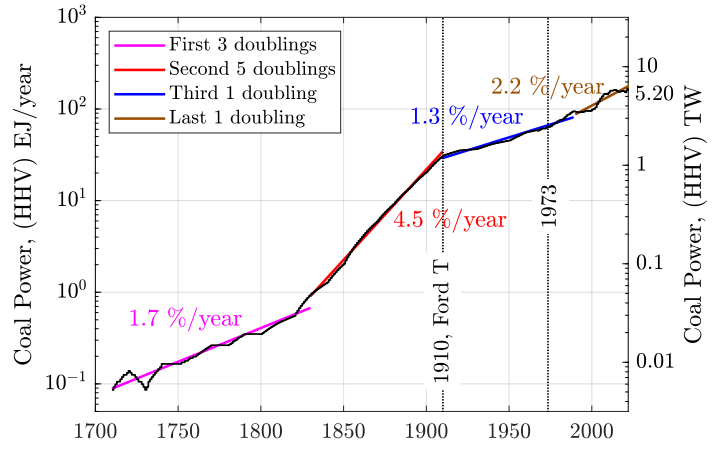

(a)

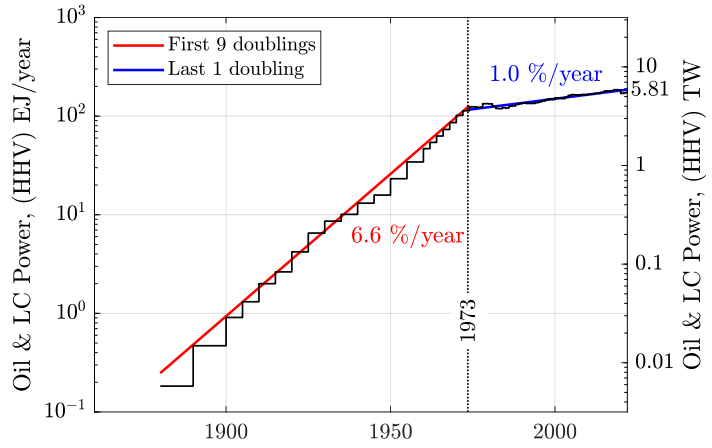

(b)

Figure 4.11: **(a)** The global rate of coal production underwent 10 doublings between 1710 and 2023, reaching 5.20 TW. Mass production of Ford T that required gasoline started in 1913 (*Ford*, 1913), one year before WWI. In 1919, a few months after the Armistice, Citroën became the first European carmaker to implement Ford-style mass production (*Citroën*, 1921). During WWI, trucks, tanks and planes became common, and the rate of expansion of coal production decreased. **(b)** The global rate of oil and lease condensate production also underwent 10 doublings between 1880 and 2023, reaching 5.81 TW. Sources: EIA, OWID, *Clark and Jacks* (2007), Patzek, accessed 11/11/2024.

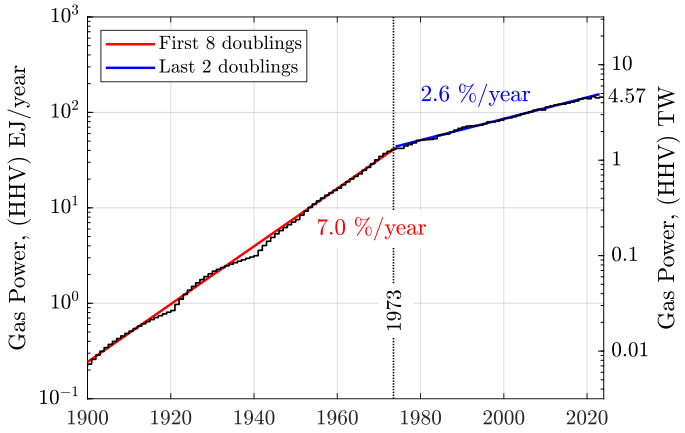

(a)

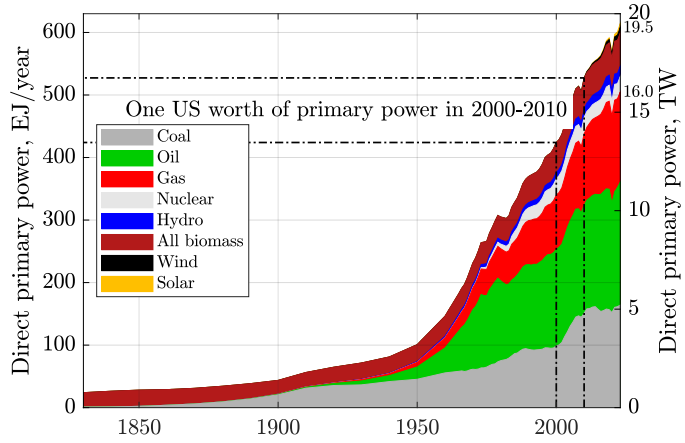

(b)

Figure 4.12: **(a)** The global rate of natural gas production underwent 10 doublings between 1900 and 2023. **(b)** Direct primary power developed by each source of primary energy since 1830. Today the human world is a giant 19 TW machine. "Direct" means that no division by average fossil fuel power plant efficiency (0.40) to convert PV and wind electricity into a "fossil fuel equivalent" is performed, essentially multiplying their output by a factor of $1/0.40 = 2.5$. Primary power is primary power, and without these accounting gimmicks solar PV and wind are almost invisible. Sources: EIA, OWID, *Clark and Jacks* (2007), Patzek, accessed 11/11/2024.

Chapter 5

Carbon dioxide and methane concentrations in the atmosphere now and in recent past

Air over Beijing.
Photo by T.W. Patzek, August 1995

We are reluctant to recognize our limitations in relation to space, to time, and to matter and energy
Nicholas Georgescu-Roegen
The Entropy Law and the Economic Process (1971, p. 6)

5.1 What are you going to learn?

In this chapter, we will examine nearly two centuries of atmospheric CO_2 and CH_4 concentrations – measured continuously at the Mauna Loa Observatory since 1974, and reconstructed over millennia from Arctic and Antarctic ice cores. These records reveal that an approximately constant fraction of cumulative anthropogenic carbon emissions remains in the atmosphere. As a result, the recent rapid increases in atmospheric CO_2 and CH_4 concentrations directly reflect the accelerating combustion of fossil fuels since 1850, alongside long-term contributions from agriculture, biomass burning, and deforestation dating back over 6,000 years.

We compare these anthropogenic emissions with two ancient natural events: the Chicxulub asteroid impact at the end of the Cretaceous, and the massive carbon release during the Paleocene-Eocene Thermal Maximum (PETM), likely driven by supervolcanism and methane hydrate destabilization.

Finally, we analyze the global, land, and ocean surface temperature anomalies since 1850 as a function of cumulative CO_2 emissions – the dominant driver of contemporary climate change – highlighting the distinct climate bifurcation that began around 1976.

5.2 Why is this important?

The central premise of this book is that cumulative emissions of greenhouse gases – primarily CO_2, and to a lesser but growing extent, CH_4 – are the principal drivers of global temperature increase. Atmospheric concentrations of these gases are determined by the total amount emitted over time and their respective atmospheric lifetimes. This chapter presents key empirical evidence supporting this relationship and compares the observed trends with those projected in the Representative Concentration Pathway (RCP) scenarios.

5.3 Preliminaries

In May–June 2025, the seasonal mixed-atmosphere molar concentration of CO_2 measured at NOAA's Mauna Loa Observatory in Figure 5.1 exceeded **430 ppm**$_v$, see Figure 5.2(a). When I was born in 1951, this concentration was approximately 310 ppm$_v$. Thus, during my lifetime, the atmospheric CO_2 concentration on planet Earth has increased by

$$\frac{430 - 310}{310} \approx 39\%.$$

This rate of increase is geologically instantaneous and likely unprecedented since the Paleocene–Eocene Thermal Maximum (PETM), approximately 56 million years ago. During the PETM, global temperatures were up to $5 - 8$ °C higher than in the late Paleocene, and as much as 12 °C higher than today (see Chapter 9 for details).

Figure 5.1 shows the Mauna Loa Observatory in Hawaii. The carbon dioxide and methane concentration data from Mauna Loa constitute the longest record of direct measurements of these greenhouse gases in the atmosphere. They were started by C. David Keeling of the Scripps Institution of Oceanography in March of 1958 at a facility of the National Oceanic and Atmospheric Administration (NOAA) (*Keeling et al.*, 1976). NOAA started its own CO_2 measurements in May of 1974, and they have run in parallel with those made by Scripps since then (*Thoning et al.*, 1989). In 2025, the Mauna Loa facility may be shut down because of deep budget cuts at NOAA.

In short, the best and longest CO_2 and CH_4 concentration data set in existence has been funded by the US government. Similar comments can be made about most other measurements related to climate change, especially the satellite measurements since 1960 onwards. Most countries do not measure global climate change or hide the data. The notable examples are China, Russia, India, the Middle Eastern countries, etc. The European Union is now very active in the collection of climate data, see, e.g., their Copernicus Climate Data Service.

Figure 5.1: The Mauna Loa Global Monitoring Observatory (MLO) on the Big Island of Hawaii. It is located on the north flank of the Mauna Loa Volcano at 3397 meters ASL. The observatory is a premier atmospheric research facility that has been continuously monitoring and collecting data related to atmospheric change since the 1950s. The observatory protrudes through the strong marine temperature inversion layer present in the region, which separates the more polluted lower portions of the atmosphere from the much cleaner free troposphere. The undisturbed air, remote location, and minimal influences of vegetation and human activity at MLO are ideal for monitoring constituents in the atmosphere that cause climate change.

We measure trace greenhouse gas concentrations in **parts per million (or per billion or trillion) by volume (ppm_v or ppb_v or ppt_v)** because they are:

1. **Direct:** The volume fraction of a dilute gas in a gaseous mixture measures directly the number of molecules of that gas per total number of gas molecules in the mixture. For example, one part per million by volume (1 ppm_v) of CO_2 in air means that, on average, one out of every million gas molecules is a CO_2 molecule. This makes volume fraction a natural and accurate way to compare the relative abundances of trace gases such as CO_2, CH_4, NO_x, and SO_x in the atmosphere.
2. **Standard:** Atmospheric gas analyzers – such as infrared sensors and gas chromatographs at Mauna Loa – detect gas concentrations based on volume fractions rather than mass, making ppm_v the standard output unit.
3. **Robust:** Volume mixing ratios remain nearly constant despite changes in pressure and temperature, unlike mass-based measures, which vary with air density.
4. **Transparent:** Reporting trace gas concentrations in ppm_v enables straightforward, consistent comparisons over time, space, and among different greenhouse gases.

5.4 CO_2 and CH_4 concentrations in recent atmosphere

Figure 5.2 shows that the December 2024 mixed-atmosphere CO_2 concentration was 425.4 ppm_v, compared with 419.0 ppm_v in December 2022. Similarly, the methane concentration increased to 1938.1 ppb_v from 1931.0 ppb_v over the same time interval.

Seven and a half parts per million by volume (ppm_v) of CO_2 per two years may not seem like much, but even this small increase drives a measurable rise in global temperature. It takes only a slight shift in the average temperature to cause the frequency of extreme events (Black Swans) to explode

Table 5.1: Methane Global Warming Potential (GWP) over different time horizons, relative to CO_2

Source	GWP (20 yr)	GWP (100 yr)	GWP (500 yr)
IPCC AR4 (2007, incl. climate-carbon feedbacks)	72	25	7.6
IPCC AR5 (2013, incl. feedbacks)	84	28	7.6
IPCC AR6 (2021, incl. feedbacks)	83.3	29.8	–

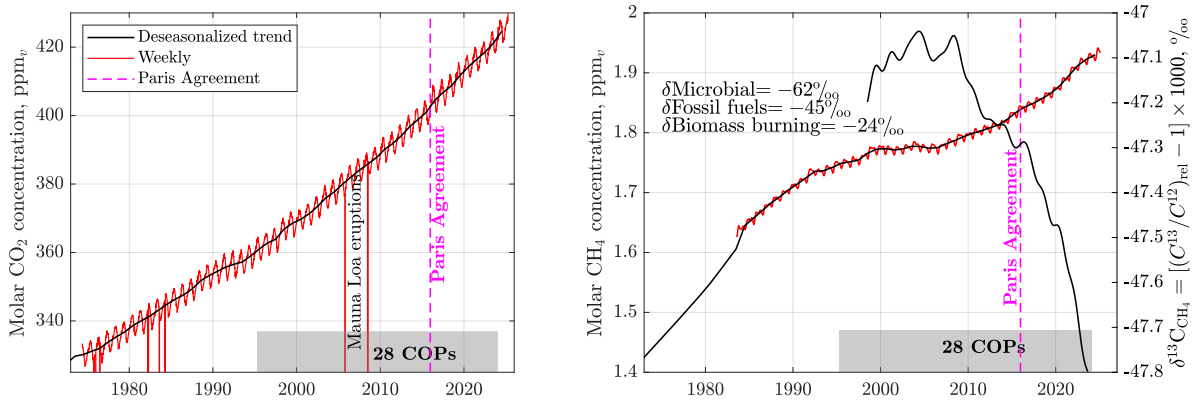

(a) (b)

Figure 5.2: **(a)** The weekly average values of mixed-atmosphere molar concentration of CO_2 and their trend. **(b)** Weekly average values of molar concentration of methane and their trend. The carbon isotopic composition of atmospheric CH_4 ($\delta^{13}C_{CH_4}$) is a powerful tool because different CH_4 sources have distinctive $\delta^{13}C_{CH_4}$ signatures (*Michel et al.*, 2024) (the right axis). Current unprecedented growth of methane concentration to almost 2 ppm_v or $2 \times 29.8 \approx 60$ ppm_v of $CO_{2,eq}$ seems to have a growing microbial component (up to 20% of the weighted average) caused by global climate change, and agriculture and land use change. The main component (∼80%) are industrial methane emissions, especially from oil and gas fields, and processing facilities. Data source: Mauna Loa, (*Lan et al.*, 2025a,b); El Niño Southern Oscillation (ENSO): Wikipedia.

– exactly what we have been observing across the Northern Hemisphere (*Tollefson*, 2023), with no signs of it abating.

Similarly, seven parts per billion of methane per two years is equivalent to adding $(7 \times 29.8)/1000 = 0.2$ ppm_v of CO_2 over a 100-year time-frame, and 0.6 ppm_v of $CO_{2,eq}$ over the next 20 years, see the AR6 recommendation (*Arias et al.*, 2021) in Table 5.1.

The annual rate of increase in the mixed-atmosphere molar concentration of CO_2 is shown in Figure 5.3(a). This rate reached its highest-ever value in early 2024. Notably, the annual increases in CO_2 concentration exhibit a near-linear trend from 1960 to 2025, accelerating at an average rate of approximately 30 $ppb_v\,yr^{-2}$. If the current business-as-usual (BAU) trajectory continues for the next 25 years, we can expect the average annual increase in atmospheric CO_2 concentration in the year 2050 to reach:

$$0.6 + 0.030 \times (2050 - 1960) = 3.3 \text{ ppb}_v\,\text{yr}^{-1},$$

which is 5.5 times greater than the rate observed in 1960.

Also shown in the figure are the 28 United Nations Conferences of the Parties (COPs), during which numerous pledges were made but rarely honored. In fact, it could be argued that emissions sometimes spiked in the weeks preceding certain COP meetings. This spiking was particularly pronounced in the lead-up to the first three COPs.

Currently, the two largest CO_2 emitters – China by far, followed by India – show no signs of slowing their expansion of coal-fired electricity generation (see Figure 5.4). In 2022, coal combustion alone accounted for approximately 15 Gt $CO_2\,yr^{-1}$, or about 40% of global fossil fuel emissions (*IEA*, 2023b).

If the annual rate of growth of CO_2 emissions is linear at 30 ppb_v per year squared, then the cumulative emissions trend must follow a quadratic trajectory. Figure 5.3(b) presents the observed mixed-atmosphere CO_2 concentrations from 1850 to 2022. Beginning in 1980, this trend is extrapolated forward using a parabolic fit through the year 2100. If this trajectory persists, we estimate with 95% confidence that by 2100, the global atmospheric CO_2 concentration will lie between 697 and 730 ppm_v, with a most likely value of 720 ppm_v.

This projection will serve as the high-emissions case in our evaluation of future global temperature increases. For comparison, Berkeley Earth projects a business-as-usual atmospheric CO_2 concentration of approximately 790 ppm_v by 2100.

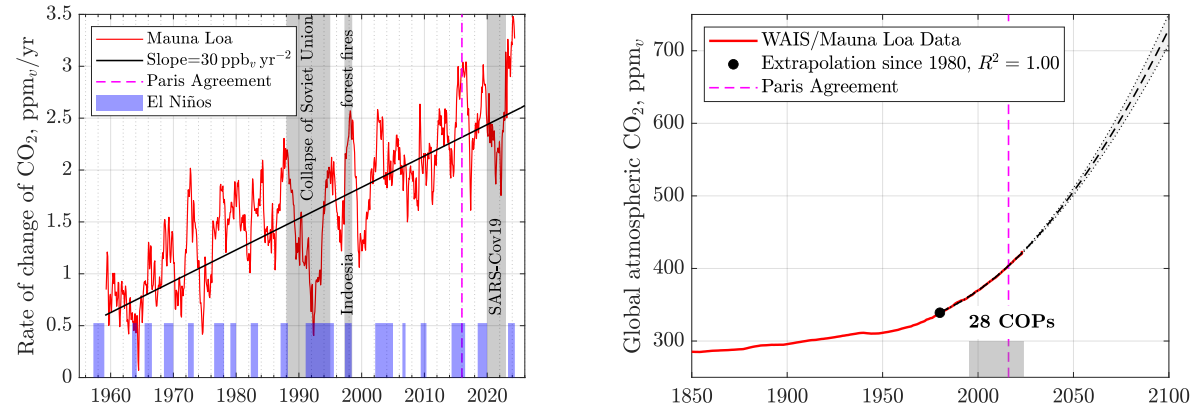

(a) (b)

Figure 5.3: **(a)** Annual increases of atmospheric CO_2 concentration. Notice that the 28 COP meetings have had zero effect on the average annual acceleration of increase of atmospheric CO_2 at (30 $ppb_v\,(yr)^{-2}$). **(b)** Mixed atmosphere CO_2 concentration since 1850. The pre-1900 global CO_2 concentrations in the atmosphere were estimated from the West Antarctic Ice Sheet ice cores, see *Ahn et al.* (2012), *Etheridge et al.* (1996). The quadratic extrapolation curve fits the CO_2 data perfectly between 1980 and 2023 and reaches 720 ppm_v by the year 2100, an increase of 300 ppm_v relative to June 2023. Also shown is the 95% confidence interval for the curve fit. If nothing changes, we are 95% certain that the predicted CO_2 concentrations will be between 697 and 733 ppm_v in the year 2100. But if a lot more coal is used to generate electricity, the likely CO_2 concentration might exceed $800-850$ ppm_v by 2100. Sources: Combined Scripps and NOAA CO_2 data, the Conference of the Parties (COP) dates from UN, calculations by Patzek.

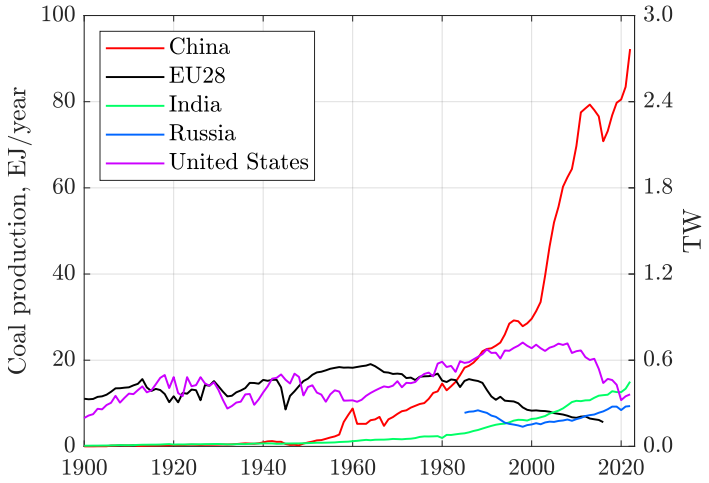

Figure 5.4: Coal production by country expressed in common energy units, because different coals have different heating values per unit mass and densities. Notice that China produces over five times more coal than any of the countries and entities in the plot. In fact, China has exceeded our own prediction of their peak coal production in ∼2011 (*Patzek and Croft*, 2010), remembering that truthfulness of Chinese coal production data reporting was questionable at times. Sometimes, the overburden rock would pass as coal. In 2022, China permitted more coal power plants than any other time in the last seven years, according to a new report released this week. "It's the equivalent of about two new coal power plants per week. The report by energy data organizations, Global Energy Monitor and the Centre for Research on Energy and Clean Air, finds the country quadrupled the amount of new coal power approvals in 2022 compared to 2021." Data sources: Energy Institute Statistical Review of World Energy (*Anonymous*, 2023b), (*Anonymous*, 2023a), and NPR.

5.5 Recent CO_2 emissions in geologic perspective

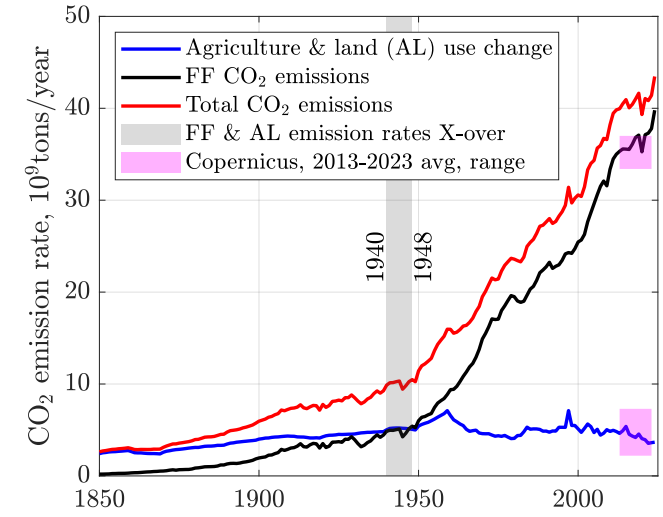

(a)

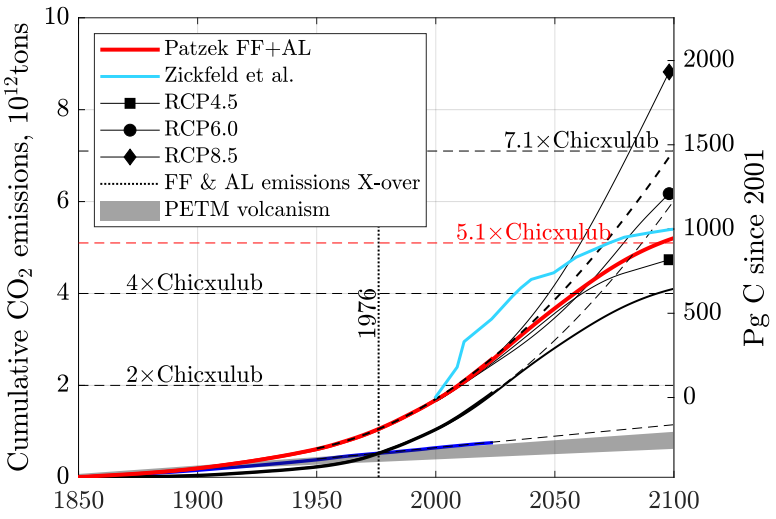

(b)

Figure 5.5: **(a)** CO_2 emissions rate from agriculture and land use change (AL) and fossil fuels (FF) since 1850. Notice that the substantial AL emissions rate is almost constant and provides the background CO_2 level in the atmosphere. **(b)** Cumulative CO_2 emissions from agriculture and land use change and fossil fuels since 1850. The Paleocene-Eocene Thermal Maximum (PETM) emissions range from 0.625 to 1 Tt C $(\text{kyr})^{-1}$. The extrapolation of FF emissions is either quadratic (the black dashed line "720 ppm_v scenario"), or it follows from our FF production model (the red "Patzek's 562 ppm_v scenario" both explained in Chapter 6). Notice that up to the year 2050, the red curve's trajectory is very close to the representative Concentration Pathway RCP4.5 (*Meinshausen et al.*, 2011) (black square), while RCP6.0 shoots up after 2060 (black circle). The most aggressive emissions scenario in Fig. 1 in *Zickfeld et al.* (2009) (blue curve) is far ahead of Patzek's scenario, despite similar cumulative total emissions of ∼1000 Pg C since 2001. Data sources: (*Anonymous*, 2023a) and Copernicus (*Friedlingstein et al.*, 2023). Calculations by Patzek.

Figure 5.5 shows CO_2 emissions from agriculture & land use change (AL) and from fossil fuels (FF) since 1850. First we note that the rate of emissions from FF began crossing those from AL only in 1940-1948.

The cumulative FF emissions crossed those of AL in 1976, the year that has special significance in the history of global heating. In 2023, *we* injected into the atmosphere 39.5 billion tons (Gt) of FF CO_2 per year (11 peta grams (Pg) C/yr), and 4 Gt/yr (1.1 Pg C/yr) of CO_2 from AL. The cumulative CO_2 emissions since 1850 have been 1,810 Gt (494 Pg C) from FF and 750 Gt (205 Pg C) from AL.

Figure 5.5(b) compares our realistic FF+AL scenario, as well as a simple quadratic extrapolation of cumulative total emissions to-date (the 720 ppm_v scenario) with IPCC's representative concentration pathways RCP4.5 (intermediate stabilization), 6 (higher stabilization), and 8.5 (worst-case scenario), and a simulation study by *Zickfeld et al.* (2009). RCPs and SSPs (Shared Socioeconomic Pathways) are both frameworks used by IPCC for climate modeling and impact assessments.

RCPs appeared first (*Meinshausen et al.*, 2011), and were incorporated in the IPCC's Fifth Assessment Report (AR5) (*Core Writing Team et al.*, 2014). SSPs were developed in the late 2010s to complement RCPs, and were integrated into the Sixth Assessment Report (AR6) by IPCC that had three (I-III) Working Group Contributions (WGCs) *Masson-Delmotte et al.* (2021), *IPCC* (2022b), *Shukla et al.* (2022) and the Synthesis Report (SYR) *Core Writing Team et al.* (2023).

The most aggressive emissions scenario from the Global Climate Model (GCM) used in *Zickfeld et al.* (2009) (the blue curves in their Fig. 1 and here) starts at an impossibly high rate, but ends at the level of cumulative total emissions similar to our scenario. We include it in our comparisons to show that (1) the global temperature anomaly depends only on the final value of cumulative total emissions, but not on the particular rates of FF production, and (2) a multiple-carbon reservoir model predicts emitted carbon partitioning into the atmosphere that is almost identical with our instantaneous (zero-delay time), simple partitioning model employed here.

To demonstrate how much human emissions have impacted the biosphere, we compare first recent CO_2 emissions with those at the Cretaceous-Paleogene (K-Pg) boundary, 66.043 ± 0.011 Ma (million years before present). This iridium-rich K–Pg boundary chronicles a massive global extinction event caused by the impact of the Chicxulub asteroid on the Yucatán peninsula (*Morgan et al.*, 1997). The star-like adiabatic compression of the impact evaporated and decomposed a huge volume of the pierced carbonate and gypsum *Yang et al.* (1996) strata:

$$\begin{aligned} \text{Limestone: } CaCO_3 &\rightarrow CaO + CO_2\uparrow \;\; 0.3 - 2 \times 10^{11} \text{ tons C} \\ \text{Anhydride: } CaSO_4 &\rightarrow CaO + SO_3\uparrow \;\; 0.5 - 2 \times 10^{11} \text{ tons S} \end{aligned} \tag{5.1}$$

The CO_2 from limestone was then 0.73×10^{12} tons ≈ 1 Tt. Other estimates of CO_2 release are $2 - 100$ Tt, with the upper limit equal to 10 times the atmospheric CO_2 mass at the time (*Agrinier et al.*, 2001). Thus, our conservative unit of human emissions is 1 Chicxulub $\doteq$ 1 Tt CO_2. If current emission trend continued to be quadratic (but it cannot), humans would have produced 7 Chicxulubs worth of CO_2 emissions by the year 2100. The likely Patzek's FF+AL scenario yields 5 Chicxulub equivalents, making humans equivalent to a slow-motion super-asteroid. The original Chicxulub asteroid was the lead cause of the extinction of approximately $75 - 80\%$ of all life on the Earth. Will we be even more destructive to the biosphere?

Second, we compare recent CO_2 emissions with the violent volcanism during the first ~20 ka of the < 200 ka-long Paleocene-Eocene Thermal Maximum (PETM) ~56 Ma (*Röhl et al.*, 2007, *McInerney and Wing*, 2011b). Teratons of carbon were released into the ocean-atmosphere system with induced changes in the carbon cycle, climate, ocean chemistry, and marine and continental ecosystems. The global temperature increased by another 5-8°C. The main source of carbon was thermogenic methane (oxidized to CO_2 in a geologic blink of an eye). Injection of magma into organic-rich sediments would have caused the explosive release of thermogenic methane from the Cretaceous-Paleocene mudstone volcanoes in the North Atlantic, but four other sources are also mentioned (*McInerney and Wing*, 2011b). The initial carbon release at the PETM onset occurred over at least 4,000 yrs (*Zeebe et al.*, 2016). Using estimates of 2.5 - 4.5 Tt C for the initial carbon release, the maximum sustained PETM carbon release rate was therefore 0.6 - 1.1 Gt C yr^{-1}. These estimates of carbon emissions during PETM (or CO_2 emissions after they are multiplied by $44/12 \approx 3.7$) are shown as the gray shaded area in Figure 5.5(b). As we can see, the highest cumulative PETM carbon emission estimates are equal to those of AL alone.

Agriculture and land-use-change have been the dominant uninterrupted source of carbon injection into the atmosphere for the last 6 thousand years, generating an almost constant $pCO_2 \approx 278$ ppm_v by 1850, see

Section 3.15.5 and Figure 5.6(a). The current FF emissions of 11 pG C yr^{-1} are one order of magnitude larger. We conclude that the present anthropogenic carbon release rate is unparalleled during the Cenozoic Era (last 66 Ma).

5.6 How much of emitted CO_2 remains in the atmosphere?

Since 1950, the historical cumulative emissions in Figure 5.5(b) have been extrapolated quadratically to the year 2100, reaching the astronomical 7×10^{12} tons or 7 Tt. This is our "720 ppm_v" scenario, similar to but increasingly behind the SSP3-7.0, see Figure 6.1. In contrast, our FF+AL scenario yields $4+1=5$ Tt of cumulative emissions. The quasi-linear dependence of pCO_2 in the atmosphere on cumulative total emissions, and with it – via the unequilibrated incremental radiative forcing – ΔT, the global air temperature anomaly, is established by a convolution integral:

$$\Delta c_a(t) \doteq c(t) - c(-\infty) = \int_{-\infty}^{+\infty} [f(t_{\max}, \tau) + r(\tau)] g(t-\tau, \tau) \mathrm{d}\tau \tag{5.2}$$

where Δc_a is the increment of molar concentration, c, of CO_2 in the atmosphere, $r(\tau)$ is the rate of total CO_2 emissions at time τ, $g(t-\tau, \tau)$ is the convolution kernel that governs the fraction of the emitted CO_2 which remains in the air given the past (the "memory function"), and $f(t_{\max}, \tau)$ is the pCO_2 relaxation function, $f > 0$ after net injection of CO_2 has ceased ($r(t > t_{\max}) = 0$), and is zero otherwise.

A simplified analytic theory behind the translation of Eq.(5.2) into ΔT was developed by *Matthews et al.* (2009) and MacDougall et al. in a series of brilliant papers (*MacDougall et al.*, 2013, *MacDougall and Friedlingstein*, 2015, *MacDougall*, 2016, 2017) as TCRE (transient climate response to cumulative CO_2 emissions metric or our ΔT per unit mass of cumulative CO_2 emissions). Focusing on GCMs (or Earth System Models), *MacDougall* (2016) stated that "The [TCRE] metric was developed once researchers noticed that the cumulative CO_2 versus temperature change curve [*inverting the cause and effect, TWP*] was nearly linear for almost all Earth system model output."

Formally

$$\begin{aligned} \mathrm{TCRE}(t) &= \frac{\Delta T(t)}{E(t)} = \frac{\Delta T}{\Delta c_a} \frac{\Delta c_a}{E} \\ E(t) &= \int_{-\infty}^{t} r(\tau) \mathrm{d}\tau \end{aligned} \tag{5.3}$$

Here $E(t)$ is the cumulative CO_2 emissions at time t and r is the rate of emissions. Notice the an operational definition of the "$-\infty$" might be the year 1850 or 1976.

In order for TCRE to be constant for the oceans since 1850, and for the Earth piecewise during 1850-1976 and 1976-2024, cf. (*MacDougall and Friedlingstein*, 2015, *MacDougall*, 2016) – both slopes on the right-hand-side of Equation $(5.3)_1$ must be constant. It turns out that $\Delta c_a/E$ is constant, see Figure 5.6(b), and so is $\Delta T/\Delta c_a$.

Both these insights are independent of GCMs and tell us that the Earth tries to maintain stasis for as long as she can. But GCMs tell us why exactly this happens. *MacDougall* (2017) showed that the path-independence of TCRE arises from the partitioning ratio of anthropogenic carbon between the ocean and the atmosphere being almost the same as the partitioning ratio of enhanced radiative forcing between the ocean and space.

A more realistic average TCRE, computed from Fig. 2C in *MacDougall* (2017), has the slope of 1.1/500 $^{\circ}C(Pg\ C)^{-1} = 0.60\ ^{\circ}C(Tt\ CO_2)^{-1}$. This slope is equal almost exactly to the purely empirical slope $0.62 \pm 0.06\ ^{\circ}C(Tt\ CO_2)^{-1}$ of the observation data-driven TCRE in Figure 5.7(c). Thus, including the oceanic carbon pool and heat uptake results in a realistic TCRE for the range of cumulative total emissions encountered in our probable fossil fuel production scenario until 2100 or 2150. To simplify our story, we will assume that the emitted CO_2 will continue to partition along the black dashed line $\tau = 0$ in Figure 5.6(b).

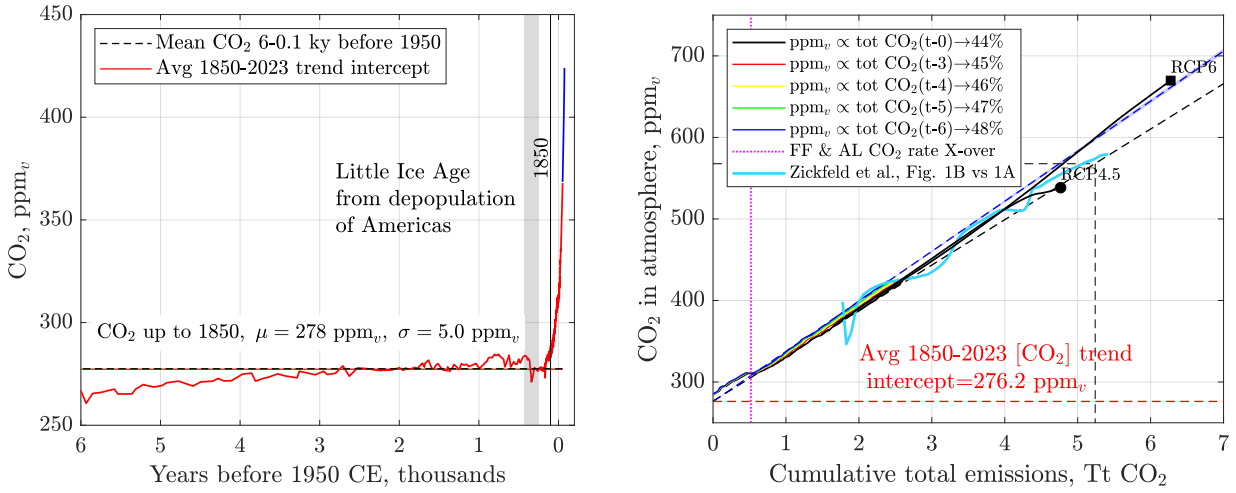

Figure 5.6: **(a)** pCO_2 from composite Antarctic ice cores between the year 1650 and 6 ka. The Mauna Loa data are in blue. Notice the almost constant level of $pCO_2 \approx 278$ ppm_v (black dashed line). We conclude that CO_2 equilibration in the oceans after the last glaciation (Section 3.15.5), and perhaps forest and savannah burning by people have been changing global climate very slowly over the last 10,000 years (*Johnston et al.*, 2023). Today, global climate change generates forest infernos *Zou et al.* (2020). Data source: NOAA *Bereiter et al.* (2015b), *Tans and Keeling* (2023). **(b)** The WAIS and Mauna Loa pCO_2 between 1850 and 2023 vs time-shifted total cumulative injection of CO_2 (FF+AL) in Figure 5.5(b). Notice that depending on the time shift (0-6 years), 44-48% of the injected CO_2 remains in the atmosphere. The break in the slopes of pCO_2 lines corresponds to the years 1940-1948, when the FF emission rate crossed over the AL emissions. The common intercept of all fit lines is ∼278 ppm_v of CO_2, the background value plotted on the left. Only two linear fits for $\tau = 0$ and $\tau = 6$ years are plotted for clarity. The 95% (2σ) confidence interval that a new observation will fall inside it is shaded. Because pCO_2 is a linear function of cumulative CO_2 emissions, this interval is small. Data sources: OWID (*Anonymous*, 2023a), Copernicus (*Friedlingstein et al.*, 2023). The thick blue curve is the pointwise division of the blue curve in Fig 1B by that in Fig 1A in *Zickfeld et al.* (2009). Their curve relaxes to the instantaneous pCO_2 here (black line), linking directly our zero-shift line of $\frac{\Delta T(t)}{E(t)}$ to GCM responses. The RCP4.5 and 6.0 scenarios also fall between the $\tau = 0$ and $\tau = 6$ lines. Calculations by Patzek.

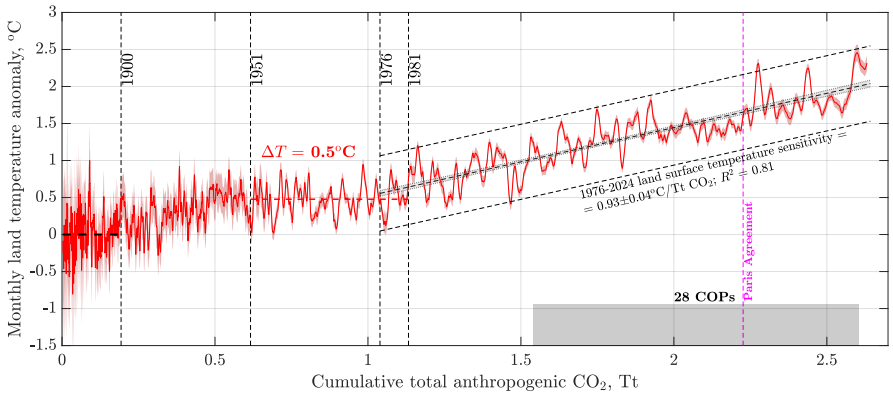

(a)

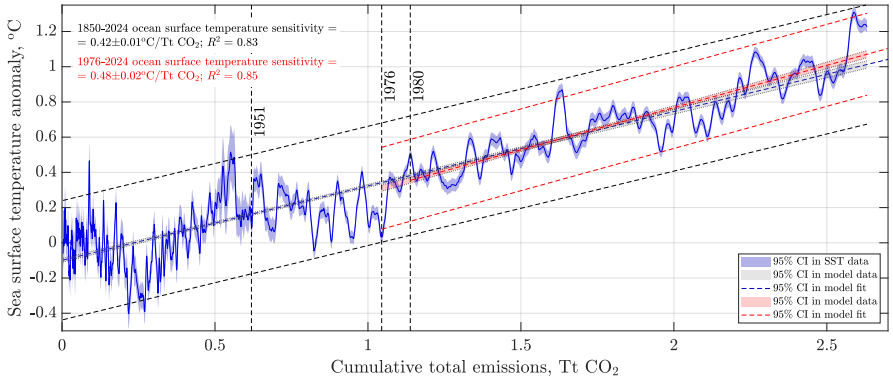

(b)

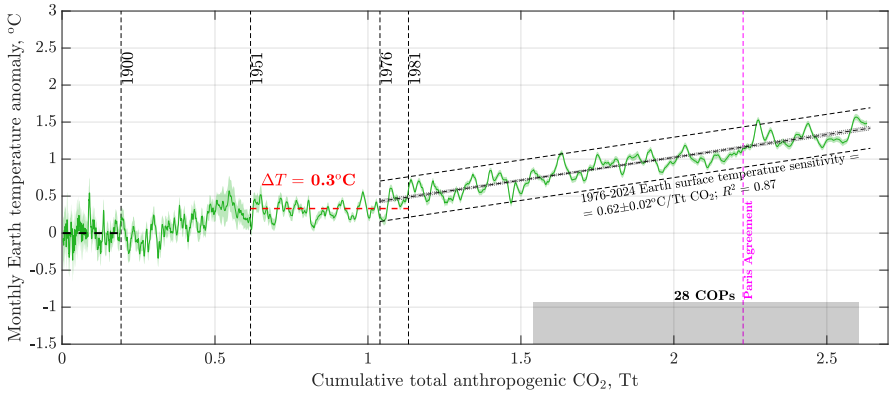

(c)

Figure 5.7: The cause (cumulative total emissions) and effect (ΔT) plot. All temperature anomalies are relative to the 1850-1900 global mean temperature (GMT). **(a)** Land mean annual temperature anomaly. The year 1976 marks a global climate bifurcation: the global land and oceans heated in unison between 1850 and 1976 in response to cumulative CO_2 emissions, and diverged at the $0.93/0.42 = 2.2 : 1$ ratio of the slopes, and at $0.93/0.58 = 1.9 : 1$ since 1976. **(b)** The Sea Surface Temperature (SST) changes slope only slightly after 1976. **(c)** The global mean annual temperature anomaly also changes slope significantly after 1976, driven by the faster rate of land heating. Data sources: Berkeley Earth, NASA GISTEMP, and HadSST.4.0.1.0. Data accessed 02/10/2025. Calculations by Patzek.

Chapter 6

Patzek's 568 and 720 ppm_v fossil fuel emissions scenarios

A better appreciation of the brevity and exceptional character of the epoch of the fossil fuels can be gained [by imagining it as] the Washington-Monument-like spike [that] represents the period of exploitation of the fossil fuels in the much longer span of human history.

Marion King Hubbert

Arguably the most influential American geologist and geophysicist of the 20^{th} century, Hubbert founded Shell Development and profoundly impacted my research persona.

Exponential Growth as a Transient Phenomenon in Human History, MIT Press, 1992

6.1 What are you going to learn?

In this chapter, we introduce two scenarios for the future trajectory of greenhouse gas concentrations through the year 2100. The first, referred to as the *Patzek 568 ppm$_v$ Scenario*, is based on a realistic model of fossil fuel depletion and emissions. The second, labeled the *720 ppm$_v$ Scenario*, is a direct parabolic extrapolation of the observed growth in cumulative atmospheric CO_2 emissions over the past 40 years.

We will relate both scenarios to the widely used frameworks developed by the Intergovernmental Panel on Climate Change (IPCC): the Shared Socioeconomic Pathways (SSPs) and the Representative Concentration Pathways (RCPs).

An **SSP** is a scenario framework consisting of both qualitative narratives and quantitative projections of key socioeconomic driverssuch as population, GDP, energy consumption, education, and inequality – constructed independently of specific climate policy assumptions. SSPs are used to drive climate models in combination with emissions trajectories and associated radiative forcing outcomes.

An **RCP**, on the other hand, describes a possible pathway of atmospheric radiative forcing (i.e., the net imbalance between incoming solar and outgoing terrestrial radiation at the top of the atmosphere) by the year 2100, expressed in watts per square meter (W/m^2). The SSP framework was introduced to complement and extend the earlier RCP system, and both are integral to the IPCC's Sixth Assessment Report (AR6).

6.2 Why is it important?

Emission scenarios determine the future warming potential of human activities. As we will demonstrate later, global warming is approximately proportional to the cumulative emissions of greenhouse gases (GHGs) – primarily CO_2 – and modulated by the cooling effects of aerosols. Therefore, a critical understanding of likely future GHG emissions and the aerosols they generate is essential for anticipating the trajectory of global climate over the next 80 years.

6.3 Overview of Patzek's and IPCC scenarios

The AR6 Report *IPCC, Full Report* (2022) (Box SPM1):

> "[Assesses] the climate response to five illustrative scenarios that cover the range of possible future development of anthropogenic drivers of climate change found in the literature. They start in 2015 *Riahi et al.* (2017), and include scenarios with high and very high GHG emissions (SSP3-7.0 and SSP5-8.5) and CO_2 emissions that roughly double from current levels by 2100 and 2050, respectively, scenarios with intermediate GHG emissions (SSP2-4.5) and CO_2 emissions remaining around current levels until the middle of the century, and scenarios with very low and low GHG emissions and CO_2 emissions declining to net zero around or after 2050, followed by varying levels of net negative CO_2 emissions (SSP1-1.9 and SSP1-2.6)."

Table 6.1 summarizes the radiative forcings and temperature increases from key SSP scenarios. Figure 6.1 depicts these IPCC scenarios together with Patzek's FF+AL 568 and 720 ppm$_v$ scenarios.

Figures 4.11 and 4.12 demonstrate that all three fossil sources of primary power (PP) for humanity reached similar power levels of ∼5 TW in 2023 (together 15.61 TW). To develop current power, coal production underwent 10 doublings since 1710, and oil and gas production underwent 10 doublings since 1860 and 1900, respectively. Current rates of exponential growth declined from their peak values by 65% for coal, 85% for oil and lease condensate, and by 64% for natural gas. In other words, the world is rapidly approaching the peak power production levels for all three fossil fuels, and there will *never* be the 11$^{\text{th}}$ doubling. Therefore, the 11 Tt of fossilfuel emissions projected by 2100 in the IPCC SSP5–8.5 scenario (see Figure 6.1) *cannot be realized directly*, regardless of the efforts of fossil-fuel consumers or producers. However, other positive climate feedbacks may still amplify the global temperature response to future cumulative emissions.

Table 6.1: Radiative forcing and temperature projections for SSP scenarios by 2100

SSP Scenario	Radiative Forcing (W/m^2)	CO_2 Concentration (ppm)	Warming by 2100 (°C)	Narrative Summary
SSP1-1.9	1.9	350-400	∼1.4	Strong mitigation; sustainability; meets 1.5°C goal
SSP1-2.6	2.6	420-460	∼1.8	Green growth; strong climate policies
SSP2-4.5	4.5	540-600	∼2.7	Continuation of historical trends; intermediate emissions
SSP3-7.0	7.0	700-850	∼3.6-4.0	Fragmented world; weak cooperation; high population growth
SSP5-8.5	8.5	900-1050	∼4.4-4.8	Fossil-fueled development; high energy demand

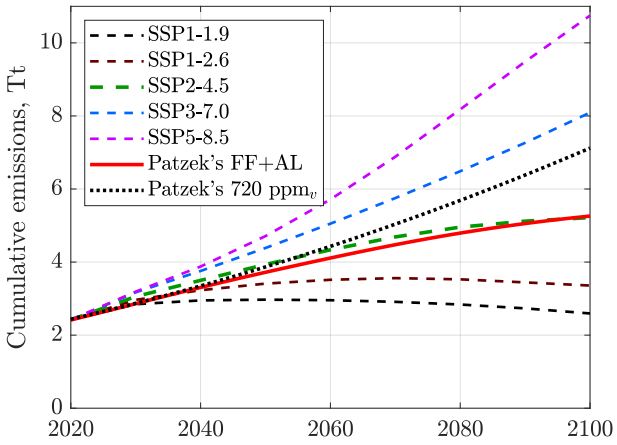

Figure 6.1: The cumulative emissions from the four IPCC Shared Socioeconomic Pathways and two Patzek's scenarios. The IPCC pathways are encoded as SSPx-y, where $x = 1, \ldots, 5$ (1 = Sustainability, 2 = Middle of the Road, 3 = Regional Rivalry, and 5 = Fossil-fueled Development) and y refers to the approximate level of radiative forcing (in W m^{-2}) resulting from the scenario in the year 2100. Notice that Patzek's FF+AL scenario is essentially a slightly decelerated SSP2-4.5, while his 720 ppm$_v$ scenario is a noticeably decelerated SSP3-7.0, with 1 Tt fewer CO_2 emissions and 150 ppm$_v$ less by 2100. The SSP5-8.5 is physically impossible with the anthropogenic CTE alone, but it well may happen with giant methane releases (up to 1 Tt of CO_2 by 2100) from permafrost (*Schuur et al.*, 2022, *Moon et al.*, 2024), reversal of other large natural sinks of carbon into carbon emitters, etc. All emission scenarios are anchored in 2020 to the current cumulative FF+AL emissions in Figure 5.5.

6.4 Patzek's physics-based CO_2 emissions scenario

Our most likely scenario of future CO_2 emissions from fossil fuels and agriculture and land-use change (FF+AL) will result in approximately 570 ppm$_v$ of CO_2 by the year 2100, or in ∼4.0 W m^{-2} of incremental radiative forcing.

For clarity, we will not attempt to scale down the emissions from this scenario, because there is little reason to believe that anything but geology and exhaustion of large oil and natural gas fields, and best coal deposits will lead to a decrease of emissions beyond the year 2100. Such a scaling down would be equivalent to moving from the IPCC SSP-4.5 to SSP-2.6 or -1.9.

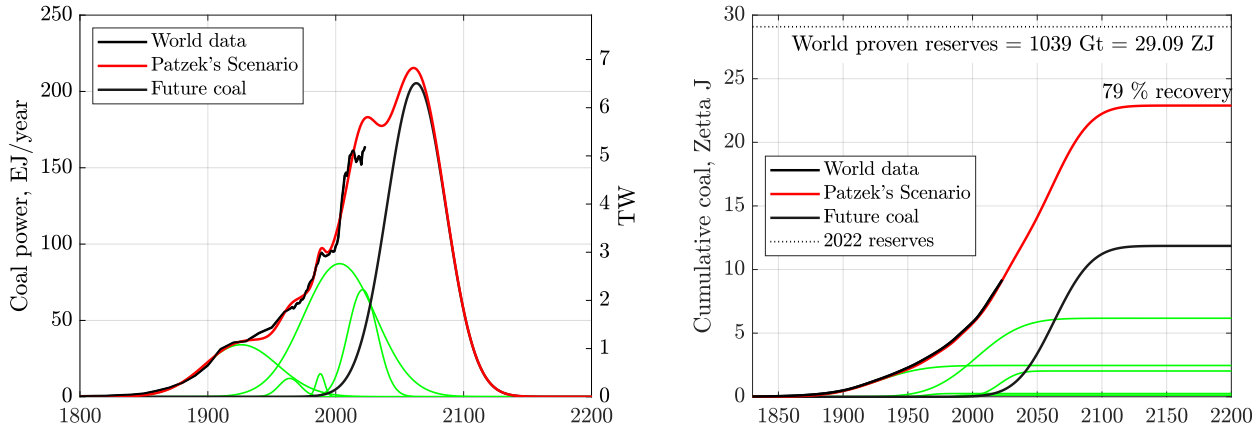

(a) (b)

Figure 6.2: **(a)** Patzek's scenario of future coal production rate. The Gaussian representing future coal production is the largest ever. **(b)** Patzek's scenario of cumulative coal production predicts that 79% of global coal reserves will be produced. Data sources: EIA, BP, OWID, accessed 08/30/2024; analysis by Patzek.

Patzek's FF+AL scenario relies on the summation of Gaussians representing each stage of historical production of a fossil fuel and assumptions about future production based on the proven reserves available at the time of making the forecast.

6.4.1 Global coal production scenario

Coal production was resolved in Figure 6.2 with 6 Gaussians. In 2010, the multi-Gaussian approach by *Patzek* (2008) was extended to global production of coal (*Patzek and Croft*, 2010). At the time, we predicted the global coal production rate to peak in 2011-2012. This was true until recently, but now China decided to commission more new coal-fired power capacity than the rest of the world combined, with 140 GW$_e$ under construction and 144 GW$_e$ permitted in 2024, according to Global Coal Plant Tracker. At a thermal efficiency of 0.4 and capacity factor of 0.8 (both high values according to our global analysis (*Bolson et al.*, 2022a)), and HHV of coal of 29 GJ/t (*Patzek and Croft*, 2010), once completed, these new power plants will burn 620 Mt/yr of new coal and emit 2.4 Gt/yr of new CO_2, increasing global emissions by 6%. The operating Chinese coal-fired power plants emit five times more CO_2 than each runner-up, India and the USA. In recognition of so many new coal-fired power plants coming on-line in dozens of countries, the future coal production Gaussian in Figure 6.2(a) is the largest in history, cf. *Patzek and Croft* (2010) and the appendices therein. Consequently, our estimate of ultimate coal production on the Earth has increased from less than 50% to more than 76% of proven global reserves, or to 22.2 ZJ, including 11 ZJ from future production in Figure 6.2(b). Other long-term uses of coal are described next.

Coal-to-Chemicals and Coal-Derived Plastics in China

China's coal use is undergoing a deep structural shift. Although power generation still dominates total coal consumption, a rapidly expanding coal-to-chemicals (CTC) and coal-to-liquids (CTL) industry is converting a growing share of coal into fuels, plastics, fertilizers, and industrial feedstocks. This trend has accelerated during the past decade and now plays a significant role in China's carbon emissions, energy security planning, and petrochemical supply chains.

A comprehensive material-flow analysis by *Zhu et al.* (2024) quantified the extent to which coal has supplanted oil and gas as a feedstock in China's chemical sector. In 2017 alone, coal-based production of methanol, ammonia, and polyvinyl chloride (PVC) generated approximately 0.27 Gt of CO_2 emissions. Coal accounted for 0.18 Gt of chemical feedstock inputs, far exceeding the fraction used in most other countries. These coal-derived pathways supply essential intermediates (methanol, olefins, syngas, ammonia) that underpin the production of plastics, fertilizers, solvents, synthetic fibers, and industrial gases.

Since 2020, the coal-to-chemicals industry has expanded further, driven by volatile global gas and oil markets and by China's desire to increase domestic control over critical materials. Several analyses report that the CTC and CTL sectors now consume roughly 6–7% of China's annual coal output, largely for methanol, synthetic natural gas (SNG), olefins, and downstream plastics production (*C&EN Staff*, 2025, *Climate Change News*, 2025). Growth in these sectors is sufficiently large that it may offset declines in coal use for power generation, thereby complicating national emissions reduction trajectories.

Another development is the rapid expansion of large integrated coal-to-gas and coal-to-olefin (CTO) complexes. As reported by *Stanway* (2025), some individual facilities process tens of millions of tonnes of coal per year, producing syngas, methanol, synthetic fuels, and petrochemical intermediates that enter plastics and rubber supply chains. Many of these projects are concentrated in coal-rich regions such as Inner Mongolia, Shaanxi, and Xinjiang, where water scarcity and local air pollution pose additional constraints on large-scale deployment.

From a global energy perspective, the International Energy Agency notes that demand for coal in chemicals production is increasing even as electricity-sector coal consumption begins to decline (*International Energy Agency*, 2025a). This structural shift suggests that coal's role in China's industrial system is not disappearing but transforming. Instead of serving primarily as a combustion fuel, coal is progressively becoming a carbon feedstock for the petrochemical industry, with significant implications for life-cycle greenhouse gas emissions and long-term carbon *lock-in*. The Entropy Law (Chapter 14) dictates that any large-scale coal-to-chemicals or liquid-fuel conversion inevitably requires enormous quantities of freshwater and generates vast streams of toxic waste; see, e.g., (*Patzek and Croft*, 2009, *Croft and Patzek*, 2009). In the context of accelerating global climate breakdown, this represents one of the worst possible outcomes.

6.4.2 Global oil and gas production scenario

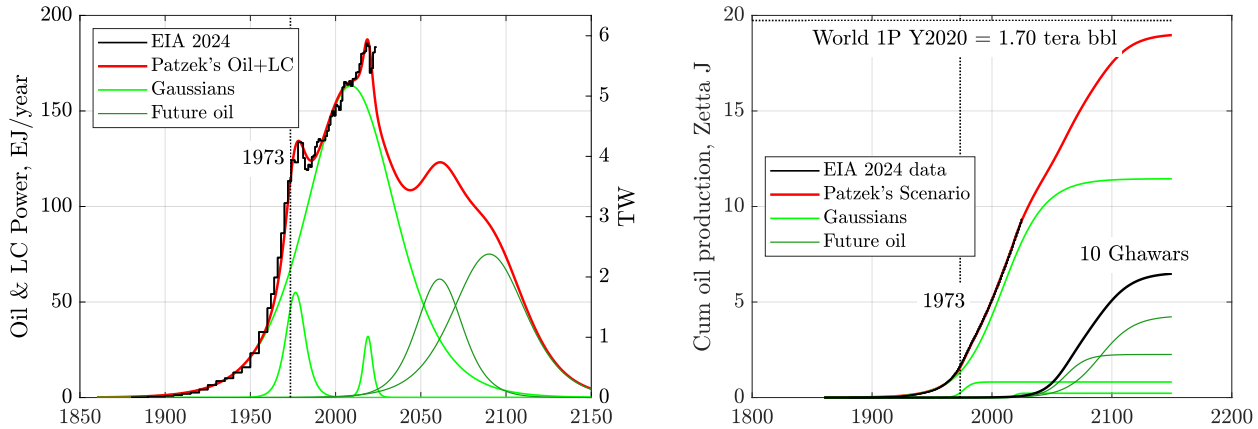

(a) (b)

Figure 6.3: **(a)** The global crude oil and lease condensate power, with two very large Gaussians representing future production. **(b)** Cumulatively the world will produce the 2020 1P reserves or ∼19 ZJ; 6.4 ZJ or 10 Ghawars at 100 billion bbl each will be produced in the future. Data sources: EIA, BP, OWID, and World Bank, accessed 9/15/2024; analysis by Patzek.

Oil production history and future production are complicated and resolved with 7 Gaussians in Figure 6.3. The fundamental Gaussian that peaked in 2009, is much larger than all other ones. The second Gaussian

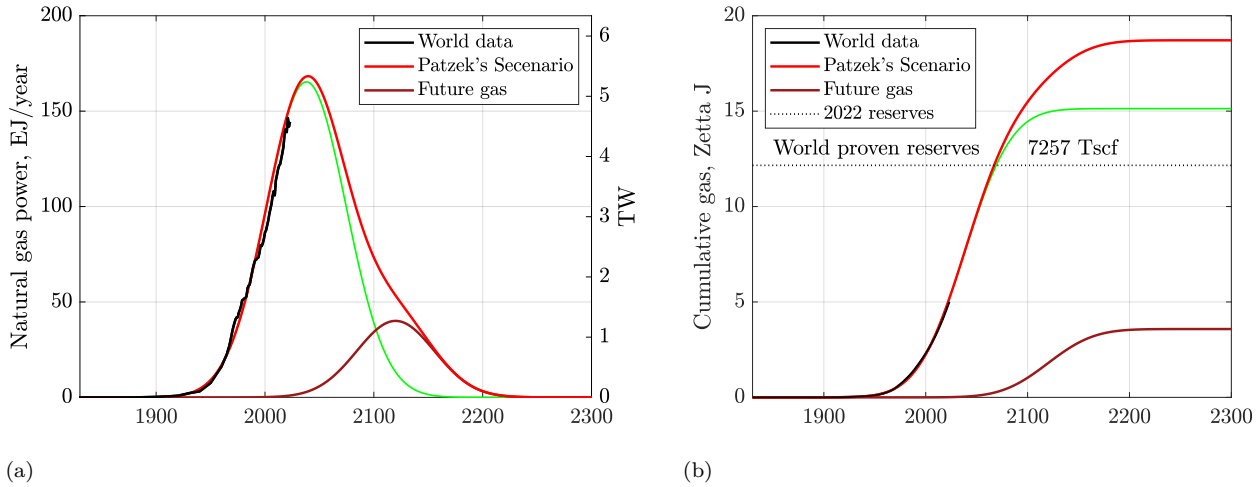

(a) (b)

Figure 6.4: **(a)** The historic rate of global gas production is represented with one green Gaussian, whose *unknown* height is set to exceed the proven 2022 gas reserves by 35%. The future production is also represented with a single Gaussian. **(b)** Cumulatively the world might produce 19 ZJ as the HHV of natural gas, including 3.6 ZJ from the future projects. Data sources: EIA, BP, OWID, and World Bank, accessed 9/15/2024; analysis by Patzek.

from the left is the fill-up with water and recharge of pressure-depleted reservoirs in the Middle-East, as well as all other new post-1973-Arab-embargo production. The third Gaussian from the left is mostly US oil shale production with new offshore production. The future production is resolved into two broad and large Gaussians that promise to deliver a new volume of crude oil equivalent to 10 Ghawars, each producing 100 billion bbl of oil. The supergiant Ghawar oil field in Saudi Arabia is by far the largest oil field on the Earth, and an outlier in every respect (*Patzek et al.*, 2022). The ultimate global recovery in this scenario will be 3 trillion bbl of oil and lease condensate, and all remaining proven oil reserves will be exhausted.

Natural gas production worldwide is modeled in Figure 6.4 with a single Gaussian. It is assumed that new discoveries and field development will permit exceeding current proven reserves by 35%, yielding cumulatively 19 ZJ, still less than the 22 ZJ from coal. It is possible that the actual future production of gas will be higher than that of coal. Sans flaring and fugitive emissions (*IEA*, 2024), natural gas is the cleanest fossil fuel, which unfortunately is not as fungible as crude oil and coal, and cannot be shipped easily around the world.

By producing its natural gas and crude oil from shales and tight reservoirs so fast and exporting them, e.g., *Patzek* (2019), *Patzek et al.* (2013), *Marder et al.* (2021), *Patzek et al.* (2019), *Saputra et al.* (2019, 2020, 2021, 2022b,a), *Saaputra et al.* (2023), *Saputra et al.* (2024), *Arias-Ortiz and Patzek* (2025), the US is undercutting its own future security in the post FF power peak world. Current short-term energy focus of the US, which boasts to be the largest oil producer and the largest natural gas producer on the Earth, will greatly weaken our country relative to Russia, which has larger reserves of both, see Table 6.2, plays the long strategic game, and spans latitudes north of the US (41°N to 82°N for Russia and 26°N to 49°N for the US). Given the rampant and accelerating climate breakdown, political tensions and wars, the current US energy policy may have dire repercussions in view of the emerging Russia-Iran/Iraq-China axis.

The heat content of oceanic water (OHC) has been estimated since mid-1950s, but beginning in the 1990s, the NOAA infrared satellite images of ocean surface water were combined with the water temperature measurements taken by thousands of floats and submersibles (*Cheng et al.*, 2019), delivering an ever-more detailed picture of ocean heat accumulation caused by the energy imbalance from anthropogenic GHG emissions (*Hansen et al.*, 2013b, *Hansen and Sato*, 2012, *Cheng et al.*, 2020, *Trenberth et al.*, 2014). Parenthetically, these essential NOAA programs are being dismantled by the chain-saw wielding DOGE

Table 6.2: Proven oil & gas reserves of key global players[a].

Country	Oil 10^9 bbl	Natural gas 10^{15} scf
Iran	151	12
Iraq	143	1
Russia	80	17
USA	35	4

[a] Source BP 2023 Outlook and OWID, accessed 05/26/2024.

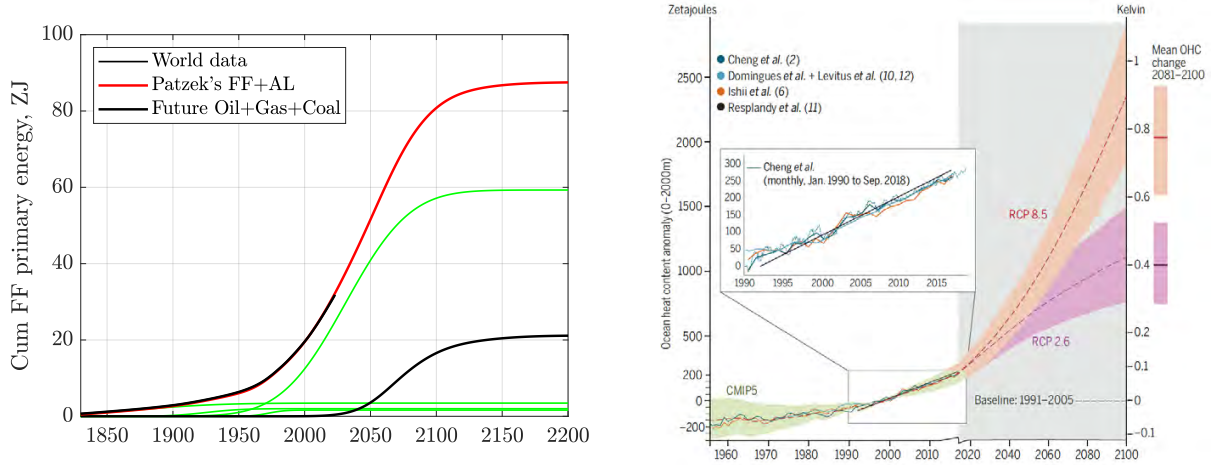

(a) (b)

Figure 6.5: **(a)** Cumulative heat generated by FF fuels until 2200. Roughly 30% of these 88 ZJ of heat is converted to work and the remaining 62 ZJ is heat generated at the Earth's surface. **(b)** Cumulative heat from incremental radiation forcing by GHGs. Ocean water heat content 0–2000 m depth is likely to reach 1500 ZJ by 2100. Image source: *Cheng et al.* (2017). Data sources: EIA, BP, OWID, and World Bank, accessed 9/15/2024; analysis by Patzek.

team.

As a result of the extreme growth of FF production rates, the world will have produced the cosmic 88 ZJ of FF primary energy by 2200, if Patzek's FF+AL scenario holds (the rightmost black future FF production curve in Figure 6.5(a)). In 2024, the amount of anthropogenic heat from FFs (23 ZJ) was roughly 5% of the 400 ZJ of incremental heat absorbed during my lifetime by the ocean water 0-2000 m deep, see Figure 6.5(b). An update by *Cheng et al.* (2020) increases the total full-depth ocean warming to 370 ± 81 ZJ (equal to a net heating of 0.38 ± 0.08 W m^{-2} over the global surface) from 1960 to 2019 (over 60 years), in good agreement with *Cheng et al.* (2019).

To put into perspective what we have done to the Earth's climate, each 1 ZJ in FF heat, and the resulting emissions of GHG gases, have *caused* an extra 20 ZJ of solar heat to be absorbed by the global ocean water. Based on this argument, the mean global climate sensitivity to FFs is 20:1!

In retrospect, Patzek's FF+AL scenario is a decelerated variant of SSP2-4.5 or RCP4.5 (Figure 6.6, in which FF production is distributed more evenly in time and lasts longer at a lower total rate. All other original IPCC scenarios are either excessive (SSP5-8.5 and SSP3-7.0), or will not be followed (SSP1-1.9 and SSP1-2.6) by the unwilling world for fear of the unknown and many other reasons *Bolson et al.* (2023).

Figure 4.9(b) explains forcefully why it will be so difficult to divorce thermal fuels power sources in real life. By continuing to consume fossil fuels at today's rate, however, the 8 billion humans living in 2024 will be in harm's way *Patzek* (2007), *Bolson et al.* (2022b), see Figure 6.6(a). Note that by the year 2200,

RCP8.5 predicts the pCO_2 level in the atmosphere to be 6.5× that in 1850, like during most of Eocene, Figures 9.8 and 9.9.

6.5 Patzek's scenario of future methane emissions

Prediction of future atmospheric methane (CH_4) concentrations is considerably more complex and uncertain than that of carbon dioxide, as illustrated in Figure 6.7. Methane is a highly potent greenhouse gas, with a global warming potential approximately 30 times greater than that of CO_2 over a 100-year time horizon. However, unlike CO_2, methane is chemically reactive: it has a relatively short atmospheric lifetime (approximately 812 years) and is gradually removed through oxidation reactions, primarily with hydroxyl radicals (OH), ultimately forming CO_2 and H_2O. Thus, its future concentration is sensitive to the biological sources of emissions, such as agriculture, farm animals, but above all permafrost melting.

The net atmospheric concentration of methane is therefore the result of a dynamic balance between multiple, often poorly constrained, sources and sinks. On the emissions side, major anthropogenic sources include agriculture (especially rice paddies), enteric fermentation from ruminant livestock, landfills, fossil fuel extraction and transport, and biomass burning. Natural sources include wetlands and geologic seepage. Among the most concerning potential contributors to future methane emissions is the thawing of high-latitude permafrost and destabilization of methane hydrates – processes that are highly sensitive to regional warming and difficult to quantify, cf. Appendix E.

On the sink side, changes in atmospheric chemistry – such as declining OH concentrations due to air pollution or climate feedbacks – could prolong methane's residence time, amplifying its radiative forcing. Finally, nonlinear feedbacks between warming, permafrost melting (*Natali et al.*, 2021), (*on Climate Change*, 2022, *Schuur et al.*, 2022, *Hugelius et al.*, 2014, *Shakhova et al.*, 2010b), and microbial activity may result in tipping-point behavior (*Schuur et al.*, 2015, *Turetsky et al.*, 2020, *Walter Anthony et al.*, 2018) that will amplify current climate change catastrophically, but is nearly impossible to model accurately.

On the sink side, changes in atmospheric chemistry – such as reductions in hydroxyl radical (OH) concentrations driven by air pollution or climate-induced feedbacks – can prolong methane's atmospheric lifetime, thereby enhancing its cumulative radiative forcing to a factor of 100 relative to CO_2. More critically, nonlinear feedbacks involving regional warming, large-scale permafrost thaw (*Natali et al.*, 2021, *on Climate Change*, 2022, *Schuur et al.*, 2022, *Hugelius et al.*, 2014, *Shakhova et al.*, 2010b), and increased microbial activity in thawed soils may trigger tipping-point dynamics. Such processes could lead to abrupt and potentially catastrophic increases in methane emissions, significantly amplifying global warming. These feedbacks are deeply uncertain and remain extremely difficult to represent accurately in current Earth system models (*Schuur et al.*, 2015, *Turetsky et al.*, 2020, *Walter Anthony et al.*, 2018).

In summary, future projections of methane concentration and climate impact are more uncertain than those for long-lived greenhouse gases like CO_2, and they introduce significant variability into scenarios of future climate forcing.

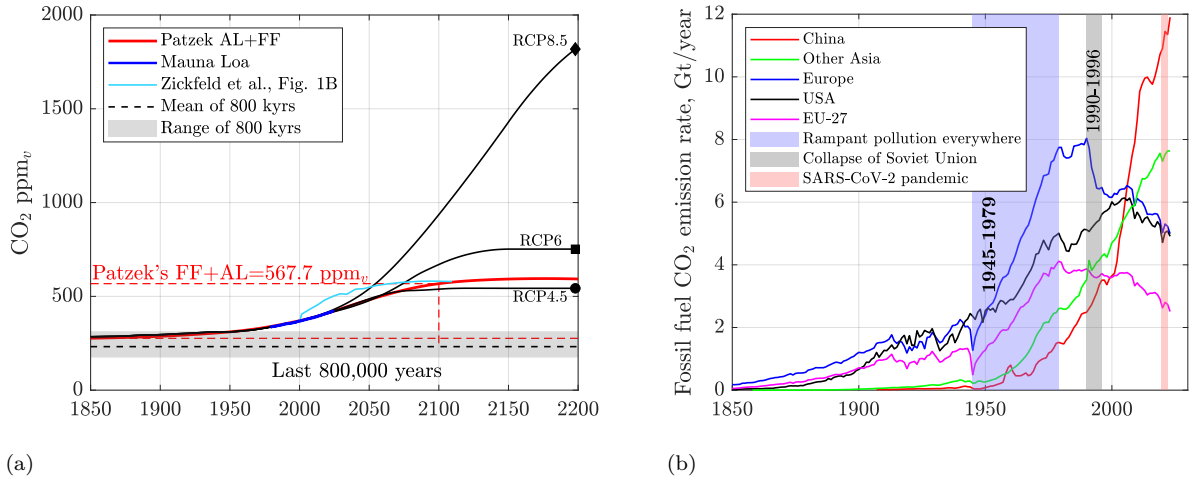

(a) (b)

Figure 6.6: **(a)** Comparison of atmospheric pCO_2 until 2200, resulting from Patzek's FF+AL scenario and RCP 4.5, 6.0 and 8.5 scenarios (*Meinshausen et al.*, 2011). The Zickfeld at al. simulation curve is also displayed for comparison, showing that equal cumulative CO_2 emissions lead to equal pCO_2s. **(b)** CO_2 FF emission rates by region or country. Europe includes the former Soviet Union and Warsaw Pact countries. Sources: EIA, NOAA, OWID, *Clark and Jacks* (2007), Patzek, accessed 02/11/2025. Calculations by Patzek.

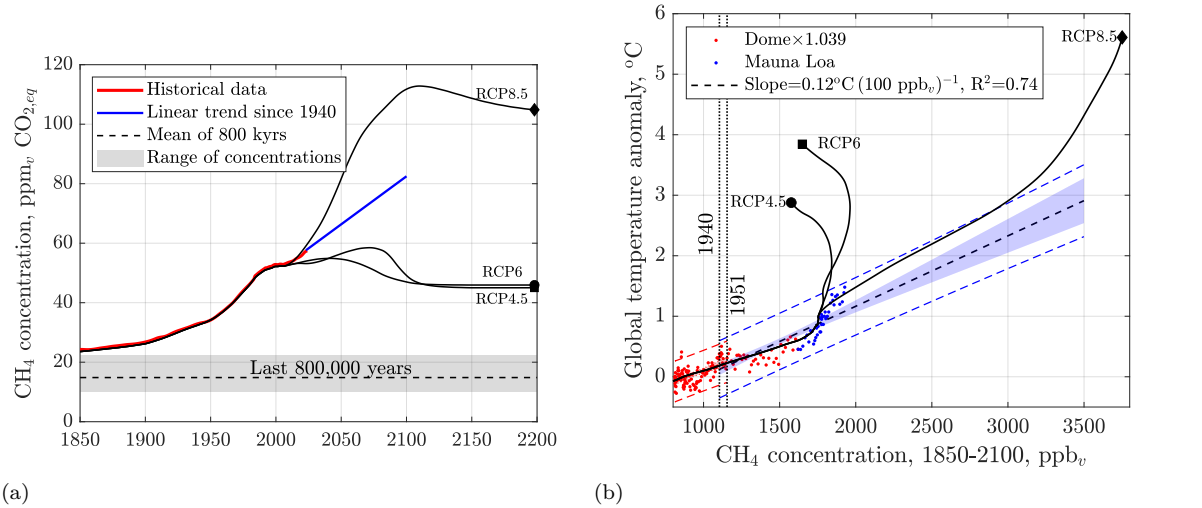

(a) (b)

Figure 6.7: **(a)** Methane concentrations are converted to $CO_{2,eq}$ by multiplying them by 29.8 (*Arias et al.*, 2021). Historic CH_4 concentrations are obtained from EPICA Dome C core data multiplied by 1.039 to align the overlapping data points with the Mauna Loa data. Very uncertain future concentrations are predicted by an extrapolation of the linear fit of historic data between 1940 and 2024. Three RCP scenarios are shown for calibration. **(b)** Global mean annual temperature anomaly vs CH_4 concentration. The plotted RCP scenarios (*Meinshausen et al.*, 2011) were converted to the corresponding temperature anomalies by multiplying their respective CTE by the average slope of 0.62 °C (Tt CO_2)$^{-1}$ in Figure 5.7(c). This calculation is well within the range of global warming probability distributions for RCP4.5, 6 and 8.5 (*Sherwood et al.*, 2020, Fig. 23). Notice that the RCP8.5 trajectory tracks historical data best, but I am quite unsure how predictive its future outcomes are. Data sources: Supplementary materials to *MacFarling Meure et al.* (2006), *PAGES* (2016), Mauna Loa (*Lan et al.*, 2025b). Calculations by Patzek.

6.6 Patzek's 720 ppm_v emissions scenario

The 720 ppm_v scenario arose from extrapolating with a parabola the last 45 years of CO_2 concentration until the year 2100, with no regard as to where this CO_2 will come from.

This scenario follows directly from Figure 5.3(b). Integrating the monotonically increasing total CO_2 emissions rate, roughly 2 trillion tons more of CO_2 will be emitted relative to the Patzek's 568 ppm_v scenario.

Chapter 7

The radiative energy budget of the Sun-Earth system

Early summer morning in Bodega Bay, California.
Photograph by T.W. Patzek, August 2007.

In nature everything is connected, everything is interwoven, everything changes with everything, everything merges from one into another.
Gotthold E. Lessing, *Beyond the Screenplay: A Dialectical Approach to Dramaturgy* (quoting from 1769)

7.1 What are you going to learn?

Here you will learn how our hot Sun produces an astonishingly constant stream of radiant energy that sustains life on Earth, and what happens to this energy when a portion of it enters the Earth's atmosphere and is ultimately re-emitted into the frigid expanse of the Universe.

7.2 Why is this important?

There is perhaps no better example of quantum mechanics shaping all life on Earth – and influencing everything about its climate – than the radiation emitted by the Sun and Earth. If you wish to explore the quantum statistical foundations of this phenomenon, please refer to Appendix B, which delves into Planck's Law of blackbody radiation and the Stefan-Boltzmann Law. The latter relates the total energy radiated per unit surface area of a blackbody to the fourth power of its absolute temperature, with the proportionality constant arising directly from quantum mechanics.

7.3 Preliminaries

This chapter introduces the energy balance of the Sun-Earth system – a fundamental starting point for any meaningful discussion of climate change. The analysis must begin with our remarkably stable and reliable star, the Sun. The Earth is powered by solar radiation emitted by the Sun, whose surface radiates approximately as a blackbody with an effective temperature of $T_1 \approx 5800$ kelvin (K)[1].

To maintain a relatively mild and stable climate, the Earth must expel very nearly as much energy as it receives. It does so by emitting longwave (infrared) radiation into the cold vacuum of space, at the effective background temperature of the Universe, $T_2 = 2.725$ K – the remnant of the Big Bang. In thermodynamic terms, this makes the Earth a remarkably efficient heat engine.

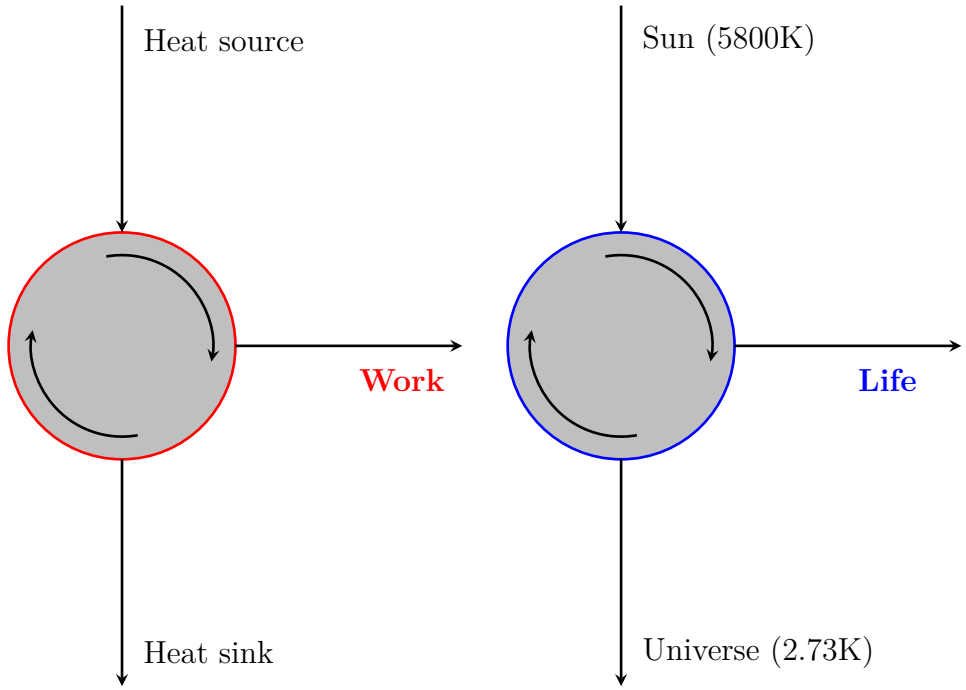

Figure 7.1: Carnot cycle for heat conversion to work by a machine (left) and the solar radiation energy conversion to life by Earth.

[1]The kelvin (K) is the absolute temperature scale, offset from the Celsius scale by 273.16 degrees: T, [K] = T, [°C]+273.16. A temperature difference of 1 K is equivalent to 1 °C.

Let's compare thermodynamic efficiency of the Sun-Earth system with that typical of a human-made machine (*Patzek*, 2004, *Patzek and Pimentel*, 2005, *Patzek*, 2007), see Figure 7.1.

- Cosmic background radiation $T_2 = 2.725$ K
- Sun blackbody temperature $T_1 = 5790$ K
- Earth engine's theoretical thermal efficiency $\eta = 1 - \frac{T_2}{T_1} = 1 - \frac{2.725}{5790} = 0.9995$
- *Theoretical* maximum of photosynthesis efficiency $\eta = 0.046$ for C3 plants (most plants, including trees and many crops), and $\eta = 0.06$ for C4 plants (e.g., maize, sugarcane), which are more efficient in hot, sunny environments
- *Practical* efficiency of photosynthesis in plants is $\eta = 0.01 - 0.02$
- Algae and cyanobacteria that use slightly different mechanisms, can have $\eta = 0.03 - 0.04$ under controlled conditions

Ecosystems are very inefficient, but very robust

And now efficiency of a steam engine:

- Ambient temperature $T_2 = 293$ K $= 20^{\circ}$C
- Steam temperature $T_1 = 473$ K $= 200^{\circ}$C
- Steam engine's theoretical thermal efficiency $\eta = 1 - \frac{T_2}{T_1} = 1 - \frac{293}{473} = 0.38$
- Newcomen's engine, $\eta = 0.005 - 0.02$ (1712), Watt's improved steam engine $\eta = 0.03 - 0.05$ (1769), compound steam engines $\eta = 0.10 - 0.15$ (1870s locomotives), high-pressure steam engines $\eta = 0.15 - 0.20$ (1950s locomotives), modern steam turbines $\eta = 0.30 - 0.45$ (power plants)

Human technology is very efficient, but very fragile

We begin with a quantitative outline of the energy balance between the Sun and Earth. Following that, we examine the radiation spectra of both bodies, the role of greenhouse gases (GHGs), and later – in Chapter 13 – address several claims made by climate denialists.

7.4 The Sun

Our G-type main-sequence star, the **Sun**, shown in Figure 7.2, ignited approximately 4.6 billion years ago and has since been the dominant source of energy for Earth. At the Earth's orbit – shown on the right edge of Figure 7.3 – the Sun delivers a continuous, globally averaged power flux of approximately $F_{\odot} \approx 1361$ W m^{-2}, known as the **solar constant** (see Figure 7.4). This value represents the average **solar irradiance** received at the top of Earth's atmosphere over a 24-hour day and across all latitudes.

The G-type stars have several common characteristics:

- **Surface temperatures** range from 5,300 K to 6,000 K.
- **Masses and radii** range between 0.84 and 1.15 times the mass of the Sun and between 0.9 and 1.1 times the Sun's radius.
- **Luminosities** range from 0.6 to 1.5 times that of the Sun.
- **Lifespans** are relatively long, around 10 billion years, allowing for the potential development of planetary systems.
- **Radiation spectra** have strong absorption lines of ionized metals like Ca II and unionized metals like Fe I and Mg I (in the outer layers of the photosphere, see Figure B5).

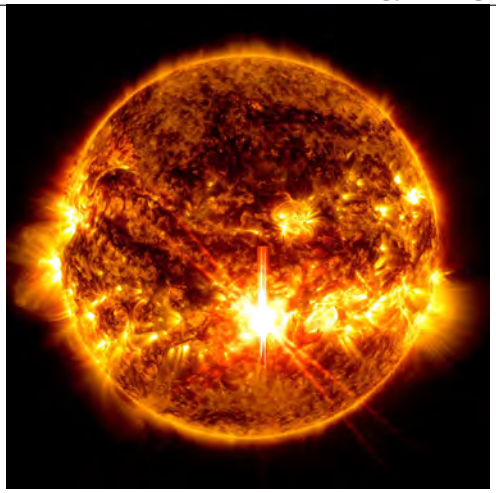

Figure 7.2: The Sun is a G-type main-sequence star, commonly referred to as a yellow dwarf. Its surface occasionally exhibits sunspots – temporary, cooler, and darker regions caused by intense magnetic activity that suppresses convective mixing. Sunspot temperatures range from 3,800 to 4,500 K, significantly cooler than the surrounding photosphere at approximately 5,800 K. In addition to sunspots, the Sun's fast-changing magnetic field powers solar flares and coronal mass ejections (CMEs) – massive bursts of solar plasma and magnetic fields. A notable example is a solar flare captured by NASA's Solar Dynamics Observatory on October 3, 2024.

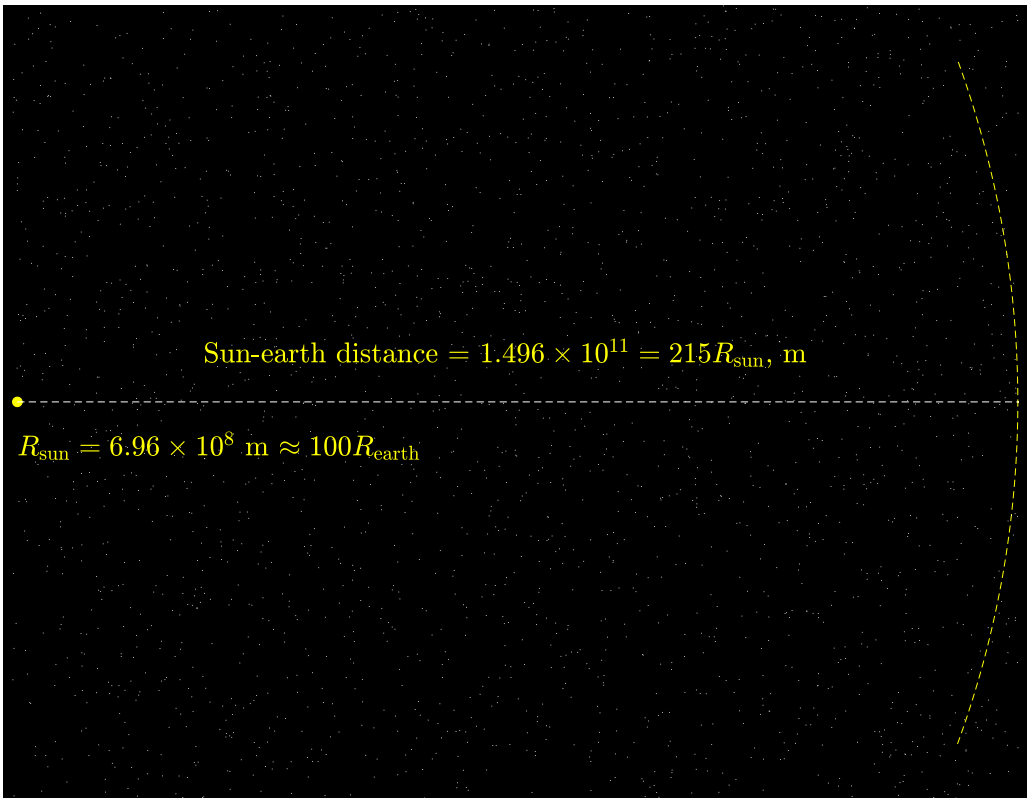

Figure 7.3: The Sun-Earth system drawn to scale. The arc on the right depicts the Earth's orbit around the Sun. At this scale the Earth is an invisible spec lost in the vast Universe. Because of its size and distance from the Sun, the Earth intercepts only one-half of one billionth of all radiation emitted by the Sun.

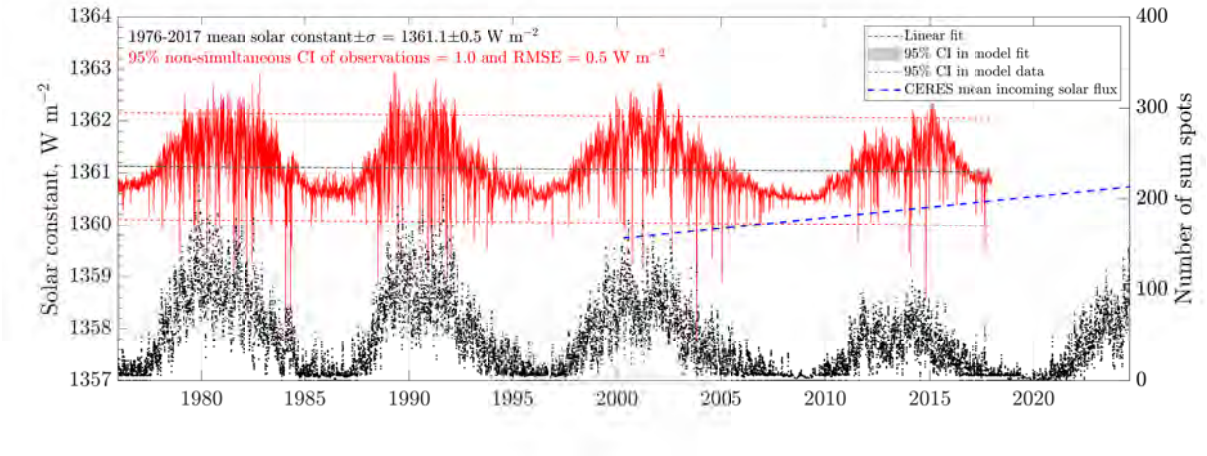

Figure 7.4: The best available reconstruction of the solar constant is based on multiple independent data sets. Over the past 42 years, the solar constant has remained remarkably stable, with a mean value of 1361.1 ± 0.5 W m^{-2} (1 standard deviation), varying by up to ± 1 W m^{-2} ($\pm 0.07\%$) in phase with the solar sunspot cycle. At top of atmosphere (TOA), Earth receives a time-averaged solar irradiance of $F_{\odot}/4 = 1361.1$ divided by four $= 340.275$W m^{-2}. The reduction factor of 1/4 arises from averaging the solar light incidence angles between the equator to the poles (1/2), and accounting for the Earth rotation (day-night cycle, 1/2). The solar constant values are derived from the supplementary data in *Gueymard* (2018). CERES radiative fluxes are based on the dataset `CERES_EBAF-TOA_Ed4.2_Subset_200003-202407.nc`, accessed on February 1, 2025. Monthly sunspot numbers were obtained from the SILSO database at `https://www.sidc.be/SILSO/datafiles`. Calculations by Patzek.

7.5 Important definitions

Definition 5. A star's **luminosity**, L, in watts, is the rate at which that star radiates energy, E:

$$L = \frac{dE}{dt}$$

The quantum distribution of radiation emitted and absorbed by a black body is required to derive the energy relationship between the Sun and Earth, as well as the Earth and Universe. Summing up black body radiation over all wavelengths and directions gives the Stefan-Boltzmann law, which in turn governs the macroscopic radiative energy transfer in the open Sun-Earth-Universe system. This two-way transfer of photons has created and sustained all life on the Earth. There isn't a more direct and important mechanism by which quantum physics defines everything that ever happened to and on the Earth. For the derivations, please see **Appendix B**.

Definition 6. The Stefan–Boltzmann Law for blackbody radiation. For a star, its luminosity is given by:

$$L = 4\pi R^2 \sigma T^4$$

where:

- R is the radius of the star (in meters),
- T is the surface temperature (in kelvin),
- σ is the Stefan–Boltzmann constant: $\sigma = 5.670 \times 10^{-8}\ \mathrm{W\,m^{-2}\,K^{-4}}$, given by Equation (B.37).

The luminosity of the Sun is a standard reference value:

$$L_\odot \approx 3.828 \times 10^{26}\ \mathrm{W}$$

Other stars' luminosities are often expressed in multiples of $L_\odot$:

$$L_{\text{star}} = \text{Factor of order of } 1\ \times L_\odot$$

The famous G-type stars are:

- **Sun (G2V)**, our father and mother.
- **Alpha Centauri A (G2V)**, the brightest star in the Alpha Centauri system 4.37 LY[2] away.
- **Tau Ceti (G8V)**, located approximately 12 LY away.

Definition 7. Irradiance, **radiant emittance**, and **radiant exitance** are radiometry terms for the power of electromagnetic radiation at a surface, per unit area, or energy flux. **Irradiance** is used when the electromagnetic radiation is incident on the surface. The other two terms are used interchangeably for radiation emerging from a surface. The SI units for all of these quantities are watts per square meter ($\mathrm{W\,m^{-2}}$) or $\mathrm{J\,s^{-1}\,m^{-2}}$

[2] 1 light-year (LY) is the distance that light travels in one year in vacuum. It is equal to 9.4607×10^{12} km or 5.879×10^{12} miles.

Definition 8. Total Solar Irradiance (TSI) is the solar irradiance at all wavelengths incident on a unit surface placed at the edge of the atmosphere (AM0) perpendicularly to the direction of sunlight. It is also called the **solar constant**. The TSI at 1 AU[3] is

$$S_0 \approx 1361 \text{ W m}^{-2},$$

as measured by the SORCE/TCTE/TSIS-1 composite record (*Kopp and Lean*, 2011, *Kopp*, 2021). Over the 11-year Schwabe solar cycle, TSI exhibits a quasi-periodic variation of only

$$\Delta S \approx 0.8\text{–}1.3 \text{ W m}^{-2},$$

corresponding to a relative amplitude of

$$\frac{\Delta S}{S_0} \approx 0.06\text{–}0.1\%.$$

The instantaneous range of daily-mean values since 1978 therefore lies between

$$S_{\min} \approx 1360.3 \text{ W m}^{-2} \quad \text{and} \quad S_{\max} \approx 1361.6 \text{ W m}^{-2},$$

depending on solar activity and instrument calibration. Long-term secular trends in TSI are negligible compared with anthropogenic radiative forcing; satellite composites (PMOD, ACRIM, and SORCE/TSIS) show stability within $\pm 0.02\%$ over the past four decades. For climate modeling, the mean value $S_0 = 1361.0 \text{ W m}^{-2}$ is now recommended by the WMO and IPCC. This value is significantly lower than the canonical value of $1365.4 \pm 1.3 \text{ W m}^{-2}$ established in the 1990s from the somewhat miscalibrated satellite measurements.

Definition 9. AM0 ("Air Mass 0") defines the solar spectrum outside Earth's atmosphere, commonly referred to as the *top-of-atmosphere (TOA)* or *extraterrestrial* solar irradiance. The AM0 spectrum is relevant for space-based applications and serves as a reference in satellite solar power systems. The total solar irradiance at AM0 is approximately 1361 W m^{-2}.

AM1 ("Air Mass 1") describes the solar spectrum at Earth's surface when the Sun is directly overhead (solar zenith angle of 0°). Under this condition, sunlight travels the shortest possible path through the atmosphere. This idealized scenario is often used in solar energy studies to represent maximum potential irradiance at sea level, typically approximated as 1000 W m^{-2}.

AM1.5 refers to the standard solar spectrum when the Sun is positioned at an elevation angle of 48.2° above the horizon. This corresponds to a solar zenith angle of 41.8°, implying that sunlight travels through the atmosphere along a path 1.5 times longer than the vertical (AM1) path. AM1.5 represents average mid-latitude conditions and is widely used for the testing and characterization of photovoltaic devices.

The solar elevation corresponding to AM1.5 occurs at different latitudes on specific days of the year: at 47.2°N or S on the equinoxes (March 21 or September 23), 66.6°N on the summer solstice (June 21), and 23.8°N on the winter solstice (December 21). These latitudes correspond roughly to the locations of cities such as Vienna or Seattle, Murmansk or Reykjavík, and Miami or Cancún, respectively.

The AM1.5 standard spectrum is widely adopted in the design and performance evaluation of terrestrial solar energy systems, particularly photovoltaic cells, as it closely approximates real-world operating conditions.

Definition 10. Insolation is the amount of direct solar radiation incident upon a unit horizontal surface at a specific latitude and level on (e.g., AM1) or above the surface of the Earth

[3] An astronomical unit (AU), defined as

$$1 \text{ AU} = 149{,}597{,}870.7 \text{ km} \approx 1.496 \times 10^{11} \text{ m},$$

is the mean distance between Earth and the Sun.

Definition 11. The Earth's **albedo** is the fraction of incoming solar radiation that is reflected back into space:

$$\alpha = \frac{E_{\text{reflected}}}{E_{\text{incoming}}}$$

where:

- α is the albedo (dimensionless, between 0 and 1),
- $E_{\text{reflected}}$ is the reflected solar energy,
- E_{incoming} is the total incident solar energy.

Currently the Earth's average albedo is:

$$\alpha_{\text{Earth}} \approx 0.30 \tag{7.1}$$

This means that in 2025, approximately 30% of incoming sunlight at TOA is reflected by clouds, ice, snow, and aerosols, while 70% is absorbed by the Earth's surface – mostly oceans – and atmosphere. The Earth maintains a uniform constant albedo (*Pierrehumbert*, 2010). The Northern and Southern Hemispheres (NH, SH) reflect the same amount of sunlight to within $\sim$0.2 W-m^{-2} out of the average solar endowment of $\sim$240 W m^{-2}. This symmetry is achieved by increased reflection from SH clouds precisely offsetting the greater reflection from the NH land masses. Clouds provide the necessary degrees of freedom to modulate the Earth's albedo, controlling the miracle of *hemispheric symmetry*. The formation of clouds and their effects are not captured well by numerical global climate models.

A break of the Earth albedo's uniformity (hemispheric symmetry) depicted in Figure 10.11, and/or its fast decrease will have dire consequences for our fragile technological global civilization. More on this subject soon.

Earth's albedo is measured using satellite-based instruments that monitor both incoming and reflected solar radiation.

a. Incoming Solar Radiation

Satellites measure the **total solar irradiance (TSI)** above the atmosphere using the following instruments:

- **SORCE/NASA** (Solar Radiation and Climate Experiment, 2003-2020)
- **TSIS-1/NASA** (Total and Spectral Solar Irradiance Sensor, 2018-). Instrument hosted on NOAA's International Space Station platform

b. Reflected Solar Radiation

Satellites detect reflected shortwave radiation using instruments such as:

- **CERES/NASA** (Clouds and the Earth's Radiant Energy System). Instruments on *Terra*, *Aqua*, Suomi NPP and JPSS satellites
- **MODIS/NASA** (Moderate Resolution Imaging Spectroradiometer). Instruments on *Terra* and *Aqua* satellites

NASA's bus-sized *Terra* and *Aqua* satellites, launched in 1999 and 2002 respectively, have far exceeded their original six-year mission lifespans, delivering over two decades of invaluable data about our home planet, Earth. Both missions are now approaching the end of their operational lifetimes. The satellites have ceased active orbit control, are drifting away from their original sun-synchronous trajectories, and are expected to conclude science operations by 2026[4] or earlier.

[4]The proposed NASA budget for 2026 includes a 25% reduction, potentially accelerating mission termination.

Despite their crucial contributions to Earth system science, no direct replacements for *Terra* and *Aqua* are currently planned, raising concerns about continuity of critical climate and environmental observations. NASA is transitioning to newer instruments, such as the *Visible Infrared Imaging Radiometer Suite* (VIIRS), to sustain Earth observation capabilities.

In this book, we primarily rely on data from the *CERES* (Clouds and the Earth's Radiant Energy System) instrument suite aboard *Terra* and *Aqua*, which has provided long-term, consistent measurements of Earth's radiative energy budget.

c. Types of albedo

- **Top-of-atmosphere (TOA) albedo**: Includes contributions from clouds, aerosols, and surface.
- **Surface albedo**: Isolated reflectivity of Earth's surface, retrieved by correcting for atmospheric effects (CERES does that).

7.6 The solar radiation spectrum

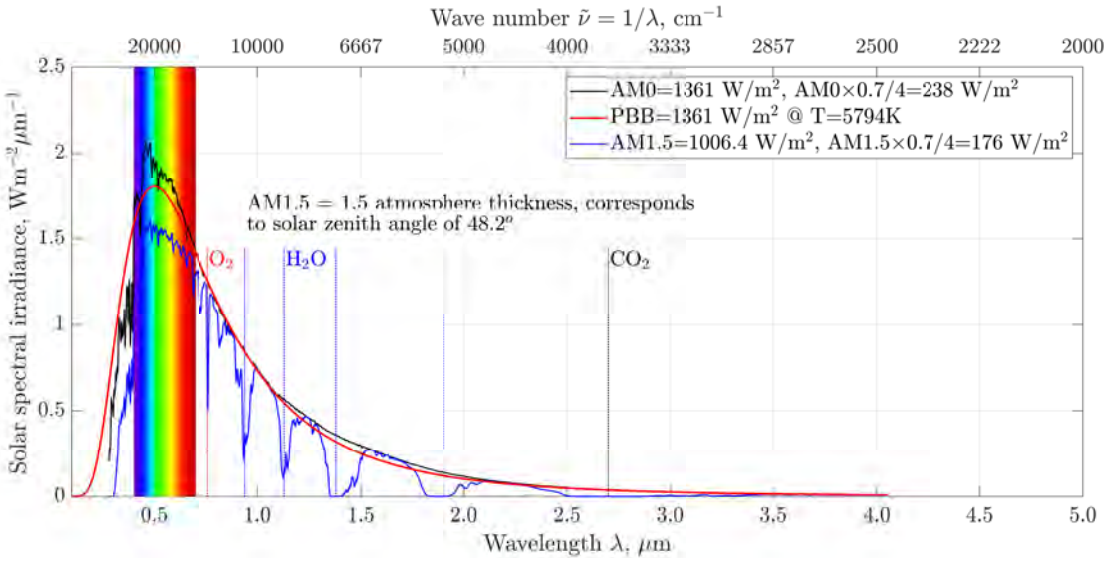

Figure 7.5: The measured and theoretical (Planck's blackbody PBB) solar radiation spectra. Sources: *NREL*, calculations by Patzek.

Figure 7.5 plots the solar spectrum irradiance[5] versus the incident light wavelength λ (the bottom x-axis), and its inverse, ν, the spectroscopic wave number as the top x-axis. At top of atmosphere (AM0, cf. Definition 9), the area under the black curve equals the total power of sunlight at all wavelengths incident on a square meter of surface perpendicular to it, or the solar constant of 1361.1 W m^{-2}. At ground level and the solar zenith angle of 48.2^o (the blue curve, AM1.5), one square meter of Earth surface perpendicular to sunlight receives only a little above 1000 W m^{-2} because of the absorption of radiation energy by atmospheric gases. The visible light part of the solar spectrum is highlighted by the rainbow from violet to dark red. Oxygen in red absorbs solar light in the near infrared. The five major absorption troughs in blue are from water vapor. Finally, a broad shallow trough by CO_2 in black is shown at the right tail end of the solar spectrum. The ozonosphere is a strong absorber of the near- and far-ultraviolet light to the left of the visible-light rainbow, see Figure 7.6(a).

Using statistical mechanics and quantum theory, see Appendix B, it is straightforward to derive the total specific[6] radiation energy, u, of a black body. Equation (B.25) describes u in terms of the photon wavelength, and Equation (B.26) in terms of the photon frequency.

[5]The power of solar radiation (light) associated with each micrometer of wavelength of sunlight incident on one square meter of surface perpendicular to the light, see Definition 7.

[6]Per unit volume of space filled with radiation.

Superimposed on the measured irradiance curves is the theoretical Planck blackbody (PBB) radiation curve u_λ in red. It was calculated at the Sun's blackbody radiation temperature of $5794 \approx 5800\mathsf{K}$, and the area under the curve is equal to the solar constant of 1361 $\mathsf{W\,m^{-2}}$. Notice that the PBB's peak energy for the Sun is at the short wavelength portion of green light.

7.7 Temperature relationship between the Earth and the Sun

To begin, we use the Stefan-Boltzmann law to find the total power the Sun is radiating:

$$P_{\text{Sun}} = (\sigma T_{\text{Sun}}^4)\ (4\pi R_{\text{Sun}}^2) \tag{7.2}$$

where σ is the Stefan-Boltzmann constant, T_{Sun} is the surface temperature of the Sun, and R_{Sun} is the average radius of the Sun.

The Sun radiates its power uniformly in all directions. Because of this, the Earth receives only a tiny fraction of the Sun's radiation. Here is the power from the Sun the Earth absorbs:

$$P_{\text{Earth absorbed}} = P_{\text{Sun}}(1-\alpha)\frac{\pi R_{\text{Earth}}^2}{4\pi d^2} \tag{7.3}$$

where R_{Earth} is the average radius of the Earth and d is the average distance between the Sun and the Earth.

Even though the Earth only absorbs as a projected circular area πR_{Earth}^2, it radiates uniformly in all directions as a sphere:

$$P_{\text{Earth emitted}} = \sigma T_{\text{Earth}}^4\ 4\pi R_{\text{Earth}}^2 \tag{7.4}$$

where T_{Earth} is the surface temperature of the Earth.

Now, by the first assumption, the Earth is in thermal equilibrium (steady state), so the power absorbed must equal to the power emitted:

$$P_{\text{Earth absorbed}} = P_{\text{Earth emitted}} \tag{7.5}$$

After plugging Eqs. (7.2) – (7.4)into Eq. (7.5) and simplification we get:

$$T_{\text{Earth}} = T_{\text{Sun}}\sqrt{\frac{R_{\text{Sun}}}{2d}\sqrt{1-\alpha}} \tag{7.6}$$

The blackbody radiation temperature of the Earth depends only on the surface temperature of the Sun and its radius, the distance between the Earth and the Sun, and the Earth's albedo.

7.7.1 Radiation temperature of the Earth

When we plug in the measured values for the Earth and Sun,

$$\begin{aligned} T_{\text{Sun}} &= 5794\ \text{K from Figure 7.5} \\ R_{\text{Sun}} &= 6.96 \times 10^8\ \text{m} \\ d &= 1.5 \times 10^{11}\ \text{m} \\ \alpha &= 0.3 \end{aligned}$$

we calculate the blackbody temperature of the Earth to be

$$T_{\text{Earth}} = 255\,\text{K}\ (\approx -18\,^\circ\text{C})$$

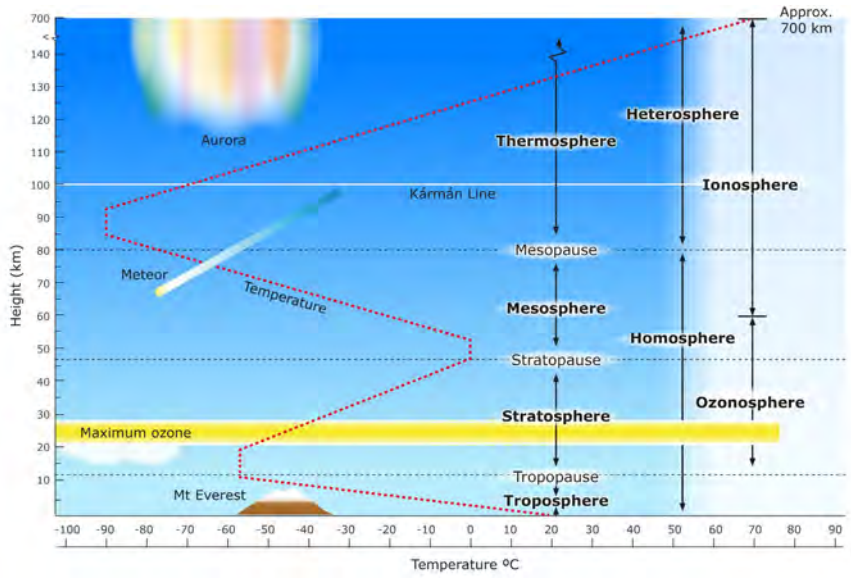

(a)

(b)

Figure 7.6: (**a**) A cartoon of the vertical profile of air temperature versus elevation above ground level. Image source: The University of Waikato – Science Learning Hub. (**b**) This spectacular image of sunset on the Indian Ocean was taken by astronauts aboard the International Space Station (ISS). The image presents an edge-on, or limb view, of the Earth's atmosphere seen from orbit. The yellow and orange layer is the troposphere, the ivory layer is the stratosphere, and the light blue and increasingly darker blue layers make up the upper atmosphere. The black top region is the outer space. Image source: NASA.

In thermal equilibrium with the intercepted solar radiation, the Earth radiates as a black body at $T_{\text{Earth}} = 255\,\text{K}$. This is the temperature the Earth's surface would have **without** an atmosphere. But the Earth has an atmosphere. In 2025, the measured mean temperature of air at the Earth surface was

$$T_{\text{surface}} \approx 288.5\,\text{K}\ (\approx 15.5\,^{\circ}\text{C})$$

The difference is due to the **greenhouse effect**:

$$\Delta T_{\text{GHG}} = T_{\text{surface}} - T_{\text{Earth}} \approx 33.5\,\text{K}$$

This ∼33.5 K warming is caused by greenhouse gases (primarily water vapor, CO_2, CH_4, O_3, and others).

In conclusion, the Earth behaves like a black body radiating from an effective spherical surface located at some elevation in the troposphere, see Figure 7.6.

7.8 The Earth infrared radiation spectrum

The idealized black-body spectra of the Sun and Earth are juxtaposed in Figure 7.7. Energy conservation requires that the *absorbed* solar flux

$$\frac{(1-\alpha)\,F_\odot}{4},$$

where $F_\odot$ is the solar constant and $\alpha \simeq 0.3$ is Earth's albedo, equals the planet's *emitted* thermal flux,

$$\sigma T_{\text{Earth}}^4 \;\approx\; 238\ \text{W m}^{-2}.$$

Thus, in radiative equilibrium the net energy exchange is zero: the incoming and outgoing fluxes are equal in magnitude and opposite in direction.

Entropy nevertheless increases. On average, each visible or near-infrared photon received from the Sun is degraded into five or six lower-energy infrared photons emitted by Earth, so the total entropy of the Universe rises in accordance with the Second Law of thermodynamics.

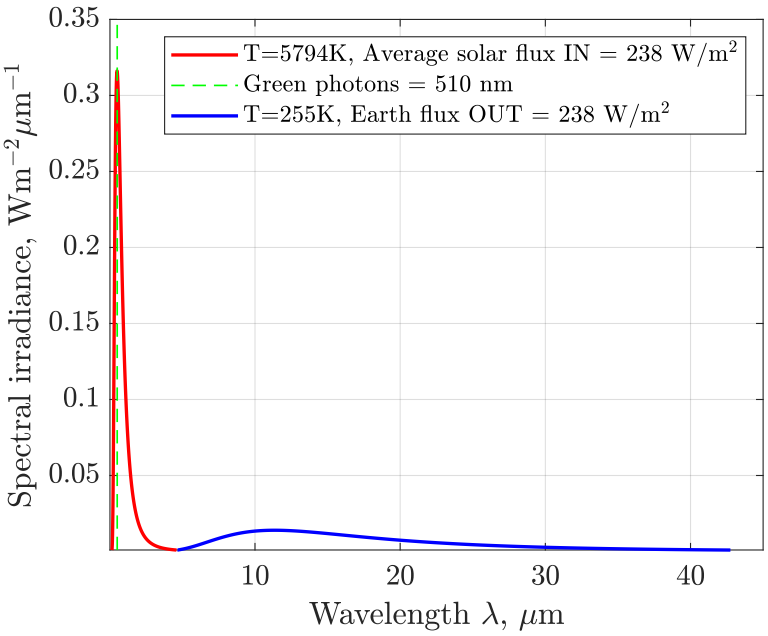

Figure 7.7: The solar radiation spectrum is scaled by the factor of $(1-\alpha)/4$ so that both areas under the irradiance spectra are equal. The Planck blackbody radiation curves in Equation (B.26) are plotted at the absolute temperatures of 5794 and 255 K, respectively. Notice that the two spectra are disjoint. The solar spectrum ends at the infrared light wavelengths at which the Earth spectrum begins. Calculations by Patzek are based on Equation (B.26).

Definition 12. The Earth's emits only infrared photons. Infrared radiation (**IR**) is divided into three main regions, characterized by specific wavenumber ranges[7]:

[7]The range of visible light wavelengths is $\lambda = 0.4 - 0.7\,\mu$m and the corresponding wavenumbers are $\tilde{\nu} = 25000 - 14280$ cm^{-1}.

1. **Near Infrared (NIR)** (water content analysis and organic compound detection):
   - Wavelength: $\lambda = 0.75 - 3\,\mu\text{m}$
   - Wavenumber: $\tilde{\nu} = 1/\lambda = 13333 - 3333\,\text{cm}^{-1}$
2. **Mid (Thermal) Infrared (MIR)** (molecular vibrations, like CO_2 absorption at 667 cm^{-1}):
   - Wavelength: $3 - 15\,\mu\text{m}$
   - Wavenumber: $3333 - 667\,\text{cm}^{-1}$
3. **Far Infrared (FIR)** (low-frequency vibrations and rotational transitions):
   - Wavelength: $15 - 1000\,\mu\text{m}$
   - Wavenumber: $667 - 10\,\text{cm}^{-1}$

7.8.1 Infrared light absorption bands for CO_2 and water vapor

The photons of infrared (IR) radiation at specific frequencies carry just the right amount of energy to induce vibrational and rotational transitions in water vapor and carbon dioxide molecules. Water, a triatomic molecule, forms a bent structure with the heavy oxygen atom at the vertex and two light hydrogen atoms separated by an angle of approximately 104.5°. This geometry results in three fundamental vibrational modes:

- **Symmetric stretch** (ν_1), in which both O–H bonds elongate and contract in unison;
- **Bending mode** (ν_2), where the H–O–H bond angle oscillates, resembling a scissoring motion;
- **Asymmetric stretch** (ν_3), where one O–H bond elongates while the other contracts, and vice versa (see Figure 7.8, left).

Continuum absorption by water (far from individual absorption lines) is significant, especially in the window region of $830 - 1250$ cm^{-1} or $12 - 8$ μm. Liquid water (e.g., cloud droplets, fog, rain) also contributes to IR absorption, but less dominantly than vapor. Clouds composed of liquid water or ice strongly absorb and reemit IR radiation. Clouds act as grey bodies. They absorb across most of the IR spectrum and emit based on their temperature.

At equilibrium, CO_2 is a linear molecule: O=C=O. Carbon is at the center, flanked symmetrically by two oxygen atoms. Because of the molecule's linearity, only the ν_2 and ν_3 vibrations are present in IR.

At lower wavenumbers (longer wavelengths), IR photons do not carry enough energy to excite vibrational modes but can still induce **rotational transitions**. As an asymmetric top molecule water has three distinct moment of inertia, each associated with a different principal axis of rotation:

- **A-axis**, perpendicular to the molecular plane;
- **B-axis**, lying in the molecular plane and bisecting the H–O–H angle;
- **C-axis**, also in the molecular plane but orthogonal to the B-axis (see Figure 7.8, right).

Because CO_2 is a linear and symmetric molecule, it behaves as a linear rigid rod that can rotate along its axis and perpendicular to it, regardless of the molecule's orientation in space. In CO_2, rotational transitions appear as a fine tooth-comb structure within vibrational bands (called rotational-vibrational spectra).

The major infrared absorption bands of water vapor and carbon dioxide are summarized in Tables 7.1 and 7.2.

7.8.2 Basics of LTE in the atmosphere

The Local Thermal Equilibrium (LTE) of a gaseous atmosphere and thermal[8] infrared radiation (IR) ($\lambda = 3 - 15$ μm or $\tilde{\nu} = 3333 - 667$ cm^{-1}) can be described as follows (*Pierrehumbert*, 2010, 2011):

[8] See Definition 12.

Table 7.1: Major infrared absorption bands of water vapor. Data adapted from *Rothman et al.* (2013).

Wavelengths (μm)	**Wavenumbers (cm^{-1})**	**Transition Type**	**Description**
2.5–3.0	4000–3333	O–H stretch overtones	Weak overtone absorption
4.5–6.5	2200–1500	Bending mode (ν_2)	Strong absorption near 6.3 μm
5.5–8.0	1800–1250	Combination bands	Complex structure, medium strength
12–20	833–500	Rotational	Rotational transitions in the IR
15	667	Overlaps with CO_2	Water vapor sidebands near strong CO_2 feature
17.9–23.8	560–420	Rotational	Rotational band tail
>20	<500	Rotational (far-IR)	Continuum and weak rotational bands

- An atmosphere is a mixed gas of **matter** and **photons**. **Radiative transfer** deals with the nonequilibrium thermodynamics of a radiation field interacting with matter and the transport of energy by the photon component of the atmosphere.
- CO_2 energy transition lifetimes are from 0.001 to 0.1 s. The typical time between collisions in an atmosphere at a pressure of 10^4 Pa and temperature of 255 K is well under 10^{-7} s. Therefore, the energy of the photon will almost always be assimilated by collisions into the general energy pool of

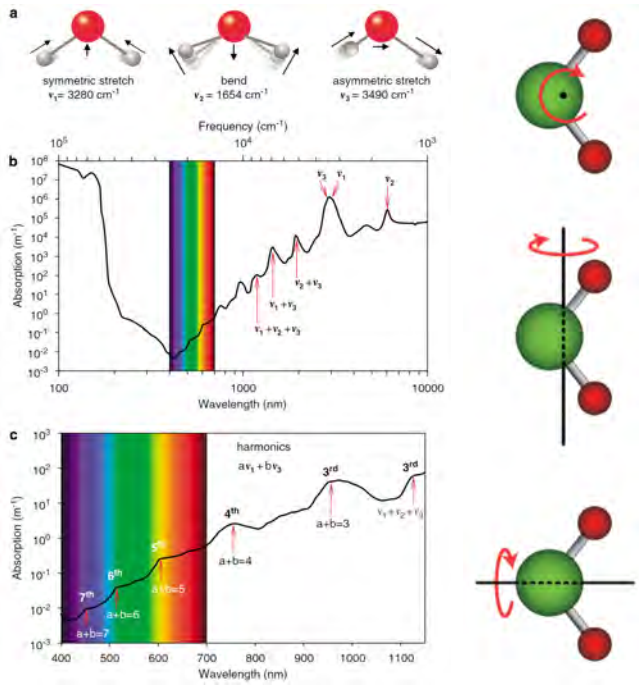

Figure 7.8: Sources: Figure 2 in *Stomp et al.* (2007) (left) and https://www.xaktly.com/Water.html (right). Radiation absorption by H_2O vapor (similar, but not identical for CO_2). **(a)** The three vibrational modes of the water molecule and their fundamental frequencies in liquid water: symmetric stretching (ν_1), bending (ν_2) and asymmetric stretching (ν_3). The atoms move in the directions indicated by arrows. **(b)** Absorption spectrum of pure water. Peaks in the absorption spectrum correspond to the fundamental frequencies and higher harmonics of the vibrations of the water molecules. **(c)** Absorption spectrum of pure water in the visible and infrared region. Shoulders in the absorption spectrum correspond to the third, fourth, fifth, sixth and seventh harmonics of the symmetric and asymmetric stretch vibrations, as indicated.

Table 7.2: Major infrared absorption bands of carbon dioxide. Data adapted from *Rothman et al.* (2013).

Wavelengths (μm)	Wavenumbers (cm^{-1})	Vibrational Mode	Description
4.0–4.5	2420–2220	ν_3 (asymmetric stretch)	Strong absorption at 4.26 μm
6.9–7.3	1450–1370	ν_1 (symmetric stretch)	IR-inactive (visible in Raman)
14.5–15.5	690–645	ν_2 (bending mode)	Strong absorption at 15 μm

the matter and establish a new Maxwell-Boltzmann distribution at a slightly higher temperature. **That is how radiation heats matter in the LTE limit**.

- Many molecules occupy higher-energy states, and over a moderately small stretch of time a large number of molecules will decay by emitting photons. If that radiation escapes without being reabsorbed, the higher-energy states are depopulated and the system is thrown out of thermodynamic equilibrium. Molecular collisions repopulate the states and establish a new thermodynamic equilibrium at a slightly cooler temperature. **That is how thermal emission of radiation cools matter in the LTE limit**.

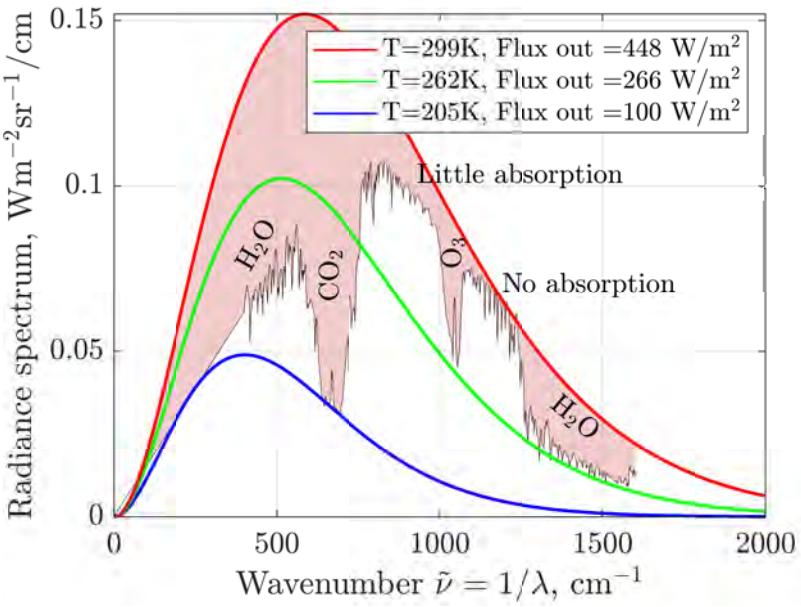

Figure 7.9: The energy-density spectrum of outgoing thermal radiation from the Earth at wave numbers ranging from 400 to 1600 cm^{-1} (black jagged curve). Equivalent wavelengths of 6.3-25 microns are in the mid- and far-infrared bands (see Definition 12). The pink area is due to net absorption of the outgoing energy flux by greenhouse gases that block parts of the Planck blackbody radiation of ground surface at the temperature of 299 K. These spectral radiance data were measured on May 5, 1970, 12:00:07 with NASA's IRIS instrument on the Nimbus 4 satellite. Here you can see one of the earliest satellite measurements of Earth's outgoing longwave radiation that have since become critical to monitoring our planet's energy balance. Data source: NASA. Calculations by Patzek.

7.9 The greenhouse effect

Figure 7.9 shows, as a jagged black curve, the Earth's top-of-atmosphere outgoing radiation captured by the Nimbus 4 satellite. The x-axis represents the spectroscopic wavenumber, $\tilde{\nu}$, defined as the inverse of the radiation wavelength in centimeters. Lower wavenumbers correspond to longer wavelengths and lower photon energies.

This particular observation was made over a swath of North Africa, where the surface (or ground) temperature was approximately 26 °C (299 K). The red curve in the figure represents the ideal Planck blackbody (PBB) emission spectrum for a surface at this temperature. If Earth had no atmosphere, the entire emission spectrum would closely follow this red curve. However, in that case, the effective emission temperature would be approximately 255 K, rather than 299 K. The difference is caused by the absorption of outgoing longwave radiation by atmospheric gases – a phenomenon known as the **greenhouse effect**. Locally, at the time the spectrum was acquired, the greenhouse effect warmed up the ground by about 44 K.

Notice that in the wavenumber ranges of approximately $790 - 974$ cm^{-1} and $1100 - 1240$ cm^{-1}, the atmosphere is nearly transparent to outgoing infrared radiation. In these "atmospheric windows," radiation escapes directly to space from the surface. The jagged structure of the black curve in these regions reflects the variability in surface emissivity.

Outside these windows, the atmosphere strongly absorbs outgoing radiation, especially in certain spectral bands corresponding to the vibrational transitions of greenhouse gases such as H_2O, CO_2, O_3, CH_4, and others. Absorption from the rotational transitions of the H_2O and CO_2 molecules is also important.

The left absorption band in Figure 7.9 is due to the rotational transitions of water molecules. Moving to the right, it is followed by the strongest absorption in the vibrational band (ν_2) of CO_2, and ν_3 of ozone O_3.[9] On the right, the wide region of absorption is due to the vibrational and rotational transitions of water, and even further to the right to those of CO_2.

The shaded pink area in Figure 7.9 represents the difference between the Planck blackbody emission from the Earth's surface and the actual outgoing longwave radiation observed at the top of the atmosphere. This difference quantifies the **greenhouse effect** – the trapping of thermal radiation by atmospheric gases.

Water is the dominant greenhouse agent in Earth's atmosphere. Approximately 50-60% of the total greenhouse effect is attributable to **water vapor**, with an additional 15-25% arising from **liquid water**, primarily in clouds *Pierrehumbert* (2010) .

The second most important greenhouse gas is carbon dioxide (CO_2), responsible for $15 - 25\%$ of the greenhouse effect. Other gases (O_3, CH_4 and N_2O) are minor contributors, but together they contribute $5 - 10\%$ of the greenhouse effect.

While less abundant than water vapor, CO_2 plays a critical role in regulating Earth's long-term climate by setting the background temperature and influencing the hydrological cycle. Specifically, a decrease in atmospheric CO_2 would cool the climate, promoting condensation of water vapor and increasing the removal of water from the atmosphere through precipitation and snowfall. In this way, CO_2 is an ultimate *knob* that controls climate by governing the amount of water vapor the atmosphere can retain.

The greenhouse effect can be explained as follows (*Pierrehumbert*, 2011):

- An atmospheric **greenhouse gas** enables a planet to radiate at a temperature *lower* than the ground's, if there is cold air aloft. It therefore causes the surface temperature in balance with a given amount of absorbed solar radiation to be *higher* than would be the case if the atmosphere were transparent to IR.
- Adding more **greenhouse gas** to the atmosphere makes higher, more tenuous, *formerly transparent* portions of the atmosphere opaque to IR and thus increases the difference between the ground temperature and the radiating temperature.
- The result, once the system comes into equilibrium, is **surface warming**.
- The greenhouse effect of CO_2 on Earth and Mars is visually manifest as the **ditch carved out of the Planck spectrum** near 667 cm^{-1}, see Figure 7.9. A similar ditch is created by O_3 near 1042

[9] The strongest IR absorption feature of ozone is the ν_3 asymmetric stretch, centered near 1042 cm^{-1} ($\sim$9.6 μm). This is the main contributor to ozone's role in the greenhouse effect and is responsible for the deep absorption feature near 1042 cm^{-1} in Earth's outgoing longwave radiation spectrum.

cm^{-1}. These ditches represent energy that would have escaped to space were it not for the opacity of CO_2 and O_3.

- On Venus, the CO_2 greenhouse effect extends well beyond the ditch, owing to the opacity of the continuum associated with so much CO_2.
- In the Earth spectrum in Figure 7.9, one can also see two broad regions in which water vapor has reduced the radiating temperature to a value well below the surface temperature.

7.10 Radiative forcing of greenhouse gases

Burning fossil fuels causes CO_2 emissions and releases combustion byproducts—such as SO_x, NO_x, volatile organic compounds (VOCs), CH_4, soot, and others—that contribute to air pollution. These substances react with atmospheric gases to form tropospheric ozone, formaldehyde, and a variety of primary and secondary aerosols, see Chapter 8.

The accumulation of CO_2 in the atmosphere is the dominant amplifier of the greenhouse effect, which warms the Earth. In contrast, aerosols primarily exert a cooling influence by scattering sunlight and enhancing cloud reflectivity, thereby offsetting part of the greenhouse-induced warming.

To quantify the cumulative impact of greenhouse gases (GHGs), NOAA has introduced the *Annual Greenhouse Gas Index* (AGGI), defined as the ratio of total effective radiative forcing by all long-lived GHGs relative to their 1990 levels. The reference year 1990 was selected because it served as the baseline for the Kyoto Protocol and coincided with the publication of the first IPCC Scientific Assessment of Climate Change (*Houghton et al.*, 1990); see Figure 7.10(a) and Figure 4.7(b). The rise in AGGI since then has been driven primarily by increased CO_2 concentrations. By 2024, the AGGI reached 1.53, indicating that the net radiative forcing from anthropogenic GHGs in 2023 was 53% greater than in 1990, consistent with Figure 4.10.

As shown in Figure 7.10(b), the radiative forcing attributed to CO_2 alone accounted for approximately 65% of the total GHG-induced forcing in 2024:

$$\frac{2.32}{3.53} \approx 0.65$$

This underscores the central role of CO_2 in driving contemporary climate change.

At first glance, an increase of just a few watts per square meter in radiative forcing might seem negligible. But to appreciate its significance, consider the energy implications of even a 1 $W\,m^{-2}$ imbalance applied uniformly across the Earth's surface:

$$\begin{aligned} 1 W\,m^{-2} \times 4\pi(6371 \times 10^3)^2 &= 510 \text{ TW} = 27 \text{ human economies in 2023} \\ 238 W\,m^{-2} \times 4\pi(6371 \times 10^3)^2 &= 121 \text{ PW} = 6.4 \text{ thousand human economies in 2023.} \\ \text{Albedo } 0.30 \Rightarrow 0.29 &= 13.6 W\,m^{-2} \to 7 \text{ PW} = 370 \text{ human economies in 2023.} \end{aligned} \tag{7.7}$$

The 1 $W\,m^{-2}$ energy flux is equivalent to:

- Total annual heat accumulation of $E_{\text{year}} = 510 \times 10^{12} W \times 5.1 \times 10^{14}$ $m^2 \times 3.15 \times 10^7$ s/year $\approx 1.6 \times 10^{22}$ J/year = 16 zetaJ/year.
- Detonation of approximately **400,000 Hiroshima bombs per day**, since each bomb released about 6×10^{13} J.
- Global ocean's net heat uptake rate over the past two decades, which has averaged roughly 0.7–0.9 $W\,m^{-2}$ of Earth's surface area, accounting for more than 90% of the excess energy trapped by greenhouse gases (*Cheng et al.*, 2020, 2022, *Arias et al.*, 2021, *von Schuckmann et al.*, 2023).

To convert this energy flux into ocean warming, consider that 93% of this energy is absorbed by the ocean. Assuming a mixed-layer ocean mass $M_{\text{ocean}} \approx 1.4 \times 10^{21}$ kg and average specific heat capacity

$c_p \approx 4,000\ \mathrm{J\,kg^{-1}\,K^{-1}}$, the temperature change over one year is

$$\Delta T \approx \frac{E_{\text{year}}}{0.93 \times M_{\text{ocean}} c_p}$$

This gives

$$\Delta T \approx \frac{1.6 \times 10^{22}}{0.93 \times 1.4 \times 10^{21} \times 4000} \approx 0.003\ \mathrm{K/year}.$$

Although this rate of ocean warming seems small, it accumulates over time and penetrates ever deeper into the water column, driving sea level rise by thermal expansion and disrupting water circulation in global ocean.

Even a small sustained 1 $\mathrm{W\,m^{-2}}$ imbalance represents a powerful and persistent planetary-scale energy balance perturbation with serious implications for the climate system.

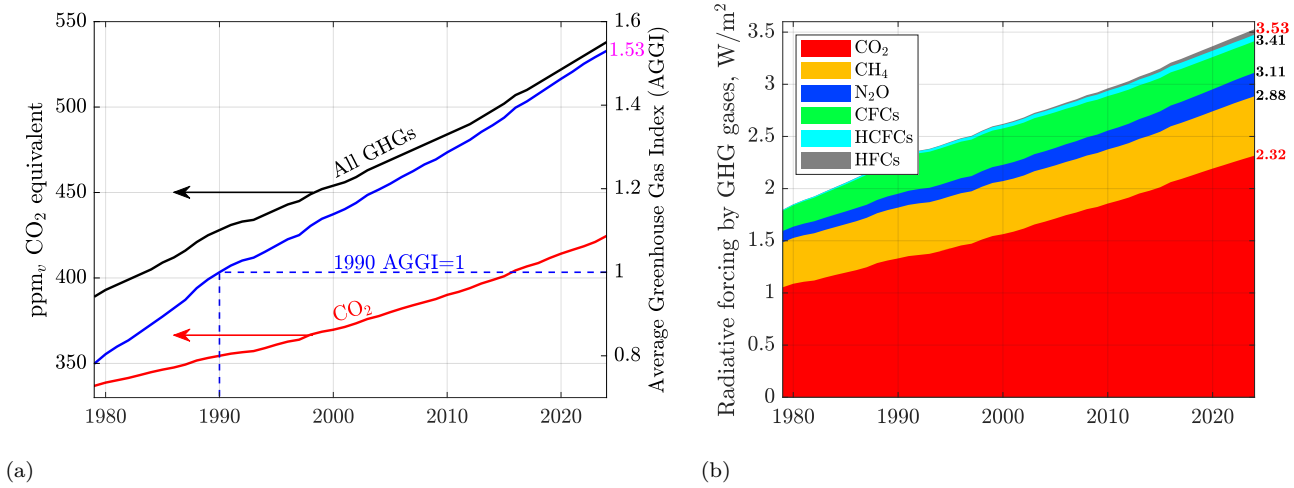

(a) (b)

Figure 7.10: **(a)** Accumulation of CO_2 and all GHG gases in the atmosphere (left y-axis) and the NOAA Annual Greenhouse Gas Index (AGGI), normalized to the year 1990 (right y-axis). **(b)** Radiative forcing, relative to 1750, of virtually all long-lived greenhouse gases. Data sources: (*Dlugokencky et al.*, 2025), see the caption of NOAA's Figure 3 for the list of key GHGs. Calculations by Patzek.

7.11 Climate sensitivity to radiative forcing

According to the conventional forcing-feedback theory of the climate system *Pierrehumbert* (2010), *Sherwood et al.* (2020), the net downward radiation imbalance ΔN at the top of the atmosphere (TOA) can be decomposed into a radiative forcing ΔF, a direct or indirect radiative feedback response ΔR caused by forced changes in temperature, and variability V unrelated to the forcing or feedback:

$$\Delta N = \Delta F + \Delta R + V \tag{7.8}$$

Variability V can arise from changes in upwelling of cold water to the surface, cloud cover, albedo, and so forth. The net radiation balance ΔN consists of the net absorbed shortwave (SW) solar radiation minus the planet's emission of longwave (LW) radiation. Assuming that the radiative response ΔR is proportional to first order to the forced change in global mean g surface air temperature (SAT), ΔT, Equation (7.8) becomes

$$\Delta N = \Delta F + \lambda \Delta T + V \tag{7.9}$$

where the climate feedback parameter λ is the sensitivity of the net TOA downward radiation N to T and dN/dt (at fixed F). If this feedback parameter is negative, the system is stable.

In equilibrium over sufficiently long time scales, with $\lambda < 0$, the net radiation imbalance ΔN and mean unforced variability V will each be negligible, leaving a balance between the constant forcing ΔF and radiative response ΔR. In this case Equation (7.9) simplifies to

$$\Delta T = -\frac{\Delta F}{\lambda} \tag{7.10}$$

The case of a doubling of CO_2 concentration defines the *climate Planck climate sensitivity*:

$$S = -\frac{\Delta F_{2\times CO_2}}{\lambda} \tag{7.11}$$

where $\Delta F_{2\times CO_2}$ is the radiative forcing per doubling of CO_2 concentration in the air.

As observed by *Sherwood et al.* (2020), effective λ (the value that satisfies Equation (7.9) for some climate change scenario) can vary significantly across scenarios even when the same feedbacks are nominally operating.

All measurements relevant to climate sensitivity come from the recent historical period during which internal variability may play a large role and the climate is far out of equilibrium; or from proxy reconstructions of past climate equilibria during which the climate differed significantly from the reference scenarios.

Finally, we note that any definition of planetary sensitivity depends on the time scale considered. The S in Equation (7.11) incorporates only feedbacks acting on time scales of order a century. Traditional ECS, see Table 7.3, allows for more complete equilibration of the system, albeit with some feedbacks explicitly excluded, see section 2.1 in *Sherwood et al.* (2020) which assumes that ECS and S are related by

$$ECS = (1 + \zeta)\, S \tag{7.12}$$

where ζ represents the net effect of climate feedback mechanisms that enhance or diminish the initial temperature response to a doubling of atmospheric CO_2. Different climate regimes lead to different ζs:

- Positive feedbacks ($\zeta > 0$): Water vapor increase (H_2O is a strong GHG); ice loss; negative albedo effect (the Earth albedo ↓); and/or decreased cloud cover (albedo ↓).
- Negative feedbacks ($\zeta < 0$): Increased cloud cover (albedo ↑); and/or glaciations (albedo ↑).

7.11.1 Range of ζ

The Planck sensitivity, S, is the baseline temperature response without feedbacks, which is approximately equal to 1.2°C for a doubling of CO_2 *Arias et al.* (2021). Since IPCC Sixth Assessment Report (AR6) (*Arias et al.*, 2021) estimates ECS to be between 2.5°C and 4°C, the corresponding range of $\zeta \in [1.08, 1.33]$, indicating that climate feedbacks amplify the initial warming by up to 2.3 times. ESS is usually somewhat higher than ECS (*Sherwood et al.*, 2020).

The relationship between ESS and ECS can be expressed as:

$$ESS = (1 + \zeta_{\text{slow}})\, ECS \tag{7.13}$$

where ζ_{slow} represents the additional climate change amplification from slow climate feedbacks.

7.11.2 How Much Higher is ESS Compared to ECS?

Studies suggest that ESS is typically 1.5 to 2 times ECS:

- ECS = 2.5-4.5°C per doubling CO_2 (best estimate: 3°C) (*Arias et al.*, 2021).
- ESS = 4-6+°C per doubling CO_2, potentially exceeding 6°C in extreme cases (*Hansen et al.*, 2008, *Lunt et al.*, 2010).

Paleoclimate data confirm that ESS is significantly higher than ECS:

Table 7.3: Comparison of sensitivity estimates of current climate

Feature	ESS (Earth System Sensitivity)	ECS (Equilibrium Climate Sensitivity)	TCR (Transient Climate Response)
Definition	Long-term temperature change including slow geologic feedbacks	Long-term temperature change after CO_2 doubling (fast + some slow feedbacks)	Short-term temperature change at CO_2 doubling under a 1% increase per year
Timescale	Thousands to millions of years	Centuries to millennia	Decades (< 100 years)
Feedbacks	Fast + slow + very slow Earth system feedbacks (e.g., carbon cycle, ice sheets, weathering)	Fast + some slow feedbacks (deep ocean, ice sheets)	Fast feedbacks only (anthropogenic, clouds, water vapor)
Typical Range (°C per $2\times CO_2$)	4 – 6°C or more (potentially higher) *Hansen et al.* (2008), *Lunt et al.* (2010)	2.5 – 4.5°C (best estimate 3°C) *Stocker et al.* (2013), *Gettelman et al.* (2019)	1.4 – 2.2°C (best estimate 1.8°C) *IPCC, Full Report* (2022)
Relevance	Deep-time climate changes, past warm climates (e.g., PETM, EECO, see Figure 9.8)	Ultimate human-caused climate change	Near-term policy and mitigation

Table 7.4: Comparison of *ESS* and *ECS* in paleoclimate records

Climate Period	ESS (°C per $2\times CO_2$)	ECS (°C per $2\times CO_2$)	ESS/ECS Ratio
Eocene (∼50 Ma)	6–9	3–4.5	∼ 2 *Hansen et al.* (2008)
Pliocene (∼3 Ma)	4.5–6	2.5–3	∼ 1.5–2 *Pagani et al.* (2010)
Last Glacial Maximum (∼20 ka)	4–5	∼ 3	∼ 1.5 *Hansen et al.* (2013a)

Table 7.5: This is a reproduction of Table 11 in *Sherwood et al.* (2020). Medians and 66% (1σ) probability ranges (in brackets) for Equilibrium Climate Sensitivity (ECS) to one doubling of CO_2, Transient Climate Response (TCR), and warming PDFs for RCP2.6, 4.5, 6, and 8.5 in Figure 23 in *Sherwood et al.* (2020). RCP = Representative Concentration Pathway scenarios by IPPC. For example, the RCP4.5 scenario results in an incremental 4.5 W/squaremeter radiative forcing by 2100. PPD = prior predictive distribution. All values are in K.

	Baseline	Uniform-S PPD
ECS	3.2 [2.6, 4.1]	3.5 [2.7, 4.6]
TCR	1.8 [1.5, 2.2]	1.9 [1.6, 2.4]
RCP2.6 warming	1.0 [0.7, 1.4]	1.2 [0.8, 1.7]
RCP4.5 warming	1.8 [1.4, 2.3]	2.0 [1.5, 2.6]
RCP6.0 warming	2.0 [1.6, 2.6]	2.3 [1.7, 3.0]
RCP8.5 warming	3.5 [3.0, 4.2]	3.8 [3.2, 4.8]

7.12 Current Earth energy imbalance

Climate forcings by greenhouse gases (see Chapter 5) and aerosols (see Chapter 8) create an imbalance at the top of the atmosphere (TOA) between the net incoming solar radiation and the outgoing longwave radiation emitted by Earth.

Figure 7.11 shows that this Earth Energy Imbalance (EEI) – a measure of the transient climate response – has increased significantly between 2001 and 2023, according to observations from NASA's *Clouds and the Earth's Radiant Energy System* (CERES) satellite instruments. Notably, the observed EEI trend increasingly diverges from the predictions made by most of *Climate Model Intercomparison Project 6* (CMIP6) models (see Section 10.4). These models generally underestimate the strong positive shortwave and strong negative longwave components of the observed TOA radiative imbalance (*Myhre et al.*, 2025).

This discrepancy implies that real-world global warming and sea level rise may be progressing faster than projected by current state-of-the-art global climate models.

It is important to emphasize that our statistical model in Chapter 11 relies exclusively on empirical observations: atmospheric CO_2 concentrations from Chapter 5 and global surface temperature anomalies from Chapter 10.

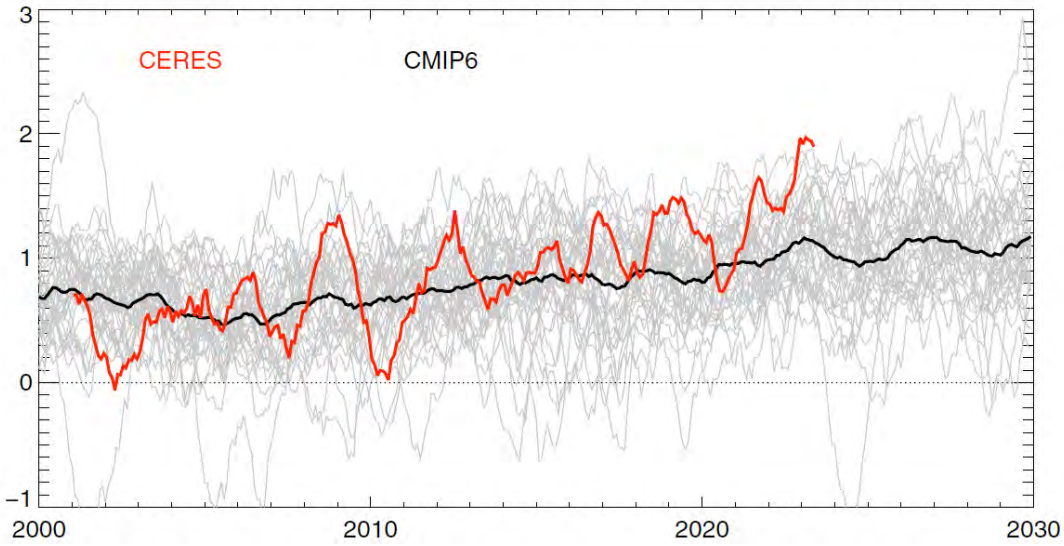

Figure 7.11: Trends in Earth energy imbalance (EEI) from CERES (in red) data and CMIP6 models (black and gray). The CERES data are shown from 2001 to 2023. The CMIP6 data are shown from 2000 to 2030. All EEI are given as 12-month running means. CMIP6 model mean is shown by a thick black line and individual models are shown in thin gray lines. Only one ensemble member for each of the models is shown. Notice that the ocean heat uptake in Figure 12.2 is referenced to zero in the year 2000, and is consistent with this figure. Source: Fig. 1 in (*Myhre et al.*, 2025), reproduced with permission.

Chapter 8

Pollution, aerosols and climate regulations

600 block of Liberty Avenue, Pittsburgh, ca. 1939-1942.
Image SCLS010, University of Pittsburgh.

Environmental pollution is not only humanity's treason to humanity but also a treason to all other living creatures on earth!
– attributed to Mehmet Murat Ìldan (source unverified; widely circulated online)

8.1 What are you going to learn?

This chapter explores the history and consequences of air pollution – the omnipresent byproduct of the Industrial Revolution – and the long-delayed governmental responses aimed at mitigating its most harmful effects. For over 170 years, little was done to curb the release of deadly toxins into the atmosphere, oceans, and soil. In addition to the key greenhouse gases, carbon dioxide and methane discussed in Chapter 5, these toxins are chiefly produced through the combustion and processing of fossil fuels in virtually every sector of human activity, including transportation, oil refining, chemical manufacturing, and agriculture.

We will examine landmark environmental legislation first enacted in Great Britain and the United States, which – after decades of industrial expansion without regulation – began to place meaningful limits on toxic emissions. Many of these laws were subsequently adapted by other nations, most notably China.

Tragically, the United States now faces a regressive policy shift, driven by isolationist leaders who reject the scientific understanding of nature's deep interconnectivity – an understanding that is essential to addressing global warming. Even more perversely, the current trend of removing toxic pollutants while continuing to release ever-larger quantities of CO_2 and CH_4 may accelerate the climate system's sprint toward a new, much hotter equilibrium – one far less hospitable to human civilization.

8.2 Why is this important?

A deeper understanding of how pervasively polluted air, water, and soil have threatened life on Earth may sharpen your perspective – especially if you have children or grandchildren whose futures are at stake. Dirty air kills, even at very low concentrations of pollutants, especially PM2.5 (*Weichenthal et al.*, 2022). It also promotes dementia (*Zhang et al.*, 2025c).

Definition 13. $PM_{2.5}$ refers to fine particulate matter with a diameter of 2.5 μm or smaller, small enough to penetrate deep into the lungs and enter the bloodstream. It is a major air pollutant, produced primarily by combustion emissions from vehicles, power plants, wildfires (*Qiu et al.*, 2025), etc., and linked to severe health risks including respiratory and cardiovascular disease.

At the global scale, the observed decline in Earth's albedo can be directly linked to the reduction in atmospheric aerosol concentrations. While aerosols have long masked some of the warming caused by greenhouse gases by reflecting sunlight back into space, their decline – driven by air pollution controls – has inadvertently unmasked the full extent of human-induced global warming. The year 2024 was the hottest on record, with 2025 following in its footsteps. Cleaner air over Europe, North America, and Asia has contributed to amplified polar warming and the decline of Arctic ice cover to an all-time low in the last 50 years, see Appendix E.

Briefly, there is no such thing as "clean CO_2 pollution" or "clean coal," or "clean combustion." Ever-increasing emissions of CO_2 and methane cause harm regardless of whether other pollutants are removed. Indeed, stripping aerosol-forming substances lays bare the full impact of CO_2 pollution. We cannot have it all, my friends! If you still choose to ignore this message, I suggest you watch the film *Don't Look Up*.

8.3 Preliminaries

Anthropogenic aerosol emissions exhibit pronounced geographical heterogeneity, with the highest concentrations originating from densely populated and industrialized regions. Major aerosol sources are scattered across East and South Asia (especially eastern China and the Indo-Gangetic Plain), parts of Africa (biomass burning in central and western regions), and industrial zones in Europe and North America. The spatially heterogeneous nature of aerosols causes strong regional variations in radiative forcing and cloud-aerosol interactions. Because aerosols have short atmospheric lifetimes (typically 1–2 weeks), their climatic impacts are primarily localized near their emission sources or downwind regions (*IPCC*, 2013, *Myhre et al.*, 2013b, *Hammer et al.*, 2020, *Li*, 2023).

Table 8.1: Estimated global aerosol effective radiative forcing (ERF_{aer}) from 2020 to 2050.

Year	ERF_{aer} [W/m^2]	Δ from 2020 [W/m^2]	Source(s)
2020	−1.3 ± 0.7	–	*Myhre et al.* (2013b), *Forster et al.* (2021b,a)
2030	−1.0 to −1.1	+0.2 to +0.3	*Samset* (2020), *Liu* (2023)
2040	−0.9 to −0.8	+0.4 to +0.5	*Li* (2023)
2050	−0.8 to −0.6	+0.5 to +0.7	*Kloster* (2022), *Lee et al.* (2021)

Table 8.1 shows that current aerosol cooling is about -1.3 $W\,m^{-2}$. Projected increase (less cooling) by 2050 is approximately 0.5 ± 0.2 $W\,m^{-2}$, largely because emissions of pollutants like SO_2 and black carbon will continue to decline. Or will they, given the pollution control rollbacks in the US and EU?

It is likely that aerosols will provide progressively **less** cooling in the coming decades, thereby **unmasking** the latent warming already "**baked in**" by accumulated greenhouse gases. Unless fossil fuel combustion is substantially reduced, this additional warming will continue to accelerate climate change.

8.4 Biomass and FF combustion, greenhouse gas (GHG) emissions and aerosols

Fossil fuel combustion and its associated CO_2, aerosol and black carbon emissions have not been distributed uniformly across the world, as illustrated in Figure 6.6(b) and Figure 8.1. According to Figure 6.6(b), the original industrial polluters – Europe and the United States – were surpassed in annual CO_2 emissions by China in 2006 and by the rest of Asia (primarily India) in 2008. By 2024, China alone was emitting CO_2 at a rate of 12 $Gt\,(yr)^{-1}$, exceeding the combined emissions of the U.S. and Europe ($2 \times 4.9 = 9.8$ Gt/yr).

In terms of cumulative fossil fuel CO_2 emissions, shown in Figure 8.1(a), Europe has been the historical leader, followed by the United States, the current EU-27, and China/other Asia – each now contributing nearly equal shares. By the end of 2024, both China and the rest of Asia will have individually surpassed the cumulative emissions of the EU-27 countries.

Figure 8.1(b) shows cumulative emissions for the world and the combined total from the high emitters identified in Figure 8.1(a). As of the end of 2023, these major emitters were responsible for approximately 84% of all global fossil fuel CO_2 emissions. This fact is crucial because the atmosphere is well-mixed, and the effective radiative forcing from greenhouse gases – see Figure 7.10(b) – depends on their cumulative atmospheric burden, not on short-term emission rates.

Finally, it is worth noting that the collapse of the Soviet Union in 1990 triggered the largest recorded drop in global anthropogenic CO_2 emissions to date, as also reflected in Figure 6.6(b).

Between the end of World War II in 1945 and the early 1970s, the world – led by the United States, Canada, Japan, and Western Europe – experienced an unprecedented period of economic expansion. This rapid growth, however, was accompanied by largely unregulated emissions and widespread industrial pollution of air, water, and soil. Before the mid-1970s, few legal constraints existed to curb environmental degradation, and it took several more years before new regulatory frameworks began to show tangible effects.

In parallel, the Soviet Union, Warsaw Pact countries, and China pursued aggressive industrialization, often relying on outdated and highly polluting technologies with no environmental safeguards. By the early 1970s, pollution levels in the Soviet Union had reached grotesque proportions (*Feshbach and Jr.*, 1992). China followed a similarly ecocidal path beginning with the Great Leap Forward in 1958 (*Smil*, 1984). The Soviet economy collapsed between 1990 and 1995, while China did not begin to implement meaningful pollution controls until the mid-1990s, with noticeable improvements emerging only in recent

decades.

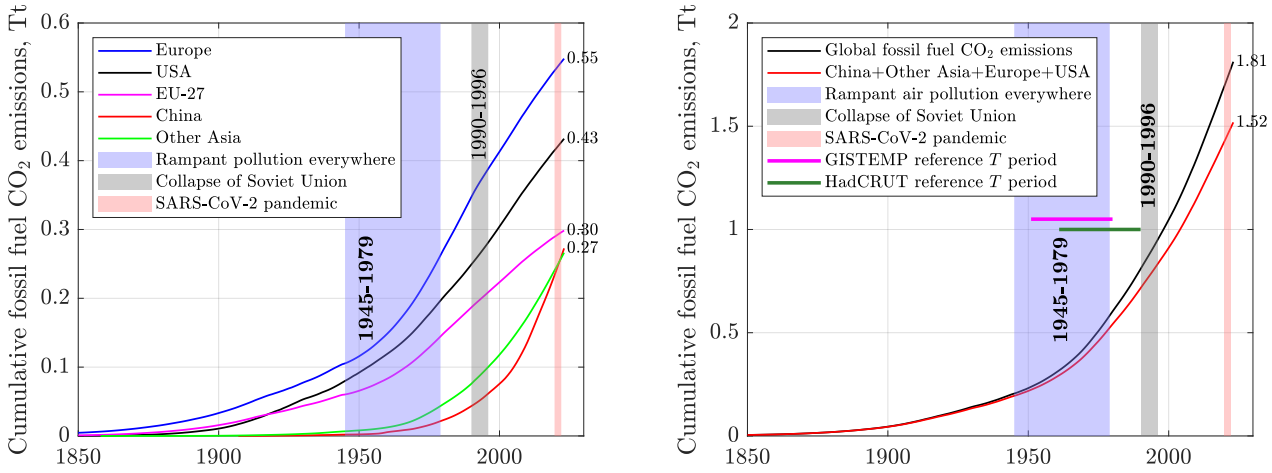

(a) (b)

Figure 8.1: Cumulative fossil fuel CO_2 emissions by **(a)** country and region, and for the world and high-emitters **(b)**. Sources: EIA, OWID, *Clark and Jacks* (2007), Patzek, accessed 01/11/2024.

As we have already observed in Section 7.10, burning fossil fuels causes CO_2 emissions and air pollution by combustion byproducts (SO_x, NO_x, VOCs, CH_4, soot, etc.) that interact with the atmospheric gases forming ozone, formaldehyde and an assortment of primary and secondary aerosols (*Ervens et al.*, 2011, *Myhre et al.*, 2013a). The CO_2 concentration buildup is the dominant amplifier of the greenhouse effect that heats up the Earth, and the air-pollution aerosols mostly shield the planet from sunlight and decrease the heating.

The annual combustion of gigatons of fossil fuels and biomass (Figure 5.5(a)) releases an estimated $400-600$ million tonnes of soot and chemically complex gases into the atmosphere each year (*Janssens-Maenhout et al.*, 2019, *IPCC*, 2019a, *Crippa et al.*, 2023). These emissions form aerosols, which play a critical role in Earth's radiative balance. Through aerosol-radiation interactions (ARIs) and aerosol-cloud interactions (ACIs), aerosols exert a negative effective radiative forcing, partially offsetting – or in some cases nearly cancelling – the positive radiative forcing from atmospheric CO_2, as illustrated in Figure 8.2.

In effect, a sufficiently polluted atmosphere – though toxic and life-threatening – can become optically thick enough to reflect or absorb a substantial portion of incoming solar radiation. We will explore this compensating but lethal for most life mechanism in more detail shortly and in Chapter 14.

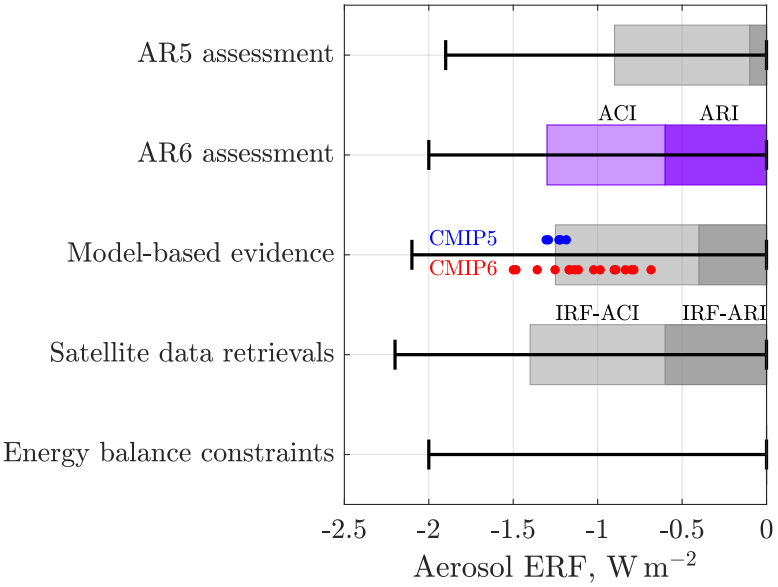

Figure 8.2: Aerosol net effective radiative forcing (ERF) from different lines of evidence. IRF ARI refers to the Instantaneous Radiative Forcing (IRF) from Aerosol-Radiation Interactions (ARI). Similarly ACI refers to Aerosol-Cloud Interactions. The headline AR6 assessment of -1.3 [-2.0 to -0.6] (mean[min to max]) W m^{-2} is highlighted in purple for 1750-2014 and compared with the AR5 assessment of -0.9 [-1.9 to -0.1] W m^{-2} for 1750-2011 (note a discrepancy between the AR5 bars in IPCC's Figure 7.5 and the supporting data). The evidence comprising the AR6 assessment consists of climate model-based evidence of -1.25 [-2.1 to -0.4] W m^{-2}; observational evidence from satellite retrievals of -1.4 [-2.2 to -0.6] W m^{-2}; and energy balance constraints [-2 to 0] W m^{-2} with no best estimate. Based on the data to Figure 7.5 in *Masson-Delmotte et al.* (2021). Calculations by Patzek.

8.5 Pollution and climate

My own childhood experience in the industrial Upper Silesia in communist Poland and other anecdotal evidence point to the main cause of stagnation of the global mean surface temperature between 1951 and 1980, chosen as a 30-year mean temperature reference period (GISTEMP) by NASA's Goddard Institute for Space Studies, (*NASA*, 2022), see Figure 8.1(b). Similarly, the period of 1961-1990 was chosen for the reference mean global temperature by the Hadley Centre of the UK Met Office in collaboration with the Climatic Research Unit (CRU) at the University of East Anglia in Norwich, England (HadCRUT) (*Brohan et al.*, 2006b, *Jones et al.*, 2012).

IPCC and our analysis eventually settled on shifting the mean surface temperature anomalies relative to GISTEMP or HadCRUT up to the 1850-1900 reference (*Arias et al.*, 2021).

Global temperature deviations from a single global reference temperature (**anomalies**) are a key metric in the study of climate change, see Chapter 10.

Because of measurement error cancellation and minimization of local and short-term fluctuations (*NASA*, 2022), these anomalies, rather than absolute temperatures, provide a clearer picture of climate trends. The GISTEMP and HadCRUT standards were chosen because they are natural references for the modern temperature measurements at roughly 30,000 weather station worldwide, most a part of the global telecommunication systems (*Ortiz-Bobea*, 2021), and by ocean buoys and submersibles (*ARGO*, 2020, *NASA and CNES*, 1992, *NOAA et al.*, 2001, 2008, 2016) etc., and satellites (*USGS and NASA*, 1972, *NASA*, 2002, 2000, *NOAA and NASA*, 2011, *NOAA*, 1975, 1978, *ESA and EUMESTAT*, 2016, *ESA*, 2010) etc.

None of these complex temperature measurement methods existed in 1850-1900, and the shift to an earlier

reference temperature is purely formal, to reflect better the pre-industrial climate. Beyond 2025, if the current US administration has its way, many of these essential satellite programs and most environmental regulations will be terminated, and most of the US public will forget about the exploding climate change until they start to choke on deadly air pollution, while eating mercury in fish, drinking carcinogens in water, and succumbing to heat strokes.

This multidecadal stagnation of global temperature amid the ever-increasing CO_2 emissions was likely caused by the runaway industrial, agricultural, residential and transportation emissions of SOx, soot particles, and other aerosols that dampened the rate of heating of the planet, cf. Figure 8.2.

In my home town, Gliwice, industrial gas aerosols and toxic effluents from chemical plants, soot and dust from iron and steel works and cement plants, and acid rain from the high-sulfur brown coal burned in power stations nearby, together caused an unimaginable today level of pollution (e.g., *Fowler et al.* (2020), Table 1), from which I still have serious health problems 50 years later.

Similar levels of pollution were present in all industrial and urban centers on the planet, dimming sunlight over Europe, and much of the US and Asia. During my 1995 visit to Tianjin, a major coastal industrial center in China, I encountered levels of air pollution that made Upper Silesia seem like a sanatorium for the convalescing TB patients. Air quality in Beijing was not much better, and I could barely see the other side of the street from my luxurious hotel windows.

By 1950, the vile industrial pollution of the entire global ecosphere accumulated enough microplastics, radionuclides and industrial toxins in lake sediments in Canada to call their geologic evidence a new epoch, the *Anthropocene* (*McCarthy et al.*, 2023).

This definition was swiftly rejected as lacking by a committee of experts (*Witze*, 2024).

Since times immemorial, climate changes, mostly long draughts, and localized environment exhaustion and pollution have been main causes of collapses of many civilizations, e.g, (*Tainter*, 1990, *Wright*, 2005, *Tainter and Patzek*, 2011). To prevent these collapses, rulers have been issuing edicts and laws, e.g., in (*Athens*, -500) (urban cleanliness and sanitation); in India (*Ashoka*, -250) (animal protection and afforestation); in England (*King Arthur*, 1215) (forest law and restrictions on deforestation), (*King Henry III*, 1217) (rights to sustainable resource use and limited deforestation) and (*King Edward I*, 1306) (restricted excessive logging in royal forests to preserve resources for shipbuilding and construction); (*Spanish Crown*, 1573) (conservation of water, forests, and land-use planning in the Americas); in France (*King Louis XIV*, 1669) (regulated logging, protected forests, and established sustainable timber management policies); in Victorian England (*UK Parliament AA*, 1863) (air pollution control law, regulating emissions from chemical industries) and (*UK Parliament RP*, 1876) (regulation of industrial water pollution in the UK); in Germany (*Council of Nuremberg*, 1334) (regulations to protect forests, prevent deforestation, and ensure sustainable timber use) and (*Emperor Wilhelm I*, 1875) (sustainable forestry practices and regulated deforestation); in USA, (*Congress*, 1872) (Yellowstone became the first national park, setting a precedent for conservation efforts worldwide); etc.

Unsurprisingly, about 40-60% of early environmental laws dealt with forests, the main source of energy-on-demand and building materials for all civilizations prior to 1760 (*Williams*, 2003, *Perlin*, 2005, *Radkau*, 2008), and the largest victim of "progress." While these laws had some impact, the global deforestation since the Neolithic times until today has claimed *46-50%* of the original forest cover (*Crowther et al.*, 2015), see Table 8.3. Most of this loss occurred in the last *300 years* due to industrialization and modern agriculture (*Hannah et al.*, 2020). Now the assertion that man has always been a nature's flame has been quantified, and nature lost.

The Industrial Revolution has not only accelerated forest losses to logging, and conversions to pastures and agricultural land, but it also added new staggering waste streams dumped into the environment. It took a century of ever-worsening pollution and direct loss of life, see Figure 8.3, for the UK legislators to start acting, e.g., (*UK Parliament CAA*, 1956, *UK Parliament CPA*, 1974, *UK Parliament EPA*, 1990, *UK Parliament CAA*, 1993). A comprehensive set of US environmental laws followed, e.g., (*EPA NEPA*, 1969, *EPA CAA*, 1970, *EPA CWA*, 1972, *EPA ESA*, 1973, *EPA RCRA*, 1976, *EPA SDWA*, 1974, *EPA TSCA*, 1976, *EPA CERCLA*, 1980, *EPA OPA*, 1990). Similarly in the EU, (*EU WFD*, 2000, *EU Treaty*, 2007, *EU EIA*, 2011); Russian Federation (*Russian Fed AP*, 1999, *Russian Fed EP*, 2002, *Russian Fed SP*,

2001, *Russian Fed WC*, 2006, *Russian Fed WM*, 1998); and in People's Republic of China, e.g., (*PRC President EPA*, 1989, *PRC President WPP*, 2008, *PRC President APP*, 2015, *PRC President SPP*, 2018, *PRC President SWPP*, 2020).

First, we must stress that the US, EU and UK have had huge successes in fighting a century of the all-out environmental pollution between 1850 and 1950. But there are several differences and challenges among them.

The United States has a unique federal system, in which the federal government and individual states share environmental responsibilities, but this creates many problems:

- **Inconsistent Enforcement:** The federal structure leads to inconsistent enforcement standards across states. The already gutted Environmental Protection Agency (EPA) sets federal guidelines, but state agencies often have the autonomy to interpret and enforce them differently (*Fiorino*, 2006, *Vig and Kraft*, 2018).
- **Judicial Constraints:** Environmental regulations in the U.S. are frequently challenged in court (*Lazarus*, 2020). Notable cases like *West Virginia v. EPA* (2022) have limited the EPA's regulatory power, creating uncertainty in environmental governance (*SCOTUS*, 2022).
- **Outdated Legislation:** Key laws, such as the Clean Air Act and the Clean Water Act, were enacted decades ago. Updating these laws requires congressional approval, which is often impossible because of extreme political polarization (*Vig and Kraft*, 2018).
- **Political Influence and Lobbying:** Corporate lobbying corrupts environmental laws *Fiorino* (2006). On March 12, 2025, the US EPA's Administrator Zeldin announced the rollback of 31 environmental regulations, targeting policies on pollution from coal-fired power plants, climate change initiatives, and electric vehicle mandates. He claimed these changes would reduce regulatory costs and boost American manufacturing, making this day a single largest abdication of ecological and human health responsibilities by a government of any developed country (AP News).

We don't know what will happen with environmental regulations in the US ca. 2025.

The EU generally has a more centralized approach to environmental regulation:

- **Centralized Enforcement:** EU directives set binding standards for all member states, which must implement these through national laws (*Jordan and Adelle*, 2013). This results in more uniform enforcement compared with the US.
- **Adaptability:** EU laws are frequently updated to address emerging environmental challenges, such as climate change. The Emissions Trading System (ETS) is a key example of this adaptability (*EEA*, 2022).
- **Legal Supremacy:** The European Court of Justice plays a crucial role in enforcing environmental laws across member states, ensuring compliance (*Jordan and Adelle*, 2013).

Since leaving the EU, the UK has faced its own set of challenges in environmental governance:

- **Transition from EU Standards:** The UK has adopted much of the EU's environmental framework, but it now needs to fund independent enforcement bodies, such as the Office for Environmental Protection (OEP) (*ClientEarth*, 2021).
- **Legal Uncertainty:** The transition has created gaps in the regulatory framework, and there are concerns about the capacity of new UK institutions to enforce environmental laws effectively (*ClientEarth*, 2021).
- Funding is short.

Both China and Russia have suffered from a weak enforcement of environmental laws and corruption, but China has made more progress, see Table 8.2.

With the extensive pollution cleanup efforts by all major emitters in Figure 8.1 and removal of aerosols, the Earth's atmosphere has become more transparent first over Europe and America, then over China

and other Asia. The removal of aerosols while increasing emissions of CO_2 accelerates Earth's warming and this is what has happened.

A recent paper (*Wang et al.*, 2024) provides more evidence for this line of reasoning by describing 10 years (2010 to 2020) of unprecedented surface seawater temperature warming in the NE Pacific. The authors present evidence that this rapid warming has been caused by a gradual cleanup of the incredibly polluted air over China. Thus, one might conclude that cleaner air over land has ushered speedier heating of the Earth's surface towards something like +10°C in thermal equilibrium, unless global emissions are curtailed dramatically *now*, cf. (*Hansen et al.*, 2023). This statement is consistent with higher sensitivity of the generally much cleaner paleoatmosphere to changes in GHG concentrations.

(a) (b)

Figure 8.3: **(a)** The 1948 Donora "yellow fog" was the worst air pollution disaster in U.S. history. It killed 20 people in one day (*Perry and Lave*, 1998), jump-started the fields of environmental and public health, drew attention to the need for industrial regulation, and launched a national conversation about the effects of pollution. But in doing so, it pitted "economic growth" against the health of people and their environment. Source: The Smisonian, Bettmann / Contributor. **(b)** A thick fog that engulfed London in December 5-9, 1952, mixed with black smoke spewed by homes and factories to create a deadly smog that killed about 12,000 people (*Bell et al.*, 2004). Source: Central Press/Hulton Archive/Getty Images.

Table 8.2: Comparison of Environmental Law Enforcement in Russia and China

Category	**Russia**	**China**
Legal Framework	Strong laws, weak enforcement	Stronger enforcement mechanisms
Key Challenges	Corruption, weak penalties	Local government interference
Public Participation	Low	Increasing activism
Court System	Weak enforcement of rulings	Development of environmental courts
Compliance Monitoring	Limited oversight	Expanding use of AI and satellites

8.6 Earth's albedo is decreasing

Because the US has discarded most of its air, water and soil pollution restrictions, while encouraging more CO_2 and methane emissions, it is worthwhile to revisit the solar constant and the Earth's albedo. Figure 7.4 shows how the solar constant has been varying in magnitude by up to ±0.07% with the number of sunspots between 1976 and 2018. NASA's Clouds and the Earth's Radiant Energy System (CERES) product, `CERES_EBAF-TOA_Ed4.2` (*Loeb et al.*, 2018), provides monthly and climatological averages of the measured top-of-atmosphere (TOA), clear-sky and all-sky radiation fluxes that are energy-balanced to the ocean heat storage term and clear-sky spatially filled, along with associated cloud properties.

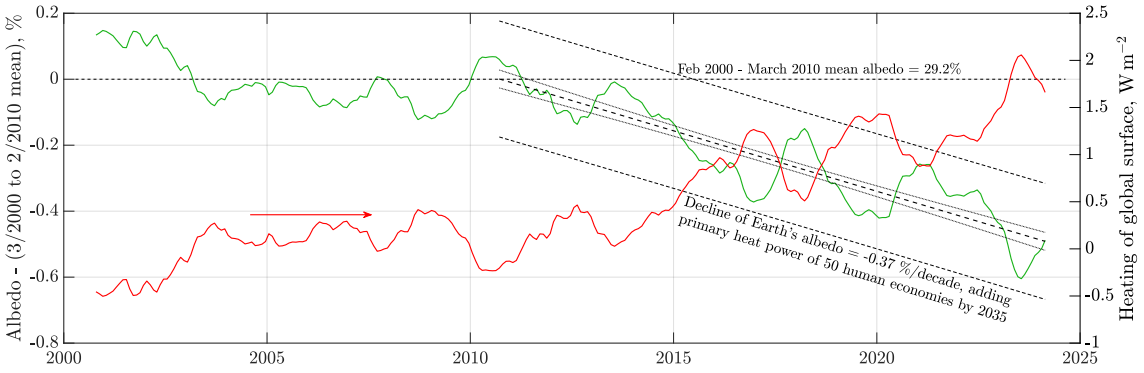

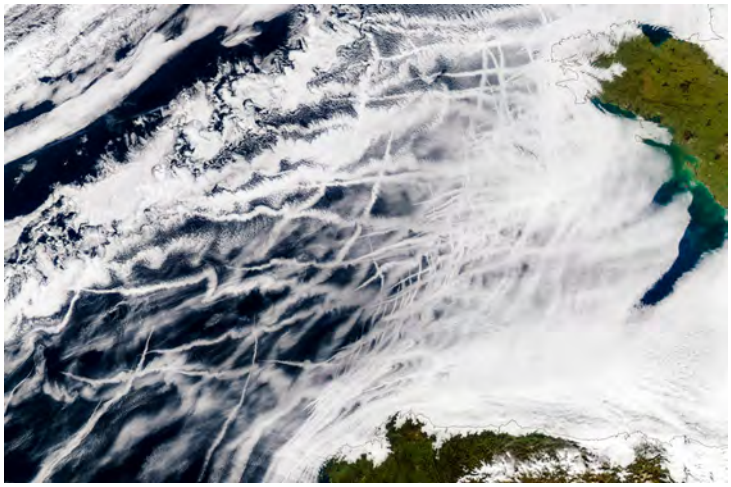

Figure 8.4: **Top:** The Earth albedo between 2/2000 and 12/2024. The albedo's deviation from the 2/2000-3/2010 mean (the green curve) is a 12-month moving average of the CERES measurements. This change of albedo is translated into more unequilibrated radiative forcing, approaching the total radiative forcing from CO_2 in Figure 7.10(b). Data source: File `CERES_EBAF-TOA_Ed4.2_Subset_200003-202407.nc`, accessed on Feb 01, 2025. Data processing and calculations by Patzek. **Bottom:** Crisscrossing clouds known as ship tracks can be seen off the coast of Spain in this 2003 satellite image. With the phasing out of high-sulfur ship fuel, these reflective clouds have become scarcer, leading to ocean warming. Source: Acques Descloitres CNRS/MODIS Land Rapid Response Team and Mark Gray/MODIS.

For details on how sea-ice melting impacts the Earth's albedo, see Appendix E.

From the CERES data, we have calculated the decline of the Earth's albedo relative to its Feb 2000 - Mar 2010 mean, see Figure 8.4. It appears that since 2010, the albedo has been declining at 0.04%/yr, or 1% by 2035. This decline will be equivalent to accumulating at the Earth's surface the heat generated by fifty 19-TW human economies that dissipate 70% of primary power as heat. Alternatively, by 2035, the change of Earth's average albedo from 0.29 to 0.28 will cause a net heating that increases more-less linearly, $1.7[0, 3.4]$ W m^{-2}, over the global surface between 2010 and 2035. The mean (1.7 W m^{-2}) is 4.5 times higher than the 0.38 W m^{-2} absorbed by the oceans thus far, likely to almost double by 2035, see Figure 6.5(b).

In summary, by 2035, the ocean heat absorption and decrease of the albedo by 1%, may add ∼4 W m^{-2} of unequilibrated radiative forcing distributed over the global surface, equivalent to that for doubling the CO_2 concentration in AR6 WGI-Box7.1, which generates an equilibrium climate sensitivity $ECS = 3$K (see Section 7.11).

The key driver of the Earth's declining albedo is the progressive deterioration of the oceans—warming rapidly, becoming increasingly acidic, and supporting less life. As marine productivity wanes, so too does the biospheric output of aerosol-precursor compounds that act as cloud condensation nuclei (CCN), thereby reducing cloud cover. The biogenic cloud-forming pathways are fantastically complex and interlinked (*de Jonge et al.*, 2024). Moreover, marine organisms and terrestrial forests interact across all climatic zones, from the polar oceans to the tropics (*Hance*, 2010, *Sheil and Murdiyarso*, 2009, *Levasseur*, 2013).

In what follows, we enumerate the principal species responsible for producing aerosol-precursor chemicals; see also Appendices A and E for further discussion of the intricate interconnections among global biosystems. Everything is connected everywhere, as John Muir famously observed. Humans, however, have evolved to devise single-hammer, disjoint solutions that yield limited local benefits while inflicting broad harm across multiple domains. This is the key reason why human-designed geoengineering schemes "to save the planet"are destined to fail miserably and to produce excessive collateral damage. see Chapter 14.

8.6.1 Marine Biological Sources of Climate-Relevant Volatiles

Dimethyl Sulfide (DMS) Producers

Phytoplankton (microalgae) are the principal producers of dimethylsulfoniopropionate (DMSP), the immediate precursor of DMS (*Stefels et al.*, 2007). High intracellular concentrations of DMSP are characteristic of dinoflagellates, coccolithophores (e.g. *Emiliania huxleyi*), and prymnesiophytes. Marine bacteria convert DMSP released from phytoplankton cells into DMS through cleavage enzymes; important groups include the *Roseobacter* clade and the *SAR11* clade (*Carpenter et al.*, 2015). Sea-ice algae also play a critical role, with polar blooms under ice acting as regional hotspots of DMSP/DMS production (*Levasseur*, 2013). Once produced, DMS is ventilated to the atmosphere, where it oxidizes to form sulfate aerosols that serve as cloud condensation nuclei (CCN) (*Charlson et al.*, 1987, *de Jonge et al.*, 2024).

Iodine- and Bromine-Containing Compounds

Macroalgae (seaweeds), particularly brown algae such as *Laminaria*, *Macrocystis*, and *Fucus*, are prolific accumulators and emitters of iodine. They release I_2, HOI, and CH_3I in response to oxidative stress, including ozone exposure and desiccation during low tide (*Saiz-Lopez and von Glasow*, 2012). Phytoplankton also emit volatile halogenated organics, including CH_3I, CH_2I_2, CH_2ICl, and CH_2IBr; these emissions are associated with prymnesiophytes[1], diatoms, and cyanobacteria (*Carpenter et al.*, 2015). Marine bacteria and fungi likewise contribute to iodocarbons and bromocarbons. These halogenated compounds photolyze rapidly in the atmosphere to release reactive iodine and bromine species, which both destroy ozone and promote the formation of ultrafine particles that can grow into CCN (*Saiz-Lopez and von Glasow*, 2012).

Other Volatile Organics of Marine Origin

Isoprene (C_5H_8) is emitted by phytoplankton, particularly diatoms, cyanobacteria, and prymnesiophytes, and constitutes an important precursor of secondary organic aerosol (SOA) (*Shaw et al.*, 2003). Methane (CH_4) is produced by methanogenic archaea inhabiting anoxic sediments and micro-niches in the water column, while nitrous oxide (N_2O) arises primarily from nitrifying and denitrifying bacteria distributed throughout the ocean interior (*Bange*, 2006).

Summary

The ocean surface hosts diverse microbial and algal communities that emit a variety of volatile compounds influencing atmospheric chemistry, aerosol formation, and climate regulation. Dimethyl sulfide (DMS), produced largely via the enzymatic cleavage of dimethylsulfoniopropionate (DMSP) synthesized by phytoplankton, is the dominant natural source of non-sea-salt sulfate aerosols (*Charlson et al.*, 1987,

[1] Unicellular algae of major global importance. Blooms of prymnesiophytes, especially coccolithophores, play a major role in both carbon cycling through calcification and photosynthesis, and climate regulation through DMS emissions and albedo effects from their reflective plates.

Stefels et al., 2007). Brown macroalgae are prolific emitters of molecular iodine and organic iodocarbons, while phytoplankton and associated bacteria also contribute to the global flux of methyl iodide and brominated compounds (*Saiz-Lopez and von Glasow*, 2012, *Carpenter et al.*, 2015). In addition, marine cyanobacteria and diatoms emit isoprene, an important precursor of secondary organic aerosols (SOA) (*Shaw et al.*, 2003). The main organismal sources and their emitted volatiles are summarized in Table 8.5.

If we irreparably damage the oceans, humanity together with all other living beings will confront an epochal peril. As this damage accelerates, we may be steering Earth toward a replay of the Permian extinction—the most severe and far-reaching of the five great mass extinctions—so vividly portrayed by *Brannen* (2025).

8.7 Summary tables

Table 8.3: Estimated percentage of global deforestation over time

Time Period	Forest Cover (%)	Deforestation (%)	Notes
Neolithic Era (~10,000 BCE)	57 – 60%	0%	Pre-agriculture, natural forest coverage. Early human activity had little impact on global forests.
Roman Empire (~1 CE)	50 – 55%	5 – 10%	Large-scale deforestation for agriculture, fuel, and construction. Heavy logging in Europe, North Africa, and the Middle East.
Medieval Period (~1000 CE)	45 – 50%	10 – 15%	Expansion of towns, farms, and monasteries led to forest loss. Shipbuilding for exploration increased timber demand.
Industrial Revolution (~1800 CE)	40 – 45%	15 – 20%	Widespread deforestation for industrial expansion, urbanization, and fuel (charcoal, coal). Major forest loss in Europe and North America.
Modern Era (2020 CE)	30 – 31%	29 – 30%	Rapid deforestation in the Amazon, Congo Basin, and Southeast Asia from agriculture, logging, and urban expansion. Nearly 50% of Earth's original forests lost.

Table 8.4: Comparison of environmental law implementation challenges in the U.S., UK, and EU

Issue	**United States (U.S.)**	**United Kingdom (UK)**	**European Union (EU)**
Governance Structure	Federal system with shared responsibility between federal and state governments, leading to inconsistent enforcement *Fiorino* (2006).	Centralized but undergoing transition post-Brexit; UK agencies assume former EU oversight roles *ClientEarth* (2021).	Centralized system where EU directives set binding minimum standards for all member states *Jordan and Adelle* (2013).
Legislative Flexibility	Many laws (e.g., Clean Air Act) are outdated and require congressional approval to amend, making updates difficult *Vig and Kraft* (2018).	Post-Brexit laws are being restructured (e.g., Environment Act 2021), but enforcement remains uncertain *ClientEarth* (2021).	EU laws are regularly updated through directives and regulations, ensuring adaptability *Jordan and Adelle* (2013).
Judicial and Legal Challenges	Frequent litigation and Supreme Court rulings (e.g., *West Virginia v. EPA*, 2022) constrain agency authority *SCOTUS* (2022).	Reliance on UK courts post-Brexit may introduce new legal uncertainties *ClientEarth* (2021).	EU law historically held supremacy over national courts, ensuring more stable enforcement *Jordan and Adelle* (2013).
Market vs. Regulatory Approaches	Mix of market-based and regulatory measures; strong corporate lobbying corrupts enforcement *Fiorino* (2006).	Historically followed EU regulatory standards, now transitioning toward independent policies *ClientEarth* (2021).	Strong regulatory approach with the Emissions Trading System (ETS) and stringent sustainability rules *EEA* (2022).
Climate Commitments	Policy shifts depending on administration (e.g., withdrawal and rejoining of Paris Agreement) *Vig and Kraft* (2018).	Committed to strong climate policies; future alignment with EU standards remains uncertain *ClientEarth* (2021).	Leads global climate efforts with ambitious legally binding targets *EEA* (2022).
Enforcement Mechanisms	EPA enforcement varies by state, often underfunded and politically constrained *Vig and Kraft* (2018).	Establishing new enforcement bodies (e.g., Office for Environmental Protection); their capacity is uncertain *ClientEarth* (2021).	Strong compliance mechanisms, with the European Court of Justice ensuring enforcement *Jordan and Adelle* (2013).

Table 8.5: Principal marine organisms producing climate-relevant volatile compounds.

Compound(s)	**Biological sources**	**Notes**
Dimethyl sulfide (DMS)	Coccolithophores (e.g. *Emiliania huxleyi*), dinoflagellates, prymnesiophytes; bacterial DMSP-lyase activity	Major source of sulfate aerosols and CCN
Iodine species (I_2, HOI, CH_3I, CH_2I_2, etc.)	Brown macroalgae (*Laminaria*, *Fucus*, *Macrocystis*); some phytoplankton; marine bacteria	Influence new particle formation, ozone destruction
Brominated organics (CH_2Br_2, $CHBr_3$, etc.)	Phytoplankton (e.g. diatoms, prymnesiophytes), bacteria, fungi	Important in marine boundary layer halogen chemistry
Isoprene (C_5H_8)	Cyanobacteria, diatoms, prymnesiophytes	Precursor of secondary organic aerosols (SOA)
Methane (CH_4)	Methanogenic archaea in anoxic sediments and micro-niches	Climatically relevant greenhouse gas
Nitrous oxide (N_2O)	Nitrifying and denitrifying bacteria in the water column	Strong greenhouse gas and ozone-depleting substance

Chapter 9

From deep time to the present: A comparison of climate states

Ancient Ammonites, Mineralogical-Geological Museum, TU Delft.
Photo by T.W. Patzek, April 2004.

All flesh is grass, and all the glory of man is the flower of grass. The grass withers, the flower fades...
Prophet Isaiah (c.760-690 B.C.), *Isaiah 40.6-8*

...Say that your main crop is the forest that you did not plant,
that you will not live to harvest.
Say that the leaves are harvested when they have rotted into the mold.
Call that profit. Prophesy such returns.
Put your faith in the two inches of humus that will build under the trees
every thousand years...
Manifesto: The Mad Farmer Liberation Front, Wendell Berry, *The Country of Marriage*, Harcourt Brace Jovanovich, Inc. 1973

9.1 What are you going to learn?

You are going to learn about reconstructions of paleoclimate during the Holocene (∼12 kyr), the Pleistocene (2.58 Ma – 12 ka), and all the way back to the Paleocene–Eocene transition (PET; 58–50 Ma), including the Paleocene–Eocene Thermal Maximum (PETM; 55.9–55.7 Ma, lasting ∼170–200 kyr). Relative abundances of the oxygen isotopes ^{18}O and ^{16}O, as well as deuterium and hydrogen, serve as thermometers guiding us through the temperatures of the air bubbles trapped in ice cores back to 800,000 years ago. For deeper geologic time we analyze isotope abundances preserved in marine sediments.

The discussion of paleoclimate changes would be incomplete without a thorough understanding of Milankovitch cycles and the ways in which orbital variations modulate incoming solar irradiance. We also compare paleoclimate sensitivities to greenhouse gases with the ones operating today.

9.2 Why is this important?

Examining geologically recent paleoclimates is akin to reconstructing a family's genealogical tree: it illuminates our ancestral past and clarifies where we came from. The reconstructions presented in this chapter warn, in no uncertain terms, that Earth could warm by as much as 10 °C in the not-too-distant future. This prospect should focus your attention on the chapters that follow.

9.3 Preliminaries

9.3.1 Isotope-ratio thermometers

In their outstanding paper, *Hansen et al.* (2013b), showed that climate sensitivity depends on the initial climate state, but potentially can be accurately inferred from the precise paleoclimate data illustrated in Figure 2 in *Zachos et al.* (2001).

Figure 9.1(a) shows the oxygen isotope composition of samples in *Grootes and Stuiver* (1997) can be expressed as the relative difference in the abundance ratios, ^{18}O/^{16}O, of the sample and Vienna standard mean ocean water (V-SMOW), expressed in parts per on thousand (per mil, ‰). The deviation of this ratio from a standard (as well as that of Deuterium D/Hydrogen H) is:

$$\begin{aligned} \delta^{18}\mathrm{O} &= \left(\frac{\left(\frac{^{18}\mathrm{O}}{^{16}\mathrm{O}}\right)_{\text{sample}}}{\left(\frac{^{18}\mathrm{O}}{^{16}\mathrm{O}}\right)_{\text{standard}}} - 1 \right) \times 1000, \ ‰ \\ \delta\mathrm{D} &= \left(\frac{\left(\frac{\mathrm{D}}{\mathrm{H}}\right)_{\text{sample}}}{\left(\frac{\mathrm{D}}{\mathrm{H}}\right)_{\text{standard}}} - 1 \right) \times 1000, \ ‰ \end{aligned} \tag{9.1}$$

As *Hoffman and Schrag* (1999) stated:

> Many lines of evidence support a theory that the entire Earth was ice-covered for long periods 600-700 million years ago. Each glacial period lasted for millions of years and ended violently under extreme greenhouse conditions. These climate shocks triggered the evolution of multicellular animal life, and challenge long-held assumptions regarding the limits of global change. ... At the height of the last glacial maximum (LGM), a mere 21,000 years ago, much of North America and Europe were covered by glaciers over 2 km thick, causing the sea level to drop by 120 meters. The chill was global: land and sea ice combined to cover 30 percent of the Earth's surface, more than at any other time in the last 500 million years. Although these are dramatic examples of the variability of Earth's climate, they pale in comparison with climatic events near the end of the Neoproterozoic eon (1000-543 million years ago, cf. Chapter 3). Those events immediately preceded the first appearance of recognizable animal life during Ediacaran around 600 million years ago.

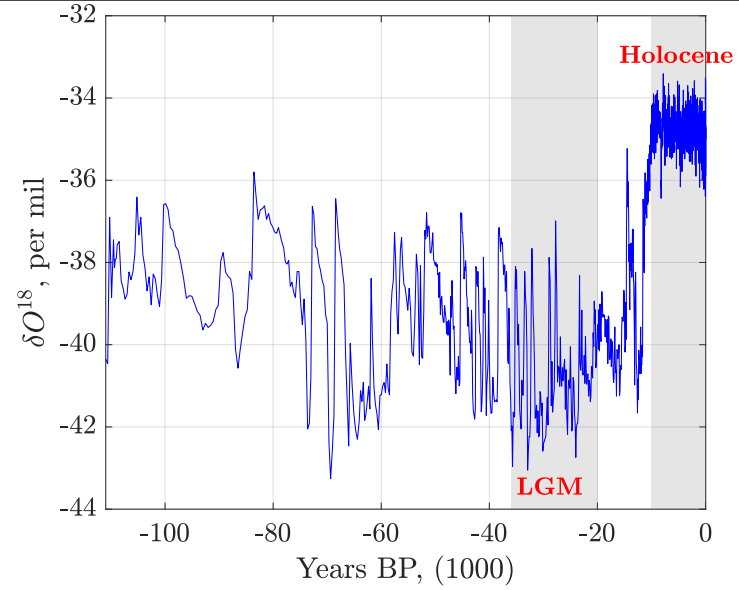

(a)

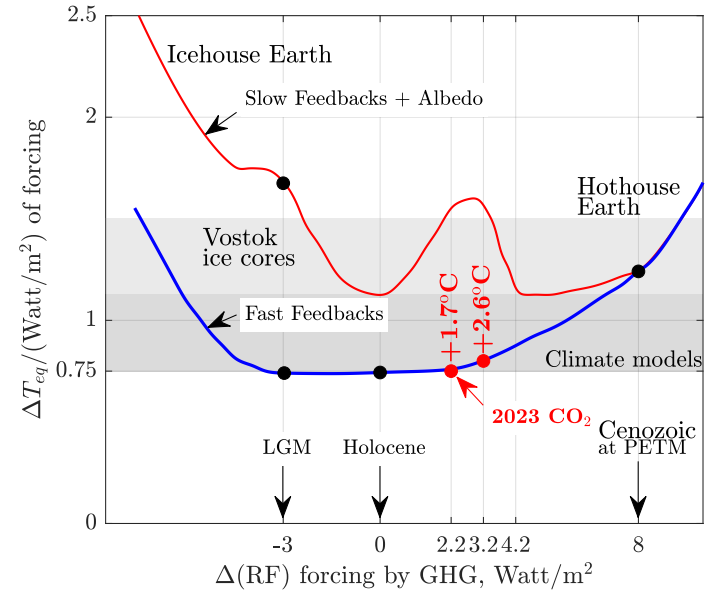

(b)

Figure 9.1: **(a)** The oxygen isotope composition of samples in *Grootes and Stuiver* (1997) is expressed as the relative difference in the abundance ratios $^{18}O/^{16}O$ of the sample and Vienna standard mean ocean water (V-SMOW). **(b)** Our adaptation of global temperature response in K to changes of equilibrium radiative forcing (RF) in $W^{-1}\,m^2$ (Fig. 7 in *Hansen and Sato* (2012)). Calculations by Patzek, 8/23/2023.

Figure 9.1(b) displays our adaptation of Figure 7 in *Hansen and Sato* (2012). It is a schematic diagram of the equilibrium fast-feedback climate sensitivity, as well as the Earth system sensitivity that includes slow feedback from the surface albedo.

- On a scale of days to months, increasing CO_2 concentration in the air causes temperatures in the stratosphere and then in the troposphere to adjust accordingly.

- On a scale of decades, the oceans take up the heat and delay global warming (and cooling in the opposite direction). On a scale of centuries to millennia, the slow climate feedback takes over, the

Arctic and Antarctic ice sheets melt, as do glaciers elsewhere, vegetation cover changes, the planet's albedo decreases, and a hothouse Earth ensues.

- Notice that these giant climate changes result from the equilibrium radiative forcing (RF) from CO_2 swinging by 11 $W\,m^{-2}$ (from -3 to +8 $W\,m^{-2}$) relative to the preindustrial Holocene. The snowball earth ensues when the CO_2 RF decreases by another few $W\,m^{-2}$.
- The temperature response of most climate models is 0.75 $K\,W^{-1}\,m^2$, but some go above 1.1 $K\,W^{-1}\,m^2$. Current equilibrium response to CO_2 alone is 1.7 K, and to all GHGs it is 2.6 K (°C and K are interchangeable).

Here

- LGM = Last Glacial Maximum that ended 20,000 years ago.
- Cenozoic PETM = The Paleocene-Eocene Thermal Maximum, was a time period approximately 56 Ma with more than $5-8$ °C global average temperature rise relative to Paleocene.

The Pleistocene[1] climate oscillations yield a fast-feedback climate sensitivity of 3 ± 1 °C for a 4 $W\,m^{-2}$ CO_2 *equilibrium* forcing if Holocene warming relative to the Last Glacial Maximum (LGM) is used as calibration. But the error (uncertainty) is substantial and partly subjective because of a poorly defined LGM global temperature and human influences in the Holocene, see Figure 5.6. Glacial-to-interglacial climate change leading to the Eemian[2] interglacial is less ambiguous and implies a sensitivity in the upper part of the above range, i.e., $3-4$ °C for each 4 $W\,m^{-2}$ CO_2 forcing.

Slow feedback, especially changes in ice sheet size and atmospheric CO_2, amplifies the total Earth system sensitivity by an amount that depends on the time scale considered. Ice sheet response times are poorly defined, but they do show that the slowness of response and hysteresis size in prevailing ice sheet models are *exaggerated*, i.e., the real polar caps melt more and faster.

Hansen et al. have used a global model, simplified to the essential processes, to investigate state dependence of climate sensitivity, finding an increased sensitivity towards warmer climates, as low cloud cover is diminished and increased water vapor elevates the tropopause (the upper limit of the troposphere that constitutes the boundary between it and the stratosphere at an elevation 10-15 km above sea level (ASL)).

Burning all fossil fuels rapidly, as concluded by Hansen et al. and supported by this author, would render much of the planet uninhabitable for humans – thereby invalidating widely promoted strategies that focus primarily on adaptation to climate change. In this context, the 2025 abandonment by the United States of most previously established environmental policies is nothing short of *suicidal*. Welcome to the US government climate and environmental policies ca. 2025.

The Earth's climate sensitivity to changing radiative forcing (RF) by CO_2 is shown in Figure 9.1(b). Please notice that the small changes in RF from CO_2 in the atmosphere cause very large changes in the energy balance of the planet. This is an excellent illustration of the disproportionate role CO_2 plays in controlling the Earth's climate.

Let's focus now on the last 800,000 years of climate history. At several sites in Antarctica, see Table 9.1, a nearly linear relationship of ^{18}O and deuterium (D), and the mean annual temperature was obtained in samples of modern firn[3] snow taken over several decades. This relationship was then used to calibrate the isotope ratio thermometer, although the calibration changed a little during ice age climates.

Plotting either ^{18}O or D with depth along the length of an ice core reveals the seasonal oscillations in temperature. Researchers can also count annual snow layers in order to date them. From the

[1] Pleistocene: 2.58 Ma → 11.7 ka BP, start of Holocene.

[2] The Eemian Interglacial, equivalent to Marine Isotope Stage (MIS) 5e, extends from roughly 129 ka to 116 ka BP, reaching maximum global warmth at ∼ 125 ka BP.

[3] Firn refers to compacted, partially metamorphosed snow that has survived one or more melt seasons. It exhibits intermediate densities and permeability, forming the transition layer (∼ 10–80 m) between the seasonal snowpack and impermeable glacial ice. Gas bubbles in firn remain connected, allowing atmospheric gases to diffuse until pore close-off occurs deeper in the firn column.

high-resolution measurements in ice cores reaching depths of 3.5 kilometers in the Antarctic ice sheet, we can clearly see the steady recurrence of the ice ages with a period of about 100,000 years. From >6,000 measurements in these ice cores (Table 9.1), over 800,000 years of paleoclimate temperatures were reconstructed (*Jouzel et al.*, 2007b), pin-pointing 8-9 ice ages, each interwoven with a warmer interglacial climate.

Table 9.1: Antarctic composite ice core sites

-51-1800 yr BP	Law Dome *Rubino et al.* (2013)
1.8-2 kyr BP	Law Dome *MacFarling Meure et al.* (2006)
2-11 kyr BP	Dome C *Monnin et al.* (2001, 2004)
11-22 kyr BP	WAIS *Marcott et al.* (2014) minus 4 ppm_v
22-40 kyr BP	Siple Dome *Ahn et al.* (2014)
40-60 kyr BP	TALDICE *Bereiter et al.* (2012)
60-115 kyr BP	EDML *Bereiter et al.* (2012)
105-155 kyr BP	Dome C Sublimation *Schneider et al.* (2013)
155-393 kyr BP	Vostok *Petit et al.* (1999b)
393-611 kyr BP	Dome C *Siegenthaler et al.* (2005)
612-800 kyr BP	Dome C *Bereiter et al.* (2015a)

9.3.2 Marine Isotope Stages

Marine Isotope Stages (MIS) are alternating warm and cold intervals in Earth's paleoclimate history, identified from the ratio of oxygen isotopes ($\delta^{18}O$) in benthic and planktonic foraminifera. Odd-numbered MIS represent interglacials, while even-numbered MIS correspond to glacials. The sequence extends back more than 5 million years, see Table 9.2.

Table 9.2: Summary of major Marine Isotope Stages (MIS 1–11). Ages approximate; benthic $\delta^{18}O$ timescale.

MIS	Age (ka)	Description
MIS 1	0–11.7	Holocene interglacial; present warm period.
MIS 2	11.7–29	Last Glacial Maximum (LGM) culminating at ∼21 ka.
MIS 3	29–57	Mild glacial interval with strong millennial variability (Dansgaard–Oeschger events).
MIS 4	57–71	Cold glacial stage preceding MIS 3.
MIS 5e	118–129	Eemian (Last Interglacial), warmest interval of the last 200 ka.
MIS 5d–a	71–118	Transition from glacial inception (5d) to warm substages (5c, 5a).
MIS 6	129–191	Penultimate glacial; ends with strong deglaciation into MIS 5e.
MIS 7	191–243	Complex interglacial with warm substages (7a, 7c, 7e).
MIS 8	243–300	Strong glacial interval.
MIS 9	300–337	Warm interglacial; strong benthic $\delta^{18}O$ minimum.
MIS 10	337–374	Cold glacial stage.
MIS 11c	398–424	Super-interglacial; exceptionally long, warm, stable interglacial.

9.3.3 Milankovitch cycles

Among the additional factors influencing long-term climate variability, the Milankovitch Cycles (*Milanković*, 1941) are among the most significant. These orbital variations modulate incoming solar

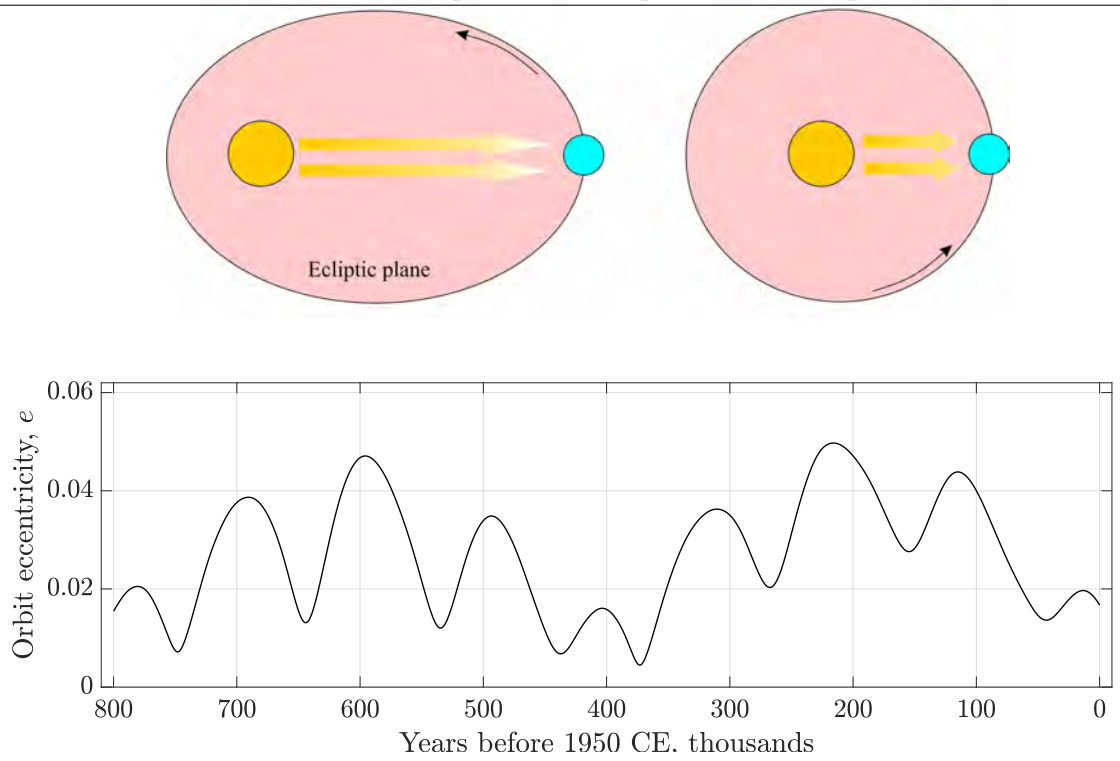

Figure 9.2: The MILANKOVITCH *eccentricity* cycle has three periods of roughly 405,000 yrs, 95,000 years and 124,000 years, with a beat period (repeat of wave dhape) of 400,000 years. They loosely combine into a 100,000-year cycle. The present eccentricity is 0.0167 and decreasing. The Earth's orbit plane (*ecliptic*) also precesses (wobbles) with a period of 112 ky due to interactions with Jupiter and Saturn. We call this wobbling *apsidal* precession. Eccentricity refers to the shape of Earth's orbit around the Sun, varying from near circular ($e = 0.0034$) to slightly elliptical ($e = 0.058$). When Earth's orbit is at its most elliptic, about 23% more incoming solar radiation reaches Earth at perihelion than at aphelion. Currently, Earth's orbit eccentricity is very slowly decreasing.

.

irradiance, as illustrated in Figures 9.2 to 9.4. As demonstrated by each Marine Isotope Stage (MIS) throughout recent climatic history of Earth, these cycles – calculated here over the past one million years from the governing orbital mechanics (e.g., *Schwarzacher* (1993)) – consistently favored the initiation of interglacial periods through specific alignments of orbital eccentricity, axial tilt (obliquity), and axial precession (wobble).

The Earth's orbit is a slightly perturbed circle, with its eccentricity e varying from nearly circular ($e = 0.0034$) to mildly elliptical ($e = 0.058$). When the orbit is at its most elliptical, approximately 23% more incoming solar radiation reaches Earth at perihelion (shortest distance to the Sun) than at aphelion. At present, Earth's orbital eccentricity is near the midpoint of this range ($e = 0.0167$) and is gradually decreasing. As a result, about 6.8% more solar energy enters the Earth's atmosphere in January (perihelion) than in July (aphelion). However, this seasonal asymmetry has a negligible short-term effect on climate. The eccentricity cycle is composed of three principal periodicities of roughly 405,000 years, 124,000 years, and 95,000 years, producing a dominant beat cycle with a period of approximately 400,000 years.

Obliquity, ϵ, is the tilt of Earth's axis relative to the plane of the ecliptic. It varies between 22.1° and 24.5° every 41,000 years. A high angle of tilt increases the seasonal contrast, most effectively at high latitudes (i.e., winters in both hemispheres will be colder and summers hotter as obliquity increases). Today, the obliquity is 23.4°, midway between its extremes and is decreasing.

The wobble of Earth's rotational axis, denoted by $\tilde{\omega}$, describes a slow circular motion in space with a

period of approximately 26,000 years. This motion defines the Milankovitch *precession* cycle. Modulated by orbital eccentricity, precession determines the position of Earth in its orbit at which the solstices and equinoxes occur – i.e., whether they align with perihelion or aphelion. This alignment alters the seasonal contrast, enhancing it in one hemisphere while reducing it in the other. The precessional effect is strongest near the equator and diminishes toward the poles. The dominant periodicities of the eccentricity-modulated precession signal are approximately 23,000 and 19,000 years, both of which are well documented in geological climate records. Currently, Earth's axis points toward the North Star (Polaris).

Over the past 800,000 years, interglacial (warm) paleoclimate cycles have generally corresponded to periods of low orbital eccentricity and low axial obliquity, with precession acting as a secondary perturbation (see Figure 9.5(a)). Today, we remain in an interglacial period – far from the onset of another glaciation – and are progressing, almost imperceptibly on human timescales, toward an even warmer climate.

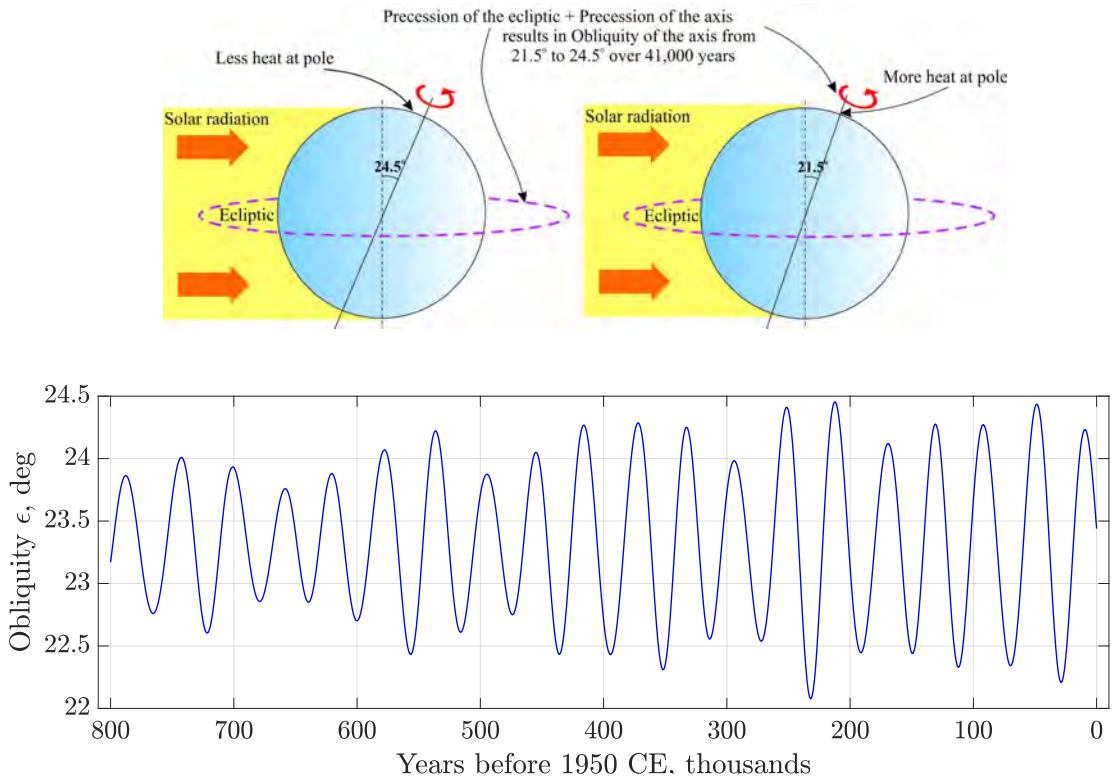

Figure 9.3: The Milankovitch *obliquity* cycle has a period of 41,000 years. Obliquity refers to the tilt of Earth's axis relative to the plane of the ecliptic varying between 22.1° and 24.5°. A high angle of tilt increases the seasonal contrast, most effectively at high latitudes (e.g., winters in both hemispheres will be colder and summers hotter as obliquity increases).

.

In the absence of anthropogenic CO_2 emissions, the next ice age could be expected in about 50,000 years from now (*Ganopolski et al.*, 2016). The cumulative CO_2 emissions until 1976, postponed this next ice age by another 100,000 years. Thus, the multidecadal climate effects of the Milankovitch cycles are nil in comparison with an overwhelming cosmic force, i.e., the fossil fuels- and planet-burning humans, 8 billions strong, and multiplying.

So what gives? Why is current climate so much less sensitive to GHG gases? The answer lies most likely in the omnipresence of severe anthropogenic pollution of the atmosphere, discussed in Chapter 8.

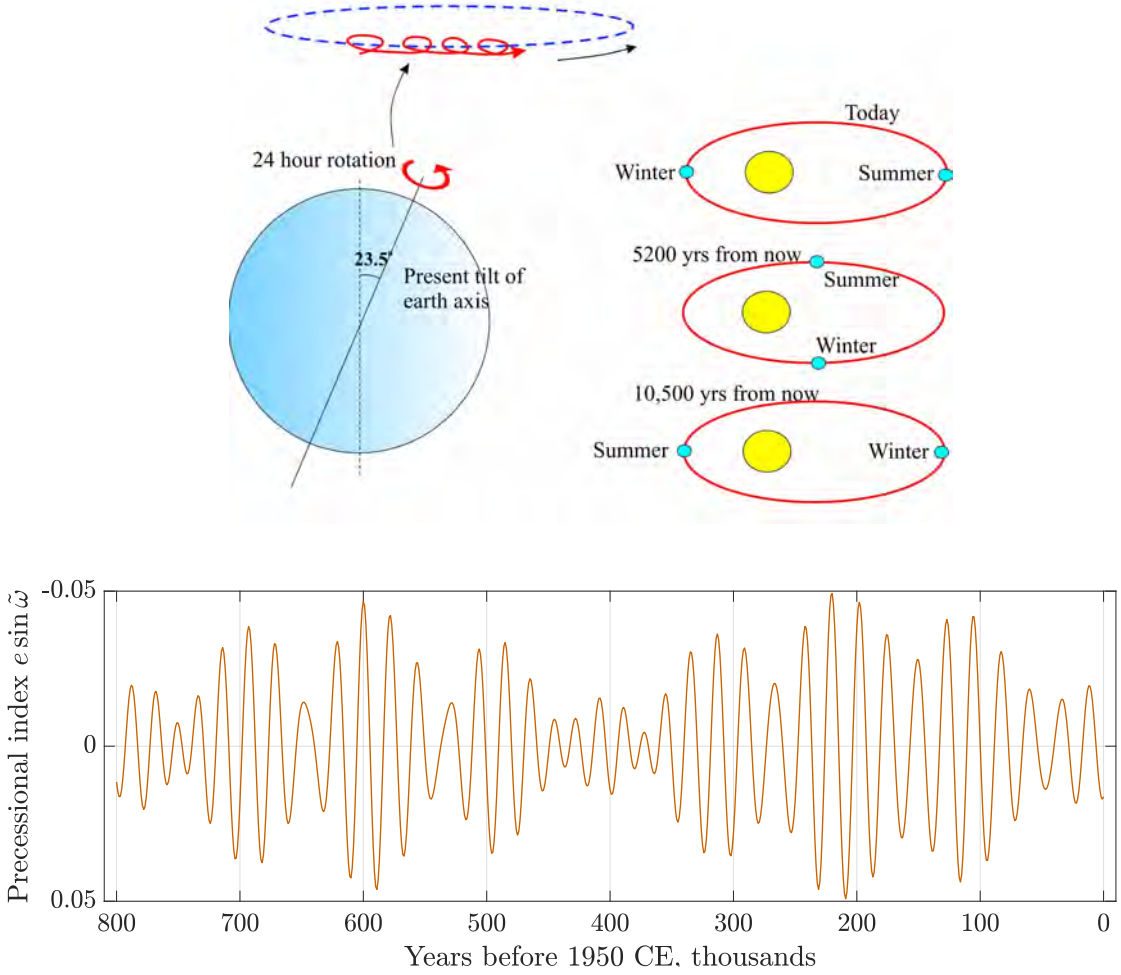

Figure 9.4: The MILANKOVITCH *precession* cycle refers to the wobble of the axis of Earth's rotation describing a circle in space with a period of 26,000 years. Modulated by orbital eccentricity, precession determines where on the orbit around the Sun (i.e., relative to aphelion or perihelion) seasons occur, thereby increasing the seasonal contrast in one hemisphere and decreasing it in the other. The effect is largest at the equator and decreases with increasing latitude. The periods of the precessional signal modulated by eccentricity are 23,000 and 19,000 years, the periods observed in geological records.

.

9.4 Comparison of interglacial climates with the Anthropocene

Figure 9.5(top) contains a wealth of paleoclimate information. It shows the reconstructed temperature anomaly relative to the mean Earth temperature over the past 1,000 years, with the corresponding Marine Isotope Stages (MIS) superimposed. It also displays the reconstructed atmospheric CO_2 concentration in ppm_v.

Figure 9.5(bottom) presents Earth's orbital eccentricity and axial obliquity, with the four major interglacial periods highlighted: the Eemian (MIS 5e), MIS 7a, MIS 9, and the Holsteinian (MIS 11).

Figure 9.6 shows the same orbital information together with the reconstructed temperature anomaly and atmospheric CH_4 concentration in ppb_v.

First, the reconstructed CO_2 concentration in the atmosphere exceeded the average CO_2 concentration during the past 6,000 years (Figure 5.6) only 5 times, two of which were longer, see Figure 9.5(a). During the Eemian, CO_2 concentration hovered at the preindustrial value for 12,000 years.

During the Holsteinian that corresponds to Marine Isotope Stage 11 (MIS-11) some 400,000 years ago,

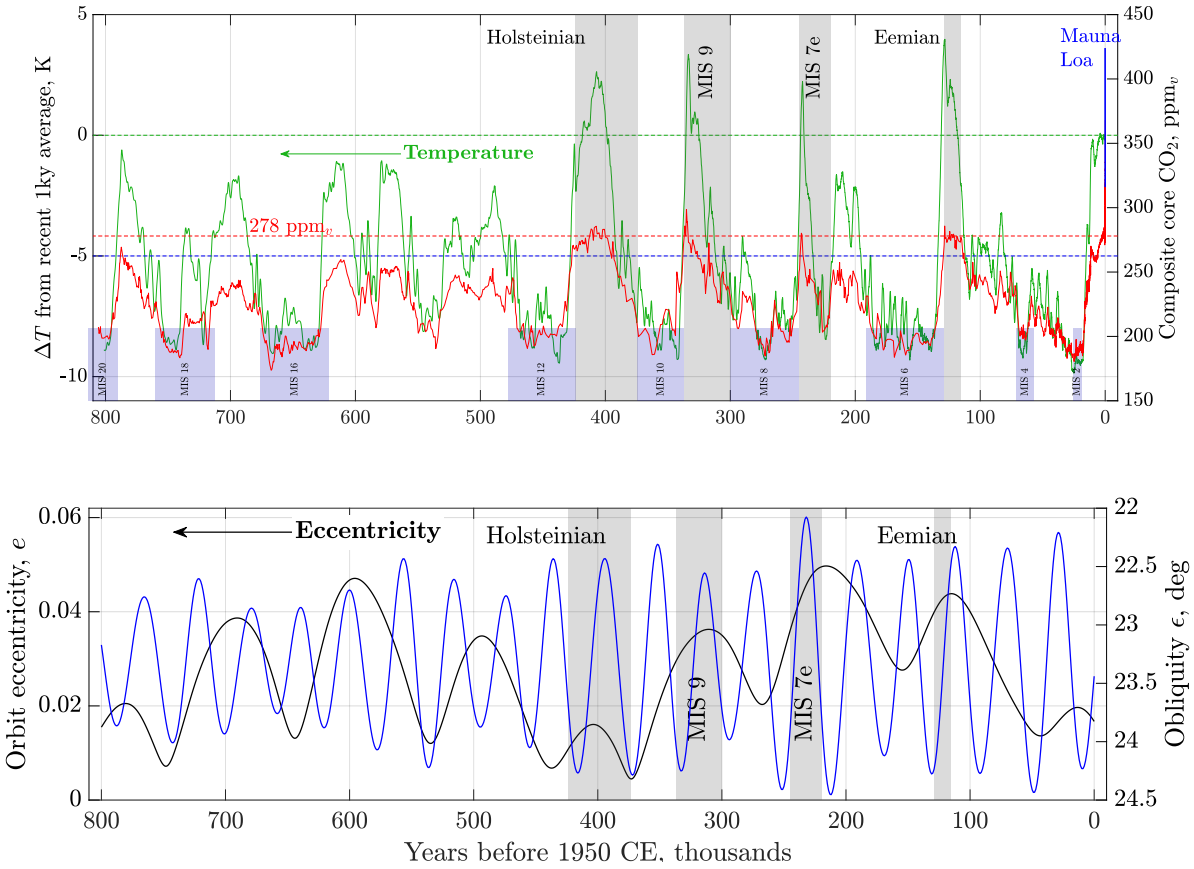

Figure 9.5: Sensitivity of paleoclimate over the last 800,000 years to pCO$_2$ **(top)** and the Milankovitch cycle forcing (**bottom**). It seems that the interglacial periods were driven usually by high orbit ellipticity (eccentricity), but not the Holsteinian, and low axis tilt (obliquity). When Earth's orbit is at its most elliptic, about 23 percent more incoming solar radiation reaches Earth each year at perihelion than does at its aphelion. The glaciation cycles were driven by low eccentricity. When eccentricity is low the glaciations become less extreme and more stable. Notice that the orbit eccentricity has a period of ∼100 kyrs and the beat period (waveform repeats) of 400 kyrs. Data source: Supplementary materials to *MacFarling Meure et al.* (2006), *PAGES* (2016), NOAA *Bereiter et al.* (2015b), *Lan et al.* (2025a), calculations by Patzek, 12/30/2023.

the CO$_2$ concentration exceeded slightly 277 ppm$_v$ for 15,000 years, and the other three CO$_2$ excursions (MIS 7, 9, and 19) were much briefer. Methane concentrations during the last 800,000 years were lower than that in Jan 2024 by factors of $2.5 - 5.5$.

The obvious conclusion is that during the periods of relatively high CO$_2$ and CH$_4$ concentrations, the average Earth temperature was also high. Both global paleo-GHG concentrations were however much lower than today (236 ppm$_v$ for CO$_2$ and 498 ppb$_v$ for CH$_4$), on average 1.8× lower for CO$_2$, and 3.9× lower for CH$_4$.

The correlation between the Earth temperature and the GHG concentrations is remarkable. Thus, it is fair to say that during the Eemian, CO$_2$ concentration was equal to ∼277 ppm$_v$, and the global temperature was warmer than today by $2 - 3$°C. It then follows that the paleoclimate was *more* sensitive to GHG concentrations than today's climate. This higher sensitivity is displayed in Figure 9.7. Compared with today's sensitivity of global climate to effective CO$_2$ concentration in Figure 11.5, the paleoclimate could have been $7.9/2.6 = 3$ times more sensitive.

Over the past 800,000 years of Earth's pristine climate history, interglacial (warm) paleoclimates appear to have been more sensitive than the present climate to atmospheric concentrations of the two key greenhouse gases, CO_2 and CH_4.

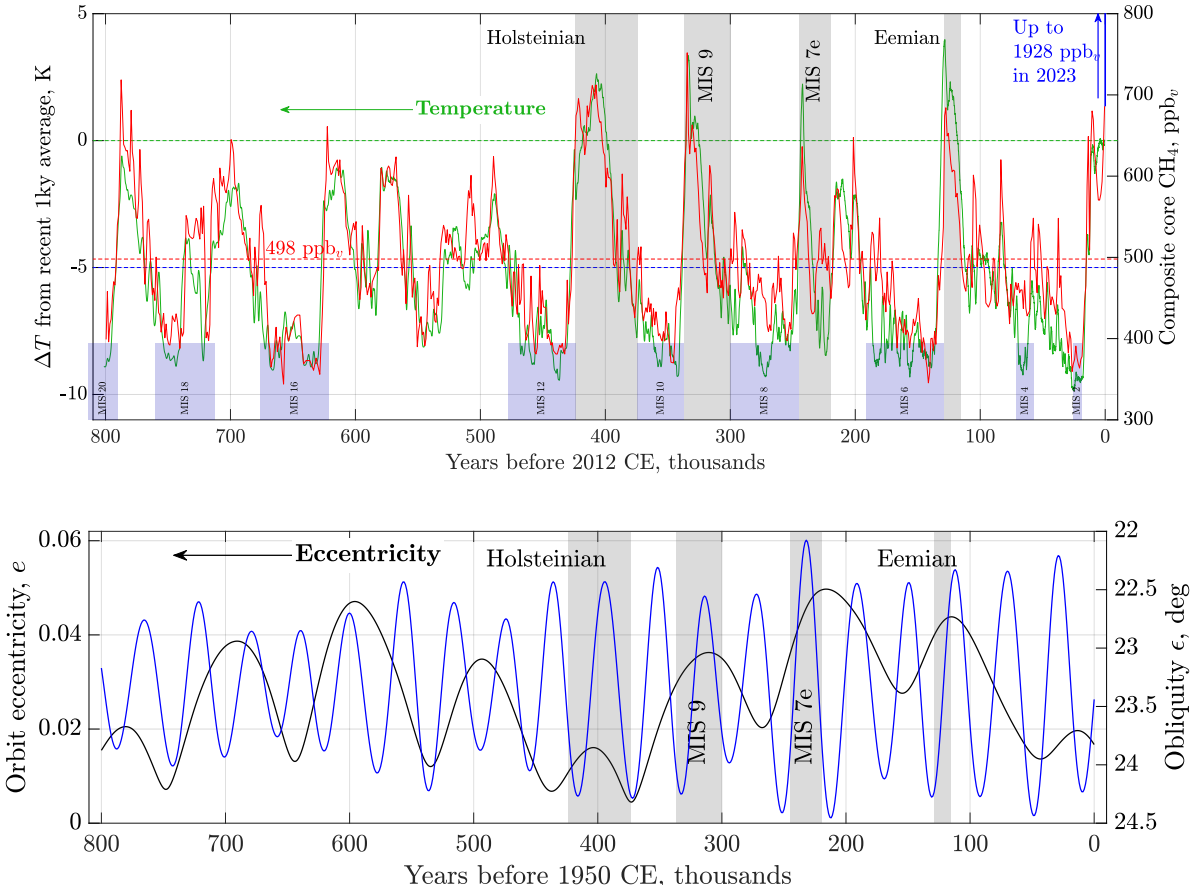

Figure 9.6: Sensitivity of paleoclimate over the last 800,000 years to ppb$_v$ of CH_4 **(top)** and the Milankovitch cycle forcing (**bottom**)). Notice that current CH_4 concentration is so high that it exceeds the scale of the plot 2.5 times (if plotted, [CH_4] would extend to the middle of the previous page). Data source: NOAA *Bereiter et al.* (2015b), calculations by Patzek, 12/30/2023.

There are several serious difficulties with comparing the singular climate of the recent 200 years (cf. Figures 5.2, 5.7 and 6.7) with the last 800,000 years of paleoclimate records acquired in Antarctica and Greenland (cf. Tables 9.3 to 9.5):

- The most recent interglacial (the Holocene) that corresponds to Marine Isotope Stage 1 (MIS 1), began *only* 11.7 kyrs ago (*Berger et al.*, 2012), after the end of the Last Glacial Period (MIS 2) and the Last Glacial Maximum (LGM, ∼26.5 kyrs ago) (*Clark et al.*, 2012), and it is far from over.
- There have been the unprecedented, breakneck accumulations of CO_2 (280 → 420 ppm$_v$) and CH_4 (800 → 1930 ppb$_v$) between 1850 and 2025 (Figure 6.6(a) and Figure 5.2) relative to their historical averages in the past 800 kyrs (CO_2: 232 [174 to 314] ppm$_v$, Figure 9.5; and CH_4: 498 [344 to 752] ppb$_v$, Figure 9.6) (*Petit et al.*, 1999b);
- The older three interglacials, the Eemian (13 kyrs); MIS 7a (25kyrs); MIS 9 (37 kyrs); and Holsteinian (50 kyrs) lasted together 125 kyrs, long enough for the Earth's orbit eccentricity and axis obliquity to play major roles in their emergence and stabilization (*Jouzel et al.*, 2007a), see Figure 9.5(bottom).

- Ice-core records of climate from Greenland and Antarctica show asynchronous temperature variations on millennial timescales beyond MIS 5. The warming during the transition from glacial to interglacial conditions was markedly different between the hemispheres, a pattern attributed to the thermal bipolar "see-saw". The more recent climate variations (MIS 1-to-5) have been synchronous, however, because of the Atlantic Meridional Overturning Circulation (AMOC), e.g., (*Stenni et al.*, 2011, *Bereiter et al.*, 2012).

- The climate records of the last 800 kyrs have been mostly acquired from ice shelves in Antarctica (EPICA Dome C and Vostok) and from Greenland (NEEM and NGRI), cf. (*EPICA Community*, 2006, *NEEM Team*, 2013, *NGRIP*, 2004). Both locations were covered most of the time with the highly-reflective ice and snow deposits and responded quickly to all external climate factors, including sun-spots. Therefore, these records are subject to the "polar amplification (PA)" of global climate responses by a factor of up to 2.2, e.g., (*Jouzel et al.*, 2007a), cf. Section 13.7. During glacial periods there was more ice, higher albedo and stronger cooling. During interglacial periods with less ice, albedo was lower and warming stronger. Figure 9.5 and Figure 9.6 show the fluctuations in GHG forcing with CO_2 concentration increasing to almost preindustrial levels during warm periods, and CH_4 contributing strongly and synchronously. Warmer periods enhanced poleward energy transport, strengthening PA. Increased cloud cover during warm periods modified longwave radiation, also increasing PA.

- Finally, the oldest ice cores spanned the last 100 kyrs of the Mid-Pleistocene Transition (MPT, ∼1.25 - 0.7 Ma), which ushered a major shift in Earth's climate system that switched from the 41,000-year glacial cycles driven by the Earth's orbit obliquity to the 100,000-year glacial cycles controlled by orbit eccentricity, seen in Figure 9.5. During MPT, the Mid-Pleistocene Warm Period (mPWP, ∼1.1 - 0.9 Ma) was the last period of a relatively warm climate (CO_2 concentrations from 250 to 300 ppm_v (*Hönisch et al.*, 2009), and CH_4 concentrations from 350 to 700 ppb_v (*Loulergue et al.*, 2008)), comparable to the preindustrial conditions in Figure 5.6, and with average seawater level (ASL) 6-15 m higher than today (*Rohling et al.*, 2009). The major, long glaciations came in 100 kyr cycles in the last 700 kyrs.

The Holsteinian (MIS 11) and Eemian (MIS 5e) interglacials were among the warmest periods in the past 500,000 years. Comparing them to the present-day Holocene provides insights into the long-term effects of greenhouse gas levels, ice sheet stability, and sea level rise. Table 9.5 summarizes key climate metrics of these periods. The warm periods were interlaced with eight major glaciations, see Figure 9.5(top).

It seems that the post-1976 acceleration of land heating was caused by the 1956 and 1963 Clean Air Acts CAAs in the UK, and the Clean Air Act (CAA) of 11/21/1963 in the Unites States. Its 12/31/1970 enhancement is now referred to as the CAA, with full compliance of all states by 1975. Several amendments in 1977, 1990 and 2012 further strengthened the CAA. Other countries followed, especially Germany (1980) and the EU (2001).

The temperature mean between 1951 (when rate of FF emissions had already exceeded that of AL) and 1980 (with the fast-increasing land temperature that had already bifurcated 4 years earlier from the ocean temperature), should never be used as a reference standard, except that it is practical and convenient. This global temperature plateau resulted from a wholesale pollution of air (like that in Figure 8.3), water and land by every industrial and urban center across the world. This deadly level of pollution blocked plenty of sunlight and deferred Earth heating for a while.

Figure 9.7 contrasts current transient climate response to [CO_2] doubling ($S \approx 1.8$[1.4 to 2.2] K), and predicted current Earth System Sensitivity (ESS) of $4-6$°C (Table 7.3), with mean ESS during the last 800 kyrs. The slowly-changing paleoclimate was perhaps twice as sensitive as current climate's ESS. Thus, decreasing aerosol content of the atmosphere (making air more transparent), while increasing cumulative total emissions (CTE) may result in a climate sensitivity that might resemble that in Figure 9.7. The calculation here is independent of those by *Snyder* (2016), but the results and conclusions are similar.

Snyder states: "Over the past 800 kyrs, polar amplification (PA) (the amplification of temperature change at the poles relative to global temperature change) has been stable over time, and global temperature and atmospheric greenhouse gas concentrations have been closely coupled across glacial cycles. A comparison of the new temperature reconstruction with radiative forcing from greenhouse gases estimates an Earth

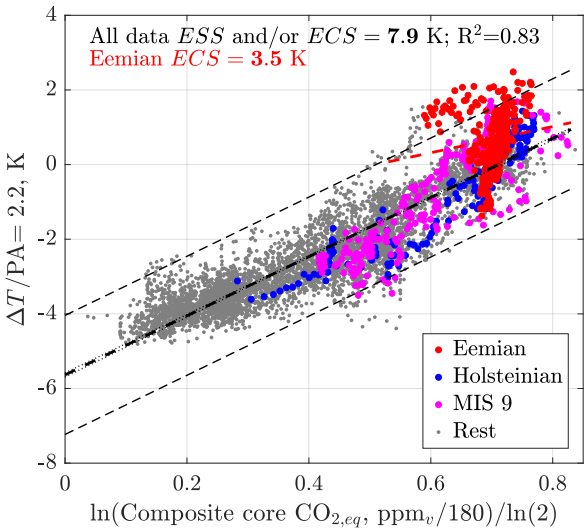

Figure 9.7: This regression shows clearly that most of the time climate during the last 800 kyrs was more sensitive to GHG forcing than today. The earth system or equilibrium climate sensitivities (ESS or ECS) defined in Section 7.11, see Table 7.4, to a *very slow* doubling of $[CO_2]+29.8[CH_4]=[CO_{2,eq}]$ for all data and the Eemian (MIS5e) data are plotted above. The warm Eemian climate response ($ESS = 3.5$ K) is comparable to today's climate, but the slope of all ice core data from the last 800 kyrs yields $ESS = 7.9$ K, much higher than today and comparable to the incongruent climates during LGM (cf. Section 9.4.1) and Eocene, see Figures 9.8 to 9.9. All temperature data from the cores were divided by the Polar Amplification (PA) factor of 2.2 (*Jouzel et al.*, 2007a).

system sensitivity of 9°C (range 7 to 13°C, 95% CI) change in global average surface temperature per doubling of atmospheric carbon dioxide over millennium timescales [*our ESS, TWP*]. This result suggests that stabilization at today's greenhouse gas levels may already commit Earth to an eventual total warming of 5°C (range 3 to 7°C, 95% CI) over the next few millennia as ice sheets, vegetation and atmospheric dust continue to respond to global warming."

In the last decade, this commitment grew closer to 10°C *Hansen et al.* (2023) and, no, it will take centuries, not millennia, to make the Earth hostile to most vertebrates, with several decades for the substantial warming to emerge globally and remain.

9.4.1 Why is it difficult to compare current climate with the distant past?

The two most-studied past climates are the Last Glacial Maximum (LGM) (~20 ka), parts[4] of Mid-Pleistocene Transition (MPT) (~1.1 - 0.9 Ma), and mPWP[5] (3.3–3.0 Ma), but there are plenty of cross-validated data for the last 800 kyrs, see Figures 9.5 and 9.6, and for the Eocene (56-33.9 Ma), Figure 9.8. The paleoclimate studies rely on equilibrium planetary energy budgets, including ocean heat content. But, over centuries or millennia one must model not only changes in GHG concentrations, but

[4]The interval MIS 28–24, spanning roughly 1.05–0.9 Ma, marks a pivotal stage in the Mid-Pleistocene Transition (MPT). During this period the Northern Hemisphere ice sheets grew larger, thicker, and more stable than in the preceding 41 kyr glacial cycles, partly because extensive glacial erosion removed the insulating regolith layer from continental surfaces. As a result, glacials MIS 28, MIS 26, and MIS 24 became progressively colder and longer, and the climate system began to deviate from its formerly regular obliquity-paced rhythm. Paleoceanographic proxies indicate that deep-ocean stratification strengthened and the Atlantic Meridional Overturning Circulation weakened during these glacials, promoting enhanced storage of dissolved inorganic carbon in the abyss. This mechanism likely contributed to lower glacial CO_2 levels and amplified global ice-volume changes. Thus the MIS 28–24 interval captures the emergence of the climate system's nonlinear response to Milankovitch forcing and marks the onset of the transition toward the large-amplitude 100 kyr glacial cycles that dominate the late Pleistocene.

[5]mPWP stands for the *mid-Piacenzian Warm Period*, a warm interval during the Pliocene, approximately 3.3–3.0 Ma, often used as an analog for near-future climate because global temperatures were 2–3 °C above preindustrial and CO_2 levels were 350–450 ppm.

also changes in land vegetation cover, ice on land and sea, land topography, and – for Eocene – the shapes and positions of continents, as well as a plethora of other forcing and climate uncertainties. For details, see *Sherwood et al.* (2020), Sections 4 and 5. Accounting for all of these factors requires Equations (7.11) to (7.13) to be augmented with several new terms, cf. *Sherwood et al.* (2020), Section 2.

A direct application of energy balance Equation (7.8) points to a moderate sensitivity having highest likelihood of ∼2.4 K. However, this standard estimate depends on the assumption that feedbacks remain constant over a wide range of climate states and forcings. As stated in *Sherwood et al.* (2020), several other studies suggest that the relationship between forcing and temperature response is nonlinear, indicating that sensitivity depends on the background climate state and/or the efficacy of the forcings.

During the LGM, a high sensitivity of the climate Planck climate sensitivity S to $[CO_2]$ (∼6 K per $[CO_2]$ doubling) could be supported by a cooler LGM temperature anomaly of around −7 K (the higher end of the range suggested from proxydata evaluations in *Snyder* (2016)). This interpretation is also supported by evidence that spans the most recent five glacial cycles *Rohling et al.* (2012).

Table 9.3: Comparison of Holsteinian, Eemian, and present-day climates

Climate Metric	Holsteinian (MIS 11)	Eemian (MIS 5e)	Present (Holocene)
Time Period (kyr BP)	424 – 374 kyr	129 – 116 kyr	11.7 kyr - Present
Global Temperature	+1-2°C vs. pre-industrial	+1-2°C vs. pre-industrial	+1.5°C (2024)
CO_2 Concentration (ppm)	280 – 300 *Bereiter et al.* (2015a)	280 – 300 *Bereiter et al.* (2015a)	420+ (2024) *NOAA* (2024)
Sea Level Change	+6 to +13 m *Dutton et al.* (2015)	+6 to +9 m *Dutton et al.* (2015)	Rising (∼0.2 m since 1900)
Ice Sheet Stability	Partial Greenland/WAIS melt	Significant Greenland/ WAIS melt	Greenland/WAIS melting faster than past interglacials *Arias et al.* (2021)
Duration (kyr)	∼50 kyr	∼13 kyr	∼11.7 kyr (ongoing)
Orbital Influence	Weak eccentricity cycle, prolonged interglacial	Strong eccentricity cycle, shorter warm period	Different orbital phase, human-driven warming

Table 9.4: Main climates of MIS 5

MIS Substage	Years Ago (kyr BP)	Climate Characteristics
MIS 5e (Eemian)	130 – 116 kyr	Warmest period; +1 – 2°C above pre-industrial; CO_2: 280 – 300 ppm *Bereiter et al.* (2015a); Sea level: +6 – 9m *Dutton et al.* (2015)
MIS 5d	116 – 106 kyr	Cooling phase; transition to glaciation
MIS 5c	106 – 92 kyr	Short warming (interstadial); temporary ice retreat
MIS 5b	92 – 87 kyr	Further cooling; glaciers advancing
MIS 5a	87 – 71 kyr	Brief warm phase before glacial expansion
Transition to MIS 4	**∼71 kyr**	Ice sheets expand, global cooling intensifies

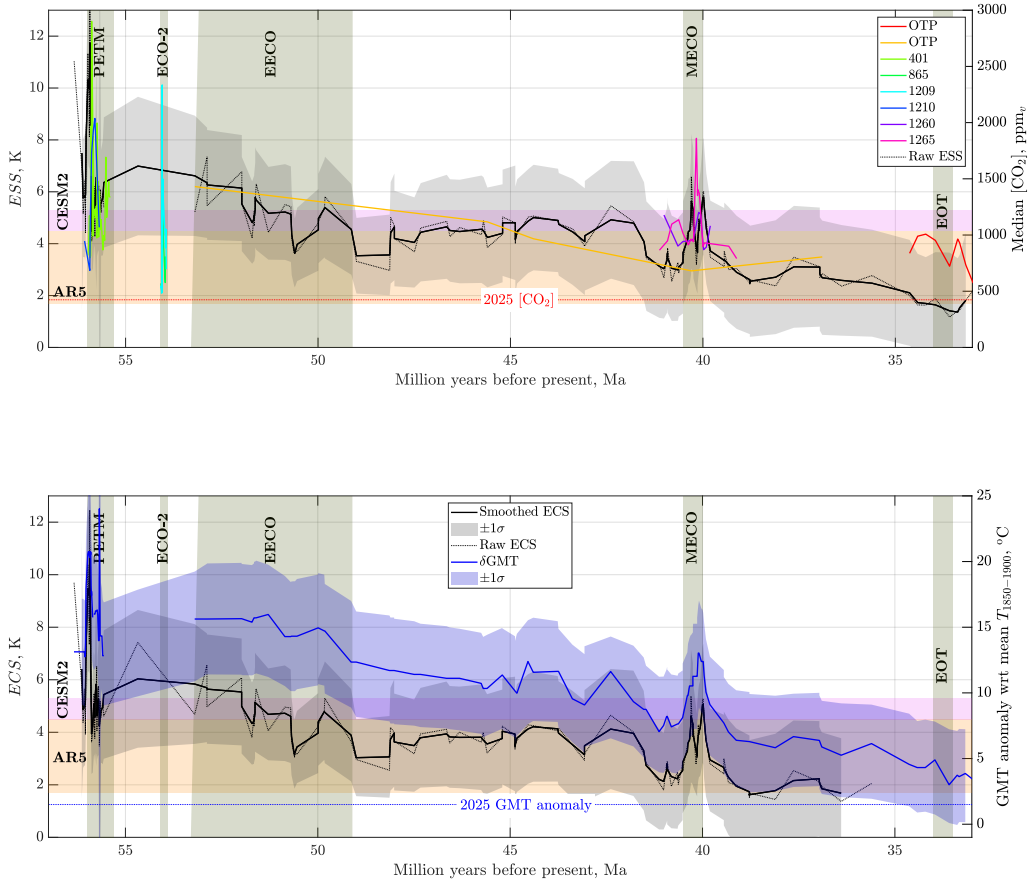

Figure 9.8: The shaded geologic periods from left to right are: PETM = Paleocene-Eocene Thermal Maximum, ECO-2 = Eocene Climatic Optimum 2, EECO = Early-Eocene Climatic Optimum, MECO = Middle-Eocene Climatic Optimum, EOT = Eocene-Oligocene Transition, during which the permanent Antarctic ice-sheets appeared. (**top**) ESS (see Table 7.3 for definitions), 4-point running average and raw data (left y-axis black) and median CO_2 concentrations in the atmosphere (color curves, with sources explained in the legend, right y-axis). (**bottom**) ECS, 4-point running average and raw data (in black, the left y-axis) and Global Mean Temperature (GMT) anomaly relative to the 1850-1900 GMT = 13.7°C *IPCC, Full Report* (2022) (the right y-axis). The orange rectangle denotes approximate range of ESS and ECS from *Stocker et al.* (2013). The magenta rectangle reflects the high-sensitivity CESM-2 simulations *Gettelman et al.* (2019). Data source: Supporting data to *Anagnostou et al.* (2020), calculations by Patzek, 02/22/2025.

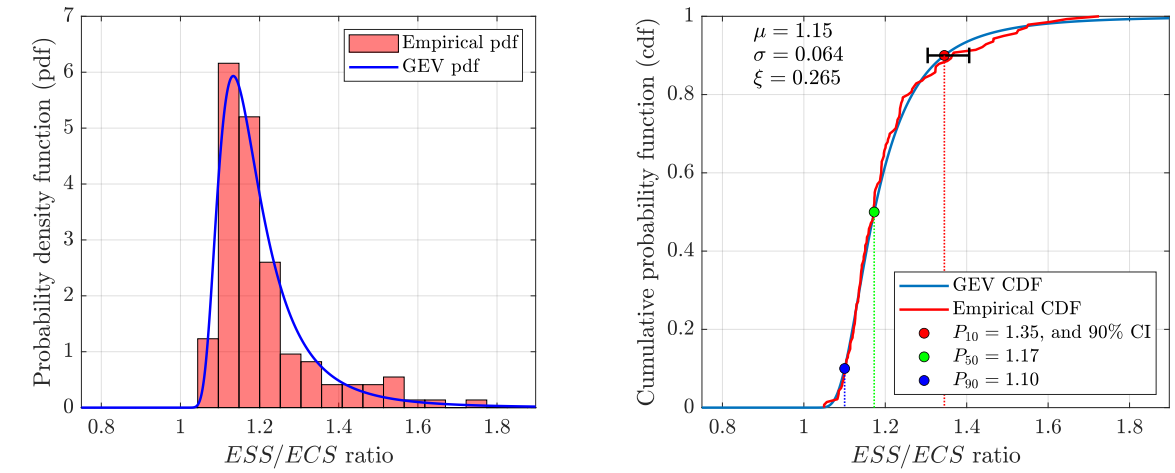

Figure 9.9: The distribution of ESS/ECS ratios for the Eocene climate data shown in Figure 9.8. The data are fit with a Generalized Extreme Value (GEV) distribution *Gumbel* (1958), which reduces to a Fréchet distribution with $\xi > 0$, left cut-off and right fat tail. **(a)** The experimental and GEV probability density functions (pdf). **(b)** The corresponding cumulative distribution functions (cdf) including a 90% confidence interval (CI) on P_{10}. Note that the median value of the ratio is 1.17, and only 10% of data exceed the $P_{10} = 1.35$. Thus, most of the time, the ratio of ESS to ECS is between 1.1 and 1.35. Calculations by Patzek.

Table 9.5: Major Glaciations of the last 800 kyrs with temperature and CO_2 estimates

Glaciation	**MIS Stage**	**Years Ago (kyr BP)**	**Global Temp Change (°C)**	**CO_2 (ppm)**
Last Glacial Maximum (LGM)	MIS 2	26 – 19 kyr	-6 to -8°C *Arias et al.* (2021)	~180 ppm *Bereiter et al.* (2015a)
Weichselian/Wisconsinan	MIS 4	71 – 57 kyr	-4 to -6°C	~190 ppm
Illinoian Glaciation	MIS 6	191 – 130 kyr	-5 to -7°C	~190 ppm
Kansan / Wolstonian	MIS 8	300 – 243 kyr	-4 to -6°C	~200 ppm
Pre-Illinoian Glaciation	MIS 10	374 – 337 kyr	-5 to -7°C	~190 ppm
Saalian Glaciation	MIS 12	478 – 424 kyr	-6 to -8°C	~180 ppm
Elsterian Glaciation	MIS 16	676 – 621 kyr	-7 to -9°C	~180 ppm

Chapter 10

Global climate data collection

Newest of the three solar PV arrays in Austin during a polar-air blast in Feb 2021.
Photo by T.W. Patzek.

To me, global warming means growing instability – of weather, agriculture, and human relations at every level. The ever more frequent and brutal heat waves, countered by sudden freezing spells, cannot possibly support the intricate web of life that evolved over millennia under a far milder and more stable climate.

Tad Patzek, May 2025

10.1 What Are You Going to Learn?

In this chapter, you will learn how to accurately represent the monthly mean global surface air temperature anomaly – defined as the deviation from a long-term standard baseline – using a single number accompanied by a standard uncertainty. Understanding how this single number is computed, and what it truly signifies, is essential. The temperature anomaly has enormous implications for government policy, infrastructure planning, and the daily choices made by individuals and families. Its simplicity masks a profound complexity, and its interpretation applies to nearly every facet of life on a warming planet.

10.2 Why Is This Important?

Mass media often distill the intricate and interconnected dynamics of climate change into a single, headline-ready figure – typically the global warming anomaly of +1.5°C or +2.0°C. But these numbers, though compact, are not trivial. They emerge from a complex and carefully constructed process of data collection, homogenization, gridding, and averaging – what might be called the "sausage-making" of climate science.

Understanding how these temperature anomalies are calculated is essential if you want to fully grasp their implications. Without this understanding, it's easy to misinterpret what +1.5°C of global warming truly means.

For example, the global average temperature anomaly of +1.55°C in 2024 – the hottest year on record – corresponded to a land-only (terrestrial) temperature anomaly of +2.28°C, with local anomalies reaching and exceeding +8°C. Between May 15 and 19, 2025, the temperature anomalies were +10°C in Iceland and +14.5°C in Greenland, resulting in an ice-melt rate that was 17× the average. Some of the peak temperatures during major 2024 heatwaves are listed in Table 10.1.

All 67 extreme heat events between May 2024 and May 2025 – identified as significant due to record-breaking temperatures or severe impacts on human populations or infrastructure – were found to have been influenced by climate change (*Giguere et al.*, 2025). These heatwaves are becoming increasingly frequent, prolonged, and lethal. Beyond the immediate threat to human health – especially for the poor, elderly, and other vulnerable populations – extreme heat also endangers crops, insects, birds, and countless other species vital to ecological stability. In Europe alone, approximately 62,000 people died from heat-related causes in 2022 (*Ballester et al.*, 2023); comparable mortality data are generally unavailable elsewhere.

Table 10.1: Worst 2024 heatwaves by continent (dates, duration, peak temperature, from *Martinez-Villalobos et al.* (2025), *Jha et al.* (2025))

Continent	Dates	Duration	Peak Temp (°C)
Europe	July 2024 (SE Europe)	13 days (record)	∼46.8 (Cyprus)
Asia	Apr-May (S/SE Asia)	Several weeks	∼53 (heat index), 43.8 (Bangl.)
North America	7 Jul (Death Valley)	Mar-Sep period	53.9 (Furnace Creek)
Africa	July (Morocco)	11 days	48 (Marrakech)
South America	Sep-Dec (Amazon,Gran Chaco)	150 days	42 (Cin Culabá)
Oceania / Aus.	Feb (West Australia)	14 days	50

Table 10.2: Temperature anomalies during the May 2025 heatwave in Iceland and Greenland relative to recent climatology and the preindustrial baseline.

Region	**vs. 1991–2020**	**vs. 1850–1900**	**Amplif. vs. GMST**
Iceland	+10 to +13°C	+11 to +14°C	∼7–9×
E. Greenland	+13°C	+13 to +14°C	∼8–9×

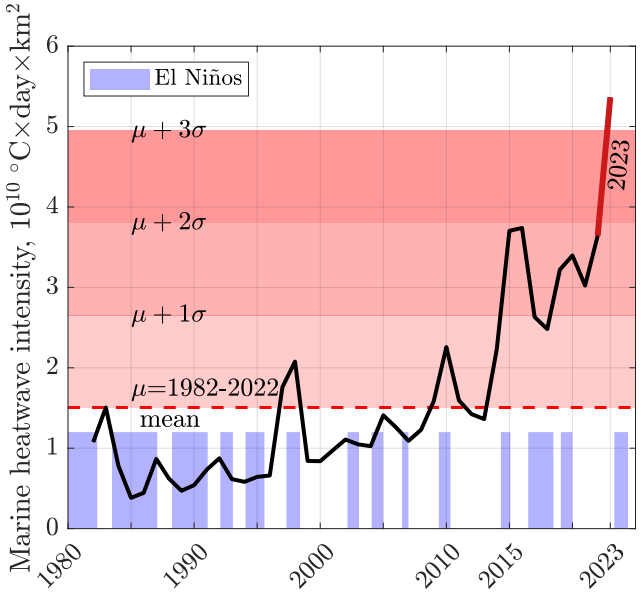

Figure 10.1: Extreme marine heatwave since 1981. Their intensity was quantified as the product of area-weighted average seawater surface temperature in °C from satellite images × heatwave duration in days × the heated area above a threshold temperature in km^2. Note a mild positive correlation with El Niños. Plotted by Patzek, using the data to Fig1a from the Supporting Online information to *Dong et al.* (2025), accessed 07/30/2025.

At the same latitude as Cairo or Lahore, Austin, Texas, experiences periodic intrusions of polar air – approximately every two years between 2020 and 2025 – with temperatures plummeting to as low as −15°C for several days. This may seem paradoxical in a warming world, but it is a consequence of Arctic amplification. As global warming accelerates the loss of Arctic sea ice, more heat escapes from the exposed ocean surface during autumn and winter. This added heat disrupts the stability of the polar vortex – a fast-spinning band of winds that normally contains frigid air around the North Pole. When weakened, the vortex becomes more erratic, allowing lobes of cold Arctic air to spill southward into mid-latitudes, reaching as far as Texas and even northern Mexico.

Figure 10.1 shows the relative power of all major marine heatwaves recorded between 1981 and 2023. This power is computed directly from high-resolution satellite records of sea surface temperature (SST), spanning latitudes from −60° to +60°. Marine heatwaves are defined as periods of at least five consecutive days during which the SST exceeds the 90th percentile of the climatological temperature distribution – using a baseline period of 1985–2014. At the end of 2023, the power of the largest ever-recorded global MHV was 53.6 billion °C days km^2 – more than three standard deviations above the historical norm since 1982. This MHW lasted for 120 days (longest since 1982 and 3× longer than the average), and spanned an ocean area of 320 million km^2, over 96% of the global marine area.

But make no mistake; the heat is on. If you're planning a vacation on Tuvalu, Kiribati, Maldives, Aruba, Dominica, Saint Vincent and the Grenadines, Grenada, Guadeloupe, Montserrat, Barbados, Antigua & Barbuda, Micronesia, Saint Kitts and Nevis, Martinique, Puerto Rico, or similar destinations, be aware that these island archipelagos – long celebrated for their stable, mild tropical climates – experienced some of the longest heatwaves on Earth in 2024–2025, driven by human-induced climate change (see Figure 10.2(a)). The lowest-ranked eleven countries with the longest periods of unusually hot weather that were statistically *not* attributed to climate change were: South Korea, Uruguay, Malta, Pakistan, Iceland, Japan, Canada, Czechia, North Korea, Vatican City, and India.

Notice that in several key countries driving current climate change – namely the United States, China, and Russia (Figure 6.6(b))– the attribution of extreme heat remains roughly split 50/50 between natural weather variability and anthropogenic climate change. This ambiguity creates fertile ground for climate denial and deliberate obfuscation. However, if a similar analysis were conducted a decade from 2025, these

countries – along with Canada, India, and Poland – would almost certainly have shifted decisively toward greater attribution to climate change, or to the right in Figure 10.2(a). That is, unless they drastically reduce their emissions. But will they? Not before their economies crash in random order is my guess.

You may be wondering – why did so many remote Pacific and Caribbean islands experience such prolonged heatwaves in 2024 and 2025? The answer is straightforward – these islands are surrounded by oceans that have been undergoing unprecedented extreme marine heatwaves (MHWs) since the early 1980s, with record-breaking intensity in 2023 (*Dong et al.*, 2025), just prior to the land-based heat extremes shown in Figure 10.2(a) between May 2024 and 2025. These MHWs have been attributed to anthropogenic climate change with near 100% certainty (*Laufkötter et al.*, 2020).

There are hundreds of private islands scattered across the Pacific and Caribbean.[1] Most were purchased as status symbols or as supposed refuges from the effects of climate change. Alas, in this world, there is no escaping climate change.

Iceland and East Greenland shifted markedly to the right in Figure 10.2(a) following the intense heatwave of May 13–22, 2025, during which local temperatures exceeded preindustrial values by

$$T_{\text{local, anomaly}} = T_{\text{local}} - T_{\text{local, preindustrial}} \approx +11 \text{ to } 14^{\circ}\text{C},$$

as shown in Table 10.2. When referenced to the global mean surface temperature (GMST), this Greenland ice-melt event – introduced at the beginning of Chapter 12 – was estimated to be approximately 40 times more likely under today's climate than under preindustrial conditions. This suggests that localized warming in the region may eventually exceed even the high-end SSP5-8.5 projections for 2100. That's why heatwaves in the polar regions matter profoundly (Appendix E) – regardless of your tropical vacation plans.

Another widespread myth holds that in already hot climates, heatwaves are merely weather – not evidence of climate change. Having lived in the Kingdom of Saudi Arabia (KSA) for a decade, I must correct this misconception. Figure 10.2(b) shows clear signs of climate change in the capital, Riyadh, by comparing the distributions of warm night temperatures (TXn) across two 20-year periods: 1950–1969 and 2001–2021. Since I was born in November 1951, the climate in Riyadh has changed markedly over my lifetime. Air conditioning is now essential 24/7 for much of the year. But what about plants and animals?

In short, knowing where that "one number" for the mean global surface temperature anomaly comes from – and the complexity it hides – is key to understanding our shared future.

[1] Listings alone suggest several hundred across major island nations. Many more are likely held privately without public sale records – particularly resorts, estates, or islands held by corporations or trusts; see, e.g., *Vladi Pacific* (2024), *Private Islands Online* (2024), *Vladi Caribbean* (2024).

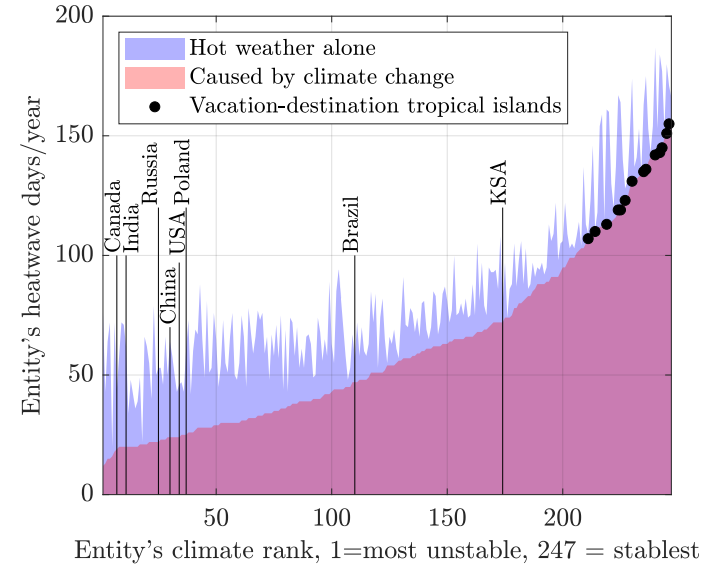

(a)

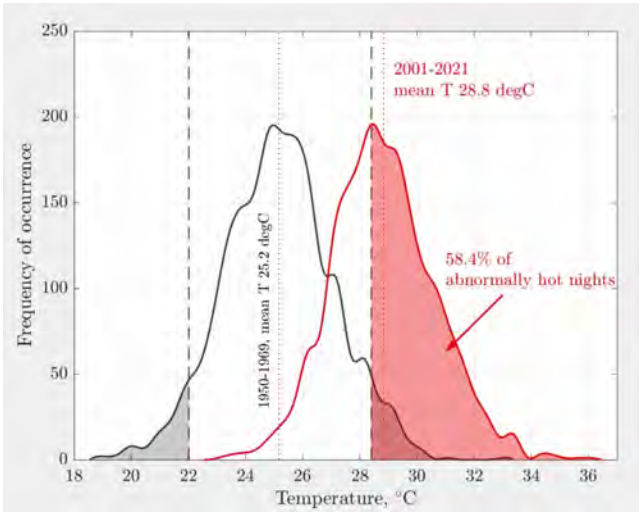

(b)

Figure 10.2: **(a)** Heatwave days were recorded for 247 countries during the one-year period from May 1, 2024, to May 1, 2025. Temperature anomalies were measured relative to the Global Mean Surface Temperature (GMST) anomaly, using the 1850–1900 reference period as the preindustrial baseline. As shown in Figure 5.7, GMST trends over land, ocean, and the entire planet have increased monotonically with cumulative total CO_2 emissions since 1850. Local temperature anomalies were calculated relative to the GMST for each specific location. A heatwave is defined as a period when local daily temperatures exceed the 90^{th} percentile of the local GMST distribution (*Gilford et al.*, 2022, *Giguere et al.*, 2025). Please notice that the Pacific and Caribbean islands experienced the longest climate change-attributed heatwaves during this interval. So, if you going to catch a wide-body jet to one of these islands, do so before it is too late to enjoy it. Diesel-powered, air-conditioned luxury accommodations will be waiting for you, and a small mountain
of your plastic trash will magically disappear. And so it goes, as Kurt Vonnegut used to say. . . Data source: Climate Change and the Escalation of Global Extreme Heat: Assessing and Addressing the Risks (2025), calculations by Patzek. **(b)** Two frequency distributions of monthly maxima of daily minimum temperatures (TXn) illustrate the occurrence of warm nights in Riyadh during the periods 1950–1969 and 2001–2021. Between these two time intervals, warm night temperatures increased by approximately $4 - 6°$C. Source: A frame from the unpublished animation of temperature data for Riyadh in *Odnoletkova and Patzek* (2021).

10.3 How climate data are collected

The essential Earth climate data are collected by satellites and surface sensor arrays. Satellites allow us to see and measure the full scope of different aspects of global climate on the Earth's surface and at top of the atmosphere (TOA), including the dynamic energy balance of the planet as a function of time, geographic location, cloud cover, aerosol presence, etc.:

$$\begin{aligned}\text{Short wavelength solar energy flux IN} = \text{Infrared Earth}'\text{s radiation flux OUT} + \\ + \text{Energy accumulation in oceans and land as heat}\end{aligned} \tag{10.1}$$

In Chapter 8 we have discussed a decline of Earth's reflectivity (albedo) measured by the CERES satellites, and the resulting extra global heating.

The high-impact images collected by satellites over the last sixty years have mobilized nations to slow down ozone depletion (*Molina and Rowland*, 1974, *Solomon*, 1999), watch passively (*Patzek*, 2004, *Patzek and Pimentel*, 2005, *Patzek*, 2007) the monstrous forest burning in the tropics, and recognize catastrophic coral reef bleaching (*Liu et al.*, 2014, *Skirving et al.*, 2019) from ocean water warming (*Heron et al.*, 2016), and acidification (*Hoegh-Guldberg et al.*, 2007, *Comiso*, 2012, *Gattuso et al.*, 2015).

Satellites have been essential in delineating and quantifying polar ice melting (*Shepherd et al.*, 2012, *McMillan et al.*, 2014, *Smith et al.*, 2020, *Markus et al.*, 2017). The landmark satellite missions that monitor ice mass loss, sea ice extent, and surface changes in Antarctica and the Arctic have been GRACE (*Velicogna*, 2009), ICESat (*Zwally et al.*, 2002), and CryoSat (*Laxon et al.*, 2013).

Yet the vast scale of human-driven climate change and ecological degradation – meticulously documented by more than 1,200 Earth-observing satellites – remains largely unknown to most of the 8 billion people now stumbling into an increasingly hostile climate regime. In what follows, I will present examples of the satellites that continuously monitor Earth's climate, along with key instruments we have used in my own research.

10.3.1 Earth-Observing Satellites

Most of what you read about climate change – beyond the noise of social media – is rooted in rigorous science and powered by advanced computer models that process vast volumes of data, expected to reach exabyte (EB)[2] scales annually by 2032.

As of 2025, approximately 1,200 operational satellites (*Pixalytics*, 2023, *Wilkinson et al.*, 2023) were in orbit, of which around 450+ were major Earth-observing platforms continuously gathering data about the planet (*Wikipedia*, n.d.); see also Table 10.3. These earth-observing satellites collect data on:

- Climate and weather, e.g., GOES, METOP, Himawari
- Ocean dynamics, e.g., Sentinel-6, Jason series
- Land surface, e.g., Landsat, Sentinel-2, MODIS
- Atmospheric composition, e.g., Aura, TROPOMI, AIR
- Greenhouse gases, e.g., OCO-2, GOSAT
- Disaster monitoring and deforestation, e.g., PlanetScope, ICEYE
- Agriculture and land use, e.g., Sentinel, TerraSAR-X
- Soil moisture and groundwater levels, GRACE and GRACE-FO
- Ice and cryosphere, e.g., ICESat-2, CryoSat

The classification of Earth observation satellite types is presented in Table 10.4, and the corresponding volumes of data they generate are summarized in Table 10.5. As aging U.S. satellites increasingly fail and NASA and NOAA face severe budgetary constraints under the current U.S. administration, the global

[2] 1 exabyte = 1 EB = 10^{18} bytes = 1000×10^{15} bytes = 1000 petabytes = 1000 PB.

Figure 10.3: Terra Earth observatory satellite collects data about the Earth's bio-geochemical and energy systems using five sensors that observe the atmosphere, land surface, oceans, snow and ice, and the planetary energy budget. The five Terra onboard sensors are: ASTER (Advanced Spaceborne Thermal Emission and Reflection Radiometer) CERES (Clouds and Earth's Radiant Energy System) MISR (Multi-angle Imaging SpectroRadiometer) MODIS (Moderate-resolution Imaging Spectroradiometer) MOPITT (Measurements of Pollution in the Troposphere). Source: NASA – Terra, accessed 11/01/2024

center of gravity for critical, life-saving Earth and climate monitoring is likely to shift toward Europe and China.

The following are key NASA satellite missions and instruments that enabled our research, see Figure 10.3. The numbers in parentheses indicate how many satellites are equipped with each instrument:

- ACRIM = Active Cavity Radiometer Irradiance Monitor (21)
- ERBS = Earth Radiation Budget Satellite (3)
- CERES = Clouds and the Earth's Radiant Energy System. Since 1997, *CERES* instruments have launched aboard the Terra, Aqua, Suomi National Polar-orbiting Partnership (S-NPP) and NOAA (20 GEOS satellites)
- GEOS = Geostationary Operational Environmental Satellite, NOAA (20)
- Terra = Earth's atmosphere, land, and water, primary productivity (MODIS = Moderate Resolution Imaging Spectroradiometer)
- Aqua/Aura = Precipitation, evaporation, and cycling of water (2)

Table 10.3: Major Earth observation satellite operators and their fleets (2025)

Operator	Country / Region	Number	Notable Missions
NASA / NOAA	United States	30+	Landsat series, Terra, Aqua, Suomi NPP, ICESat-2, JPSS, SWOT, GRACE, GRACE-FO
ESA / EUMETSAT	Europe	20+	Sentinel series (1-6), CryoSat-2, EarthCARE, Meteosat
ISRO	India	15+	Oceansat, Cartosat, RISAT, INSAT
CNSA	China	20+	Gaofen series, Haiyang, Fengyun, CBERS (with Brazil)
JAXA	Japan	10+	GCOM, GOSAT, ALOS, Himawari
Planet Labs	United States	195	Dove (Flock) CubeSats for daily Earth imaging
Spire Global	United States	126	GNSS-RO, weather and maritime tracking
CNES	France	5+	SPOT, Pléiades, Megha-Tropiques
CSA	Canada	3+	RADARSAT-2, RCM (RADARSAT Constellation Mission)
DLR	Germany	3+	TerraSAR-X, TanDEM-X, EnMAP
ASI	Italy	4+	COSMO-SkyMed constellation, PRISMA

- InSAR-1/2 = Interferometric synthetic aperture radar (2)

10.3.2 Earth surface sensors

Earth's surface climate monitoring network includes vast arrays of sensors deployed on land, in oceans, and in freshwater systems, see Table 10.6:

- Land-based surface meteorological stations measure air temperature, precipitation, humidity, wind speed and direction, pressure, etc. Most stations belong to the Global Observing System (GOS) – coordinated by World Meteorological Organization (WMO). In this network, there are some 170 primary climate stations, 11,000 synoptic[3] stations, and 120,000 automated weather stations (AWS) and climate reference sites[4].
- Ocean sensors measure sea surface temperature (SST), salinity, sea level, pH, currents, biological and chemical water composition etc., see Figure 10.4. Their global network consists of the US National Oceanic and Atmospheric Agency's (NOAA's) Argo Float Network with ∼4,000 profiling floats worldwide (sea surface to 2,000 m of water depth) that upon surfacing transmit data through NOAA's Jason satellites, see Figure 10.5. The more sophisticated floats in the Deep Argo and

[3]Synoptic stations are the standardized meteorological observation sites that report comprehensive weather data at regular intervals, typically every 6 hours.

[4]Climate reference sites are the high-quality, long-term observation stations specifically designed to monitor climate trends with high accuracy, consistency, and continuity over time. They are a core component of the Global Climate Observing System (GCOS) and are often referred to as climate reference networks or baseline stations. Climate reference sites are essential for detecting climate change signals (such as warming trends, droughts, snow loss),validating satellite data, bias-correcting reanalysis (like ERA5 (*Hersbach et al.*, 2020) used in our research, e.g., (*Odnoletkova and Patzek*, 2021)) and climate model outputs. These sites support IPCC assessments and climate services worldwide.

Table 10.4: Important Earth-observing satellites and their key functions and operators

Satellite	Operator	Primary Function	Reference
MODIS (on Terra/Aqua)	NASA	Land, ocean, and atmospheric monitoring	*Salomonson and Appel* (2002)
Landsat 8	USGS/NASA	Land surface imaging	*Roy* (2014)
Sentinel-2A/B	ESA	High-resolution multispectral land imaging	*Drusch* (2012)
GOES-16	NOAA	Geostationary weather observation	*Schmit* (2017)
OCO-2	NASA	CO_2 concentration measurement	*Eldering* (2017)
ICESat-2	NASA	Ice sheet elevation and vegetation height	*Magruder* (2020)
GOSAT	JAXA	Greenhouse gas monitoring	*Yokota* (2009)
PlanetScope	Planet Labs	Daily high-res land monitoring	*Fisher* (2020)
CryoSat-2	ESA	Polar ice thickness	*Wingham* (2006)
JPSS-1 (NOAA-20)	NOAA/NASA	Atmospheric, oceanic, and land data for weather	*Goldberg* (2013)
GRACE, GRACE-FO	NASA	Understanding terrestrial water storage and mega-droughts	*Chandanpurkar et al.* (2025)

Table 10.5: Estimated annual data volumes from Earth-observing satellites

Source	Estimated Annual Volume	Reference
NASA Earth Science Data Systems (ESDS) archive	128+ petabytes (as of 2025)	*NASA Earthdata* (2025)
SWOT and NISAR missions	∼36.5 petabytes/year (100 TB/day)	*NASA JPL* (2022)
Commercial satellites (e.g., Planet, Maxar)	36+ petabytes/year	*Miller* (2020)
Projected global EO data volume	2,000 petabytes/year by 2032	*Mason* (2022)

Biogeochemical Argo programs profile water column down to 6,000 m of depth and measure CO_2, pH, O_2, as well as biomarkers and water chemistry. In addition there are drifting surface buoys; ∼1,000 - 1,200 buoys are active at any time. Then there are ∼1,500 global tide gauge stations (e.g., GLOSS) that monitor sea level rise. There are also global moored arrays with $\sim 200 - 300$ buoys (e.g., TAO/TRITON, RAMA, PIRATA) that measure tropical ocean-atmosphere interactions.

- The inland and coastal water systems monitor hydrological variables (river levels, lake salinity/temperature groundwater)

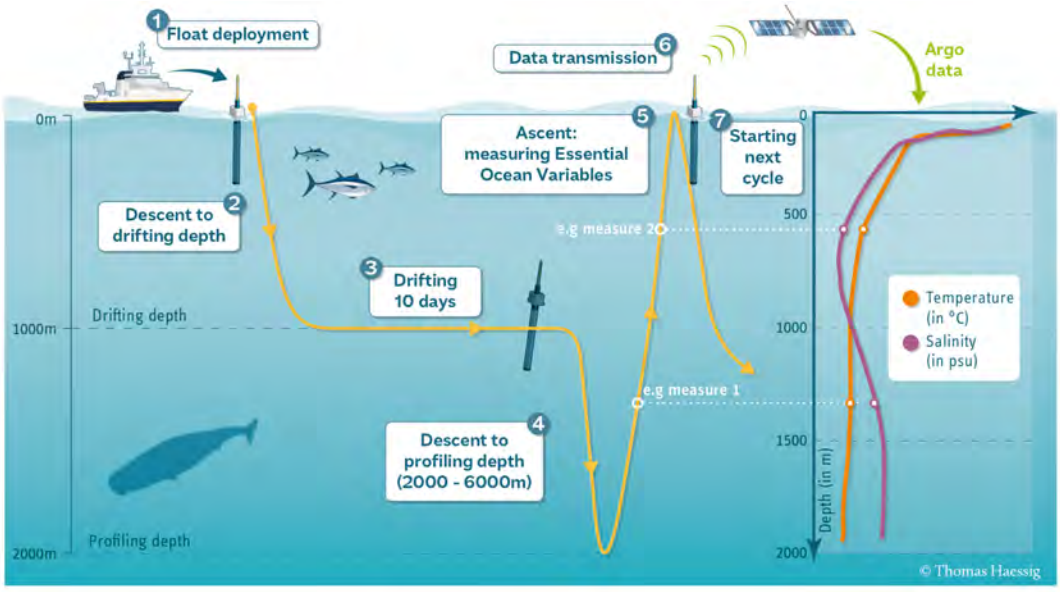

Figure 10.4: Argo float water column profiling cycles. Source: UCSD.

- About 10,000 river gauge stations report to the Global Runoff Data Center (GRDC).
- Finally, there are tens of thousands of stream, salinity, and groundwater sensors that comprise the

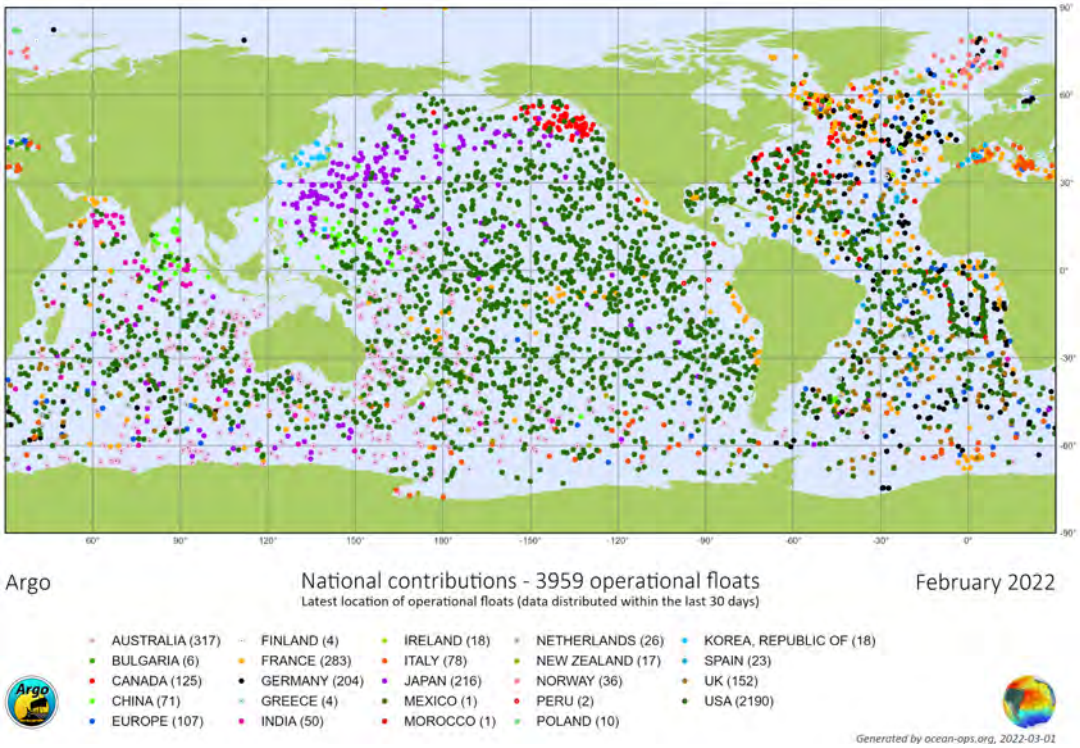

Figure 10.5: Active Argo floats in Feb 2022. Each float that costs between $20,000 and $150,000, depending on its capabilities, is launched from a ship. There is no central funding for Argo. Each of the 30 countries that operate floats obtains their own national funding to buy floats, prepare and launch them and to process and distribute the data. Argo is part of the Global Ocean and Global Climate Observing Systems. The total annual cost of Argo is estimated at $40million/year. Source: UCSD.

US Geological Survey (USGS) network and its global equivalents.

10.4 Models

Today's scientific and engineering models are extraordinarily complex, and they operate on high-dimensional manifolds where nonlinear interactions among variables often obscure intuitive understanding. To many users, these models appear as black boxes: they absorb historical data and produce projections of the future. This raises a fundamental question – how can we be confident that these models are telling the truth?

Generally, the answer lies in model comparison and calibration. Scientists compare the outputs of different models using similar – but not identical – input datasets. Because each model varies in complexity and dimensionality, their inputs are tailored accordingly. Models are then "appropriately calibrated" against historical data to ensure their responses are plausible, and only then are they used to project the future.

Back in the 1980s, I was a leading reservoir engineer at Shell. I experienced firsthand how difficult it was to forecast oil and gas production, even with the most advanced, thoroughly calibrated simulation models – often exceeding a million lines of code and involving millions of grid blocks. The lesson was clear: complex, multi-parameter models are often excellent at reproducing the past but frequently struggle to predict the future with high accuracy.

Table 10.6: Estimated global counts of Earth surface climate sensors

Sensor Type	**Estimated Count**	**Example Networks / Sources**
Land Weather and Climate Stations	$> 130,000$	GOS, GSN, AWS (*World Meteorological Organization*, 2023, *Global Climate Observing System*, 2022)
Ocean Profiling Floats (Argo)	$\sim 4,000$	Argo Project (*Argo Steering Team*, 2023)
Surface Drifting Buoys	~1,000 - 1,200	Global Drifter Program (*Global Drifter Program*, 2023)
Moored Ocean Buoys	$\sim 200 - 300$	TAO, RAMA, PIRATA (*NOAA*, 2022)
Tide Gauges	~1,500	GLOSS (*UNESCO/IOC*, 2022)
River and Hydrological Gauges	$10,000 - 50{,}000+$	GRDC, USGS (*GRDC*, 2021, *USGS*, 2023)

Forecasting Earth's climate future is one of science's hardest problems – everything is interconnected, nonlinear, and constantly evolving. To address this challenge, large-scale model intercomparison projects have emerged, focusing on sophisticated Global Coupled Models (GCMs), some comprising up to two million lines of code (see Table 10.7), as well as simpler, more conceptual models like the one proposed in this book. These state-of-the-art GCMs simulate the physics, chemistry, and biology of the atmosphere, land, and oceans with increasing fidelity, and are executed on the world's most powerful supercomputers.

The prevailing scientific approach relies on running ensembles of diverse climate models under comparable forcing scenarios, and systematically comparing their outputs to assess the consistency, variability and uncertainty of the model responses – see, for example, *Touzé-Peiffer et al.* (2020) and the references therein.

The Atmospheric Model Intercomparison Project (AMIP) in 1990, was the first attempt to coordinate such an activity in modeling current climate. Among other climate intercomparison projects, the Coupled Model Intercomparison Projects (CMIP 1–6), are now considered as "...the foundational elements of climate science" (*Eyring et al.*, 2016). For example, an output of a CMIP6 full-suite simulation is between 100 and 1000+ TB of numbers (*Eyring et al.*, 2016, *ESGF Consortium*, 2024). Such giant output data sets are inaccessible to humans and can only be processed by computers. The simple models of climate

Table 10.7: Approximate size and structure of major Global Climate Models (GCMs)

Model	Lines of Code	Languages	Notes
CESM (*NCAR*, 2024)	1.5 - 2 million	Fortran, C, Python	Modular Earth system model with components for atmosphere (CAM), ocean (POP), land (CLM), sea ice (CICE), and coupler (CPL7)
GISS ModelE (*NASA*, 2024)	500k - 1M	Fortran, Python	Used by NASA GISS. Simplified compared to CESM. Publicly available
HadGEM3 / UM (*HAD*, 2024)	∼1.2 million	Fortran	Unified Model with ocean (NEMO), land (JULES), and atmospheric physics. Closed-source but documented
IPSL-CM	∼1 million	Fortran	French consortium. Uses OASIS coupler. Widely used in CMIP[a]
MPI-ESM (*MP*, 2024)	∼1 million	Fortran	German model used in CMIP. Atmosphere: ECHAM, ocean: MPIOM
EC-Earth (*EC*, 2024)	1.5 million	Fortran	Based on ECMWF IFS[b] and ARPEGE[c]; maintained by European consortium

[a]CMIP = Climate Model Intercomparison Project
[b]ECMWF IFS = the Integrated Forecasting System developed and maintained by the European Centre for Medium-Range Weather Forecasts (*ECMWF*, 2022)
[c]ARPEGE = Action de Recherche Petite Échelle Grande Échelle, or Research Project on Small and Large Scales (*Dejardin et al.*, 2022)

change use the processed and averaged satellite and surface sensor data sets, with inputs and outputs measured in kilobytes (kB) or megabytes (MB)[5].

Climate modeling teams worldwide either participate in or depend heavily on coordinated Coupled Model Intercomparison Projects (CMIPs). These global collaborations form the backbone of modern climate science, generating a vast and rapidly expanding literature. As of January 3, 2025, Google Scholar listed over 10.1 million scientific articles and reports referencing "climate change." The monumental Sixth Assessment Report (AR6) of the Intergovernmental Panel on Climate Change (IPCC) is considered to be the most authoritative source. It includes three Working Group Contributions (WGI-III) *Masson-Delmotte et al.* (2021), *IPCC* (2022b), *Shukla et al.* (2022) and a Synthesis Report (SYR) *Core Writing Team et al.* (2023) that together have amassed more than 570,000 citations and span 7,519 pages. The AR6 reports reflect the enormous scope and complexity of contemporary climate model outputs – rich in data yet often impenetrable to non-specialists, including policymakers, students, and researchers from other disciplines. In contrast, our goal is to use greatly simplified input datasets to generate climate projections that are robust, transparent, and accessible to a broad audience.

[5]Recall that 1 kB = 1 nano TB and 1 MB = 1 micro TB. Thus these reduced data sets are quite easily managed by humans.

10.5 Calculation of Monthly Global Temperature Anomalies

The monthly global anomaly of surface air temperature is calculated by comparing the average temperature for a given month to a long-term reference period, often 30 years. Because of the wealth of data and the relatively stable global temperature, the 1951-1980 mean global temperature reference is often used. The calculation process involves the following steps:

1. **Data Collection**: Temperature data from weather stations, satellites, and ocean buoys are gathered, see, e.g., Figures 10.6 and 10.7.
2. **Averaging**: For each location, an average temperature is calculated for each month.
3. **Baseline Period**: A long-term baseline period (e.g., 1951-1980) is chosen to represent reference conditions.
4. **Anomaly Calculation**: The temperature for each month is compared with the corresponding average in the baseline period. The difference between the monthly temperature and the baseline is the anomaly.
5. **Global Averaging**: These anomalies are averaged across all locations globally to produce a single global value for the month.

For example, the U.S. has thousands of weather stations operated by various entities, including the National Weather Service (NWS), the Federal Aviation Administration (FAA), and private entities. Some of the major networks are:

- **National Weather Service (NWS)**: Over 900 automated stations in the Automated Surface Observing Systems (ASOS) network.
- **Cooperative Observer Program (COOP)**: More than 8,700 volunteer-based stations provide long-term climate data.
- **Mesonet Networks**: States like Oklahoma, Texas, and others have local networks, with hundreds of stations each. Oklahoma's Mesonet, for example, has 120 stations.

In total, the U.S. has over 10,000 weather stations, although the exact number varies with the inclusion of private and unofficial stations. In Texas, I relied on a Mesonet weather station owned by a neighbor next to my property.

Key studies on the topic are:

- *Hansen and Lebedeff* (1987) and *Hansen et al.* (2010), who provide an in-depth explanation of how NASA's GISTEMP[6] dataset calculates global temperature anomalies, see Figure 10.8 or NASA's GISTEMP website. It describes methods used to collect, process, and average temperature data, as well as how anomalies are compared to a baseline period.
- *Brohan et al.* (2006b), *Jones et al.* (2012) detail the methodology behind the HadCRUT[7] temperature dataset, including historical reconstruction of global temperatures, the baseline used for anomaly calculations, and the treatment of uncertainties.

[6] GISTEMP is the GISS Surface Temperature Analysis algorithm that was developed by NASA's Goddard Institute for Space Studies (GISS) in New York.

[7] HadCRUT Sets 1, 2, and 3 are the historical datasets of global surface temperatures developed by the Hadley Centre of the UK Met Office in collaboration with the Climatic Research Unit (CRU) at the University of East Anglia in Norwich, England.

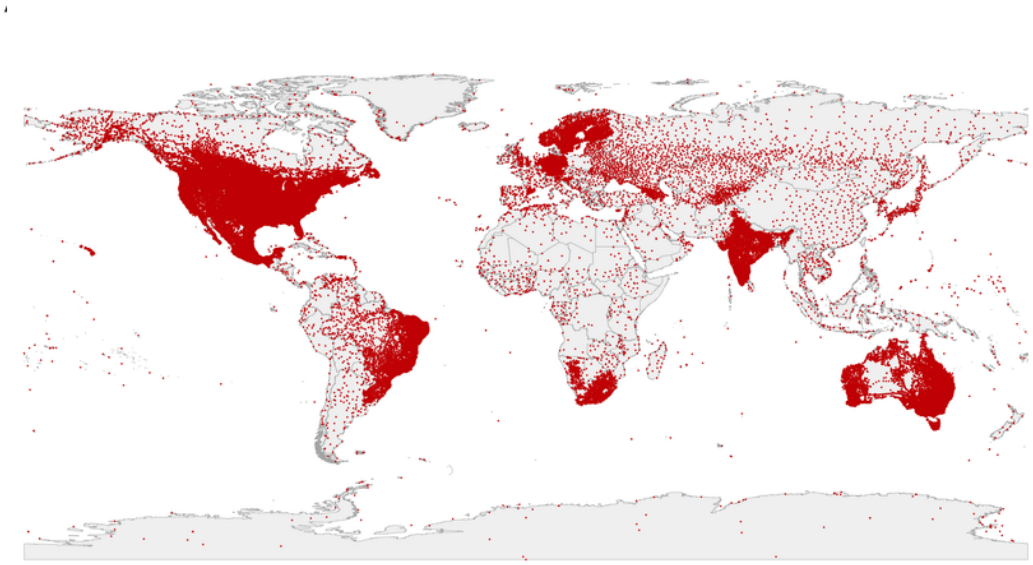

Figure 10.6: Spatial distribution of weather stations in the Global Historical Climatology Network in 2020. Today there are roughly 30,000 weather station worldwide, most a part of the global telecommunication systems. Fig. 1 in (*Ortiz-Bobea*, 2021) reproduced with permission. Also see Fig 1 in (*Brohan et al.*, 2006a).

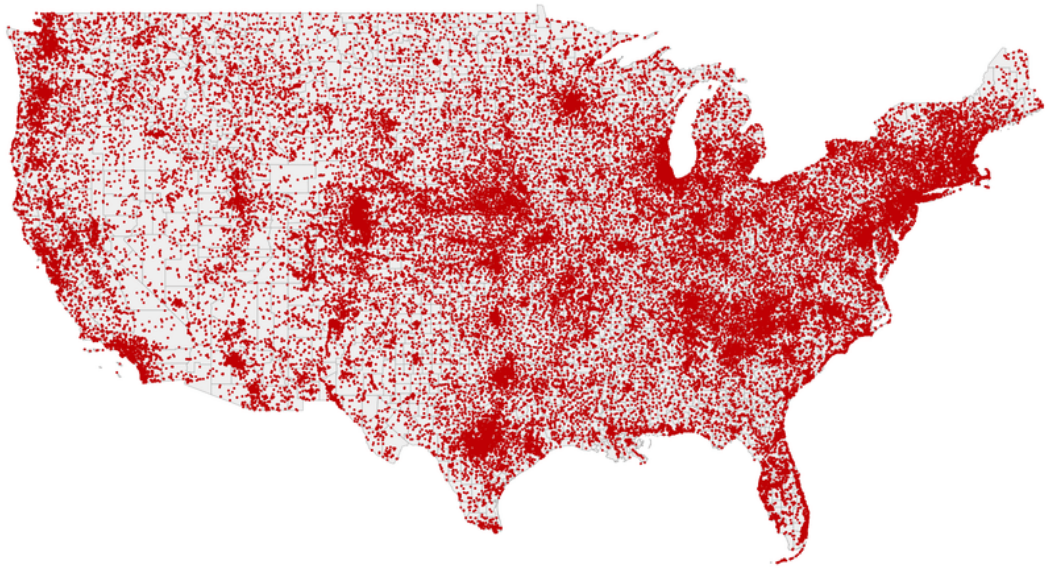

Figure 10.7: Spatial distribution of US weather stations in the Global Historical Climatology Network in 2020. Fig. 1 in (*Ortiz-Bobea*, 2021) reproduced with permission. Also see Fig. 3 in (*Connor et al.*, 2010).

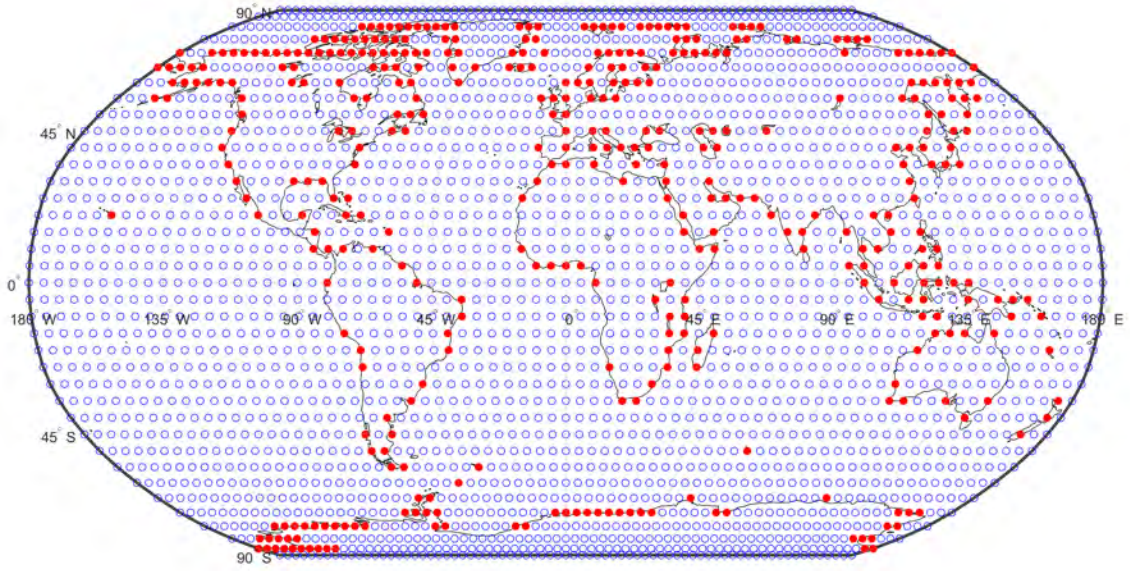

Figure 10.8: The HadCRUT grid, 3 degrees of latitude-by-5 degrees of longitude, is used to calculate mean monthly surface air temperature anomaly for each cell. The red circles denote coastal weather stations. In contrast, in NASA's GISTEMP grid the Earth's surface is divided into 80 equal-area boxes, each further subdivided into 100 equal-area subboxes, totaling 8,000 subboxes globally (*Lenssen et al.*, 2019). This design ensures uniform area representation across different latitudes. Here the mapping and calculations are by Patzek.

10.6 Anomaly Calculation

Algorithm 1 Mean temperature calculation in a grid cell

Input: Temperature anomalies T_i for stations $i = 1, 2, \ldots, N$ within the grid cell
Input: Weighting factors w_i for stations (optional)
Identify stations with latitude and longitude within the grid cell boundaries
Apply quality control and homogenization* to T_i
if weighting factors w_i are provided **then**
    Calculate weighted mean temperature anomaly:

$$T_{\text{mean}} = \frac{\sum_{i=1}^{N} w_i T_i}{\sum_{i=1}^{N} w_i}$$

else
    Calculate unweighted mean temperature anomaly:

$$T_{\text{mean}} = \frac{1}{N} \sum_{i=1}^{N} T_i$$

end if
Handle missing data by excluding stations with missing values
Output: Mean temperature anomaly T_{mean} for the grid cell

*Homogenization in climate research means the removal of non-climatic changes. Next to changes in the climate itself, raw climate records also contain non-climatic jumps and changes, for example due to relocations or changes in instrumentation. Source: Wikipedia.

A temperature **anomaly** is the difference between an observed value of temperature and a reference or baseline value. The calculation process has the following steps:

1. **Baseline Period**: A baseline period is chosen. This period represents the "zero" reference temperature or average climate conditions for consistent comparisons of all temperature anomalies. For each location (weather station or grid point), the average temperature for each month over the entire baseline period is calculated. For instance, the average of all January temperatures from 1951 to 1980 is computed, and this becomes the baseline *January* temperature that is subtracted from the mean monthly temperature for January of year *xxxx*.

   Different datasets use different reference periods, each with unique characteristics based on data availability and historical significance.

   1951–1980 Baseline (NASA GISTEMP). This period is chosen due to its good data coverage and its position before the significant rise in global temperatures in recent decades (*Hansen et al.*, 2010). An example of the 1951-1980 reference temperature for the entire planet is shown in Figure 10.9.

   1961–1990 Baseline (HadCRUT and IPCC).The 1961–1990 baseline is regarded as a standard climatological reference period (*Jones et al.*, 2012).

   1850–1900 Baseline (Pre-industrial).This baseline is used in climate change discussions, particularly with respect to the Paris Agreement's +1.5°C and +2°C targets (*Hawkins et al.*, 2017). Berkeley Earth and this book use this standard, see Figure 10.10. For example, the 1850-1900 mean temperature is shifted down by −0.3°C with respect to the 1951-1980 global mean temperature, −0.2°C with respect to the 1951-1980 global seawater surface mean temperature, and −0.5°C with respect to the 1951-1980 global land mean temperature. Thus, the temperature anomalies calculated relative to the preindustrial mean **are higher**.

2. **Current Month's Temperature**: The actual temperature is measured at the same location during a specific month in a given year (e.g., January 2024). The algorithm for calculating the

mean temperature anomaly for a GISTEMP cell, whose center is located at $(\text{lat}_{\text{grid}}, \text{lon}_{\text{grid}})$ is given by **Algorithms 1 and 2**.

3. **Calculate the Anomaly**: The anomaly is found by subtracting the baseline temperature from the current month's temperature:

$$\text{Anomaly} = \text{Current Month's Temperature} - \text{Baseline Month's Temperature}$$

For example, if the average January temperature during the baseline period was 2°C and the current January temperature is 3°C, the anomaly would be:

$$3^{\circ}\text{C} - 2^{\circ}\text{C} = +1^{\circ}\text{C}$$

A positive anomaly means the current temperature is higher than the baseline, indicating warming. A negative anomaly means it's cooler than the baseline.

Algorithm 2 Weight calculation for a GISTEMP grid cell

Input: Latitude and longitude of the grid cell center $(\text{lat}_{\text{grid}}, \text{lon}_{\text{grid}})$
Input: Latitude and longitude of each station $i = 1, 2, \ldots, N$ $(\text{lat}_i, \text{lon}_i)$
Input: Reliability scores r_i for each station (optional)
Step 1: Calculate distance of each station from grid center:
for each station i **do**
    Calculate great-circle distance d_i using the Haversine formula:

$$d_i = 2R \arcsin(\alpha)$$

$$\alpha = \sqrt{\sin^2\left(\frac{\text{lat}_i - \text{lat}_{\text{grid}}}{2}\right) + \cos(\text{lat}_i)\cos(\text{lat}_{\text{grid}})\sin^2\left(\frac{\text{lon}_i - \text{lon}_{\text{grid}}}{2}\right)}$$

$R = 6371$ km is the Earth radius

end for
Step 2: Calculate inverse distance weight:
for each station i **do**
    Assign weight $w_i = \frac{1}{d_i}$
end for
Step 3: Normalize weights:
for each station i **do**
    Normalize weight $w_i = \frac{w_i}{\sum_{j=1}^{N} w_j}$
end for
Step 4 (Optional): Apply reliability factors:
if reliability factors r_i are provided **then**
    for each station i **do**
        Adjust weight $w_i = w_i \cdot r_i$
    end for
    Normalize the adjusted weights again
end if
Output: Final weights w_i for each station

After two decades of extensive research and teaching a graduate course on Earth systems, energy supply for humanity, geologic time and climate, I have concluded that it is very difficult to add anything truly new to the existing body of knowledge of climate change. But writing a compelling short story of climate change based on the simple interpretations of observations and complex numerical models is urgently needed, and this is what I set out to do here. I want to link directly the severity of climate change today to our historical use of biomass and fossil fuels in all areas of life, and show in a simple convincing way what will happen next if we decide to pretend that it is not too late yet, and those scientists are often wrong and keep on changing their esoteric arguments we never understood. This work might be called "A Primer on how Resource Use Impacts Climate Change and All of Us."

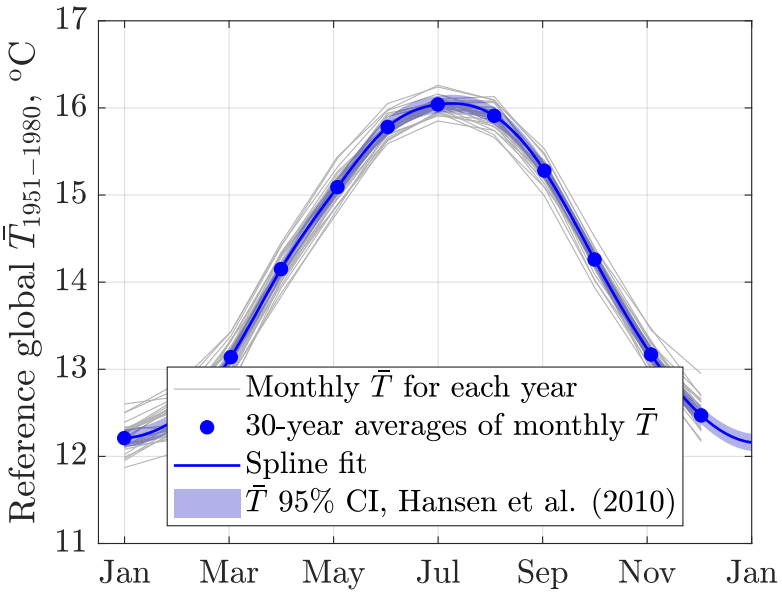

Figure 10.9: The 1951-1980 reference temperature for the Earth. For each grid cell in Figure 10.8, a cell-area analog of this global reference temperature must be used. Here, each monthly temperature anomaly anywhere on the Earth was averaged over 30 years and an average absolute global annual temperature of 14°C was added.

The key idea is to average a variety of high-resolution climate data to formulate an algebraic model of climate change, and predict the most probable future global and land temperature increases, given a CO_2 concentration pathways based on the physically possible – and probable – future production rates of fossil fuels (FFs). Thus, our approach complements the generally accepted Coupled Model Intercomparison Projects. The averaged input data encode climate complexities, and a simple transparent model quantifies only one aspect of future climate, the global mean anomalies of surface air temperature over land, sea, and the planet. The crucial insight here is that the practical aspects of climate change that will matter to you and your children become obvious when measured in terms of a single driver: the cumulative CO_2 emissions from power production and all other human activities. Such a parametrization of these climate aspects linearizes or almost linearizes all of them, making it plain that we are undergoing a fast climate deregulation driven by the anthropogenic CO_2 (and CH_4) emissions.

Figure 10.10 shows that the Earth's mean temperature is increasing fast, exceeded the +1.5°C warming cap (*UNFCCC*, 2015) in 2024, and +2°C will be exceeded by 2050, as we will show soon. In 1976, the global land started heating faster than the oceans, and the global climate *bifurcated* for the first time in millennia. On April 15, 2025, the UN-backed Net Zero Banking Alliance (*United Nations Environment Programme Finance Initiative*, 2021) voted to abandon a more stringent target to align all sector financing with +1.5°C above the pre-industrial average by 2050, and said that it would align their businesses with a well-below +2.0°C target. The major financial US-based institutions that withdrew from the +1.5°C goal were Goldman Sachs, Vanguard, Wells Fargo, Citi, Bank of America, Morgan Stanley and JPMorgan.

The global average temperatures are warming up uniformly with time, see Figure 10.11, because the Southern and Northern hemispheres (SH and NH) reflect the same amounts of sunlight to within 0.2 $W\,m^{-2}$. This symmetry is achieved by increased reflection from SH clouds offsetting precisely the greater reflection from the NH land masses (*Pierrehumbert*, 2010). The dynamic cloud cover keeps the Earth's albedo remarkably uniform, but this albedo is slowly declining. We will quantify how a decline in the aerosol component of anthropogenic air emissions might accelerate global warming.

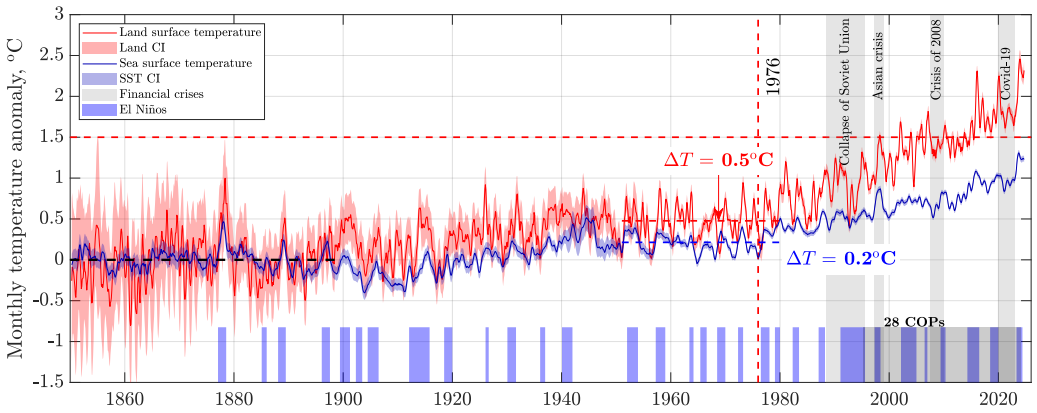

(a)

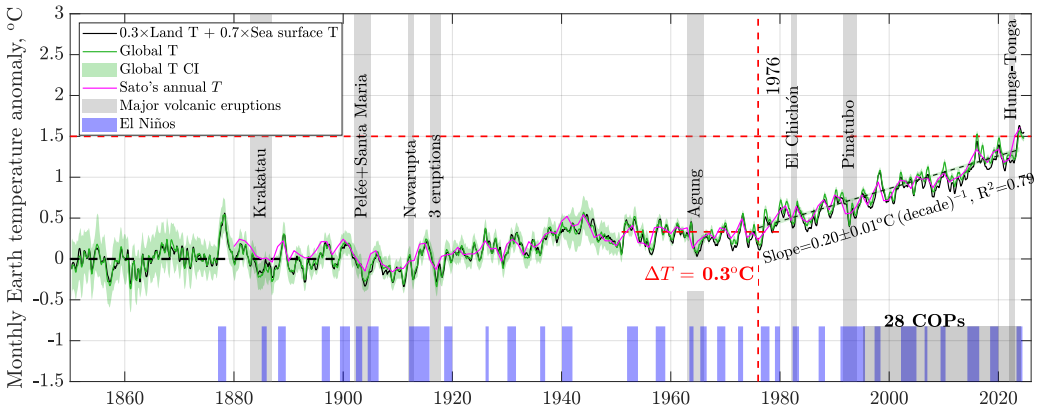

(b)

Figure 10.10: All temperature anomalies are relative to the 1850-1900 mean global surface temperature. The 1951-1980 temperature plateau anomalies are shown as the dashed horizontal lines offset by +0.5°C for global land, +0.2°C for SST, and +0.3°C for the Earth. **(a)** Anomalies of the global land temperature (Land) and sea surface temperature (SST) vs. time. Notice that in 1976, the global land temperature started increasing faster than SST, and the global climate bifurcated. **(b)** Global monthly temperature anomaly (more precisely, global mean surface air temperature (GMSAT) anomaly) vs. time. As a cross-check, also plotted are the ocean and land areas-weighted average of SST and land temperature anomaly (black curve), and (*Sato*, 2025) annual temperature anomaly (magenta). All these global anomaly histories are self-consistent. Data sources: Berkeley Earth and HadSST.4.0.1.0, accessed 02/10/2025. Calculations by Patzek.

10.7 Climate change and temperature extremes

Figure 10.12 shows the 10-year moving averages of the Earth and global land temperature anomalies. These or multidecadal averages are used to define climate change as a significant variation of weather conditions that persists after the averaging. It is this long-term trend that differentiates climate change from natural weather variability. Recall that the breaks in slope in Figure 10.12(a,b) disappear in Figure 10.12(c,d) when the anomalies are replotted against cumulative total CO_2 emissions (CTE), whose acceleration caused these slope breaks to emerge against calendar time.

The extrema of mean temperature anomalies for the Earth and global land are plotted in Figure 10.13.

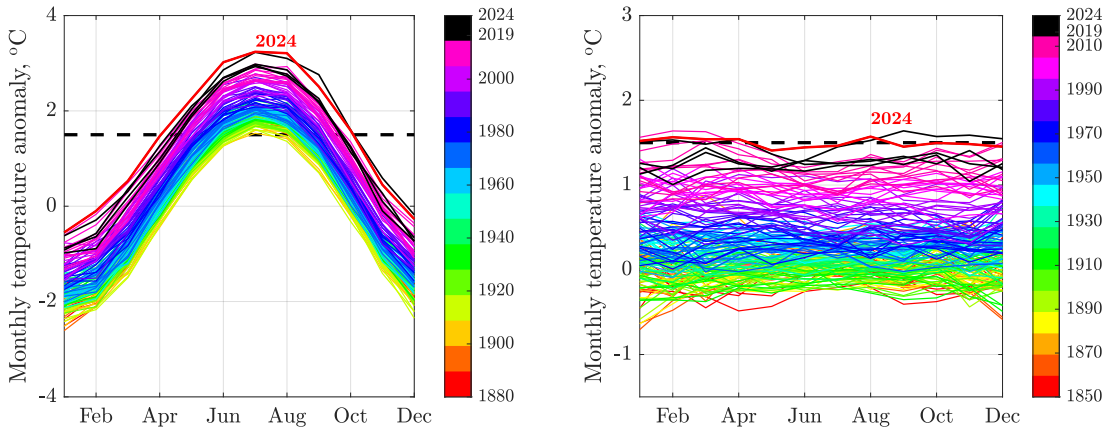

Figure 10.11: Stacked global temperatures colored by decade. The years 2020-2023 are shown in black and the record-breaking 2024 is a thick red curve. The thick horizontal dashed line is the +1.5°C temperature anomaly. **(a)** Seasonal temperatures of both hemispheres. **(b)** The stacked monthly global temperatures eerily resemble increasing water level in a tub filling with water that is warming most of the time. The almost horizontal water surface in this analogy has been controlled by clouds that make the Earth's albedo uniform. Data sources: NASA GISTEMP (*NASA*, 2015) and Berkeley Earth, accessed 2/10/2025. Calculations by Patzek.

These extrema are the minima and maxima of the monthly temperature anomaly data between 1850 and 2023, organized into 12 one-month blocks. Thus, these extrema *should* follow two GEV distribution functions[8] (one for the left tail of the parent temperature distribution and the other for its right tail) *Gumbel* (1958), *Patzek et al.* (2019), *if* they belonged to the same population of temperature anomalies. But they do *not*, because of the 1976 climate bifurcation depicted in Figure 10.10.

For a more detailed explanation of the statistics of extremes, see Appendix D, which also examines 132 years of extreme events and the impacts of climate change in Dallas, TX.

Thus, these temperature extremes belong to two disjoint subsets of global temperatures, one for 1850 - 1976, and another for 1976 - 2023. For example, the P_{10} global maximum temperature of the pre-1976 distribution, 0.57°C, is lower than the P_{90} temperature of the post-1976 distribution, 0.68°C. The resulting distributions for the Earth and global land are shown in Figure 10.14. All distributions have negative shape factors, ξ, and thus they are the fat-left-tail Weibull distributions weighted by cold temperatures. Notice the large jumps in the P_{50} values between the pre- and post-1976 temperature anomalies: 0.72°C for the Earth and 0.93°C for the land. The cooler global temperatures are less frequent now and are disappearing fast in favor of heat waves.

The minima and maxima in Figure 10.13 show most clearly the climate-defining role of the 1976 FF cumulative emissions crossover in Figure 5.5, aided by global air cleaning post 1970, and consequent climate bifurcation. For the entire planet, the slope of the maximum temperature, 0.03°C/decade, which persisted for 126 years, jumped six-fold in 1976 to 0.18°C/decade. In 2011, it may have jumped to 0.32°C/decade or ten-fold! The minimum Earth temperature was increasing even faster at 0.05°C/decade, and its slope jumped four-fold to 0.20°C/decade in 1976 and to 0.24°C/decade in 2011.

[8] *Kaufman and Roston* (2025) reported: At one panel on extreme weather, the moderators put up a slide with regional wind and hail events just in May and June of this year. Two had damages in the hundreds of millions of dollars. One crosses the billion-dollar threshold. "Historical data is not lining up with what we're seeing right now" in terms of damages, said Chambers. "I think that is a huge concern for a lot of risk managers, because insurance carriers – you know, they've got 250 years of data, but that data looks very different now." Good observation; weather extremes follow very different distributions explained in Appendix D.

To prove that the cumulative total CO_2 emissions are the primary driver of Earth heating, let's compare the plots of temperature extremes vs. time in Figure 10.13(a,b) and the same plots vs. the CO_2 emissions in Figure 10.13(c,d). In the latter two figures, the dramatic slope changes disappear since 1950, simply because they are the response of the Earth climate system to the ever-increasing rate of CO_2 injection into the atmosphere and little else.

The "fat-tail" extreme value statistics govern real tails, or extremes, of random phenomena people attempt to describe with "nice" distributions like Gaussians that make events $2-3\sigma$s away from the mean impossible in practice. But such extreme events, rare as they might be, do exist. As discussed here, we have already exceeded the $\Delta T = +1.5^oC$ anomaly for the Earth and $+2^oC$ for the global land. But both these extremes are still the P_{10} category events in Figure 10.14(b) and (d). So what about an extremely extreme event with $\Delta T = +40^oC$?!

In March 2022, Antarctica experienced an extraordinary heatwave *Bergstrom* (2024), see Figure 10.15. Over three million square kilometers of East Antarctica – the area of India – experienced temperature increases of up to 40^oC above normal, shattering all extreme temperature anomaly records. It was the most intense heatwave ever recorded anywhere in the world. Despite the La Niña conditions, hot air over the Indian Ocean created 12 tropical storms. Five of these storms became tropical cyclones, and heat and moisture from some of these cyclones merged. A fortuitously meandering jet stream picked up this hot air and shot it across the planet to Antarctica. This extraordinary event caused the vulnerable Conger Ice Shelf east of Dome C (where the famous ice cores presented in Chapter 9 were drilled) to finally collapse. But the heatwave's impact was not nearly as bad as it could have been, because it occurred in March, the month when Antarctica begins its dark, extremely cold winter (there are only two seasons there: summer and winter). Thus air temperature over land remained negative (-47+40=-7°C). If a future heatwave arrives in Antarctica in summer – which is increasingly likely after the 1976 climate bifurcation – the results will be catastrophic simply because $-7+20 = 13^oC$ and ice will melt fast.

A climate tipping point was reached in 1976, ushering a new era of global warming, but only a few noticed. A climate tipping point can be defined as a critical point in the global climate system beyond which significant, abrupt, and often unstoppable changes occur.

The global land extreme temperatures were heating up even faster. The slope of the warmest temperatures jumped in 1976 from 0.05^oC/decade to 0.31^oC/decade, or six-fold, and possibly to 0.53^oC/decade in 2011, or ten-fold. The slope of the coldest temperatures jumped in 1976 from 0.10^oC/decade to 0.31^oC/decade, or three-fold, and possibly to 0.45^oC/decade in 2011, or four-fold.

Figure 10.12 reveals another secret of global warming. Until 1976, the coldest Earth temperatures were heating up at the rate 33% faster on average than the hottest temperatures. This means that the coldest nights and winters were getting warmer faster than the hottest days and summers. After 1976, the rates of heating of the warmest and coldest temperatures became closer, but also several-fold higher. As we showed elsewhere *Odnoletkova and Patzek* (2021) in regional calculations, the respite night cooling brings to animals and people has been disappearing almost imperceptibly until 1976, and quite visibly thereafter. This fact alone should have given a major pause to governments and policy makers. Did it?

The slopes of the temperature anomaly profiles in Figures 5.7, 10.12 and 10.13 are listed in Table 10.8, and are compared with Hansen et al.'s results *Hansen et al.* (2023). Notice that the color-coded current results are very close to their analogs in Hansen et al. *Hansen et al.* (2023). All these slopes should be viewed as the *low* bounds on climate change, simply because they reflect an increase of pCO_2 by 94 ppm_v between 1976 and 2024, and are linear not quadratic when pCO_2 changes by 300-400 ppm_v.

Table 10.8: Slopes of climate change plots

Quantity	Earth			Global Land		
	Slope °C/decade	$\pm 2\sigma$ °C/decade	R^2	Slope °C/decade	$\pm 2\sigma$ °C/decade	R^2
Figure 10.10(b), ΔT	0.20	0.02	0.89	0.30	0.04	0.86
Figure 10.12(a) ΔT	0.20	0.01	0.97	0.29	0.02	0.97
Figure 10.13, Max ΔT, 1976-2011	0.18			0.32		
Figure 10.13, Max ΔT, 2011-2023	0.32			0.53		
Figure 10.13, Min ΔT, 1976-2011	0.20			0.24		
Figure 10.13, Min ΔT, 2011-2023	0.24			0.45		
Hansen et al. (2023) Fig. 24, ΔT	0.18					
Hansen et al. (2023) Fig. 24, Max ΔT	0.36					
Hansen et al. (2023) Fig. 24, Min ΔT	0.27					

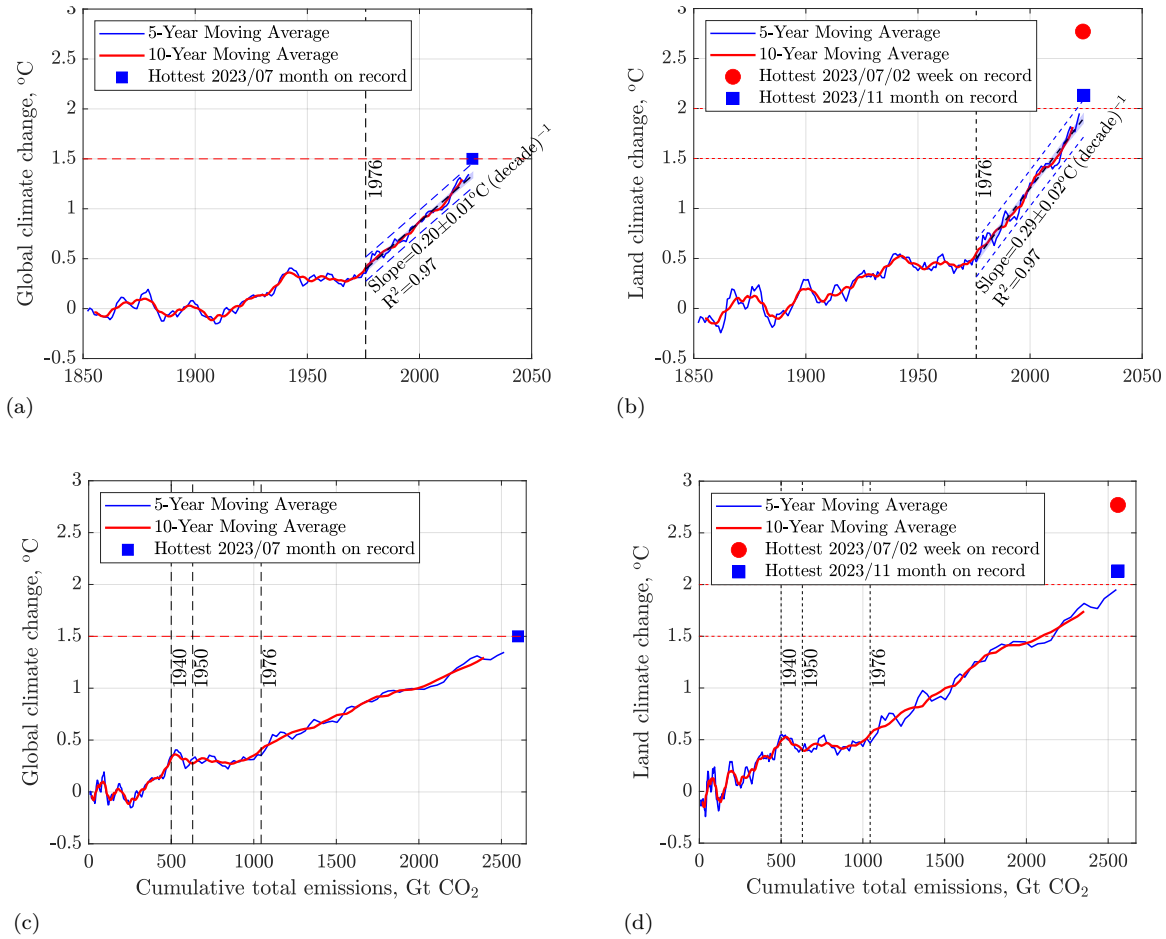

Figure 10.12: Global and land climate change, 1850-2024. The climate temperature anomalies relative to 1850-1900 are calculated as the moving 10-year averages of the annual anomaly data to smooth out the effects of weather. The five-year running averages are also shown for comparison. **(a)** Global climate temperature anomaly. **(b)** Land climate temperature anomaly. In 1951, the FF emissions rate exceeded that of AL and in 1976 cumulative FF emissions exceeded those of AL. Notice that the sharp kinks in global temperatures in 1976 (Figure 10.10) are smeared by the moving averages. The post-1976 temperature slopes are **(a)**, 0.2 ± 0.01°C (decade)$^{-1}$, and **(b)** 0.3 ± 0.02°C (decade)$^{-1}$. The 95% certainty ($\pm 2\sigma$) intervals for the models are shaded in blue and for the observations appear as dashed blue lines. **(c)** and **(d)** same as (a) and (b) but plotted vs. cumulative CO_2 emissions. The 1940-1976 hiatus reflects the uncontrolled global air pollution that dampened temporarily solar irradiation of much of the Earth's surface.

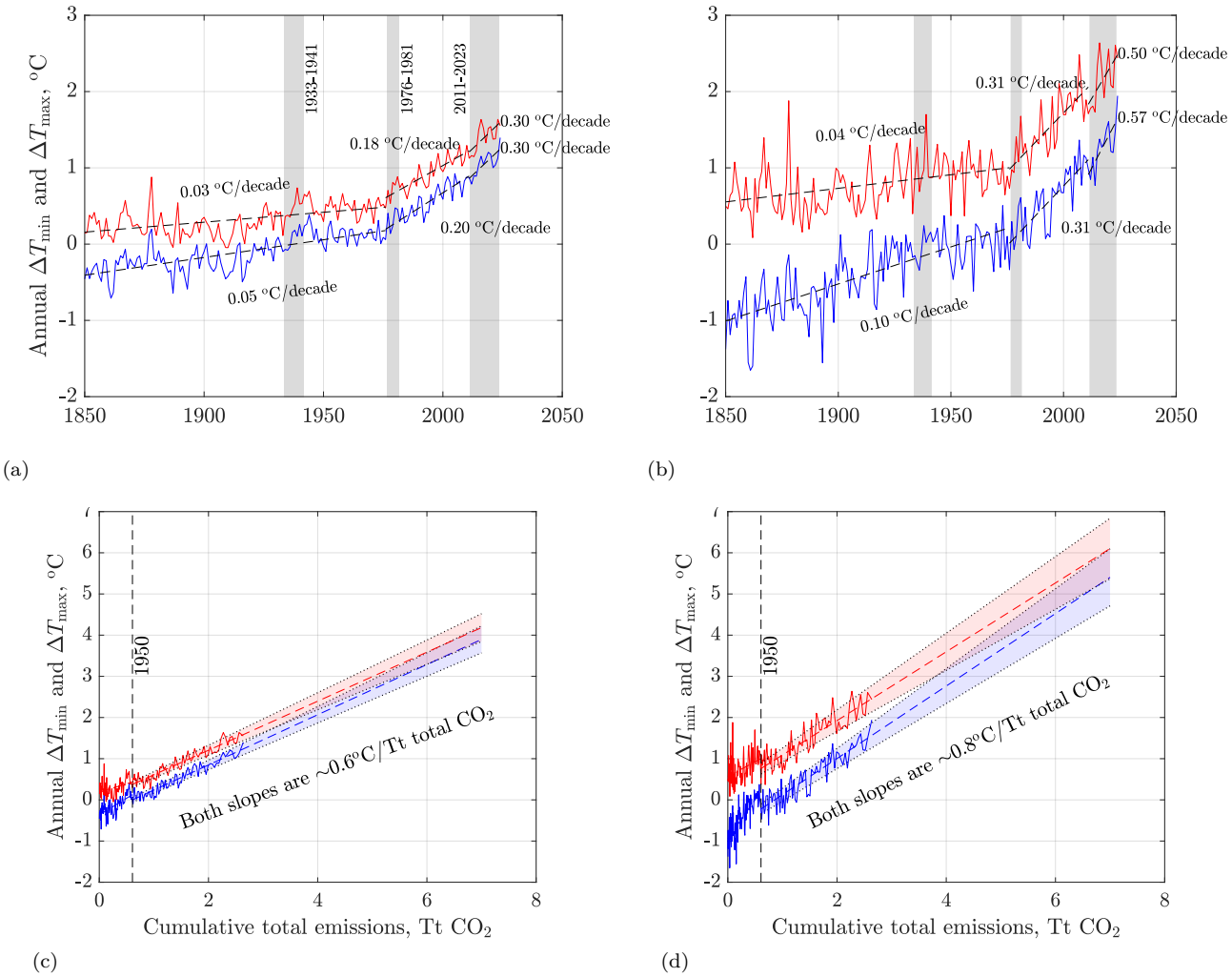

Figure 10.13: The annual maximum (red) and minimum (blue) temperatures between the years 1850 and 2024. Notice that both linear trends have been increasing slowly, with a significant break in the slope around 1976, after which the hottest temperatures have increased at 2.6°C/century and the coldest ones have increased at 2.9°C/century for the Earth **(a)**, and at 3.1°C/century for the land **(b)**. The slopes of the warmest temperatures may have increased again in 2011 to 3.2°C/century for the Earth and 5.3°C/century (!) for the global land. The slopes of the coldest temperatures jumped in 2011 to 2.4°C/century for the Earth and 4.5°C/century for the land. This means that winters and nights have been heating up faster than summers and days. In other words, the heat misery indices have been increasing faster during winters and nights, denying people rest and regeneration in most parts of the world. For example, soon majority of people will not be able to survive without AC year-long in most parts of the Middle East. In sub-Saharan Africa, India, Pakistan and Bangladesh, ~1 billion people will have no access to AC and will be increasingly dying from severe heat exposure and strokes. **(c)** and **(d)** same as (a) and (b) but plotted vs. cumulative CO_2 emissions.

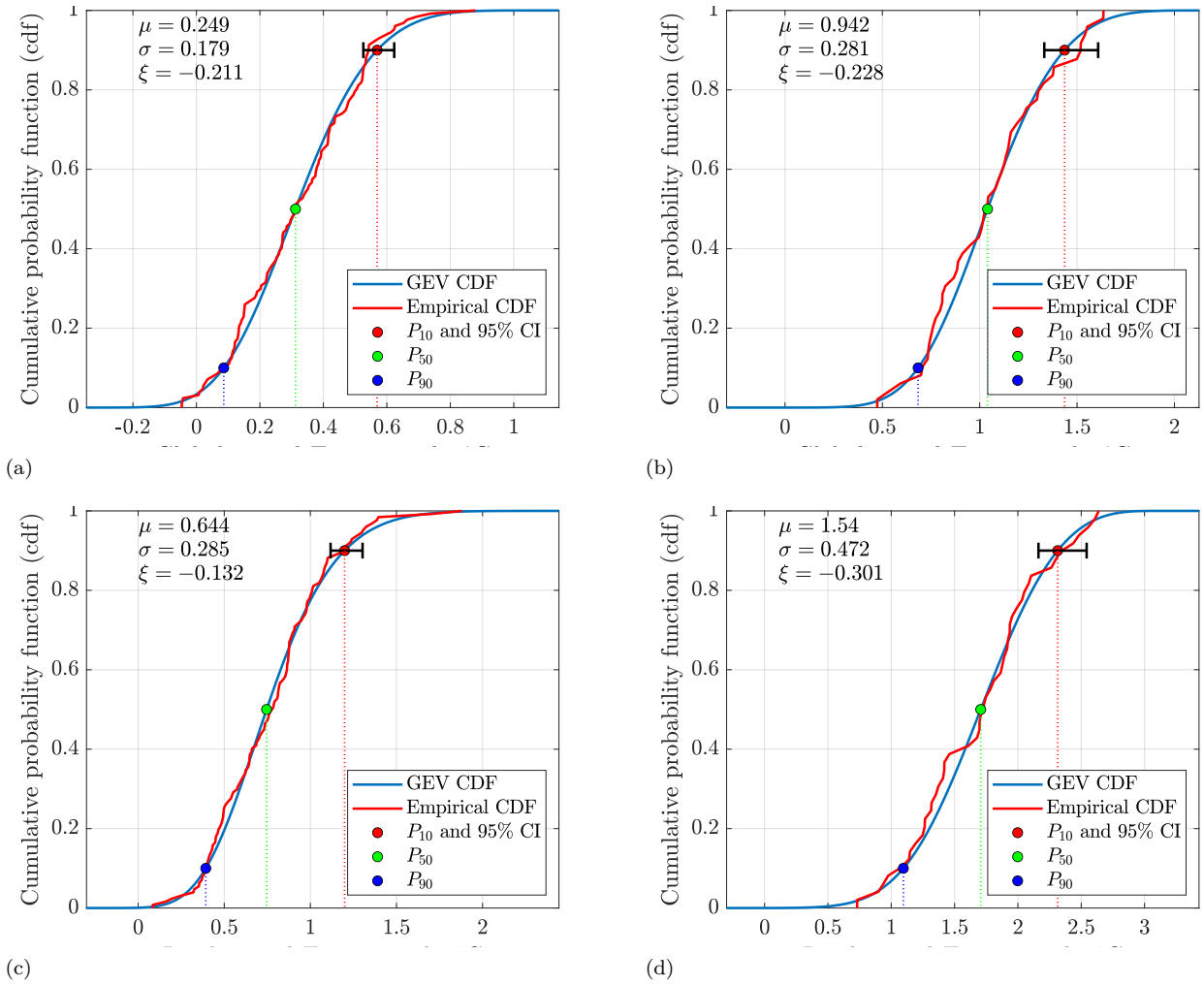

Figure 10.14: Theoretical and empirical (data-driven) GEV cumulative probability distribution functions (CDF) with the highlighted median value (P_{50}), and P_{90} (90% of the CDF values $\geq P_{90}$) and P_{10} (10% of CDF values $\geq P_{10}$). The bar around each P_{10} is the 95% confidence interval (CI). Notice that this interval is obtained from two minimizations of the function $R10$ subject to nonlinear constraints. The first minimization finds the maximum lower bound on CI, and the second one minimizes $-R10$ to find the minimum upper bound. Therefore this 95% CI can be asymmetrical with respect to the CDF. **(a)** CDF of 12-month data block maxima ($T_{\max}$) of global temperature anomaly, 1850-1976. $T_{50} = 0.31$°C, $T_{90} = 0.09$°C, and $T_{10} = 0.57 \pm 0.05$°C. **(b)** CDF of monthly-block $T_{\max}$ of global temperature anomaly, 1976-2023. $T_{50} = 1.03$°C, $T_{90} = 0.68$°C, and $T_{10} = 1.42 \in [1.32, 1.59]$°C. **(c)** CDF of monthly-block $T_{\max}$ of global land anomaly, 1850-1976. $T_{50} = 0.75$°C, $T_{90} = 0.39$°C, and $T_{10} = 1.20 \pm 0.09$°C. **(d)** CDF of monthly-block $T_{\max}$ of global land anomaly, 1976-2023. $T_{50} = 1.68$°C, $T_{90} = 1.09$°C, and $T_{10} = 2.30 \in [2.14, 2.54]$°C.

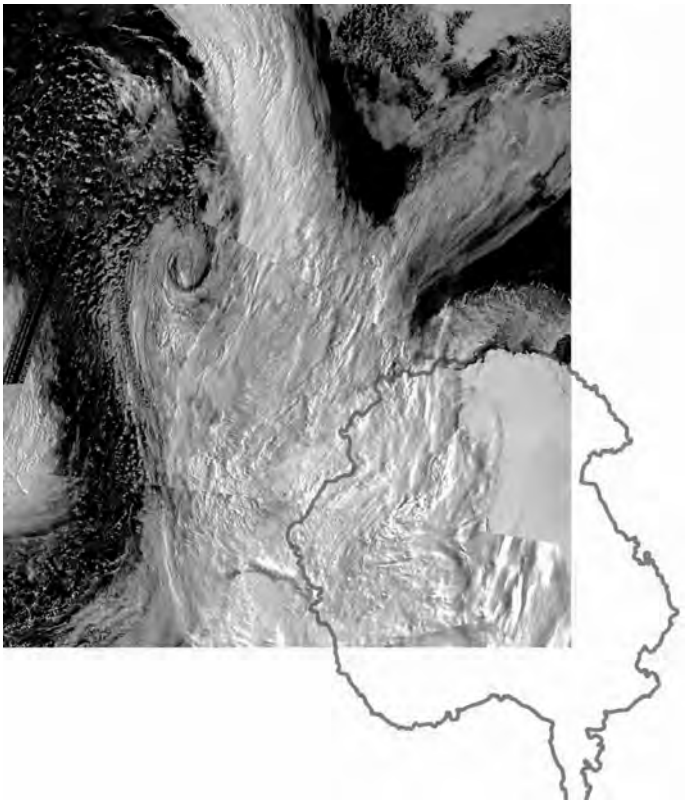

(a)

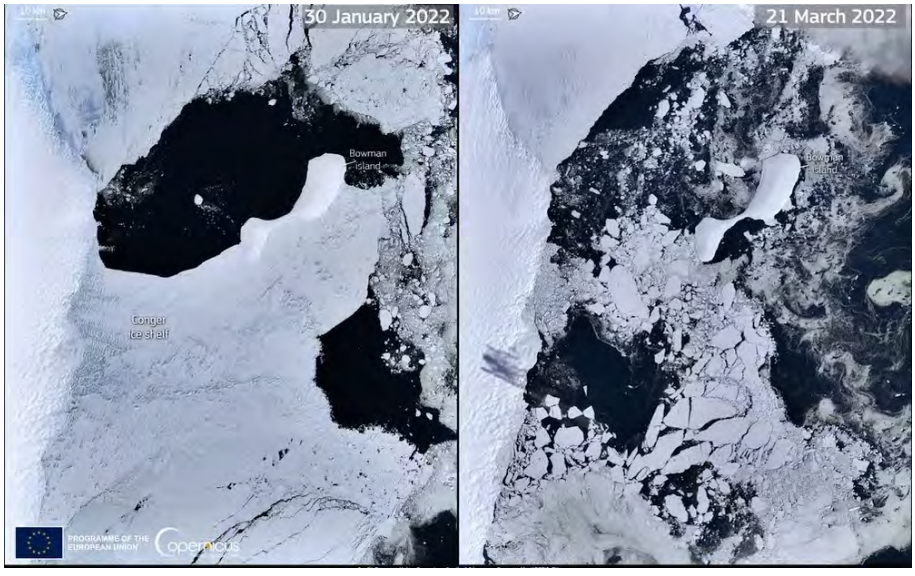

(b)

Figure 10.15: The largest ever recorded heatwave in the world occurred in March 2022 over east Antarctica. **(a)** The atmospheric torrent that transported hot air from the equator. **(b)** The fast collapse of the Conger Ice Shelf, offshore east of Dome C. Image sources: Copernicus, reproduced from *Bergstrom* (2024), CC-BY.

Chapter 11

Simple model of global warming

A bleaching coral reef in the Red Sea north of Yanbo in Saudi Arabia.
Photo by Łukasz Jaremko, a KAUST professor and avid scuba diver, Aug 20, 2022.

We may never see the heat stress that causes bleaching drop below the threshold that triggers a global event. We're looking at something that's completely changing the face of our planet and the ability of our oceans to sustain lives and livelihoods

Mark Eakin

Coral Reef Watch program of the U.S. National Oceanic and Atmospheric Administration

AP News, April 23, 2025.

11.1 What are you going to learn?

You will see that global temperature anomalies and cumulative atmospheric CO_2 emissions – primarily from fossil fuel combustion – are sufficient to predict with great accuracy global warming trends through the year 2100.

11.2 Why is this important?

Violent weather events intensified by climate warming are becoming increasingly expensive. For example, the two hurricanes that struck Florida just two weeks apart in 2024 caused an estimated $113 billion in damages.

According to *The Climate Economy: 2025 Outlook*, a report released by Bloomberg Intelligence on June 16, 2025, the United States spent nearly $1 trillion on disaster recovery and other climate-related expenditures over the 12 months ending May 1. That figure represents approximately 3% of U.S. GDP – money that households and businesses might otherwise have spent on preferred goods and services. As Bloomberg analysts note, this amounts to "a stealth tariff on consumer spending."

Since 2000, global disaster-related spending has reached an astonishing $18.5 trillion. In the United States, the primary drivers of this trend include rapidly rising insurance premiums – which have doubled since 2017 –, post-disaster reconstruction costs, and expanding federal aid programs.

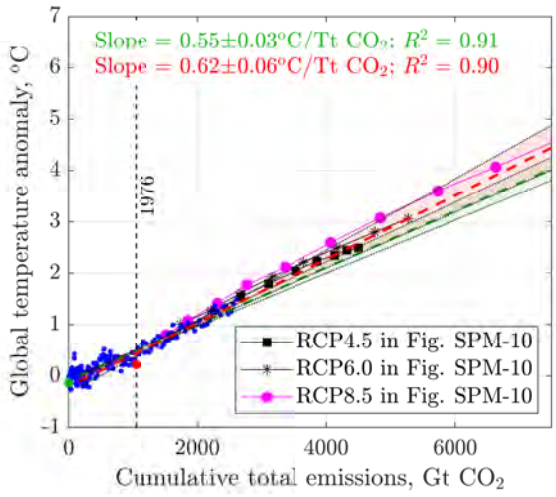

Figure 11.1: Global temperature anomaly vs CO_2 emissions, given ΔT vs. time in Figure 10.10(b) and cumulative CO_2 emissions vs time in Figure 5.5(b) (the red curve for Patzek's 568 ppm_v scenario). The 95% (2σ) confidence intervals that the fitted lines explain the data are shaded. The red color and dot signify the post-bifurcation fit, 1976-2023, and the green color signifies the 1850-2023 fit.

11.3 Results

The key results of our analysis of fossil fuel combustion-driven climate change are summarized in Figure 11.1-Figure 11.4. Figure 11.1 demonstrates that the global mean annual temperature anomaly increases approximately linearly with the cumulative CO_2 emissions from fossil fuel combustion, with an observed slope of $0.55 - 0.62$;°C per teratonne (Tt) of CO_2, depending on whether all available data or only post-1976 data are used. It is important to note that this is an **effective empirical slope**, derived directly from observational temperature anomaly records. These anomalies reflect the combined radiative forcing of all greenhouse gases, as illustrated in Figure 7.10.

For comparison, the commonly accepted sensitivity of global temperature to atmospheric CO_2 concentration is approximately 0.45 °C$(\text{Tt CO}_2)^{-1}$, based on climate model simulations and assessments such

as the IPCC AR6 WG1 report (*Arias et al.*, 2021). Over the past two centuries, however, the observed temperature response corresponds to a transient climate response (TCR) that is somewhat lower than the equilibrium scaling estimate of

$$\frac{2.32}{3.53} \times 0.45 \approx 0.68\ ^\circ\text{C}\ (\text{Tt CO}_2)^{-1}$$

as inferred from the radiative forcing breakdown in Figure 7.10(b). This disparity is consistent with the values reported in Table 7.3 and Table 7.5.

Finally, we emphasize that anthropogenic climate change, GHG emissions, and most environmental degradation – including deforestation, soil depletion, and ocean acidification – are fundamentally linked to fossil fuel combustion and the **large-scale destruction** of terrestrial and marine ecosystems, as discussed in Section 4.4.

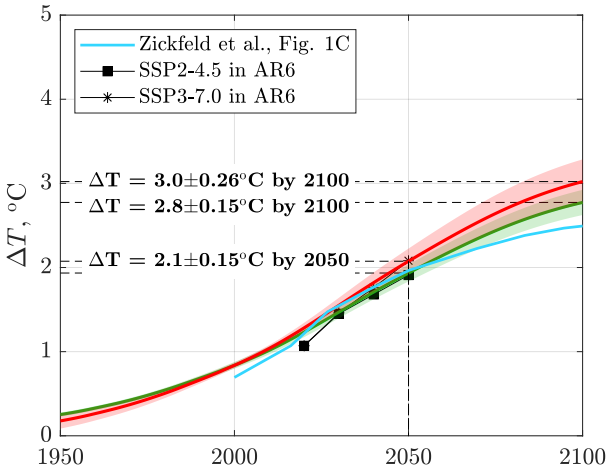

Figure 11.2: Global temperature anomaly vs time, given ΔT vs. CO_2 emissions in Figure 11.1 and cumulative CO_2 emissions vs time in Figure 5.5(b) (the red curve for Patzek's 568 ppm_v scenario). The 95% (2σ) confidence intervals that fitted curves explain the data are shaded. The Zickfeld at al.'s data fall below our prediction because their CTE was ∼2 Tt of CO_2 less than that in the 568 ppm_v scenario, cf. Figure 5.5(b).

By contrast, if we extrapolate current CO_2 emissions from Figure 5.5(b) to reach 720 ppm_v by 2100, our statistical model projects a global mean temperature anomaly of 2.0 ± 0.14,°C in 2050 and 4.3 ± 0.5,°C in 2100, with 95% confidence intervals, as shown in Figures 11.5 and 11.6. For the global land area, the projected anomalies are even higher: 3.0 ± 0.33,°C in 2050 and 6.2 ± 1.1,°C in 2100.

These projections exhibit slightly greater scatter when plotted against calendar years rather than cumulative emissions, highlighting that time-based parametrizations are less predictive than those based on total carbon released.

Notably, the most probable outcomes from the CMIP5 ensemble and the IPCC AR6 report (see Figure 11.7) are in good agreement with Patzek's 720 ppm_v scenario. However, our model's uncertainty envelope (green band) effectively excludes the upper-end climate responses predicted by the most extreme GCMs, suggesting that some of these outcomes may overstate the likely range of warming under this emissions trajectory.

The linear growth of global temperature extrema shown in Figure 10.13(c,d) follows the post-1976 trend. Given Patzek's 568 ppm_v emissions scenario, our projected warming lies below the upper-range predictions of the complex climate models evaluated in *Shukla et al.* (2023) for CMIP5 and CMIP6, as illustrated in Figure 11.7. These models are generally weighted toward high-emissions scenarios that result in atmospheric CO_2 concentrations of 800-1000+ ppm_v by 2100 or 2150. However, our predictions align closely with those of the SSP2-4.5 pathway, as shown in Figure 11.8.

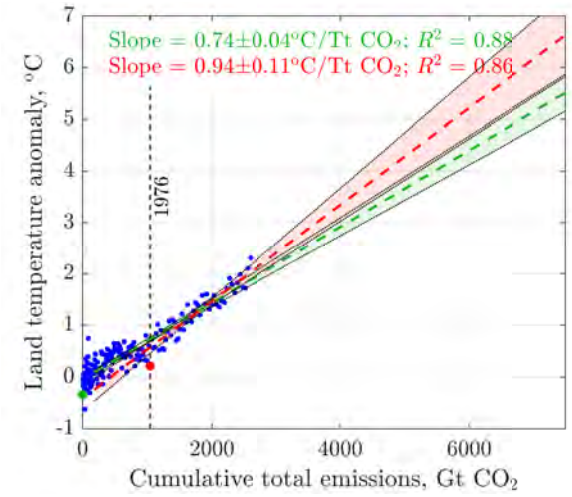

Figure 11.3: Global land temperature anomaly vs CO_2 emissions, given ΔT vs. time in Figure 10.10(a) and cumulative CO_2 emissions vs time in Figure 5.5(b) (the red curve for Patzek's 568 ppm_v scenario). The 95% (2σ) confidence intervals that the fitted curves explain the data are shaded. All data since 1850 were used in the green fit, and in the red one, only the post-1976 bifurcation data were used. Since the bifurcation was caused by land heating up over two times faster than the oceans, the slope difference is large.

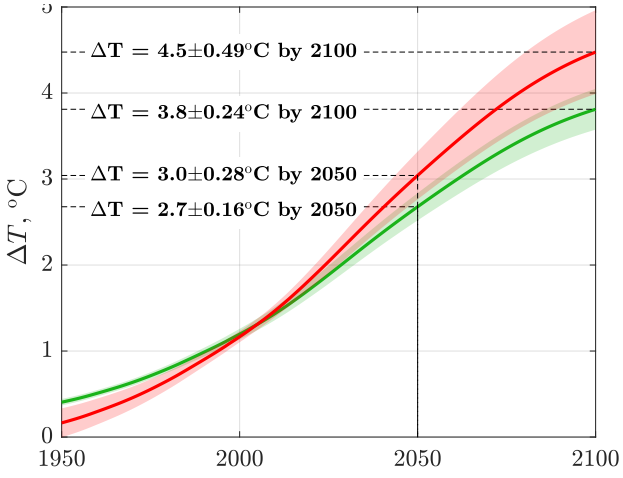

Figure 11.4: Global land temperature anomaly vs. time, given ΔT vs. CO_2 emissions in Figure 11.3 and cumulative CO_2 emissions vs time in Figure 5.5. The 95% (2σ) confidence intervals that the fitted curves explain the data are shaded. The land temperature data have a higher variance than global temperatures, and their 2σ intervals are wider.

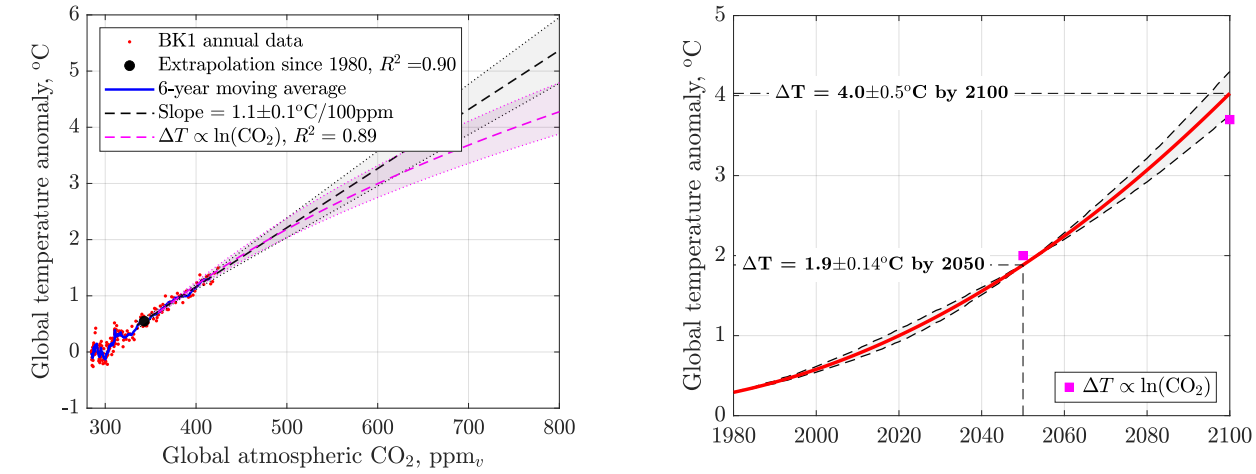

Figure 11.5: Patzek's 720 ppm_v scenario. **(a)** Global temperature anomaly vs. CO_2 emissions, given ΔT vs. time in Figure 10.10(b) and cumulative CO_2 emissions vs. time in Figure 5.5(b), the black parabola. **(b)** Global temperature anomaly vs. time, given ΔT vs. CO_2 emissions in Figure 10.10(a) and cumulative CO_2 emissions vs. time in Figure 5.5(b). The 95% (2σ) confidence intervals that the polynomial fits explain the data are shaded.

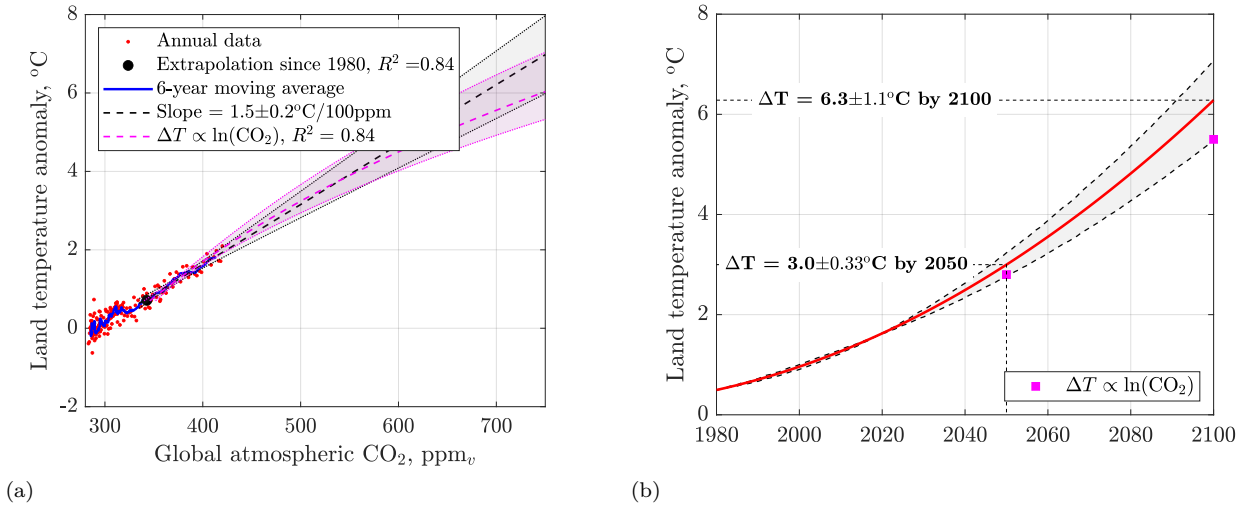

Figure 11.6: Patzek's 720 ppm_v scenario. **(c):** Global land temperature anomaly vs. CO_2 emissions, given ΔT vs. time in Figure 10.10(a) and cumulative CO_2 emissions vs. time in Figure 5.5(b). **(d)** Global land temperature anomaly vs. time, given ΔT vs. CO_2 emissions in Figure 10.10 and cumulative CO_2 emissions vs. time in Figure 5.5(b).

11.4 Dependence of annual mean temperature on CO_2 concentration

Here is our surface temperature- and CO_2 concentration-driven predictive model of climate change:

$$\begin{aligned}&\text{STEP 1}: \\ &\underbrace{\Delta T(1850-2023)}_{\text{Global T anomaly Berkeley Earth}} + \underbrace{[CO_2](1850-2100)}_{\text{WAIS+MLO+our extrapolation}} \Rightarrow \underbrace{\Delta T\left([CO_2](1850-2100)\right)}_{\text{Cross-plot of } \Delta T \text{ vs. } [CO_2]} \\ &\text{STEP 2}: \\ &\underbrace{\Delta T\left([CO_2](1850-2100)\right)}_{\text{Cross-plot of } \Delta T \text{ vs. } [CO_2]} + \underbrace{[CO_2](1850-2100)}_{\textit{Our } [CO_2] \text{ scenarios}} \Rightarrow \underbrace{\Delta T(1850-2100)}_{\text{Our climate change predictions}}\end{aligned} \tag{11.1}$$

The following illustration is for Patzek's 720 ppm_v scenario. The mean global surface temperature and the mean land surface temperature anomalies in Figure 10.12 were correlated with the mean annual mixed-atmosphere CO_2 concentration in Figure 5.6(b). The resulting cross-plots are shown in Figure 11.5. By analogy to radiative forcing (RF) from CO_2 in the atmosphere that depends on the logarithm of CO_2 concentration, and if global/land temperature anomalies *were* simple functions of only RF (not multi-valued functionals), one *might* stipulate that

$$\Delta T = T - T_0 \propto RF \propto \ln\left(\frac{[CO_2]}{[CO_2]_0}\right) \propto \ln[CO_2] \tag{11.2}$$

where $T_0 = 14.1^{\circ}C$ is the 1850-1900 global mean temperature; $[CO_2]$ ppm_v is the mixed-atmosphere CO_2 concentration in the air; and $[CO_2]_0 = 278$ ppm_v is the average CO_2 concentration over the same reference period.

The magenta semilogarithmic curve in Figure 11.5(a) yields the mean anomaly of 3.8°C at 790 ppm_v of CO_2 in the air, identical to this Berkeley Earth (BE) figure.

We would like to caution against overanalyzing the purely data driven cross-plots in Figure 11.5. The global temperature anomaly is the result of a combination of all factors, led by CO_2 concentration in the air, but also by other greenhouse gases (of which CH_4 is highlighted in Figure 7.10), by aerosols and dust, by melting of ice, and changes in ocean currents, global cloud cover (albedo), etc. From this point of view, the linear trend seems more defensible than the semi-logarithmic one, but they differ by less than one °C in the year 2100. We maintain that this difference is statistically insignificant given the length of the extrapolation of 76 years.

The emergence of a semi-logarithmic dependence of infrared absorption on greenhouse gas concentration, resulting from the response of a stratified atmosphere to a sudden increase in CO_2, is derived in Appendix C.

In light of recent temperature data, a semi-logarithmic trend may **not** emerge during the current transient climate response (TCR), particularly over short time scales comparable to the duration of ongoing CO_2 accumulation in the atmosphere (see TCR in Table 7.3). If the global temperature anomaly depended *only* on CO_2 concentration ($= c$), we would expect its rate dT/dt to *decrease* with increasing CO_2 concentration in the air, simply because $d\ln(c)/dt = c^{-1}dc/dt$. Since, currently, $c(t) \propto t^2$, $c^{-1}dc/dt \propto t^{-1}$, and dT/dt must decrease uniformly. But the opposite is true from looking at the bare temperature data. For example, Figure 10.13 shows that in 1976 the planet reached a significant tipping point, and the rate of global heating increased uniformly *manyfold*. The changes of temperature slopes in Figure 10.13 hide in several other figures if you look carefully. Thus, the semilogarithmic scaling of temperature with CO_2 concentration in Eq. (11.2), used by Berkeley Earth and reproduced here, may be too conservative on a century timescale. But the error would still be small, if you *believed* the highly improbable Patzek's 720 ppm_v scenario or BE's 790 ppm_v scenario.

Figures 11.5 and 11.6 depict our 720 ppm_v scenario of global heating relative to the 1850-1900 average. The temperature anomaly averages are 2.0°C in 2050 and 4.3°C in 2100. Berkeley Earth predicts a little

less, 3.8°C in 2100 at a higher CO_2 concentration, but overall both results are quite similar. We also provide the 95% (2σ) certainty bands around our predictions. The predictions here agree well with the complex CMIP5 and 6 simulation sets, summarized in Figure 11.8.

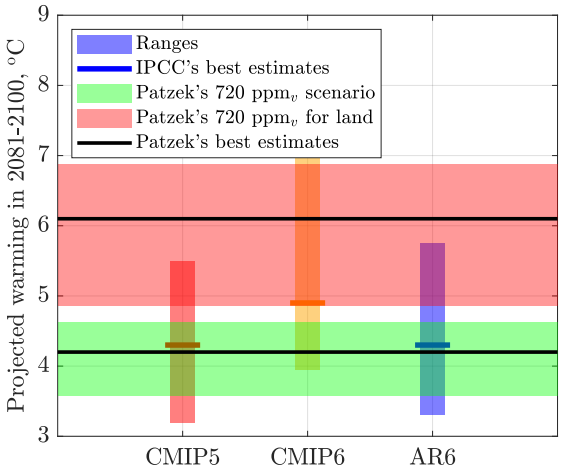

Figure 11.7: Comparison of Patzek's 720 ppm$_v$ scenario with IPCC's Sixth Assessment Report (AR6), and CMIP5 and 6. Agreement of Patzek's most probable global ΔT with those from CMIP5 and AR6 is remarkable. The Climate Model Intercomparison Project, Phase 6 (CMIP6) consists of some 100 distinct climate models produced by 49 different modelling groups. The earlier CMIP5 protocol consisted of thirty five climate model experiments designed to (i) assess the mechanisms responsible for model differences in poorly understood feedbacks associated with the carbon cycle and with clouds, (ii) examine climate "predictability", and (iii) determine why similarly forced models produce different responses. Data source: AR6-Chapter 7 Figures, accessed 09/23/2023.

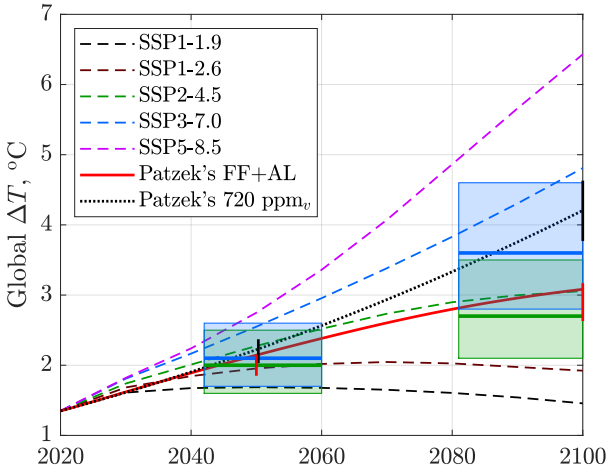

Figure 11.8: Comparison of our emission- and temperature-data-driven model predictions (red) with IPCC's Sixth Assessment Report (AR6). All temperature anomalies are referenced to +1.35°C in 2020. The incremental CO_2 emissions since 2020 are converted into the corresponding ΔTs by the multiplication by $0.61°C\,(\text{Tt } CO_2)^{-1}$. The color-coded horizontal lines and rectangles are the most likely temperature ranges over the ∼18-year intervals in AR6-Table SPM.1, accessed 01/24/2024. The vertical bars are the 95% confidence intervals from the more detailed calculations here.

Chapter 12

Ocean heating and polar ice melting

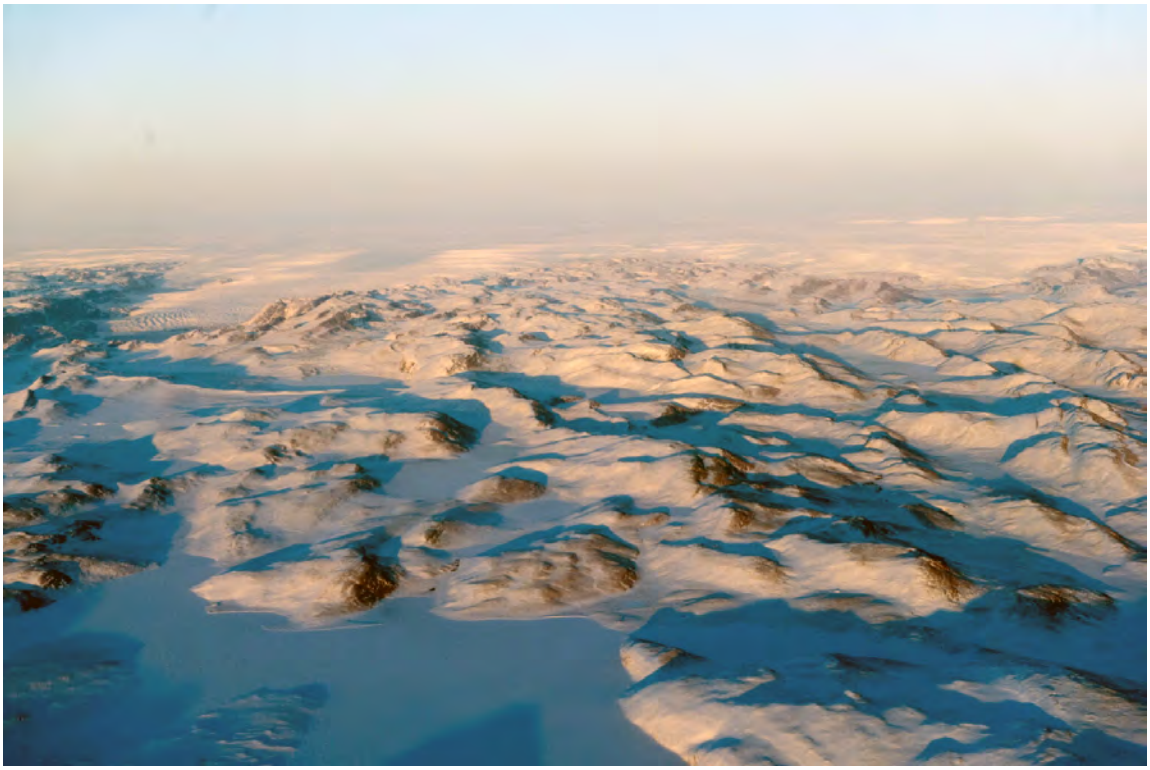

On May 15-21, 2025, the Greenland ice sheet melted 17 times faster than the 1991-2020 average for this period (blue is melt water).
Image by UN Photo/Mark Garten.

Where the glacier meets the sky, the land ceases to be earthly, and the earth becomes one with the heavens; no sorrows live there anymore, and therefore joy is not necessary; beauty alone reigns there, beyond all demands.

Halldór Laxness

World Light, Book Four: The Beauty of the Heavens, Vintage Books, 2002

12.1 What are you going to learn?

You are going to learn that modern melt of ice is dominated by anthropogenic emissions of CO_2 (*Slangen et al.*, 2016). Table 12.1 shows that ice is melting everywhere in the world at the average rate that is still 1/3 of that after the Last Glacial Maximum (LGM, ∼26.5–19 ka BP). Modern ice melt may be understated and is accelerating. According to *IPCC* (2019b), under RCP8.5 the highest future average ice melt rate could be twice that during post glacial melt, see the last row in Table 12.1).

- After LGM, global sea level rose by approximately 120–130 meters 13 ky (see the first row of Table 12.1). The average rate of sea level rise was

$$\frac{130 \text{ m}}{13{,}000 \text{ years}} \approx 10 \text{ mm/year}.$$

  During specific intervals such as Meltwater Pulse 1A ∼14.5 ka ago (*Liu et al.*, 2004), the rate of rise reached peaks of approximately 40–50 mm/year.

- Since 1993, the global mean sea level has been rising at a rate of approximately 3.4 mm/year, based on satellite altimetry observations discussed in this chapter. The contribution from land ice melt includes: Greenland (∼270 Gt/year), Antarctica (∼150 Gt/year), and mountain glaciers (∼220 Gt/year), giving a total of about 640 Gt/year. For the reasons explained later this estimate is likely too low. Current sea level rises at approximately 1.8 mm/year from ice melt and 1.6 mm/year from thermal expansion of seawater.

Table 12.1: Comparison of global ice melt and sea level rise rates: Past vs. present

Period / Event	**Time (ka BP / CE)**	**Rate (mm/yr)**	**Cause / Notes**
LGM and early Holocene (avg.)	∼21–8 ka BP	∼10	Natural deglaciation over millennia
Meltwater Pulse 1A	∼14.5 ka BP	40–50	Abrupt postglacial sea level jump
Pre-Industrial	8 ka BP–1900 CE	<0.5	Near equilibrium, minor natural changes
20th Century (avg)	1901–1990 CE	∼1.4	Early anthropogenic forcing
Satellite Era	1993–present	∼3.4	Accelerated ice melt and thermal expansion
Current Ice Melt	2020s	∼1.8	Greenland, Antarctica, and mountain glaciers
Projected (High Emissions)	2000–2100 CE	10–20+	Continued warming and feedbacks

Appendix E analyzes 46 years of satellite-derived maps of Arctic and Antarctic sea-ice concentration and their trends. It also summarizes the global impacts of polar sea-ice loss, including albedo, ocean circulation, decline of fisheries, and climate feedbacks.

12.2 Why is this important?

It is difficult to fully grasp the cascading implications of ongoing global ice melt on oceanic and atmospheric circulation, marine ecosystems and fisheries, the global supply of freshwater to billions of people, and the eventual displacement of hundreds of millions from gradually inundated coastal regions.

For example, *Silvano et al.* (2025) remind us that the surface of the polar Southern Ocean has been freshening due to ice melt since the early 1980s, coinciding with an expansion of Antarctic sea ice. This phenomenon has frequently been misused by climate change deniers as "proof" that global warming is not occurring. However, this Antarctic ice expansion reversed abruptly after 2015, culminating in a record-low sea ice extent in late 2016. Since then, Antarctic sea ice has undergone sustained retreat, with multiple record minima observed during both summer and winter (*Hobbs et al.*, 2024), see, e.g., Figure E6.

Several hypotheses have been proposed to explain this reversal, including changes in atmospheric heat transport, wind patterns, and upper-ocean warming. The increased spatial (i.e., circumpolar) coherence, variance, and persistence of sea ice anomalies suggest a critical transition within the Antarctic ice system

(*Hobbs et al.*, 2024) – a shift that may represent a new regime or "state". In lay terms, the Antarctic sea ice may already have undergone what is described in dynamical systems theory as a *catastrophe* – a sudden, nonlinear change of state – and may now be collapsing at an accelerating average rate. This unfolding catastrophe has the potential to affect climatic, ecological, and socioeconomic systems worldwide. No matter where we live, we may soon feel the consequences of this unraveling.

12.3 Preliminaries

A recent study by *Zekollari et al.* (2025) demonstrates that under Patzek's AL+FF scenario (a global temperature increase of +3 °C by 2100), the committed ice loss from all of the world's glaciers will reach approximately 77% of their total mass (range: $60-85\%$). All 19 glaciated regions (including the Arctic, Antarctic, Alaska, Siberia, the Himalayas, etc.) are projected to lose more than two-thirds of their present-day ice mass, with nine of these regions expected to lose over 90%.

In many regions, the tail end of the committed ice loss will materialize much later, as the current global transient climate response to atmospheric greenhouse gas accumulation approaches equilibrium (see Section 7.11). What follows is a brief explanation of the underlying causes of this unfolding global catastrophe, which will directly affect nearly half of humanity.[1]

Figure 10.10(a) plots the last 149 years of global average of surface sea water temperatures (SSWT) relative to the 1850-1900 mean temperature standard. Since 2023 was the record year for global and land temperatures, see Figure 10.12, it is possible that the SSWT anomaly will exceed 1°C for decades. As surface sea water becomes warmer, so does the subsurface water that absorbs astronomic quantities of heat, Figure 12.1. Recall that the oceans absorb over 90% of the solar power available at the earth surface, causing a large radiant energy imbalance and long-term heating of the planet's surface, see Figures 9.1 and 12.2.

The heat content of oceanic water has been estimated since the 1960s, but beginning in the 1990s, the infrared satellite images of ocean surface water were combined with the water temperature measurements taken by thousands of floats and submersibles (*Cheng et al.*, 2019), delivering an ever-more detailed picture of heat uptake by the oceans. Figure 12.1(a) shows the ocean heat content (OHC) accumulated in water 0-700 m deep since 1994. This OHC gain was 160 ZJ, roughly 2.5× the total heat generated by FF until 2200, Figure 6.4(b). Figure 12.1(a) compares OHC with the cumulative FF heat, and shows that each 1 ZJ in FF HHV increments the OHC by 14-27 ZJ, if CO_2 emissions from these FF are the key driver of climate change. Here we have presented ample evidence that they are.

Figure 12.1(b) shows OHC in water 0-2000 m since the year 1960. In this case, the OHC until 2020 was 200 ZJ, or almost three times the predicted heat generated by humanity until 2200. While the Representative Concentration Pathway (RCP)8.5 requires burning fossil fuels at rates that are impossible to realize physically and geologically, human emissions will likely track RCP4.5 (RCP4.5 is a scenario closely related to SSP2.-4.5 that stabilizes radiative forcing at 4.5 $\mathrm{W\,m^{-2}}$ in the year 2100 without ever exceeding that value. Simulated with the Global Change Assessment Model (GCAM), RCP4.5 includes long-term, global emissions of greenhouse gases, short-lived species, and land-use-land-cover in a global economic framework *Thomson et al.* (2011).) Thus our cautious estimate of the OHC anomaly is 1500 ZJ by the year 2100, or 19 times all the heat generated by humans until 2200.

The inset in Figure 12.1(b) shows a linear trend of heat absorption by the ocean as a function of time between 1990 and 2015. During this period, the oceans absorbed on average 10 ZJ/year. The "heat gain" from converting fossil fuels burned between 2015 and 2022 into the ocean heat content increased therefore from $10/0.4 = 25$ to $15/0.4 = 37$, respectively.

[1] The Tibetan Plateau, often referred to as the "Water Tower of Asia," is the source of several major rivers – including the Yangtze, Yellow, Mekong, Indus, Ganges, and Brahmaputra – that collectively support the freshwater needs of nearly 2 billion people across Asia. This extensive water supply system is crucial for China, India, Pakistan, Bangladesh, Nepal, Bhutan, and nations in Southeast Asia, where it underpins agriculture, drinking water, and energy production (*Li et al.*, 2022b).

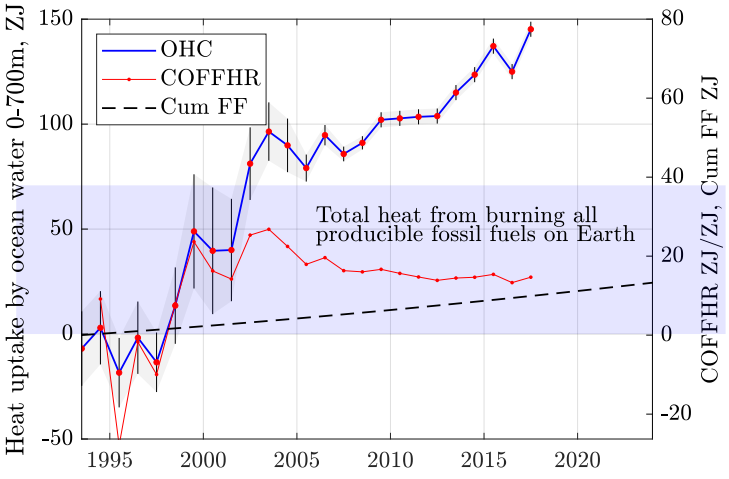

(a)

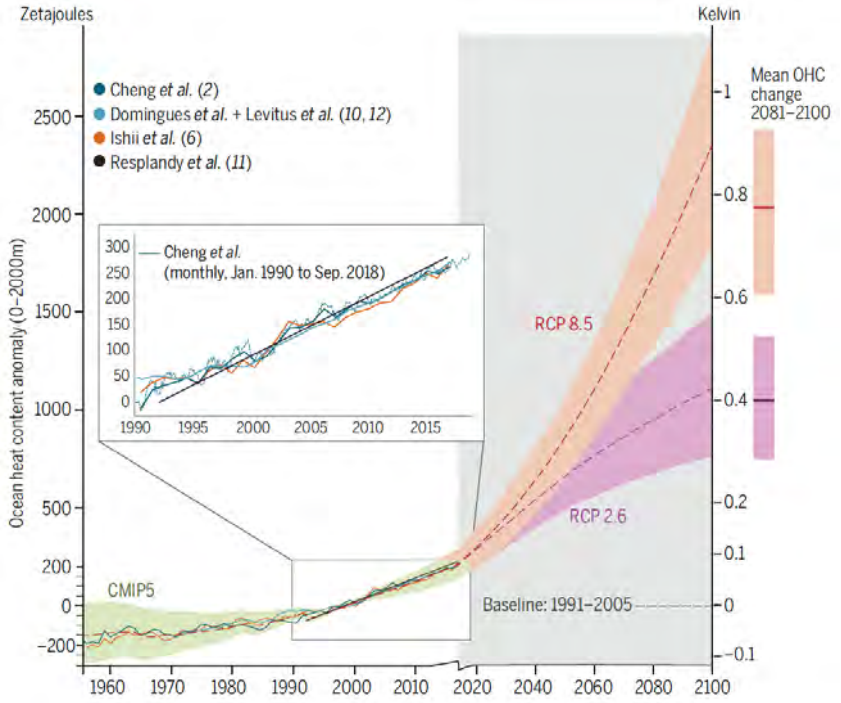

(b)

Figure 12.1: **(a)** *Left axis:* Cumulative ocean heat content (OHC) in the upper $0-700$ m reached approximately 150 ZJ by 2018. According to *Cheng et al.* (2017), the 0–2000 m ocean layer has already absorbed incremental heat equal to approximately 4× the ∼67 ZJ of energy ever generated by fossil fuels, as shown in Figure 6.5(a). *Right axis:* Cumulative fossil fuel high heating value (HHV) from 1994 to 2024, and the ratio of cumulative ocean heat to fossil fuel heat. The data indicate that each 1 ZJ of fossil fuel HHV corresponds to $15-27$ ZJ of heat retained in the upper $0-700$ m of the ocean. *Data sources: NOAA*, EIA. **(b)** Ocean heat content (OHC) for the $0-2000$ m depth layer. If current trends continue, the thermal burden on the ocean will intensify to levels incompatible with the survival of global industrial civilization. *Image source: Cheng et al.* (2017).

The heat absorbed by the Earth is mostly caused by the accumulation of CO_2 in the atmosphere. Most of this CO_2 is generated by combusting fossil fuels. The disproportionate effect of this combustion (25:1 in 2015 and 37:1 in 2022) has been converted mostly into the exploding global ocean heat content that will be with us for another $500 - 1000$ years.

What will this gigantic heat absorbed by the oceans do to the planet? Here is how *Loeb et al.* (2021) explains this phenomenon:

> Climate is determined by how much of the Sun's energy the Earth absorbs [+] and how much energy the Earth sheds through emission of thermal infrared radiation [-]. Their [difference] determines whether the Earth heats up or cools down. Continued increases in concentrations of well-mixed greenhouse gasses in the atmosphere and the long time-scales time required for the ocean, cryosphere, and land to come to thermal equilibrium with those increases result in a net gain of energy, hence warming, on the Earth. Most of this excess energy (about 90%) warms the ocean, with the remainder heating the land, melting snow and ice, and warming the atmosphere. We compare satellite observations of the net radiant energy absorbed by the Earth with a global array of measurements used to determine heating within the ocean, land and atmosphere, and melting of snow and ice. We show that these two independent approaches yield a decadal increase of 0.5 ± 0.47 W/m^2 in the rate of energy uptake by Earth from mid-2005 through mid-2019, which we attribute to decreased reflection of energy back into space by clouds and sea ice, increases in well-mixed greenhouse gases and water vapor, and heating of the planet.

Figure 12.2 shows that over the last two decades the Earth has gained an extra 1 W/m^2 of the still unequilibrated radiative forcing from the warming ocean. This gain is more than the increment of 0.7 W/m^2 in the radiative forcing from the atmospheric CO_2 since the year 2000. This means that the Earth will continue to heat up for centuries. If humanity finally acts and the radiative forcing from greenhouse gases decreases, the oceans will eventually cool down over centuries.

This centuries-lasting Earth cooling period is analogous to the cooling of a big brick masonry heater, like the ones in my childhood house. Each was warmed up during the day by burning a bucket of coal inside it for 1-2 hours, and cooled down slowly during the night for 8-12 hours. As a child, I had no idea about the obscene emissions from these coal heaters and I loved their unmatched pleasant warmth.

When ocean water heats up, the polar ice shelves melt faster, and global oceanic currents change fluxes and rearrange trajectories. Figure 12.4 presents the most recent updates to the Ice sheet Mass Balance Inter-comparison Exercise (IMBIE, supported by the ESA Climate Change Initiative and the NASA Cryosphere Program *Shepherd et al.* (2021)) for the Antarctic ice shelves (AntIS) and Greenland (GrIS). All ice melt masses are plotted as *positive* vs calendar time and the corresponding cumulative total CO_2 emissions. For Greenland, 26 different surveys were used to produce this single community estimate; 24 were used for Antarctica. Common spatial and temporal domains were used to compute the satellite data to support the aggregation of the individual datasets.

For the AntIS, the mean loss rate of ice was 117 Gt year^{-1} between 2003 and 2018, with melt accelerating on average by 6 Gt year^{-2}. An increase in the variability of El Niño Southern Oscillation (ENSO) leads to reduced warming near the surface, but accelerated warming of deeper ocean waters *Cai et al.* (2023). Thus, climate change is expected to warm up the water impinging against the Antarctic continent and returning under the ice shelves, accelerating their melt. Recall that WAIS is melting at 4× the overall melt rate of AntIS, see Figure 12.5.

IMBIE's estimate of the mean loss rate of ice in Greenland was 221 Gt year^{-1} between 2003 and 2018, with melt accelerating on average at 11 Gt year^{-2}. Further, it was found *Greene et al.* (2024) that, over the same period, glacier terminus retreat caused a further 43 Gt year^{-1} of ice loss that was not captured by any of the three independent satellite-based techniques (altimetry, gravimetry and input-output method) used in the IMBIE consensus, has not been accounted for in any large study of GrIS mass balance and represents a source of solid freshwater flux that has not been included in previous budgets of

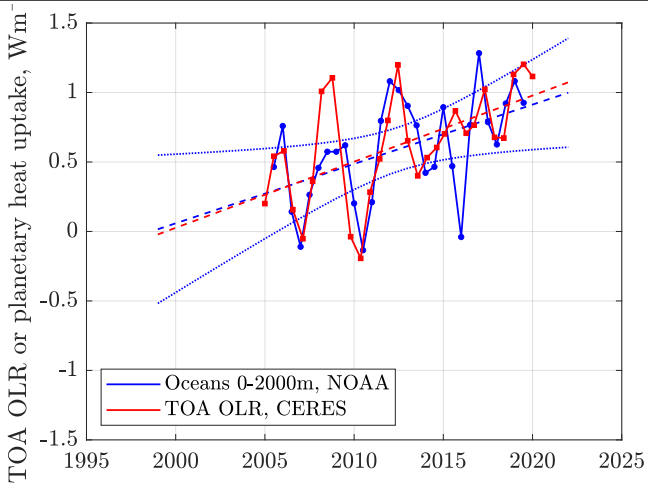

Figure 12.2: Outgoing Longwave Radiation (OLR) forcing by heated ocean water. In the last two decades, the Earth stored $\Delta RF = +1$ Wm^{-2}, or half of incremental CO_2 forcing since 1750, see Figure 9.1(b). The global climate is controlled by the amount of sunlight absorbed by Earth and the amount of infrared energy emitted to space. These quantities – together with their difference – define Earth's radiation budget (ERB). TOA OLR CERES = the Top-Of-the-Atmosphere Outgoing Longwave Radiation from the US Clouds and the Earth's Radiant Energy System (CERES), a project that provides satellite-based observations of ERB and clouds. It uses measurements from CERES instruments flying on several satellites along with data from many other instruments to produce a comprehensive set of ERB data products for climate, weather and applied science research. The CERES instruments provide direct measurements of reflected solar radiation and emission of thermal infrared radiation to space across all wavelengths between the ultraviolet and far-infrared. Data sources: NOAA1, NOAA2, and NASA CERES *Loeb et al.* (2021), calculations by Patzek.

discharge to the ocean. The massive ice melt discharge from Greenland disturbs and weakens fast one of the most important oceanic currents, the surface branch of AMOC or Gulf Stream *van Westen et al.* (2024). Greenland's warming and ice loss slowed down between 2010 and late 2016, suggesting a negative correlation with the ENSO events in the Pacific *Matsumura et al.* (2021), but this slowdown reversed sharply between 2017 and 2021.

By analogy with petroleum Enhanced Oil Recovery processes, we define the cumulative ice-CO_2 ratio as:

$$\text{CICO}_2\text{R}(t) = \frac{\text{Cumulative ice melt mass up to time } t}{\text{Cumulative total CO}_2 \text{ emissions up to time } t} \tag{12.1}$$

and the instantaneous ice-CO_2 ratio as

$$\text{ICO}_2\text{R}(t) = \frac{\text{Ice melt mass rate at time } t}{\text{Total CO}_2 \text{ emissions rate at time } t} \tag{12.2}$$

The cumulative ice-CO_2 ratios have been increasing monotonically since 1992, and by 2022, they reached 1 t/t and 2 t/t for Antarctica and Greenland, respectively. More ominously, the instantaneous ice-CO_2 ratios reached 4 and 12 (t/year)/(t/year), respectively, for Antarctica and Greenland.

In 2020, on average, Greenland's ice was melting at 1.8 times the rate of Antarctic ice loss, and the acceleration of melt in Greenland was also twice as high. Subsequent findings by *Greene et al.* (2024) indicate an additional 20% increase in ice loss – primarily due to glacier retreat – with the trend likely continuing to grow. In terms of polar ice response to greenhouse gas forcing, each ton per year of global CO_2 emissions in 2020 corresponded to approximately 4 tons per year of ice melt in Antarctica and 12 tons per year in Greenland.

In summary, the rate of ice loss in Greenland is catastrophic and significantly exceeds most projections

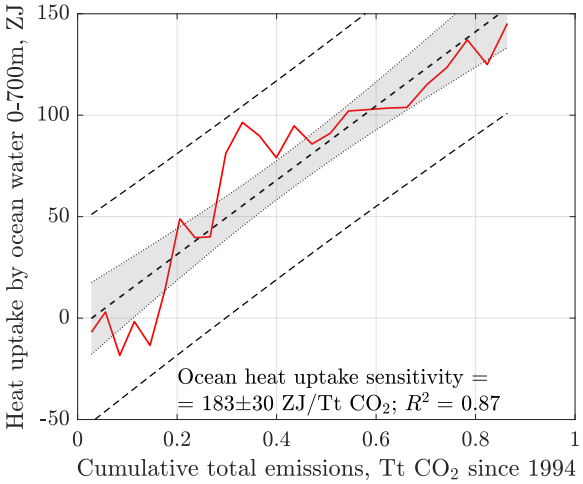

Figure 12.3: Heat absorption by the ocean water in Figure 12.1(a) replotted vs cumulative total CO_2 emissions.

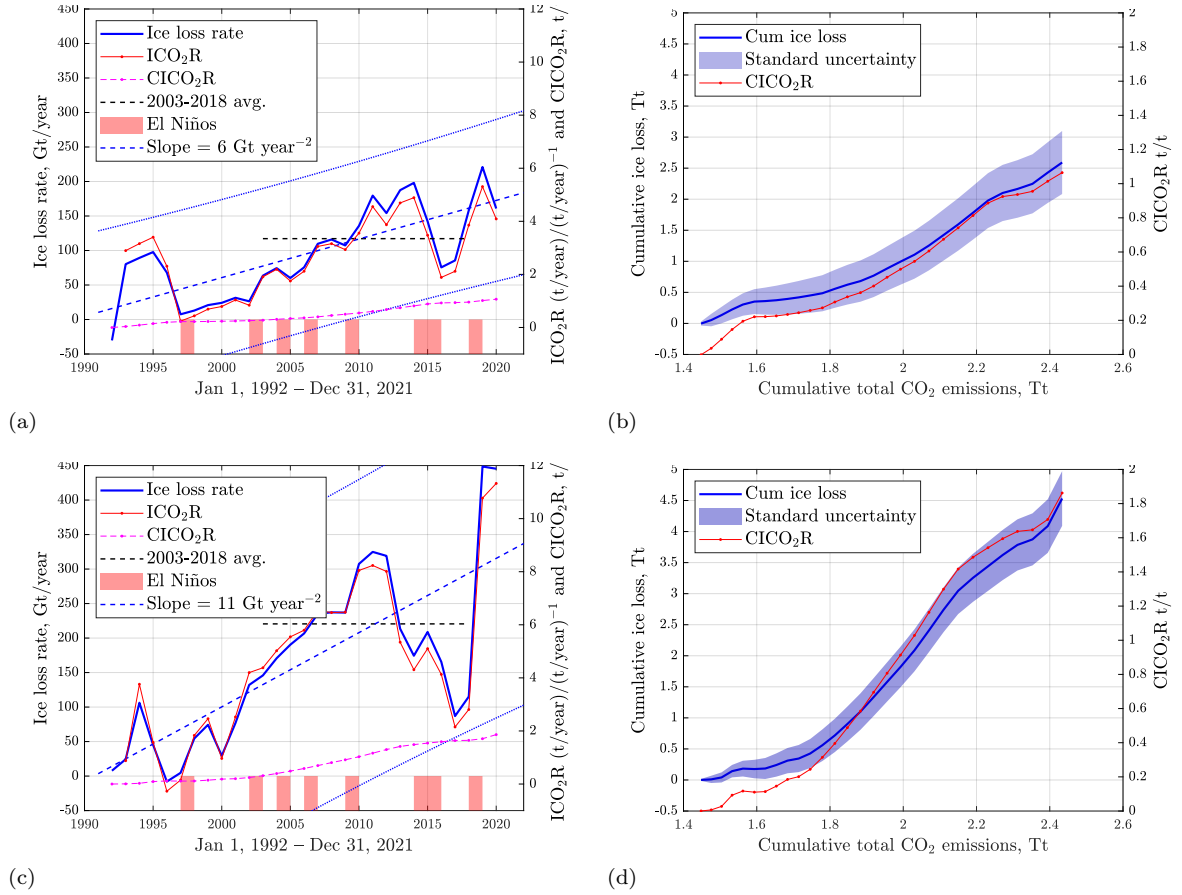

Figure 12.4: Differential **(a)** and cumulative **(b)** ice mass losses in Antarctica and Greenland, **(c)** and **(d)**, between January 1 1992, and December 31 2020. The acronym ICO_2R stands for the instantaneous ice-CO_2 ratio of annual mass rates. $CICO_2R$ abbreviates the cumulative ice-CO_2 ratio. Between 1979 and 2021, Antarctica lost 5372 ± 1046 km^3 of ice, while Greenland lost 5850 ± 575 km^3 between 1972 and 2021. Data sources: *IMBIE*, *Shepherd et al.* (2021) and Wikipedia, calculations by Patzek.

.

from IPCC climate models. As a result, global sea level is expected to rise substantially faster than predicted in those assessments.

In stark contrast to petroleum enhanced oil recovery (EOR) processes – where oil-to-injectant ratios typically decline over time – the two climate-related ratios discussed above continue to increase monotonically. This is because atmospheric CO_2, amplified by CH_4 and rising water vapor concentrations, becomes increasingly effective at deicing the planet.

Figure 12.6 shows the rise in mean sea level since 1900, based on coastal tide gauge measurements referenced by the author to the mean sea level during 1900–1910. The satellite altimetry data beginning in 1993 have been shifted upward by 106 mm to align with the gauge record at the point of overlap.

The TOPEX/Poseidon altimeter satellite – a joint mission between NASA and CNES, the French space agency – was launched on August 10, 1992, as the first major satellite mission dedicated to mapping global ocean surface topography. Its successors, the NOAA Jason satellite series, continue this mission by combining satellite radar altimetry with data transmitted from thousands of Argo submersibles deployed around the world. Together, these systems provide sustained, high-precision measurements of sea surface height (SSH), accurate to within a few centimeters globally, allowing scientists to monitor variations in surface and deep-ocean circulation over time.

The Jason satellite missions can detect changes in global mean sea level with millimeter-scale accuracy and are a vital tool for monitoring climate change. Currently, altimetry data are available only between 66°S and 66°N. Estimates of sea level rise do not account for the effects of glacial isostatic adjustment (GIA) on the geoid – modeled to be in the range of +0.2 to +0.5 mm/year – which, when averaged globally, contribute an additional 20–50 mm of sea level rise per century.

Given the accelerating rates of polar ice melt, it is reasonable to project that global mean sea level could rise by at least 800 mm by 2100 – and potentially 2–3× more in some regions. Under a low-CO_2 emissions scenario that limits warming to below 1.5°C by 2100, sea level rise may follow the linear trajectory shown in Figure 12.6(b) or (d). However, if current high-CO_2 emissions persist, mean sea level in the United States could rise by 1–2 m by 2100 (*Sweet et al.*, 2017), likely following the parabolic extrapolation depicted in Figure 12.6(d).

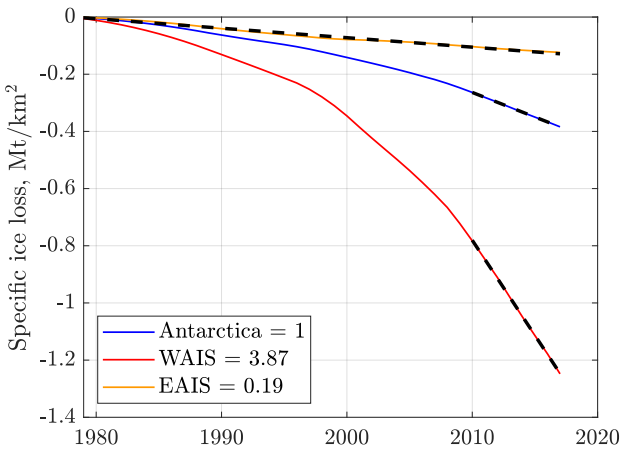

Figure 12.5: The slopes of the dashed lines are the specific rates of ice loss in Mt (yr km^2)$^{-1}$ between 2010 and 2017. The West Antarctic Ice Sheet (WAIS) lost ice at the rate four times higher than Antarctica, while the East Antarctic Ice Sheet (EAIS) lost ice at the rate five times lower. Data source: Supplementary data set `pnas.1812883116.sd01.xlsx` to *Rignot et al.* (2019), accessed on 01/06/2024, calculations by Patzek.

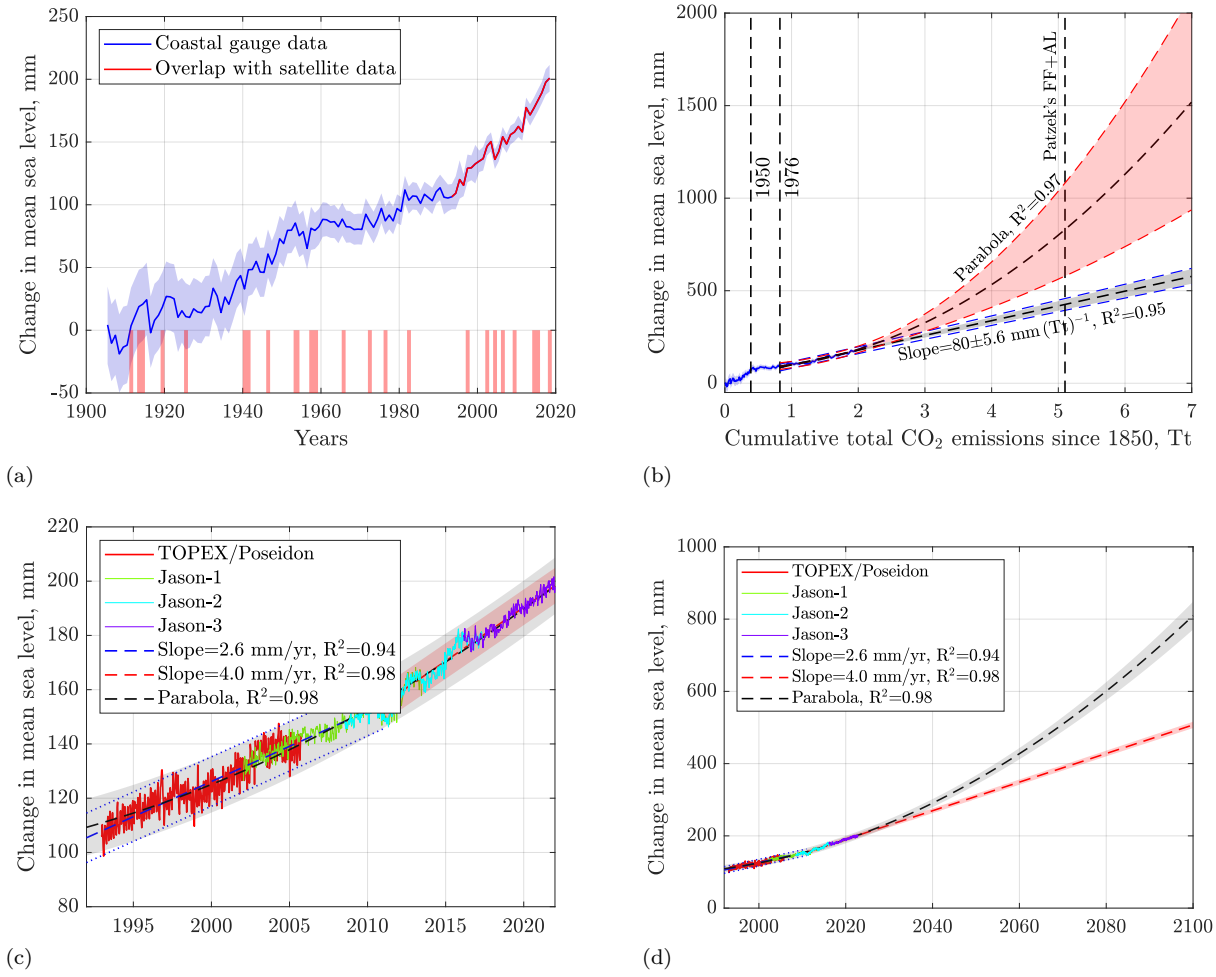

Figure 12.6: **(a)** Mean global sea level rise 1900-2022. The 1900-1910 mean sea level is zero. This reference makes it easier to understand that in 120 years AL+FF emissions already caused over 20 cm of average sea level rise with much more to come soon to a coast near you. There might be a correlation with some of the El Niños. **(b)** Same as (a), but now plotted against cumulative total CO_2 emissions. The new parametrization compresses the 1900-1950-time interval (lower emissions) and linearizes better the post-1976 level rise. Of the two extrapolations, the linear one is more conservative and stable, while the parabola captures better the residual curvature of the post 1976-data, i.e., the acceleration of sea level rise, and predicts 830 ± 244 mm of sea level raise by the year 2100 or 5.1 Tt of CO_2 emissions in Patzek's FF+AL scenario. **(c)** Mean global sea level rise 1993-2023, shifted upwards by 106 mm to coincide the coastal gauge data zeroed in 1900. **(d)** same as (c) but now extrapolated to 2100. There are two linear fits of data (1993-2011 and 2011-2023) and one parabolic fit (1993-2023). The second linear fit and the parabolic fit are extrapolated to 2100. In 2100, the linear extrapolation falls within 15 mm of that in (b) at 7 Tt, but the quadratic one is 2σ lower than that in (b). The 95% confidence intervals ($\pm 2\sigma$) are shaded. Data sources: NASA (coastal gauges), NOAA (satellites), NOAA references and Wikipedia, calculations by Patzek.

Chapter 13

The long fight: climate change science and its denial

At the moment, all we can say for sure is that the cause of cancer isn't known and that there is absolutely no proof that smoking causes human cancer.
Tobacco Institute, *Frank Statement to Cigarette Smokers*, January 1954.

There does not exist today a general scientific consensus about the importance of greenhouse warming from rising levels of carbon dioxide. On the contrary, most scientists now accept the fact that actual observations from earth satellites show no climate warming whatsoever.
A statement by the Global Climate Coalition (sponsored by Exxon, Chevron et al.), 1995

13.1 What Are You Going to Learn?

In this chapter, we return to the foundations of modern climate science. It began with Svante Arrhenius, who in 1896 made the first quantitative estimates of how atmospheric CO_2 affects Earth's temperature. While his predicted warming from a doubling of CO_2 was somewhat exaggerated, his framework was scientifically robust and remarkably prescient.

At the same time, two pioneering experimentalists – Anders and Knut Ångström – pushed the boundaries of spectroscopy by attempting to measure the infrared absorption properties of CO_2 and H_2O. Despite their ingenuity, the limited spectral resolution of their instruments led them to incorrect conclusions. Most notably, Knut Ångström claimed that the effect of CO_2 on Earth's climate was negligible and quickly saturated – a conclusion later refuted by advances in radiative transfer modeling and high-resolution spectroscopy.

Though the Ångströms were meticulous scientists who made honest errors, Knut's outdated conclusion has since been co-opted by modern climate denialists. It continues to be cited – out of context and without regard for a century of subsequent science – to mislead the public and even some scientists. Today, climate denialism has evolved into a well-funded industry whose primary purpose is to validate the comforting illusion that climate change is either insignificant or unreal.

In this chapter, you will learn how to recognize and resist such deception by grounding your understanding in the physical principles and empirical evidence that define real climate science.

13.2 Why Is This Important?

If we fail to confront the accelerating challenge of climate change – individually and collectively – then the consequences for future generations will be catastrophic. Inaction today will condemn our children and grandchildren to lead unhealthy, unstable lives in societies strained by ecological collapse and economic disarray, even in nations that now consider themselves "developed."

Examples of this fragility are already evident: the United Kingdom, still grappling with the aftershocks of Brexit, and the United States, now reeling under the second Trump administration, both show how quickly political and societal norms can unravel.

After studying this chapter, you will be better equipped to distinguish rigorous science from manipulative rhetoric, and to recognize when scientific uncertainty is being twisted to sow confusion. Staying informed is the first step toward action and resilience.

13.3 Arrhenius's Hypothesis on the Greenhouse Effect

The story of modern climate science – and of the immediate and persistent denial of the possibility or significance of climate change – begins with the Swedish physicist and chemist Svante Arrhenius (1859–1927), whose portrait appears in Figure 13.1(a). *Arrhenius* (1896) published a landmark paper titled *On the Influence of Carbonic Acid in the Air upon the Temperature of the Ground*, in which he was the first to quantify the effect of atmospheric CO_2 concentrations on Earth's surface temperature. Drawing upon the earlier insights of Joseph Fourier on terrestrial heat retention and John Tyndall's experiments on infrared absorption by gases, Arrhenius integrated observational evidence with mathematical modeling to estimate how changes in CO_2 levels could alter the global climate.

Arrhenius concluded that a doubling of atmospheric CO_2 would raise Earth's average surface temperature by approximately $5-6$ °C, a value that exceeds today's best estimates of Equilibrium Climate Sensitivity (ECS), which range from 2.5 to 4.5 °C (see Section 7.11.2). This phenomenon, now known as the **greenhouse effect**, is explored in more detail in Chapter 7. Arrhenius's work laid the groundwork for modern climate science by introducing the concept of climate sensitivity and emphasizing the potential consequences of anthropogenic greenhouse gas emissions.

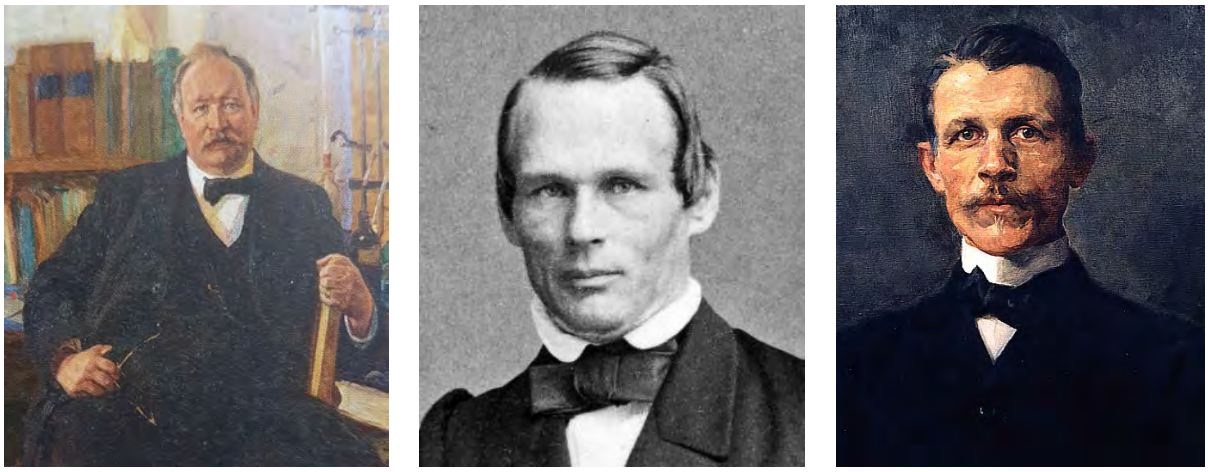

(a) (b) (c)

Figure 13.1: **(a)** Svante Arrhenius. **(b)** Anders Jonas Ångström, the father of **(c)** Knut Ångström.

13.4 Legacy of the Ångströms: Father and son

Anders Jonas Ångström (1814 – 1874), whose 1862 portrait by Mathias Hansen is shown in Figure 13.1(b), was a pioneering Swedish physicist and one of the founders of modern spectroscopy. He developed high-precision spectroscopic instruments that were considered state-of-the-art in the mid-19$^{\text{th}}$ century. He advanced optical spectroscopy and influenced subsequent research, including his son's. However, the spectral resolution and sensitivity of his equipment were limited by the technological constraints of his time.

The first significant scientific response to Arrhenius's work came almost immediately from Anders Jonas's son, Knut Ångström, a Swedish physicist depicted in Figure 13.1(c). Active at the turn of the 20$^{\text{th}}$ century, Knut conducted some of the earliest laboratory experiments on infrared absorption by atmospheric gases. His state-of-the-art laboratory at Uppsala University had been established by his father. In a widely cited publication, Knut *Ångström* (1901) challenged Arrhenius's hypothesis, asserting that increases in atmospheric CO_2 would have minimal impact on Earth's climate due to what he believed was the saturation of its infrared absorption bands. Knut Ångström's key conclusions were incorrect, and his reasoning was based on several critical misunderstandings.

1. **Light path length too short:** Ångström used laboratory absorption cells with path lengths of only a few centimeters, far shorter than the multi-kilometer path lengths of infrared radiation through the actual atmosphere. As a result, he failed to capture the cumulative effect of CO_2 absorption.

2. **Misunderstanding of absorption saturation:** He assumed that once a spectral band was "saturated," further increases in CO_2 would have no additional radiative effect. This ignores the importance of the band wings, where absorption continues to increase with concentration and where much of the greenhouse effect operates.

3. **Neglect of vertical temperature profile:** Ångström did not account for the vertical structure of the atmosphere, shown in Figure 7.6. Radiative transfer depends not just on total absorption, but on how high in the atmosphere absorption and re-emission occur, especially given the steep temperature gradient (lapse rate) from surface to upper troposphere, see Table 13.1.

4. **Inadequate instrumentation:** The detectors of the time, including thermopiles and early bolometers,[1] lacked the spectral resolution and sensitivity needed to distinguish fine-scale variations

[1] A bolometer is a thermal radiation detector that measures the power of incident electromagnetic radiation by converting it into heat. The absorbed radiation raises the temperature of an absorbing element, usually a thin metal or semiconductor film, whose electrical resistance changes with temperature. This resistance change is then measured – typically using

in absorption and to quantify small radiative differences depicted in Figure 13.2.

A detailed discussion of his four major errors is beyond the scope of this brief overview, but an excellent analysis is provided by *Pierrehumbert* (2011).

13.4.1 Anders Jonas Ångström's approach

In his monumental work (*Ångström*, 1868), titled in English *Researches on the Solar Spectrum: With an Atlas Containing the Wavelengths of Solar Lines and Emission Spectra Obtained with Different Chemical Elements*, Ångström described the instrumentation he developed for high-resolution solar spectroscopy. He primarily employed a prism-based spectrometer, often incorporating a Bunsen–Kirchhoff diffraction grating and a scale-mounted telescope. His apparatus could resolve spectral features separated by approximately 0.1–0.2 nm – sufficient for many atomic spectral lines, but inadequate for distinguishing the overlapping molecular absorption bands characteristic of atmospheric gases such as CO_2 and H_2O. In his 1868 solar spectrum atlas, Ångström achieved a wavelength calibration accuracy of about 0.05 nm, although systematic errors in the range of 0.1–0.2 nm were typical. Spectral detection relied on photographic plates, which imposed further limitations due to their low sensitivity, limited dynamic range, and nonlinear response, all of which constrained both the qualitative and quantitative precision of his spectroscopic measurements.

13.4.2 Limitations of early greenhouse gas studies

While Anders Jonas Ångström's equipment was adequate for analyzing solar and stellar atomic spectra, it lacked the spectral resolution required to study the fine rotational–vibrational absorption bands characteristic of greenhouse gases in the infrared (*Goody and Yung*, 1989). For example, the 15 μm (667 cm^{-1}) bending-mode band of CO_2, shown in Figures 7.9 and 13.2, and the 6.3 μmeter (1588 cm^{-1}, see Figure 13.3) vibrational band of H_2O both exhibit intricate line structures with individual features spaced by less than 0.01 nm. Resolving these bands requires high-resolution infrared spectroscopy, such as that provided by modern Fourier-transform spectrometers or high-dispersion gratings – technologies far beyond the reach of 19^{th}-century optics. Ångström's conclusion that atmospheric CO_2 played a negligible role in infrared absorption arose not from a flaw in physical theory, but from the severe limitations of his instrumentation. In contrast, modern spectroscopic techniques, employing detectors with high dynamic range and sophisticated calibration, have conclusively demonstrated the dominant role of CO_2 in longwave radiative transfer, see Figure 13.2.

13.4.3 Knut Ångström's improvements to spectroscopic instrumentation of his father

Knut Ångström (1857–1910), expanded upon his father's legacy by conducting several atmospheric and infrared radiation experiments at Uppsala University. While much of his work was foundational, it has since been criticized for methodological limitations. Nonetheless, he made some notable refinements to the spectroscopic tools and experimental techniques available in the late 19^{th} century.

Knut Ångström introduced several important methodological advances over his father's earlier work. To detect changes in infrared radiation intensity, he employed sensitive thermopiles – arrays of thermocouples – connected to galvanometers. This configuration enabled rudimentary quantitative measurements of radiant heat and marked an improvement over photographic plates, though thermopiles are broadband detectors and cannot resolve individual wavelengths. He also implemented controlled absorption cells filled with CO_2, H_2O vapor, or air, through which infrared radiation from a heated metal plate, used as a reproducible blackbody source, was passed. These gas-filled tubes allowed him to compare the transmittance of different gas concentrations. Additionally, he adopted a differential measurement approach by systematically varying the gas concentration in the absorption cells to detect changes in transmitted radiation – a technique that foreshadowed modern differential spectroscopy.

a sensitive Wheatstone bridge or superconducting transition edge sensor (TES) – to infer the incident radiation power. Bolometers can detect extremely small changes in radiant energy and are widely used in astronomy, atmospheric science, and laboratory spectroscopy. In contrast to thermopiles, bolometers offer significantly higher sensitivity and, when cryogenically cooled, can resolve subtle spectral features across the infrared and submillimeter ranges.

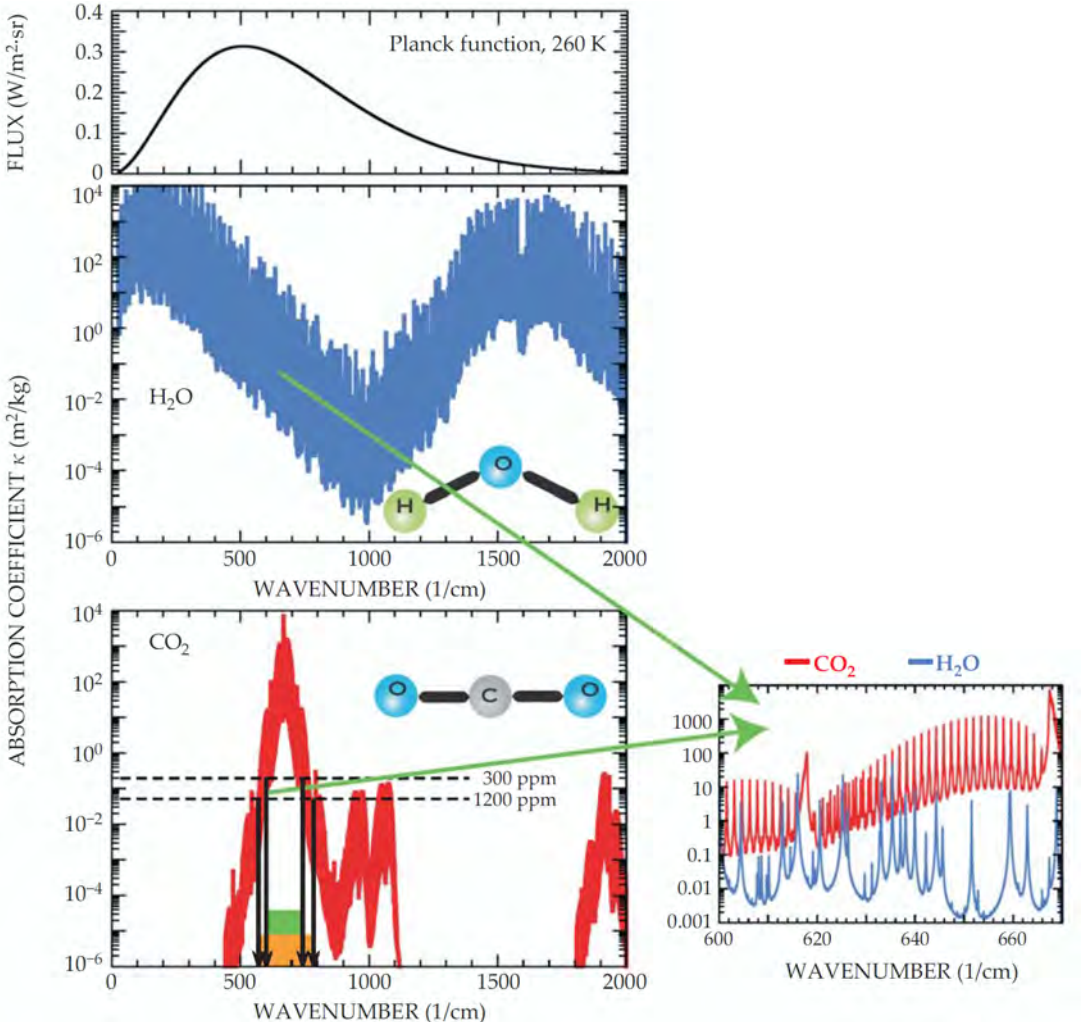

Figure 13.2: The upper panel displays the Planck blackbody function $B(f,T)$ for a 260 K surface, spanning the spectral regions critical to planetary energy balance. Here, the wavenumber $\tilde{\nu}$ is proportional to frequency f. If an atmospheric layer contains M kilograms of absorbing gas per square meter at its base, the intensity of transmitted radiation is attenuated by a factor $\exp(-\kappa M)$, where κ is the absorption coefficient. This coefficient is related to the molecular absorption cross-section σ discussed in Section 13.5.1, and depends on the gas density, molecular weight, and Avogadro's number. In the lower plot, horizontal dashed lines indicate the threshold values of κ beyond which the atmosphere becomes strongly absorbing for CO_2 concentrations of 300 ppm and 1200 ppm. The green rectangle highlights the spectral region where the atmosphere is already optically thick at 300 ppm, while the orange rectangle shows how this region expands with increased CO_2 concentration. This figure and its caption are reproduced from Figure 2 in *Pierrehumbert* (2011).

While Knut Ångström introduced several innovations beyond his father's original spectroscopic setup, his experiments were limited by insufficient spectral resolution, low sensitivity, and shortcomings in experimental design. These constraints led him to underestimate the infrared absorption of CO_2 and draw incorrect conclusions about its role in atmospheric radiative forcing. Although his results were influential at the time, they were later refuted by Svante Arrhenius, (*Callendar*, 1938), and the development of mid-20$^{\text{th}}$-century high-resolution infrared spectroscopy, shown in Figures 13.2 and 13.3.

13.4.4 Knut Ångström and modern climate denialism

Ångström (1901) cast doubt on the warming potential of atmospheric CO_2, arguing that its infrared

absorption bands were already saturated and that additional CO_2 would therefore have little to no effect on climate. However, this conclusion was based on experiments with limited spectral resolution, short path lengths, and an incomplete understanding of radiative transfer. His claims were soon refuted by better instrumentation and theoretical advances (see *Arrhenius* (1896), *Callendar* (1938), *Plass* (1956)).

High-precision spectroscopic measurements of the absorption cross-sections of CO_2, CH_4, and H_2O now fully resolve line broadening, overlapping absorption bands, and their dependencies on temperature and pressure. Advances in radiative transfer modeling – particularly through detailed layer-by-layer simulations – have shown that CO_2 remains radiatively active in the upper troposphere and lower stratosphere, where water vapor is scarce and saturation effects do not occur. In addition, a vast body of observational evidence from satellite remote sensing, long-term surface temperature records, and energy balance models confirms the dominant role of CO_2 in driving climate change, largely through its regulation of atmospheric water vapor via feedback mechanisms.

Despite numerous scientific refutations, some modern climate change deniers continue to cite Ångström's outdated arguments as "proof" that CO_2 cannot significantly influence Earth's climate.

Outright denial of climate change is intellectually indefensible and would verge on the absurd – were it not endorsed by the Trump II administration, which has systematically dismantled environmental regulations and promoted fossil fuel combustion wherever feasible. More insidious, however, is the strategy of climate obfuscation: the deliberate sowing of doubt and confusion under the guises of scientific objectivity and skepticism. The recent DOE report on climate change is a good example of such obfuscation (*Christy et al.*, 2025).

I hope that this book, and the very simplicity and transparency of our global warming model, will make it more difficult for such climate obfuscators to dismiss out of hand the robust global climate response to rising CO_2 concentrations. Consider the following illustrative statement:

> I would have offered a somewhat different statement, based upon my familiarity with the assessment reports and literature: The earth has warmed during the past century, partly because of natural phenomena and partly in response to growing human influences. These human influences (most importantly the accumulation of CO_2 from burning fossil fuels) exert a physically *small effect* on the complex climate system. Unfortunately, our *limited observations and understanding are insufficient [italics, TWP]* to usefully quantify either how the climate will respond to human influences or how it varies naturally. (*Koonin*, 2021)

Such language exemplifies a deliberate attempt to undermine the scientific consensus by portraying the well-established radiative forcing of CO_2 as negligible and by casting doubt on the reliability of modern climate science. This rhetorical strategy aligns more closely with public manipulation and ideological propaganda than with genuine scientific inquiry.

13.4.5 Modern understanding and refutation

The Ångströms were aware of the Lambert–Beer's Law, named after the two key contributors *Goody and Yung* (1989), *Liou* (2002). Johann Heinrich Lambert (Swiss mathematician and physicist) formulated the exponential attenuation of light in an absorbing medium in 1760 in his book *Photometria*. August Beer (German physicist) expanded on Lambert's work in 1852, showing that absorbance is proportional to the concentration of the absorbing species.

But Ångström's spectrometric equipment had insufficient resolution of the IR spectra of water vapor and CO_2. Therefore, modern critiques of Knut Ångström's dismissal of atmospheric CO_2 absorption are grounded in the clear inadequacy of 19th-century instrumentation for infrared atmospheric spectroscopy and theoretical understanding of his time. Notable refinements include:

- **Pressure Broadening:** In the lower atmosphere, molecular collisions broaden the absorption lines of gases—a phenomenon known as pressure broadening. This effect allows CO_2 to absorb infrared radiation across a wider spectral band than could be resolved by Ångström's early 20^{th}-century instrumentation.

- **Altitude Dependence:** While absorption by CO_2 may appear saturated at low altitudes, higher in the atmosphere (above ∼6 km; see Table 13.1) – where the Earth emits strongly in the infrared – CO_2 becomes the dominant greenhouse gas. This is because water vapor concentrations drop rapidly with height, while CO_2 remains well mixed.
- **Radiative Forcing:** Modern radiative transfer models demonstrate that the greenhouse effect of CO_2 increases logarithmically with concentration. As a result, each doubling of atmospheric CO_2 leads to a predictable and quantifiable increase in global surface temperature.

13.5 Discussion of relative IR absorption by H_2O and CO_2

The atmosphere's temperature, pressure, air density, water vapor mole fraction, CO_2 mole fraction and their ratio are listed in Table 13.1, assuming the following:

- Atmospheric air pressure and temperature are from U.S. Standard Atmosphere model *NOAA et al.* (1976),
- This model applies to mid-latitude, static atmosphere under no weather influence. Temperature is linear only in the troposphere ($0 - 11$ km above ground level (AGL)). Above that, different lapse rates and isothermal layers occur,
- Saturated H_2O mole fraction is estimated using empirical saturation vapor pressure at the air temperature, and
- CO_2 concentration is fixed at 420 ppm_v. In the real atmosphere, carbon dioxide (CO_2) is well-mixed up to at least $80 - 100$ km AGL, due to turbulent mixing in the homosphere ($0 - 100$ km)[2]. Therefore:

$$x_{CO_2}(z) \approx 420 \text{ ppm}_v = 0.00042 \quad \text{for } 0 \leq z \leq 50 \text{ km}$$

This means that the mole fraction of CO_2 is approximately constant with height in the troposphere and stratosphere, including up to 50 km, while the water mole fraction declines exponentially and becomes less than that of CO_2 at elevations exceeding 6 km above ground level.

13.5.1 Beer's law for a mixture of gases

For a homogeneous mixture of gases, the total spectral absorbance at a given wavelength λ is the sum of the individual contributions from each gas species:

$$A_\lambda = \sum_i A_{\lambda,i} = \sum_i \varepsilon_{\lambda,i}\, c_i\, \ell \tag{13.1}$$

where:

- A_λ is the total spectral absorbance at wavelength λ,
- $\varepsilon_{\lambda,i}$ is the molar absorptivity of gas i at wavelength λ ($\text{m}^2\text{mol}^{-1}$),
- c_i is the molar concentration of gas i (mol/m^3),

[2]The concentration of carbon dioxide (CO_2) is observed to be nearly constant up to approximately 50 km above ground level (AGL), a region encompassing the troposphere, stratosphere, and lower mesosphere – collectively known as the *homosphere*. This vertical uniformity is maintained by turbulent mixing, large-scale atmospheric circulation, and molecular diffusion, all of which act on timescales much shorter than those of most radiative or chemical processes. Unlike water vapor, which condenses and precipitates out of the atmosphere, CO_2 is a non-condensable gas under Earth's atmospheric conditions and does not participate in phase changes that would locally alter its concentration. Empirical confirmation of this vertical uniformity comes from a range of balloon-borne, aircraft-based, and satellite observations, including data from the Atmospheric Infrared Sounder (AIRS), the Stratospheric Aerosol and Gas Experiment (SAGE), and limb-sounding instruments on ENVISAT and the Aura satellite. These observations consistently show that the volume mixing ratio of CO_2 remains stable throughout the homosphere, typically around 400–420 ppm in recent years, with significant deviations only appearing in the thermosphere, where diffusive separation begins to dominate over mixing.

Table 13.1: Standard atmosphere with air density, saturated H_2O and CO_2 mole fractions

Altitude (km)	**Pressure** (kPa)	**Temperature** (°C)	**Air Density** ($kg\,m^{-3}$)	**H_2O (ppm_v)** (saturated)	**CO_2 (ppm_v)** (assumed)	**H_2O/CO_2** (ratio)
0	101.3	15.0	1.225	17038	420	40.6
1	89.9	8.5	1.112	10869	420	25.9
2	79.5	2.0	1.007	6672	420	15.9
3	70.1	-4.5	0.909	3950	420	9.4
4	61.6	-11.0	0.819	2268	420	5.4
5	54.1	-17.5	0.736	1255	420	3.0
6	47.4	-24.0	0.660	673	420	1.6
7	41.5	-30.5	0.590	345	420	0.82
8	36.5	-37.0	0.525	170	420	0.40
9	32.3	-43.5	0.467	85	420	0.20
10	28.7	-50.0	0.413	41	420	0.10
11	25.8	-56.5	0.365	19	420	0.045

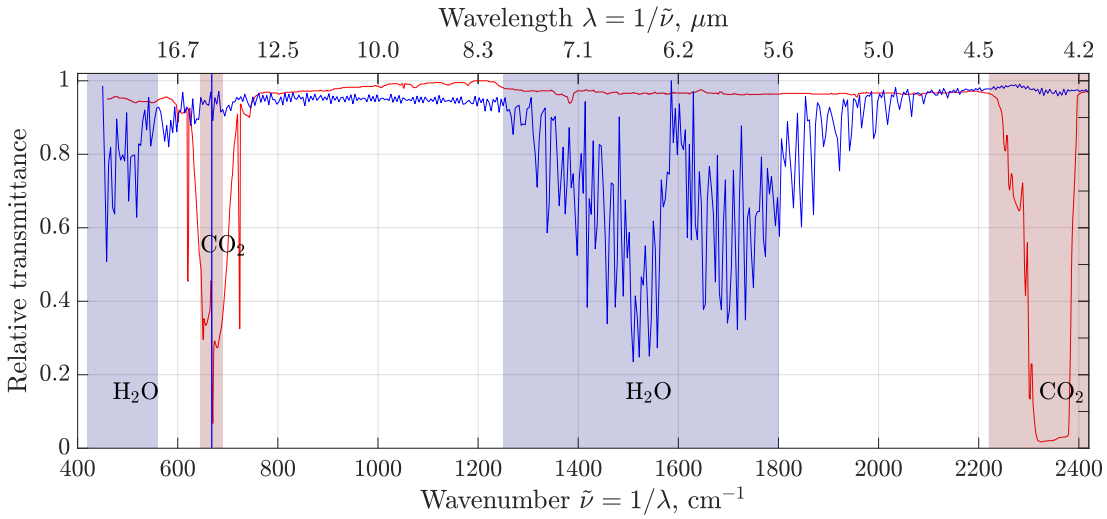

Figure 13.3: The infrared relative transmittance of pure gaseous CO_2 and pure water vapor. The displayed range of wave numbers covers that in Figure 7.9. The CO_2 spectrum was obtained at the CO_2 pressure of 200 mmHg diluted to a total pressure of 600 mmHg with N_2. Calculations by Patzek. Source: The US National Institute of Standards and Technology (NIST) Chemistry WebBook.

- ℓ is the path length through the gas (m).

In terms of spectral transmittance T and the molecular absorption cross-section $\sigma_{\lambda,i}$ (in m^2/molecule), we can also write:

$$T = \frac{I}{I_0} = \exp\left(-\sum_i \sigma_{\lambda,i}\, n_i\, \ell\right) \tag{13.2}$$

where:

- I_0 is the incident radiation intensity,
- I is the transmitted radiation intensity,

- n_i is the number density of gas i (molecule/m^3),
- $\sigma_{\lambda,i}$ is the spectral absorption cross-section of gas i (m^2 (molecule)$^{-1}$).

Taking the natural logarithm, the total absorbance becomes:

$$A_\lambda = -\ln T = \sum_i \sigma_{\lambda,i}\, n_i\, \ell \tag{13.3}$$

For non-uniform atmospheres, the total absorbance is obtained by vertical integration:

$$A_\lambda = \int_0^\ell \sum_i \sigma_{\lambda,i}(z)\, n_i(z)\, dz \tag{13.4}$$

13.5.2 Absorption cross-sections σ of H_2O, CO_2, and CH_4

Accurate measurement of infrared (IR) absorption cross-sections of greenhouse gases, such as CO_2, H_2O, and CH_4, has been critical to understanding and quantifying their radiative forcing in the Earth's atmosphere.

These cross-sections, typically in units of cm^2 (molecule)$^{-1}$, describe how strongly a molecule absorbs infrared radiation over specific wavenumber ranges (typically 400 cm^{-1} to 4000 cm^{-1}). They are especially important in modeling the atmospheric greenhouse effect and interpreting satellite radiance measurements.

The accurate values of infrared (IR) absorption cross-sections of greenhouse gases were unknown to Knut Ångström, whose experiments predated the development of high-resolution infrared spectroscopy and systematic spectroscopic databases such as HITRAN.

Historically, significant advances were made in the 1970s and 1980s with the development of high-resolution Fourier Transform Infrared (FTIR) spectroscopy, used routinely in my laboratory at the King Abdullah University of Science & Technology (KAUST) to detect components of liquid mixtures. These advances enabled precise measurements of molecular vibrational and rotational transitions under atmospheric pressure and temperature conditions.

The `HITRAN` (High-resolution Transmission) database, first released in 1973, has played a foundational role in compiling and updating absorption cross-sections and spectroscopic parameters for key atmospheric species. It remains a central reference for climate models and radiative transfer codes.

Recent updates, including `HITRAN2016`, incorporate improved measurements of line intensities, pressure broadening coefficients, and temperature-dependent cross-sections. Laboratory techniques such as cavity ring-down spectroscopy and advanced FTIR systems have further refined these values, particularly in the 400 cm^{-1} to 2000 cm^{-1} range where major greenhouse gas absorption bands are found.

Here are the key references for more in-depth reading:

- *Rothman et al.* (1998) presents the 1996 `HITRAN` database update and methodology.
- *Gordon et al.* (2017) provides the `HITRAN2016` update, including expanded line lists and IR cross-sections.
- *Allen et al.* (1976) reports laboratory measurements of CO_2 and H_2O IR absorption under atmospheric conditions.
- *Shine et al.* (1995) discusses how IR cross-sections relate to global warming potentials.

Table 13.2: Typical peak IR absorption bands and cross-sections for major greenhouse gases *Rothman et al.* (2013)

Gas	Absorption Band	Wavenumber	Wavelength	Mode	σ (cm^2/molecule)
H_2O	6.3 ţm	1587 cm^{-1}	6.3 ţm	Bending	1×10^{-20}
	2.7 ţm	3700 cm^{-1}	2.7 ţm	Stretching	1×10^{-21}
	0.94 ţm	10 600 cm^{-1}	0.94 ţm	Overtone	1×10^{-22}
CO_2	15 ţm	667 cm^{-1}	15 ţm	Bending	1×10^{-19}
	4.3 ţm	2349 cm^{-1}	4.3 ţm	Stretching	1×10^{-20}
	2.7 ţm	3700 cm^{-1}	2.7 ţm	Overtone	5×10^{-22}
CH_4	7.7 ţm	1300 cm^{-1}	7.7 ţm	Deformation	1×10^{-19}
	3.3 ţm	3030 cm^{-1}	3.3 ţm	Stretching	1×10^{-19}
	1.65 ţm	6050 cm^{-1}	1.65 ţm	Overtone	1×10^{-21}

13.6 Houston, we have a problem

This book distills the author's two-decade-long journey from the relative comfort of working as a petroleum reservoir engineer, earth scientist, and ecologist to the more unsettling role of a climate analyst. It culminates in the formulation of a simple, quantitative, and predictive model that links anthropogenic CO_2 emissions to the progressive destabilization of Earth's climate system. The model illustrates – graphically and unequivocally – the extent of planetary damage driven by what the author's old friend, Nate Hagens, has called the global *Fossil Amoeba* (*Hagens*, 2020), a perennially insatiable global system powered predominantly by the industrial economies of the global North.

The earliest comprehensive and scientifically accurate account of the role of fossil fuels in altering the global climate dates to an internal report released on November 12, 1982, by Marvin B. Glaser, then Manager of Environmental Affairs Programs at the Exxon Corporate Research Center in New Jersey (*Glaser*, 1982). This remarkably prescient document, along with other key internal publications and peer-reviewed papers coauthored by Exxon scientists and academic collaborators (e.g., *Hoffert et al.* (1980), *Flannery* (1984), *Hoffert et al.* (1983)), not only predated many core insights of modern climate science but arguably surpassed the academic consensus for over a decade, as discussed in *Song et al.* (2015). The Intergovernmental Panel on Climate Change (IPCC) was established six year later, on December 6, 1988, by the United Nations Environment Programme (UNEP) and the World Meteorological Organization (WMO).

It is perhaps unsurprising that the first scientists to rigorously address the epochal challenge of fossil fuel-induced climate change were employed by the largest oil company in the United States. Equally unsurprising – but deeply troubling – is that after 1989, Exxon's corporate leadership began to cast doubt on, and actively downplay, the very findings its own researchers had helped to establish. Under institutional pressure and financial incentives, some of these same scientists publicly reversed their earlier positions. One can only speculate how different the trajectory of global climate policy might have been had the world heeded Exxon's internal warnings and initiated corrective action as early as 1980 or 1982.

The author joined Shell's historic Bellaire Research Center in Houston in 1983 and, by 1986, had encountered the internal resource limitation reports authored by M. King Hubbert – the earliest dating back to 1943. In Hubbert's memory, the author later resolved U.S. crude oil, lease condensate, and natural gas production into multiple "Hubbert cycles" (Gaussians) (*Patzek*, 2008).

13.7 Vanilla climate disinformation

Figure 13.4 claims to demonstrate that carbon emissions are not the primary driver of global warming, attributing observed temperature changes instead to variations in sunspot numbers. Polar air temperature

is selectively used to support this claim. Debunking such disinformation requires a basic understanding of climate physics.

> Sea ice has a much higher albedo than the surrounding ocean. A typical ocean albedo is approximately 0.06, while bare sea ice ranges from 0.5 to 0.7. This means that the ocean reflects only 6% of incoming solar radiation, absorbing the rest, whereas sea ice reflects 50–70%. When covered by snow, the albedo of sea ice increases further to about 90%. The ice surface temperature responds rapidly to changes in the solar constant.

In addition:

- Sunspots modulate the solar constant; see Figure 7.4.
- During polar winter in particular, Arctic surface temperatures are highly sensitive to changes in the solar constant (*Roy*, 2018). This phenomenon is part of what is known as "polar amplification"; see Section 9.4.
- However, sunspot variability does not significantly affect surface temperatures across most of the rest of the Earth.
- The Arctic has been warming at approximately 2× the global average rate, contributing directly to an unfolding global climate crisis.

In words of Max Bazerman of Harvard, *Positive illusions lead us to conclude that a problem doesn't exist or is not severe enough to merit action... we try desperately to maintain the status quo.*

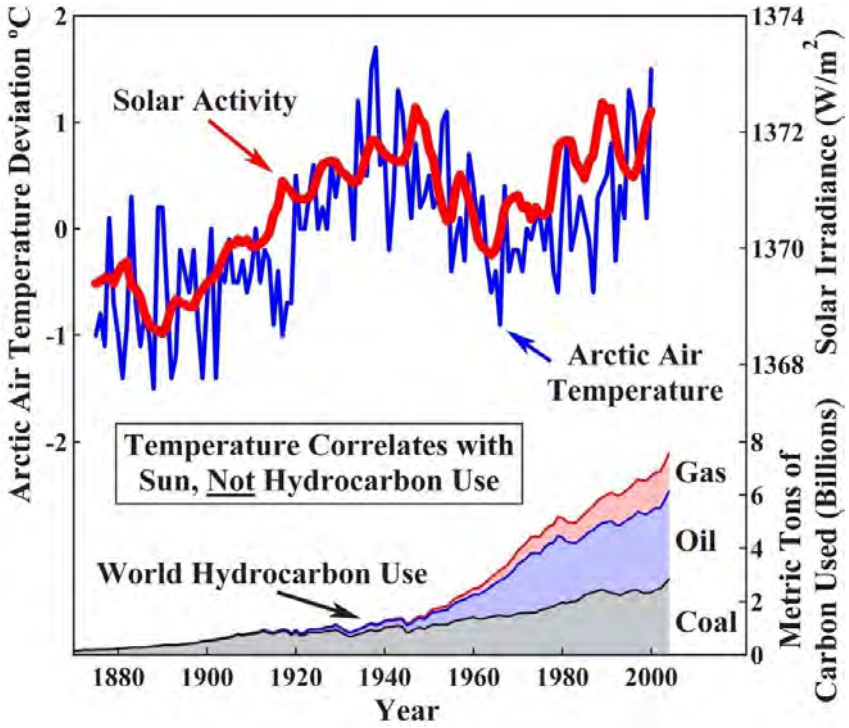

Figure 13.4: Disinformation here is using the polar ice temperature changes that respond readily to the changes in solar activity to correlate global temperature anomaly with the number of sun spots. Local coincidence is **not** global causality! Source: Fahad Almotairi from Twitter, http://polarportal.dk/en/sea-ice-and-icebergs/sea-ice-temperature/

Chapter 14

Geoengineering

Photo illustration by Juliana Jimenez Jaramillo. Photo by Frank Bienewald/LightRocket via Getty Images

Geoengineering is like trying to cure obesity by tightening your belt. Yes, it might make you look thinner, but it does nothing to address the underlying problem – and can cause serious harm.
Pierrehumbert (2015), "Climate Hacking Is Barking Mad", Slate, 2015.

The law that entropy increases – the Second Law of Thermodynamics – holds, I think, the supreme position among laws of nature. If someone points out to you that your pet theory of the universe is in disagreement with Maxwell's equations – then so much the worse for Maxwell's equations. If it is contradicted by observation – well, these experimentalists do bungle things sometimes. But if your theory is found against the Second Law of Thermodynamics, I can give you no hope; there is nothing for it but to collapse in deepest humiliation
Sir Arthur Stanley Eddington
The Nature of the Physical World (1953, p. 74)

14.1 What are you going to learn?

First, you should know that the two scientists quoted on the title page of this chapter are exceptional. Dr. Pierrehumbert is among the world's leading atmospheric physicists, and Sir Eddington was a famous astrophysicist, mathematician and historian of science in early twentieth century.

Now you are ready to learn about **geoengineering**. This term was coined in 1977 by the Italian physicist Cesare Marchetti in his seminal paper "On geoengineering and the CO_2 problem," where he proposed deep-ocean CO_2 disposal as a means to counteract greenhouse-gas emissions (*Marchetti*, 1977). Today, geoengineering denotes the deliberate, large-scale manipulation of the Earth system – principally the atmosphere, hydrosphere, cryosphere, and biosphere – with the explicit objective of modifying the planetary energy balance or atmospheric composition to counteract anthropogenic climate change (*Royal Society*, 2009, *Shukla et al.*, 2022). Conceptually, geoengineering is divided into two classes:

- *Solar radiation management* seeks to alter shortwave radiative forcing by increasing the planetary albedo through interventions such as stratospheric aerosol injection or marine cloud brightening (*Crutzen*, 2006, *Kravitz et al.*, 2015);
- *Carbon removal* aims to reduce long-lived greenhouse gas burdens via biological or geochemical enhancement of natural sinks, engineered capture technologies, or ocean-based sequestration (*National Academies of Sciences, Engineering, and Medicine*, 2015, *IPCC*, 2018).

Both solar radiation management and carbon removal involve substantial uncertainties in climate-system response, multi-scale feedbacks, environmental side effects, and governance challenges, and are therefore subject to significant ethical and regulatory scrutiny *GESAMP* (2019), *Strong et al.* (2009);

The dependably techno-optimistic journal *Science* (*White*, 2025) offers the following commentary on geoengineering:

> Currently, carbon-removal efforts soak up about 2 gigatons of CO_2 from the atmosphere each year[1], mostly through the planting of new forests. That amount would likely need to quadruple by 2050 in order to limit warming to 1.5°C, according to a 2024 report from the University of Oxford, requiring the rapid scale-up of new carbon-removal methods. "It's got to go from something that most people have never heard of to the biggest industry the world has ever seen in a really short time," says[2] climate scientist David Ho, a professor at the University of Hawaii at Manoa.

The author laments that scientists are clumsy in communicating their unproven, **global** and potentially very harmful technologies to the **local**, preferably indigenous, communities expected to host them. She concludes that such technologies will eventually gain broad social acceptance, "But first scientists need to learn how to talk to the public about it [geoengineering]."

To balance this assertion, Prof. *Rees* (2023) argues:

> [H]uman brain and associated cognitive processes are functionally obsolete to deal with the human eco-crisis [*caused by overshoot, see Appendix A, TWP*]. H. sapiens tends to respond to problems in simplistic, reductionist, mechanical ways. Simplistic diagnoses lead to simplistic remedies. Politically acceptable technical 'solutions' to global warming assume fossil fuels are the problem, require major capital investment and are promoted on the basis of profit potential, thousands of well-paying jobs and bland assurances that climate change can readily be rectified. If successful, this would merely extend overshoot. Complexity demands a systemic approach; to address overshoot requires unprecedented international cooperation in the design of coordinated policies to ensure a socially just economic contraction, mostly in high-income countries, and significant population reductions everywhere.

[1] This statement is not quite true in general (*Patzek and Pimentel*, 2005, *Smith et al.*, 2016, *Griscom et al.*, 2017), but reforestation is the only large-scale method of geoengineering available to humans, other than the obvious deep cutbacks in CO_2 emissions.

[2] A reductionist scientist's testimonial to how irreformable the Fossil Amoeba is.

Keep this in mind: the reductionist scientist—as most of us are trained to be—is far less free than the jazz musician who improvises without a script or the indigenous shaman. What is required now to break out of the inherited reductionist cage of our own making is nothing less than a global explosion of deliberate, collective free will and systems thinking.

Figure 14.1: Azerbaijan reduces sulphur in fuel used to prevent toxic gas emissions from ships. Image source: https://www.azernews.az/business/220169.html, accessed 11/25/2025.

14.2 Why is this important?

In Chapter 13 we outlined several shades of climate change denial. Here we move one level higher, to a form of arrogant negation: the ability to deflect the consequences of climate change away from our profit-making schemes and offload them onto poorer nations and even our own citizens. It is crucial to view much of the geoengineering hype through this lens. Remember that the real strength of capitalism lies in its capacity to morph – or metastasize –into whatever configuration yields the highest profit, regardless of circumstance or consequence.

Several years ago, when I was still on the faculty at UC Berkeley, I had a telephone conversation with a prominent Australian proponent of ocean fertilization. We sparred for a while, and when he finally ran out of arguments he concluded, "Look, we have already f. . . d up [the global] land, so now we have to fertilize the ocean." His remark was revealing. The good Australian professor seemed not to have noticed that humanity had *also* damaged the global ocean beyond recognition, as documented amply throughout this book.

From the previous chapters you have learned that in nature everything is connected to everything else, and that every action is accompanied—often swiftly and unexpectedly—by interlinked reactions. A telling example is the recent acceleration of ocean warming that followed the international effort to remove sulfur from ship fuel. Having spent a fortune cleaning up this source of sulfate aerosols (Figure 14.1), we now hear loud voices calling for injecting sulfur *into the stratosphere* to compensate for the resulting loss of atmospheric cooling. Despite 30 COP meetings, no one in power is willing to state publicly the obvious: cleaning up the air—a wise and necessary policy—while simultaneously pouring ever-increasing amounts of CO_2 into that same air cannot help but produce unintended and ever more severe side effects.

In this chapter you will confront the stark reality of a technological fantasy pursued in defiance of

common sense and ecological prudence: the notion that global geoengineering can rescue us from the consequences of our own excess. As *Jasanoff* (2010) warns, such schemes amount to "playing God with the climate," a posture of reckless hubris in which stratospheric aerosol injection and similar interventions are promoted with an air of technical omniscience. In practice, these proposals sidestep or trivialize the most difficult questions – the ethical stakes, the unresolved physical and chemical complexities, the absence of democratic consent, and the stark dichotomy between the planet's complex, fragile climate system and our ignorance.

14.3 Ocean fertilization

The idea of deliberate iron fertilization of the ocean emerged from John Martin's famous quip: "Give me half a tanker of iron, and I will give you an ice age" (*Martin*, 1990).

14.3.1 Background

The biological gravitational pump (BGP) has traditionally been studied at selected ocean sites using a variety of particle-interception techniques, including sediment traps (deep-moored, surface-tethered free-drifting, or neutrally buoyant). Over the past decade, new observational tools – such as gliders and profiling floats equipped with biogeochemical (BGC) and bio-optical sensors (BGC-Argo; see Section 10.3.2) – have greatly increased the temporal and spatial resolution of particle-field measurements in the mesopelagic[3] zone. During this same period, efforts to characterize the diverse mesopelagic fauna using bioacoustics and trawling have also expanded. Together, these complementary approaches are yielding increasingly robust estimates of carbon sequestration by the BGP (*Boyd et al.*, 2019).

Paraphrasing somewhat *DeVries et al.* (2012), the conversion of dissolved nutrients and carbon to organic matter by phytoplankton in the surface ocean, and its downward transport by sinking particles, produces the BGP that reduces the concentration of atmospheric CO_2. Global rates of organic matter export are a *poor* indicator of biological carbon storage however, because organic matter gets distributed across water masses over *diverse pathways* and *timescales* of return to the surface.

DeVries et al. (2012) show that organic matter export and carbon storage can be related through a sequestration efficiency, which measures how long regenerated nutrients and carbon will be stored in the interior ocean before being returned to the surface. We write their definition (1) of this sequestration efficiency η_{bio} as a convolution integral integrated over the water surface A:

$$\eta_{\text{bio}}(t) = \frac{1}{I_{tot}(t)} \int_A da(\boldsymbol{r}) \int_0^\infty \mathcal{E}(\tau|\boldsymbol{r}) \Phi_{ex}(\boldsymbol{r}, t-\tau)\, d\tau \tag{14.1}$$

where t is time; I_{tot} is the ocean's total inventory of nutrients; $\boldsymbol{r}$ is a point on the water surface; $da(\boldsymbol{r})$ is a water surface element centered at point $\boldsymbol{r}$; $\Phi_{ex}(\boldsymbol{r}, t)$ is the rate of organic matter export at that point; $\mathcal{E}(\tau|\boldsymbol{r})$ is the sequestration efficiency of nutrients regenerated in the water column below point $\boldsymbol{r}$ at time τ. $\mathcal{E}(\tau|\boldsymbol{r})$ is the fraction of nutrients regenerated from organic matter exported out the euphotic (sun-lit and mixed) near-surface layer at point $\boldsymbol{r}$ that remains sequestered below the surface for a period of at least τ.

By construction, $\mathcal{E} = 1$ everywhere at $\tau = 0$. As τ increases, upwelling and eddy-diffusion return nutrients to the surface, where they are removed from the regenerated pool (converted back to CO_2), so that $\mathcal{E} \to 0$ as $\tau \to \infty$. At $\tau = 1$ year, regions of persistent upwelling, in Peru and some parts of the Southern Ocean lose as much as 50% of the initial pool of regenerated nutrients (have high emissions of CO_2).

Upwelling regions are typically strong natural sources of atmospheric CO_2 on the order of 0.7–1.5 PgC/yr depending on the dataset. Deep waters rich in dissolved inorganic carbon and respired CO_2 are brought to the surface, where their partial pressure exceeds that of the atmosphere, leading to net outgassing. Although these localized emissions are large, they are more than offset by high-latitude uptake[4], leaving the global ocean as a net sink for atmospheric CO_2.

[3] Mesopelagic: The 200–1000 m "twilight zone" of the ocean, too dark for photosynthesis but biologically active and central to carbon remineralization.

[4] The Southern Ocean and the Sub-Arctic and Arctic Ocean.

At $\tau = 100$ years, the areas which feed the deep ocean circulation increasingly stand out, with $\mathcal{E}$ exceeding 50% in areas where North Atlantic Deep Water and Antarctic Bottom Water are produced. Sequestration efficiencies over most of the rest of the ocean drop to around 10–30% after 100 years.

By $\tau = 1000$ years, only small amounts of regenerated nutrients remain, mainly originating from regions of deep convection in the Labrador Sea and Greenland-Iceland- Norwegian seas in the North Atlantic, and from the Weddell Sea in the Southern Ocean[5].

Over long time scales, only few areas of the global ocean have sequestration times $\geq$ 250 years, with the rest having sequestration times 50–150 years, see Fig 2 in (*DeVries et al.*, 2012).

Note that the regions with long sequestration times lie primarily in the Arctic, which is not iron-deficient, and around Antarctica, which is iron-deficient over most of its extent. The 10,000 year-time scales of quasi-static glacial-interglacial carbon exchange between the ocean and atmosphere are discussed in Section 3.15.1.

Boyd et al. (2019) identified several additional particle injection pumps (PIPs) beyond the classical BGP, as illustrated in Figure 14.2. These pumps provide distinct pathways for the mineralization and downward transport of organic carbon. Taken together, the various PIPs may inject nearly as much carbon to depth as the primary BGP, and they merit far more detailed investigation – provided that common sense, ethical constraints, and robust self-governance are in place (*Boyd and Bressac*, 2016, *National Academies of Sciences, Engineering, and Medicine*, 2022) to prevent damage to the affected ecosystems (*Tagliabue et al.*, 2023).

14.3.2 Ocean iron fertilization (OIF)

To apply iron fertilization in the open ocean, certain criteria must be met, see Table 14.1. Dissolved (d) iron (Fe) concentration in Fe-deficient water is dFe$<$ 0.1 nanomolar (nM), and in moderately Fe-limited water it is $0.1 - 0.2$ nM.

To date, 13 major ocean iron-fertilization experiments have been conducted between 1993 and 2009 (*Yoon et al.*, 2018), as summarized in Table 14.2. Of these, seven took place in different sectors of the Southern Ocean, three in the Subarctic/Arctic Ocean, and three in the tropical and subtropical oceans. All but one were carried out in Fe-deficient, high-nutrient, low-chlorophyll (HNLC) waters.

These first-generation open-ocean iron enrichments shared a broadly similar design. Experimental patches were typically on the order of 10 km in horizontal extent, and the field campaigns lasted for only a few weeks. These scales were dictated by what could realistically be achieved from research vessels while using tracers to follow Lagrangian patches of injected iron.

However, extrapolating results from such short-duration, small-scale studies to the spatial and temporal scales required for meaningful carbon sequestration introduces substantial uncertainties. Addressing these uncertainties demands experiments of longer duration (months–years) and at much larger spatial scales (100–200 km), as emphasized by *Watson et al.* (2008a).

To extrapolate the results of present-day iron enrichments to decadal timescales and to the scale of entire ocean basins, such experiments must be carried out in parallel with—and, where possible, assimilated into—high-resolution models of the physics and biogeochemistry of the fertilized waters. Current understanding indicates that any net carbon sequestration, *if it occurs at all*, will emerge only from the integrated air–sea CO_2 flux over millions of square kilometres and over many years, a quantity that can be assessed realistically only through modelling.

The primary role of observational studies is therefore to constrain, test, and improve these models so that their simulations and predictions become increasingly reliable. For this reason, next-generation iron-fertilization experiments have been proposed that would extend over several years (*Yoon et al.*, 2018) and/or incorporate novel design and monitoring features (*Watson et al.*, 2008a, *Buesseler et al.*, 2024).

[5]Definition in Table 3.15.

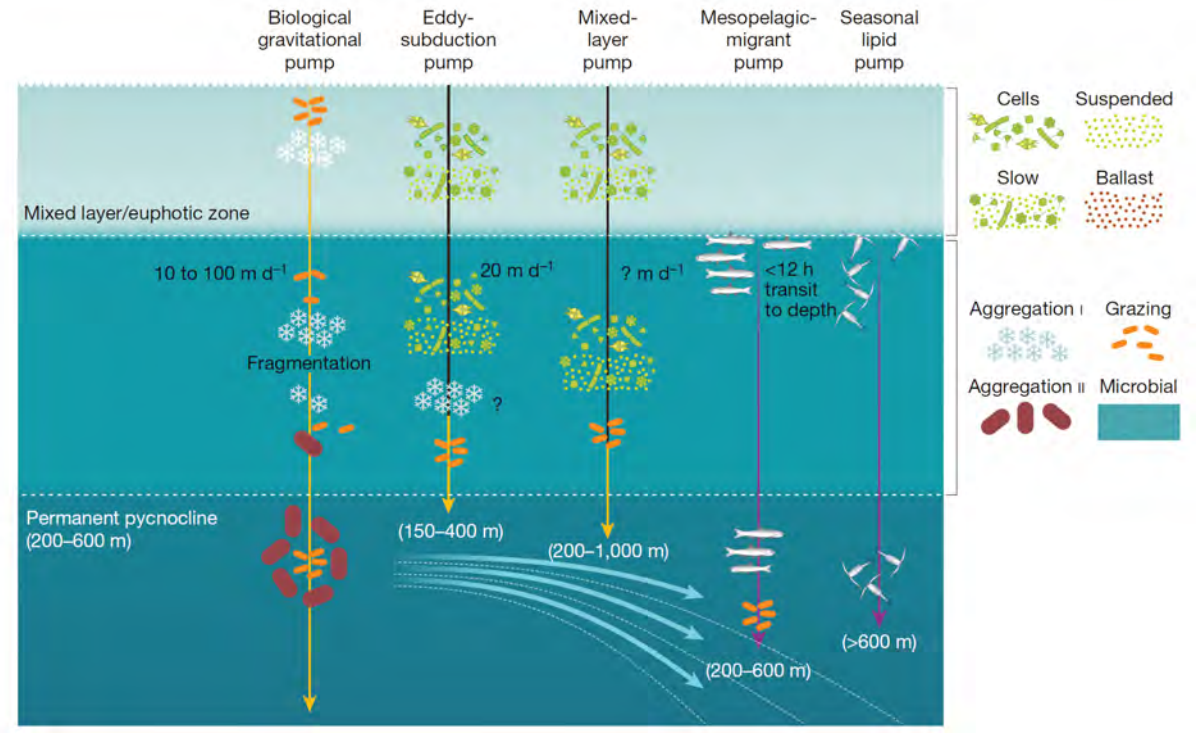

Figure 14.2: Interplay between particle characteristics, mode of export, biological gravitational pump (BGP) or particle injection pump, (PIP), delivery depth and larger-scale ocean circulation for a range of pumps. In the upper layer, the box at the top right represents mixed-layer particle types, which either form large sinking particles (that is, within the BGP; such as faecal pellets and marine snow) or are injected to depth (that is, by PIPs; such as suspended and/or slow-settling heterogeneous particles and cells (including healthy, slow-sinking phytoplankton89)). The vertical yellow arrow signifies the BGP; black lines indicate physically mediated PIPs; and purple lines indicate biologically mediated PIPs. The delivery rates of particles to subsurface strata (in m d^{-1}; ? denotes not known) are presented for each pump. Patchiness in the distribution of vertically migrating animals (top right) has a role in driving three-dimensional particle delivery to depth, and is denoted by different fish or copepod stocks in the upper ocean. The box to the right of the middle layer presents different particle transformations that are central to the BGP. This figure and its caption have been reproduced from Fig. 2 in (*Boyd et al.*, 2019).

Between 2009 and late 2025 no large-scale, open-ocean iron-fertilization experiments were conducted. Nevertheless, efforts to revive this line of research – and to design potential future trials within far stricter governance and monitoring frameworks – are actively underway (see Table 14.3).

None of the 13 iron-fertilization experiments were designed as fishery-support projects, and most were deliberately located far from regions of intense fishing effort. If one asks more broadly how many were conducted within the same large-scale biogeographic provinces as major fisheries or fisheries under stress, only a subset qualifies. In the Southern Ocean, arguably two of the seven experiments (SAGE and LOHAFEX) lay closest to commercially exploited regions (the New Zealand fisheries sector and the Atlantic krill sector), although both remained well away from the most heavily harvested Antarctic krill grounds near the Antarctic Peninsula and Scotia Sea (CCAMLR Area 48). In the Subarctic Pacific, all three experiments (SEEDS-1, SERIES, SEEDS-2) occurred within classic subarctic high-productivity zones that support major salmon and groundfish fisheries and have experienced long-term ecological variability. In contrast, the two IronEx experiments in the Equatorial Pacific were situated in broad tuna-fishing regions but far offshore and not associated with localized fishery distress, and the FeeP experiment was conducted in a low-productivity subtropical gyre with no significant local fishery. Thus, depending on how broadly one defines "in or near major fishery provinces," roughly five to six of the thirteen experiments occurred within large-scale oceanic provinces that also host important fisheries, but none were placed within the most heavily exploited krill grounds, and none were intended to ameliorate

Table 14.1: Operational thresholds for iron limitation in the open ocean, based on dissolved iron (dFe) and transient Fe(II) concentrations. Values reflect typical ranges in the High Nutrient, Low Chlorophyll (HNLC) regions and GEOTRACES[a] climatologies.

Category	Typical Fe Concentration	Oceanographic Interpretation
Strong Fe limitation	$d\mathrm{Fe} < 0.10\,\mathrm{nM}$	HNLC conditions; macronutrients remain unused; phytoplankton growth, $\mathrm{F}_v/\mathrm{F}_m$[b], and nitrate drawdown strongly Fe-limited.
Moderate Fe limitation	0.10–0.20 nM	Physiological Fe stress; growth partially Fe-limited; diatoms unable to reach maximal productivity.
Weak Fe limitation / Fe-replete	0.20–0.60 nM	Mixed limitation; Fe availability generally adequate but not abundant; typical of oligotrophic gyres and some upwelling regions.
High Fe / Fe-rich	0.60–> 1 nM	Coastal, shelf, or dust-influenced waters; Fe not limiting.
Post-fertilization Fe levels	1–3 nM (target)	Common target concentrations in iron-fertilization experiments (IronEx, SOFeX, SERIES).
Fe(II) in natural surface waters	< 10–100 pM	Fe(II) is transient; rapidly oxidizes; its concentration does *not* define Fe limitation in oceanography.
Fe(II) after artificial addition	0.1–1 nM (minutes–hours)	Short-lived spike after Fe(II) sulfate addition; quickly reverts to ligand-bound Fe(III).

[a] GEOTRACES is an international oceanographic program whose goal is to identify sources, sinks, and internal cycling of trace elements and their isotopes in the global ocean. Through a coordinated set of basin-scale transects, GEOTRACES has produced high-resolution distributions of dissolved and particulate species (including iron, manganese, aluminum, zinc, rare earth elements, and their isotopes), providing an unprecedented view of micronutrient supply pathways, particle dynamics, and ocean circulation.

[b] $\mathrm{F}_v/\mathrm{F}_m$ is the maximum photochemical efficiency of photosystem II in dark-adapted phytoplankton, defined as the ratio of variable fluorescence ($F_v = F_m - F_0$) to maximum fluorescence (F_m). F_0 is the dark-adapted minimal fluorescence. $\mathrm{F}_v/\mathrm{F}_m$ measures the fraction of absorbed photons that can be used for photochemistry under optimal conditions. In the open ocean, low values of $\mathrm{F}_v/\mathrm{F}_m$ are a diagnostic signature of iron stress.

Table 14.2: Large-scale iron-fertilization experiments.

Exp.	Time	Location	Initial Fe (nM)	Patch (km^2)	Duration (days)	Region
Southern Ocean						
3	SOIREE (Feb 1999)	61°S, 140°E	0.08	50	13	HNLC
4	EisenEx (Nov 2000)	48°S, 21°E	0.06	50	23	HNLC
5	SOFeX-N (Jan–Feb 2002)	56.23°S, 172°W	< 0.01	225	40	HNLC/LSi_a
6	SOFeX-S (Jan–Feb 2002)	66.45°S, 171.8°W	< 0.01	225	28	HNLC
7	EIFEX (Feb–Mar 2004)	50°S, 2°E	0.08–0.20	167	39	HNLC
8	SAGE (Mar–Apr 2004)	46.5°S, 172.5°E	0.09	36	15	HNLC/LSi_a
9	LOHAFEX (Jan–Mar 2009)	48°S, 15°W	0.06	300	40	HNLC/LSi_a
Subarctic / Arctic Ocean						
10	SEEDS-1 (Jul–Aug 2001)	48.5°N, 165°E	0.05	80	13	HNLC
11	SERIES (Jul–Aug 2002)	50.14°N, 144.75°W	< 0.10	77	25	HNLC
12	SEEDS-2 (Jul–Aug 2004)	48°N, 166°E	0.17	64	26	HNLC
Tropical & Subtropical Oceans						
1	IronEx-1 (Oct 1993)	5°S, 90°W	0.06	64	10	HNLC
2	IronEx-2 (May 1995)	3.5°S, 104°W	0.02	72	17	HNLC
13	FeeP (Apr–May 2004)	27.5°N, 22.5°W	0.20–0.40	25	21	LNLC

declining fisheries. In summary, good science does not cause harm testing unproven technologies, see Figure 14.3.

Table 14.3: Selected iron-fertilization (OIF) activities, proposals, and planning efforts (2020–2025). No authorized large-scale open-ocean Fe additions have occurred since the 2009 LOHAFEX experiment.

Type	Project / Group	Location	Start	Status (2025)	Notes
Planned OIF (not executed)	ExOIS (Exploring Ocean Iron Solutions) proposed large-scale OIF trial	NE Pacific, near OSP (Ocean Station Papa)	2022–2025 planning	**Planned** (not permitted)	Modern, heavily monitored OIF experiment (up to 10^4 km^2). Requires London Protocol permitting. No Fe added as of 2025.
Planned small-scale Fe additions	Independent university-led micro-OIF studies (e.g., Fe-limited mesocosms)	Coastal NE Pacific / subarctic Pacific	2023–2025	**In preparation**	Shipboard and mesocosm Fe-dosing experiments for physiology; *not* open-ocean fertilization. No patch-scale Fe release.
Concept development / feasibility only	Ocean Nourishment Foundation (renewed proposals)	Western Pacific	2020–2025	**Concept only**	The group has periodically proposed Fe-urea additions since the 2000s; no permitted or executed trials in 2020–2025. Widely rejected by scientists/regulators.
Unpermitted / commercial claims	Eco-restoration / carbon-credit start-ups (various)	Global oceans (claimed)	2021–2025	**No verified Fe trials**	Several start-ups made vague claims about nutrient additions, but no documented or permitted Fe-fertilization events occurred. Regulators watch these closely.
Geopolitical / unauthorized	No documented rogue Fe-fertilization additions (postHaida 2012)	—	2013–2025	**None confirmed**	After the 2012 Haida salmon-boosting Fe dump, no comparable unauthorized large-scale Fe additions have been verified. London Protocol decisions tightened controls.

In my view, commercial iron/phosphate fertilization of the fragile ecosystems of the Southern Ocean should not be pursued, given the risk of disrupting and damaging one of the planet's most important natural carbon-sequestration regions. As we show below, the Arctic is not iron-limited, and there are many additional reasons to avoid haphazard or illegal iron dumps aimed at boosting fishery yields. I have little confidence that such commercial attempts will not recur in the future, with potentially severe consequences, see the last column in Table 14.3.

Because all first-generation experiments were carried out between 1993 and 2009, most of the seminal papers cited in the next two sections date from that period. Please do not treat them as old news.

14.3.3 Iron fertilization of the Southern Ocean

Martin's core physical insight was sound. Large parts of the Southern Ocean, the equatorial Pacific, and the subarctic North Pacific are high-nutrient, low-chlorophyll (HNLC) regions: macronutrients such as nitrate and phosphate are abundant, but phytoplankton biomass is suppressed because of a chronic shortage of bioavailable iron. In such regions, adding traces of dissolved iron can trigger striking phytoplankton blooms.

Over the last three decades, a series of purposeful iron-addition experiments in the Southern Ocean—including SOIREE, SOFeX, EIFEX, and LOHAFEX—have confirmed that iron is indeed the proximate limiting nutrient there (*Boyd et al.*, 2007, *Watson et al.*, 2008b, *Wallace et al.*, 2010). Within days of fertilization, surface chlorophyll often increases by factors of three to ten, surface CO_2 partial pressure declines, and export fluxes of particulate organic carbon are measurably enhanced. At first glance, this appears to validate Martin's vision: add iron, grow plankton, pull down atmospheric CO_2.

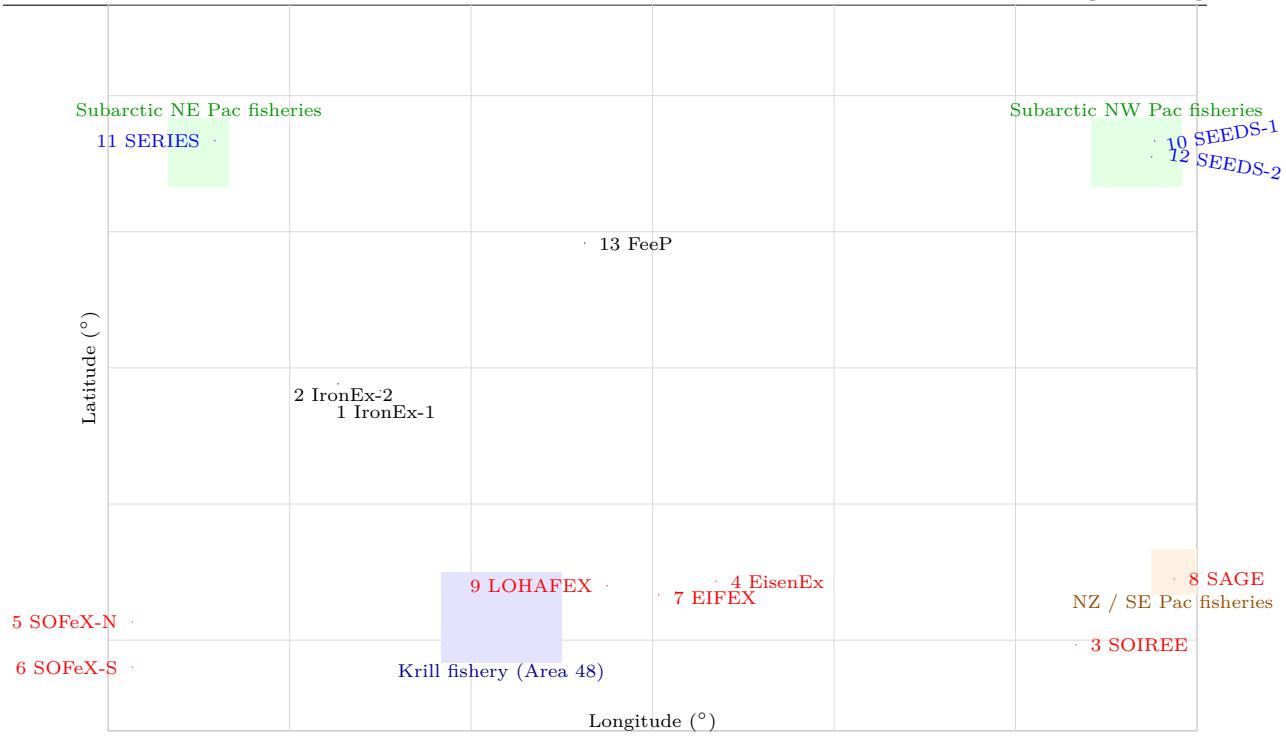

Figure 14.3: Schematic locations of major open-ocean iron-fertilization experiments (1993–2009) and broad regions of intense or sensitive fisheries (shaded). Coordinates are approximate; map is not to scale.

However, closer analysis shows that the net climate benefit of large-scale Southern Ocean iron fertilization would be modest, uncertain, and accompanied by significant ecological and governance risks (*Buesseler et al.*, 2008, *Boyd et al.*, 2000). Only a small fraction of the additional organic matter produced in fertilized patches actually sinks below the depth of winter mixing or the main thermocline, where the associated carbon would be sequestered from contact with the atmosphere for centuries. Most of the bloom is grazed by zooplankton or respired by microbes in the upper few hundred meters, returning CO_2 to waters that re-equilibrate with the atmosphere on decadal timescales.

Figure 14.4 schematically compares the natural and iron-fertilized biological pumps in the Southern Ocean. In the unfertilized state (left), primary production is limited by low iron supply, and the biological pump exports only a modest flux of organic carbon into the twilight zone. When iron is added (right), the surface bloom intensifies and export increases, but only a small fraction of this additional flux penetrates to depth. The ratio of *permanently* sequestered carbon to iron added turns out to be much smaller than early back-of-the-envelope estimates suggested.

In addition, iron fertilization does not act in isolation. It changes the species composition of phytoplankton communities, with a tendency to favor large diatoms and, in some circumstances, even harmful or toxic taxa (*Boyd et al.*, 2000). It perturbs food webs, alters biogeochemical cycling of nitrogen, phosphorus, and silica, and may enhance production of nitrous oxide, a potent greenhouse gas, in subsurface waters.

Because the Southern Ocean plays a central role in ventilating the global deep ocean and setting the planetary inventory of dissolved inorganic carbon, large-scale geoengineering there would amount to a risky experiment on one of Earth's primary climate control systems.

From a purely physical standpoint, the Southern Ocean is the *best-case* region for iron-based carbon removal: it is genuinely iron-limited, and iron addition reliably produces large blooms. Yet even under these favorable conditions, the net climate leverage is weak once ecological feedbacks, partial remineralization, and century-scale storage requirements are taken into account. In the Arctic (Section 14.3.4), where light and stratification—not iron—limit productivity, iron seeding fails even more completely.

The lesson is clear: tinkering with micronutrient supply to the ocean cannot substitute for rapid reductions in fossil fuel combustion and land-use emissions.

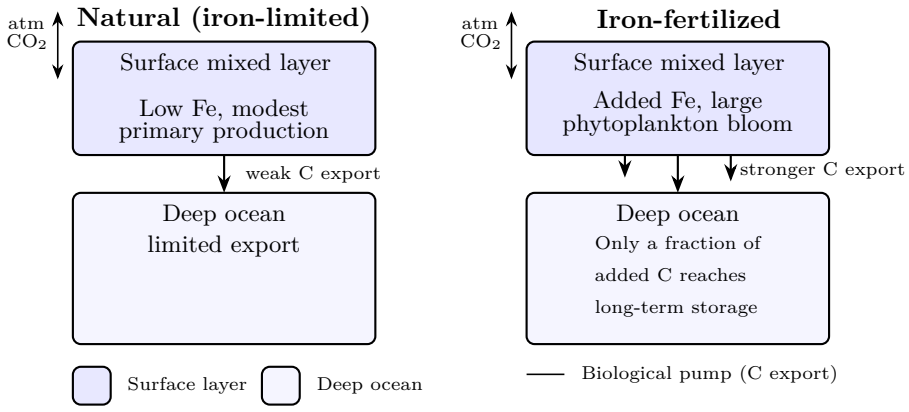

Figure 14.4: Schematic comparison of the natural (iron-limited) and iron-fertilized biological pump in the Southern Ocean. In the natural state (left), low iron availability limits phytoplankton growth and carbon export. Iron addition (right) stimulates a large surface bloom and increases export, but only a fraction of the additional organic carbon is transported to depths where it would be sequestered from the atmosphere for centuries.

14.3.4 Iron Fertilization and the Arctic Ocean

In contrast to the Southern Ocean (Section 14.3.3), the Arctic Ocean is a *poor* candidate for deliberate iron fertilization. Although the basic idea is the same—stimulate phytoplankton blooms by adding dissolved iron and enhance the biological pump—the controlling physical and biogeochemical constraints in the Arctic make meaningful CO_2 sequestration highly unlikely.

The conceptual basis of iron fertilization rests on two linked elements. First, in high-nutrient, low-chlorophyll (HNLC) regions such as the Southern Ocean and parts of the equatorial Pacific and subarctic North Pacific, macronutrients (nitrate, phosphate, silicate) are abundant while bioavailable iron is scarce, so modest iron additions can trigger large phytoplankton blooms (*Martin*, 1990, *Boyd et al.*, 2007, *Moore et al.*, 2013). Second, for such blooms to actually remove CO_2 from the atmosphere, a non-trivial fraction of the newly fixed organic carbon must sink below the main thermocline and be stored in the deep ocean for centuries. This is the so-called biological gravitational pump (BGP): phytoplankton fix carbon, some of it is packaged into fast-sinking particles, and a small fraction escapes remineralization in the upper ocean (*Buesseler et al.*, 2008, *Boyd et al.*, 2000, 2019). Even in ideal HNLC settings, artificial stimulation of the pump has proven to be weak and inefficient; in the Arctic it is weaker still.

The Arctic is not iron-limited

Unlike classic HNLC regions, the Arctic Ocean is *not* generally iron-limited. Observations and modeling studies indicate that Arctic phytoplankton are primarily constrained by light availability, stratification, and seasonal macronutrient depletion, rather than trace-metal scarcity (*Arrigo*, 2015, *Wassmann and Reigstad*, 2011, *Popova et al.*, 2012). For much of the year the high latitudes experience low sun angles, long periods of darkness, and extensive sea-ice cover, all of which severely limit light for photosynthesis. During the brief melt season, sea-ice retreat and freshwater input from rivers and ice melt strengthen the halocline[6], capping the surface layer and restricting vertical nutrient supply.

As a result, Arctic productivity tends to peak in a short window of two to three months, when light is abundant and macronutrients have not yet been exhausted. Once the initial bloom has stripped the surface layer of nitrate and phosphate, productivity declines rapidly (*Arrigo*, 2015). Adding iron does not

[6] Halocline: A vertical layer in the ocean where salinity changes rapidly with depth, producing a strong salinity gradient that contributes to density stratification and inhibits vertical mixing.

relax these seasonal and physical constraints; it cannot create light in polar night, nor can it overcome the strong stratification that isolates the surface from deeper nutrient reservoirs.

Short growing seasons and weak export

Even during the productive season, the Arctic biological pump is relatively inefficient. Most of the organic matter produced in surface blooms is rapidly consumed by zooplankton or remineralized by bacteria within the shallow mixed layer. Only a small fraction—on the order of a few percent—is exported to depths where it could contribute to long-term carbon storage (*Wassmann and Reigstad*, 2011, *Huffard et al.*, 2020). In shelf regions, much of the production is recycled locally over sediments rather than exported into the deep basins.

In contrast to the Southern Ocean, where iron fertilization experiments have at least demonstrated enhanced particle fluxes below the sun-lit interval (*Buesseler et al.*, 2008), there is no compelling evidence that artificial iron inputs in the Arctic would significantly increase export to depths that matter on century timescales. The short growing season, strong stratification, and efficient upper-ocean recycling combine to suppress deep sequestration.

Stratification, hypoxia, and methane risk

The Arctic halocline—maintained by river discharge, sea-ice melt, and low-salinity surface waters—is among the strongest on the planet (*Aagaard and Carmack*, 1989). This density structure inhibits vertical mixing and limits the penetration of sinking particles. Organic matter that does reach subsurface or benthic layers is often remineralized in relatively shallow, poorly ventilated waters. Artificially enhancing surface productivity in such settings risks intensifying oxygen consumption and promoting local hypoxia, with adverse consequences for benthic ecosystems (*Wassmann and Reigstad*, 2011).

On Arctic shelves, additional deposition of organic matter into sediments could also stimulate methanogenesis and increase methane fluxes to the water column and atmosphere. Given methane's high global warming potential on decadal timescales, any such enhancement would erode or even reverse whatever small climate benefit iron-induced CO_2 drawdown might achieve (*Shakhova et al.*, 2010a).

Ecosystem disruption and harmful blooms

Iron is not a neutral addition to the Arctic marine environment. As in other regions, it would alter phytoplankton community composition, favoring taxa best able to exploit pulses of micronutrients, such as certain diatoms (*Boyd et al.*, 2000, *Moore et al.*, 2013). In some cases iron enrichment has been associated with the proliferation of *Pseudonitzschia*, a toxic diatom genus capable of producing domoic acid toxin, with implications for higher trophic levels and human health (*Harðardóttir et al.*, 2015). As shown in Appendix E, the Arctic marine ecosystem is already under intense pressure from rapid warming, sea-ice loss, ocean acidification, and shifting species distributions; adding large-scale, deliberate micronutrient perturbations would add another layer of stress and uncertainty.

Moreover, enhanced recycling in the microbial loop, rather than increased export, is a likely outcome of additional organic matter production under strong stratification. This would further weaken the link between surface blooms and deep-ocean carbon storage.

Low efficiency and governance concerns

Experience from Southern Ocean and subarctic iron-addition experiments suggests that for each ton of iron added, only tens of tons of CO_2 are taken up biologically in the fertilized patch. Published analyses of Southern Ocean and subarctic iron-addition experiments indicate that only a small fraction—typically of order 1–10%—of the biologically fixed carbon in the fertilized patch is exported below the depth of winter mixing (*Boyd et al.*, 2007, *Buesseler et al.*, 2008, *Boyd et al.*, 2000).

Suppose that 50 t of CO_2 are taken up per tonne of iron added, noting that the biogeochemically active iron in $FeSO_4{\cdot}7H_2O$ is only ∼20% by mass. Even assuming optimistically that 10% of this CO_2 is sequestered for more than a century, only $50 \times 0.1 = 5$ t of CO_2 would be stored per 5 t of

iron sulfate deployed. Thus, sequestering **1 Gt** of CO_2 would require **1 Gt** of iron sulfate spread over the the high latitude, vulnerable oceans.

Reliable – and just defunded – US government sources (*USGS, National Minerals Information Center*, 2025b,a, *U.S. EPA*, 2022a) indicate that global production of iron sulfate is only a few million tonnes per year, whereas market reports place total consumption at $\sim$10 Mt yr^{-1}. Therefore, the material requirement for large-scale ocean iron fertilization exceeds current global supply by a factor of **about 100**—the difference between running at 8 km h^{-1} and flying at 800 km h^{-1}.

Given that the Arctic is not iron-limited and is subject to stronger physical constraints on export, any realistic sequestration efficiency there would be lower still.

In addition to biophysical limitations, Arctic iron fertilization raises serious governance and ethical issues. Ocean fertilization activities are subject to regulation under the London Convention and its 1996 Protocol, which restrict large-scale iron addition to legitimate scientific research under strict permitting and oversight (*GESAMP*, 2019, *Strong et al.*, 2009). The Arctic Ocean is bordered by multiple coastal states, indigenous communities, and competing geopolitical interests; unilateral geoengineering interventions there would almost certainly be contentious. Framing iron seeding as a climate solution risks encouraging moral hazard by suggesting that continued high fossil fuel use can be offset by speculative, high-risk interventions in one of Earth's most fragile marine environments.

Summary: iron fertilization is a dead end in the Arctic

Taken together, the physical, biogeochemical, ecological, and legal arguments against Arctic iron fertilization are compelling. The region is not iron-limited; its primary productivity is constrained by light, stratification, and seasonal macronutrient exhaustion. The biological pump is weak and shallow, with minimal export to depths where carbon can be stored on climate-relevant timescales. Enhanced production risks local hypoxia, altered food webs, and increased methane emissions from sediments. Governance frameworks already recognize these risks and substantially limit ocean fertilization activities.

If the Southern Ocean represents the best-case scenario for iron-based carbon removal, the Arctic represents something close to the worst case. In both regions, and especially in the Arctic, iron seeding offers negligible CO_2 removal at the cost of significant ecological and political risk. It cannot substitute for the only robust strategy we possess: rapid, sustained reductions in anthropogenic greenhouse gas emissions at their sources.

Regardless of the scientific arguments presented above, any commercial attempt at large-scale ocean fertilization will run headlong into a fundamental constraint: the severely limited global supply of iron sulfate heptahydrate.

14.4 Direct CO_2 capture from air (DAC)

Like the earlier designs for perpetuum mobile machines, contemporary DAC technologies are a valiant – but ultimately futile – attempt to sidestep the Second Law of Thermodynamics.

All DAC technologies attempt the same fundamentally difficult task: to separate (*unmix*) a trace gas component with a molar fraction of only 0.0042 from a mixture dominated by nitrogen and oxygen. As Sir Eddington explained long ago, the true thermodynamic cost of unmixing is inevitably large, because each mole of separated CO_2 carries a substantial entropy[7] penalty. The Second Law of Thermodynamics is unequivocal: *no invention* in the Universe can eliminate this cost.

In 2007, while returning from a Ministerial OECD meeting in Paris, I found myself sitting next to a young government lawyer who accompanied Ms Paula Dobriansky, Under Secretary of State for Global Affairs and chief US climate negotiator at the time. The meeting had examined the real ecological costs

[7] If you want to learn more about the Entropy Law, please read Part I of the fascinating book by *Penrose* (2010).

of biofuels, and he had seen my rather unsettling presentation. At one point he remarked, with complete confidence: "Best entrepreneurs can always invent something that circumvents the laws of physics." In his view, just as a skilled lawyer can outmaneuver human law, a clever inventor could simply bypass the laws of nature. It took me a few hours to explain to the young man the cruel Laws of Nature—a realm that admits no exceptions whatsoever, where the Entropy Law reigns supreme—and I remain unconvinced that he ever accepted the lesson.

In total, only four DAC plants worldwide currently operate at or above the 1,000 $t_{CO_2}\,yr^{-1}$ scale, all located in Iceland and the United States, while more than 100 large-scale projects remain at the planning or construction stage (*International Energy Agency*, 2025b, *Energy Futures Initiative Foundation*, 2024). Two large DAC systems, Orca and Mammoth, operate in Iceland, and two much smaller ones operate in the United States, in Colorado and California (see Table 14.4).

Let us consider what would have to occur if DAC machines were actually capable of capturing *just* 5 Gt $CO_2\,yr^{-1}$ from the 18 Gt annual excess of anthropogenic CO_2 that accumulates in the atmosphere, raising its average molar fraction by roughly $2.3 - 2.5\ ppm_v\,yr^{-1}$. Annual anthropogenic emissions are about 40,000 Mt_{CO_2}, roughly *seven orders of magnitude larger* than the capacity (not the realized performance) of the largest DAC installation on Earth, the Mammoth plant. The annual accumulation of CO_2 in the atmosphere is approximately 18,000 Mt (see Figure 3.7). To offset just 27% of this annual accumulation, the world would need roughly 150,000 Mammoth-scale DAC machines operating continuously at their full nameplate capacity, and we would have to sequester those 5 billion tonnes of captured CO_2 every year.

At a compressed CO_2 pressure of 150 bar, a typical geothermal gradient of 30 °C km^{-1}, and an injection depth of 1.5 km (giving a downhole CO_2 temperature of about 70 °C), the density of supercritical CO_2 is roughly 350 $kg\,m^{-3}$. Thus, under representative subsurface conditions, we would have to inject an annual supercritical CO_2 volume of

$$\frac{5 \times 10^{12}\ \text{kg}}{350\ \text{kg}\,\text{m}^{-3}} \approx 1.45 \times 10^{10}\ \text{m}^3 \approx 9 \times 10^{10}\ \text{reservoir barrels.}$$

For comparison, global crude oil production in 2024 was about 30 billion stock-tank[8] barrels per year. Across major petroleum provinces (Middle East, North America, Russia, West Africa, Latin America), reservoir-engineering data show a mean oil formation volume[9] factor of ~ 1.3, implying an annual withdrawal of roughly 40 billion reservoir barrels. In other words, capturing and storing the annual CO_2 buildup in the atmosphere would require injecting *twice the downhole volume of all crude oil produced globally each year* as supercritical CO_2.

This is not merely impractical – it is impossible by a factor of 100–1000.

The giant DAC toys provide a convenient illusion of progress, soothing an apathetic, mostly clueless public in affluent countries into believing that "technology will save us," while doing essentially nothing to address the actual emissions problem.

14.4.1 Minimum reversible work to separate CO_2 from air

In an isothermal, isobaric ideal-gas mixture, the minimum reversible work required to separate a dilute component from an ideal mixture is equal to the decrease in Gibbs free energy associated with unmixing. For CO_2 in air with mole fraction $x_{CO_2} \approx 420\ ppm_v = 4.2 \times 10^{-4}$, the minimum work per mole of CO_2 to obtain pure CO_2 at the same total pressure is(*Krekel et al.*, 2018, *House et al.*, 2011, *Sanz-Pérez et al.*, 2016)

$$w_{\min} = RT \ln\left(\frac{1}{x_{CO_2}}\right), \tag{14.2}$$

[8]Stock-tank conditions refer to standard surface conditions of pressure and temperature (typically 1 atm and 60 °F or 15.6 °C) at which crude oil volumes are measured after gas has been liberated and the fluid has stabilized.

[9]The oil formation volume factor B_o is the ratio of the volume of crude oil at reservoir conditions (pressure and temperature) to its corresponding stock-tank volume at standard surface conditions.

Table 14.4: Operating DAC plants with nameplate capacity $\geq 1{,}000\ t_{CO_2}\ yr^{-1}$ as of 2025. Capacities are nominal.

Operator / Plant	Country	Location	Capacity $t\,yr^{-1}$	Start	Notes
Climeworks *Mammoth*	Iceland	Hellisheiði (near Reykjavík)	36,000	2024	Second commercial Climeworks plant; powered by geothermal energy; designed as modular units.(*Climeworks AG*, 2024)
Climeworks *Orca*	Iceland	Hellisheiði (near Reykjavík)	4,000	2021	First commercial DAC+storage plant; partnered with Carbfix for in situ mineralization of CO_2.(*Birnbaum*, 2021, *Climeworks AG*, 2024)
Heirloom Tracy facility	United States	Tracy, California	1,000	2023	First commercial Heirloom plant; limestone-based DAC with storage in concrete products.(*Heirloom*, 2023)
Global Thermostat Commerce City plant	United States	Commerce City / Denver area, Colorado	$\gtrsim 1{,}000$	2022	Commercial-scale demonstration unit at company HQ; amine-based DAC for testing and offtake partnerships.(*Global Thermostat*, 2023, *Sumitomo*, 2023)

where R is the universal gas constant and T is the absolute temperature. Evaluated at $T = 298$ K and $x_{CO_2} = 4.2 \times 10^{-4}$,

$$w_{\min} = \left(8.314\ \mathrm{J\,mol^{-1}\,K^{-1}}\right)(298\ \mathrm{K}) \ln\left(\frac{1}{4.2 \times 10^{-4}}\right) \tag{14.3}$$

$$\approx 1.9 \times 10^{4}\ \mathrm{J\,mol_{CO_2}^{-1}} \;=\; 19\ \mathrm{kJ\,mol_{CO_2}^{-1}}. \tag{14.4}$$

On a per-tonne basis,

$$w_{\min} \;\approx\; 0.44\ \mathrm{GJ\,t_{CO_2}^{-1}} \;\approx\; 120\ \mathrm{kWh\,t_{CO_2}^{-1}}. \tag{14.5}$$

This value represents the *absolute thermodynamic minimum* for separating very, very slowly ~420 ppm_v CO_2 from air at constant temperature into a pure CO_2 stream at the same pressure.

14.4.2 Real work of direct CO_2 capture

Real direct-air-capture systems necessarily consume substantially more energy than this ideal minimum because of finite driving forces, irreversibilities, sorbent regeneration, non-isothermal compression, and other process losses. Contemporary engineering analyses of chemical-sorbent DAC technologies report that separation alone typically requires 3–7 $\mathrm{GJ\,t_{CO_2}^{-1}}$ of low-grade heat (for sorbent regeneration) and 0.5–1.5 $\mathrm{GJ\,t_{CO_2}^{-1}}$ of electricity (for fans, pumps, and controls), with total process energy commonly in the range 4–9 $\mathrm{GJ\,t_{CO_2}^{-1}}$ (*House et al.*, 2011, *Sanz-Pérez et al.*, 2016, *Krekel et al.*, 2018). Further compression of the captured CO_2 to pipeline or sequestration pressures (100–150 bar) requires an additional 0.4–0.8 $\mathrm{GJ\,t_{CO_2}^{-1}}$ of electricity. Taken together, present DAC systems therefore demand approximately 5–10 $\mathrm{GJ\,t_{CO_2}^{-1}}$ of useful energy[10] (Table 14.5), corresponding to roughly a factor of 10 ± 5 above the reversible separation limit.

The giant, cityblock-sized DAC machines (Figure 14.5), must operate continuously and – outside of Iceland or Norway – are powered largely by thermal power plants whose average thermal efficiency is

[10]The thermodynamic minimum of 0.44 $\mathrm{GJ\,t^{-1}}$ reflects the *exergy* required to reverse the entropy of mixing of dilute CO_2 in air. Real systems require far more because heat at ~ 100–900 °C has lower exergy content than electricity, and because all practical devices operate with finite driving forces and irreversible losses.

Table 14.5: Representative energy requirements for direct-air-capture (DAC) systems based on published engineering analyses. All values in $\mathrm{GJ\,t_{CO_2}^{-1}}$.

Energy Component	Typical Range	Dominant Use	Representative Sources
Heat for sorbent regeneration	3–7	Amine/carbamate or carbonate cycle regeneration	(*House et al.*, 2011, *Sanz-Pérez et al.*, 2016)
Electricity for fans & pumps	0.5–1.5	Moving ∼20,000 m^3 air per tonne CO_2	(*House et al.*, 2011, *Krekel et al.*, 2018)
Electricity for CO_2 compression	0.4–0.8	Compression to 100–150 bar for transport/storage	(*House et al.*, 2011)
Total practical energy	5–10	Combined heat + electricity	(*House et al.*, 2011, *Krekel et al.*, 2018, *Sanz-Pérez et al.*, 2016)

Figure 14.5: Climeworks, a Swiss company specializing in solid-sorbent direct air capture (DAC), has developed and operated a sequence of progressively larger plants in Europe and Iceland. In 2021 the company commissioned *Orca* in Iceland, the first industrial-scale DAC plant, with a nominal capacity of 4,000 $\mathrm{t_{CO_2}\,yr^{-1}}$, powered by geothermal heat and electricity. This was followed in 2023-2024 by *Mammoth*, also in Iceland, designed as a modular array of twelve containerized DAC units with a projected capacity of 36,000 $\mathrm{t_{CO_2}\,yr^{-1}}$ once fully operational (*Climeworks AG*, 2024). The company has announced plans for future hundred-thousand-tonne-scale facilities later in the 2020s, but as of 2025 its operating plants collectively capture well under 50,000 $\mathrm{t_{CO_2}\,yr^{-1}}$ – orders of magnitude below what would be required for any meaningful contribution to global carbon-removal targets. Image source: Climeworks, 2022.

∼ 38% (*Bolson et al.*, 2022a). Converting the electrical requirements of DAC to a primary-energy basis therefore yields

$$3\text{–}7 \;+\; \frac{0.5\text{–}1.5}{0.38} \;+\; \frac{0.4\text{–}0.8}{0.38} \;\approx\; 5.4\text{–}13\ \mathrm{GJ\,t_{CO_2}^{-1}}.$$

Given that the average high heating value of coal is 29 $\mathrm{GJ\,t^{-1}}$ (*Patzek and Croft*, 2010), capturing one tonne of CO_2 requires the combustion of approximately

$$\frac{5.4\text{–}13}{29} \;\times\; 1000\ \mathrm{kg} \;=\; 185\text{–}450\ \mathrm{kg}$$

of coal, which emits an additional 690–1650 kg of CO_2.[11]

Current estimates place the cost of direct air capture in the range of \$600–\$1,200 USD $t_{CO_2}^{-1}$ for commercially deployed plants, depending on energy prices, sorbent chemistry, and capital intensity (*National Academies of Sciences, Engineering, and Medicine*, 2019, *Keith et al.*, 2018, *Fasihi et al.*, 2019). Even under optimistic future learning rates, most techno-economic analyses project long-term costs of \$200–\$400 USD $t_{CO_2}^{-1}$, assuming abundant low-carbon heat and electricity and large-scale manufacturing and deployment (*IPCC*, 2022a). A substantial fraction of total cost arises from energy demand: present DAC systems require 5–13 GJ $t_{CO_2}^{-1}$ of primary energy, which strongly couples cost to the price of zero-carbon power (that is generally unavailable at scale and continuously).

We leave it to the reader to judge whether such material-intensive, very expensive, continuously operated DAC machines make any climatic or energetic sense whatsoever. Remember that ignoring the Second Law of Thermodynamics can only end in the deepest humiliation.

14.5 Stratospheric sulfur injection: Arguments for and against

Stratospheric sulfur injection (SSI) is the most widely discussed form of solar radiation management (SRM). The basic idea is to inject sulfur-containing gases (typically SO_2) into the lower stratosphere, where they oxidize to form sulfate aerosols that increase planetary albedo and cool the surface. The proposal is motivated by observations of major volcanic eruptions such as Mount Pinatubo in 1991 (Figure 14.6), which produced a short-lived global cooling of about 0.5 °C (*McCormick et al.*, 1995, *Robock*, 2000).

Stratospheric sulfate injection might cool the planet, but it would do so by creating a dangerous new climate deregulation that ordinary people would feel directly. First, SSI would shift rainfall patterns on a continental scale, worsening droughts in some regions and intensifying floods in others, with severe consequences for food and water security. Second, by thinning parts of the ozone layer, SSI would increase harmful ultraviolet radiation at the surface, raising rates of skin cancer and cataracts and damaging crops and marine life. Third, SSI requires continuous operation: if it were halted abruptly, global temperatures would rebound in just a few years, producing a shock far faster than societies or ecosystems could withstand. In short, SSI trades one problem for three that strike at human health, food, and basic safety. Even Faust, in the end, did not escape his bargain.

The Second Law of Thermodynamics says that you can never get something for nothing. Any time you try to "unmix" things, clean things up, or make them more or *differently* organized—whether it's separating CO_2 from air, desalinating water, injecting sulfur into the stratosphere, charging a battery, or running a machine—you must spend energy, and you always waste some (usually most) of it as heat. Nature can only run backwards at a very high cost of entropy export and creation of disorder (trash, toxic waste, pollution) elsewhere. You cannot trick Nature, negotiate with it, or lawyer your way around it. The Second Law is the Universe's non-negotiable rule that all clean-up, concentration, and ordering takes real work, and always creates excessive mess somewhere else. So, my friends, cutting CO_2 emissions rapidly and deeply is the only path forward. There is no loophole, no clever workaround, and no way to weasel out of this requirement if we are to stabilize—let alone lower—the mean temperature of the world.

14.5.1 Arguments in favor

- **High radiative efficiency.** Sulfate aerosols in the stratosphere scatter incoming solar radiation effectively. Model studies show that a sustained injection of several teragrams of sulfur per year could offset a substantial fraction of anthropogenic warming (*Kravitz et al.*, 2015).
- **Fast climatic response.** Unlike mitigation or CO_2 removal, which act over decades to centuries, SSI produces measurable cooling within months. This rapid response is often cited as a potential emergency measure in the event of extreme warming or abrupt climate impacts.

[11] Assuming 2.3–2.5 $t_{CO_2}\, t_{coal}^{-1}$, depending on carbon content and combustion efficiency.

Figure 14.6: The 1991 eruption of Mount Pinatubo in the Philippines was the largest volcanic event of the twentieth century and injected roughly 17–20 Tg of SO_2 into the lower stratosphere (*McCormick et al.*, 1995, *Robock*, 2000). Oxidation of this SO_2 formed a global veil of sulfate aerosols that increased planetary albedo and produced a transient ∼0.4–0.6 °C drop in global mean surface temperature during 1992–1993, alongside marked reductions in incoming shortwave radiation. The aerosols also warmed the lower stratosphere, perturbed atmospheric circulation, and accelerated heterogeneous chemical reactions that depleted ozone, especially at high latitudes. The Pinatubo eruption remains the most informative natural analogue for stratospheric aerosol injection, offering real-world constraints on radiative forcing, aerosol microphysics, and the climatic side effects of large sulfate perturbations. Image source: USGS Archives.

- **Low direct material cost.** The sulfur mass required is modest compared to industrial sulfur production, and lofting it into the stratosphere would require tens to hundreds of aircraft – not impossible for current aerospace technology (*Smith and Wagner*, 2020).
- **Analogous natural precedents.** Large volcanic eruptions demonstrate both the feasibility of aerosol formation and the radiative effect, providing a partial empirical basis for model validation.

14.5.2 Arguments against

- **Does not address the root cause.** SSI does nothing to reduce atmospheric CO_2; ocean acidification, ecosystem stress, and long-term warming from accumulated greenhouse gases remain unmitigated (*Royal Society*, 2009, *IPCC*, 2022a).
- **Uneven regional climate effects.** Climate models consistently show non-uniform changes in precipitation, monsoons, and circulation patterns. Some regions become drier or wetter in ways that cannot be globally optimized, raising issues of inequity and geopolitical conflict (*Kravitz et al.*, 2015, *MacMartin and Keith*, 2019).
- **Termination shock.** If SSI were abruptly stopped while greenhouse gases remain high, global temperatures would rapidly rebound to the unmasked warming trajectory within a few years, causing extreme impacts (*Matthews et al.*, 2014), like cutting off drug supply from a heroine addict.
- **Stratospheric chemistry risks.** Sulfate aerosols enhance heterogeneous chemical reactions that deplete stratospheric ozone, particularly in polar regions, delaying ozone recovery (*Tilmes et al.*, 2008).

- **Stratospheric heating and circulation changes.** Absorption of infrared and near-infrared radiation by sulfate aerosols warms the lower stratosphere and can alter the Brewer-Dobson circulation[12], with uncertain dynamical consequences.
- **Governance and moral hazard.** SSI would constitute a planetary-scale intervention with no precedent in international law. The prospect of a technological "fix" may reduce the political will for emission reductions (*Reynolds*, 2019).
- **Annual commitment.** Because stratospheric aerosols fall out on a timescale of 1–2 years, SSI would require permanent annual injections for as long as greenhouse gas concentrations remain elevated, that is for decades or centuries.

In summary, while stratospheric sulfur injection could rapidly cool the planet, the technique introduces serious physical, chemical, social, and political risks.

Stratospheric sulfur injection may temporarily mask warming, but it cannot replace deep reductions in greenhouse-gas emissions and sustained efforts to restore Earth's energy balance.

14.6 Conclusion

Writing this chapter, I found myself imagining the industrialized world – *us* – as a terminal drug addict: out of usable veins, unable or unwilling to pause and confront the consequences of *our* own dependence, yet still desperate enough to rob the poor and the weak to satisfy our insatiable thirst for fossil power and for resources from every corner of Earth. What we need now is a giant dose of environmental Methadone to wake up before we destroy ourselves – and to allow others to live.

Then come the inevitable *what if* questions posed at the level of commanders, not the foot soldiers (graduate students, postdocs) who march as they are told: *What if* ocean iron fertilization were never truly about CO_2 sequestration, but instead – often illegally – about reviving collapsing fisheries in the Southern Ocean and off Newfoundland? *What if* direct air capture were less a climate solution than a "green" alibi for major emitters, a convenient palliative that reassures affluent publics while masking runaway costs? *What if* SO_2 injection into the stratosphere became the last-ditch maneuver of the super-polluting nations to shield their own territories, all while imposing severe collateral damage on their citizens and neighbors? The current posture of the U.S. government suggests that these questions merit serious, and perhaps unsettling, answers.

I am not alone in my scepticism towards geoengineering. In the past, the JASON group—the elite scientific advisory panel founded in 1960 to advise the U.S. national-security establishment—intersected with climate science in several important ways. Beginning in the late 1970s, JASON produced some of the earliest rigorous assessments of CO_2-driven global warming, parallel to the Charney Report, and later issued influential analyses of climate sensitivity, sealevel rise, and the risks of abrupt climate change. During the 1990s and 2000s, JASON reports evaluated the feasibility and strategic implications of geoengineering approaches such as stratospheric sulfate injection and ocean fertilization, and helped shape U.S. climate-monitoring programs, including satellite altimetry and ocean-observing systems. (Remember the TOPEX/Poseidon program and Jason-1, Jason-2 satellites described in Chapter 12?) They assessed physical plausibility, strategic risks, and potential weaponization of geoengineering. Their reports significantly influenced U.S. government caution around geoengineering. In short, JASON served as a quiet bridge between cutting-edge climate science and the national-security community. I first intersected with the JASON group in the early 2000s, when Dr. Steven Koonin, then its director, invited me to brief them on biofuels.

[12]The *Brewer–Dobson circulation* is the large-scale meridional overturning flow in the stratosphere, characterized by tropical upwelling, poleward transport in the upper stratosphere, and subsidence in the extratropics (23.5°–66.5° latitude. It is driven primarily by the breaking and dissipation of planetary-scale waves and controls the global distribution and lifetime of stratospheric trace gases, including ozone and long-lived greenhouse gases.

Chapter 15

Epilogue

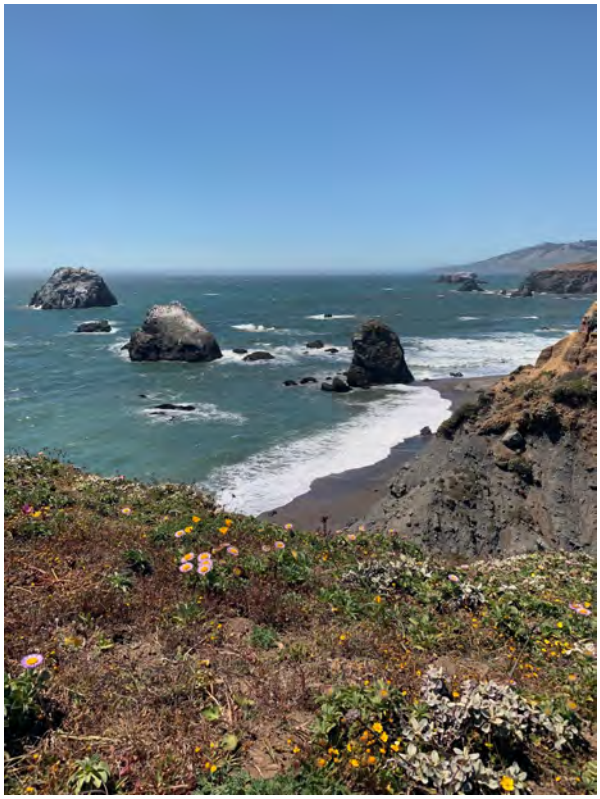

Our beloved Pacific coast near Mammoth Rock in California, and a community concert in Half Moon Bay, a small coastal town south of San Francisco, California.
Photos by T.W. Patzek, June and August 2025.

Wouldn't you be willing to change – just a little – to protect the places you love and ensure your family and friends can thrive?
Tad Patzek, 2025

After two decades of writing and speaking about the unfolding environmental catastrophe we have brought upon ourselves through brazen myopia and greed, I am fully aware that this book will be dismissed by many as catastrophic naysaying or undue pessimism. The key reason is that the Fossil Amoeba – the technological-human system that shapes our perceptions and clouds our judgment (enframes us) – insists that the only acceptable message must be one of hope, carefully crafted to anesthetize, not awaken. Hope fosters complacency and inaction, ensuring that the status quo continues undisturbed.

To set the stage with conclusions rather than postpone them, consider the following blunt summary – tinged with cautious hope. It was generated by DeepSeek in response to a question about the future trajectories of our global system (*Aramburu*, 2025). Both DeepSeek and ChatGPT have been trained on nearly the entire corpus of publicly available human knowledge and are designed to draw reasoned inferences from it. And reason they did:

> The collapse of the current [global economic] model is inevitable, but humanity will not vanish. It will be a painful journey toward simpler, more localized systems. The question is **not** whether this transformation will occur, but **how** we choose to navigate it – to reduce suffering and plant the seeds of a post-growth world.

A key conclusion of this book is that global climate change, compounded by growing resource limitations, will be the dominant force behind the eventual collapse of our current global system.

Digging deeper and assuming you have read most of this book and absorbed its key, interlinked figures and tables, you have likely come to the realization that the breakdown of the current climate regime is the most complex and deeply interconnected set of processes within Earth's delicately balanced system. Most of the planet's natural checks and balances – including multiscale negative feedbacks and the stability manifolds that restrict climate and ecosystem control parameters – have now been violated or disrupted. Unsurprisingly, the current climate trajectory is becoming increasingly chaotic and more dangerous than ever – even for those of us living in developed countries. So here is the bottom line:

> The climate regime I was born into 74 years ago has been unraveling – quietly but inexorably. Global climate disintegration has been swift since 1976, when global land temperatures began rising at nearly twice the rate of ocean temperatures. Like the proverbial frogs in a pot of water slowly brought to a boil, we tend to ignore the creeping, cumulative changes: soaring atmospheric CO_2 levels, rising seas, warming oceans, parched soils, catastrophic wildfires, stronger hurricanes, and sudden "rain bombs." These changes do not arrive all at once; they accumulate year after year, driven by relentless human-caused greenhouse gas emissions.

In words of *Brannen* (2025): "It's not just the amount of CO_2 that enters the system that matters, it's also the flux. Put a lot in over a very long time and the planet can manage. But put more than a lot in over a brief enough period of time and you can short-circuit the biosphere. Unfortunately, the rate at which humans are now injecting CO_2 into the oceans and atmosphere today far surpasses the planet's ability to keep pace. We are now at the initial stages of a system failure. If we keep at it for much longer, we might see what actual failure really means."

In fairness, though, most readers of this book – scientists and non-scientists alike – have not spent the past forty years thinking daily about global energy supply, overpopulation, climate change and ecological collapse. As a result, your perception of the complex, evidence-based detective story I have just presented may be something like: "He is such a pessimist," or "His alarmism is hard to digest," or "I don't see any signs of imminent social breakdown or collapse of the systems that have kept me safe and comfortable, so he must be exaggerating."

For the record, I'm a realist – neither pessimist nor optimist. We remain on a course of about $\sim$40 Gt $CO_2\,y^{-1}$, and rising, as major emitters race ahead and offload the damage onto the entire world. Power-hungry AI data centers are just the newest driver of the ever-growing ecological overshoot.

Even McKinsey & Company – long a trusted advisor to the fossil fuel industry – recognizes the existential threat posed by unchecked greenhouse gas emissions. In a recent report, they outline concrete strategies to avoid greenhouse gas (GHG) emissions and assess the associated costs, please read the 8 pages of

Helmcke et al. (2025).

McKinsey introduced the first marginal abatement cost curve (MACC) in 2007 to assist a Swedish utility in optimizing its GHG mitigation strategy. Each potential abatement measure was assigned a cost per metric ton of avoided GHG emissions – primarily CO_2 – and weighted by the quantity of emissions it could reduce. MACCs have since become essential tools for evaluating and prioritizing the most cost-effective pathways to decarbonization across sectors and regions worldwide.

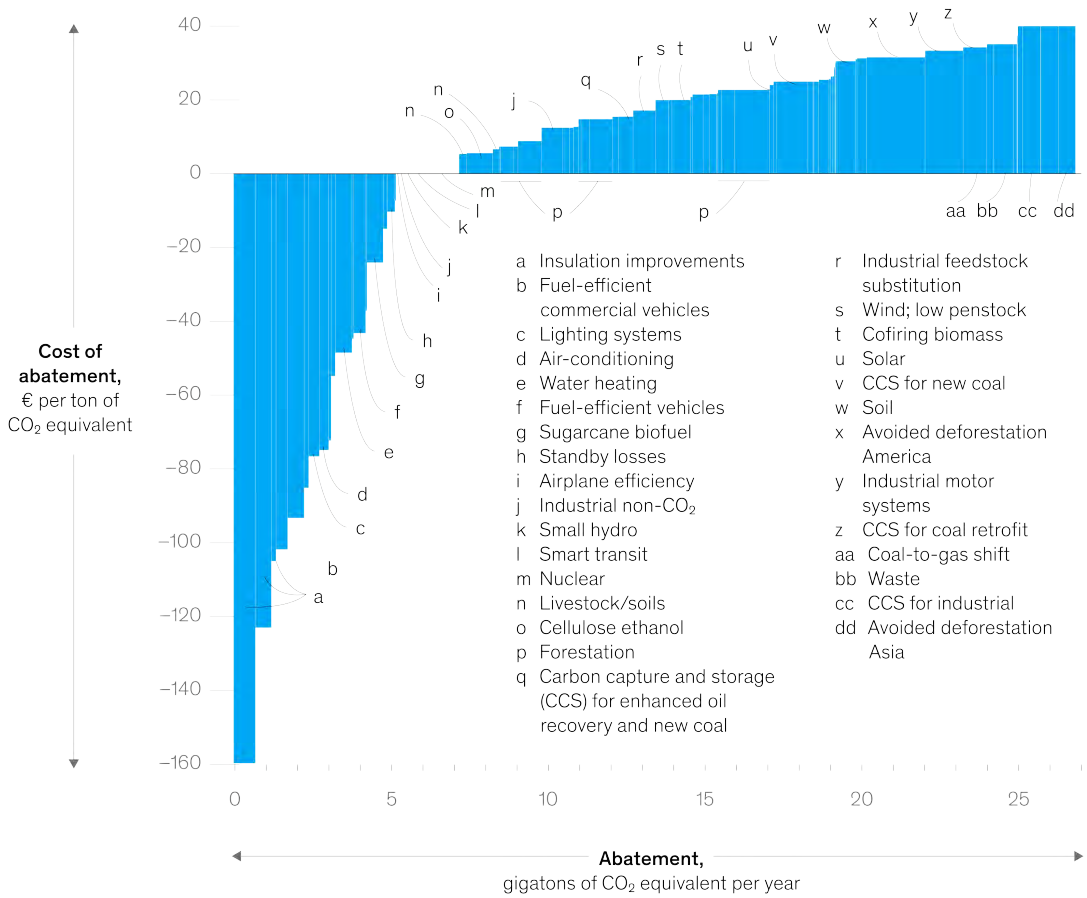

Figure 15.1: Marginal cost distribution of greenhouse gas abatement opportunities beyond business as usual. Source: Exhibit 1 in (*Helmcke et al.*, 2025).

Figure 15.1 illustrates how various technological solutions – including nuclear power – can generate substantial economic returns while abating up to 7 billion metric tons of CO_2 annually. The most cost-effective and impactful measure is improving building insulation worldwide, followed by increasing the efficiency of vehicles. At the lower end of the marginal cost spectrum, global reforestation offers the potential to remove an additional 5 billion tons of CO_2 per year. In contrast, avoiding deforestation in Asia provides a small abatement potential, albeit at significantly higher costs.

I am not the only one whose scientific work has led to profound despair and emotional exhaustion. There are many of us who carry this burden. For example, consider the following excerpt from a recent blog post by my Spanish comrade-in-arms, Professor Antonio Turiel:

> . . . [T]he emphasis remained on the need to promote hope. Not optimism about the situation – that would be absurd, given the data – but rather the hope that we might be able to reverse the situation. A hope, in truth, quite unfounded given how things have gone over the last few decades and how little attention has been paid to us scientists working on the Environmental Crisis. . . .
>
> What is the point of the widely accepted mantra in academia that we must transmit a message

> of hope? Even more troubling: when people like me present the plain, raw data in stark terms, it's not unusual for even fellow scientists to label such discourse as "catastrophist" or "pessimistic," even though what is being shown are just plain, factual data. Facts, in the end. It's as if every time someone shows that the situation is dire, they're required to offer some sort of incantation about the power of Science (capital S) and the ingenuity of Humanity (capital H), to *absolve responsibility and make it clear that things will get fixed (italics TWP)* – though we have no clue how, at least for now.
>
> *Hope and Defeatism*, Antonio Turiel, 2025-05-21,
> `https://www.15-15-15.org/webzine/2025/05/21/hope-and-defeatism/`

Here, then, are the key conclusions derived from my dispassionate, science-based analysis, grounded solely in hard evidence drawn from a multitude of independent sources:

- We live in an unprecedented climate regime – one in which humanity has emerged as a geological force rivaling the most powerful natural drivers over the past 60 million years. For more than two centuries, we have been flooding the atmosphere and biosphere with the carbon that life gradually sequestered over hundreds of millions of years. The scale of this transformation – equivalent to the metabolic activity of 260 billion people – has gone largely unnoticed. Equally overlooked is the fact that humanity has now breached most of the global constraints that stabilized Earth's climate over millennia. While the precise future trajectory remains uncertain, we now have a clear understanding of what must unfold.

- We have analyzed 6000 years of human biomass and fossil fuel combustion, with a particular focus on the explosive growth of fossil fuel production and emissions in the last 200 years (Figures 4.5 and 5.5(a)). We demonstrated that the chaotic, additive nature of energy transitions – combined with poor governmental communication – has made it exceedingly difficult to wean societies off thermal sources of energy, which have provided approximately 85% of global primary power over the past several decades (Figures 4.9 and 8.2). Including the energy delivered by fossil fuels and biomass, humanity today operates as 260 billion person-equivalents (Figure 4.7).

- To place the last two centuries of CO_2 emissions in context, we introduced a new unit: **1 Chicxulub**, defined as 1 trillion tonnes of CO_2 emissions emitted by the Chicxulub asteroid impact that finished off the dinosaurs and most life on Earth. Depending on the future emissions trajectory, humanity's cumulative impact may reach $5-8$ Chicxulubs (Figure 5.5(b)). We have also shown that the most intense volcanism during the Paleocene–Eocene Thermal Maximum (PETM) – Earth's warmest climate of the last 60 million years – released an amount of CO_2 comparable to that generated solely by modern agriculture and land-use change (Figure 5.5(b)).

- Through a simple mass-balance model, we constrained the fraction of emitted CO_2 that remains in the atmosphere and showed that, on a century-scale, this proportion remains stable at approximately 45% of cumulative emissions, with no measurable time delay (Figure 5.6). This model agrees well with IPCC's RCP4.5 and RCP6.0 pathways and with simulations by *Zickfeld et al.* (2009).

- The geometry of the Sun-Earth system determines that our blue-and-green Mothership intercepts only about one-half of one-billionth of the Sun's total radiant output (Figure 7.3). Fortunately, our remarkably stable star emits energy at an almost constant rate of $1361.1 \pm 0.5\ \mathrm{W\,m^{-2}}$ at the top of Earth's atmosphere (Figure 7.4), a value known as the solar constant. When this incoming solar radiation is averaged over the entire surface of the Earth and across all seasons and latitudes, the planet absorbs approximately $238\ \mathrm{W\,m^{-2}}$ of solar energy. That is the total energy budget available to power the Earth's climate system, sustain ecosystems, and support all life.

> Given the steady flow of solar energy, Earth maintains a delicate radiative balance – it endures, transforms, and recycles, but it does **not grow**.

- The stable equilibrium with incoming solar radiation requires that Earth emits infrared radiation from its entire surface, averaging $238\ \mathrm{W\,m^{-2}}$ – corresponding to a blackbody temperature of 255 K ($\approx -18\,^{\circ}\mathrm{C}$). If Earth lacked an atmosphere, this would be its average surface temperature.

- But Earth possesses a complex, layered atmosphere in which temperature decreases rapidly with

altitude up to about 12 km. This atmosphere contains gases that absorb outgoing infrared radiation, most notably H_2O, CO_2, and CH_4.

Carbon dioxide plays a disproportionately large role in regulating Earth's climate. Its concentration sets the baseline temperature profile of the Earth's atmosphere, thereby controlling the amount of water vapor – the atmosphere's most abundant greenhouse gas.

- The absorbing atmosphere forces Earth to shed heat by radiating infrared energy from an altitude of several kilometers above the surface. Greenhouse gases block a substantial portion of this outgoing radiation, thereby warming Earth's surface by approximately 33 °C above its blackbody equilibrium temperature. See the important Figure 7.9.
- When various indicators of climate change are plotted against combustion-driven thermal emissions – the apparent single dominant driver – many relationships become linear (Figures 10.13, 11.1 and 11.3) or show a single, abrupt break in slope (Figures 5.7 and 10.12). The most significant of these breaks reflects the climate bifurcation that began around 1976, when global land temperatures began rising at twice the rate of ocean surface warming (Figure 5.7(a,b)).
- We compared two fossil fuel scenarios developed by Patzek – a physics- and geology-constrained fossil fuel combustion (FF) plus agriculture and land use (AL) change pathway leading to 568 ppm_v by 2100, and a simpler extrapolated trajectory reaching 720 ppm_v – with several IPCC scenarios. The 568 ppm_v pathway closely tracks the delayed SSP2-4.5 trajectory (Figures 6.1, 11.2 and 11.8), while the 720 ppm_v scenario parallels the decelerated SSP3-7.0 or RCP6.0 scenarios (Figures 6.1, 11.5 and 11.8).
- To date, each of the three main fossil fuel sources – coal, oil, and natural gas – has undergone approximately ten doublings in power output, reaching nearly 5 TW each. We show that an eleventh doubling is neither physically feasible nor geologically justified. In Section 4.4, we developed the details of Patzek's fossil fuel production scenarios by fitting future production of each resource using the minimum number of Gaussian functions required for accurate approximation (Figures 6.2 to 6.4).
- We further examined the global distribution of GHG and aerosol emissions, identifying the top cumulative emitters – Europe, the United States, the EU-27, China, and other parts of Asia – which collectively account for more than 80% of total emissions (Figure 8.1–Figure 8.2). We reviewed several cases of prolonged, runaway air pollution over the past century in Europe (including England, Germany, Eastern Europe, and Russia), the United States, and Asia, and analyzed how this pollution temporarily masked global warming (Figures 7.10 and 8.2).
- In addition, we examined the eventual effects of air-quality legislation in the highest-emitting countries. By reducing anthropogenic aerosols, cleaner air can further depress Earth's planetary albedo. We estimate that this albedo decline adds, between 2010 and 2035, a cumulative heat uptake equivalent to powering ∼50 current global economies (Figure 8.4).
- We highlighted the challenges of comparing today's anomalous climate state with paleoclimates over the past 800,000 years, across the Mid-Pleistocene Transition (MPT; (∼1.25 – 0.7 Ma), and through Paleocene-Oligocene climates spanning the last ∼57 Myr (Figures 9.5, 9.6 and 9.8). Our analysis suggests that the equilibrium climate sensitivity (ECS) inferred for past warm interglacials exceeded today's, in part because their atmospheres were, on average, less aerosol-polluted.
- We explained the complex process of constructing a regular grid covering the globe (Figure 10.8) and calculating the average monthly temperature anomaly within each grid cell, followed by its calibration against reference data sets.
- We analyzed the outdated and scientifically invalid theories underlying vanilla climate denialism. We also showed how geoengineering serves as a "green" fig leaf for polluting industries in affluent countries and is marketed to an apathetic public as a credible technological remedy for the already severe impacts of climate change.
- Finally, we quantified the dramatic ice losses occurring in the polar regions and directly linked them

to cumulative carbon emissions. The associated rise in global sea level appears to be outpacing most climate model projections, placing hundreds of millions of people living in low-lying coastal areas at serious risk within the next decade or two (Figure 12.6).

Because we have directly linked ongoing climate warming to its principal driver – the **combustion-dominated total emissions** of CO_2 – we were able to construct a simple regression/interpolation model of global warming through 2100, complete with 2σ confidence intervals. This model translates Patzek's FF+AL scenario (568 ppm_v) and the 720 ppm_v trajectory into well-defined warming pathways (Figure 11.1–Figure 11.4, Figures 11.5 and 11.6). Both scenarios align well with their corresponding IPCC analogs (Figures 11.7 and 11.8).

But the real conclusions and human actions will not be driven by science alone. They will result from moral outrage and sense of self-preservation of ordinary people. Here is a random selection of leading environmental news on May 22, 2025, from The Guardian:

> From the Congo rainforest to the boreal forests of the far north, an area the size of Italy disappeared last year. It was land lost to fire, expanding agricultural frontiers, mining and logging. In 2021, at COP26 in Glasgow, world leaders promised to end the destruction of these ecosystems – the most alive places on Earth – by the end of the decade. But we are way off track. We would need to reduce forest loss by one-fifth each year from today's levels to meet it, something which feels incredibly unlikely at the time of writing. (Patrick Greenfield)
>
> The loss of ice from the giant Greenland and Antarctic ice sheets has quadrupled since the 1990s due to the climate crisis and is now the principal driver of sea level rise.
>
> The international target to keep global temperature rise below 1.5°C is already almost out of reach. But the new analysis found that even if fossil fuel emissions were rapidly slashed to meet it, sea levels would be rising by 1cm a year by the end of the century, faster than the speed at which nations could build coastal defences.
>
> ...
>
> Today, about 230 million people live within 1 metre above current sea level, and 1 billion live within 10 metres above sea level. Even just 20 centimeters[1] of sea level rise by 2050 would lead to global flood damages of at least $1tn a year for the world's 136 largest coastal cities and huge impacts on people's lives and livelihoods. (Damian Carrington)

If not science and investigative journalism at their best, then what other means do we have to confront the accelerating deterioration of the very places where we live – and where we dare to dream?

Politics, at its most constructive, has led to some degree of public awareness and education, depending on the country. But it has failed to restrain the relentless rise of atmospheric greenhouse gases, whose growth now traces an ever-steepening parabola (Figure 5.3). The 30 Conferences of the Parties (COPs) have yielded no genuine breakthroughs – despite endless proclamations to the contrary. These gatherings have often functioned as theatrical performances appealing to humanity's better angels. But Europe, in particular, has made substantial environmental progress in the last forty years, followed to varying extents by the United States and China.

Today, however, the belligerent, populist United States – still the most voracious consumer of Earth's resources – openly disregards climate science, and indeed, science itself. It is systematically dismantling decades of environmental protections. My country, instead of moving toward sustainability, is heading in the opposite direction.

Ironically, the only arguably positive outcome of the Trump-era tariffs has been the disruption of global supply chains, which in theory could have reduced resource consumption, just like the recent COVID-19 pandemic. But in practice, this disruption has not yet led to lower emissions. On the contrary, more coal is now being burned worldwide than ever before, and the exponential growth of AI-driven computation – powered largely by massive server farms in the US, Europe and China – more than offsets emissions reductions elsewhere.

[1] Compare with Figure 12.6(b) and (d).

Moral codes and art can and do exist outside of religion, encouraging self-discipline as well as helping others and finding happiness in contributing to their well-being. What we need is a stronger sense of social cohesion, where trust can be built and, through trusting relationships, people can find the support to make difficult and frightening decisions. For many, however, the strength to face such challenges may be difficult to summon, and religion often provides a familiar source of comfort and guidance. Thus, at this point, I believe that only religion remains to help most of us cope with fundamental traits of the human soul – our greed and aggression – which also make the core of global capitalism and the global Fossil Amoeba. Religion, at its best, can offer a powerful moral counter-force, as demonstrated by the actions and writings of three recent popes: John Paul II, Francis, and (though less frequently cited) Leo XIII.

However, at its worst, religion, when fused with political power, fear, or nationalism, has often fueled endless wars, deadly persecution, oppression, and dehumanization of "the other," as in "Gott mit uns."[2] These are idols of the theater and marketplace in Bacon's terms (cf. Chapter 1); the belief systems solidified into dogmas that stifle education, reason and compassion. For balance, religion has also inspired some of humanity's best – abolitionism, nonviolence (Gandhi, Martin Luther King Jr.), social justice movements, and humanitarian work.

So here is a balancing quote from the Dalai Lama:

> It is therefore in our interest to look after [*Mother Earth, TWP*]. This is common sense. But only recently have the size of our population and the power of science and technology grown to the point that they have a direct impact on nature. To put it another way, until now, Mother Earth has been able to tolerate our sloppy house habits. However, the stage has now been reached where she can no longer accept our behaviour in silence. The problems caused by environmental disasters can be seen as her response to our irresponsible behaviour. She is warning us that there are limits even to her tolerance.
> *Excerpt from Ancient Wisdom, Modern World: Ethics for the New Millennium by Tenzin Gyatso, the Fourteenth Dalai Lama. Published by Little, Brown and Company, United Kingdom J 999. (pp 2 J 3 -220).*

We close with another example that brings together both religion and art – a passage from a deeply spiritual blog posted on Good Friday, 2025. For now, let us set aside the serious scientific and environmental concerns about "green methanol" and "green hydrogen."

> But maybe this [*stench of death, TWP*] is what resurrection smells like before it is beautiful.
>
> What if it begins in the sewage? In the things we call too filthy, too far gone? What if new life doesn't start with glory but with decay? What if redemption isn't about escape, but transformation?
>
> Germany's scientists call it [*a fuel from sewage, TWP*] "climate-neutral methanol," produced by capturing biogas from sewage, purifying it, and combining it with green hydrogen to create a clean-burning fuel. The kind that can carry vessels across oceans – waste, now bearing witness to renewal.
>
> But I call it gospel. The kind that tells us the tomb isn't the end. That even the discarded can be harnessed for life. That what we cast off as waste may yet become fuel. The crucified Christ – abandoned, reviled, buried – becomes the vessel through which all things are being made new. This is not optimism. This is sacred paradox.
> *Death Tilled the Soil – on energy, waste, and renewal*, by Kat Armas, Apr 18, 2025,
> `https://katarmas.substack.com/p/death-tilled-the-soil`

Since this book is rich in imagery, let us end it with the following allegory:

[2] While the Wehrmacht used *Gott mit uns* ("God with us") on their belt buckles, the SS used *Meine Ehre heißt Treue* ("My honor is loyalty"), a surprisingly contemporary branding.

Figure 15.2: Photo by Etienne Girardet on Unsplash

Appendix A

Carrying capacity of Earth

Tops of mostly hexagonal basalt columns in Devil's Stockpile near Mammoth Lake, CA. They are the result of a volcanic eruption 80,000 years ago.

The human enterprise is in potentially disastrous 'overshoot', exploiting the ecosphere beyond ecosystems' regenerative capacity and filling natural waste sinks to overflowing. Economic behavior that was once 'rational' has become maladaptive. This situation is the inevitable outcome of humanity's natural expansionist tendencies reinforced by ecologically vacuous growth-oriented 'neoliberal' economic theory. *Rees (2020)*.

A.1. What are you going to learn?

In wildlife biology, the term carrying capacity generally refers to the maximum number of individual animals that a given area of land can support. This definition may be refined by distinguishing between the *subsistence density*—the upper limit set by the environment's ability to provide food and water—and the *optimum density*, which is lower and takes into account the health, growth, and fecundity of the population (*Dhondt*, 1988).

In human societies, however, exosomatic resource and energy consumption is both substantial and highly variable, depending on a society's level of economic development and an individual's position within the socioeconomic hierarchy. Incorporating humans into Earth's ecological accounts therefore complicates the very notion of carrying capacity beyond measure. Across 160 countries, our two-decade assessment found widespread unsustainability and weak resilience for the eight dimensionless indicators we chose (*Bolson et al.*, 2022b). Consistent with this, (*Fanning and Raworth*, 2025) report that the richest 20 % of nations (15 % of the population) generate >40 % of ecological overshoot, while the poorest 40 % (42 %) incur >60 % of the global social shortfall.

Interestingly, until the 1990s the dominant definitions of carrying capacity were almost entirely anthropocentric, with *Mothership Earth* entering only as an afterthought—if at all. It was due in no small measure to the work of my old friend, Professor William Rees, that the Earth itself was reintroduced into the neoliberal economic gobbledygook.

As a result, *global carrying capacity* came to be defined as the maximum size of the human population that could be sustained *indefinitely* at a specified standard of living, without degrading the essential biophysical stocks and flows—such as soils, freshwater, biodiversity, net primary production, and climate-regulating sinks—that underpin that standard of living (*Daily and Ehrlich*, 1992, *Cohen*, 1995, *Catton*, 1980a, *Arrow et al.*, 1995, *Wackernagel and Rees*, 1996). At that time, this carrying capacity was estimated to be:

- **Scale- and standard-of-living–dependent**: higher per-capita consumption lowers capacity, all else being equal (*Cohen*, 1995, *Wackernagel and Rees*, 1996).
- **Technology- and institution–contingent**: innovations and governance can shift capacity up or down, but often trade off against waste assimilation by the environment and long-term ecosystem integrity (*Arrow et al.*, 1995, *Daily and Ehrlich*, 1992).
- **Dynamic and uncertain**: it changes over time with ecology, energy availability, and social systems; global trade can raise local carrying capacity yet cannot relax global biophysical limits (*Catton*, 1980a, *Cohen*, 1995).

Today we know better and you will learn here about a more physical, comprehensive definition of global carrying capacity.

A.2. Why is this important?

Before addressing the multitudinous aspects of climate change, we must recognize that it is but one symptom of humanity's overshoot beyond the global carrying capacity: *No human society can endure beyond the health of the biosphere.* The carrying capacity of humanity is therefore strictly a subset of Earth's capacity to sustain all life.

Every apparent gain achieved by degrading soils, waters, climate, or other species subtracts more from future survival than it contributes to the present.

Since 1922, many definitions of carrying capacity have been proposed (*Dhondt*, 1988), but regardless of anything else, we now understand that global carrying capacity, K_{glob}, is:

- **All-life-centered**: the needs of non-human species and the integrity of ecological networks determine carrying capacity of the planet. Human numbers and activities are nested within the much larger community of all life (*Leopold*, 1949, *Wackernagel and Rees*, 1996).

- **Limited by the finite Earth system**: the fluxes of energy and matter set hard upper limits; overshoot erodes soils, waters, climate stability, and biodiversity that constitute the real foundations of capacity (*Catton*, 1980a, *Haberl et al.*, 2007, *Rockström et al.*, 2009).
- **Co-evolutionary and dynamic**: climate, ecosystems, and species distributions shift, and the safe space for humans shifts as well. The Anthropogenic Sixth Extinction underway and ecosystem collapse reduce future capacity far more than incremental technological gains can increase it.
- **Shared among all species**: global carrying capacity must include equitable space for other species to thrive, not just survive, if Earth's life-support system is to remain functional.

Formally, for human population P, per-capita consumption vector $\mathbf{c}$[1], technology/institutions $\mathcal{T}$[2], and Earth-system state $\mathbf{E}$, the global carrying capacity K_{glob} at welfare level W^* is

$$K_{\text{glob}}(W^*) \;=\; \max_{P,\,\mathbf{c},\,\mathcal{T}} P \quad \text{s.t.} \quad W(\mathbf{c},\mathcal{T}) \geq W^*,\; \dot{\mathbf{E}} = \mathbf{F}(\mathbf{E},P,\mathbf{c},\mathcal{T}) \geq 0,\; \mathbf{E} \in \mathcal{B}, \tag{A.1}$$

where $\mathcal{B}$ is the biosphere's safe operating space, explicitly including other species' viability and evolutionary potential (*Rockström et al.*, 2009, *Steffen et al.*, 2015). Equation (A.1) is a complicated generalization of Ehrlich-Holdren's $I = PAT$ identity.

Notice that in general K_{glob} is a non-unique (one-to-many), nonlinear *functional*[3] of the input vector functions, such as the Earth-system state function, $\mathbf{E}$, that has critical points, stationary points, bifurcation nodes, etc. Each of these points and nodes can be local or global, introducing the bewildering scale-dependent complexity into $\mathbf{E}$'s mathematical description and behavior.

Most policymakers, and nearly all politicians at every level, are either (i) unaware of this complexity, or (ii) willfully ignore it and mislead others. Most people are all too eager to embrace any falsehood that permits them to carry on with business-as-usual, even if only for another month. The IPCC focuses on understanding and modeling those components of $\mathbf{E}$ that directly affect Earth's climate. This book introduces cumulative total emissions of CO_2 as the primary control parameter driving the present climate transition toward a new quasi-steady state: a hot(ter) Earth, see Chapter 11.

A.3. United Nations Sustainable Development Goals

By their nature, these goals are intimately linked to the global carrying capacity defined in Equation (A.1). In 2015, the United Nations adopted the *2030 Agenda for Sustainable Development*, centered on 17 Sustainable Development Goals (SDGs). These goals provide a comprehensive framework to address global challenges with poverty, inequality, health, education, economic growth, climate change, and environmental protection (*United Nations General Assembly*, 2015, *United Nations*, 2024).

The 17 SDGs are:

1. No Poverty
2. Zero Hunger (*)
3. Good Health and Well-being (*)
4. Quality Education
5. Gender Equality
6. Clean Water and Sanitation (*)
7. Affordable and Clean Energy (*)
8. Decent Work and Economic Growth

[1] $\mathbf{c}$ is a vector analog of the scalar Affluence in the original $I = PAT$ paper by *Ehrlich and Holdren* (1971).
[2] Same as in (*Ehrlich and Holdren*, 1971).
[3] *Function*: input = number (or vector, element), output = number (or vector, element). *Functional*: input = function, output = number (scalar).

9. Industry, Innovation, and Infrastructure
10. Reduced Inequalities
11. Sustainable Cities and Communities (*)
12. Responsible Consumption and Production
13. Climate Action (*)
14. Life Below Water (*)
15. Life on Land (*)
16. Peace, Justice, and Strong Institutions (*)
17. Partnerships for the Goals

The goals highlighted by an asterisk are explicitly dependent on the climate aspects of $\mathbf{E}$. These interlinked goals aim to balance social, economic, and environmental dimensions of sustainable development, with the explicit commitment to "leave no one behind."

Contrast these goals with the September 2025 address to the United Nations General Assembly by President Donald Trump, who dismissed climate change as "the greatest con job ever perpetrated on the world," criticizing multilateral climate initiatives and accusing the United Nations, scientists, and green energy proponents of economic damage and ideological excess. Trump warned that renewable energy policies would wound economies – particularly in Europe – and urged a return to fossil fuels while rejecting forecasts of catastrophic warming as alarmist. Trump framed global climate efforts as unfair to the US, and used his speech to challenge the legitimacy of climate science, promote national sovereignty over international cooperation, and position the American approach as one unconstrained by what he called "green scams" (*Slattery and Holland*, 2025, *Associated Press*, 2025). The global reaction to this speech underscored how gravely the United States under President Trump had become isolated from the rest of the world on climate change – perhaps more than on any other issue.

A.4. Drilling deeper

The planet's carrying capacity controls our life styles, health, prosperity, and daily coffee supply. To understand more how closely it is interwoven with global climate change, we begin with a few useful definitions.

Definition 14 (Critical Point in Multivariable Calculus). For $f : \mathbb{R}^n \to \mathbb{R}$, a point $\mathbf{x}_0$ is a *critical point* if the gradient vanishes:

$$\nabla f(\mathbf{x}_0) = \mathbf{0}.$$

Classification (max/min/saddle) is made via the Hessian (second partial derivative) matrix.

Definition 15 (Critical Point in Dynamical Systems). A point $\mathbf{E}_0$ is a *critical point* (or equilibrium point) of a dynamical system

$$\dot{\mathbf{E}} = \mathbf{F}(\mathbf{E}, \dots)$$

if $\mathbf{F}(\mathbf{E}_0) = \mathbf{0}$. That is, the system remains at rest if started at $\mathbf{E}_0$.

Definition 16 (Fixed Point). Let $f : X \to X$ be a mapping. A point $x^* \in X$ is called a *fixed point* of f if

$$f(x^*) = x^*.$$

In dynamical systems, fixed points correspond to states that do not change over time:

- **Discrete time:** For $x_{n+1} = f(x_n)$, a fixed point x^* satisfies $f(x^*) = x^*$. If the system is started at x^*, it remains there indefinitely.

- **Continuous time:** For $\dot{x} = F(x)$, a fixed point (or equilibrium point) x^* satisfies $F(x^*) = 0$. At such a point the system does not evolve in time.

Examples:

- Predator–prey models: equilibria represent steady population levels of interacting species.
- Climate energy-balance models: equilibria correspond to stable climate states, such as snowball Earth vs. ice-free Earth.

A key distinction between a fixed point and a critical point is the following: a *fixed point* is a location in state space where the system can "sit still," whereas a *critical point* is sometimes used synonymously with "fixed point" in mathematics and ODE theory, but more generally denotes the parameter value or state at which a qualitative change occurs—such as a bifurcation, stability loss, or phase transition.

Definition 17 (Bifurcation). In the study of dynamical systems

$$\dot{\mathbf{E}} = \mathbf{F}(\mathbf{E}, \ldots, \mu),$$

a *bifurcation* is a qualitative change in the structure or stability of equilibria or periodic orbits that occurs as the control parameter μ passes through a critical value μ_c.

Formally, at a bifurcation point $(\mathbf{E}_c, \mu_c)$ the Jacobian

$$J = \left.\frac{\partial \mathbf{F}}{\partial \mathbf{E}}\right|_{(\mathbf{x}_c, \mu_c)}$$

has at least one eigenvalue with zero real part, leading to the creation, destruction, or stability change of invariant sets.

Common examples include:

- **Saddle–node bifurcation:** Two equilibria collide and annihilate each other.
- **Pitchfork bifurcation:** One equilibrium splits into three as symmetry is broken.
- **Hopf bifurcation:** A fixed point loses stability and a periodic orbit emerges.

A.4.1. Saddle–node bifurcation

Common examples of saddle–node bifurcations at different spatial scales are listed in Table A1. The impending collapse of the Amazon rainforest is listed in the second row of this table. The last four rows in Table A1 have global implications.

A.4.2. Pitchfork bifurcation

Pitchfork bifurcations are less common in messy real-world systems than saddle–nodes, because they require an underlying symmetry in the governing equations. But these bifurcations are more interesting, and they do appear in physics, ecology, and climate contexts when symmetry is present. A few instructive examples are listed in Table A2 and the formation of hexagonal fracture patterns in drying soil or cooling lava is next.

As soil or mud dries, the loss of water produces tensile stresses. For small stresses, the uniform unfractured state remains stable. Once a critical threshold is exceeded, however, the homogeneous state loses stability and periodic fractures emerge.

This transition can be understood as a symmetry-breaking or *pattern-forming* bifurcation: the symmetric state (no cracks) bifurcates into a spatially periodic fracture network. Nonlinear interactions among cracks favor hexagonal tiles (as those on the first page of this appendix), which minimize elastic energy. This is analogous to pattern-forming bifurcations seen in convection (Rayleigh-Bénard) and reaction-diffusion systems. Mathematically, the periodic fracture emergence is often modeled as a Turing-type (pattern-forming) bifurcation or as a subcritical pitchfork bifurcation in elastic fracture fields.

Table A1: Examples of saddle–node bifurcations in natural systems.

System	Driver / Feedback	Alternative States and Transition	References
Lake eutrophication	Nutrient loading, P/N cycling, loss of macrophytes	Clear-water vs. turbid, algal-dominated; sudden collapse of clear state under rising nutrients	*Scheffer et al.* (1993)
Savanna–forest mosaics	Rainfall, fire frequency, grazing	Forest vs. savanna; drying or increased fire eliminates forest equilibrium	*Higgins et al.* (2000), *Scheffer et al.* (2001)
Slowdown of AMOC[a]	Freshwater input, salt-advection feedback	Strong vs. weak/off circulation; excess freshwater collapses strong mode	*Stommel* (1961), *Notz and Doerr* (2023)
Arctic sea ice	Ice–albedo feedback	Seasonal ice cover vs. ice-free state; loss of stable ice equilibrium with warming	*Notz* (2009), *Notz and Doerr* (2023)
Permafrost carbon release	Warming, GHG release	Frozen vs. thawed permafrost; disappearance of frozen equilibrium	*Schuur et al.* (2015), *Notz and Doerr* (2023)

[a] AMOC = Atlantic Meridional Overturning Circulation

Similar processes occur in cooling lava flows, where hexagonal basalt columns emerge. The lava that formed the Devil's Postpile columns was some 120 m thick. Cooling was uniform and gradual, over thousands of years. As a result, the beautifully regular, tall (12-18 m) hexagonal columns, about 0.5-1 m wide emerged. In permafrost regions, repeated freeze–thaw cycles generate polygonal ground. In all these cases, a symmetry-breaking bifurcation underlies the sudden emergence of ordered hexagonal fracture patterns.

Table A2: Examples of pitchfork bifurcations in ecological and climate systems. Symmetry breaking is the hallmark of these transitions.

System	Driver / Feedback	Symmetric vs. Asymmetric States	References
Population dispersal in symmetric patches	Nonlinear competition, migration costs	Even distribution across two identical habitats vs. asymmetric dominance of one patch	*Cantrell and Cosner* (1991), *Hastings* (1991)
Vegetation pattern formation	Reaction–diffusion feedbacks between water, biomass, and soil	Uniform vegetation cover bifurcates into symmetric patterned states (stripes/spots, differing orientations)	*Meron* (2012), *Rietkerk et al.* (2004)
Equatorial Hadley circulation	North–south radiative forcing symmetry, angular momentum conservation	Symmetric two-cell circulation vs. asymmetric dominance of one hemisphere cell	*Bordoni and Schneider* (2008), *Emanuel* (2007)
ENSO[a] conceptual models	Symmetric Pacific background state, coupled ocean–atmosphere feedbacks	Neutral symmetric state vs. asymmetric El Niño or La Niña regimes	*Tziperman et al.* (1995), *Wang and Picaut* (2004)

[a] ENSO = El Niño–Southern Oscillation

A.4.3. Symmetry breaking for heating rate of land and surface seawater

Figure 5.7 shows a symmetry-breaking bifurcation of global land and surface seawater temperatures. The land temperature anomaly started growing at the rate that is ∼2× that for surface seawater, see Table A3 for a summary. The mean ocean temperature (MOT) started growing at the rate of 2 °C $(\text{kyr})^{-1}$.

The many reasons for this land–ocean divergence during periods of climate instability, both today and over geologic time, are summarized in Table A4. Briefly, the ocean's vast heat capacity, efficient vertical and lateral mixing, and strong latent-heat flux distribute and store the imposed energy, damping sea-surface trends. By contrast, continents are often dried-up; the active thermal layer is shallow, so diminished evaporation shifts more of the radiative imbalance into sensible heating of the boundary layer. Consequently, for comparable radiative forcing, land warms faster than the ocean. Only on sufficiently long timescales – when ocean heat uptake approaches equilibrium – do land and SST evolve more nearly in tandem. This was happening between 1850 and prior millenia, and 1976.

Table A5 summarizes land and SST heating rates across major episodes of climatic instability over the last 59 Myr, including the 25 abrupt Greenland warmings between 115 and 12 ka BP. During these events, coastal and shelf seas around Greenland shed sea ice rapidly, while the high interior of the ice sheet remained well below thaw. As a concrete benchmark, between the Last Glacial Maximum and the onset of the Holocene (roughly 19–11 ka; 8 kyr), representative rates are ~ 0.70 and ~ 0.45 °C kyr^{-1} for land and SST, respectively, yielding a land-to-ocean heating ratio of $\sim 0.70/0.45 \approx 1.6$. Ratios inferred specifically from Greenland during Dansgaard–Oeschger events are highly uncertain and not directly comparable to global land–SST contrasts. Most other paleo land-to-ocean ratios were smaller than the contemporary value (currently > 2), consistent with the ocean's large heat capacity, strong latent-heat buffering, efficient vertical and lateral mixing, and generally lower greenhouse-gas concentrations.

Cumulative sealevel rise during Termination I.

Stepwise global mean sealevel rose by roughly 70–80 m between ∼19 and 11.7 ka (Termination I in the last row of Table A5), embedded within a total rise of about 120 m from ∼16.5 to 7 ka *Lambeck et al.* (2014) (with a ∼18–20 m pulse at ∼14.6 ka *Lin et al.* (2021), *Stanford et al.* (2006) and continued early Holocene rise of ∼38 m from 11 to 3 ka) *Hijma et al.* (2025).

But the really frightening conclusion follows from the estimates of average ocean heating over the entire water column (MOT). The MOT rate is calculated from the multi-year mean ocean heat content:

$$\frac{\mathrm{d}T}{\mathrm{d}t} = \frac{Q_{oc}}{M_{oc} c_p}$$

Using $Q_{oc} \approx 11.2 - 12.1$ ZJ/yr (2005–2024), $M_{oc} \approx 1.4e^{21}$ kg, $c_p \approx 3990$ J kg^{-1} K^{-1}

$$\frac{dT}{dt} \approx \frac{(11.2\text{–}12.1) \times 10^{21}\ \text{J yr}^{-1}}{(1.4 \times 10^{21}\ \text{kg})(3990\ \text{J kg}^{-1}\,\text{K}^{-1})} \approx (2.0\text{–}2.2) \times 10^{-3}\ \text{K yr}^{-1}.$$

$$\text{Deglacial MOT (20-10 ka): } \Delta T = 2.57 \pm 0.24\ ^\circ\text{C} \ \Rightarrow\ \frac{dT}{dt} \approx 0.257 \pm 0.024\ ^\circ\text{C kyr}^{-1}.$$

$$\text{Ratio (recent/deglacial)} \approx 7.8\text{–}8.4\times\ \ (>10\times\ \text{only if using 2024's single-year spike}).$$

Currently, the mean ocean temperature (MOT) is rising roughly an **order of magnitude faster** than during the last deglaciation (multi-year average ∼8×; individual recent years >10×). A conservative estimate is 2.0–2.2 °C per 1000 yr today, versus 0.26 °C per 1000 yr during 20–10 ka. This contrast reflects a large, persistent top-of-atmosphere energy imbalance driven by high and fast-increasing greenhouse-gas concentrations, see Chapter 7 and Appendix B. Because the ocean absorbs about 90% of the excess heat, global warming gradually penetrates the full water column, see Chapter 12 and Appendix E. Continued fossil-fuel emissions at present rate accelerate climate warming impacts and social disintegration. Also note that the early-Holocene sealevel rise was 38 m.

A.4.4. Loss of hemispheric symmetry of Earth's albedo

In Chapter 7 we reviewed the near-hemispheric symmetry of Earth's planetary reflectivity (albedo). The energetics incorporated into the Earth system state **E** in Equation (A.1) imply that, on multi-year averages, the Southern Hemisphere (SH) and Northern Hemisphere (NH) reflect nearly the same fraction of incoming shortwave radiation, while the NH emits more outgoing longwave radiation (OLR). Yet, as Figure 8.4 shows, since about 2010 the planetary albedo has declined at roughly 0.04% yr^{-1}, implying a ∼1% drop by 2035 if the trend persists. In other words, a substantial increase in absorbed shortwave radiation is already "baked in," as Dr. Hansen would say.

Most of Earth's planetary albedo is set by clouds rather than by the surface. As a result, atmospheric reflection can compensate for large NH–SH surface-albedo contrasts (land–ocean area ratio, snow, sea ice) (*Voigt et al.*, 2013, *Datseris and Stevens*, 2021). In practice, the ocean-dominated, darker-surface SH hosts extensive, bright cloud fields along storm tracks and in persistent subtropical low-cloud layers, whereas the NH's brighter surface (more land, seasonal snow and sea ice) requires less cloud reflectance. To first order, these opposing contributions offset, yielding similar hemispheric-mean reflected shortwave radiation.

The coupled atmosphere–ocean system tends to minimize the mean cross-equatorial energy transport. Keeping absorbed shortwave radiation levels similar in the two hemispheres reduces the required north–south energy flux. Cloud reflectance co-adjusts with ocean and atmospheric circulation to maintain near-symmetry in reflected shortwave.

At the surface, NH snow cover and Arctic sea ice raise albedo, while the SH is anchored by Antarctica and seasonally extensive sea ice. Historically, these cryospheric contrasts complemented the primary cloud compensation, see Appendix E, but their balancing role is weakening as snow and sea-ice areas decline.

Secondary compensation arises from natural marine aerosols (sea salt) and biogenic sulfur (e.g., dimethyl sulfide from phytoplankton) that seed clouds over the oceans; anthropogenic aerosols have historically brightened NH clouds. Nonlinear cloud microphysics (Twomey and related effects[4]) saturates albedo susceptibility to aerosols,[5] limiting sensitivity and helping avoid large hemispheric imbalances. In other words, clean, thin clouds are highly sensitive to added aerosols, but in already bright, optically thick clouds further cloud condensation nuclei produce little additional reflectance.

Oceanic and atmospheric circulation co-adjust to the vertical and horizontal distribution of radiative heating over the oceans. Using satellite observations, *Loeb et al.* (2025) show that both hemispheres are losing reflectivity (darkening; see Section 8.6), with the NH darkening faster. This break in hemispheric symmetry of reflected solar radiation underscores that the near-symmetry is not a fundamental constraint of the Earth system, but an emergent outcome of its long evolution.

A symmetry-breaking pitchfork bifurcation in hemispheric albedo would reorganize the climate system, shifting the ITCZ[6] and monsoons, altering storm tracks, and amplifying cryosphere feedbacks.

Possible reasons for emerging hemispheric albedo asymmetry are:

- Declining anthropogenic aerosols and ship sulfur emissions. Air-quality regulations and the 2020 International Maritime Organization sulfur cap reduced aerosol scattering and cloud droplet numbers,

[4] *Twomey (first indirect) effect.* More cloud condensation nuclei (CCN) increase cloud droplet number N_d, which reduces droplet radius r_e for a given vertically-integrated cloud liquid water (LWP in mass of water per unit area of cloud). Since dimensionless optical depth $\tau \propto \mathrm{LWP}/r_e$, τ increases and cloud albedo R rises. *Related effects.* The Albrecht (second indirect) effect: higher N_d suppresses drizzle, extending cloud lifetime and often increasing cloud fraction and LWP. Additional adjustments include changes in turbulence and entrainment that can either enhance or offset brightening, depending on regime.

[5] *Saturating susceptibility.* Albedo susceptibility to aerosol, $S_{N_d} \equiv \partial R/\partial \ln N_d$, is largest in clean, optically thin clouds and declines as clouds become brighter and thicker. A simple scaling for fixed LWP is $\tau \propto N_d^{1/3}$, so $R(\tau)$ approaches an asymptote as τ grows, implying $S_{N_d} \to 0$ at high N_d. In practice, once droplets are already small and τ is large, more CCN yield little additional brightening.

[6] The Intertropical Convergence Zone (ITCZ) is a narrow belt of low-level convergence and deep convection near the equator where the NE and SE trade winds meet the ascending branch of the Hadley circulation. It features deep cumulonimbus, heavy rainfall, high cloud cover, and low outgoing longwave radiation. Seasonally, the ITCZ migrates toward the warmer, moister hemisphere (typically northward in boreal summer, southward in austral summer).

weakening cloud brightening, especially along NH shipping corridors) (*Quaas et al.*, 2022, *Gettelman et al.*, 2024, *Yoshioka et al.*, 2024, *NOAA Climate.gov*, 2024).

- Cryosphere changes. Strong Arctic sea-ice and snow-cover loss lowers NH albedo; Antarctic changes are more variable, altering the historical compensation between hemispheres (*Pistone et al.*, 2014, *Duspayev et al.*, 2024, *Jenkins and Dai*, 2021).

- Cloud-regime shifts. Changes in storm-track cloudiness and subtropical low clouds can erode the cloud-based compensation that previously masked clear-sky NH–SH surface-albedo differences (*Voigt et al.*, 2013, *Datseris and Stevens*, 2021, *Crueger et al.*, 2023).

- Energy-transport and ITCZ, and its mean latitude shifts toward the hemisphere that gains more net energy from a lower albedo and/or higher absorbed shortwave radiation adjustments. A growing hemispheric energy imbalance (NH absorbing more shortwave) can shift circulation and cloud fields, further perturbing albedo (*Loeb et al.*, 2025, *Voigt et al.*, 2014).

- Other aerosol variability. Regionally increasing dust and wildfire intensities modulate shortwave reflection with hemispheric biases, in addition to the mechanisms listed above. (*Wild*, 2009, 2012).

Worst outcomes of persistent hemispheric albedo asymmetry

- ITCZ displacement and rainfall reorganization: a darker (lower-albedo) hemisphere absorbs more shortwave, pulling the ITCZ toward it. Expect hemispheric-scale shifts in tropical rainfall and monsoons, with drought on one side and flood risk on the other. For example, if the NH darkens, mean ITCZ shifts northward.

  - **Wetter (flood risk up):** Sahel and West Africa; South Asia (India, Bangladesh); parts of the East Asian monsoon belt (e.g., Yangtze-Huaihe basin); northern tropical Americas and northern South America near 5–10° N (Caribbean and Venezuela-Guyana).

  - **Drier (drought risk up):** Southern Hemisphere monsoons – southern Africa (Angola-Botswana-Zimbabwe-South Africa's summer rainfall zone), northern Australia and the southern Maritime Continent;[7] northeast and central-eastern Brazil (including Nordeste) and parts of the southern Amazon.

  If the Southern Hemisphere darkens, the process reverses, resulting in wetter southern Africa, Australia, and the South American monsoon belt, but drier Sahel, South Asia, East Asia, and the northern tropical Americas.

- Amplified cryosphere feedbacks: sustained excess absorption in the Northern Hemisphere accelerates Arctic sea-ice and snow loss, strengthening the albedo feedback, and further darkening and heating the NH.

- Cloud-circulation coupling: cloud-cover adjustments that once compensated NH-SH surface differences may fail, reinforcing the asymmetry and uncertainty in tropical precipitation response.

- Energy-transport and overturning adjustments: altered cross-equatorial energy transport follows ITCZ shifts and interacts with ocean overturning (e.g., AMOC) and storm-track structure, raising risk of persistent regional hydroclimate anomalies (excessive flooding or droughts).

- Shortwave "unmasking" from aerosol declines: reduced sulfate from shipping and cleaner-air policies weakens cloud brightening over the busy NH oceans, adding to absorbed shortwave radiation and potentially intensifying marine heat extremes along shipping corridors[8].

[7] The Southern Maritime Continent (SMC) stands for the portion of the Maritime Continent south of the equator (roughly 0–15° S, 90–150° E). It includes the southern halves of Sumatra and Borneo (Kalimantan), Java, Bali and the Nusa Tenggara islands, Timor-Leste, southern New Guinea (Papua), and adjacent seas (Java, Banda, Arafura, Timor). In monsoon and ITCZ-shift contexts, authors sometimes extend the SMC to include northern Australia's Top End and Torres Strait; the term has no strict official boundary and is used pragmatically in tropical meteorology and oceanography.

[8] We have paid dearly to reduce sulfur in marine fuels, yet some geoengineering advocates now propose very expensive schemes for adding SO_2 to the upper troposphere and lower stratosphere. And so it goes...

Table A3: Current annual ΔT rates for land, SST, and MOT. Windows chosen to reflect modern trends.

Metric	Window	Rate (C $(\mathrm{yr})^{-1}$)	Notes
Land surface air temperature	1995-2024	0.041 ± 0.009	ERA5 land-only trend 0.41 ± 0.09 C per decade.
Sea-surface temperature SST (global)	1982-2023	0.013 ± 0.001	Global SST trend 0.13 ± 0.01 C per decade.
Mean ocean temperature MOT (full depth)	2006-2020	0.0020 ± 0.0002	Inferred from Earth energy imbalance 0.66-0.76 W m^{-2} and ocean heat uptake; conversion uses ocean mass $1.4\mathrm{e}^{21}$ kg and $c_p \approx 3990$ J kg^{-1} K^{-1}.

Table A4: Why land warms faster than the ocean: concise mechanism-by-mechanism summary.

Mechanism	**Land (Surface Air)**	**Ocean (SST / Mixed Layer)**
Heat capacity & thermal inertia	Low heat capacity; thin active layer → rapid sensible warming	Very high heat capacity; heat mixed downward → slower surface warming
Latent vs. sensible heat	Often water-limited; reduced evaporation → more energy becomes sensible heat	Abundant evaporation; large latent heat flux → damps SST rise
Moisture / drying amplification	Soil drying lowers evaporative cooling; boundary layer warms and deepens	Surface remains moist; weaker drying feedback in marine boundary layer
Aerosols & pollution trends	Emissions mainly over land; historical cooling mask decreased with air-quality gains → faster warming	Indirect cloud effects persist; aerosol burdens over remote oceans decline more slowly
Lapserate & water-vapor feedbacks	Drier troposphere; less negative lapse-rate feedback → larger surface response	Moister troposphere; stronger negative lapse-rate feedback moderates SST
Albedo / cryosphere	Snow cover loss on land yields sharp seasonal albedo drops; permafrost retreat adds heat	Sea-ice loss spreads heat into mixed layer; local SST increase moderated by mixing
Circulation & heat transport	No lateral heat buffer; reacts locally to forcing	Currents + overturning subduct heat to depth and across basins; delays SST rise
Forcing pattern & geography	Continental interiors far from evaporative sources; stronger continentality	Vast area & proximity to moisture keep SST changes spatially smoother, slower
Energy storage share	Small fraction of excess energy stored on land	∼90% of excess energy stored in the ocean → muted surface trend
Net effect (observational)	Warming rate ≈ 2× ocean over recent decades (3× since 1995)	Warming rate slower due to buffering and mixing

Table A5: Approximate land and sea-surface temperature SST[a] heating-cooling rates across selected geologic intervals. Rates are ΔT divided by interval duration and are order-of-magnitude guides. Proxy and regional *uncertainties are large.*

Interval	Window and duration	Land ΔT and rate	Ocean SST or MOT[b] ΔT and rate	Ratio
LGM[c] to Holocene global	19 ka to 11 ka (8 kyr)	Warming approx +6 C giving approx +0.7 C per kyr	Global mean SST warming approx +3.6 C giving approx +0.45 C per kyr[e]	1.7
Abrupt DO[d] warmings (Greenland land)	10 to 50 yr	+8 to +16 C in decades giving order 0.2 to 1.6 C per yr	N Atlantic SST rises order 1 to 3 C within centuries giving order 0.01 to 0.03 C per yr[f]	$5-8$[k]
PETM onset	approx 6 kyr onset	Terrestrial sites show approx +5 C giving approx +0.8 C per kyr	Marine SST approx +4 to +5 C giving approx +0.7 to +0.8 C per kyr[g]	1
Mid Pliocene Warm Period then cooling	3.3 Ma to 2.7 Ma (0.6 Myr)	Land warmer by approx +4.3 C then cooled giving approx -0.007 C per kyr	Ocean warmer by approx +2.8 C then cooled giving approx -0.005 C per kyr[h]	1.4
Last Interglacial early SST peak	129 ka to 124 ka (5 kyr)	NA	Global mean SST peak approx +0.9 C giving approx +0.18 C per kyr[i]	NA
Termination I[l] mean ocean temperature MOT	20 ka to 10 ka (10 kyr)	NA	MOT warming 2.6 ± 0.24 C giving approx +0.26 C per kyr[j]	NA

[a] SST = Seawater Surface Temperature
[b] MOT = The volume-weighted global-average temperature of the entire ocean water column, distinct from SST which samples only the surface skin. MOT is inferred mainly from noble-gas ratios trapped in polar ice (solubility depends on ocean temperature), so it reflects whole-ocean heat content and integrates changes over centuries to millennia. For example, MOT rose by about 2.6 ± 0.24 C from 20 ka to 10 ka (*Bereiter et al.*, 2018).
[c] LGM is Last Glacial Maximum
[d] DO = Dansgaard–Oeschger events. About 25 abrupt warmings (10-50 yrs) during the last glacial period, roughly 115-11.7 ka BP. In Greenland records they are expressed as alternations of Greenland Stadials (GS, cold) and Greenland Interstadials (GI, warm); the final GI-1 corresponds to the Bølling-Allerød around ∼14.7 ka BP, and the Younger Dryas is GS-1 just before the Holocene begins at 11.7 ka BP. BP means years before AD 1950. (*Dansgaard et al.*, 1993, *NGRIP*, 2004, *Rasmussen et al.*, 2014)
[e] (*Seltzer et al.*, 2021, *Loland et al.*, 2022, *Tierney et al.*, 2020, *Osman et al.*, 2021)
[f] (*Severinghaus et al.*, 1998, *Rasmussen et al.*, 2014)
[g] (*Li et al.*, 2022a, *Zeebe et al.*, 2016, *McInerney and Wing*, 2011a)
[h] (*Haywood et al.*, 2020)
[i] (*Turney et al.*, 2020)
[j] (*Bereiter et al.*, 2018)
[k] Probably unreliable and misleading, because of the arctic ΔT amplification and vastly different time scales for land and ocean heating. The actual ratio might be ∼2 is my guess
[l] Termination I = the last glacial termination, or the transition from the Last Glacial Maximum to the Holocene, spanning roughly 19–11.7 ka BP. It includes Heinrich Stadial 1 (HS-1), the Bølling-Allerød warm interval (GI-1), and the Younger Dryas (GS-1), and is marked by rapid regional warming, rising CO_2, large ice-sheet retreat, and stepwise global sealevel rise by up to 120 m.

A.4.5. Hopf bifurcation

A Hopf bifurcation occurs when a fixed point loses stability as a parameter passes a threshold, giving rise to a stable or unstable limit cycle (oscillations). Common oscillatory states are Milankovitch-driven glaciations and interglacials (described in Chapter 9) and emergence of El Niño cycles, see Table A6.

Table A6: Examples of Hopf bifurcations in ecological and climate systems.

System	Driver / Feedback	Transition	References
Predator–prey dynamics	Nonlinear feedback between prey growth and predator consumption	Steady coexistence equilibrium loses stability; system enters sustained population cycles	*Rosenzweig and MacArthur* (1963), *May* (1974)
Insect outbreak dynamics	Plant—herbivore feedbacks, density dependence, delayed responses	Equilibrium forest state destabilizes; oscillatory outbreaks of herbivores (e.g. spruce budworm) emerge	*Ludwig et al.* (1978), *Ghaffari et al.* (2011)
Climate glacial cycles (conceptual models)	Ice sheet mass balance, albedo feedback, ocean CO_2	Stable climate equilibrium destabilizes; system enters self-sustained glacial–interglacial oscillations	*Saltzman and Maasch* (1991), *Tziperman et al.* (2006)
ENSO[a]	Coupled ocean–atmosphere feedback, delayed thermocline adjustment	Neutral Pacific equilibrium destabilizes; oscillatory ENSO events appear as limit cycles	*Jin* (1997), *Timmermann et al.* (2003)

[a] ENSO = El Niño–Southern Oscillation

A.5. Summary

It should now be clear that human well-being hinges on the state of the global climate, which our collective actions are driving via bifurcations away from a human-friendly stable regime. A hardwired human imperative toward expansion – more people and higher throughput – is amplified by growth-centric economic doctrines, religious narratives, and techno-optimism that equate growth with good. The result is overshoot: the Earth system responds with warming, extremes, and threshold crossings that lower carrying capacity and force contractions in consumption and, ultimately, population. Against such biophysical constraints, political rhetoric of unbounded economic growth collides with physical reality. Whoever wagers against the Second Law of Thermodynamics – as neoliberal economic doctrine does – always meets the same end: utter collapse and humiliation.

Rees (2023) argues that

> [H]uman brain and associated cognitive processes are functionally obsolete to deal with the human eco-crisis [*caused by overshoot, TWP*]. H. sapiens tends to respond to problems in simplistic, reductionist, mechanical ways. Simplistic diagnoses lead to simplistic remedies. Politically acceptable technical solutions to global warming assume fossil fuels are the problem, require major capital investment and are promoted on the basis of profit potential, thousands of well-paying jobs and bland assurances that climate change can readily be rectified. If successful, this would merely extend overshoot. Complexity demands a systemic approach; to address overshoot requires unprecedented international cooperation in the design of coordinated policies to ensure a socially-just economic contraction, mostly in high-income countries, and significant population reductions everywhere.

Keep this in mind: the reductionist scientist—as most of us are trained to be–is far less free than the jazz musician who improvises without a script. What is required now to break out of the inherited reductionist cage of our own making is nothing less than a global explosion of deliberate, collective free will.

Appendix B

Black Body Radiation

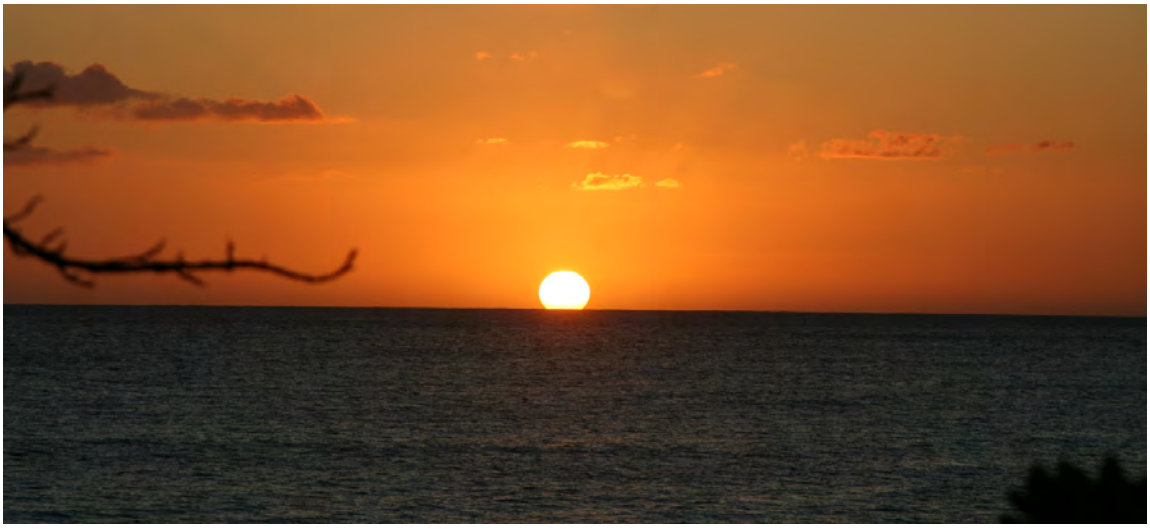

A sunset over the Red Sea seen from our house in KAUST, north of Jeddah, Saudi Arabia.
Photo by T.W. Patzek, Oct 2024.

Non-scientists should stop looking for shortcuts around the hard work of learning the science
Christopher Essex and Ross McKitrick
Taken by Storm, The Troubled Science, Policy and Politics of Global Warming (BPR Publishers, 2002)

B.1. What are you going to learn?

You are going to learn about the quantum PLANCK Law of Black Body Radiation and macroscopic STEFAN-BOLTZMANN Law of Radiation. These two laws are intricately related. We will also introduce the macroscopic quantities, irradiance, spectral irradiance and radiance that are used to calculate radiation power fluxes (see the definitions in Section 7.5). We will calculate these quantities for the Sun and Earth's radiation spectra and compare them with the satellite-measured spectra.

B.2. Why is it important?

This appendix provides background information for Chapter 7. The quantum distribution of radiation emitted and absorbed by a black body is required to derive the energy relationship between the Sun and Earth as well as the Earth and Universe. Summing up black body radiation over all wavelengths and directions gives the Stefan-Boltzmann law, which in turn governs the macroscopic radiative energy transfer in the open Sun-Earth-Universe system. This two-way transfer of photons has created and sustained all life on the Earth. There isn't a more direct and important mechanism by which quantum physics defines everything that ever happened to and on the Earth.

B.3. Background

This derivation follows Chapter XIV in *Thermodynamics* by *Guggenheim* (1950) and *Statistical Thermodynamics* by *Fowler and Guggenheim* (1949).

Radiation is regarded as a collection of photons. Each photon is characterized by a frequency ν, a direction of propagation, and a plane of polarization. In vacuum all photons have speed of light $c = 299792458$ m/s. Each photon has specific energy u_i related to its frequency ν_i by Planck's relation

$$u_i = h\nu_i \quad \text{J/photon} \tag{B.1}$$

and a momentum of magnitude $h\nu_i/c$. Here $h = 6.626068 \times 10^{-34}$ J s is Planck's constant.

It is convenient to group all photons having equal frequencies, thus equal energies, but different directions of propagation and planes of polarization.

We denote by

$$g_i \, d\nu_i$$

the number of distinguishable photons having frequencies between ν_i and $\nu_i + d\nu_i$, and energies between u_i and $u_i + du_i$.

Suppose that the radiation photons reside in a rectangular box defined by $0 \le x \le a$, $0 \le y \le b$, and $0 \le z \le c$.

Then for a wave traveling in the x-direction, the half-wave length $\frac{1}{2}\lambda$ must be an integer sub-multiple of the length a of the box, see Figure B1,

$$\frac{2}{\lambda} = \frac{l}{a}, \quad l = 1, 2, 3, \ldots \tag{B.2}$$

For a wave traveling in any direction it turns out that the boundary conditions along the box walls restrict the wavelengths to

$$\left(\frac{2}{\lambda}\right)^2 = \left(\frac{l}{a}\right)^2 + \left(\frac{m}{b}\right)^2 + \left(\frac{n}{c}\right)^2, \quad l, m, n = 1, 2, 3, \ldots \tag{B.3}$$

Hence the number of possible wavelength greater than λ_0 is equal to the number of positive integers l, m, n, satisfying

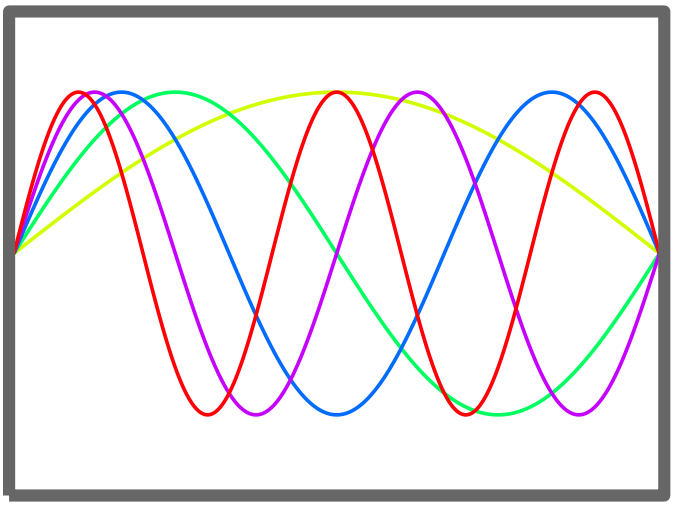

Figure B1: Five standing wave modes in the x-direction of a rectangular cavity.

$$\left(\frac{l}{a}\right)^2 + \left(\frac{m}{b}\right)^2 + \left(\frac{n}{c}\right)^2 \leq \left(\frac{2}{\lambda_0}\right)^2 \tag{B.4}$$

This number is equal to the number of points ξ, η, ζ with the positive integer coordinates inside the ellipsoid

$$\left(\frac{\xi}{a}\right)^2 + \left(\frac{\eta}{b}\right)^2 + \left(\frac{\zeta}{c}\right)^2 = \left(\frac{2}{\lambda_0}\right)^2 \tag{B.5}$$

and therefore to the volume of the positive octant of this ellipsoid:

$$\frac{1}{8}\,\frac{4\pi}{3}\,\frac{abc}{\left(\frac{1}{2}\lambda_0\right)^3} = \frac{4\pi}{3}\,\frac{V}{\lambda_0^3} \tag{B.6}$$

where V is the volume of the box.

It can be further shown that this dependence on V is independent on the shape of the box as soon as the wavelength becomes small compared with the dimensions of the box, and it is only such modes of the photon vibration which are numerous enough to matter.

In vacuum

$$\lambda\nu = c \tag{B.7}$$

Hence the number of possible frequencies less than ν_0 for two transverse directions of vibrations (two planes of polarization) is

$$2\,\frac{4\pi}{3}\,\frac{\nu_0^3}{c^3}V \tag{B.8}$$

and

$$g_i d\nu_i = 2\,\frac{4\pi V}{c^3}\nu_i^2 d\nu_i \tag{B.9}$$

B.4. Energy and Entropy in Terms of g_i's

Let's denote by n_i the number of photons having energies between u_i and $u_i + du_i$, and the corresponding frequencies ν_i, see Eq. (B.1). Then the total energy of all photons is

$$U = \sum_i n_i u_i \tag{B.10}$$

From the fact that the photons obey the Bose-Einstein statistics, it can be shown that the entropy of the photons is

$$\frac{S}{k} = \sum_i \ln\left[\frac{(g_i + n_i)!}{g_i! n_i!}\right] \tag{B.11}$$

Differentiating Eqs. (B.10) and (B.11) at constant g_i, i.e., constant V, we get

$$dU = \sum_i u_i dn_i \tag{B.12}$$

and

$$\frac{dS}{k} = \sum_i \ln\left[\frac{(g_i + n_i)}{n_i}\right] dn_i \tag{B.13}$$

The condition for equilibrium at a fixed V is that U be minimum and S maximum *Kestin* (1979), page 21. Hence, for the most general variation, both expressions (B.12) and (B.13) must vanish simultaneously. Therefore the coefficients of all dn_i's must be proportional:

$$\frac{u_i}{\ln\left[\frac{(g_i + n_i)}{n_i}\right]} = \frac{u_k}{\ln\left[\frac{(g_k + n_k)}{n_k}\right]}, \quad \text{for all } i, k \tag{B.14}$$

and, consequently, using Eqs. (B.10) and (B.11)

$$\frac{u_i}{\ln\left[\frac{(g_i + n_i)}{n_i}\right]} = \frac{\sum_k u_k dn_k}{\sum_k \ln\left[\frac{(g_k + n_k)}{n_k}\right] dn_k} = k\frac{dU}{dS} = kT \tag{B.15}$$

since at constant volume

$$dU = TdS \tag{B.16}$$

From Eq. (B.15) we obtain

$$\frac{n_i}{g_i + n_i} = e^{-u_i/kT} \tag{B.17}$$

and so

$$n_i = \frac{g_i}{e^{u_i/kT} - 1} \tag{B.18}$$

and

$$U = \sum_i n_i u_i = \sum_i \frac{g_i u_i}{e^{u_i/kT} - 1} \tag{B.19}$$

For the entropy we can obtain from Eq. (B.11), using a simple approximation for the factorials:

$$\frac{S}{k} \approx \sum_i n_i \ln\left[\frac{(g_i + n_i)}{n_i}\right] + \sum_i g_i \ln\left[\frac{(g_i + n_i)}{g_i}\right] \tag{B.20}$$

Using Eqs. (B.15) and (B.17) in Eq. (B.20) we get

$$\frac{S}{k} \approx \sum_i \frac{n_i u_i}{kT} - \sum_i g_i \ln\left(1 - e^{-u_i/kT}\right) \tag{B.21}$$

For the free energy, we deduce from (B.10) and (B.21)

$$F = U - TS = kT \sum_i g_i \ln\left(1 - e^{-u_i/kT}\right) \tag{B.22}$$

B.5. Thermodynamic Functions

In the previous sections we have obtained formulæ for the energy, entropy and free energy in terms of the specific photon energies u_i and their number distribution function g_i, without making use of Eqs. (B.1) and (B.9). If we now substitute the values of u_i and g_i given by the latter two equations into Eqs. (B.21) and (B.19), we will get

$$F = \frac{8\pi V}{c^3}\, kT \int_0^\infty \ln\left(1 - e^{-h\nu/kT}\right) \nu^2 d\nu \tag{B.23}$$

$$U = \frac{8\pi V}{c^3} \int_0^\infty \frac{h\nu^3 d\nu}{e^{h\nu/kT} - 1} \tag{B.24}$$

We can also write Eq. (B.24) in the form

$$\frac{U}{V} = u = \int_0^\infty u_\nu d\nu, \text{ where } u_\nu := \frac{8\pi}{c^3} \frac{h\nu^3}{e^{h\nu/kT} - 1} \tag{B.25}$$

This is the original Planck formula from which the quantum theory started. u_ν is the radiation energy per unit volume per unit frequency ν in $\mathsf{J\ m^{-3}\ s}$.

Alternatively,

$$\begin{aligned} u &= -\int_\infty^0 u'_\nu \frac{c}{\lambda^2} d\lambda, \text{ and one may define} \\ u_\lambda &:= u'_\nu \frac{c}{\lambda^2} = \frac{8\pi hc}{\lambda^5} \frac{1}{e^{hc/(\lambda kT)} - 1} \end{aligned} \tag{B.26}$$

u_λ is the radiation energy per unit volume per unit wavelength in $\mathsf{J\ m^{-3}\ m^{-1}}$.

B.6. Evaluation of Integrals

We can rewrite Eq. (B.23) as

$$F = -\frac{8\pi V k^4 T^4}{c^3 h^3}\, I \tag{B.27}$$

where

$$I := -\int_0^\infty \ln\left(1 - e^{-\xi}\right) \xi^2 d\xi \tag{B.28}$$

Using the Taylor series for the logarithm and then integrating term-by-term, we obtain

$$I := \int_0^\infty \frac{\xi^2}{n} e^{-n\xi} d\xi = \sum_{n=1}^\infty \frac{1}{n^4} \int_0^\infty \xi^2 e^{-\xi} d\xi = 2 \sum_{n=1}^\infty \frac{1}{n^4} = \frac{\pi}{45} \tag{B.29}$$

Substituting Eq. (B.29) into (B.27) we finally obtain

$$F = -\frac{8\pi^5 k^4}{45 c^3 h^3}\, T^4 V \tag{B.30}$$

B.7. Stefan-Boltzmann Law

We could derive fromulæ for U and S in a similar manner, but it is easier to obtain them by differentiation of Eq. (B.30)

For historical reasons, let's write Eq. (B.30) in the following form:

$$F = -\frac{1}{3} a T^4 V \tag{B.31}$$

where a is a universal constant defined as

$$a := \frac{8\pi^5 k^4}{15c^3h^3} = 7.569 \times 10^{-16} \quad \mathsf{J\,m^{-3}\,K^{-4}} \tag{B.32}$$

In the universal Stefan-Boltzmann constant, a, hidden are relativity (the speed of light, c), statistical mechanics (the Boltzmann constant k), and quantum mechanics (the Planck constant, h).

From Eq. (B.31) we deduce immediately

$$S = -\left(\frac{\partial F}{\partial T}\right)_V = \frac{4}{3}aT^3V \tag{B.33}$$

$$U = F + TS = aT^4V \tag{B.34}$$

$$p = -\left(\frac{\partial F}{\partial V}\right)_T = \frac{1}{3}\frac{U}{V} \tag{B.35}$$

$$G = F + pV = 0 \tag{B.36}$$

The equation for radiation pressure can be derived from classical electromagnetic theory. The equation for the radiation energy was discovered by Stefan and derived theoretically by Boltzmann. It is therefore called the Stefan-Boltzmann law. We can see from Eq. (B.34) that aT^4 is the equilibrium value of the radiation energy per unit volume in an enclosure. If a small hole is made in such an enclosure then it can be shown by simple geometrical considerations that the radiation flux, $\mathcal{F}_U$ (radiation energy emitted through the hole per unit area and per unit time) is σT^4, where

$$\sigma = \frac{1}{4}ac = 5.6703 \times 10^{-8} \quad \mathsf{J\,m^{-2}}\ s^{-1}\ \mathsf{K^{-4}} \tag{B.37}$$

where c is the speed of light. The constant σ is called the Stefan-Boltzmann constant.

B.8. Solved examples

1. Prove Eq. (B.5).

   We seek a standing wave solution to the three dimensional wave equation for radiation energy:

   $$\frac{\partial^2 U}{\partial x^2} + \frac{\partial^2 U}{\partial y^2} + \frac{\partial^2 U}{\partial z^2} = \frac{1}{c^2}\frac{\partial^2 U}{\partial t^2} \tag{B.38}$$

   subject to the boundary condition

   $$\begin{aligned} &U(x, y, z, t) = 0 \text{ along the walls of the rectangular box:} \\ &0 \le x \le a, \quad 0 \le y \le b, \quad 0 \le z \le c \end{aligned} \tag{B.39}$$

   A nonzero value of U along the walls would dissipate radiation energy and violate the assumption of a standing wave. Since the wave is a steady oscillation, we do not need initial condition (the wave keeps on oscillating forever as a sine function of time).

   Guess a standing wave solution of the form

   $$U = U_0 \sin\left(\frac{l\pi x}{a}\right) \sin\left(\frac{m\pi y}{b}\right) \sin\left(\frac{n\pi z}{c}\right) \sin\left(\frac{2\pi ct}{\lambda}\right) \tag{B.40}$$

   Substitute this solution into the wave equation (B.38) and obtain directly condition (B.5).

2. Demonstrate the approximate equality in Eq. (B.20).

   By definition,

$$\ln N! = \ln 1 + \ln 2 + \cdots + \ln N \tag{B.41}$$

   For a large N, the sum above may be viewed as a Riemann sum for the following definite integral:

$$\int_1^N \ln x dx = N \ln N - N + 1 \approx N \ln N - N \tag{B.42}$$

   Thus

$$\ln N! \approx N \ln N - N \tag{B.43}$$

   Now use this approximation in the entropy equation (B.11) and group terms.

$$\ln \left[\frac{(g_i + n_i)!}{g_i! n_i!} \right] \approx (n_i + g_i) \ln(n_i + g_i) - n_i - g_i - \ln(g_i) + g_i - n_i \ln(n_i) + n_i \tag{B.44}$$

   Thus Eq. (B.11) is proved.

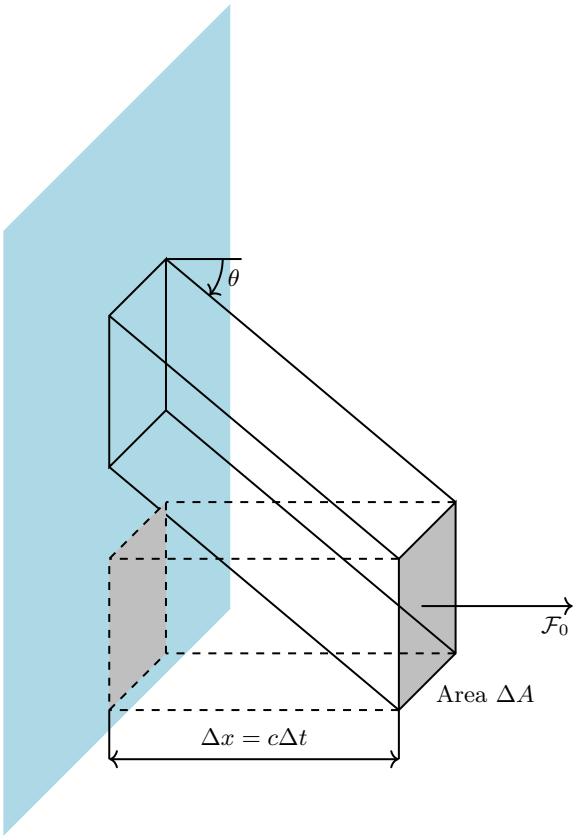

Figure B2: We start from radiation fluxes through two gray ends of the control box perpendicular to the hot plane in equilibrium with radiation. We then balance radiation fluxes from a tilted box, and average over all orientations.

3. Demonstrate that when a small hole is made in a rectangular box, the radiation flux (radiation energy emitted through the hole per unit area and per unit time) is σT^4, where $\sigma = \frac{1}{4}ac$, see Figure B2.

For a rectangular box filled with radiation of total energy U, the radiated energy flux $\mathcal{F}_0$ (perpendicular to both gray ends) is

$$U = \mathcal{F}_0 \Delta t \underbrace{2\Delta A}_{\substack{\text{Count}\\ \text{Both ends}}} = \mathcal{F}_0 2 \underbrace{\frac{\Delta x \Delta A}{c}}_{\text{Volume}} = \mathcal{F}_0 \frac{2V}{c}$$
$$\mathcal{F}_0 = \frac{c}{2}\frac{U}{V} = \frac{c}{2} a T^4 \tag{B.45}$$

For an arbitrary tilted box, the areas of both gray ends are larger than the areas of ends perpendicular to the other edges by a factor $1/\cos(\theta)$. The time to sweep the longer tilted box is $\Delta t/\cos(\theta)$. The total flux in half-space (one side of the hot plane) is the average of fluxes in all directions from $-\pi/2$ to $\pi/2$ radians

$$\underbrace{\frac{U}{\cos\theta}}_{\substack{\text{Larger}\\ \text{volume}}} \underbrace{\cos\theta}_{\substack{\text{Smaller}\\ \text{x-section}}} = \mathcal{F}_\theta \frac{\Delta t}{\cos\theta}\frac{2\Delta A}{\cos\theta} = \mathcal{F}_\theta \frac{2\Delta x \Delta A}{c\cos^2\theta} = \mathcal{F}_\theta \frac{2V}{c\cos^2\theta}$$

$$\mathcal{F}_\theta = \frac{c}{2}\frac{U}{V}\cos^2\theta = \frac{c}{2} a T^4 \cos^2\theta \tag{B.46}$$
$$\mathcal{R} = \frac{1}{\pi}\int_{-\pi/2}^{\pi/2} \mathcal{F}_\theta d\theta = \frac{c}{2} a T^4 \underbrace{\frac{1}{\pi}\int_{-\pi/2}^{\pi/2} \cos^2(\theta)\, d\theta}_{=1/2} = \left(\frac{c}{4}\right) a T^4$$

Here $\mathcal{R}$ is *irradiance* or the total power per unit area (surface power density) or the total radiation flux received from a source in the form of electromagnetic radiation in the wavelength range of the measuring instrument. Irradiance is measured in watts per square metre, $\mathsf{W\,m^{-2}}$.

4. Assuming that Sun surface has the black body temperature[1], and using Planck's formula for the density of radiation energy converted to radiation flux in half-pace $\theta \in [-\pi/2, \pi/2]$, or irradiance, by multiplying it by $c/4$, calculate how much energy is received by the Earth, if the average distance between the Sun and Earth is $d_{SE} = 149.598 \times 10^9$ m, and the Sun radius is $R_{\text{sun}} = 6.955 \times 10^8$ m.

   Assume Planck's constant $h = 6.626068 \times 10^{-34}$ $\mathsf{J\,s}$, the speed of light in vacuum $c = 299792458$ $\mathsf{m\,s^{-1}}$, and Boltzmann's constant $k = 1.3806503 \times 10^{-23}$ $\mathsf{J\,K^{-1}}$.

   The flux of solar radiation at the edge of Earth's atmosphere is obtained from the that at the Sun's surface by applying the law of energy conservation to radial geometry

$$\frac{4\pi R_{\text{sun}}^2}{4\pi d_{SE}^2} \tag{B.47}$$

   Thus, the function we plot is

$$\mathcal{R}_\lambda = u_\lambda \frac{c}{4}\frac{R_{\text{sun}}^2}{d_{SE}^2} = \frac{8\pi hc}{\lambda^5}\frac{1}{e^{hc/(\lambda k T)} - 1}\frac{c}{4}\frac{R_{\text{sun}}^2}{d_{SE}^2} \quad \mathsf{W\,m^{-2}\,m^{-1}} \tag{B.48}$$

   where $\mathcal{R}_\lambda$ is *spectral irradiance* per unit wavelength. Plot this density function from 1 nm to 4000 nm. Calculate the area underneath the curve. It should equal approximately the solar constant at the edge of the Earth's atmosphere, ∼1362 $\mathsf{W\,m^{-2}}$. The measured solar radiation flux density is provided in Figure 7.5. Only the black body radiation of the sun at $T = 5794$K is shown in Figure B3. Note very close similarity of the measured solar irradiance distributions and the Planck black body radiation.

[1] The Sun is not a perfect black body; instead, it is a gray body with surface emissivity of 0.93. Disregarding this small discrepancy for the time being, I have found by trial-end-error that the temperature of the Sun's surface of approximately ∼5794 K yields the solar constant of 1361.4 $\mathsf{W\,m^{-2}}$ when integrating from 1 to 30000 nm.

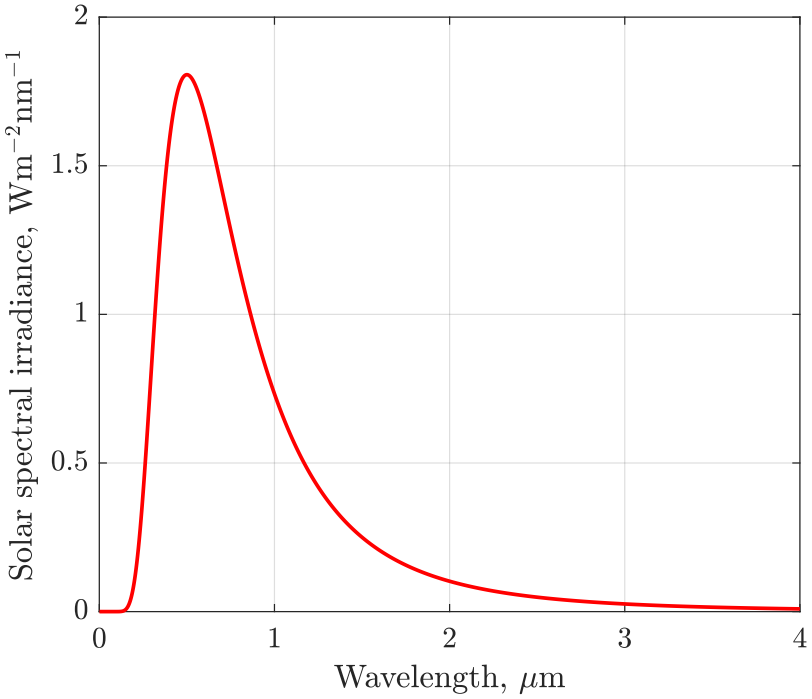

Figure B3: Solar radiation flux density function calculated from Eq. (B.48).

5. Assuming that the visible light is contained between 400 nm (purple) and 700 nm (deep red), calculate what fraction of total solar radiation falls in this range. In your calculations, use Equation (B.48). This fraction is related to the *Photosynthetically Active Radiation* (PAR) used by plants. **Answer:** ∼37%.

6. Assuming the same physical constants as in Example 4 and $T_E = 255$ K as the black body temperature of the outer layers of Earth's atmosphere, generate the plot in Figure B4. Notice that this plot was generated versus the spectroscopic wave number $\tilde{\nu} = 1/\lambda$, customarily presented in the units of cm^{-1}. The function you want to plot now is

$$\mathcal{R}_{\tilde{\nu}} = \lambda^2 u_\lambda \, \frac{c}{4} \, \frac{R_{\text{sun}}^2}{d_{SE}^2} = 8\pi h c \tilde{\nu}^3 \frac{1}{e^{hc\tilde{\nu}/(kT)} - 1} \, \frac{c}{4} \, \frac{R_{\text{sun}}^2}{d_{SE}^2} \quad \mathsf{W\ m^{-2}\ m} \tag{B.49}$$

where $\mathcal{R}_{\tilde{\nu}}$ is *spectral irradiance* per unit wavenumber. Plot this density function from 0 to 2000 cm^{-1}. The distribution functions in Eq. (B.48) and (B.49) have essentially different shapes and locations of peaks. The wavenumber corresponding to the distribution peak is ($\tilde{\nu}_{\max}$ in cm^{-1}) = $1.95T$. The corresponding wavelength ($\lambda_{\max}$ in cm)$T = 0.2897$.

The curve $\mathcal{R}(T_E)_{\tilde{\nu}}$ is the spectral Earth radiance. Because of the rotational symmetry, $\mathcal{R}_{\tilde{\nu}}$ per *steradian* is $\mathcal{R}_{\tilde{\nu}}/\pi$, see Figure B4. This new directional function is called *spectral radiance*. Calculate the area underneath this curve. It should be close to 238 $\mathsf{W\ m^{-2}}$. This is roughly how much power is radiated from each square meter of the Earth's surface in every direction. Note that Earth's radiation spectrum is mostly in intermediate and far infrared. Also note that the Earth is a system open to radiation flow, but closed to mass flow. An analogous plot for the Sun is shown in Figure B5.

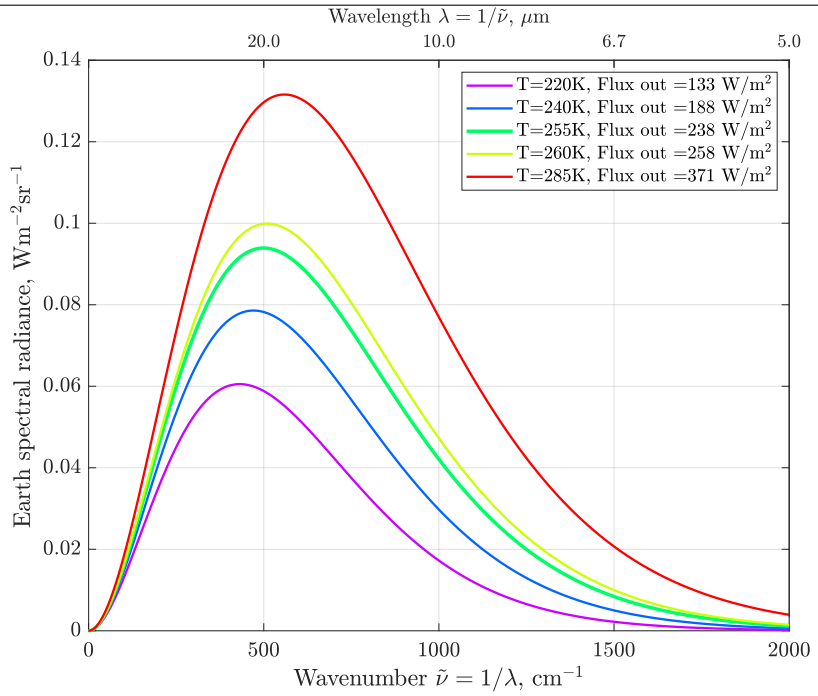

Figure B4: The Earth's spectral radiance versus radiation wavenumber in cm^{-1}. Note that the radiation wavelength *decreases* from left to right. Radiance is the radiant power emitted, reflected, transmitted or received by a given surface, per unit solid angle per unit projected area. The SI unit of radiance is watt per steradian per square meter (W sr^{-1} m^{-2}). Radiance of a surface is a directional quantity, because it depends on the direction from which it is being observed. The function related to radiance is the radiance of a surface per unit frequency, wavelength or wavenumber, depending on the units of the spectrum. This type of radiance is called *spectral radiance* or *specific radiance*.

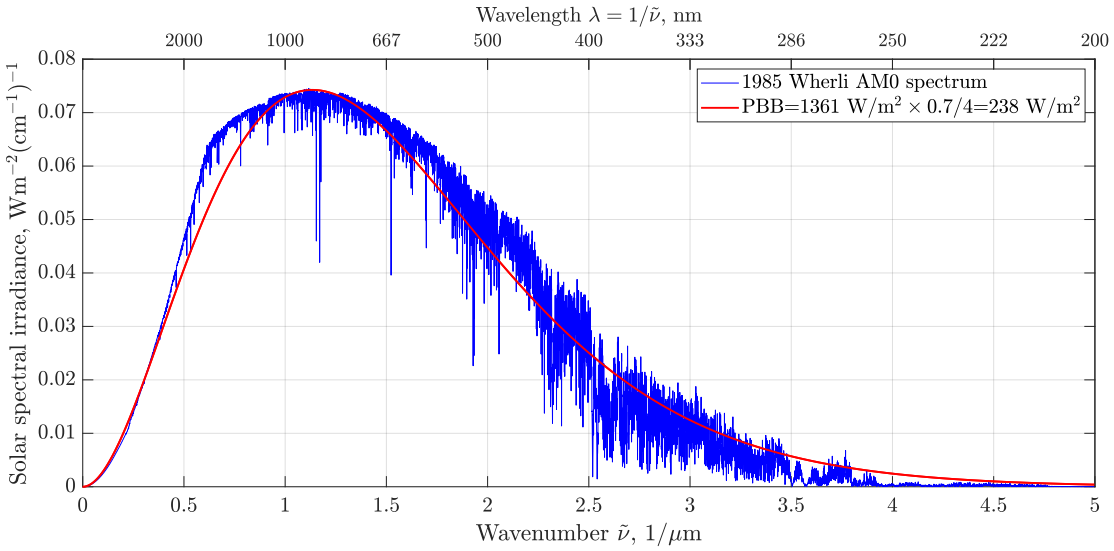

Figure B5: The Sun's spectral radiance versus radiation wavenumber in $\mu\mathrm{m}^{-1}$. The Sun temperature is $T_S = 5790$K. The area under the curve is 1361.4 $\mathsf{W\ m}^{-2}$. The blue curve is the 1985 Wehrli Standard Extraterrestrial (Top-of-Atmosphere) Solar Irradiance Spectrum (*Wehrli*, 1985, *Neckel and Labs*, 1981). The multiple absorption spikes that belong to Ca, Mg, Fe and H are typical of the G and K stars, like the Sun *Griffin* (1961), also see Chapter 7. *Question:* How did I map the Wehrli standard $(\lambda, \mathcal{R})$ spectrum onto this $(\tilde{\nu}, \mathcal{R})$ plot? *Hint*: Look at Eq. (B.49).

Appendix C

Plane-parallel model of absorption of IR radiation

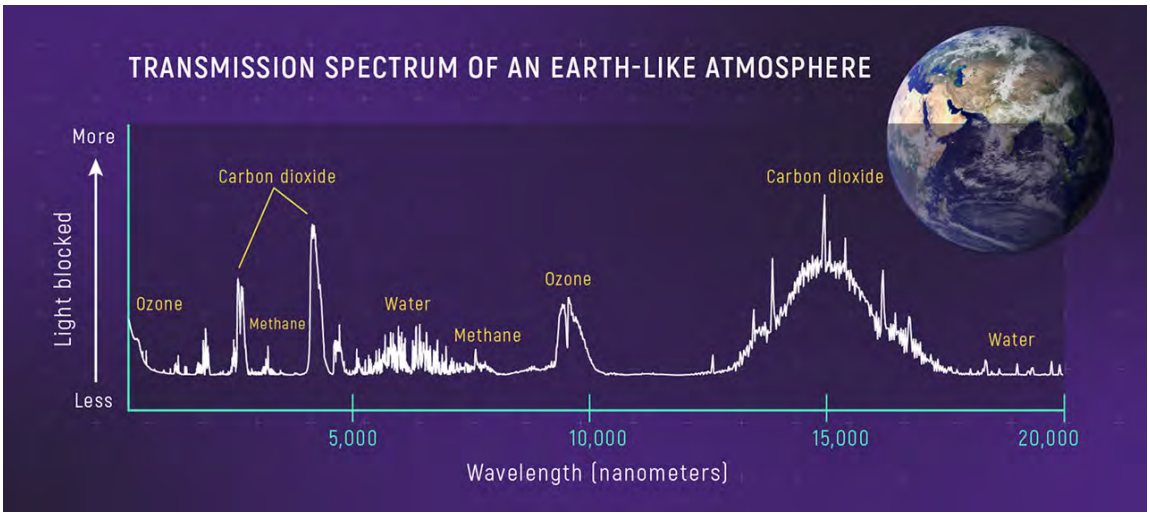

A transmission spectrum of an Earth-like atmosphere shows wavelengths of sunlight that molecules like ozone (O_3), water (H_2O), carbon dioxide (CO_2), and methane (CH_4) absorb. (Notice that on this graph, the y-axis shows amount of light blocked by Earth's atmosphere rather than brightness of sunlight that travels through the atmosphere: Brightness decreases from bottom to top.)
Lisa Kaltenegger and Zifan Lin, *Model transmission spectrum, 2021 ApJL 909* (Credits: NASA, ESA, CSA, Leah Hustak (STScI))

C.1. What are you going to learn?

The radiative forcing due to a change in atmospheric CO_2 concentration follows a logarithmic relationship:

$$\Delta F \approx 5.35 \ln\left(\frac{c}{c_0}\right) \ \mathrm{W\,m^{-2}}, \tag{C.1}$$

where c is the new concentration, c_0 is the baseline (typically 280 ppm_v), and the coefficient 5.35 is derived from line-by-line radiative transfer models (*Myhre et al.*, 1998, *Forster et al.*, 2021b).

The climate system responds to this forcing on multiple timescales. Two standard metrics are used to quantify the resulting warming from a doubling of CO_2:

- **Transient Climate Response (TCR)** is the global mean surface temperature change at the time of CO_2 doubling when concentrations increase by 1% per year, capturing fast feedbacks and ocean heat uptake on a time scale of years and decades but not full equilibration.
- **Equilibrium Climate Sensitivity (ECS)** is the steady-state temperature change after the system has fully equilibrated to doubled CO_2, accounting for all fast feedbacks on a time scale of centuries.

C.2. Why is this important?

Both TCR and ECS scale approximately linearly with the radiative forcing, and thus logarithmically with CO_2 concentration:

$$\Delta T \propto \ln\left(\frac{c}{c_0}\right), \tag{C.2}$$

though the magnitude of ΔT differs depending on the response timescale and feedbacks included.

C.3. Scaling derivation

The atmosphere is modeled as a series of stacked, homogeneous layers, each characterized by distinct composition, density, and temperature, all of which are functions of elevation z. In the derivation that follows, we will display explicitly only the dependence of all variables on z. With minor modifications, the treatment presented here follows the elegant formulation of *Huang and Bani-Shahabadi* (2014).

For monochromatic radiation of frequency ν, optical depth of a homogenous layer is given by Beer's law:

$$\tau_\nu = \ln \frac{I_\nu(z)}{I_{\nu,0}(z)} = -\ln T_r(z), \text{ where } T_r \text{ is layer's transmittance.} \tag{C.3}$$

Here $\tau_\nu = \tau$ is measured from top-of-atmosphere (TOA) to an arbitrary altitude z, $I_\nu(z)$ is the spectral radiance (monochromatic intensity) of radiation of frequency ν transmitted at the altitude z (in units of $\mathrm{W\,m^{-2}\,Hz^{-1}\,sr^{-1}}$), and $I_{\nu,0}(z)$ is that of the incident radiation.

For a layer at z_i, the "weighting function" is

$$W_i = \frac{dT_r(z_i)}{dz} = -\mathrm{e}^{-\tau} \frac{d\tau}{dz}\bigg|_{z=z_i} > 0 \tag{C.4}$$

For m layers, the radiative transfer equation (RTE) can be approximated as

$$\mathcal{R} \approx \sum_{i=1}^{m} B_\nu[T(\tau_i)] W_i = \sum_{i=1}^{m} B_\nu(\tau_i) W_i, \text{ where } \mathcal{R} \text{ is the outgoing radiance, } \mathrm{Wsr^{-1}m^{-2}} \tag{C.5}$$

where $B_\nu(\tau_i$ is the Planck blackbody function of layer i, When the molar CO_2 gas concentration c in the atmospheric column is uniformly increased to $a = c_{\text{new}}/c_{\text{old}}$ times its original value, so does the optical depth at any given level

$$\tau_i^{'} = a\tau_i \tag{C.6}$$

We can still find m layers whose weighting functions $W_i^{'}$ are identical to those in the unperturbed atmosphere; i.e., $W_i^{'} = W_i$. Because W is only a function of τ, these layers in the perturbed atmosphere correspond to where $\tau = \tau_i/a$ in the unperturbed atmosphere. Because B_i are also functions of τ, this new set of source functions becomes $B(\tau_i/a)$

$$\mathcal{R}_{\text{new}} = \sum_{i=1}^{m} B_\nu(\tau_i/a)W_i \tag{C.7}$$

In the far infrared spectrum, and at terrestrial temperatures, the Planck blackbody function, B_ν, is an *almost linear* function of temperature. B_ν is then also a linear function of altitude z, given a constant temperature lapse rate:

$$B_\nu \approx C_1 + C_2 z,\ C_2 < 0 \tag{C.8}$$

Moreover, if the absorption cross-section σ is also constant or varies exponentially with z, it follows that the optical depth can be expressed as an exponential function of z:

$$\tau = C_3 \mathrm{e}^{C_4 z},\ C_4 < 0 \tag{C.9}$$

Combining Equation (C.8) and Equation (C.9) yields

$$B_\nu \approx C_5 + C_6 \ln \tau,\ C_6 = \frac{C_2}{C_4} > 0 \tag{C.10}$$

Subtracting Equation (C.5) from Equation (C.7) yields

$$\begin{aligned} \Delta\mathcal{R} = \mathcal{R}_{\text{new}} - \mathcal{R}_{\text{o}} = \sum_{i=1}^{m} \underbrace{[B_\nu(\tau_i/a) - B_\nu(\tau_i)]}_{-C_6 \ln a} W_i \propto -C_6 \ln a \propto -\ln\left(\frac{c_{\text{new}}}{c_{\text{o}}}\right) \\ \Delta F = -\Delta\mathcal{R} \propto \ln\left(\frac{c_{\text{new}}}{c_{\text{o}}}\right) \end{aligned} \tag{C.11}$$

where ΔF is the increment of radiative forcing due to a rapid increase of molar concentration of CO_2. The incremental radiance $\Delta\mathcal{R}$ and ΔF have a **logarithmic dependence** on the CO_2 concentrations at a reference state and after increasing CO_2 concentration a times.

Appendix D

Generalized Extreme Value (GEV) Distributions

On July 4th, 2025, in the Texas Hill Country town of Hunt – home to Camp Mystic – the Guadalupe River surged in 45 minutes from roughly 2 m to nearly 9 m, drowning 27 children and the camp director.

Human subtlety will never devise an invention more beautiful, more simple or more direct than does Nature, because in her inventions nothing is lacking and nothing is superfluous.
Leonardo da Vinci, Notebooks, Book 1.

D.1. What are you going to learn?

Generalized Extreme Value (GEV) distributions are widely used to model extreme events by analyzing blocks of data, such as the highest monthly rainfall over decades, weather and climate extrema, floods, earthquakes, the formation of large pores or fractures in a rock mass, or gas production from shales. When the extremes are sharply bounded below by zero (e.g., no rainfall, zero days per year above 100°F), they are best modeled with the Frèchet distribution, or Type II GEV. Conversely, for extremes that are more strongly bounded above than below (e.g., temperature maxima), the Weibull distribution, or Type III GEV, is more appropriate.

Here, we first analyze 85 years of monthly maxima of daily rainfall in Sealy, TX, as shown in **Figure D1**. Our objective is to determine the probability distribution of the largest daily rainfall events over many years. A Type II GEV probability density function fits the monthly maxima exceptionally well (**Figure D2**). The corresponding cumulative probabilities of extreme monthly rainfall are presented in **Figure D3**.

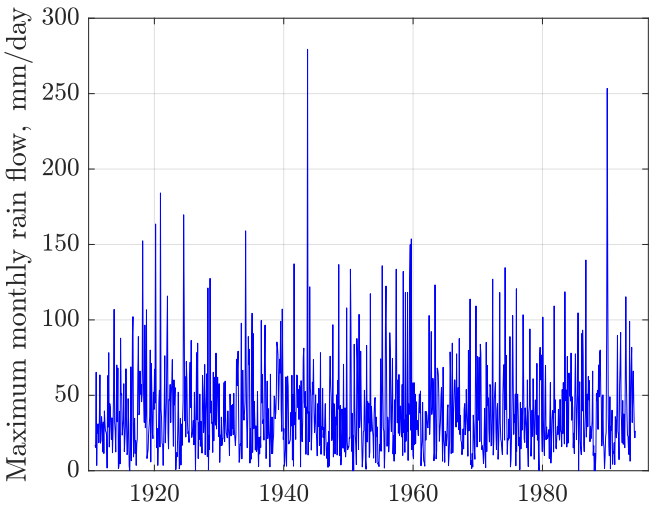

Figure D1: Monthly maxima of daily rainfall in 85 years of daily rainfall data in Sealy, TX. The question we ask is what is the likelihood of getting a certain maximum rainfall in a month?

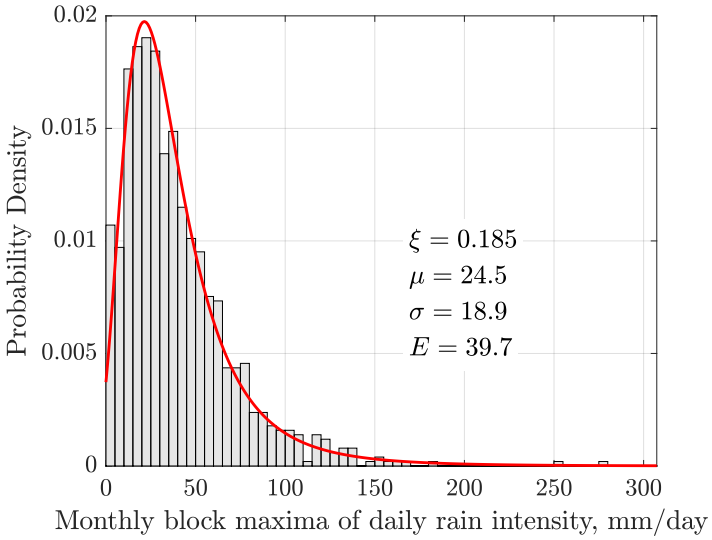

Figure D2: The monthly maxima of daily rainfall intensities in Sealy, TX, are fit with the Fréchet distribution. The expected maximum daily rainfall in a month is ∼40 mm/day.

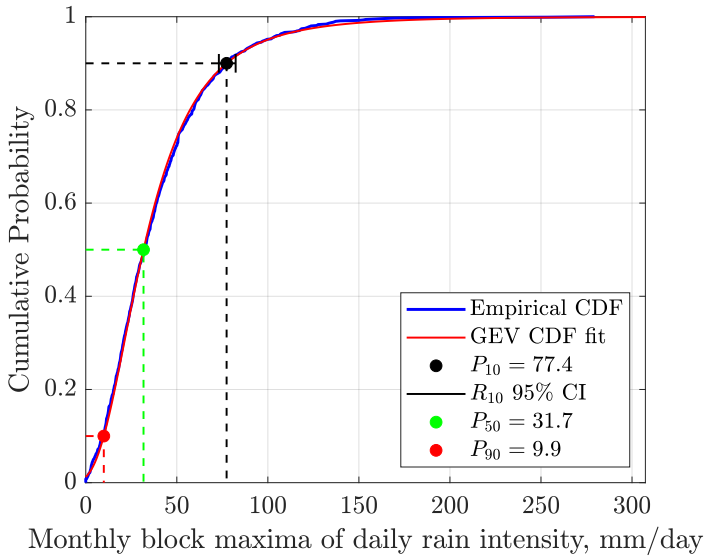

Figure D3: Cumulative probability of monthly maxima of daily rainfall in Sealy, TX. The black bar denotes the 95% confidence limits, indicating that only 10% of maximum monthly rainfall events exceed this value. Thus, 90% of maximum rainfall intensity in any month is less than 77 mm day^{-1}. For comparison, in July 2025, Hunt in the Texas Hill Country, 320 km west of Sealy, received 8 cm of rain in three hours, equivalent to 2000 mm day^{-1}. Such an intensity would have been extremely rare based on the 1911–1994 daily rainfall record, but not anymore. The same July 2025 storm, supercharged by anomalously warm Gulf of Mexico waters, delivered 35 cm of rain to Austin, half-way between Hunt and Sealy, in just five hours – an intensity of 1680 mm day^{-1}. Under global warming, rainfall events of this magnitude are no longer exceptional.

D.2. Why is this important?

In the second week of August 2025, the Maricopa County (Arizona) Heat Surveillance webpage reported that, in both 2023 and 2024, over 600 people per year died during the unrelenting June–October heatwaves, with temperatures reaching up to 123°F (50°C). Most of these fatalities were attributed to heatstroke. The victims were predominantly county residents, mostly men, and largely aged 35 years and older. Heatwaves and cold snaps are extreme events, which will be examined here in greater detail using approximately 130 years (Jan-01-1894 to Aug-05-2025) of temperature and rainfall data, downloaded from NOAA's National Centers for Environmental Information[1] and cleaned up.

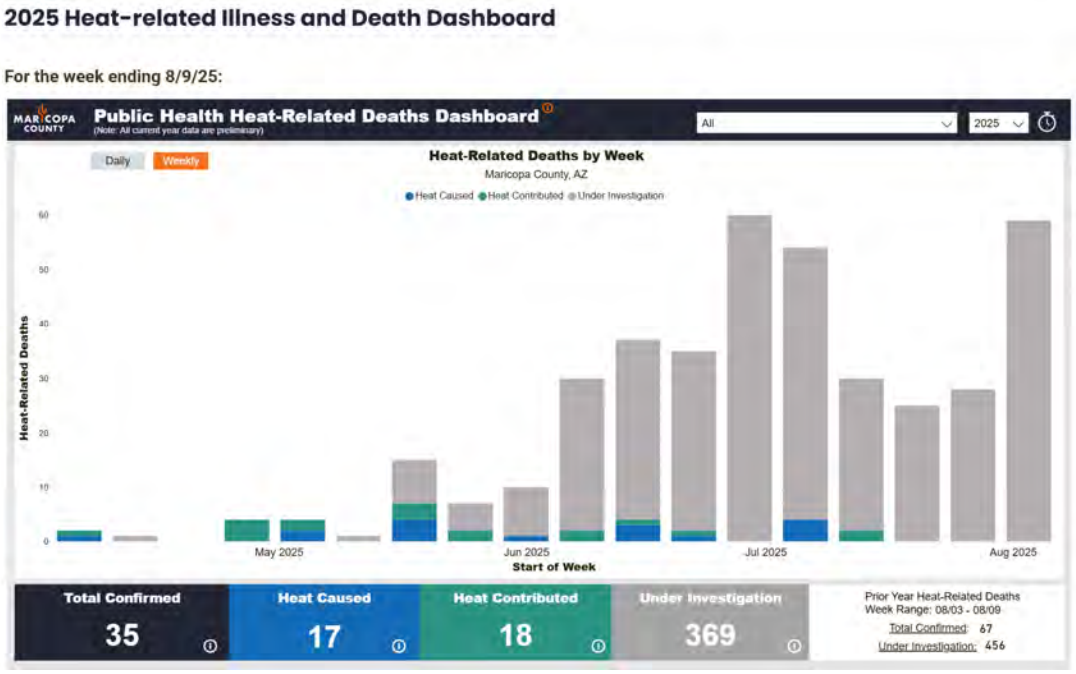

Figure D4: A screenshot of the dashboard of the Maricopa County Department of Public Health, showing heat-related deaths in May-August 2025. For earlier deaths, please consult *Maricopa County* (2025).

At the same time, in Juneau, the capital of Alaska, residents were asked to evacuate because of the imminent danger of an ice-dam failure. On August 18, the dam partially breached, but temporary flood barriers protected most homes from inundation. The fast-melting[2] Mendenhall Glacier occupies a large valley north of Juneau, forming an ice dam that impounds a meltwater lake in Suicide Basin. Since 2011, annual outburst floods from this basin have poured into Mendenhall Lake and surged down the river toward Juneau. In 2023, such an event flooded 300 homes. This extreme event was driven by climate change, as are many others worldwide.

In the distant Himalayas, a severe glacial lake outburst flood (GLOF) – an extreme event – occurred in October 2023, when the moraine-dammed South Lhonak Lake breached during heavy monsoon rains. The resulting flash flood destroyed the Teesta-III hydropower dam at Chungthang, inundating downstream areas, causing widespread infrastructure damage, and tragically claiming 55 lives, with 74 individuals still missing. In affected areas, water levels rose by 5–6 m.

This appendix provides the essential background for predicting statistical trends in the otherwise unpredictable weather and climate extremes, such as those shown in Figure 10.2. In the context of

[1] For the Dallas–Fort Worth area, see https://www.ncei.noaa.gov/access/past-weather/dallas%2C%20%20tx.

[2] From the 1750s to the present, the glacier has retreated by approximately 4 km, including 700 m between 1946 and 2009. Mendenhall Glacier's retreat is part of a widespread regional trend: the Juneau Icefield is losing snow and ice nearly five times faster than it did in the 1980s. Across the icefield, annual ice-melt volumes are increasing, with spring melt alone rising by about 16% per decade.

global warming, these extremes follow a Generalized Extreme Value (GEV) distribution, which assigns substantially higher probabilities to extreme heatwaves and rainfalls than does a Gaussian distribution. In words of Nassim Nicholas Taleb:

> Almost everything in social life [*and natural science, TWP*] is produced by rare but consequential shocks and jumps; all the while almost everything studied about social life focuses on the 'normal,' particularly with 'bell curve' methods of inference that tell you close to nothing. Why? Because the bell curve ignores large deviations, cannot handle them, yet makes us confident that we have tamed uncertainty. Its nickname in this book is GIF, Great Intellectual Fraud.
>
> *The Black Swan: The Impact of the Highly Improbable*, 2007, 2010.

D.3. Background

The Generalized Extreme Value (GEV) *Gumbel* (1958) probability density function, depicted in **Figure D5**, models distributions of extrema (minima or maxima) of blocks of data. For example, the Weibull distribution with $\xi < 0$, can be used to model the distribution of pore throats in carbonate macroporosity in the Ghawar with the capillary pressure data from *Clarke et al.* (2008), see (*Patzek et al.*, 2022).

In a generalized extreme value distribution, $\mu \in \mathbb{R}$ is the *location parameter*, $\sigma > 0$ the *scale parameter*, and $\xi \in \mathbb{R}$ (often denoted by k) is the *shape parameter*. The generalized extreme value (GEV) distribution is a family of continuous probability distributions developed within extreme value theory to combine the Gumbel ($\xi = 0$), Fréchet ($\xi > 0$) and Weibull ($\xi < 0$) families also known as type I, II and III extreme value distributions.

Always

$$\frac{y}{y_0} := \begin{cases} 1 + \xi \dfrac{(x-\mu)}{\sigma}, & \text{if } \xi > 0,\ c = \dfrac{1}{\xi} \\ 1 - \xi \dfrac{(x-\mu)}{\sigma}, & \text{if } \xi < 0,\ c = -\dfrac{1}{\xi} \end{cases} \tag{D.1}$$

where a new random variable, y, and its scaling parameter, y_0, are defined by Eq. (D.1). Here $y = x + (\mu - \sigma/|\xi|)$ and $y_0 = \sigma/|\xi|$.

The GEV probability density function is defined as:

$$\begin{aligned} f(x;\mu,\sigma,\xi) = &\frac{1}{\sigma}\left[1 + \xi\left(\frac{x-\mu}{\sigma}\right)\right]^{(-1/\xi)-1} \times \\ &\times \exp\left\{-\left[1 + \xi\left(\frac{x-\mu}{\sigma}\right)\right]^{-1/\xi}\right\} \end{aligned} \tag{D.2}$$

For $\xi < 0$ and with $c = -1/\xi$, the Type III GEV distribution can be transformed into the classical Weibull distribution:

$$f_W(y;c,y_0) = \frac{1}{\sigma}\left(\frac{y}{y_0}\right)^{c-1} \exp\left[-\left(\frac{y}{y_0}\right)^{c}\right], \tag{D.3}$$

also known as the *stretched exponential* distribution for $c < 1$. With $c = 1$, this distribution reduces to a simple exponential distribution

$$f(x;c) = \begin{cases} ce^{-cx}, & x \geq 0, \\ 0, & x < 0, \end{cases}$$

with a constant failure rate, c. For $c < 1$, the failure rate decreases over time, i.e., the defective items are weeded out from the population early on. Conversely, for $c > 1$, the failure rate increases with time.

The Weibull distribution with $c \leq 1$ has been used to model pretty much everything in the Universe *Laherrère and Sornette* (1998), including the distribution of hydrocarbon volumes in the Gulf of Mexico

and die-off of dinosaurs. Its cumulative probability distribution function is particularly simple:

$$cdf_W(y; c, y_0) = \int_0^y f_W(y; c, y_0)\, dy = 1 - \exp\left[-\left(\frac{y}{y_0}\right)^c\right] \tag{D.4}$$

For $c < 1$, the cumulative distribution (D.4) presents a clear curvature on a log-log plot while exhibiting a relatively extensive apparent linear behavior, all the more so, the smaller c is. It can thus be used to account both for a limited power-law scaling regime and a cross-over to non-scaling.

The GEV distribution's *mode* (pdf's peak value) is

$$\text{Mode(X)} = \mu + \frac{\sigma}{\xi}\left[(1+\xi)^{-\xi} - 1\right], \quad \xi \neq 0 \tag{D.5}$$

Median is

$$\text{Median(X)} = \mu + \sigma\frac{(\ln 2)^{-\xi} - 1}{\xi}, \quad \xi \neq 0 \tag{D.6}$$

Mean or *expected value* of the GEV distribution is

$$\text{E(X)} = m = \mu - \frac{\sigma}{\xi} + \frac{\sigma}{\xi}\Gamma(1-\xi), \quad \xi \neq 0 \tag{D.7}$$

Variance of the GEV distribution is

$$\text{V(X)} = \frac{\sigma^2}{\xi^2}\left[\Gamma(1-2\xi) - \Gamma^2(1-\xi)\right], \quad \xi \neq 0,\ \xi < \frac{1}{2} \tag{D.8}$$

if $\xi = 0$

$$\text{V(X)} = \frac{\pi^2}{6}\sigma^2 \tag{D.9}$$

and V does not exist ($= \infty$) otherwise.

The *standard deviation* is

$$s = \sqrt{\text{V}} \tag{D.10}$$

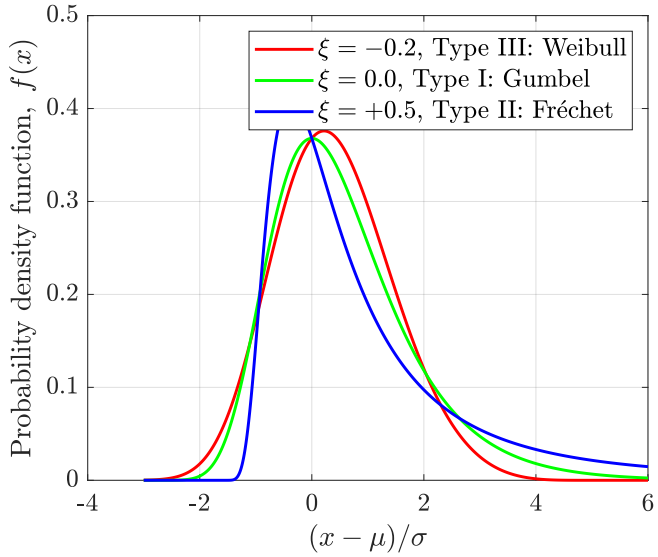

Figure D5: Examples of the three GEV distributions with three values of the shape parameter, ξ, and with a zero location parameter, $\mu = 0$, and unit scale parameter, $\sigma = 1$. Notice that for $\xi < 0$ or $\xi > 0$, the density has zero probability above or below, respectively, the upper or lower bound -$(1/\xi)$. In the limit as ξ approaches 0, the GEV is unbounded. These cases can be summarized as the constraint that $1 + \xi(x - \mu)/\sigma$ must always be positive.

D.4. Temperature and rainfall extrema in Dallas, Texas

Let us examine the weather and climate in Dallas within the broader context of global warming. For example, the summer of 2025 is poised to become another record-breaker. Two intense heatwaves have swept across Europe, causing hundreds of heatstroke deaths each month, amplifying wildfires, and pushing electrical grids to their limits. From mid-June to early July, Western Europe experienced its highest average temperatures for this period in decades, as well as the hottest June on record. For weeks on end, persistent high-pressure "heat domes" kept temperatures above 104°F (40°C), and up to 115°F (46°C) in Spain and Portugal.

To conduct our analysis, we partition each year into a warm season (May-September, denoted "Hot Season" or "HS") and a cool season (October-March, denoted "Cold Season" or "CS"). For each period, we compute the four quantities listed in Table D1. While other combinations are possible – for example, computing the first two rows of Table D1 for the cool season and the second two rows for the warm season – these alternatives are omitted here for brevity.

Table D1: Definitions of four temperature extrema considered in this example

Definition	**Symbol**	**Duration**	**Meaning**
Monthly maxima of daily maxima	T_{maxmax}	Hot Season (HS)	Hottest days
Monthly minima of daily maxima	T_{maxmin}	Hot Season	Coolest warm days
Monthly maxima of daily minima	T_{minmax}	Cold Season (CS)	Warmest cold nights
Monthly minima of daily minima	T_{minmin}	Cold Season	Coldest nights

Let us begin by asking the following question: *How many dangerously hot days, with maximum tempera-*

tures at or above 100°F *(∼* 38°C*), have occurred each year since 1894?*

First, in Figure D6, note that the 1899 record, as well as Apr–Sep 1901 and 1902, are missing. The disappearance of very hot days—together with cool days and nights—during those intervals should be disregarded. Incomplete data obscure the climate signal from coeval major volcanic eruptions that caused significant cooling. Fortunately, the 1902 and 1912 data are intact and capture this cooling.

Figure D6(a) shows the temporal distribution of extreme heat days. The pattern is surprisingly complex: clusters of years with many hot days are separated by intervals with few or none. The cooler intervals correlate reasonably well with El Niño events.

The primary volcanic cooling signals in the late 19th century arose from the 1883 Krakatau eruption (VEI-6[3]) and the 1886 Tarawera eruption (VEI-5), whose effects lingered into the early 1890s. In the early 20th century, the largest eruptions by volume and climatic impact were the "colossal" Santa María (VEI-6, 1902) and Novarupta (VEI-6, 1912), the latter being the largest eruption of the entire century. Their cooling influence, together with El Niño events, is clearly visible in Figure D6(a) up to about 1908 and again in 1912.

Since 1918, the 5-year moving average of hot days has resembled the teeth of an upside-down, upward-tilted saw—some teeth broken or missing—with an average slope of ∼ +1.6 days per decade. Over the 130 years of available data, this amounts to an increase of roughly 10 very hot days per year, or 17 days if the count begins in 1918. Within this period, five strong and five weak cycles of elevated temperatures can be distinguished.

Figure D6(b) demonstrates that pleasant night and day temperatures in Dallas have been disappearing at an alarming rate: approximately −2.6 days per decade overall, and as much as −9.4 days per decade since 1976. In total, about 56 cool days have been lost since 1894, including 28 days since the mid-1970s, when the global climate bifurcated. This is climate change in action—slow but unrelenting.

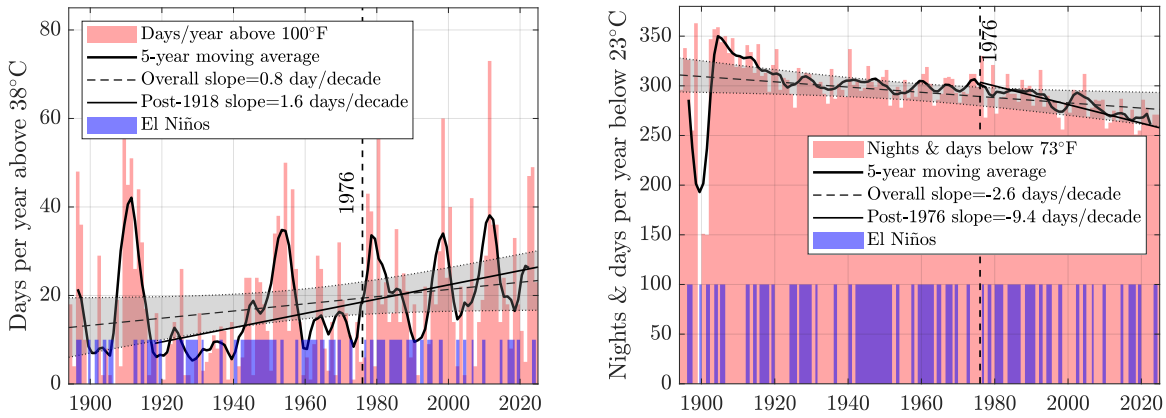

(a) (b)

Figure D6: **(a)** The number of days per year in Dallas with maximum temperatures above 100°F. This number varies from zero to 73 days/year. Its temporal distribution is complex, quasi-cyclic, and correlates negatively with the El Niño years. There is an overall upward trend of +0.8 days per decade of rising hottest temperatures, increasing to +1.6 days per decade after 1918, adding on average 17 very hot days. **(b)** The number of nights and days per year with minimum temperatures below 73°F. The pleasant climate in the Dallas area has been disappearing uniformly at 2.6 days per decade, and at 9.4 days per decade after the 1976 global climate bifurcation described in Chapter 10. Since 1894, climate change has erased 56 cool nights and days, or a little less than two months of mild weather.

[3]The Volcanic Explosivity Index (VEI) is a logarithmic scale introduced by *Newhall and Self* (1982) to standardize eruption magnitude. It combines (i) erupted tephra volume, (ii) cloud column height, and (iii) qualitative descriptors such as "gentle," "cataclysmic," or "colossal."

Let's analyze now the four classes of extreme events listed in Table D1. They all must follow the Type III (Weibull) GEV distribution we are guessing. T_{maxmax} and T_{maxmin} go together and we compare them first.

D.4.1. Temperature extremes in Dallas

Distributions of of T_{maxmax} and T_{maxmin}

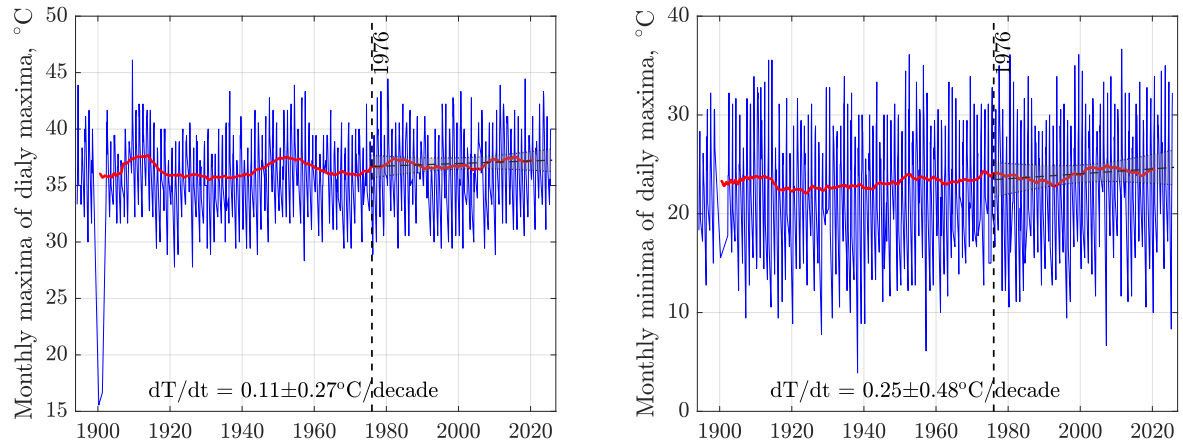

(a) (b)

Figure D7: Histories of T_{maxmax} **(a)** and of T_{maxmin} **(b)** in Dallas. The red curves show 5-year moving averages. The broken black line represents the linear regression fit to the blue curve, and the shaded gray region denotes the 95% confidence interval of the linear model. Notice the missing data around the year 1900.

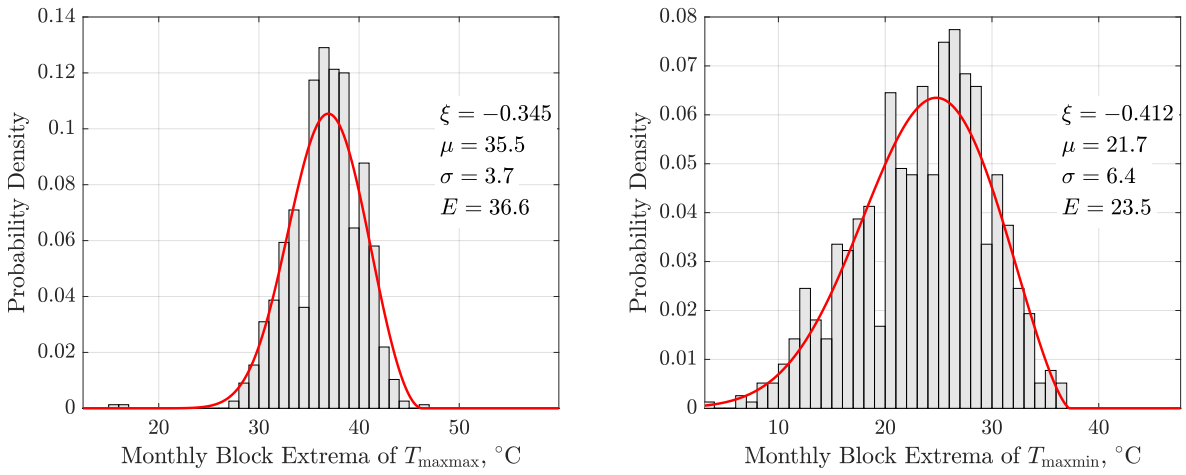

(a) (b)

Figure D8: Probability density functions (PDFs) of T_{maxmax} **(a)**, and T_{maxmin} **(b)** in Dallas. The gray bars are the scaled histograms of the temperature data. The red curves are the best fits of the data with a GEV distribution in Equation (D.2). ξ, μ and σ are the GEV distributions's shape. location, and scale parameters, respectively, and E is defined in Equation (D.7).

Figure D7(a) shows the history of the monthly maxima of daily maxima (T_{maxmax}), i.e., the hottest daytime temperatures in Dallas. Since 1976, these temperatures have increased nearly uniformly, with a

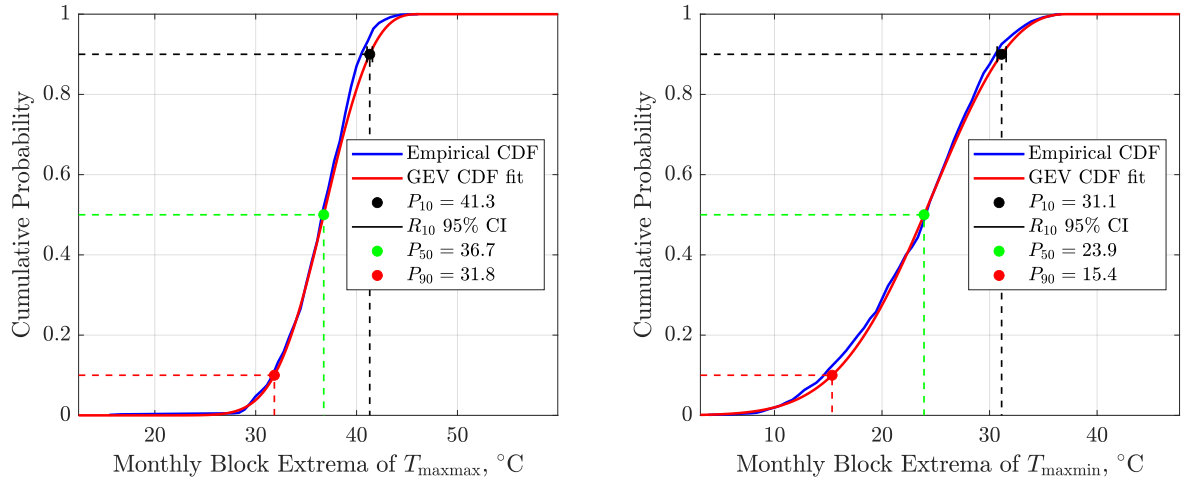

Figure D9: Cumulative probability density functions (CDFs) of T_{maxmax} **(a)**, and T_{maxmin} **(b)** in Dallas. The blue curve shows the empirical CDF obtained by integrating the scaled temperature data. The red curve represents the optimal GEV distribution fit, with parameters estimated from the PDF (see, e.g., Equation (D.4)). The black bar indicates the 95% confidence interval (CI) of the residuals of the optimization function at the level of P_{10}. Here, P_{90}, P_{50}, and P_{10} denote the cumulative probabilities corresponding to the 10th percentile (90% of the data exceed this probability), the median, and the 90th percentile (only 10% of the data exceed this probability), respectively.

mean slope of 0.11°C per decade and a substantial standard deviation (scatter) of ±0.27°C per decade. On average, the hottest daytime temperatures in Dallas have risen by about 0.6°C since 1976.

The history of the monthly minima of daily maxima (T_{maxmin}), shown in Figure D7(b), displays even greater variability. Post-1976, the linear trend of these nighttime maxima has a slope of 0.25 ± 0.48°C per decade. Overall, nighttime hot-season temperatures have increased by approximately 1.25°C since 1976.

Figure D8 shows, respectively, the probability density functions (PDFs) of the hottest days (a), and the hottest nights (b). The expected (mean) temperature of the hottest days is $E = 36.6$°C, while that of the hottest nights is $E = 23.5$°C. The probability of distribution of the hottest night temperatures is wider, because there is more temperature variability in Figure D7(b).

Figure D9 presents the respective cumulative probability functions (CDFs) for T_{maxmax} (a) and T_{maxmin} (b). The respective median values, see Equation (D.8), of the hottest day- and nighttime temperatures are 36.7°C and 23.9°C. The medians are slightly higher than the means, because the GEV distributions have fat left tails.

Distributions of of T_{minmax} and T_{minmin}

Figure D10(a) shows the history of the monthly maxima of daily minima (T_{minmax}), i.e., the warmest daytime temperatures in Dallas during the cold season. Since 1976, these temperatures have increased nearly uniformly, with a mean slope of 0.44°C per decade and a standard deviation of ±0.33°C per decade. On average, the warmest daytime temperatures during cold season in Dallas have risen by about 0.6°C since 1976.

The history of the monthly minima of daily minima (T_{minmin}), shown in Figure D10(b), exhibits more variation. Post-1976, the linear trend of these nighttime minima has a slope of 0.25 ± 0.48°C per decade. Overall, nighttime cold-season temperatures have increased by approximately 2.2°C since 1976.

Figure D11 shows, respectively, the probability density functions (PDFs) of the coldest days (a), and the coldest nights (b). The expected (mean) temperature of the coldest days is $E = 16.5$°C, while that of

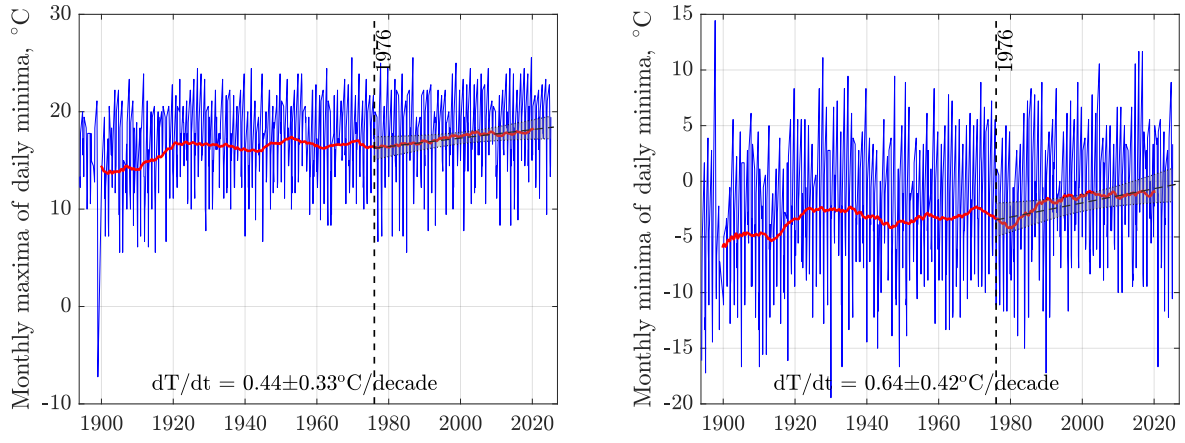

(a) (b)

Figure D10: Histories of T_{minmax} **(a)** and T_{minmin} **(b)** in Dallas. The red curves show 5-year moving averages. The broken black line represents the linear regression fit to the blue curve, and the shaded gray region denotes the 95% confidence interval of the linear model.

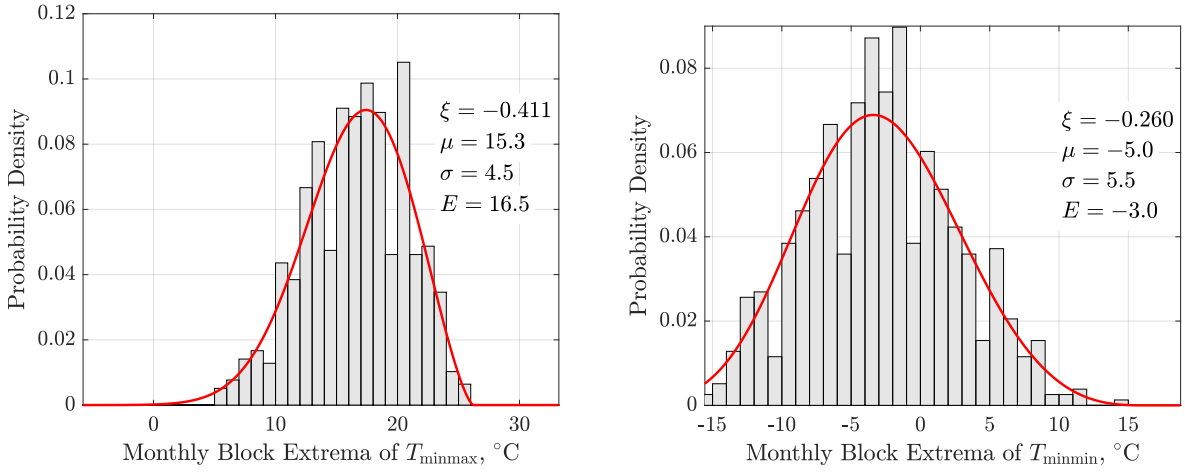

(a) (b)

Figure D11: Probability density functions (PDFs) of T_{minmax} **(a)**, and T_{minmin} **(b)** in Dallas.

the coldest nights is $E = -3.0$°C The probability of distribution of the coldest night temperatures is wider, because there is more temperature variability in Figure D10(b).

Figure D12 displays the respective cumulative probability functions (CDFs) for T_{minmax} (a) and T_{minmin} (b). The respective median values of the coldest day- and nighttime temperatures are 16.8°C and -3.1°C.

D.4.2. Distribution of maximum monthly rainfall data in Dallas

Figure D13 shows the monthly maxima of daily rainfall in Dallas since January 1, 1894. The variability is high, but since 1976 there has been a slight upward trend in maximum daily rainfall, with a slope of about 1 mm day^{-1} decade^{-1}, corresponding to an increase of roughly 5 mm day^{-1}. Nevertheless, over the full 132 years of record, the average annual rainfall in Dallas has remained remarkably constant at 316 mm yr^{-1} ($R^2 = 0.999$).

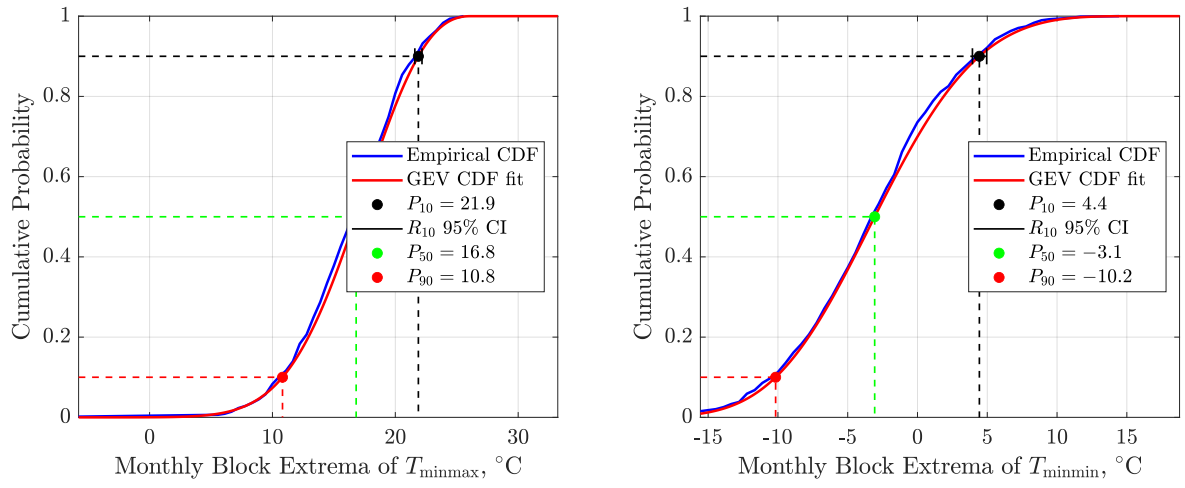

Figure D12: Cumulative probability density functions (CDFs) of T_{minmax} **(a)**, and T_{minmin} **(b)** in Dallas.

Figure D14(a) indicates that the expected (mean) intensity of the monthly maximum daily rainfall is 33.6 mm day^{-1}. By contrast, the median maximum rainfall intensity, shown in Figure D14(b), is only 27.5 mm day^{-1}, because the Fréchet distribution that fits the monthly maxima well exhibits a long, heavy right tail.

On average, about 10% of annual rainfall has historically fallen in a single extreme ($\geq$ 1 day) event, a proportion that has increased slightly since 1976 to roughly 12%. Occasionally, as shown in Figure D14(a), as much as one-half of the annual rainfall can be delivered in a single extreme event. This proportion is likely to increase, because of global – and local – warming of climate.

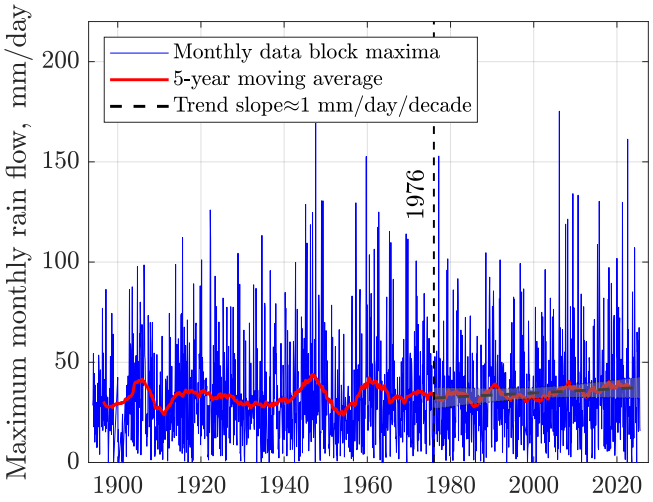

Figure D13: Monthly maxima of daily rainfall in 132 years of daily rainfall data in Dallas, TX. The red curves show 5-year moving averages. The broken black line represents the linear regression fit to the blue curve, and the shaded gray region denotes the 95% confidence interval of the linear model.

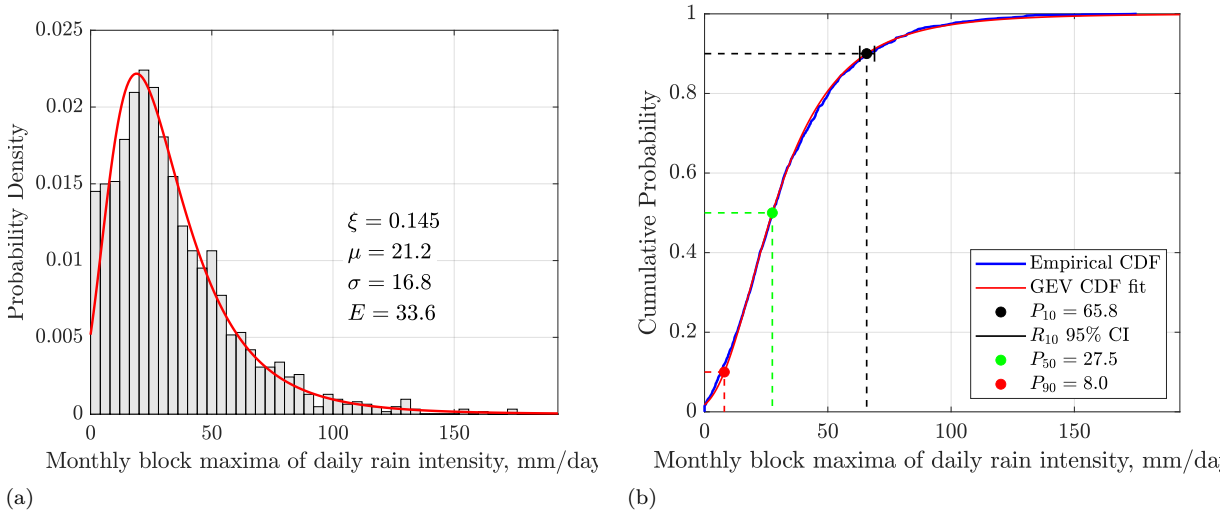

Figure D14: .**(a)** Probability density function (PDF) of maximum rainfall each month in Dallas, and **(b)** The corresponding CDF.

D.5. Conclusions

We have analyzed extreme weather events and climate change in Dallas, TX. Over the past 132 years, the climate in Dallas has warmed steadily, as shown in Figure D6. The most important changes have been an increase in the frequency of very hot days above 100°F and the disappearance of mild days and nights below 73°F. Since 1894, an average of 17 very hot days have emerged per year, while 56 mild days and nights have vanished. The coldest nights have been disappearing at the fastest rate since 1976, when the global climate bifurcated (see Figure D10).

Although the average annual rainfall in Dallas has remained essentially unchanged since 1894, the proportion of extreme rainfall events has been increasing slowly since 1976.

Practically speaking, the risks of extreme heatwaves and rain bombs (including heavy thunderstorms and tornadoes) have been rising in Dallas, along with the city's reliance on air conditioning. In Texas overall, climate change is projected to increase residential electricity use by 50–57% by 2050, largely to power air conditioning *Texas 2036* (2023). In 2024, the average Dallas household consumed approximately 937 kWh per month, with A/C representing a significant share of this demand *Rhythm Energy* (2024). For comparison, residents of Austin used on average 1,530 kWh per month in 2024. Residents of Houston used 1,300 kWh every month. Here in Oakland, CA, our household consumed only about 334 kWh in July 2025, since no A/C was required.

It is well known that California has the highest average electricity cost per kWh in the United States – more than twice that in Texas. However, the average 2024 monthly residential electricity bills in Dallas, Austin, and Houston were approximately $174, $219, and $241, respectively. By comparison, our July bill was only $167. There are, after all, fringe benefits to living next to a giant cooler like the Pacific Ocean.

Appendix E

Sea ice extent in the Arctic and Antarctic

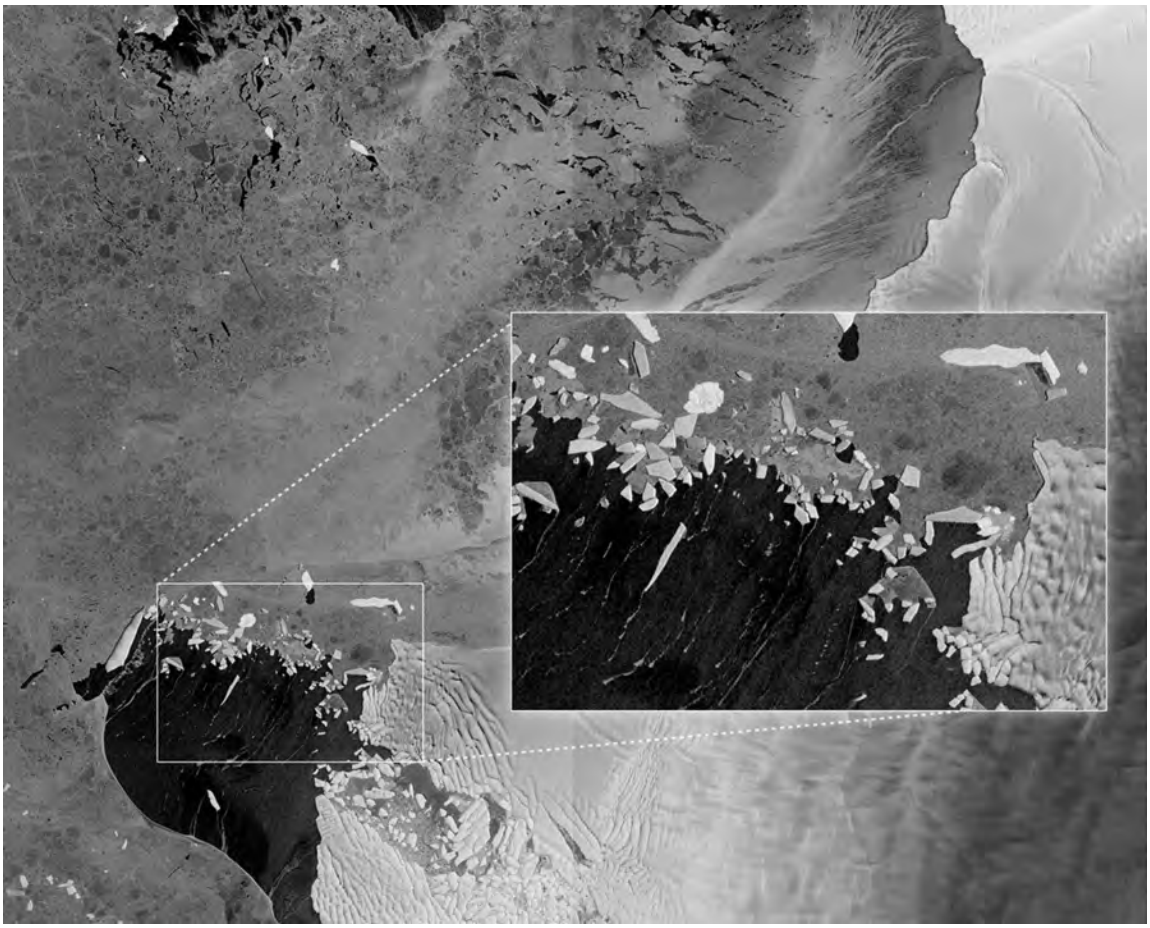

Parts of Pine Island Glacier and Thwaites Glacier in West Antarctica.
Image acquired on 13 April 2014 at 09:03 GMT (11:03 CEST) by the newly launched ESA Sentinel 1A satellite.

The oceans and the icy parts of the world are in big trouble, and that means we're all in big trouble, too.
Oppenheimer et al. (2019).

E.1. What are you going to learn?

The 2014 image on the previous page shows that Antarctica's fastest-flowing glacier has, unexpectedly, halted its thinning at the terminus, while a neighboring glacier continued to lose mass at a rapid pace, according to recent satellite analyses (*Vaughan*, 2019). The Pine Island and Thwaites glaciers in West Antarctica have been retreating at alarming rates and, over the long term, could collectively contribute substantially to global sea-level rise. Here, we place the melting of these two glaciers within the broader context of decreasing total sea-ice areas and shifting rates of ice loss across both polar regions. At present, the trends are opposite: Arctic ice loss is decelerating, while Antarctic ice loss is accelerating. Our assessment relies exclusively on satellite observations of sea-ice extent at both poles curated by NOAA. We deliberately refrain from offering forecasts or speculations about future sea-level rise—see, e.g., (*Bamber et al.*, 2019)—that are based on highly improbable, extreme-emission IPCC scenarios discussed earlier in this book.

E.2. Why is this important?

The NOAA satellites and their associated databases are in grave danger of being dismantled by the current Trump administration. In addition, a new DOE report *Christy et al.* (2025) contains extensive misleading claims and cherry-picked disinformation that must be addressed. For example, on page 90, the DOE report asserts:

- Arctic sea ice extent has declined by only about 5% since 1980 (https://nsidc.org/data/seaice_index/images/s_plot_hires.png), and that since 2007 there has been a "pause" in Arctic sea ice decline (*England et al.*, 2025).
- With respect to Antarctic sea ice, the IPCC AR6 states: "There has been no significant trend in Antarctic sea ice area from 1979 to 2020 due to regionally opposing trends and large internal variability" (Summary for Policymakers, A.1.5).

In light of satellite data and analyses readily available after 2020, both of these statements are demonstrably false. Furthermore, the paper by (*England et al.*, 2025), whose key features are summarized in

Table E1: Summary of strengths and limitations of (*England et al.*, 2025).

Aspect	Strengths	Limitations
Observational Evidence	Strong, multi-metric, multi-season confirmation	Volume decrease suggests deeper degradation
Model Support	Frequent slowdowns in ensemble projections	Attribution to forced vs. internal factors unclear
Prognostic Insights	Probabilistic outlook reinforced with caution	Broad uncertainty in projections
Communication Impact	Emphasizes ongoing risk and need for action	Could be and was misused to disregard long-term sea ice collapse

Table E1, invites misinterpretations and is cited in the DOE report in a way that distorts the paper's detailed reasoning. To set the record straight, we have accessed NOAA National Sea Ice Date Center (NSIDC) datasets directly and performed an independent analysis, the results of which are presented in this appendix.

E.3. Background

Let us begin with a few useful observations:

1. As explained in Chapter 10, for several reasons – one being error cancellation – it is preferable to express most aspects of climate change as deviations from well-established baselines (anomalies)

rather than as absolute values. Figure E1 shows two baselines for sea-ice extents in the Arctic and Antarctica, respectively. Our eyes are much better at recognizing changes in pattern or deviations from an existing trend.

2. Polar sea-ice extent is typically reported in millions of square kilometers, but such large numbers are difficult to grasp intuitively. It is therefore more effective to express them in familiar large-area units. Here we choose the area of Texas—the second-largest U.S. state—which covers 0.695 million km^2. In what follows, all anomalies will be expressed as multiples of the area of Texas, beginning with Figure E1. For reference, the total area of the United States is 9.83 million km^2, or a little more than 14 Texases. Between 1979 and 2025, the largest measured winter sea-ice area in Antarctica grew to about three times the U.S. area in 2014. In 1979, the peak Arctic sea-ice area reached roughly 2.4 U.S. areas, and has declined ever since.

3. The polar regions experience only two seasons: a cold, dark winter and a relatively warmer summer when the Sun remains above the horizon.

4. Between 1979 and 2025, the largest measured winter sea-ice area in Antarctica grew to two times the US area in 2014 and has since declined to 1.7 US areas by June 2025. In February 1979, the winter Arctic sea-ice area reached a maximum of 1.7 US areas, but has since declined to 1.5 US areas by February 2025.

5. The smallest observed summer sea-ice areas were 5 Texases in the Arctic, following the Great Arctic Cyclone of early August 2012, and 2.7 Texases in Antarctica during the record 2022 heatwave, repeated under the record-warm conditions of 2023.

6. NOAA's NSIDC data[1] and images use passive microwave data from the Defense Meteorological Satellite Program (DMSP) F17 and F18 Special Sensor Microwave Imager/Sounder (SSMIS) and Japan's Aerospace Exploration Agency (JAXA) Advanced Microwave Scanning Radiometer 2 (AMSR2). Data sets include the Sea Ice Index, AMSR2 Daily Polar Gridded Sea Ice Concentrations, and the NASA-produced Sea Ice Concentrations from Nimbus-7 SMMR and DMSP SSM/I Passive Microwave Data. Sea-ice extent is an area of ocean with at least 15 percent sea ice concentration. These NSIDC data were used both by (*England et al.*, 2025) and here, and all of our conclusions should be identical, but they are not.

7. Changes in sea-ice concentration are not only variations of areal extent, but also changes in thickness. Sea-ice thickness is a fundamental climate state variable, providing an integrated measure of the high-latitude energy balance (*Lindsay and Schweiger*, 2015). *Lindsay and Schweiger* (2015) estimated that the trend in annual mean ice thickness over the Arctic Basin was -0.58 ± 0.07 m decade^{-1} during the period 2000–2012. For the period 1975–2012 in the central Arctic Basin, they found that the annual mean ice thickness declined from 3.59 m in 1975 to 1.25 m in 2012—a 65% reduction. This critical indicator of Arctic sea-ice collapse is only mentioned in passing (*England et al.*, 2025) and here.

8. The phenomenon of "polar amplification" is more pronounced in the Northern Hemisphere, yet the Southern Hemisphere climate is more sensitive to its smaller polar amplification (*Caporale et al.*, 2025). Since 1979, for each 1°C of global warming, the Arctic has warmed by about 4°C (*Rantanen et al.*, 2022), with the Barents Sea warming by as much as 7°C, and Svalbard experiencing similarly extreme amplification (*Bradley et al.*, 2025). Polar amplification accelerates sea-ice thinning and loss through multiple processes, including enhanced melting by warmer surface waters, the spatial rearrangement of ocean currents, and stronger storms and waves.

9. According to *Rocha et al.* (2018), Arctic sea-ice melting represents a structurally interdependent stability regime shift: with one-way interactions that act as domino effects, and two-way interactions that produce hidden feedbacks. Together, these dynamics make the Arctic open sea-ice system a leading candidate for worst-case collapse.

10. In March 2022, Antarctica experienced an extraordinary heatwave *Bergstrom* (2024), described in Chapter 12.

[1] See https://nsidc.org/sea-ice-today/sea-ice-tools/charctic-interactive-sea-ice-graph.

11. The Southern Ocean absorbs nearly half of all ocean-stored human CO_2, but its future role is uncertain (*Alfred Wegener Institute*, 2025), as are the complex spatial and temporal mechanisms of CO_2 absorption and degassing (*Zhang et al.*, 2025a).

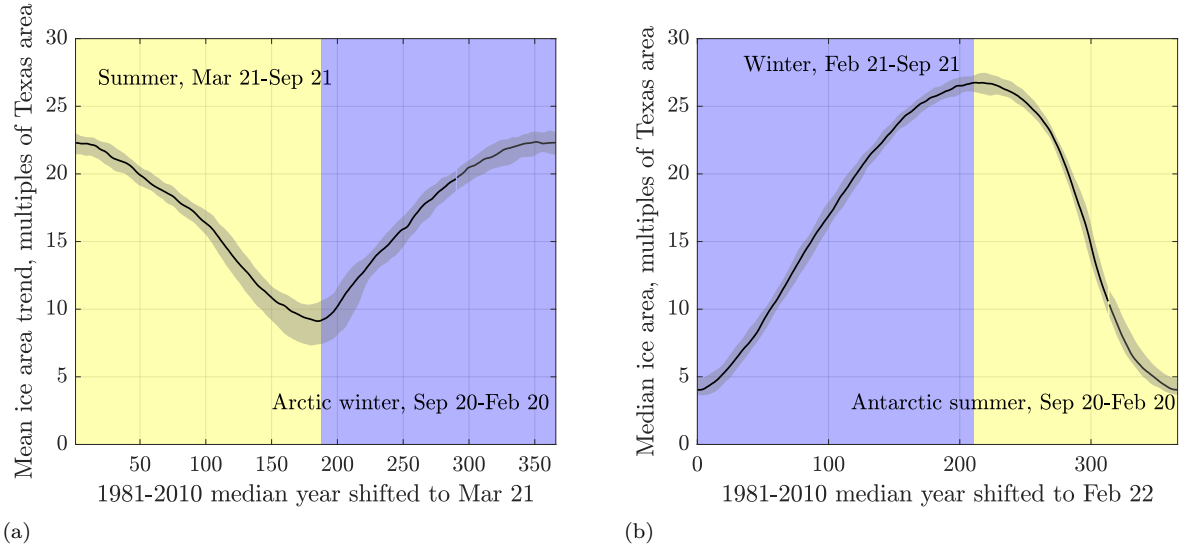

Figure E1: The 1981–2010 median annual sea-ice extents in **(a)** the Arctic and **(b)** Antarctica, expressed in units of the area of Texas. Note that the two polar seasonal cycles are offset by approximately six months relative to one another. The gray bands around the median curves indicate the P_{10} (upper) and P_{90} (lower) deciles, which exclude 10% of outliers from the right and left tails of the probability density function of ice extents (see, e.g., Figure D9). During 1981–2010, the median sea-ice extents ranged from 9 to 22 Texases in the Arctic, and from 4 to 27 Texases in Antarctica. Keep these numbers in mind, because from now on we will be showing mostly the deviations – or anomalies – from these two curves.

E.4. Approach and results

The polar ice-extent data were imported from the NOAA NSIDC database into a custom MATLAB R2024b program that performed linear regression of secular trends with associated error bounds, computed a Fourier-series expansion of the cumulative net ice extent in the Arctic, and generated all plots. The NASA CERES-EBAF data file `CERES_EBAF-TOA_Ed4.2_Subset_200003-202407.nc` was used to calculate global albedo in Figure 8.4.

Figure E2 shows the stacked 1979–2024 sea-ice area anomalies in the Arctic and Antarctica, relative to the 1981–2010 median annual sea-ice areas in Figure E1. The temporal distributions of these anomalies differ markedly: in the Arctic, sea-ice area declines on average each year, with the rate of loss slowing after 2007. In contrast, Antarctic anomalies indicate that sea-ice area initially increased, reached a maximum in 2014, and has since declined rapidly on average.

If the anomalies in Figure E2 are unfolded into a continuous time series, as in Figure E3, our previous observations are confirmed. It becomes especially clear that the 2007–2025 decline in the Arctic ice-area anomaly is accompanied by the largest annual swings in this record.

Relative to the first 30 years of observations, the post-2007 Arctic sea-ice area has become increasingly out of tune with the 1981–2010 annual median, indicating greater instability and susceptibility to abrupt failure.

In Antarctica, the post-2015 decline in sea-ice area was briefly interrupted by a short-lived rebound in 2021, before reverting to its previous downward trend. The warming subsurface ocean appears to be the

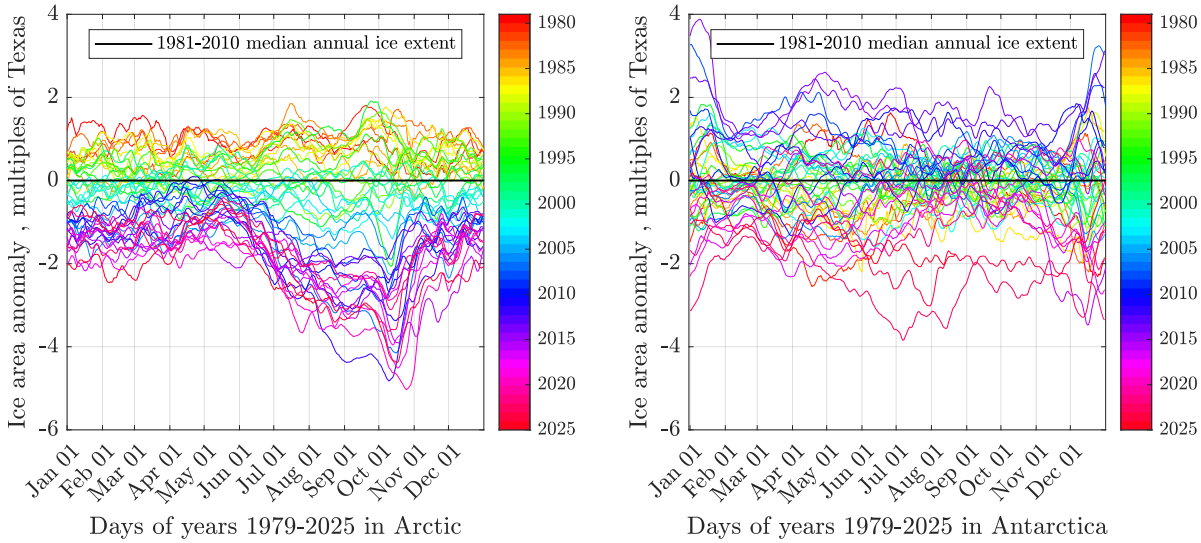

Figure E2: Stacked annual sea-ice area anomalies between 1979 and 2025 in **(a)** the Arctic and **(b)** Antarctica in multiples of Texas area. Each year is color-coded from red (earliest) to purple (latest). In the Arctic, all anomaly records after 2003 shift uniformly downward to about −5 Texases. By contrast, Antarctic anomalies are distributed more evenly, ranging from approximately −2 to +2 Texases, with the 2014–2016 records peaking near +4 Texases and the post-2020 records reaching lows of about −4 Texases. This comparison underscores how removing the baseline trend makes the underlying patterns of ice behavior more apparent.

key driver of this loss (*Purich and Doddridge*, 2023). Because most researchers have emphasized numerical model predictions over direct observations, the rapid decrease in Antarctic sea-ice extent remains highly controversial (*Jeong et al.*, 2025). No coupled climate model has yet successfully reproduced this abrupt decline, and the IPCC could offer only a limited, insufficient summary—later cited uncritically in the DOE report.

Since we aim to compare our conclusions with those of (*England et al.*, 2025) and to refute the two sweeping statements on page 90 of the DOE report, a plot of absolute ice areas in both polar regions is provided in Figure E4. Note that the 1979–2025 median sea-ice areas in both the Arctic and Antarctica are nearly identical, at ∼17 Texases, offering yet another testament to the hemispheric symmetry of the Earth's climate system (*Pierrehumbert*, 2010).

It is immediately apparent that the Arctic exhibits a long-term downward trend in both peak and trough ice areas, with the rate of decline slowing after 2007, whereas no such persistent trend is visible in Antarctica. The annual swings in ice area are also significantly larger in Antarctica than in the Arctic.

In the Arctic, the winter maximum ice area decreased from 23.45 Texases in 1979 to 21.43 Texases in 2024, corresponding to a decline of

$$\frac{21.43 - 23.45}{23.45} \times 100 \approx -8.5\%.$$

Over the same period, the summer minimum ice area decreased from 10.02 to 6.12 Texases, a decline of

$$\frac{6.12 - 10.02}{10.02} \times 100 \approx -39\%.$$

IPCC (2021), in Figure SPM.8, reaches an identical conclusion.

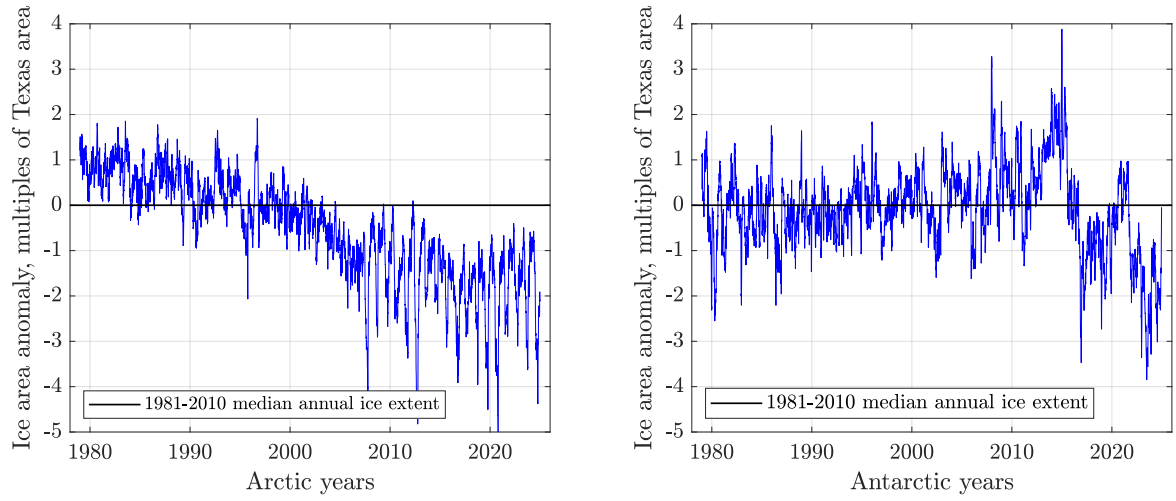

Figure E3: A time series of sea-ice area anomalies between 1979 and 2025 in **(a)** the Arctic and **(b)** Antarctica in multiples of Texas area. The Arctic time series shows a linear decline until 2007, after which it stabilizes, though with very large differences between summer and winter ice extents. We will return to this point later. In contrast, Antarctic sea-ice extent decreased until about 1994, then increased steadily until reaching a peak in 2013–2015, and has since undergone a rapid decline.

Based on the satellite data cited in the DOE report, its imprecise claim that "Arctic sea-ice extent has declined by only about 5% since 1980" is demonstrably false.

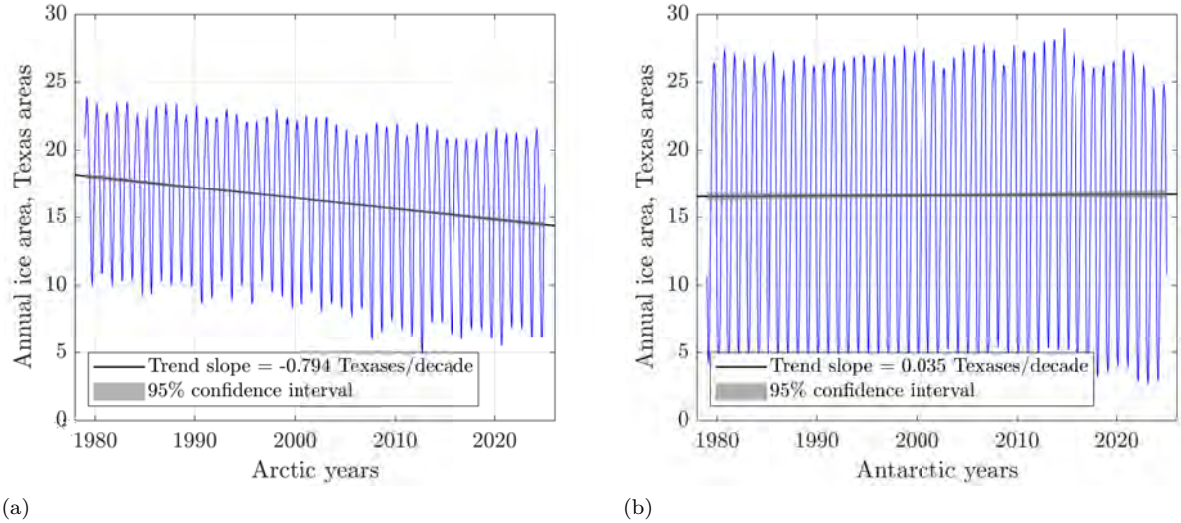

Figure E4: A time series of absolute sea-ice area between 1979 and 2025 in **(a)** the Arctic and **(b)** Antarctica in multiples of Texas area. The annual maxima occur in February for the Arctic and in September for Antarctica, while the corresponding minima occur in September and February, respectively. Antarctica exhibits greater seasonal variability—larger swings between maxima and minima—than the Arctic. In the Arctic, both maxima and minima show a steady decline, although the rate of loss slows after 2007. By contrast, in Antarctica a pronounced decline of ice area does not begin until after 2015.

The peaks and troughs in Figure E4 are replotted in Figure E5. The red September curve for the Arctic reproduces Fig. 1a of (*England et al.*, 2025). The post-2007 slowdown of the 45-year trends is evident and shown as thick dashed lines. However, as we have just demonstrated in Figure E4, the post-2007 Arctic ice extent has become increasingly chaotic, and the likelihood is high that it will soon give way to renewed acceleration of ice loss, which the authors admit. Therefore, it is safer to use the full 1979–2024 trends to project the rates of melting in February and September. Of particular interest is the linear September trend of $-1.14[-1.31$ to $-0.96]$ Texases per decade, with square brackets denoting the 95% confidence interval. If this trend continues on average, the Arctic will become ice-free in September of approximately the year

$$\frac{236.16}{0.114} \approx 2070\,.$$

Using a sigmoid approximation, *IPCC* (2021) project in Figure SPM.8 that the Arctic could be nearly "ice-free" in September by around 2050, but 2070 is certainly within the range of dates presented in Table 1 of (*Jahn et al.*, 2024). This catastrophic loss of Arctic summer sea ice is a cascade of interlinked, nested regime-shifts (*Rocha et al.*, 2018).

The story of ice melt in Antarctica is far more complex, with growing evidence of rapid, interacting, and sometimes self-perpetuating changes in the Antarctic environment. As Figure E5(b) illustrates, the post-2014 summer ice-melt trend has a slope of $-2.55[-4.33$ to $-0.77]$ Texases per decade, which would imply an ice-free condition by approximately

$$\frac{541.4}{0.255} \approx 2120\,.$$

In contrast to this linear projection, and based on satellite observations together with regional climate simulations up to 2020, IPCC WGI Chapter 9 (*Fox-Kemper et al.*, 2021) states:

> For Antarctic sea ice, regionally opposing trends and large interannual variability result in no significant trend in satellite-observed sea ice area from 1979 to 2020 in both winter and summer (high confidence). The regionally opposing trends result primarily from changing regional wind forcing (medium confidence). There is low confidence in model simulations of future Antarctic sea ice decrease, and lack of decrease, due to deficiencies of process representation, in particular at the regional level. ...
>
> ... The Antarctic Ice Sheet has lost 2670 [1800 to 3540] Gt mass over the period 1992-2020, equivalent to 7.4 [5.0 to 9.8] mm global mean sea level rise.

Today, however, we have five additional years of satellite observations that reveal a continued precipitous decline of Antarctic sea ice.

Given the cumulative evidence from the satellite data, together with a growing body of new research (*Abram et al.*, 2025), the IPCC AR6 claim that "There has been no significant trend in Antarctic sea-ice area from 1979 to 2020 due to regionally opposing trends and large internal variability" can no longer be regarded as valid—nor can the corresponding claim in the DOE report. The emerging evidence instead points to the nested, coupled, nonlinear stability regime changes that may drive the disappearance of the West Antarctic Ice Sheet within decade (*Zhang et al.*, 2025a). Recall that the Conger Ice Shelf, offshore east of Dome C in Western Antarctica already collapsed between Jan 31 and Mar 21 2022.

The last question we addressed based solely on satellite data is this:

How much sea-ice area accumulated in the Arctic and Antarctica relative to their respective linear secular trends of $-0.79[-0.85$ to $-0.74]$ *Texases per decade and* $+0.035[-0.057$ to $0.127]$ *Texases per decade?*

Integrating the annual sea-ice areas relative to these trends yields the net cumulative ice areas in the Arctic and Antarctica, from which an interesting picture emerges (see Figure E6).

In the Arctic, the relative cumulative sea-ice area oscillates with a beat period of roughly 30 years (28.4 years with an optimized 7-term Fourier series expansion).

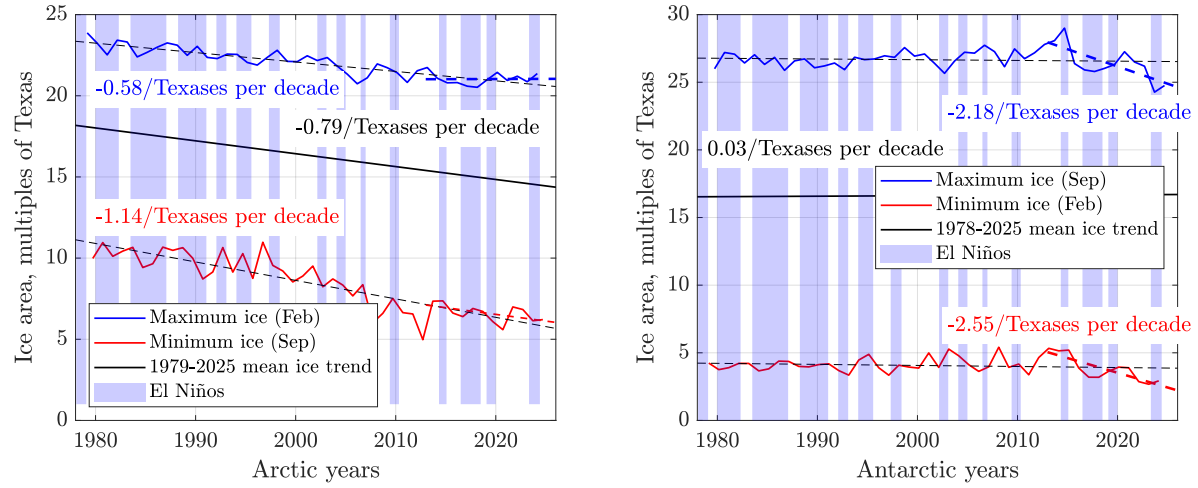

(a) (b)

Figure E5: A time series of minimum and maximum sea-ice area anomalies between 1979 and 2025 in **(a)** the Arctic and **(b)** Antarctica in multiples of Texas area. The red September curve in **(a)** reproduces Fig. 1a of (*England et al.*, 2025). After 2007, the decline in summer sea-ice area in the Arctic slows, as indicated by the thick dashed trend line. In Antarctica, the extreme ice extents decrease rapidly only after 2014, as shown by the thick dashed trend lines. The correlation between sea-ice extent and El Niño events appears weak. Even so, the exceptionally stormy summer of 2012 in the Northern Hemisphere and the unusually cold summer of 2014 in the Southern Hemisphere stand out. In both polar regions, warmer El Niño years generally delay the onset of freezing and accelerate ice melt.

Over the beat period of 30 years, there is no net accumulation of sea-ice area relative to the *always* decreasing trend, which on average would render the Arctic ice-free within about half a century. Of course, a sequence of extreme heat waves could drive the Arctic ice-free much sooner, but such a complete meltdown would likely be intermittent.

Relative to the long-term drift in sea-ice data, the post-2007 slowdown of Arctic melting appears as a natural phase of the oscillatory cycle. Figure E6(a) shows that after 2010, the net cumulative sea-ice area increased slightly faster than predicted by a single-term Fourier series expansion, yet the fundamental beat-cycle behavior remained unchanged.

In Antarctica, by contrast, the net cumulative sea-ice area increased by approximately ten Texases between 1979 and 2014. After 2015, however, a possibly self-amplifying switch flipped: this area has since declined precipitously at a rate equivalent to one US area every 17 years.

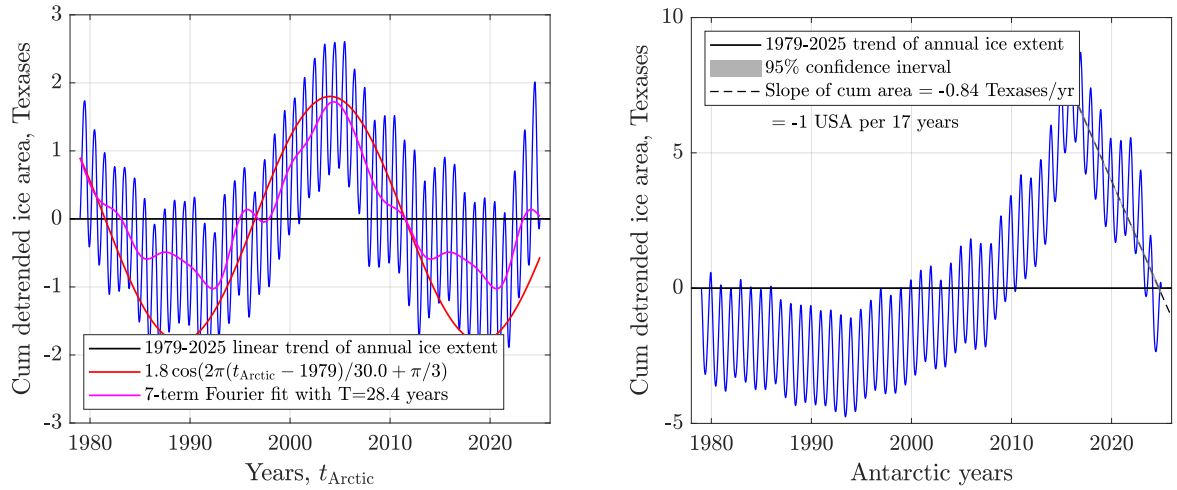

Figure E6: Detrended, net cumulative sea-ice areas between 1979 and 2025 in **(a)** the Arctic and **(b)** Antarctica in multiples of Texas area. The subtracted linear 1979-2025 trends refer to a strong negative drift in the Arctic and a weak positive drift in Antarctica, see Figure E5. In the Arctic, the detrended cumulative sea-ice area oscillates around the trend with a beat period of approximately 30 years. In contrast, the detrended cumulative sea-ice area in Antarctica increased by over 10 Texas areas from 1979 until 2014, after which it began a precipitous decline at a rate of roughly $-0.84[-0.86$ to $-0.82]$ Texases $(\text{year})^{-1}$, or one US area every 17 years. Note that the 95% confidence interval for the slope is extremely narrow and therefore barely discernible.

E.5. Discussion

Shifts in the remote polar ice inevitably send ripples throughout the entire Earth system. The most immediate ripple is sea-level rise, driven not only by thermal expansion of warming ocean waters but also by the accelerated melting of land ice, especially from Greenland. Open sea ice does not directly raise sea level, but it buttresses surrounding ice shelves and glaciers; its loss destabilizes them and accelerates ice-sheet discharge. This is happening for example at Pine Island and Thwaites glaciers in West Antarctica, and along Greenland's margins.

Unfortunately, the loss of sea ice sets off waves of change that are closer to tsunamis than to ripples. Foremost among them is the rapid decrease of Earth's albedo, see Figure 8.4. Within the next decade, this decrease will add to Earth's energy balance an amount of heat equivalent to the output of fifty human economies, each producing 20 TW of primary power, 70% of which is released as heat. Snow-covered sea ice reflects up to 90% of incoming solar radiation, whereas the dark, open ocean reflects barely 6%. This stark albedo contrast drives a powerful positive feedback that accelerates planetary warming.

Loss of sea ice further amplifies the already-strong Arctic warming ("polar amplification"), and contributes to global positive feedback loops and cascading climate instabilities (*Notz and Stroeve*, 2016, *Rocha et al.*, 2018). Increased freshwater input from melting sea ice and land ice stratifies the oceans and weakens large-scale overturning circulations such as the Atlantic Meridional Overturning Circulation (AMOC) (*Sévellec and Fedorov*, 2017, *Abram et al.*, 2025). These changes directly increase flooding risks along the Gulf Coast of the United States, where much of the nation's refining capacity is located, and they disrupt global heat transport, monsoon systems, and cause extreme weather patterns across Asia, including China, India, Pakistan, and Bangladesh.

Polar ecosystems, tightly linked to seasonal sea-ice cycles, are also at risk. Sea-ice loss undermines algae, krill, fish, and marine mammals, triggering cascading impacts on global biodiversity and fisheries (*Post and et al.*, 2013). Already, blue whales are starving because Norwegian trawlers vacuum krill from

the Antarctic waters near the Coronation Islands (*Sea Shepherd*, 2025). For hundreds of millions of people worldwide, particularly in coastal regions, declining fisheries threaten food security and protein availability.

Sea-ice algae also play a critical role, with polar blooms under ice acting as regional hotspots of DMSP/DMS production (*Levasseur*, 2013). Once produced, DMS is ventilated to the atmosphere, where it oxidizes to form sulfate aerosols that serve as cloud condensation nuclei (CCN) (*Charlson et al.*, 1987, *de Jonge et al.*, 2024) that stimulate, e.g., the boreal forests in Canada and Siberia. If these algae slow down, these boreal forests will burn.

Arctic sea-ice retreat also alters atmospheric dynamics. It disrupts large-scale atmospheric wave propagation and weakens the polar jet stream, increasing the frequency of mid-latitude extremes such as heatwaves and deep freezes (*Screen and Simmonds*, 2010). The deadly winter freezes in Texas in 2021 and 2022—from which recovery on our property required months and cost thousands of dollars—stand as stark testimony to these far-reaching consequences.

Finally, retreating sea ice in shallow Arctic seas, such as the East Siberian Shelf and the Alaskan coast, exposes sediments and may accelerate methane release, amplifying global warming (*Shakhova et al.*, 2019). Inhabitants of sinking coastal villages in northern Alaska already face relocation (*Alaska Climate Assessment and NOAA*, 2025). As a member of the Macondo Well Advisory Committee to the U.S. Department of the Interior, I personally witnessed the dire consequences of permafrost melt at Point Barrow in Alaska, the most northward human settlement in the US.

This quote about permafrost melting around the Prudhoe Bay oilfield in Alaska, 400 km north the Arctic Circle, is from Danielle Bochove with Bloomberg (https://www.bloomberg.com/graphics/2025-arctic-global-warming-permafrost, Nov 3, 2025):

> . . . [A]s sea levels rise and storms get more violent, the ocean is washing over the tundra with increasing frequency.
>
> The team is studying knock-on effects, including the impact that inundation may be having on permafrost. [*Globally, TWP*] the frozen layer of mineral soil, rock and undecomposed organic material stretches across millions of acres and contains roughly **1.4 trillion tons of carbon**. Understanding how fast it's thawing is key to gauging how much previously frozen carbon is being released into the atmosphere, and ultimately the state of the global carbon budget.

See also the global carbon budget estimate in Chapter 3.

E.6. Conclusions

Our analysis of the 1979–2025 satellite records of sea-ice extent in the Arctic and Antarctica demonstrates beyond reasonable doubt that:

- The sea-ice area in the Arctic is declining irreversibly with a long-term trend of $-0.79[-0.85$ to $-0.74]$ Texas areas per decade. The minimum summer ice area has been shrinking at a fast rate of $-1.14[-1.31$ to $-0.96]$ Texases per decade; thus far, a 39% decline relative to 1979, which may render the Arctic completely ice-free during summer by 2070. Superimposed on this long-term secular decline is an oscillation with an amplitude of ± 1.8 Texases and a beat period of roughly 30 years. Within this framework, the post-2007 slowdown in Arctic summer melting appears to be a natural phase of this 30-year cycle.
- The sea-ice area in Antarctica increased with a nearly imperceptible long-term trend of $+0.035[-0.057$ to $0.127]$ Texases per decade. Relative to this trend, the net accumulation of sea ice reached $\sim$10 Texases by 2014, after which it reversed into a precipitous decline of approximately -1 US area every 17 years. If this trend continues, Antarctica could become seasonally sea-ice-free during summer early in the next century.
- The assertions in the DOE report (*Christy et al.*, 2025) that Arctic and Antarctic sea-ice extents show no significant changes beyond natural variability are therefore invalid and should be retracted.

Bibliography

Aagaard, K., and E. Carmack, The role of sea ice and other fresh water in the Arctic circulation, *Journal of Geophysical Research*, *94*(C10), 14,48514,499, doi:10.1029/JC094iC10p14485, 1989.

Ångström, A. J., *Recherches sur le spectre solaire: avec atlas contenant les longueurs d'onde des raies du spectre solaire, et des spectres d'émission obtenus au moyen des différents éléments chimiques*, Norstedt & Söner, Upsala, published with an accompanying spectral atlas, 1868.

Ångström, K., Ueber die bedeutung des wasserdampfes und der kohlensäure bei der absorption der erdwärme, *Annalen der Physik*, *309*(6), 720–732, doi:10.1002/andp.19013090610, 1901.

Abbott, M. M., and H. C. Van Ness, *Thermodynamics*, McGraw-Hill Book Company, New York, 1972.

Abram, N. J., et al., Emerging evidence of abrupt changes in the antarctic environment, *Nature*, *644*(8077), 621–633, doi:10.1038/s41586-025-09349-5, 2025.

Adams, R., Coal and Pottery: Early Use by Native Americans, *American Antiquity*, *35*(4), 433–445, examines the Hopi tribe's use of coal for pottery production as early as the 12th century., 1970.

Agrinier, P., A. Deutsch, U. Schärer, and I. Martinez, Fast back-reactions of shock-released CO_2 from carbonates: an experimental approach, *Geochimica et Cosmochimica Acta*, *65*(15), 2615–2632, doi:10.1016/S0016-7037(01)00617-2, 2001.

Ahn, J., E. J. Brook, L. Mitchell, J. Rosen, J. R. McConnell, K. Taylor, D. Etheridge, and M. Rubino, Atmospheric CO_2 over the last 1000 years: A high-resolution record from the West Antarctic Ice Sheet (WAIS) Divide ice core, *Global Biogeochemical Cycles*, *26*(2), doi:10.1029/2011GB004247, data set: https://www.ncei.noaa.gov/access/metadata/landing-page/bin/iso?id=noaa-icecore-12949, 2012.

Ahn, J., E. J. Brook, and C. Buizert, Response of atmospheric co_2 to the abrupt cooling event 8200 years ago, *Geophysical Research Letters*, *41*(2), 604–609, doi:10.1002/2013GL058177, 2014.

Alaska Climate Assessment and NOAA, Coastal Permafrost Erosion in Alaska: Impacts and Rates, Online report, erosion rates up to 3.3 m/yr in Shishmaref; widespread Arctic permafrost coastal retreat, 2025.

Alberts, B., A. Johnson, J. Lewis, D. Morgan, M. Raff, K. Roberts, and P. Walter, *Molecular Biology of the Cell*, 6th ed., Garland Science, New York, ch. 13, "Energy Conversion: Mitochondria and ATP", 2015.

Alfred Wegener Institute, Melting Ice Is Hiding a Massive Climate Secret Beneath Antarctica, press release summary of AWI research, published by *ScienceDaily*, 2025.

Allen, M. D., J. W. Cross, and J. M. Cessna, Infrared absorption by $CO_2$and H_2O at atmospheric conditions, *Applied Optics*, *15*(1), 116–120, doi:10.1364/AO.15.000116, 1976.

Allen, R. C., *The Industrial Revolution: A Very Short Introduction*, Oxford University Press, doi:10.1093/actrade/9780198706786.001.0001, 2017.

Anagnostou, E., et al., Proxy evidence for state-dependence of climate sensitivity in the Eocene greenhouse, *Nature Communications*, *11*(1), 4436, doi:10.1038/s41467-020-17887-x, 2020.

Ångström, K., On Atmospheric Absorption, *Monthly Weather Review*, *29*(6), 268, doi:10.1175/1520-0493(1901)29[268a:KAOAA]2.0.CO;2, 1901.

Anonymous, Ergonomics of the thermal environment–determination of metabolic rate, *International Standard ISO 8996:2021*, ISO, https://www.iso.org/standard/74443.html, 2021.

Anonymous, Global CO_2 emissions from fossil fuels and land use change, Our World in Data, last updated December 5, 2023, 2023a.

Anonymous, Energy institute statistical review of world energy, https://www.energyinst.org/statistical-review/resources-and-data-downloads, 2023b.

Aramburu, S., AI again: practical duel between two models (in Spanish), https://esencialomenos.blogspot.com/2025/07/ia-de-nuevo-duelo-practico-entre-dos.html, accessed: 2025-07-22, 2025.

Archer, D., Fate of Fossil Fuel CO_2 in Geologic Time, *Journal of Geophysical Research: Oceans*, *110*(C09S05), doi:10.1029/2004JC002625, 2005.

Archer, D., and V. Brovkin, The Millennial Atmospheric Lifetime of Anthropogenic CO_2, *Climatic Change*, *90*, 283–297, doi:10.1007/s10584-008-9413-1, 2008.

Ardhuin, F., A. D. Jenkins, and K. A. Belibassakis, Comment on "On the estimation of ocean wave energy potential along the North Atlantic coast", *Journal of Geophysical Research: Oceans*, *114*(C9), C09,008, doi:10.1029/2008JC005170, 2009.

ARGO, Argo: The global array of profiling floats, *Annual Review of Marine Science*, *12*, 401–427, doi:10.1146/annurev-marine-010419-010913, argo is an international program that deploys profiling floats to monitor ocean temperature, salinity, and currents., 2020.

Argo Steering Team, Argo Float Data and Status: 2023 Update, https://argo.ucsd.edu, 2023.

Arias, P., et al., Climate change 2021: The physical science basis. contribution of working group i to the sixth assessment report of the intergovernmental panel on climate change, *Intergovernmental Panel on Climate Change (IPCC)*, doi:10.1017/9781009157896.002, includes reference temperature periods such as 18501900 (pre-industrial) and 19952014 (modern baseline)., 2021.

Arias-Ortiz, D., and T. W. Patzek, Physics-based, data-driven production forecasting in the Utica and Point Pleasant Formation, *Geoenergy Science and Engineering*, *246*, 213,491, doi:10.1016/j.geoen.2024.213491, 2025.

Arrhenius, S., On the Influence of Carbonic Acid in the Air upon the Temperature of the Ground, *Philosophical Magazine and Journal of Science*, *41*(251), 237–276, translated from the original Swedish publication, 1896.

Arrigo, K. R., Environmental controls of marine productivity hot spots around Antarctica and the Arctic, *Journal of Geophysical Research: Oceans*, *120*(5), 3376–3397, doi:10.1002/2015JC010888, 2015.

Arrow, K., et al., Economic Growth, Carrying Capacity, and the Environment, *Science*, *268*(5210), 520–521, doi:10.1126/science.268.5210.520, 1995.

Ashoka, Edicts of Ashoka on Environmental Protection, Maurya Empire, India, 250 BC (Before Common Era), -250.

Associated Press, Fact check: Ap's director of climate news breaks down trump's remarks at the un on climate change, *AP News*, accessed: 2025-09-26, 2025.

Athens, Edict of Athens on Public Cleanliness, Ancient Greek City-State Regulation, Athens, 500 BC (Before Common Era), -500.

Ballerini, M., et al., Interaction ruling animal collective behavior depends on topological rather than metric distance: Evidence from a field study, *Proceedings of the National Academy of Sciences*, *105*(4), 1232–1237, doi:10.1073/pnas.0711437105, 2008.

Ballester, J., et al., Heat-related mortality in Europe during the summer of 2022, *Nature Medicine*, *29*(7), 1857–1866, doi:10.1038/s41591-023-02419-z, 2023.

Bamber, J. L., M. Oppenheimer, R. E. Kopp, W. P. Aspinall, and R. M. Cooke, Ice sheet contributions to future sea-level rise from structured expert judgment, *Proceedings of the National Academy of Sciences*, *116*(23), 11,195–11,200, doi:10.1073/pnas.1817205116, 2019.

Bange, H. W., Nitrous oxide and methane in european coastal waters, *Estuarine, Coastal and Shelf Science*, *70*, 361–374, doi:10.1016/j.ecss.2006.05.042, 2006.

Barjavel, R., *Ashes, Ashes*, Doubleday, originally published in French as *Ravage* in 1943 by Denoël, 1967.

Beer, C., M. Reichstein, E. Tomelleri, et al., Terrestrial Gross Carbon Dioxide Uptake: Global Distribution and Covariation with Climate, *Science*, *329*(5993), 834–838, doi:10.1126/science.1184984, 2010.

Beerling, D. J., and D. L. Royer, Convergent Cenozoic CO_2 History, *Nature Geoscience*, *4*, 418–420, doi:10.1038/ngeo1186, 2011.

Behrenfeld, M. J., and P. G. Falkowski, Photosynthetic Rates Derived from Satellite-Based Chlorophyll Concentration, *Limnology and Oceanography*, *42*(1), 1–20, doi:10.4319/lo.1997.42.1.0001, 1997.

Bell, M. L., D. L. Davis, and T. Fletcher, A Retrospective Assessment of Mortality from the London Smog Episode of 1952: The Role of Influenza and Pollution, *Environmental Health Perspectives*, *112*(1), 6–8, doi:10.1289/ehp.6539, 2004.

Bereiter, B., D. Lüthi, M. Siegrist, S. Schüpbach, T. F. Stocker, and H. Fischer, Mode change of millennial CO_2 variability during the last glacial cycle associated with a bipolar marine carbon seesaw, *Proceedings of the National Academy of Sciences*, *109*(25), 9755–9760, doi:10.1073/pnas.1204069109, 2012.

Bereiter, B., S. Eggleston, J. Schmitt, C. Nehrbass-Ahles, T. F. Stocker, H. Fischer, S. Kipfstuhl, and J. Chappellaz, Revision of the EPICA Dome C CO_2 record from 800 to 600 kyr before present, *Geophysical Research Letters*, *42*(2), 542–549, doi:10.1002/2014GL061957, 2015a.

Bereiter, B., S. Shackleton, D. Baggenstos, K. Kawamura, and J. Severinghaus, Mean global ocean temperatures during the last glacial transition, *Nature*, *553*, 39–44, doi:10.1038/nature25152, 2018.

Bereiter, S., B.and Eggleston, J. Schmitt, C. Nehrbass-Ahles, T. Stocker, H. Fischer, S. Kipfstuhl, and J. Chappellaz, Antarctic Ice Cores Revised 800KYr CO_2 Data, NOAA Archive: Ice Cores, 2015b.

Berger, A., M.-F. Loutre, and H. Gallee, The Last Interglacial, the Holocene and the future, *Quaternary Science Reviews*, *29*, 6–9, doi:10.1016/j.quascirev.2010.09.006, 2012.

Bergstrom, D., A heatwave in Antarctica totally blew the minds of scientists. They set out to decipher it and here are the results, https://modernsciences.org/a-heatwave-in-antarctica-totally-blew-the-minds-of-scientists-they-set-out-to-decipher-it-and-here-are-the-results/, 2024.

Berner, R. A., and Z. Kothavala, GEOCARB III: A Revised Model of Atmospheric CO_2 over Phanerozoic Time, *American Journal of Science*, *301*(2), 182–204, doi:10.2475/ajs.301.2.182, 2001.

Birnbaum, M., World's Largest Plant Capturing CO_2 from Air Starts in Iceland, *Reuters*, accessed 2025-04-22, 2021.

Bogdanova, S. V., S. A. Pisarevsky, and Z. X. Li, Assembly and Breakup of Rodinia (Some Results of IGCP Project 440), *Stratigraphy and Geological Correlation*, *17*(3), 259–274, doi:10.1134/S0869593809030015, 2009.

Bolson, N., P. Prieto, and T. Patzek, Capacity factors for electrical power generation from renewable and nonrenewable sources, *Proceedings of the National Academy of Sciences*, *119*(52), e2205429,119, doi:10.1073/pnas.2205429119, 2022a.

Bolson, N., M. Yutkin, W. Rees, and T. Patzek, Resilience rankings and trajectories of world's countries, *Ecological Economics*, *195*, 107,383, doi:https://doi.org/10.1016/j.ecolecon.2022.107383, 2022b.

Bolson, N., M. Yutkin, and T. Patzek, Primary power analysis of a global electrification scenario, *Sustainability*, *15*(19), doi:10.3390/su151914440, 2023.

Bordoni, S., and T. Schneider, Monsoons as eddy-mediated regime transitions of the tropical overturning circulation, *Nature Geoscience*, *1*, 515–519, doi:10.1038/ngeo248, 2008.

Boudreau, B. P., T. Tyrrell, and R. E. Zeebe, Climate change and the shoaling of the carbonate compensation depth, *Geophysical Research Letters*, *48*(12), e2021GL093,255, doi:10.1029/2021GL093255, 2021.

Boyd, P. W., and M. Bressac, Developing a test-bed for robust research governance of geoengineering: the contribution of ocean iron biogeochemistry, *Philosophical Transactions of the Royal Society A: Mathematical, Physical and Engineering Sciences*, *374*(2081), 20150,299, doi:10.1098/rsta.2015.0299, 2016.

Boyd, P. W., H. Claustre, M. Levy, D. A. Siegel, and T. Weber, Multi-faceted particle pumps drive carbon sequestration in the ocean, *Nature*, *568*(7752), 327–335, doi:10.1038/s41586-019-1098-2, 2019.

Boyd, P. W., et al., A mesoscale phytoplankton bloom in the polar Southern Ocean stimulated by iron fertilization, *Nature*, *407*(6805), 695–702, doi:10.1038/35037500, 2000.

Boyd, P. W., et al., Mesoscale Iron Enrichment Experiments 1993-2005: Synthesis and Future Directions, *Science*, *315*(5812), 612–617, doi:10.1126/science.1131669, 2007.

Bradley, J. A., et al., Svalbard winter warming is reaching melting point, *Nature Communications*, *16*, 6409, doi:10.1038/s41467-025-60926-8, 2025.

Bradshaw, C. J. A., et al., Underestimating the challenges of avoiding a ghastly future, *Frontiers in Conservation Science*, *1*, 9, doi:10.3389/fcosc.2020.615419, 2021.

Brannen, P., 'A climate of unparalleled malevolence': are we on our way to the sixth major mass extinction? Churning quantities of carbon dioxide into the atmosphere at the rate we are going could lead the planet to another Great Dying, *The Guardian*, EDT: Published Tue 19 Aug 2025 00:01, last modified Tue 19 Aug 2025 00:20 ET, 2025.

Broecker, W. S., and T.-H. Peng, The Role of $CaCO_3$ Compensation in the Glacial to Interglacial CO_2 Change, *Global Biogeochemical Cycles*, *1*(1), 15–29, doi:10.1029/GB001i001p00015, 1987.

Brohan, P., J. Kennedy, I. Haris, S. F. B. Tett, and P. D. Jones, Uncertainty estimates in regional and global observed temperature changes: a new dataset from 1850, *J. Geophysical Research*, *111*, D12,106, doi:10.1029/2005JD006548, 2006a.

Brohan, P., J. J. Kennedy, I. Harris, S. F. B. Tett, and P. D. Jones, Uncertainty estimates in regional and global observed temperature changes: A new data set from 1850, *Journal of Geophysical Research: Atmospheres*, *111*(D12), doi:10.1029/2005JD006548, 2006b.

Buesseler, K. O., et al., Environment and biogeochemical responses to iron fertilization in the Southern Ocean, *Science*, *319*(5860), 162–166, doi:10.1126/science.1154640, 2008.

Buesseler, K. O., et al., Next steps for assessing ocean iron fertilization for marine carbon dioxide removal, *Frontiers in Climate*, *6*, 1430,957, doi:10.3389/fclim.2024.1430957, 2024.

Cai, W., et al., Antarctic shelf ocean warming and sea ice melt affected by projected El Niño changes, *Nature Climate Change*, *13*(3), 235–239, doi:10.1038/s41558-023-01610-x, 2023.

Callendar, G. S., The Artificial Production of Carbon Dioxide and Its Influence on Temperature, *Quarterly Journal of the Royal Meteorological Society*, *64*(275), 223–240, doi:10.1002/qj.49706427503, 1938.

Canadell, J. G., P. M. S. Monteiro, C. Sabine, et al., Global Carbon and other Biogeochemical Cycles and Feedbacks, in *Climate Change 2021: The Physical Science Basis. Contribution of Working Group I to the Sixth Assessment Report of the IPCC*, edited by V. Masson-Delmotte et al., pp. 673–816, Cambridge University Press, Cambridge, UK and New York, USA, doi:10.1017/9781009157896.007, 2021.

Cantrell, R. S., and C. Cosner, The effects of spatial heterogeneity in population dynamics, *Journal of Mathematical Biology*, *29*(4), 315–338, doi:10.1007/BF00164052, 1991.

Caporale, G. M., L. A. Gil-Alana, and N. Carmona-González, Some new evidence using fractional integration about trends, breaks and persistence in polar amplification, *Scientific Reports*, *15*(1), 8327, doi:10.1038/s41598-025-92990-x, 2025.

Carpenter, L. J., S. D. Archer, and R. Beale, Ocean-atmosphere trace gas exchange, *Chemical Society Reviews*, *41*, 6473–6506, doi:10.1039/c2cs35121h, 2015.

Catton, W. R., *Overshoot: The Ecological Basis of Revolutionary Change*, University of Illinois Press, Urbana, 1980a.

Catton, W. R., *Overshoot: The Ecological Basis of Revolutionary Change*, University of Illinois Press, Urbana, IL, 1980b.

Cavalli-Sforza, L. L., and F. Cavalli-Sforza, *The Great Human Diaspora: The History of Diversity and Evolution*, Perseus Press, Cambridge, Mass., 1995.

C&EN Staff, Coal is set to surge as a chemical raw material, *Chemical & Engineering News*, accessed 2025-12-04, 2025.

Chandanpurkar, H. A., J. S. Famiglietti, K. Gopalan, D. N. Wiese, Y. Wada, K. Kakinuma, J. T. Reager, and F. Zhang, Unprecedented continental drying, shrinking freshwater availability, and increasing land contributions to sea level rise, *Science Advances*, *11*(30), eadx0298, doi:10.1126/sciadv.adx0298, 2025.

Charlson, R. J., J. E. Lovelock, M. O. Andreae, and S. G. Warren, Oceanic phytoplankton, atmospheric sulphur, cloud albedo and climate, *Nature*, *326*, 655–661, doi:10.1038/326655a0, 1987.

Cheng, L., K. E. Trenberth, J. Fasullo, T. Boyer, J. Abraham, and J. Zhu, Improved estimates of ocean heat content from 1960 to 2015, *Science Advances*, *3*(3), e1601,545, doi:10.1126/sciadv.1601545, 2017.

Cheng, L., J. Abraham, Z. Hausfather, and K. E. Trenberth, How fast are the oceans warming?, *Science*, *363*(6423), 128–129, doi:10.1126/science.aav7619, 2019.

Cheng, L., J. Abraham, K. E. Trenberth, et al., Record-Setting Ocean Warmth Continued in 2019, *Advances in Atmospheric Sciences*, *37*(2), 137–142, doi:10.1007/s00376-020-9283-7, 2020.

Cheng, L., J. Abraham, Z. Hausfather, and K. E. Trenberth, Record-setting ocean warmth continued in 2021, *Advances in Atmospheric Sciences*, *39*, 373–385, doi:10.1007/s00376-022-1461-3, 2022.

Christian, H. J., et al., Global frequency and distribution of lightning as observed from space by the Optical Transient Detector, *Journal of Geophysical Research: Atmospheres*, *108*(D1), ACL 4–1–ACL 4–15, doi:10.1029/2002JD002347, 2003.

Christy, J., J. Curry, S. Koonin, R. McKitrick, and R. Spencer, A Critical Review of Impacts of Greenhouse Gas Emissions on the U.S. Climate, *Report*, Climate Working Group, United States Department of Energy, 2025.

Ciais, P., C. Sabine, G. Bala, et al., Carbon and Other Biogeochemical Cycles, in *Climate Change 2013: The Physical Science Basis. Contribution of WG I to the Fifth Assessment Report of the IPCC*, edited by T. F. Stocker et al., pp. 465–570, Cambridge University Press, Cambridge, UK and New York, USA, doi:10.1017/CBO9781107415324.015, 2013.

Citroën, A., Industrial Methods for Automobile Mass Production in France, *Annales de l'Automobile*, *3*, 15–30, discusses Citroën's adoption of Fordist production techniques in France., 1921.

Clark, G., and D. Jacks, Coal and the Industrial Revolution, 17001869, *European Review of Economic History*, *11*(1), 39–72, doi:10.1017/S1361491606001870, 2007.

Clark, P. U., J. D. Shakun, N. A. Lifton, et al., The Last Glacial Maximum, *Science*, *325*, 710–714, doi:10.1126/science.1172873, 2012.

Clarke, E. A., H. W. Mueller III, E. C. Phillips, R. W. Eyvazzadeh, D. H. Jones, R. Ramamoorthy, and A. Srivastava, Application of Thomeer Hyperbolas to decode the pore systems, facies and reservoir properties of the Upper Jurassic Arab D Limestone, Ghawar field, Saudi Arabia: A "Rosetta Stone" approach, *GeoArabia*, *13*(4), 113 – 160, www.spwla-abudhabi.com/SPWLA2010_Material/-GeoArabia%202008_Clerke_v13_no4_113-160.pdf, 2008.

Clarke, M. R., Cephalopods in the diet of sperm whales of the southern hemisphere and their bearing on sperm whale biology, *Discovery Reports*, *37*, 1–324, 1980.

ClientEarth, The UK Environment Act: A New Era for Environmental Law?, 2021.

Climate Change News, China's emissions fall but growing coal-to-chemicals sector raises concern, *Climate Change News*, accessed 2025-12-04, 2025.

Climeworks AG, Direct Air Capture Projects: Orca and Mammoth, company publications and technical fact sheets, 2024.

Cohen, J. E., *How Many People Can the Earth Support?*, W. W. Norton, New York, 1995.

Comiso, J. C., Large decadal decline of the Arctic multiyear ice cover, *Journal of Climate*, *25*(4), 1176–1193, doi:10.1175/JCLI-D-11-00113.1, 2012.

Congress, U., Yellowstone National Park Protection Act, United States Congress, 1872.

Connor, S., J. Omumbo, C. Green, J. DaSilva, G. Mantilla, C. Delacollette, S. Hales, D. Rogers, and M. Thomson, Health and Climate Needs, *Procedia Environmental Sciences*, *1*, 27–36, doi:10.1016/j.proenv.2010.09.004, world Climate Conference - 3, 2010.

Cook, E. R., C. A. Woodhouse, M. N. Eakin, D. M. Meko, and D. W. Stahle, Long-Term Aridity Changes in the Western United States, *Science*, *306*(5698), 1015–1018, doi:10.1126/science.1102586, 2004.

Core Writing Team, R. K. Pachauri, and L. Meyer, Climate Change 2014 Synthesis Report, Contribution of Working Groups I, II and III to the Fifth Assessment Report of the Intergovernmental Panel on Climate Change, *Tech. rep.*, Intergovernmental Panel on Climate Change (IPCC), Geneva, Switzerland, epic.awi.de/id/eprint/37530/1/IPCC_AR5_SYR_Final.pdf, 2014.

Core Writing Team, H. Lee, and J. Romero (Eds.), *Climate Change 2023: Synthesis Report. Contribution of Working Groups I, II and III to the Sixth Assessment Report of the Intergovernmental Panel on Climate Change*, 1–184 pp., IPCC, Geneva, Switzerland, doi:10.59327/IPCC/AR6-9789291691647, 2023.

Council of Nuremberg, Ordinance of Nuremberg on Forest Conservation, Municipal Ordinance, Holy Roman Empire, 1334.

CRED, Em-dat: The international disaster database, accessed 2025-10-26, 2024.

Crippa, M., et al., *GHG emissions of all world countries*, Publications Office of the European Union, doi:10.2760/953322, 2023.

Croft, G. D., and T. W. Patzek, Potential for Coal-to-Liquids Conversion in the U.S. – Resource Base, *Nat. Resour. Res.*, *18*(3), 173 – 180, dOI: 10.1007/s11053-009-9097-x, 2009.

Crowther, T. W., H. B. Glick, and K. R. C. et al., Mapping tree density at a global scale, *Nature*, *525*, 201–205, doi:10.1038/nature14967, 2015.

Crueger, T., H. Schmidt, and B. Stevens, Hemispheric Albedo Asymmetries across Three Phases of CMIP, *Journal of Climate*, *36*(15), 5267–5280, doi:10.1175/JCLI-D-22-0923.1, 2023.

Crutzen, P. J., Albedo Enhancement by Stratospheric Sulfur Injections: A Contribution to Resolve a Policy Dilemma?, *Climatic Change*, *77*, 211–219, doi:10.1007/s10584-006-9101-y, 2006.

Daily, G. C., and P. R. Ehrlich, Population, Sustainability, and Earth's Carrying Capacity, *BioScience*, *42*(10), 761–771, doi:10.2307/1311995, 1992.

Daily, G. C., A. H. Ehrlich, and P. R. Ehrlich, Optimum human population size, *Population and Environment*, *15*(6), 469–475, doi:10.1007/BF02211719, 1994.

Daniels, R., *Coming to America: A History of Immigration and Ethnicity in American Life*, 2nd ed., Harper Perennial, New York, a comprehensive history of immigration to the United States, from colonial times through the 20th century., 2002.

Dansgaard, W., et al., Evidence for general instability of past climate from a 250-kyr ice-core record, *Nature*, *364*, 218–220, doi:10.1038/364218a0, 1993.

Datseris, G., and B. Stevens, Earth's Albedo and Its Symmetry, *AGU Advances*, *2*(3), e2021AV000,440, doi:10.1029/2021AV000440, 2021.

Davies, J. H., Global map of solid Earth surface heat flow, *Geochemistry, Geophysics, Geosystems*, *14*(10), 4608–4622, doi:10.1002/ggge.20271, 2013.

Davies, J. H., and D. R. Davies, Earth's surface heat flux, *Solid Earth*, *1*(1), 5–24, doi:10.5194/se-1-5-2010, 2010.

de Jonge, R. W., et al., Natural Marine Precursors Boost Continental New Particle Formation and Production of Cloud Condensation Nuclei, *Environmental Science & Technology*, *58*(25), 10,956–10,968, doi:10.1021/acs.est.4c01891, epub 2024 Jun 13, 2024.

Dejardin, T., et al., The ARPEGE global numerical weather prediction and climate model: Configuration and recent developments, *Geoscientific Model Development*, *15*, 1885–1912, doi:10.5194/gmd-15-1885-2022, 2022.

DeVries, T., F. Primeau, and C. Deutsch, The sequestration efficiency of the biological pump, *Geophysical Research Letters*, *39*(13), doi:10.1029/2012GL051963, 2012.

Dhondt, A. A., Carrying Capacity: A Confusing Concept, *Acta Oecologica (Oecologia Generalis)*, *9*(4), 337–346, 1988.

Dlugokencky et al., E., Annual Greenhouse Gas Index (AGGI), accessed: 2025-10-25, 2025.

Dong, T., et al., Record-breaking 2023 marine heatwaves, *Science*, *389*(6758), 369–374, doi:10.1126/science.adr0910, 2025.

Donnadieu, Y., Y. Goddéris, G. Ramstein, A. Nédélec, and J. G. Meert, A 'snowball Earth' climate triggered by continental break-up through changes in runoff, *Nature*, *428*, 303–306, doi:10.1038/nature02408, 2004.

Drusch, M. e. a., Sentinel-2: ESAs Optical High-Resolution Mission for GMES Operational Services, *Remote Sensing of Environment*, 2012.

Durand, J. D., The Early Use of Coal in Britain and Europe, *Journal of Historical Energy Studies*, *12*(3), 45–67, focuses on the archaeological and textual evidence of coal use during the Roman times the Roman and Bronze Ages., 1993.

Duspayev, A., , et al., Earth's Sea Ice Radiative Effect From 1980 to 2023, *Geophysical Research Letters*, p. e2024GL109608, doi:10.1029/2024GL109608, 2024.

Dutton, A., A. E. Carlson, A. J. Long, G. A. Milne, P. U. Clark, R. DeConto, B. P. Horton, S. Rahmstorf, and M. E. Raymo, Sea-level rise due to polar ice-sheet mass loss during past warm periods, *Science*, *349*(6244), aaa4019, doi:10.1126/science.aaa4019, 2015.

EC, European Community Earth Consortium (EC)-Earth Climate Model, accessed April 2025, 2024.

ECMWF, IFS Documentation CY48R1: Part I Operational Configuration, *Tech. rep.*, European Centre for Medium-Range Weather Forecasts, accessed April 2025, 2022.

EEA, European Environment Agency: Trends and Projections in Europe 2022: Tracking Progress Towards Climate Targets, 2022.

Egleston, E. S., C. L. Sabine, and F. M. M. Morel, Revelle revisited: Buffer factors that quantify the response of ocean chemistry to changes in DIC and alkalinity, *Global Biogeochemical Cycles*, *24*(1), GB1002, doi:10.1029/2008GB003407, 2010.

Ehrlich, P. R., and J. P. Holdren, Impact of population growth, *Science*, *171*(3977), 1212–1217, doi:10.1126/science.171.3977.1212, 1971.

Eldering, A. e. a., The Orbiting Carbon Observatory-2 (OCO-2): Mission overview, *Atmospheric Measurement Techniques*, 2017.

Eltis, D., and D. Richardson, *Atlas of the Transatlantic Slave Trade*, Yale University Press, New Haven, definitive visual and statistical documentation of the Atlantic slave trade., 2010.

Emanuel, K., Increasing destructiveness of tropical cyclones over the past 30 years, *Nature*, *436*, 686–688, doi:10.1038/nature03906, 2005.

Emanuel, K., Ocean's Role in Hurricane Energy Budget and Climate Impacts, *Annual Review of Marine Science*, *12*, 71–93, doi:10.1146/annurev-marine-010419-010845, 2020.

Emanuel, K. A., An air-sea interaction theory for tropical cyclones. part i: Steady-state maintenance, *Journal of the Atmospheric Sciences*, *43*(6), 585–604, doi:10.1175/1520-0469(1986)043<0585:AAITFT>2.0.CO;2, 1986.

Emanuel, K. A., The dependence of hurricane intensity on climate, *Nature*, *326*(6112), 483–485, doi:10.1038/326483a0, 1987.

Emanuel, K. A., The Power of a Hurricane: An Example of Reckless Driving on the Information Superhighway, *Weather*, *54*, 107–108, 1998.

Emanuel, K. A., On the dynamics of the Hadley circulation, *Reviews of Geophysics*, *45*(RG2007), 1–31, doi:10.1029/2006RG000188, 2007.

Emperor Wilhelm I, German Forest Protection Act, German Empire, 1875.

Energy Futures Initiative Foundation, Direct Air Capture: A Case Study of Deployment, Costs, and Commercial Pathways, *Tech. rep.*, Energy Futures Initiative Foundation, Washington, DC, accessed 2025-04-22, 2024.

England, M. R., L. M. Polvani, J. Screen, and A. C. Chan, Minimal Arctic Sea Ice Loss in the Last 20ăYears, Consistent With Internal Climate Variability, *Geophysical Research Letters*, *52*(15), e2025GL116,175, doi:https://doi.org/10.1029/2025GL116175, 2025.

EPA CAA, Clean Air Act, 42 U.S.C. §7401 et seq., 1970.

EPA CERCLA, Comprehensive Environmental Response, Compensation, and Liability Act (Superfund), 42 U.S.C. §9601 et seq., 1980.

EPA CWA, Clean Water Act, 33 U.S.C. §1251 et seq., 1972.

EPA ESA, Endangered Species Act, 16 U.S.C. §1531 et seq., 1973.

EPA NEPA, National Environmental Policy Act, Public Law 91-190, 42 U.S.C. §4321 et seq., 1969.

EPA OPA, Oil Pollution Act, 33 U.S.C. §2701 et seq., 1990.

EPA RCRA, Resource Conservation and Recovery Act , 42 U.S.C. §6901 et seq., 1976.

EPA SDWA, Safe Drinking Water Act, 42 U.S.C.§300f et seq., 1974.

EPA TSCA, Toxic Substances Control, 15 U.S.C. §2601 et seq., 1976.

EPICA Community, One-to-one coupling of glacial climate variability in Greenland and Antarctica, *Nature*, *444*(7116), 195–198, doi:10.1038/nature05301, 2006.

Ervens, B., B. J. Turpin, and R. J. Weber, Secondary organic aerosol formation in cloud droplets and aqueous particles (aqsoa): a review of laboratory, field and model studies, *Atmospheric Chemistry and Physics*, *11*(21), 11,069–11,102, doi:10.5194/acp-11-11069-2011, 2011.

ESA, CryoSat-2 Mission, ESA Earth observation mission, monitors ice sheet temperatures and thickness in polar regions., 2010.

ESA, and EUMESTAT, Sentinel-3 Mission - Copernicus Programme, ESA-EU Earth observation satellite, measures sea and land surface temperature using the SLSTR instrument., 2016.

ESGF Consortium, Earth System Grid Federation (ESGF) CMIP6 Archive, accessed April 2025, 2024.

Etheridge, D. M., L. P. Steele, R. L. Langenfelds, R. J. Francey, J.-M. Barnola, and V. I. Morgan, Natural and anthropogenic changes in atmospheric CO_2 over the last 1000 years from air in Antarctic ice and firn, *Journal of Geophysical Research: Atmospheres*, *101*(D2), 4115–4128, doi:10.1029/95JD03410, 1996.

EU EIA, Environmental Impact Assessment (EIA) Directive 2011/92/EU (as amended by 2014/52/EU), Directive 2011/92/EU of the European Parliament and of the Council on the assessment of the effects of certain public and private projects on the environment, 2011.

EU Treaty, Treaty on the Functioning of the European Union (TFEU) - Environmental Provisions, Articles 191-193, Consolidated Version of the Treaty on the Functioning of the European Union (TFEU), Official Journal C 326, 26/10/2012, 2007.

EU WFD, Water Framework Directive 2000/60/EC, Directive 2000/60/EC of the European Parliament and of the Council establishing a framework for Community action in the field of water policy, 2000.

Evans, D. A. D., The palaeomagnetically viable, long-lived and all-inclusive Rodinia supercontinent reconstruction, *Geological Society, London, Special Publications*, *327*, 371–404, doi:10.1144/SP327.16, 2009.

Eyring, V., S. Bony, G. A. Meehl, C. A. Senior, B. Stevens, R. J. Stouffer, and K. E. Taylor, Overview of the Coupled Model Intercomparison Project Phase 6 (CMIP6) experimental design and organization, *Geoscientific Model Development*, *9*(5), 1937–1958, doi:10.5194/gmd-9-1937-2016, 2016.

Fagan, B., *The Long Summer: How Climate Changed Civilization*, Basic Books, 2004.

Fajzel, W., et al., The global human day, *Proceedings of the National Academy of Sciences*, *120*(25), e2219564,120, doi:10.1073/pnas.2219564120, 2023.

Fanning, A. L., and K. Raworth, Doughnut of social and planetary boundaries monitors a world out of balance, *Nature*, *646*(8083), 47–56, doi:10.1038/s41586-025-09385-1, 2025.

FAO/WHO/UNU Expert Consultation, Human Energy Requirements, *Tech. rep.*, Food and Agriculture Organization of the United Nations, 2004.

Fasihi, M., O. Efimova, and C. Breyer, Techno-Economic Assessment of CO_2 Direct Air Capture Plants, *Journal of Cleaner Production*, *224*, 957–980, doi:10.1016/j.jclepro.2019.03.086, 2019.

FEMA National Risk Index, Heat wave risk index map, high heat-wave risk in southern and western states, n.d.

Feshbach, M., and A. F. Jr., *Ecocide in the USSR: Health and Nature Under Siege*, Basic Books, comprehensive study on Soviet environmental degradation, covering pollution, deforestation, and health impacts., 1992.

Field, C. B., M. J. Behrenfeld, J. T. Randerson, and P. Falkowski, Primary Production of the Biosphere: Integrating Terrestrial and Oceanic Components, *Science*, *281*, 237–240, doi:10.1126/science.281.5374.237, 1998.

Fiorino, D. J., *The New Environmental Regulation*, MIT Press, 2006.

Fisher, J. I. e. a., PlanetScope data for land surface monitoring at scale, *Environmental Research Letters*, 2020.

Flannery, B. P., Energy balance models incorporating transport of thermal and latent energy, *Journal of Atmospheric Sciences*, *41*(3), 414 – 421, doi:10.1175/1520-0469(1984)041<0414:EBMITO>2.0.CO;2, 1984.

Ford, H., Mass Production and the Modern Automobile Industry, *Ford Company Archive*, historical record of Ford's introduction of the moving assembly line in 1913., 1913.

Forster, P. M., C. J. Smith, and T. Walsh, The Earth's energy imbalance and its implications, *Annual Review of Earth and Planetary Sciences*, *49*, 509–535, 2021a.

Forster, P. M., et al., Chapter 7: The Earth's Energy Budget, Climate Feedbacks, and Climate Sensitivity, in *Climate Change 2021: The Physical Science Basis. Contribution of Working Group I to the Sixth Assessment Report of the Intergovernmental Panel on Climate Change*, edited by V. Masson-Delmotte, P. Zhai, A. Pirani, S. L. Connors, C. Péan, S. Berger, N. Caud, Y. Chen, L. Goldfarb, M. I. Gomis, M. Huang, K. Leitzell, E. Lonnoy, J. B. R. Matthews, T. K. Maycock, T. Waterfield, O. Yelekçi, R. Yu, and B. Zhou, pp. 923–1054, Intergovernmental Panel on Climate Change, Geneva, Switzerland, doi:10.1017/9781009157896.009, 2021b.

Foster, G. L., D. L. Royer, and D. J. Lunt, Future climate forcing potentially without precedent in the last 420 million years, *Nature Communications*, *8*, 14,845, doi:10.1038/ncomms14845, 2017.

Fouda, M., Spain and Portugal hit by sweeping power outage: Here is what we know, Euronews, published on April 29, 2025.

Fowler, D., et al., A chronology of global air quality, *Phil. Trans. R. Soc. A*, *378*, 328–334, doi:110.1098/rsta.2021.0113, 2020.

Fowler, S. R., and E. A. Guggenheim, *Statistical Thermodynamics*, At the University Press, Cambridge, 1949.

Fox-Kemper, B., et al., Ocean, Cryosphere and Sea Level Change, in *Climate Change 2021: The Physical Science Basis. Contribution of Working Group I to the Sixth Assessment Report of the Intergovernmental Panel on Climate Change*, edited by V. Masson-Delmotte, P. Zhai, A. Pirani, S. L. Connors, C. Péan, S. Berger, N. Caud, Y. Chen, L. Goldfarb, M. I. Gomis, M. Huang, K. Leitzell, E. Lonnoy, J. B. R. Matthews, T. K. Maycock, T. Waterfield, O. Yelekçi, R. Yu, and B. Zhou, pp. 1211–1362, Cambridge University Press, Cambridge, United Kingdom and New York, NY, USA, doi:10.1017/9781009157896.011, 2021.

Freese, B., *Coal: A Human History*, Penguin Books, New York, NY, USA, a broad historical overview of coal use from ancient civilizations to the modern era., 2004.

Friedlingstein, P., P. Cox, R. Betts, et al., Climate–Carbon Cycle Feedback Analysis: Results from the C^4MIP Model Intercomparison, *Journal of Climate*, *19*(14), 3337–3353, doi:10.1175/JCLI3800.1, 2006.

Friedlingstein, P., et al., Global Carbon Budget 2023, *Earth System Science Data*, *15*(12), 5301–5369, doi:10.5194/essd-15-5301-2023, 2023.

Friedlingstein, P., et al., Global carbon budget 2024, *Earth System Science Data*, *17*(3), 965–1039, doi:10.5194/essd-17-965-2025, 2025.

Furlong, K. P., and D. M. J. S. Brown, Heat Flow, Heat Generation, and the Thermal State of the Lithosphere, *Annual Review of Earth and Planetary Sciences*, *41*, 385–410, doi:10.1146/annurev-earth-050212-123608, 2013.

Ganopolski, A., R. Winkelmann, and H. J. Schellnhuber, Critical insolation–CO_2 relation for diagnosing past and future glacial inception, *Nature*, *529*(7585), 200–203, doi:10.1038/nature16494, 2016.

Gattuso, J.-P., A. Magnan, L. Bopp, W. W. L. Cheung, C. M. Duarte, J. Hinkel, et al., Contrasting futures for ocean and society from different anthropogenic co_2 emissions scenarios, *Science*, *349*(6243), aac4722, doi:10.1126/science.aac4722, 2015.

Gernon, T. M., S. Brune, T. K. Hincks, M. R. Palmer, C. J. Spencer, E. J. Watts, and A. Glerum, Enriched mantle generated through persistent convective erosion of continental roots, *Nature Geoscience*, doi:10.1038/s41561-025-01843-9, 2025.

GESAMP, Impacts of Ocean Fertilization on Marine Ecosystems, *Tech. Rep. S94*, IMO/FAO/UNESCOIOC/UNIDO/WMO/IAEA/UN/UNEP Joint Group of Experts on the Scientific Aspects of Marine Environmental Protection, 2019.

Gettelman, A., et al., High climate sensitivity in the Community Earth System Model version 2 (CESM2), *Geophysical Research Letters*, *46*(14), 8329–8337, doi:10.1029/2019GL083978, 2019.

Gettelman, A., et al., Has Reducing Ship Emissions Brought Forward Global Warming?, *Geophysical Research Letters*, *51*(15), e2024GL109,077, doi:10.1029/2024GL109077, 2024.

Ghaffari, M., R. Kooloth, and G. Dwyer, Insect outbreaks and population cycles: a review of the theory, *Ecological Modelling*, *222*(19), 3482–3495, doi:10.1016/j.ecolmodel.2011.06.009, 2011.

Giguere, A., F. E. L. Otto, T. Tannenbaum, M. Vahlberg, et al., Climate Change and the Escalation of Global Extreme Heat: Assessing and Addressing the Risks, https://www.climatecentral.org/report/climate-change-and-the-escalation-of-global-extreme-heat-2025, accessed 2025-07-09, 2025.

Gilford, D. M., A. Pershing, B. H. Strauss, K. Haustein, and F. E. L. Otto, A multi-method framework for global real-time climate attribution, *Advances in Statistical Climatology, Meteorology and Oceanography*, *8*(1), 135–154, doi:10.5194/ascmo-8-135-2022, 2022.

Glaser, M., CO_2 "Greenhouse" Effect, *Internal Report 82EAP 256*, Exxon Research and Engineering Company, e.o. Box 1o1, Florham Park, New Jersey, 07932, 1982.

Glassner, J.-J., *The Babylonian Chronicles*, Eisenbrauns, 2004.

Global Climate Observing System, Status of the Global Climate Observing System 2022, gCOS Report No. 265, https://gcos.wmo.int, 2022.

Global Drifter Program, Drifter Data Assembly Center: Annual Report 2023, https://www.aoml.noaa.gov/phod/gdp, 2023.

Global Thermostat, Global Thermostat's Colorado DAC Facility: Project Overview, https://globalthermostat.com, accessed 2025-04-22, 2023.

Goldberg, M. D. e. a., The Joint Polar Satellite System: The United States next generation civilian polar-orbiting environmental satellite system, *Journal of Atmospheric and Oceanic Technology*, 2013.

Goody, R. M., and Y. L. Yung, Atmospheric Radiation: Theoretical Basis, *Oxford University Press*, 1989.

Gordon, I. E., L. S. Rothman, C. Hill, and et al., The hitran2016 molecular spectroscopic database, *Journal of Quantitative Spectroscopy and Radiative Transfer*, *203*, 3–69, doi:10.1016/j.jqsrt.2017.06.038, 2017.

Gould, C. F., S. Heft-Neal, A. K. Heaney, E. Bendavid, C. W. Callahan, M. V. Kiang, J. G. Zivin, and M. Burke, Temperature extremes impact mortality and morbidity differently, *Science Advances*, *11*(31), eadr3070, doi:10.1126/sciadv.adr3070, 2025.

GRDC, GRDC Overview and Data Status Report, https://www.bafg.de/GRDC, 2021.

Greene, C. A., A. S. Gardner, M. Wood, and J. K. Cuzzone, Ubiquitous acceleration in Greenland Ice Sheet calving from 1985 to 2022, *Nature*, *625*(7995), 523–528, doi:10.1038/s41586-023-06863-2, 2024.

Griffin, R. F., Photoelectric measurements of the λ5250A Fe I triplet and the D lines in G and K stars, *Monthly Notices of the Royal Astronomical Society*, *122*, 181, doi:10.1093/mnras/122.3.181, 1961.

Griscom, B. W., et al., Natural Climate Solutions, *Proceedings of the National Academy of Sciences*, *114*(44), 11,645–11,650, doi:10.1073/pnas.1710465114, 2017.

Grootes, P. M., and M. Stuiver, Oxygen 18/16 variability in Greenland snow and ice with 10^{-3}- to 10^5-year time resolution, *Journal of Geophysical Research: Oceans*, *102*(C12), 26,455–26,470, doi:10.1029/97JC00880, 1997.

Gueymard, C. A., A reevaluation of the solar constant based on a 42-year total solar irradiance time series and a reconciliation of spaceborne observations, *Solar Energy*, *168*, 2–9, doi:10.1016/j.solener.2018.04.001, advances in Solar Resource Assessment and Forecasting, 2018.

Guggenheim, E. A., *Thermodynamics – An Advanced Treatment for Chemists and Physicists*, North-Holland Publishing Company, New York, 1950.

Guidoboni, E., and A. Comastri, Catalogue of Ancient Earthquakes in the Mediterranean Area up to the 10th Century, *Annals of Geophysics*, *37*(2), 477–485, 1994.

Gumbel, E. J., *Statistics of Extremes*, Columbia University Press, New York, 1958.

Guyton, A. C., and J. E. Hall, *Textbook of Medical Physiology*, 14 ed., Elsevier, 2020.

Haberl, H., K.-H. Erb, F. Krausmann, V. Gaube, A. Bondeau, C. Plutzar, S. Gingrich, W. Lucht, and M. Fischer-Kowalski, Quantifying and Mapping the Human Appropriation of Net Primary Production in Earth's Terrestrial Ecosystems, *Proceedings of the National Academy of Sciences*, *104*(31), 12,942–12,947, doi:10.1073/pnas.0704243104, 2007.

HAD, Uk hadley meteorological office (had) hadgem3 model documentation, accessed April 2025, 2024.

Hagens, N. J., Economics for the futurebeyond the superorganism, *Ecological Economics*, *169*, 106,520, publisher: Elsevier, 2020.

Hain, M. P., D. M. Sigman, and G. H. Haug, The Biological Pump in the Past, *Nature Geoscience*, *7*, 248–255, doi:10.1038/ngeo2116, 2014.

Hammer, M. S., et al., Global Estimates and Long-Term Trends of Fine Particulate Matter Concentrations (1998–2018), *Environmental Science & Technology*, *54*(13), 7879–7890, doi:10.1021/acs.est.0c01764, 2020.

Hance, J., Healthy coral reefs produce clouds and precipitation, mongabay News, Australia, 2010.

Hannah, L., D. B. Z. Kuemmerle, and S. L. P. et al., The impacts of 21st-century deforestation on climate and biodiversity, *Science Advances*, *6*(36), doi:10.1126/sciadv.abc9221, 2020.

Hansen, J., M. Sato, P. Kharecha, D. Beerling, V. Masson-Delmotte, M. Pagani, M. Raymo, D. L. Royer, and J. C. Zachos, Target atmospheric CO_2: Where should humanity aim?, *The Open Atmospheric Science Journal*, *2*, 217–231, doi:10.2174/1874282300802010217, 2008.

Hansen, J., R. Ruedy, M. Sato, and K. Lo, Global surface temperature change, *Reviews of Geophysics*, *48*(4), doi:10.1029/2010RG000345, 2010.

Hansen, J., P. Kharecha, and M. Sato, Climate forcing growth rates: Doubling down on our Faustian bargain, *Environmental Research Letters*, *8*(1), 011,006, doi:10.1088/1748-9326/8/1/011006, 2013a.

Hansen, J., M. Sato, G. Russell, and P. Kharecha, Climate sensitivity, sea level and atmospheric carbon dioxide, *Philosophical Transactions of the Royal Society A: Mathematical, Physical and Engineering Sciences*, *371*(2001), 20120,294, doi:10.1098/rsta.2012.0294, 2013b.

Hansen, J. E., and S. Lebedeff, Global trends of measured surface air temperature, *Journal of Geophysical Research*, *92*, 13,345–13,372, doi:10.1029/JD092iD11p13345, 1987.

Hansen, J. E., and M. Sato, Climate sensitivity estimated from earth's climate history, NASA Goddard Institute for Space Studies and Columbia University Earth Institute, New York, 2012.

Hansen, J. E., et al., Global warming in the pipeline, *Oxford Open Clim. Change*, *3*(1), kgad008, doi:10.1093/oxfclm/kgad008, 2023.

Harðardóttir, S., M. Pančić, A. Tammilehto, B. Krock, E. F. Møller, T. G. Nielsen, and N. Lundholm, Dangerous Relations in the Arctic Marine Food Web: Interactions between Toxin Producing Pseudo-nitzschia Diatoms and Calanus Copepodites, *Marine Drugs*, *13*(6), 3809–3835, doi:10.3390/md13063809, 2015.

Hastings, A., Structured models of metapopulation dynamics, *Biological Journal of the Linnean Society*, *42*(1-2), 57–71, doi:10.1111/j.1095-8312.1991.tb00553.x, 1991.

Hatcher, J., *Plague, Population and the English Economy, 1348–1530*, Studies in Economic and Social History, London: Macmillan, 1983.

Hauck, J., C. Völker, and D. A. WolfGladrow, Revisiting the Revelle factorObservations and model results for the modern ocean, *Biogeosciences*, *17*, 4481–4499, doi:10.5194/bg-17-4481-2020, 2020.

Hawkins, E., P. Ortega, S. I. Seneviratne, et al., Estimating changes in global temperature since the preindustrial period, *Bulletin of the American Meteorological Society*, *98*(9), 1841–1856, 2017.

Hays, J. N., *Epidemics and Pandemics: Their Impacts on Human History*, 513 pp., ABC-CLIO, Santa Barbara, CA, USA, 2005.

Haywood, A. M., H. J. Dowsett, A. M. Dolan, and et al., The Pliocene Model Intercomparison Project Phase 2: large scale climate features and climate sensitivity, *Climate of the Past*, *16*, 2095–2123, doi:10.5194/cp-16-2095-2020, 2020.

Heaton, C. A., Oil and Bitumen in Ancient Greece and Rome, *Journal of Archaeological Science*, *32*(6), 873–889, explores the use of oil and bitumen in ancient Greek and Roman technology and culture., 2005.

Heidegger, M., The Question Concerning Technology, in *The Question Concerning Technology and Other Essays*, pp. 3–35, Harper & Row, original German essay was in 1954, English translation in 1977, 1977.

Heirloom, Heirloom Opens First Commercial Direct Air Capture Facility in California, https://www.heirloomcarbon.com, press release; Accessed 2025-04-22, 2023.

Helmcke, S., T. Nauclér, S. Pendrey, and T. Vroman, Understanding the Price of Decarbonization, mcKinsey Sustainability Insights, 2025.

Hemelrijk, C. K., D. A. P. Reid, H. Hildenbrandt, and J. T. Padding, The Increased Efficiency of Fish Swimming in a School, *Fish and Fisheries*, *16*(3), 511–521, doi:10.1111/faf.12072, 2015.

Henderson, T. J., *A Glorious Defeat: Mexico and Its War with the United States*, Hill and Wang, New York, 2007.

Herodotus, and A. de Sélincourt (translator), *The Histories*, Penguin Classics, 1996.

Heron, S. F., J. A. Maynard, R. van Hooidonk, and C. M. Eakin, Warming trends and bleaching stress of the world's coral reefs 19852012, *Scientific Reports*, *6*, 38,402, doi:10.1038/srep38402, 2016.

Hersbach, H., et al., The ERA5 global reanalysis, *Quarterly Journal of the Royal Meteorological Society*, *146*(730), 1999–2049, doi:10.1002/qj.3803, 2020.

Higgins, S. I., W. J. Bond, and W. S. W. Trollope, Fire, resprouting and variability: a recipe for grasstree coexistence in savanna, *Journal of Ecology*, *88*(2), 213–229, doi:10.1046/j.1365-2745.2000.00435.x, 2000.

Hijma, M. P., et al., Global sea-level rise in the early Holocene revealed from North Sea peats, *Nature*, *639*, 652–657, doi:10.1038/s41586-025-08769-7, 2025.

History Learning, The Lifestyle of a Roman Slave, accessed: 2025-04-23, n.d.

Hobbs, W., et al., Observational evidence for a regime shift in summer antarctic sea ice, *Journal of Climate*, *37*(7), 2263 – 2275, doi:10.1175/JCLI-D-23-0479.1, 2024.

Hodell, D. A., J. H. Curtis, and M. Brenner, Possible Role of Climate in the Collapse of Classic Maya Civilization, *Nature*, *375*(6530), 391–394, doi:10.1038/375391a0, 1995.

Hoegh-Guldberg, O., et al., Coral reefs under rapid climate change and ocean acidification, *Science*, *318*(5857), 1737–1742, doi:10.1126/science.1152509, 2007.

Hoffert, M. I., A. J. Callegari, and C.-T. Hsieh, The role of deep sea heat storage in the secular response to climatic forcing, *Journal of Geophysical Research: Oceans*, *85*(C11), 6667–6679, doi:https://doi.org/10.1029/JC085iC11p06667, 1980.

Hoffert, M. I., B. P. Flannery, A. J. Callegari, C. T. Hsieh, and W. Wiscombe, Evaporation-limited tropical temperatures as a constraint on climate sensitivity, *Journal of Atmospheric Sciences*, *40*(7), 1659 – 1668, doi:10.1175/1520-0469(1983)040<1659:ELTTAA>2.0.CO;2, 1983.

Hoffman, P. F., and D. P. Schrag, The Snowball Earth, 1999.

Hoffman, P. F., and D. P. Schrag, The Snowball Earth hypothesis: Testing the limits of global change, *Terra Nova*, *14*(3), 129–155, doi:10.1046/j.1365-3121.2002.00408.x, 2002.

Hoffman, P. F., A. J. Kaufman, G. P. Halverson, and D. P. Schrag, A Neoproterozoic Snowball Earth, *Science*, *281*(5381), 1342–1346, doi:10.1126/science.281.5381.1342, 1998.

Hoffman, P. F., G. P. Halverson, D. P. Schrag, et al., Snowball Earth climate dynamics and Cryogenian geology: State of the field, *Geological Society, London, Special Publications*, *475*, 1–43, doi:10.1144/SP475.16, 2017.

Hönisch, B., N. G. Hemming, D. Archer, M. Siddall, and J. F. McManus, Atmospheric CO_2 during the Mid-Pleistocene Transition, *Science*, *324*(5934), 1551–1554, doi:10.1126/science.1171477, 2009.

Houghton, J., G. Jenkins, and J. Ephraums (Eds.), *Climate Change: The IPCC Scientific Assessment*, Cambridge University Press, Cambridge, UK, first Assessment Report (FAR), Working Group I, 1990.

House, K. Z., A. C. Baclig, M. Ranjan, E. A. van Nierop, J. Wilcox, and H. J. Herzog, Economic and energetic analysis of capturing CO_2 from ambient air, *Proceedings of the National Academy of Sciences*, *108*(51), 20,428–20,433, doi:10.1073/pnas.1012253108, 2011.

HowStuffWorks Staff, The 10 Hottest States in the U.S., Based on 2023 Data, based on NOAA/NCEI average daily temperature data, 2023.

Hu, W., Z. Hao, P. Du, F. D. Vincenzo, G. Manzi, J. Cui, Y.-X. Fu, Y.-H. Pan, and H. Li, Genomic inference of a severe human bottleneck during the Early to Middle Pleistocene transition, *Science*, *381*(6661), 979–984, doi:10.1126/science.abq7487, 2023.

Huang, Y., and M. Bani-Shahabadi, Why logarithmic? A note on the dependence of radiative forcing on gas concentration, *Journal of Geophysical Research: Atmospheres*, *119*(24), 13,683–13,689, doi:10.1002/2014JD022466, 2014.

Hubbert, M. K., Energy resources, *Report 1000-D*, National Academy of Sciences-National Research Council, Washington, DC, 1962.

Hubbert, M. K., *Resources and Man*, chap. 8, National Academy of Sciences and National Research Council, Freeman, San Francisco, 1969.

Huffard, C. L., C. A. Durkin, S. E. Wilson, P. R. McGill, R. Henthorn, and K. L. Smith, Temporally-Resolved Mechanisms of Deep-Ocean Particle Flux and Impact on the Seafloor Carbon Cycle in the Northeast Pacific, *Deep Sea Research Part II: Topical Studies in Oceanography*, *173*, 104,763, doi:10.1016/j.dsr2.2020.104763, 2020.

Hugelius, G., J. Strauss, S. Zubrzycki, J. W. Harden, E. A. G. Schuur, C. Tarnocai, and P. M. Kuhry, Estimated stocks of circumpolar permafrost carbon with quantified uncertainty ranges and identified data gaps, *Biogeosciences*, *11*(23), 6573–6593, 2014.

IEA, World Energy Outlook 2023, *IEA Annual Report*, provides data on primary energy sources and conversion efficiency., 2023a.

IEA, CO_2 Emissions in 2022, https://www.iea.org/reports/co2-emissions-in-2022, iEA, Paris, 2023b.

IEA, Methane tracker, https://www.iea.org/data-and-statistics/data-tools/methane-tracker, 2024.

International Energy Agency, World Energy Statistics 2024: Global Primary Energy Data, https://www.iea.org/data-and-statistics, accessed 2025-10-25, 2024.

International Energy Agency, Global Energy Review 2025: Coal, *Tech. rep.*, International Energy Agency (IEA), accessed 2025-12-04, 2025a.

International Energy Agency, Direct Air Capture: Project Tracker and Global Status Update 2025, *Tech. rep.*, International Energy Agency, Paris, accessed 2025-04-22, 2025b.

IPCC, Summary for Policymakers, In: Climate Change 2013: The Physical Science Basis, Contribution of Working Group I to the Fifth Assessment Report of the IPCC, 2013.

IPCC, *Global Warming of 1.5°C*, World Meteorological Organization, Geneva, 2018.

IPCC, *Climate Change and Land: An IPCC Special Report on Climate Change, Desertification, Land Degradation, Sustainable Land Management, Food Security, and Greenhouse Gas Fluxes in Terrestrial Ecosystems*, Intergovernmental Panel on Climate Change (IPCC), 2019a.

IPCC, IPCC Special Report on the Ocean and Cryosphere in a Changing Climate, *Intergovernmental Panel on Climate Change*, 2019b.

IPCC, Summary for Policymakers, in *Climate Change 2021: The Physical Science Basis. Contribution of Working Group I to the Sixth Assessment Report of the Intergovernmental Panel on Climate Change*, edited by V. Masson-Delmotte, P. Zhai, A. Pirani, S. L. Connors, C. Péan, S. Berger, N. Caud, Y. Chen, L. Goldfarb, M. I. Gomis, M. Huang, K. Leitzell, E. Lonnoy, J. B. R. Matthews, T. K. Maycock, T. Waterfield, O. Yelekçi, R. Yu, and B. Zhou, pp. 3–32, Cambridge University Press, Cambridge, United Kingdom and New York, NY, USA, doi:10.1017/9781009157896.001, 2021.

IPCC, Chapter 4: Solar Radiation Modification, in *Climate Change 2022: Mitigation of Climate Change*, Cambridge University Press, 2022a.

IPCC, Climate change 2022: Impacts, adaptation and vulnerability, in *Working Group II Contribution to the Sixth Assessment Report of the Intergovernmental Panel on Climate Change*, Cambridge University Press, Cambridge, UK, doi:10.1017/9781009325844, 2022b.

IPCC, Full Report, Climate Change 2022: Mitigation of Climate Change. Contribution of Working Group III to the Sixth Assessment Report of the Intergovernmental Panel on Climate Change , *Tech. rep.*, Intergovernmental Panel on Climate Change (IPCC), Cambridge University Press, doi: 10.1017/9781009157926, 2022.

Irwin, D. A., The Nixon Shock After Forty Years: The Import Surcharge Revisited, *World Trade Review*, *10*(3), 319–339, doi:10.1017/S1474745611000071, 2011.

Jahn, A., M. M. Holland, and J. E. Kay, Projections of an ice-free Arctic Ocean, *Nature Reviews Earth & Environment*, *5*(3), 164–176, doi:10.1038/s43017-023-00515-9, 2024.

Janssens-Maenhout, G., et al., EDGAR v4.3.2 Global Atlas of the three major greenhouse gas emissions for the period 19702012, *Earth System Science Data*, *11*(3), 959–1002, doi:10.5194/essd-11-959-2019, 2019.

Jasanoff, S., A New Climate for Society, *Theory, Culture & Society*, *27*(2–3), 233–253, doi:10.1177/0263276409361910, 2010.

Jenkins, M., and A. Dai, The Impact of Sea-Ice Loss on Arctic Climate Feedbacks and Their Role for Arctic Amplification, *Geophysical Research Letters*, *48*(17), e2021GL094,599, doi:10.1029/2021GL094599, 2021.

Jeong, H., H.-S. Park, S. M. Kang, and E.-S. Chung, The greater role of Southern Ocean warming compared to Arctic Ocean warming in shifting future tropical rainfall patterns, *Nature Communications*, *16*(1), 2790, doi:10.1038/s41467-025-57654-4, 2025.

Jha, R., S. E. Perkins-Kirkpatrick, D. Singh, J. Kimutai, R. Libonati, and A. Mondal, Extreme terrestrial heat in 2024, *Nature Reviews Earth & Environment*, *6*(4), 234–236, doi:10.1038/s43017-025-00661-2, 2025.

Jin, F.-F., An equatorial ocean recharge paradigm for ENSO. Part I: Conceptual model, *Journal of the Atmospheric Sciences*, *54*(7), 811–829, doi:10.1175/1520-0469(1997)054<0811:AEORPF>2.0.CO;2, 1997.

Johnston, J. D., M. R. Schmidt, A. G. Merschel, W. M. Downing, M. R. Coughlan, and D. G. Lewis, Exceptional variability in historical fire regimes across a western Cascades landscape, Oregon, USA, *Ecosphere*, *14*(12), e4735, doi:10.1002/ecs2.4735, 2023.

Jones, P. D., D. H. Lister, T. J. Osborn, et al., Hemispheric and large-scale surface air temperature variations: An extensive revision and an update to 2010, *Journal of Geophysical Research: Atmospheres*, *117*(D5), D05,127, 2012.

Joos, F., R. Roth, J. S. Fuglestvedt, et al., Carbon Dioxide and Climate Impulse Response Functions for the Computation of Greenhouse Gas Metrics: A Multi-Model Analysis, *Atmospheric Chemistry and Physics*, *13*, 2793–2825, doi:10.5194/acp-13-2793-2013, 2013.

Jordan, A., and C. Adelle, *Environmental Policy in the EU: Actors, Institutions and Processes*, Routledge, 2013.

Jouzel, J., V. Masson-Delmotte, O. Cattani, et al., Orbital and millennial Antarctic climate variability over the past 800,000 years, *Science*, *317*(5839), 793–796, doi:10.1126/science.1141038, 2007a.

Jouzel, J., et al., Orbital and Millennial Antarctic Climate Variability over the Past 800,000 Years, *Science*, *317*(5839), 793–796, doi:10.1126/science.1141038, 2007b.

Kanamori, H., The Energy Release in Great Earthquakes, *Journal of Geophysical Research*, *82*(20), 2981–2987, doi:10.1029/JB082i020p02981, 1977.

Kanamori, H., and E. E. Brodsky, The Physics of Earthquakes, *Reports on Progress in Physics*, *67*(8), 1429–1496, doi:10.1088/0034-4885/67/8/R03, 2004.

Karlsen, K. S., T. Nissen-Meyer, and K. Sigloch, Spatiotemporal Variations in Surface Heat Loss Imply a Variable Oceanic Heat Flux, *Geophysical Research Letters*, *48*(8), e2020GL092,119, doi:10.1029/2020GL092119, 2021.

Kaufman, L., and E. Roston, Risk Management Is a Burgeoning Billion-Dollar Business Opportunity, *Bloomberg*, accessed: 2025-08-08, 2025.

Keeling, C. D., R. B. Bacastow, A. E. Bainbridge, C. A. Ekdahl Jr., P. R. Guenther, L. S. Waterman, and J. F. S. Chin, Atmospheric carbon dioxide variations at Mauna Loa Observatory, Hawaii, *Tellus*, *28*(6), 538–551, doi:10.1111/j.2153-3490.1976.tb00701.x, 1976.

Keenan, O. J., O. Soroka, D. Abramson, M. Safford, M. F. Shapiro, and A. K. Ghosh, Long-term impacts of hurricanes on mortality among Medicare beneficiaries: evidence from Hurricane Sandy, *Frontiers in Public Health*, *Volume 13*, doi:10.3389/fpubh.2025.1523941, 2025.

Keith, D. W., G. Holmes, D. St. Angelo, and K. Heidel, A Process for Capturing CO_2 from the Atmosphere, *Joule*, *2*(8), 1573–1594, doi:10.1016/j.joule.2018.05.006, 2018.

Keller, E. A., and D. E. DeVecchio, *Natural Hazards: Earth's Processes as Hazards, Disasters, and Catastrophes*, Pearson, 2012.

Kestin, J., *A Course of Thermodynamics, Revised Printing, Volume II*, Hemisphere Publishing Corporation, Washington, 1979.

King Arthur, Magna Carta (Environmental Provisions), King John of England, 1215.

King Edward I, Royal Decree on Logging in Royal Forests, Royal Decree, 1306.

King Henry III, Charter of the Forest, Issued by King Henry III of England, 1217.

King Louis XIV, French Royal Ordinance on Waterways and Forests, Issued by King Louis XIV of France, 1669.

Kleidon, A., How does the Earth system generate and maintain thermodynamic disequilibrium and what does it imply for the future of the planet?, *Philosophical Transactions of the Royal Society A*, *370*(1962), 1012–1040, doi:10.1098/rsta.2011.0316, 2012.

Klein, H. S., *The Atlantic Slave Trade*, 2nd ed., Cambridge University Press, Cambridge, a comprehensive overview of the economics, logistics, and human impact of the Atlantic slave trade., 2010.

Kloster, S. e. a., The climate response to future reductions in anthropogenic aerosol emissions: a multimodel study, *Atmospheric Chemistry and Physics*, *22*, 3845–3862, doi:10.5194/acp-22-3845-2022, 2022.

Koonin, S. E., *Unsettled: What Climate Science Tells Us, What It Doesnt, and Why It Matters*, BenBella, Dallas, TX, 2021.

Kopp, G., An assessment of the solar irradiance record for climate studies, *Journal of Space Weather and Space Climate*, *11*, 39, doi:10.1051/swsc/2021036, 2021.

Kopp, G., and J. L. Lean, A new, lower value of total solar irradiance: Evidence and climate significance, *Geophysical Research Letters*, *38*, doi:10.1029/2010GL045777, 2011.

Kossin, J. P., and M. Sitkowski, An objective model for identifying secondary eyewall formation in hurricanes, *Monthly Weather Review*, *137*(3), 876–892, doi:10.1175/2008MWR2701.1, 2009.

Kravitz, B., et al., A Multi-Model Assessment of Regional Climate Disparities Caused by Solar Geoengineering, *Environmental Research Letters*, *10*(9), 094,008, doi:10.1088/1748-9326/10/9/094008, 2015.

Krekel, D., R. C. Samsun, and R. Peters, The separation of CO_2 from ambient air – A techno-economic assessment, *Applied Energy*, *218*, 361–381, doi:10.1016/j.apenergy.2018.02.144, 2018.

Kump, L. R., J. F. Kasting, and R. G. Crane, *The Earth System*, 2 ed., Pearson Prentice Hall, Upper Saddle River, NJ, 2004.

Laherrère, J., and D. Sornette, Stretched exponential distributions in nature and economy: "fat tails" with characteristic scales, *The European Physical Journal B - Condensed Matter and Complex Systems*, *2*(4), 525–539, doi:10.1007/s100510050276, 1998.

Lambeck, K., H. Rouby, A. Purcell, Y. Sun, and M. Sambridge, Sea level and global ice volumes from the last glacial maximum to the holocene, *Proceedings of the National Academy of Sciences*, *111*(43), 15,296–15,303, doi:10.1073/pnas.1411762111, 2014.

Lan, X., P. Tans, and K. Thoning, Trends in globally-averaged CO_2 determined from NOAA Global Monitoring Laboratory measurements, doi:10.15138/9N0H-ZH07, 2025a.

Lan, X., K. Thoning, and E. Dlugokencky, Trends in globally-averaged CH_4, N_2O, and SF_6 determined from NOAA Global Monitoring Laboratory measurements, doi:10.15138/P8XG-AA10, 2025b.

Landsea, C. W., and J. L. Franklin, Atlantic hurricane database uncertainty and presentation of a new database format, *Monthly Weather Review*, *141*(10), 3576–3592, doi:10.1175/MWR-D-12-00254.1, 2013.

Lane, N., Life Ascending: The Ten Great Inventions of Evolution, *Profile Books*, chapter 4: Powering the Cell – The Electric Cell, 2009.

Lane, N., and W. Martin, The Power and Speed of Eukaryotic Bioenergetics and the Origin of Complexity, *Nature*, *467*, 929–934, doi:10.1038/nature09486, 2010.

Langenkamp, R. D., Petroleum in the Ancient Americas, *Oil-Industry History*, *3*(1), 14–25, documents the use of natural oil seeps by Indigenous tribes for waterproofing, medicine, and ceremonial purposes., 2002.

Laufkötter, C., J. Zscheischler, and T. L. Frölicher, High-impact marine heatwaves attributable to human-induced global warming, *Science*, *369*(6511), 1621–1625, doi:10.1126/science.aba0690, 2020.

Laxon, S. W., K. A. Giles, A. L. Ridout, et al., Cryosat-2 estimates of arctic sea ice thickness and volume, *Geophysical Research Letters*, *40*(4), 732–737, doi:10.1002/grl.50193, 2013.

Lay, T., C. J. Ammon, H. Kanamori, K. D. Koper, O. Sufri, and A. Hutko, Teleseismic Inversion for Rupture Process of the 2011 Tohoku Earthquake, *Earth, Planets and Space*, *63*(7), 637–642, doi:10.5047/eps.2011.05.013, 2011.

Lazarus, R. J., *The Rule of Five: Making Climate History at the Supreme Court*, Harvard University Press, Cambridge, MA, 2020.

Lee, J.-Y., et al., Chapter 4: Future Global Climate: Scenario-based Projections and Near-term Information, in *Climate Change 2021: The Physical Science Basis. Contribution of Working Group I to the Sixth Assessment Report of the Intergovernmental Panel on Climate Change*, edited by V. Masson-Delmotte, P. Zhai, A. Pirani, S. L. Connors, C. Péan, S. Berger, N. Caud, Y. Chen, L. Goldfarb, M. I. Gomis, M. Huang, K. Leitzell, E. Lonnoy, J. B. R. Matthews, T. K. Maycock, T. Waterfield, O. Yelekçi, R. Yu, and B. Zhou, pp. 553–672, Intergovernmental Panel on Climate Change, Geneva, Switzerland, doi:10.1017/9781009157896.006, 2021.

Lenssen, N. J. L., G. A. Schmidt, J. E. Hansen, M. J. Menne, A. Persin, R. Ruedy, and D. Zyss, Improvements in the GISTEMP Uncertainty Model, *Journal of Geophysical Research: Atmospheres*, *124*(12), 6307–6326, doi:https://doi.org/10.1029/2018JD029522, 2019.

Leopold, A., *A Sand County Almanac*, Oxford University Press, New York, 1949.

Levasseur, M., Impact of arctic meltdown on the microbial cycling of sulphur, *Nature Geoscience*, *6*, 691–700, doi:10.1038/ngeo1910, 2013.

Li, C. e. a., Projected climate response to future aerosol reductions, *Environmental Research Letters*, *18*(5), doi:10.1088/1748-9326/acd2a1, 2023.

Li, M., K. G. Miller, J. V. Browning, and et al., Astrochronology of the Paleocene-Eocene Thermal Maximum on the Atlantic Coastal Plain, *Proceedings of the National Academy of Sciences*, *119*(40), e2202429,119, doi:10.1073/pnas.2202429119, 2022a.

Li, X., D. Long, B. R. Scanlon, et al., Climate change threatens terrestrial water storage over the Tibetan Plateau, *Nature Climate Change*, *12*, 783–790, doi:10.1038/s41558-022-01443-0, 2022b.

Li, Z.-X., S. V. Bogdanova, A. S. Collins, A. Davidson, B. D. Waele, R. E. Ernst, I. C. W. Fitzsimons, et al., Assembly, configuration, and break-up history of Rodinia: A synthesis, *Precambrian Research*, *160*(1-2), 179–210, doi:10.1016/j.precamres.2007.04.021, 2008.

Liang, Q., *A History of Coal in China*, Beijing University Press, Beijing, China, discusses the early use of coal in China, including archaeological evidence dating back to 4000 BCE., 2006.

Lin, Y., I. Shennan, N. L. M. Barlow, E. A. Hill, R. Ranasinghe, C. D. Woodroffe, and B. P. Horton, A reconciled solution of Meltwater Pulse 1A sources using sea-level fingerprinting, *Nature Communications*, *12*, 2015, doi:10.1038/s41467-021-21990-y, 2021.

Lindsay, R., and A. Schweiger, Arctic sea ice thickness loss determined using subsurface, aircraft, and satellite observations, *The Cryosphere*, *9*(1), 269–283, doi:10.5194/tc-9-269-2015, 2015.

Liou, K. N., *An Introduction to Atmospheric Radiation*, 2nd ed., Academic Press, 2002.

Liu, G., A. E. Strong, W. J. Skirving, L. F. Arzayus, J. Sapper, and J. Li, Near-real-time satellite monitoring of global coral bleaching using the NOAA Coral Reef Watch Decision Support System, *Coral Reefs*, *33*(1), 85–94, doi:10.1007/s00338-013-1114-6, 2014.

Liu, J., G. Milne, R. Kopp, and J. Mitrovica, Sea level contributions from Antarctica during meltwater pulse 1A, *Quaternary Science Reviews*, *23*(13-14), 1521–1531, doi:10.1016/j.quascirev.2004.04.003, 2004.

Liu, X. e. a., Unmasking the warming role of aerosol decline over 20012019, *Nature Climate Change*, *13*, 377–384, doi:10.1038/s41558-023-01636-w, 2023.

Loeb, N. G., G. C. Johnson, T. J. Thorsen, J. M. Lyman, F. G. Rose, and S. Kato, Satellite and Ocean Data Reveal Marked Increase in Earths Heating Rate, *Geophysical Research Letters*, *48*(13), e2021GL093,047, doi:10.1029/2021GL093047, e2021GL093047 2021GL093047, 2021.

Loeb, N. G., T. J. Thorsen, S. Kato, F. G. Rose, Ø. Hodnebrog, and G. Myhre, Emerging hemispheric asymmetry of Earth's radiation, *Proceedings of the National Academy of Sciences*, *122*(40), e2511595,122, doi:10.1073/pnas.2511595122, 2025.

Loeb, N. G., et al., Clouds and the earth's radiant energy system (ceres) energy balanced and filled (ebaf) top-of-atmosphere (toa) edition-4.0 data product, *Journal of Climate*, *31*(2), 895 – 918, doi:10.1175/JCLI-D-17-0208.1, 2018.

Loland, M. H., S. Affolter, O. Kwiecien, and et al., Evolution of tropical land temperature across the last glacial termination, *Nature Communications*, *13*, 5103, doi:10.1038/s41467-022-32712-3, 2022.

Lorenz, E. N., Available Potential Energy and the Maintenance of the General Circulation, *Tellus*, *7*, 157–167, doi:10.3402/tellusa.v7i2.8796, 1955.

Loulergue, L., et al., Orbital and millennial-scale features of atmospheric CH_4 over the past 800,000 years, *Nature*, *453*(7193), 383–386, doi:10.1038/nature06950, 2008.

Lucazeau, F., Heat flow and geothermics, the current state of knowledge, *Geosciences*, *9*(1), 38, doi:10.3390/geosciences9010038, 2019.

Ludwig, D., D. D. Jones, and C. S. Holling, Qualitative analysis of insect outbreak systems: spruce budworm and forest, *Journal of Animal Ecology*, *47*(1), 315–332, doi:10.2307/3939, 1978.

Lunt, D. J., A. M. Haywood, G. A. Schmidt, U. Salzmann, P. J. Valdes, and H. J. Dowsett, Earth system sensitivity inferred from pliocene modelling and data, *Nature Geoscience*, *3*, 60–64, doi:10.1038/ngeo706, 2010.

Lüthi, D., et al., High-resolution carbon dioxide concentration record 650,000–800,000 years before present, *Nature*, *453*(7193), 379–382, doi:10.1038/nature06949, 2008.

Macdonald, F. A., et al., Calibrating the Cryogenian, *Science*, *327*(5970), 1241–1243, doi:10.1126/science.1183325, 2010a.

Macdonald, F. A., et al., Supporting Online Material for "Calibrating the Cryogenian", Science Online Supplement, doi:10.1126/science.1183325, available as supplementary material to *Science* **327**, 1241–1243 (2010), 2010b.

MacDougall, A. H., The Transient Response to Cumulative CO_2 Emissions: a Review, *Current Climate Change Reports*, *2*(1), 39–47, doi:10.1007/s40641-015-0030-6, 2016.

MacDougall, A. H., The oceanic origin of path-independent carbon budgets, *Scientific Reports*, *7*(1), 10,373, doi:10.1038/s41598-017-10557-x, 2017.

MacDougall, A. H., and P. Friedlingstein, The origin and limits of the near proportionality between climate warming and cumulative co2 emissions, *Journal of Climate*, *28*(10), 4217 – 4230, doi:10.1175/JCLI-D-14-00036.1, 2015.

MacDougall, A. H., M. Eby, and A. J. Weaver, If anthropogenic co2 emissions cease, will atmospheric co2 concentration continue to increase?, *Journal of Climate*, *26*(23), 9563 – 9576, doi:10.1175/JCLI-D-12-00751.1, 2013.

MacFarling Meure, C., D. Etheridge, C. Trudinger, P. Steele, R. Langenfelds, T. van Ommen, A. Smith, and J. Elkins, Law Dome CO_2, CH_4 and N_2O ice core records extended to 2000 years BP, *Geophysical Research Letters*, *33*(14), doi:10.1029/2006GL026152, 2006.

MacMartin, D. G., and D. W. Keith, Solar geoengineering for climate intervention: Scientific, ethical, and governance challenges, *Annual Review of Earth and Planetary Sciences*, *47*, 1–25, doi:10.1146/annurev-earth-082517-010021, 2019.

Magruder, L. A. e. a., ICESat-2 mission overview and early performance, *Remote Sensing of Environment*, 2020.

Makarieva, A. M., V. G. Gorshkov, A. V. Nefiodov, D. Sheil, A. Nobre, P. Bunyard, and B. Li, The key physical parameters governing frictional dissipation in a precipitating atmosphere, *Atmospheric Chemistry and Physics*, *13*(7), 4003–4015, doi:10.5194/acp-13-4003-2013, 2013.

Makarieva, A. M., V. G. Gorshkov, A. V. Nefiodov, D. Sheil, A. D. Nobre, and B.-L. Li, Quantifying the global atmospheric power budget, arXiv:1603.03706, see also ACP Discussions preprint; reports global atmospheric power order $\sim$1 $\mathrm{W\,m^{-2}}$., 2016.

Mankoff, R., and T. C. Bank, *The New Yorker Book of Technology Cartoons (with CD-Rom)*, Bloomberg Press, New Jersey, first edition; includes a CD-Rom, 2000.

Marchetti, C., On geoengineering and the CO_2 problem, *Climatic Change*, *1*(1), 59–68, doi:10.1007/BF00162777, 1977.

Marcott, S. A., et al., Centennial-scale changes in the global carbon cycle during the last deglaciation, *Nature*, *514*(7524), 616–619, doi:10.1038/nature13799, 2014.

Marder, M., T. Patzek, and S. W. Tinker, Physics, fracking, fuel, and the future, *Physics Today*, *69*(7), 46–52, doi:10.1063/PT.3.3236, 2016.

Marder, M., B. Eftekhari, and T. W. Patzek, Solvable model of gas production decline from hydrofractured networks, *Phys. Rev. E*, *104*, 065,001, doi:10.1103/PhysRevE.104.065001, 2021.

Maricopa County, 2024 Heat-Related Deaths Report, *Tech. rep.*, Maricopa County Department of Public Health, Epidemiology & Informatics, 2025.

Markus, T., T. Neumann, H. J. Zwally, et al., NASA's role in monitoring polar ice change, *Earth and Space Science News (EOS)*, *98*, doi:10.1029/2017EO081547, 2017.

Marshall, T. C., W. D. Rust, and M. Stolzenburg, Electric Field Measurements Near Cloud Base Before Lightning, *Geophysical Research Letters*, *33*(L16808), doi:10.1029/2006GL027169, 2006.

Martin, J. H., Glacial-interglacial CO_2 change: the iron hypothesis, *Paleoceanography*, *5*(1), 1–13, doi:10.1029/PA005i001p00001, 1990.

Martinez-Villalobos, C., D. Fu, P. C. Loikith, and J. D. Neelin, Accelerating increase in the duration of heatwaves under global warming, *Nature Geoscience*, doi:10.1038/s41561-025-01737-w, 2025.

Marvel, K., B. Kravitz, and K. Caldeira, Geophysical limits to global wind power, *Nature Climate Change*, *3*, 118–121, doi:10.1038/nclimate1683, 2013.

Mason, A., The Implications of Increasing Earth Observation Data, https://www.analysysmason.com/research/content/articles/the-implications-of-increasing-earth-observation-data, accessed April 14, 2025, 2022.

Masson-Delmotte, V., et al. (Eds.), *Climate Change 2021: The Physical Science Basis. Contribution of Working Group I to the Sixth Assessment Report of the Intergovernmental Panel on Climate Change*, 1–2409 pp., Cambridge University Press, Cambridge, United Kingdom and New York, NY, USA, doi:10.1017/9781009157896.002, 2021.

Matsumura, S., K. Yamazaki, and K. Suzuki, Slow-down in summer warming over Greenland in the past decade linked to central Pacific El Niño, *Communications Earth & Environment*, *2*(1), 257, doi:10.1038/s43247-021-00329-x, 2021.

Matthews, H. D., N. P. Gillett, P. A. Stott, and K. Zickfeld, The proportionality of global warming to cumulative carbon emissions, *Nature*, *459*(7248), 829–832, doi:10.1038/nature08047, 2009.

Matthews, H. D., et al., Solar geoengineering impacts and risks, *Nature Climate Change*, *4*, 637–639, doi:10.1038/nclimate2278, 2014.

May, R. M., Biological populations with nonoverlapping generations: stable points, stable cycles, and chaos, *Science*, *186*(4164), 645–647, doi:10.1126/science.186.4164.645, 1974.

McCarthy, F. M., et al., The varved succession of Crawford Lake, Milton, Ontario, Canada as a candidate Global boundary Stratotype Section and Point for the Anthropocene series, *The Anthropocene Review*, *10*(1), 146–176, doi:10.1177/20530196221149281, 2023.

McCormick, M. P., L. W. Thomason, and C. R. Trepte, Atmospheric effects of the Mount Pinatubo eruption, *Nature*, *373*, 399–404, doi:10.1038/373399a0, 1995.

McInerney, F. A., and S. L. Wing, The Paleocene-Eocene Thermal Maximum: A Perturbation of Carbon Cycle, Climate, and Biosphere with Implications for the Future, *Annual Review of Earth and Planetary Sciences*, *39*, 489–516, doi:10.1146/annurev-earth-040610-133431, 2011a.

McInerney, F. A., and S. L. Wing, The Paleocene-Eocene Thermal Maximum: A Perturbation of Carbon Cycle, Climate, and Biosphere with Implications for the Future, *Annual Review of Earth and Planetary Sciences*, *39*(1), 489–516, doi:10.1146/annurev-earth-040610-133431, 2011b.

McMillan, M., A. Shepherd, A. V. Sundal, K. Briggs, A. Muir, and A. Ridout, Rapid and synchronous ice loss from the Greenland and Antarctic ice sheets, *Nature Geoscience*, *7*, 732–735, doi:10.1038/ngeo2236, 2014.

Meinshausen, M., et al., The RCP greenhouse gas concentrations and their extensions from 1765 to 2300, *Climatic Change*, *109*(1), 213, doi:10.1007/s10584-011-0156-z, 2011.

Meron, E., Pattern-formation approach to modelling spatially extended ecosystems, *Ecological Modelling*, *234*, 70–82, doi:10.1016/j.ecolmodel.2011.05.035, 2012.

Michel, S. E., et al., Rapid shift in methane carbon isotopes suggests microbial emissions drove record high atmospheric methane growth in 20202022, *Proceedings of the National Academy of Sciences*, *121*(44), e2411212,121, doi:10.1073/pnas.2411212121, 2024.

Mifflin, M. D., S. T. St Jeor, L. A. Hill, B. J. Scott, S. A. Daugherty, and S. Y. Koh, A New Predictive Equation for Resting Energy Expenditure in Healthy Individuals, *Am. J. Clin. Nutr.*, *51*, 241–247, doi:10.1093/ajcn/51.2.241, 1990.

Milanković, M. M., *Canon of Insolation and the Ice-Age Problem*, Königlich Serbische Academie, 1941.

Miller, R., Terabytes from Space: Satellite Imaging is Filling Data Centers, https://www.datacenterfrontier.com/internet-of-things/article/11429032/terabytes-from-space-satellite-imaging-is-filling-data-centers, accessed April 14, 2025, 2020.

Milman, O., and A. Witherspoon, Climate disasters in first half of 2025 costliest ever on record, research shows, *The Guardian*, published 10:00 EDT, 2025.

Milo, R., and R. Phillips, Cell Biology by the Numbers, *Garland Science*, see Table 2.2 and Section 1.3 on ATP turnover rates, 2015.

Mission Instruments, Electric Fields Mission Instruments, 2024.

Molina, M. J., and F. S. Rowland, Stratospheric sink for chlorofluoromethanes: chlorine atom-catalyzed destruction of ozone, *Nature*, *249*, 810–812, doi:10.1038/249810a0, 1974.

Monnin, E., A. Indermühle, A. Dällenbach, J. Flückiger, B. Stauffer, T. F. Stocker, D. Raynaud, and J.-M. Barnola, Atmospheric CO_2 Concentrations over the Last Glacial Termination, *Science*, *291*(5501), 112–114, doi:10.1126/science.291.5501.112, 2001.

Monnin, E., et al., Evidence for substantial accumulation rate variability in Antarctica during the Holocene, through synchronization of CO2 in the Taylor Dome, Dome C and DML ice cores, *Earth and Planetary Science Letters*, *224*(1), 45–54, doi:10.1016/j.epsl.2004.05.007, 2004.

Moon, T. A., M. L. Druckenmiller, and R. L. Thoman, Arctic Report Card 2024, accessed: 2025-04-05, 2024.

Moore, C. M., et al., Processes and patterns of oceanic nutrient limitation, *Nature Geoscience*, *6*, 701–710, doi:10.1038/ngeo1765, 2013.

Morgan, J., et al., Size and morphology of the Chicxulub impact crater, *Nature*, *390*(6659), 472–476, doi:10.1038/37291, 1997.

MP, Max Planck (MP) Institute for Meteorology Earth System Model (MPI-ESM), accessed April 2025, 2024.

Myhre, G., E. J. Highwood, K. P. Shine, and F. Stordal, New estimates of radiative forcing due to well mixed greenhouse gases, *Geophysical Research Letters*, *25*(14), 2715–2718, doi:10.1029/98GL01908, 1998.

Myhre, G., C. Myhre, B. Samset, and T. Storelvmo, Aerosols and their relation to global climate and climate sensitivity, *Nature Education Knowledge*, *4*(5), 7, 2013a.

Myhre, G., Ø. Hodnebrog, N. Loeb, and P. M. Forster, Observed trend in Earth energy imbalance may provide a constraint for low climate sensitivity models, *Science*, *388*(6752), 1210–1213, doi:10.1126/science.adt0647, 2025.

Myhre, G., et al., Anthropogenic and Natural Radiative Forcing, in *Climate Change 2013: The Physical Science Basis*, edited by T. F. e. a. Stocker, pp. 659–740, Cambridge University Press, 2013b.

NASA, Terra Satellite - Earth Observing System (EOS), NASA Earth Observing System Mission, equipped with MODIS and ASTER, monitoring land surface temperatures and climate change., 2000.

NASA, Aqua Satellite - Earth Observing System (EOS), NASA Earth Observing System Mission, part of the A-Train satellite constellation, measuring atmospheric and surface temperature via MODIS, AIRS, and AMSR-E., 2002.

NASA, Global modeling and assimilation office: inst3_3d_asm_cp: Merra-2 3d iau state, meteorology instantaneous 3-hourly (p-coord, 0.625x0.5l42), version 5.12.4, 2015.

NASA, GISS Surface Temperature Analysis – The Elusive Absolute Surface Air Temperature (SAT), 2022.

NASA, NASA Goddard Institute for Space Studies (GISS) ModelE Climate Model, accessed April 2025, 2024.

NASA, and CNES, TOPEX/Poseidon Ocean Surface Topography Mission, Joint satellite altimetry mission, tOPEX/Poseidon revolutionized satellite altimetry, providing the first precise global measurements of sea level and ocean circulation., 1992.

NASA Earth Observatory, Sea Surface Temperature: warmest ∼35 °C, coolest ∼-2 °C, SST map showing cooler waters ∼35 °C, coolest ∼-2 °C., 2023.

NASA Earthdata, Nasa earth science data systems: Data holdings, https://www.earthdata.nasa.gov/, accessed April 14, 2025, 2025.

NASA JPL, Nasa turns to the cloud for help with next-generation earth missions, https://sealevel.nasa.gov/news/226/nasa-turns-to-the-cloud-for-help-with-next-generation-earth-missions, accessed April 14, 2025, 2022.

Natali, S. M., et al., Large loss of co in winter observed across the northern permafrost region, *Nature Climate Change*, *11*(9), 705–711, doi:10.1038/s41558-021-01073-2, 2021.

National Academies of Sciences, Engineering, and Medicine, *Climate Intervention: Carbon Dioxide Removal and Reliable Sequestration*, National Academies Press, doi:10.17226/18805, 2015.

National Academies of Sciences, Engineering, and Medicine, *Negative Emissions Technologies and Reliable Sequestration: A Research Agenda*, National Academies Press, Washington, DC, doi:10.17226/25259, 2019.

National Academies of Sciences, Engineering, and Medicine, *A Research Strategy for Ocean-based Carbon Dioxide Removal and Sequestration*, chap. Nutrient Fertilization, The National Academies Press, Washington, DC, doi:10.17226/26278, 2022.

NCAR, National Center for Atmospheric Research (NCAR) Community Earth System Model (CESM), accessed April 2025, 2024.

NCEI (NOAA), Billion-Dollar Weather and Climate Disasters, accessed 2025-10-26, 2024.

Neckel, H., and D. Labs, Improved Data of Solar Spectral Irradiance from 0.33 to 1.25 μm, *Solar Physics*, *74*, 231–249, doi:10.1007/BF00151270, 1981.

Needham, J., *Science and Civilization in China: Volume 4, Physics and Physical Technology*, Cambridge University Press, Cambridge, UK, describes the use of natural gas and oil in early Chinese industries such as salt extraction., 1964.

NEEM Team, Eemian interglacial reconstructed from a greenland folded ice core, *Nature*, *493*, 489–494, doi:10.1038/nature11789, 2013.

Newhall, C. G., and S. Self, The Volcanic Explosivity Index (VEI): An Estimate of Explosive Magnitude for Historical Volcanism, *Journal of Geophysical Research*, *87*(C2), 1231–1238, doi:10.1029/JC087iC02p01231, 1982.

NGRIP, High-resolution record of Northern Hemisphere climate extending into the last interglacial period, *Nature*, *431*, 147–151, doi:10.1038/nature02805, 2004.

Nicholls, D. G., and S. J. Ferguson, *Bioenergetics 4*, Academic Press, Amsterdam, chapters on protonmotive force and ATP synthesis, 2013.

NOAA, Geostationary Operational Environmental Satellites (GOES), NOAA Geostationary Satellite Program, provides real-time atmospheric temperature and sea surface temperature data for weather forecasting and climate monitoring., 1975.

NOAA, Polar-Orbiting Environmental Satellites (POES), NOAA Low-Earth Orbit Satellite Program, provided long-term global temperature records via AVHRR and other sensors., 1978.

NOAA, Global Tropical Moored Buoy Array Overview, https://www.pmel.noaa.gov/gtmba, 2022.

NOAA, NASA, NOAA Confirm 2023 as Earth's Hottest Year on Record, *NOAA Climate Report*, 2024.

NOAA, and NASA, Suomi National Polar-orbiting Partnership (NPP), Joint NASA-NOAA Earth observation satellite, monitors global temperature trends using VIIRS, CrIS, and ATMS instruments., 2011.

NOAA, NASA, and USAF, *U.S. Standard Atmosphere*, U.S. Government Printing Office, Washington, D.C., nOAA-S/T 76-1562, NASA-TM-X-74335, USAF-R-TR-76-067, 1976.

NOAA, NASA, and CNES, Jason-1 Ocean Surface Topography Mission, Joint satellite altimetry mission, jason-1 was the successor to TOPEX/Poseidon, measuring sea surface height, ocean circulation, and climate variability., 2001.

NOAA, NASA, CNES, and EUMETSTAT, Jason-2 / ocean surface topography mission (ostm), Joint satellite altimetry mission, jason-2 continued high-precision altimetry measurements for sea level rise monitoring, operational oceanography, and climate studies., 2008.

NOAA, NASA, CNES, and EUMETSTAT, Jason-3 ocean surface topography mission, Joint satellite altimetry mission, jason-3 continues sea surface height measurements for climate monitoring, ocean circulation studies, and weather forecasting., 2016.

NOAA Climate.gov, Unintended warming: How reduced ship emissions may accelerate climate change, https://www.climate.gov/news-features/feed/unintended-warming-how-reduced-ship-emissions-may-accelerate-climate-change, 2024.

Notz, D., The future of ice sheets and sea ice: Between reversible retreat and unstoppable loss, *PNAS*, *106*(49), 20,590–20,595, doi:10.1073/pnas.0902356106, 2009.

Notz, D., and J. Doerr, Chapter 9 of the working group i contribution to the ipcc sixth assessment report – data for figure 9.15 (v20220712), doi:10.5285/65c832a5eeda4ed7a9b0a8af6cf5058d, 2023.

Notz, D., and J. Stroeve, Observations reveal external driver for arctic sea-ice retreat, *Geophysical Research Letters*, *43*(10), 109–116, doi:10.1002/2016GL069317, 2016.

Odnoletkova, N., and T. W. Patzek, Data-driven analysis of climate change in Saudi Arabia: trends in temperature extremes and human comfort indicators, *Journal of Applied Meteorology and Climatology*, *60*(8), 1055–1070, 2021.

Ogilvy, C. S., and A. B. DuBois, The hydrodynamic drag of swimming bluefish (*Pomatomus saltatrix*) in different intensities of turbulence: Variation with changes of buoyancy, *Journal of Experimental Biology*, *92*, 67–85, doi:10.1242/jeb.92.1.67, 1981.

on Climate Change, U. N. F. C., Current and future permafrost emissions as large as major emitters, accessed: 2025-04-06, 2022.

Oppenheimer, M., et al., Sea Level Rise and Implications for Low-Lying Islands, Coasts and Communities, in *IPCC Special Report on the Ocean and Cryosphere in a Changing Climate*, edited by H.-O. Pörtner, D. C. Roberts, V. Masson-Delmotte, P. Zhai, M. Tignor, E. Poloczanska, K. Mintenbeck, M. Nicolai, A. Okem, J. Petzold, B. Rama, and N. M. Weyer, pp. 321–445, Cambridge University Press, Cambridge, United Kingdom and New York, NY, USA, doi:10.1017/9781009157964.006, coordinating Lead Author: M. Oppenheimer (ORCID: 0000-0002-9708-5914), 2019.

Ortiz-Bobea, A., Climate, Agriculture and Food, 2021.

Osman, M. B., J. E. Tierney, J. Zhu, R. Tardif, G. J. Hakim, J. King, and C. J. Poulsen, Globally resolved surface temperatures since the Last Glacial Maximum, *Nature*, *599*, 239–244, doi:10.1038/s41586-021-03984-4, 2021.

Pagani, M., Z. Liu, J. LaRiviere, and A. C. Ravelo, High Earth-system climate sensitivity determined from Pliocene carbon dioxide concentrations, *Nature Geoscience*, *3*, 27–30, doi:10.1038/ngeo724, 2010.

PAGES, Interglacials of the last 800,000 years, *Reviews of Geophysics*, *54*(1), 162–219, doi:10.1002/2015RG000482, 2016.

Patzek, T., *Barnett Shale in Texas: Promise and Problems, May 26, 2011, Seminar at the Bureau of Economic Geology, UT Austin*, Texas Data Repository Dataverse, doi:10.18738/T8/3MLRLO, 2019.

Patzek, T., W. Saputra, W. Kirati, and M. Marder, Generalized Extreme Value Statistics, Physical Scaling, and Forecasts of Gas Production in the Barnett Shale, *Energy Fuels*, *33*(12), 12,154–1216, doi:10.1021/acs.energyfuels.9b01385, 2019.

Patzek, T. W., Thermodynamics of the corn-ethanol biofuel cycle, *Crit. Rev. Plant Sci.*, *23*(6), 519–567, 2004.

Patzek, T. W., How can we outlive our way of life?, in *20th Round Table on Sustainable Development of Biofuels: Is the Cure Worse than the Disease?*, OECD, Paris, https://np-net.pbworks.com/f/Patzek+(2007)+How+to+outlive+way+of+life+-+Paper+for+OECD+Roundtable+on+biofuels,+Berkeley.pdf, 2007.

Patzek, T. W., Exponential growth, energetic Hubbert cycles, and the advancement of technology, *Arch. Min. Sci.*, *53*(2), 131 – 159, 2008.

Patzek, T. W., and G. D. Croft, Potential for Coal-to-Liquids Conversion in the U.S. – Fischer-Tropsch Synthesis, *Nat. Resour. Res.*, *18*(3), 181 – 191, dOI: 10.1007/s11053-009-9098-9, 2009.

Patzek, T. W., and G. D. Croft, A Global Coal Production Forecast with Multi-Hubbert Cycle Analysis, *ENERGY*, *35*, 3109 – 3122, 2010.

Patzek, T. W., and D. Pimentel, Thermodynamics of energy production from biomass, *Crit. Rev. Plant Sci.*, *24*(5–6), 329–364, 2005.

Patzek, T. W., F. Male, and M. Marder, Gas production in the Barnett shale obeys a simple scaling theory, *Proceedings of the National Academy of Sciences*, *110*(49), 19,731–19,736, doi:10.1073/pnas.1313380110, 2013.

Patzek, T. W., A. M. Saad, and A. Hassan, Multimodal Carbonates: Distribution of Oil Saturation in the Microporous Regions of Arab Formations, *Energies*, *15*(3), 1243, doi:10.3390/en15031243, 2022.

Penrose, R., *Cycles of Time: An Extraordinary New View of the Universe*, Alfred A. Knopf, New York, 2010.

Perlin, J., *A Forest Journey: The Role of Wood in the Development of Civilization*, Harvard University Press, 2005.

Perry, K., and L. Lave, Donora, Pennsylvania: An Environmental Disaster of the 20th Century, *Public Health Reports*, *113*(1), 32–37, 1998.

Petit, J. R., J. Jouzel, D. Raynaud, et al., Climate and Atmospheric History of the Past 420,000 Years from the Vostok Ice Core, Antarctica, *Nature*, *399*, 429–436, doi:10.1038/20859, 1999a.

Petit, J. R., et al., Climate and atmospheric history of the past 420,000 years from the Vostok ice core, Antarctica, *Nature*, *399*(6735), 429–436, doi:10.1038/20859, 1999b.

Pielke, R. A., and C. W. Landsea, Normalized Hurricane Damages in the United States: 1925–95, *Weather and Forecasting*, *13*(3), 621–631, doi:10.1175/1520-0434(1998)013<0621:NHDITU>2.0.CO;2, 1998.

Pierrehumbert, R. T., *Principles of Planetary Climate*, first ed., Cambridge Univ Pr, 2010.

Pierrehumbert, R. T., Infrared radiation and planetary temperature, *Physics Today*, *64*(1), 33–38, doi:10.1063/1.3541943, 2011.

Pierrehumbert, R. T., Climate Hacking Is Barking Mad, *Slate*, accessed via archived URL, 2015.

Pistone, K., I. Eisenman, and V. Ramanathan, Observational determination of albedo decrease caused by vanishing Arctic sea ice, *Proceedings of the National Academy of Sciences*, *111*(9), 3322–3326, doi:10.1073/pnas.1318201111, 2014.

Pitcher, T. J., and J. K. Parrish, Functions of Shoaling Behaviour in Teleosts, in *Behaviour of Teleost Fishes*, pp. 363–439, Chapman & Hall, doi:10.1007/978-94-011-1578-0_13, 1993.

Pixalytics, Earth Observation Satellites Orbiting in 2023, accessed April 16, 2025, 2023.

Plass, G. N., The carbon dioxide theory of climatic change, *Tellus*, *8*(2), 140–154, doi:10.3402/tellusa.v8i2.8967, 1956.

Pollack, H. N., S. J. Hurter, and J. R. Johnson, Heat Flow from the Earth's Interior: Analysis of the Global Data Set, *Reviews of Geophysics*, *31*(3), 267–280, doi:10.1029/93RG01249, 1993.

Popova, E. E., et al., What controls primary production in the Arctic Ocean? Results from the Arctic model intercomparison project (AMIP), *Journal of Geophysical Research: Oceans*, *117*(C00D12), doi:10.1029/2011JC007112, 2012.

Post, E., and et al., Ecological consequences of sea-ice decline, *Science*, *341*(6145), 519–524, doi:10.1126/science.1235225, 2013.

Powell, M. D., P. J. Vickery, and T. A. Reinhold, Reduced drag coefficient for high wind speeds in tropical cyclones, *Nature*, *422*, 279–283, doi:10.1038/nature01481, 2003.

PRC President APP, Air Pollution Prevention and Control Law of the People's Republic of China (2015), Order No. 31 of the President of the People's Republic of China, 2015.

PRC President EPA, Environmental Protection Law of the People's Republic of China (1989, amended 2014), Order No. 9 of the President of the People's Republic of China, 1989.

PRC President SPP, Soil Pollution Prevention and Control Law of the People's Republic of China (2018), Order No. 31 of the President of the People's Republic of China, 2018.

PRC President SWPP, Solid Waste Pollution Prevention and Control Law of the People's Republic of China (2020), Order No. 31 of the President of the People's Republic of China, 2020.

PRC President WPP, Water Pollution Prevention and Control Law of the People's Republic of China (2008, amended 2017), Order No. 87 of the President of the People's Republic of China, 2008.

Private Islands Online, Caribbean private islands for sale, listings of private islands across the Caribbean including Bahamas, BVI, Grenada, and more, 2024.

Purich, A., and E. W. Doddridge, Record low Antarctic sea ice coverage indicates a new sea ice state, *Communications Earth & Environment*, *4*(1), 314, doi:10.1038/s43247-023-00961-9, 2023.

Qiu, M., et al., Wildfire smoke exposure and mortality burden in the US under climate change, *Nature*, doi:10.1038/s41586-025-09611-w, 2025.

Quaas, J., et al., Robust evidence for reversal of the trend in aerosol effective climate forcing, *Atmospheric Chemistry and Physics*, *22*, 12,221–12,239, doi:10.5194/acp-22-12221-2022, 2022.

Radkau, J., *Wood: A History*, Polity Press, Cambridge, UK, 2008.

Rakov, V. A., and M. A. Uman, *Lightning: Physics and Effects*, Cambridge University Press, 2003.

Rantanen, M., A. Y. Karpechko, A. Lipponen, K. Nordling, O. Hyvärinen, K. Ruosteenoja, T. Vihma, and A. Laaksonen, The arctic has warmed nearly four times faster than the globe since 1979, *Communications Earth & Environment*, *3*(1), 168, doi:10.1038/s43247-022-00498-3, 2022.

Rasmussen, S. O., M. Bigler, S. P. Blockley, and et al., A stratigraphic framework for abrupt climatic changes during the Last Glacial period based on three synchronized Greenland ice core records, *Quaternary Science Reviews*, *106*, 14–28, doi:10.1016/j.quascirev.2014.09.007, 2014.

Rees, W. E., Ecological economics for humanity's plague phase, *Ecological Economics*, *169*, 106,519, doi:10.1016/j.ecolecon.2019.106519, 2020.

Rees, W. E., Overshoot: Cognitive Obsolescence and the Population Conundrum, *The Journal of Population and Sustainability*, *7*(1), 15–38, doi:10.3197/JPS.63799953906865, 2023.

Revelle, R., and H. E. Suess, Carbon Dioxide Exchange Between Atmosphere and Ocean and the Question of an Increase of Atmospheric CO_2 During the Past Decades, *Tellus*, *9*(1), 18–27, doi:10.1111/j.2153-3490.1957.tb01849.x, 1957.

Reynolds, J. L., Solar geoengineering governance: A challenge for the twenty-first century, *Climate Policy*, *19*(7), 857–865, doi:10.1080/14693062.2019.1591774, 2019.

Rhythm Energy, Average kWh Usage in Texas: Estimating Your Home's Usage, accessed: 2025-08-15, 2024.

Riahi, K., et al., The Shared Socioeconomic Pathways and their energy, land use, and greenhouse gas emissions implications: An overview, *Global Environmental Change*, *42*, 153–168, doi:10.1016/j.gloenvcha.2016.05.009, 2017.

Ricklefs, R. E., and R. A. Relyea, *Ecology: The Economy of Nature*, 7th ed., W. H. Freeman and Company, New York, 2011.

Ridgwell, A., and R. E. Zeebe, The role of the global carbonate cycle in the regulation and evolution of the Earth system, *Earth and Planetary Science Letters*, *234*, 299–315, doi:10.1016/j.epsl.2005.03.006, 2005.

Rietkerk, M., S. C. Dekker, P. C. de Ruiter, and J. van de Koppel, Self-organized patchiness and catastrophic shifts in ecosystems, *Science*, *305*(5692), 1926–1929, doi:10.1126/science.1101867, 2004.

Rignot, E., J. Mouginot, B. Scheuchl, M. van den Broeke, M. J. van Wessem, and M. Morlighem, Four decades of Antarctic Ice Sheet mass balance from 1979-2017, *Proceedings of the National Academy of Sciences*, *116*(4), 1095–1103, doi:10.1073/pnas.1812883116, 2019.

Robock, A., Volcanic eruptions and climate, *Reviews of Geophysics*, *38*(2), 191–220, doi:10.1029/1998RG000054, 2000.

Rocha, J. C., G. Peterson, Örjan Bodin, and S. Levin, Cascading regime shifts within and across scales, *Science*, *362*(6421), 1379–1383, doi:10.1126/science.aat7850, 2018.

Rockström, J., et al., A Safe Operating Space for Humanity, *Nature*, *461*, 472–475, doi:10.1038/461472a, 2009.

Röhl, U., T. Westerhold, T. J. Bralower, and J. C. Zachos, On the duration of the Paleocene-Eocene thermal maximum (PETM), *Geochemistry, Geophysics, Geosystems*, *8*(12), doi:10.1029/2007GC001784, 2007.

Rohling, E. J., K. Grant, M. Bolshaw, A. P. Roberts, M. Siddall, C. Hemleben, and M. Kucera, Antarctic temperature and global sea level closely coupled over the past five glacial cycles, *Nature Geoscience*, *2*(7), 500–504, doi:10.1038/ngeo557, 2009.

Rohling, E. J., M. Medina-Elizalde, J. G. Shepherd, M. Siddall, and J. D. Stanford, Sea surface and high-latitude temperature sensitivity to radiative forcing of climate over several glacial cycles, *Journal of Climate*, *25*(5), 1635–1656, doi:10.1175/2011JCLI4078.1, 2012.

Rosenzweig, M. L., and R. H. MacArthur, Graphical representation and stability conditions of predatorprey interactions, *The American Naturalist*, *97*(895), 209–223, doi:10.1086/282272, 1963.

Roser, M., and E. Ortiz-Ospina, Life Expectancy, historical data on global life expectancy, including estimates for 1920. Retrieved January 19, 2025., 2023.

Rothman, L. S., D. Jacquemart, and et al., The HITRAN molecular spectroscopic database and HAWKS (HITRAN Atmospheric Workstation): 1996 edition, *Journal of Quantitative Spectroscopy and Radiative Transfer*, *60*(5), 665–710, doi:10.1016/S0022-4073(98)00078-8, 1998.

Rothman, L. S., et al., The HITRAN2012 molecular spectroscopic database, *Journal of Quantitative Spectroscopy and Radiative Transfer*, *130*, 4–50, doi:10.1016/j.jqsrt.2013.07.002, 2013.

Roy, D. P. e. a., Landsat-8: Science and product vision for terrestrial global change research, *Remote Sensing of Environment*, 2014.

Roy, I., Solar Cyclic Variability Can Modulate Winter Arctic Climate, *Scientific Reports*, *8*(1), 4864, doi:10.1038/s41598-018-22854-0, 2018.

Roy, S. B., and J. J. Traiteur, Impacts of wind farms on surface air temperatures, *Proceedings of the National Academy of Sciences*, *107*(42), 17,899–17,904, doi:10.1073/pnas.1000493107, includes a global mean surface KE dissipation estimate $\sim$2.1 W m^{-2}., 2010.

Royal Society, *Geoengineering the Climate: Science, Governance and Uncertainty*, Royal Society, London, 2009.

Rubin, R., *The Creative Act: A Way of Being*, Penguin Press, New York, hardcover edition, published January 17, 2023., 2023.

Rubino, M., et al., A revised 1000 year atmospheric δ^{13}C-CO_2 record from Law Dome and South Pole, Antarctica, *Journal of Geophysical Research: Atmospheres*, *118*(15), 8482–8499, doi:10.1002/jgrd.50668, 2013.

Running, S. W., A Measurable Planetary Boundary for the Biosphere: The Net Primary Production Limit, *Ecology and Society*, *17*(2), 16, doi:10.5751/ES-05035-170216, 2012.

Russian Fed AP, Federal Law on the Protection of Atmospheric Air (1999, amended 2021), Federal Law No. 96-FZ of the Russian Federation, 1999.

Russian Fed EP, Federal Law on Environmental Protection (2002, amended 2021), Federal Law No. 7-FZ of the Russian Federation, 2002.

Russian Fed SP, Federal Law on Land Protection (2001, amended 2020), Federal Law No. 101-FZ of the Russian Federation, 2001.

Russian Fed WC, Water Code of the Russian Federation (2006, amended 2022), Federal Law No. 74-FZ of the Russian Federation, 2006.

Russian Fed WM, Federal Law on Production and Consumption Waste (1998, amended 2022), Federal Law No. 89-FZ of the Russian Federation, 1998.

Saaputra, W., T. Patzek, and C. Torres-Verdín, URTEC-3858983-MS: Physics-Based and Data-Driven Production Forecasting in the Eagle Ford Shale, in *Proceedings*, Society of Petroleum Engineers, SPE/AAPG/SEG Unconventional Resources Technology Conference, doi:0.15530/urtec-2023-3858983, 2023.

Saiz-Lopez, A., and R. von Glasow, Reactive halogen chemistry in the troposphere, *Chemical Society Reviews*, *41*(19), 6448–6472, doi:10.1039/c2cs35208g, 2012.

Salomonson, V. V., and I. R. Appel, MODIS: Moderate Resolution Imaging Spectroradiometer, *Remote Sensing of Environment*, 2002.

Saltzman, B., and K. A. Maasch, A first-order global model of late Cenozoic climatic change, *Transactions of the Royal Society of Edinburgh: Earth Sciences*, *81*(4), 315–325, doi:10.1017/S0263593300020824, 1991.

Samset, B. H. e. a., Climate impacts from a removal of anthropogenic aerosol emissions, *Geophysical Research Letters*, *47*(12), doi:10.1029/2020GL088125, 2020.

Sanz-Pérez, E. S., C. R. Murdock, S. A. Didas, and C. W. Jones, Direct Capture of CO_2 from Ambient Air, *Chemical Reviews*, *116*(19), 11,840–11,876, doi:10.1021/acs.chemrev.6b00173, 2016.

Saputra, W., W. Kirati, and T. Patzek, Generalized Extreme Value Statistics, Physical Scaling and Forecasts of Oil Production in the Bakken Shale, *Energies*, *12*(19), 3641, doi:10.3390/en12193641, 2019.

Saputra, W., W. Kirati, and T. Patzek, Physical Scaling of Oil Production Rates and Ultimate Recovery from All Horizontal Wells in the Bakken Shale, *Energies*, *13*(8), 2052, doi:10.3390/en13082052, 2020.

Saputra, W., W. Kirati, and T. W. Patzek, Generalized extreme value statistics, physical scaling and forecasts of gas production in the Haynesville shale, *Journal of Natural Gas Science and Engineering*, *94*, 104,041, doi:10.1016/j.jngse.2021.104041, 2021.

Saputra, W., W. Kirati, and T. Patzek, Forecast of Economic Tight Oil and Gas Production in Permian Basin, *Energies*, *15*(1), 43, doi:10.3390/en15010043, 2022a.

Saputra, W., W. Kirati, and T. Patzek, Generalized Extreme Value Statistics, Physical Scaling and Forecasts of Oil Production from All Vertical Wells in the Permian Basin, *Energies*, *15*(3), 904, doi:10.3390/en15030904, 2022b.

Saputra, W., W. Kirati, D. Hughes, and T. Patzek, Forecast of Economic Gas production in the Marcellus, *AAPG Bulletin*, *108*, 15–40, doi:10.1306/10242221078, 2024.

Sarmiento, J. L., and N. Gruber, *Ocean Biogeochemical Dynamics*, Princeton University Press, Princeton, NJ, 2006.

Sato, M., Global Mean Surface Temperature Relative to 1951-1980 (degC), Columbia University), accessed: 2025-02-10, 2025.

Scheffer, M., S. H. Hosper, M.-L. Meijer, B. Moss, and E. Jeppesen, Alternative equilibria in shallow lakes, *Trends in Ecology & Evolution*, *8*(8), 275–279, doi:10.1016/0169-5347(93)90254-M, 1993.

Scheffer, M., S. Carpenter, J. A. Foley, C. Folke, and B. Walker, Catastrophic shifts in ecosystems, *Nature*, *413*(6856), 591–596, doi:10.1038/35098000, 2001.

Schmit, T. J. e. a., GOES-16: First year of operations, *Bulletin of the American Meteorological Society*, 2017.

Schneider, R., J. Schmitt, P. Koehler, F. Joos, and H. Fischer, A reconstruction of atmospheric carbon dioxide and its stable carbon isotopic composition from the penultimate glacial maximum to the glacial inception, doi:10.1594/PANGAEA.817041, supplement to: Schneider, R et al. (2013): A reconstruction of atmospheric carbon dioxide and its stable carbon isotopic composition from the penultimate glacial maximum to the glacial inception. Climate of the Past, 9(6), 2507-2523, https://doi.org/10.5194/cp-9-2507-2013, 2013.

Schrag, D. P., R. A. Berner, P. F. Hoffman, and G. P. Halverson, On the initiation of a Snowball Earth, *Geochemistry, Geophysics, Geosystems*, *3*(6), 1036, doi:10.1029/2001GC000219, 2002.

Schuur, E. A., et al., Climate change and the permafrost carbon feedback, *Nature*, *520*(7546), 171–179, doi:10.1038/nature14338, 2015.

Schuur, E. A. G., A. D. McGuire, C. Schädel, et al., Permafrost and Climate Change: Carbon Cycle Feedbacks From the Warming Arctic, *Annual Review of Environment and Resources*, *47*, 343–371, accessed: 2025-04-06, 2022.

Schwarzacher, W., *The Milankovitch Theory*, *Developments in Sedimentology*, vol. 52, chap. 3, pp. 29–48, Elsevier, doi:10.1016/S0070-4571(08)70418-7, 1993.

Scott, R. B., and D. P. Marshall, Update on the Global Energy Dissipation Rate of the DeepOcean Circulation, *Journal of Physical Oceanography*, *48*(6), 13011323, doi:10.1175/JPOD160287.1, 2018.

SCOTUS, West Virginia v. Environmental Protection Agency, 2022.

Screen, J. A., and I. Simmonds, The central role of diminishing sea ice in recent arctic temperature amplification, *Nature*, *464*, 1334–1337, doi:10.1038/nature09051, 2010.

Sea Shepherd, Sea Shepherd Fights Krill Trawlers in the Last Wild Ocean, accessed 2025-04-02, 2025.

Seltzer, A. M., J. Ng, W. Aeschbach, R. Kipfer, J. T. Kulongoski, J. P. Severinghaus, and M. Stute, Widespread six degrees Celsius cooling on land during the Last Glacial Maximum, *Nature*, *593*, 228–232, doi:10.1038/s41586-021-03467-6, 2021.

Severinghaus, J. P., T. Sowers, E. J. Brook, R. B. Alley, and M. L. Bender, Timing of abrupt climate change at the end of the Younger Dryas interval from thermally fractionated gases in polar ice, *Nature*, *391*, 141–146, doi:10.1038/34346, 1998.

Shakhova, N., I. Semiletov, A. Salyuk, D. Kosmach, and N. Belcheva, Extensive methane venting to the atmosphere from sediments of the East Siberian Arctic Shelf, *Science*, *327*(5970), 1246–1250, doi:10.1126/science.1182221, 2010a.

Shakhova, N., I. Semiletov, A. Salyuk, V. Yusupov, D. Kosmach, and O. Gustafsson, Geological methane emissions at the east siberian shelf, *Nature Geoscience*, *3*, 189–192, 2010b.

Shakhova, N., I. Semiletov, and et al., Current rates and mechanisms of subsea permafrost degradation in the east siberian arctic shelf, *Nature Communications*, *10*, 1–14, doi:10.1038/s41467-018-07864-6, 2019.

Shakun, J. D., P. U. Clark, F. He, et al., Global Warming Preceded by Increasing CO_2 During the Last Deglaciation, *Nature*, *484*, 49–54, doi:10.1038/nature10915, 2012.

Shaw, S. L., B. Gantt, and N. Meskhidze, Production and emissions of marine isoprene and monoterpenes: a review, *Advances in Meteorology*, pp. 1–12, doi:10.1155/2010/408696, 2003.

Sheil, D., and D. Murdiyarso, How Forests Attract Rain: An Examination of a New Hypothesis, *BioScience*, *59*(4), 341–347, doi:10.1525/bio.2009.59.4.12, 2009.

Shepherd, A., E. R. Ivins, A. Geruo, and et al., A reconciled estimate of ice-sheet mass balance, *Science*, *338*(6111), 1183–1189, doi:10.1126/science.1228102, 2012.

Shepherd, A., et al., *Antarctic and Greenland Ice Sheet mass balance 1992-2020 for IPCC AR6 (Version 1.0)*, UK Polar Data Centre, Natural Environment Research Council, UK Research & Innovation, doi:10.5285/77b64c55-7166-4a06-9def-2e400398e452, data set, 2021.

Sherwood, S., M. Webb, W. J. Ingram, et al., An assessment of Earth's climate sensitivity using multiple lines of evidence, *Reviews of Geophysics*, *58*(4), e2019RG000,678, doi:10.1029/2019RG000678, 2020.

Shine, K. P., I. J. Barton, M. D. Hurley, and T. J. Wallington, Global warming potentials: the role of IR absorption cross sections, *Climate Dynamics*, *11*, 133–140, doi:10.1007/BF00223490, 1995.

Shukla, C., et al. (Eds.), *Climate Change 2022 - Mitigation of Climate Change: Working Group III Contribution to the Sixth Assessment Report of the Intergovernmental Panel on Climate Change*, 2042 pp., Cambridge University Press, doi:10.1017/9781009157926, 2023.

Shukla, P., et al. (Eds.), *Climate Change 2022: Mitigation of Climate Change. Contribution of Working Group III to the Sixth Assessment Report of the Intergovernmental Panel on Climate Change* , 1–3068 pp., Cambridge University Press, Cambridge, UK and New York, USA, doi:10.1017/9781009157926, 2022.

Siegenthaler, U., E. Monnin, K. Kawamura, R. Spahni, J. Schwander, B. Stauffer, T. F. Stocker, J.-M. Barnola, and H. Fischer, Carbon dioxide concentrations for the Last Millennium, Antarctica, doi:10.1594/PANGAEA.728135, supplement to: Siegenthaler, U et al. (2005): Supporting evidence from the EPICA Dronning Maud Land ice core for atmospheric CO_2 changes during the past millennium. Tellus Series B-Chemical and Physical Meteorology, 57(1), 51-57, https://doi.org/10.1111/j.1600-0889.2005.00131.x, 2005.

Silvano, A., et al., Rising surface salinity and declining sea ice: A new Southern Ocean state revealed by satellites, *Proceedings of the National Academy of Sciences*, *122*(27), e2500440,122, doi:10.1073/pnas.2500440122, 2025.

Skirving, W. J., S. F. Heron, B. L. Marsh, G. Liu, J. L. De La Cour, and E. F. Geiger, CoralTemp and the Coral Reef Watch Coral Bleaching Heat Stress Product Suite Version 3.1, *Remote Sensing*, *11*(11), 1323, doi:10.3390/rs11111323, 2019.

Skulachev, V. P., An Electric Concept of Life: The Essence of Mitochondrial Function, *Membrane and Cell Biology*, *12*, 305–324, 1999.

Slangen, A., J. Church, C. Agosta, X. Fettweis, B. Marzeion, and K. Richter, Anthropogenic forcing dominates global mean sea-level rise since 1970, *Nature Climate Change*, *6*, 701–705, doi:10.1038/nclimate2991, 2016.

Slattery, G., and S. Holland, Trump tells world leaders their countries are 'going to hell' in combative un speech, *Reuters*, accessed: 2025-09-25, 2025.

Smil, V., *The Bad Earth: Environmental Degradation in China*, M. E. Sharpe, one of the earliest Western analyses of China's growing pollution crisis. Covers industrial waste, deforestation, and soil degradation., 1984.

Smil, V., *Harvesting the Biosphere: What We Have Taken from Nature*, 32–35 pp., MIT Press, table 2.3 gives average human metabolic rate of 175 W for moderate activity., 2013.

Smil, V., How the World Really Works: The Science of Energy and Civilization, *Nature Energy*, *2*, 1–12, doi:10.1038/nenergy.2017.34, breaks down global energy consumption, conversion, and waste heat., 2017.

Smith, B. E., H. A. Fricker, A. S. Gardner, and et al., Pervasive ice sheet mass loss reflects competing ocean and atmosphere processes, *Proceedings of the National Academy of Sciences*, *117*(22), 12,156–12,163, doi:10.1073/pnas.1912905117, 2020.

Smith, P., et al., Biophysical and economic limits to negative CO_2 emissions, *Nature Climate Change*, *6*, 42–50, doi:10.1038/nclimate2870, 2016.

Smith, W., and G. Wagner, Stratospheric aerosol injection tactics and costs in the 2020s, *Environmental Research Letters*, *15*(10), 104,063, doi:10.1088/1748-9326/aba7b3, 2020.

Snyder, C. W., Evolution of global temperature over the past two million years, *Nature*, *538*, 226–228, doi:10.1038/nature19798, 2016.

Solomon, L., *The Deniers: The World-Renowned Scientists Who Stood Up Against Global Warming Hysteria, Political Persecution, and Fraud... and Those Who Are Too Fearful to Do So*, Richard Vigilante Books, 2008.

Solomon, S., Stratospheric ozone depletion: A review of concepts and history, *Reviews of Geophysics*, *37*(3), 275–316, doi:10.1029/1999RG900008, 1999.

Song, L., N. Banerjee, and D. Hasemyer, Exxon Confirmed Global Warming Consensus in 1982 with In-House Climate Models, 2015.

Spanish Crown, Laws of the Indies (Environmental and Urban Planning Provisions), Spanish Crown, Spain, 1573.

Speight, J. G., *The Chemistry and Technology of Petroleum*, 4th ed., CRC Press, Boca Raton, FL, USA, includes historical accounts of the use of natural oil and gas seeps in ancient civilizations., 2007.

Stanford, J. D., R. Hemingway, E. J. Rohling, P. G. Challenor, M. Medina-Elizalde, and A. J. Lester, Timing of Meltwater Pulse 1A and climate responses to meltwater injections, *Paleoceanography*, *21*, PA4103, doi:10.1029/2006PA001340, 2006.

Stanway, D., Chinese alchemy: Cheap fuel powers coal-to-gas and chemicals boom, *Reuters*, accessed 2025-12-04, 2025.

Stefels, J., M. Steinke, M. D. Keller, and et al., Environmental constraints on the production and removal of the climatically active gas dimethylsulphide (dms) and implications for ecosystem modelling, *Biogeochemistry*, *83*, 245–275, doi:10.1007/s10533-007-9091-5, 2007.

Steffen, W., et al., Planetary Boundaries: Guiding Human Development on a Changing Planet, *Science*, *347*(6223), 1259,855, doi:10.1126/science.1259855, 2015.

Steil, B., *The Battle of Bretton Woods: John Maynard Keynes, Harry Dexter White, and the Making of a New World Order*, Princeton University Press, Princeton, a detailed account of the Bretton Woods Conference and its major figures., 2013.

Stenni, B., V. Masson-Delmotte, S. Rohrbeck, et al., The expression of the bipolar seesaw in Antarctica during the last deglaciation, *Nature Geoscience*, *4*, 46–49, doi:10.1038/ngeo1026, 2011.

Stephanson, A., *Manifest Destiny: American Expansion and the Empire of Right*, Hill and Wang, New York, 1995.

Stocker, T. F., et al., *Climate Change 2013: The Physical Science Basis. Contribution of Working Group I to the Fifth Assessment Report of the Intergovernmental Panel on Climate Change*, 1–1535 pp., Cambridge University Press, Cambridge, United Kingdom and New York, NY, USA, doi:10.1017/CBO9781107415324, 2013.

Stommel, H., Thermohaline convection with two stable regimes of flow, *Tellus*, *13*(2), 224–230, doi:10.3402/tellusa.v13i2.9491, 1961.

Stomp, M., J. Huisman, L. J. Stal, and H. C. P. Matthijs, Colorful niches of phototrophic microorganisms shaped by vibrations of the water molecule, *The ISME Journal*, *1*(4), 271–282, doi:10.1038/ismej.2007.59, 2007.

Strong, C., et al., Ocean fertilization: a strategic research plan for 20092015 and beyond, *Marine Policy*, *33*(3), 529541, doi:10.1016/j.marpol.2008.12.012, 2009.

Sumitomo, Investment in direct air capture technology: Partnership with global thermostat, https://www.sumitomocorp.com, accessed 2025-04-22, 2023.

Sweet, W., R. Kopp, C. Weaver, T. Obeysekera, R. Horton, E. Thieler, and C. Zervas, Global and Regional Sea Level Rise Scenarios for the United States, *Tech. Rep. NOS CO-OPS 083*, National Oceanic and Atmospheric Administration, National Ocean Service, Silver Spring, MD., 2017.

Sévellec, F., and A. V. Fedorov, Amoc sensitivity to arctic sea ice loss, *Climate Dynamics*, *49*, 3605–3619, doi:10.1007/s00382-017-3531-6, 2017.

Tagliabue, A., et al., Ocean iron fertilization may amplify climate-driven declines in tropical ocean productivity and ecosystem biomass, *Science Advances*, *9*(14), eadd6123, doi:10.1126/sciadv.add6123, 2023.

Tainter, J. A., *The Collapse of Complex Societies (New Studies in Archaeology)*, first ed., Cambrige University Press, New York & Cambridge, 1990.

Tainter, J. A., and T. W. Patzek, *Drilling Down: The Gulf Oil Debacle and Our Energy Dilemma*, Springer Verlag, New York, 2011.

Takahashi, T., et al., Climatological distributions of pH, pCO_2, total CO_2, alkalinity, and $CaCO_3$ saturation in the global surface ocean, and temporal changes at selected locations, *Marine Chemistry*, *164*, 95–125, doi:10.1016/j.marchem.2014.06.004, 2014.

Tans, P., and R. Keeling, Mauna Loa Annual CO_2 trend data, NOAA Mauna Loa/Scripps Intitute, 2023.

Texas 2036, The Heat, Our Air Conditioners, and the Grid, accessed: 2025-08-15, 2023.

The Honest Sorcerer, The Two Achilles Heels of Complex Systems: Tight Coupling and Limits to Human Comprehension, https://thehonestsorcerer.substack.com/p/the-two-achilles-heels-of-complex, accessed: 2025-05-25, 2025.

Thomson, A. M., et al., RCP4.5: a pathway for stabilization of radiative forcing by 2100, *Climatic Change*, *109*(1), 77, doi:10.1007/s10584-011-0151-4, 2011.

Thoning, K. W., P. P. Tans, and W. D. Komhyr, Atmospheric carbon dioxide at Mauna Loa Observatory: 2. Analysis of the NOAA GMCC data, 19741985, *Journal of Geophysical Research: Atmospheres*, *94*(D6), 8549–8565, doi:10.1029/JD094iD06p08549, 1989.

Tierney, J. E., J. Zhu, J. King, S. B. Malevich, G. J. Hakim, and C. J. Poulsen, Glacial cooling and climate sensitivity revisited, *Nature*, *584*, 569–573, doi:10.1038/s41586-020-2617-x, 2020.

Tilmes, S., R. Müller, and R. Salawitch, The sensitivity of polar ozone depletion to proposed geoengineering schemes, *Science*, *320*(5880), 1201–1204, doi:10.1126/science.1153966, 2008.

Timmermann, A., F.-F. Jin, and J. M. Abshagen, A nonlinear theory for El Niño bursting, *Journal of the Atmospheric Sciences*, *60*(1), 152–165, doi:10.1175/1520-0469(2003)060<0152:ANTFEN>2.0.CO;2, 2003.

Tollefson, J., Earth's hottest month: these charts show what happened in July and what comes next, *Nature*, *620*, 703–704, doi:10.1038/d41586-023-02552-2, 2023.

Tooze, A., Trouble Transitioning, *London Review of Books*, *47*(1), accessed: 2025-01-23, 2025.

Torres, R., R. Waldman, J. Mak, and R. Séférian, Global Estimation of the Eddy Kinetic Energy Dissipation From Satellite- and In-Situ-Based Observation Data, *Geophysical Research Letters*, *50*(12), e2023GL104,688, doi:10.1029/2023GL104688, 2023.

Touzé-Peiffer, L., A. Barberousse, and H. Le Treut, The Coupled Model Intercomparison Project: History, uses, and structural effects on climate research, *WIREs Climate Change*, *11*(4), e648, doi:10.1002/wcc.648, 2020.

Treaty of Guadalupe Hidalgo, Treaty of Peace, Friendship, Limits, and Settlement between the United States of America and the Mexican Republic, signed February 2, 1848. United States National Archives, Washington, D.C., 1848.

Trenberth, K. E., J. T. Fasullo, and J. Kiehl, Earth's Global Energy Budget, *Bulletin of the American Meteorological Society*, *90*(3), 311–323, doi:10.1175/2008BAMS2634.1, 2009.

Trenberth, K. E., J. T. Fasullo, and M. A. Balmaseda, Earth's Energy Imbalance, *Journal of Climate*, *27*(9), 3129–3144, doi:10.1175/JCLI-D-13-00294.1, 2014.

Trust, S., L. Saye, O. Bettis, G. Bedenham, O. Hampshire, T. M. Lenton, and J. F. Abrams, Planetary Solvency: Finding Our Balance with Nature – Global risk management for human prosperity, *Report*, Institute and Faculty of Actuaries, University of Exeter, 2025.

Tucker, G. S. L., English Pre-Industrial Population Trends, *The Economic History Review*, *16*(2), 205–218, 1963.

Turetsky, M. R., et al., Carbon release through abrupt permafrost thaw, *Nature Geoscience*, *13*(2), 138–143, doi:10.1038/s41561-019-0526-0, 2020.

Turney, C. S. M., J. R. Palmer, J. T. F. Costin, et al., Early last interglacial ocean warming drove substantial ice mass loss from antarctica, *Nature*, *583*, 559–564, doi:10.1038/s41586-020-2484-5, 2020.

Tziperman, E., L. Stone, M. A. Cane, and S. Jarosh, El niño chaos: Overlapping of resonances between the seasonal cycle and the pacific oceanatmosphere oscillator, *Science*, *264*(5155), 72–74, doi:10.1126/science.264.5155.72, 1995.

Tziperman, E., M. E. Raymo, P. Huybers, and C. Wunsch, Consequences of pacing the Pleistocene 100 kyr ice ages by nonlinear phase locking to Milankovitch forcing, *Paleoceanography*, *21*(4), PA4206, doi:10.1029/2005PA001241, 2006.

UK Parliament AA, Alkali Act of 1863, United Kingdom Parliament, 1863.

UK Parliament CAA, Clean Air Act 1956, United Kingdom Parliament, 1956.

UK Parliament CAA, Clean Air Act 1993, UK Public General Acts, c. 11, 1993.

UK Parliament CPA, Control of Pollution Act 1974, UK Public General Acts, c. 40, 1974.

UK Parliament EPA, Environmental Protection Act 1990, UK Public General Acts, c. 43, 1990.

UK Parliament RP, Rivers Pollution Prevention Act, United Kingdom Parliament, one of the first laws to regulate industrial water pollution in the UK., 1876.

UNESCO/IOC, GLOSS Program Summary 2022, https://www.gloss-sealevel.org, 2022.

UNFCCC, United Nations Framework Convention on Climate Change (UNFCCC): The Paris Agreement, Adopted at COP 21, Paris, France, 2015.

United Nations, The 17 Goals | Sustainable Development Goals, https://sdgs.un.org/goals, accessed: 2025-09-01, 2024.

United Nations Environment Programme Finance Initiative, Net-Zero Banking Alliance (NZBA), accessed: 2025-04-14, 2021.

United Nations General Assembly, Transforming Our World: The 2030 Agenda for Sustainable Development, https://sdgs.un.org/2030agenda, resolution A/RES/70/1 adopted on 25 September 2015, 2015.

U.S. EPA, Ferrous Sulfate Supply Chain Profile, *Tech. rep.*, EPA, public report, freely available, 2022a.

U.S. EPA, Climate change indicators: Heat waves, heat-wave frequency and intensity rising across U.S. West regions, 2022b.

USGS, USGS Water Data for the Nation, https://waterdata.usgs.gov, 2023.

USGS, and NASA, Landsat Program, Joint NASA-USGS satellite program, landsat thermal sensors provide long-term records of land surface temperature and urban heat islands., 1972.

USGS, National Minerals Information Center, Historical Global Statistics for Mineral and Material Commodities, https://www.usgs.gov/centers/national-minerals-information-center/historical-global-statistics-mineral-and-material, 2025a.

USGS, National Minerals Information Center, Mineral Commodity Summaries 2025, https://www.usgs.gov/centers/national-minerals-information-center/mineral-commodity-summaries, 2025b.

van Westen, R. M., M. Kliphuis, and H. A. Dijkstra, Physics-based early warning signal shows that amoc is on tipping course, *Science Advances*, *10*(6), eadk1189, doi:10.1126/sciadv.adk1189, 2024.

Vaughan, A., Part of a Vital Antarctic Glacier Has Unexpectedly Stopped Thinning, *New Scientist*, 2019.

Velicogna, I., Increasing rates of ice mass loss from the Greenland and Antarctic ice sheets revealed by GRACE, *Geophysical Research Letters*, *36*(19), L19,503, doi:10.1029/2009GL040222, 2009.

Verhulst, P. F., Notice sur la loi que la population suit dans son accroissement, *Corr. Math. et Phys. publ. par A. Quetelet, T. X. (also numbered T. II of the third series)*, 113–121, 1838.

Verma, S., G. Novati, and P. Koumoutsakos, Efficient collective swimming by harnessing vortices through deep reinforcement learning, *Proceedings of the National Academy of Sciences*, *115*(23), 5849–5854, doi:10.1073/pnas.1800923115, 2018.

Vig, N. J., and M. E. Kraft, *Environmental Policy: New Directions for the Twenty-First Century*, CQ Press, 2018.

Villarini, G., and G. A. Vecchi, North atlantic power dissipation index (pdi) and accumulated cyclone energy (ace): Statistical modeling and sensitivity to sea surface temperature changes, *Journal of Climate*, *25*(2), 625–638, doi:10.1175/JCLI-D-11-00146.1, 2012.

Vladi Caribbean, Caribbean Region Private Islands, private islands available in the Caribbean region, 2024.

Vladi Pacific, Pacific Ocean Private Islands Archive, archived and for-sale private islands across the Pacific region, 2024.

Voigt, A., B. Stevens, J. Bader, and T. Mauritsen, The Observed Hemispheric Symmetry in Reflected Shortwave Irradiance, *Journal of Climate*, *26*(2), 468–477, doi:10.1175/JCLI-D-12-00132.1, 2013.

Voigt, A., B. Stevens, J. Bader, and T. Mauritsen, The radiative impact of clouds on the shift of the Intertropical Convergence Zone, *Geophysical Research Letters*, *41*(12), 4308–4315, doi:10.1002/2014GL060354, 2014.

von Schuckmann, K., et al., Heat stored in the Earth system 1960–2020: where does the energy go?, *Earth System Science Data*, *15*(4), 1675–1709, doi:10.5194/essd-15-1675-2023, 2023.

Wackernagel, M., and W. Rees, *Our Ecological Footprint: Reducing Human Impact on the Earth*, New Society Publishers, Gabriola Island, BC, 1996.

Wallace, D. W. R., et al., Ocean fertilization: A scientific summary for policy makers, *IOC/UNESCO Reports and Studies*, *196*, 1–20, 2010.

Walter Anthony, K. M., et al., 21st-century modeled permafrost carbon emissions accelerated by abrupt thaw beneath lakes, *Nature Communications*, *9*(1), 3262, doi:10.1038/s41467-018-05738-9, 2018.

Wang, C., and J. Picaut, Understanding enso physics: A review, *Geophysical Monograph Series*, *147*, 21–48, doi:10.1029/147GM02, 2004.

Wang, H., et al., Atmosphere teleconnections from abatement of china aerosol emissions exacerbate northeast pacific warm blob events, *Proceedings of the National Academy of Sciences*, *121*(21), e2313797,121, doi:10.1073/pnas.2313797121, 2024.

Wassmann, P., and M. Reigstad, Future Arctic Ocean seasonal ice zones and implications for pelagicbenthic coupling, *Oceanography*, *24*, 222–231, doi:10.5670/oceanog.2011.74, 2011.

Watson, A. J., P. W. Boyd, S. M. Turner, T. D. Jickells, and P. S. Liss, Designing the next generation of ocean iron fertilization experiments, *Marine Ecology Progress Series*, *364*, 303–309, doi:10.3354/meps07552, 2008a.

Watson, A. J., et al., Ocean Fertilization: A Scientific Summary for Policy Makers, *Oceanography*, *22*(3), 36–47, doi:10.5670/oceanog.2009.67, 2008b.

Webb, R. H., *Introduction to Oceanography: Temperature*, OpenText RWU Press, chapter 6.2 states ocean surface ranges ∼30 °C, coolest ∼-2 °C., 2021.

Wehrli, C., Extraterrestrial Solar Spectrum, *Tech. Rep. Publication No. 615*, Physikalisch-Meteorologisches Observatorium and World Radiation Center, Davos Dorf, Switzerland, 1985.

Weibel, E. R., *The Pathway for Oxygen: Structure and Function in the Mammalian Respiratory System*, Harvard University Press, Cambridge, MA, 2005.

Weichenthal, S., et al., How low can you go? Air pollution affects mortality at very low levels, *Science Advances*, *8*(39), eabo3381, doi:10.1126/sciadv.abo3381, 2022.

Weihs, D., Hydromechanics of fish schooling, *Nature*, *241*(5387), 290–291, doi:10.1038/241290a0, 1973.

White, J. P., Pacific Island: *Tikopia*. The Prehistory and Ecology of a Polynesian Outlier. Patrick Vinton Kirch and D. E. Yen. Bishop Museum Press, Honolulu, 1982. xviii, 398 pp., illus. Paper, $28. Bernice P. Bishop Museum Bulletin 238., *Science*, *220*(4599), 836–837, doi:10.1126/science.220.4599.836, 1983.

White, R., Failure to communicate: Geoengineering could be crucial in the fight against climate change, *Science*, *388*(6742), doi:10.1126/science.z0g6jc4, 2025.

Whittaker, R. H., and G. E. Likens, *Carbon in the Biota*, 281–302 pp., U.S. Atomic Energy Commission, CONF-720510, Washington, D.C., 1973.

Wikipedia, List of Earth Observation Satellites, accessed April 16, 2025, n.d.

Wild, M., Global dimming and brightening: A review, *Journal of Geophysical Research: Atmospheres*, *114*, D00D16, doi:10.1029/2008JD011470, 2009.

Wild, M., Enlightening Global Dimming and Brightening, *Bulletin of the American Meteorological Society*, *93*(1), 27–37, doi:10.1175/BAMS-D-11-00074.1, 2012.

Wild, M., D. Folini, M. Z. Hakuba, C. Schär, S. I. Seneviratne, S. Kato, D. Rutan, and C. Ammann, The Energy Balance Over Land and Oceans: An Assessment Based on Direct Observations and CMIP5 Climate Models, *Climate Dynamics*, *40*, 3107–3134, doi:10.1007/s00382-012-1569-2, 2013.

Wilkinson, R., M. Mleczko, B. Brewin, K. Gaston, M. Mueller, J. Shutler, X. Yan, and K. Anderson, Environmental impacts of earth observation data in the constellation and cloud computing era, *Science of The Total Environment*, *909*, 168,584, doi:10.1016/j.scitotenv.2023.168584, 2023.

Williams, M., *Deforesting the Earth – From Prehistory to Global Crisis*, The University of Chicago Press, Chicago, 2003.

Wingham, D. J. e. a., CryoSat: A mission to determine the fluctuations in Earth's land and marine ice fields, *Advances in Space Research*, 2006.

Witze, A., Geologists reject the Anthropocene as Earth's new epoch – after 15 years of debate, *Nature*, *627*(8002), 240–250, doi:10.1038/s10.1038/d41586-024-00675-8, 2024.

World Bank, and OWID, GDP per capita World Bank In constant 2017 international $ [dataset], retrieved January 19, 2025, 2023.

World Meteorological Organization, Global Observing System Status Report 2023, https://public.wmo.int/en, 2023.

Wright, R., *A Short History of Progress*, Carroll and Graf Publishers, New York, 2005.

Wrigley, E. A., *Opening Pandora's Box: A New Look at the Industrial Revolution*, Cambridge University Press, Cambridge, UK, 2016.

Wrigley, E. A., and R. S. Schofield, *The Population History of England 1541-1871: A reconstruction*, Cambridge Studies in Population, Economy and Society in Past Time, Cambridge University Press, 1989.

Yang, W., T. Ahrens, and G. Chen, Shock Vaporization of Anhydrite and Calcite and the Effect on Global Climate from K/T Impact Crater at Chicxulub, in *Lunar and Planetary Science Conference*, *Lunar and Planetary Science Conference*, vol. 27, p. 1473, provided by the SAO/NASA Astrophysics Data System, 1996.

Yokota, T. e. a., Global concentrations of CO_2 and CH_4 retrieved from GOSAT: First results, *SOLAE*, 2009.

Yoon, J.-E., et al., Reviews and syntheses: Ocean iron fertilization experiments – past, present, and future looking to a future Korean Iron Fertilization Experiment in the Southern Ocean (KIFES) project, *Biogeosciences*, *15*(19), 5847–5889, doi:10.5194/bg-15-5847-2018, 2018.

Yoshioka, M., D. P. Grosvenor, B. B. B. Booth, C. P. Morice, and K. S. Carslaw, Warming effects of reduced sulfur emissions from shipping, *Atmospheric Chemistry and Physics*, *24*, 13,681–13,692, doi:10.5194/acp-24-13681-2024, 2024.

Zachos, J., M. Pagani, L. Sloan, E. Thomas, and K. Billups, Trends, rhythms, and aberrations in global climate 65 ma to present, *Science*, *292*(5517), 686–693, doi:10.1126/science.1059412, 2001.

Zeebe, R. E., and A. Ridgwell, Past Changes of Ocean Carbonate Chemistry Due to Natural and Anthropogenic CO_2, *Geochimica et Cosmochimica Acta*, *75*(23), 6353–6384, doi:10.1016/j.gca.2011.07.023, 2011.

Zeebe, R. E., A. Ridgwell, and J. C. Zachos, Anthropogenic carbon release rate unprecedented during the past 66 million years, *Nature Geoscience*, *9*(4), 325–329, doi:10.1038/ngeo2681, 2016.

Zekollari, H., et al., Glacier preservation doubled by limiting warming to 1.5°C versus 2.7°C, *Science*, *388*(6750), 979–983, doi:10.1126/science.adu4675, 2025.

Zhang, S., et al., Substantially underestimated winter CO_2 sources of the Southern Ocean, *Science Advances*, *11*(45), eaea0024, doi:10.1126/sciadv.aea0024, 2025a.

Zhang, T., W. Wang, and B. An, Glacial Lake Survey with Supplementary Geospatial Layers, Data combined from: Glacial lake survey (Zhang, Wang & An); OpenStreetMap roads and administrative boundaries; Landsat and Copernicus satellite imagery, includes Landsat (USGS/NASA) and Copernicus Sentinel data (ESA)., 2025b.

Zhang, X., et al., Lewy body dementia promotion by air pollutants, *Science*, *389*(6764), eadu4132, doi:10.1126/science.adu4132, 2025c.

Zhang, Y., S. Li, R. Ding, et al., Collective Movement of Schooling Fish Reduces the Costs of Locomotion in Turbulent Conditions, *PLOS Biology*, *22*(6), e3002,501, doi:10.1371/journal.pbio.3002501, 2024.

Zhu, X., C. Ma, W. Chen, and E. G. Hertwich, Tracing fossil-based plastics, chemicals and fertilizers in China, *Nature Communications*, *15*(1), 47,930, doi:10.1038/s41467-024-47930-0, 2024.

Zickfeld, K., M. Eby, H. D. Matthews, and A. J. Weaver, Setting cumulative emissions targets to reduce the risk of dangerous climate change, *Proceedings of the National Academy of Sciences*, *106*(38), 16,129–16,134, doi:10.1073/pnas.0805800106, 2009.

Zou, Y., Y. Wang, Y. Qian, H. Tian, J. Yang, and E. Alvarado, Using CESM-RESFire to understand climate–fire–ecosystem interactions and the implications for decadal climate variability, *Atmospheric Chemistry and Physics*, *20*(2), 995–1020, doi:10.5194/acp-20-995-2020, 2020.

Zwally, H. J., B. E. Schutz, W. Abdalati, et al., ICESat's laser measurements of polar ice, atmosphere, ocean, and land, *Journal of Geodynamics*, *34*(3–4), 405–445, doi:10.1016/S0264-3707(02)00042-X, 2002.